ESRF
The European Synchrotron

ESRF-EBS
Extremely Brilliant Source

# EBS Storage Ring Technical Report


# Table of contents

## Introduction

The general design of the ESRF's Extremely Brilliant Source project was published as the 'Orange Book' in 2016, following the approval of the project (available at the following link: http://www.esrf.eu/Apache_files/Upgrade/ESRF-orange-book.pdf). Since publishing the Orange Book, a lot of design details have been modified and finalized.

In order to have a document describe as much as possible the real new machine, it was decided to update the Orange Book and write a ***"EBS Storage Ring Technical Report".*** The emphasis of this report is to give the detailed specifications of the new storage ring and therefore the focus is on figures and tables. The parameters of the existing and the new storage ring are presented in Table 1, Table 2 gives the parameters of the source point from the middle of the straight section (insertion devices) and the bending magnet.

Table 1: Parameters for the existing (ESRF) and the upgrade storage ring (ESRF-EBS)

| Storage Ring Parameters | |
|---|---|
| | ESRF-EBS |
| Energy [GeV] | 6 |
| Circumference [m] | 843.977 |
| Beam current [mA] | 200 |
| Natural emittance [pmrad] | 132 |
| Damping time (H/V/L0 [ms] | 8.8/13/9.1 |
| Bunch length [mm] | 2.91 |
| Energy spread | 9.30E-04 |
| Eloss/turn [MeV] | 2.52 |
| RF voltage [MV] | 6 |
| Synchrotron frequency [kHz] | 1.3 |
| Momentum compaction | 8.50E-05 |
| Tunes (H/V) | 76.21/27.34 |
| Natural chromaticity | -109/-82 |
| Operation chromat. (H/V) | 6/4 |
| Oper. Emittance (H/V) [pmrad] | 110/5 |
| Multibunch lifetime [h] | 19.3 |
| 16-bunch lifetime [h] | 1.8 |
| 4-bunch lifetime [h] | 1.2 |

Table 2: Beam parameters at the insertion device and bending magnet source point for the existing (ESRF) and the upgrade of storage ring (ESRF-EBS)

| ID Source Point | |
|---|---|
| | ESRF-EBS |
| Horizont. beam size [µm] | 30.2 |
| Horiz. beam diverg. [µrad] | 4.37 |
| Vertical beam size [µm] | 3.64 |
| Vertic. beam diverg. [µrad] | 1.37 |

| BM Source Point | |
|---|---|
| | ESRF-EBS |
| Horizont. beam size [µm] | 23 |
| Horiz. beam diverg. [µrad] | 24 |
| Vertical beam size [µm] | 3.6 |
| Vertic. beam diverg. [µrad] | 3.1 |

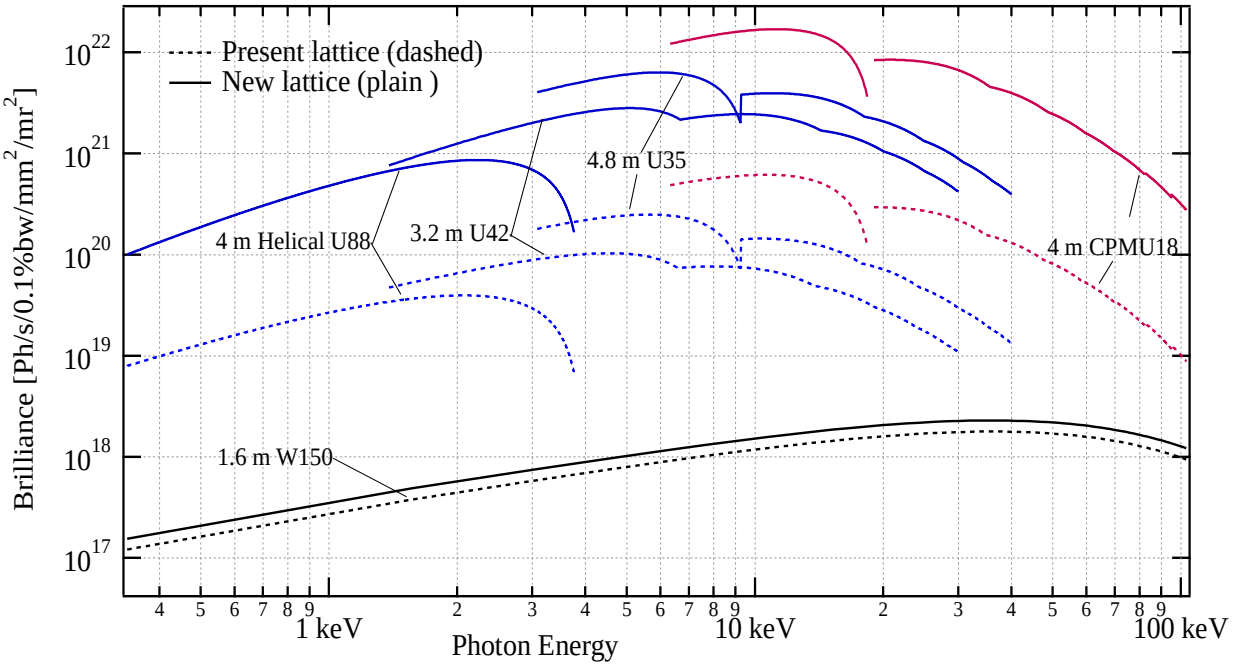


Figure 1: Brilliances presently achieved with typical ID sources in the present lattice (dashed) and with the ESRF-EBS (plain)

With the application of the new HMBA lattice (developed at the ESRF), the emittance can be reduced by a factor of roughly 36 and increasing the brilliance by roughly 2 orders of magnitude (see Figure 1) and the coherence of the emitted light by a factor of 20. This opens the area for a lot of new applications and science

The HMBA lattice will also be used for the upgrade of most of the new and existing light sources.

This Technical Design Report was written in parallel to the planning, procurement, manufacturing, and other aspects of the project, hence it was additional work for the members of the EBS team. As such it is to be considered an internal, working document until such time as it is officially published.

Many thanks to the work package leaders and their teams for their contributions to the contents of this **"EBS Storage Ring Technical Design Report"**:

**Beam Dynamics:** Laurent Farvacque

**Magnet System:** Gael Le Bec

**Accelerator Engineering:** Jean-Claude Biasci

**Power Supplies and Electrical Engineering:** Jean-Francois Bouteille

**Radio Frequency System:** Jörn Jacob

**Control System:** Jean-Michel Chaize

**Diagnostics:** Kees Scheidt

**Photon Sources:** Joel Chavanne

**Booster and Storage Ring Injection:** Thomas Perron and Simon White

**Vacuum System:** Michael Hahn

**Alignment:** David Martin

The activities of the planning, assembling, dismantling, installation, building and infrastructure are not described in this report.

**Pantaleo Raimondi**
**Director of ASD-Division**

**Dieter Einfeld,**
**Editor.**

# 1 Beam Dynamics

## 1.1 Cell design

The equilibrium emittance of an electron storage ring can be minimised by increasing the number of bending magnets. While most of the present lattices are based on two or three bending magnets per cell, recent projects have focused on six or seven bending magnets per cell. The number of bending magnets is limited by the space needed to accommodate the quadrupoles that provide the necessary focusing between the dipoles.

However, applying this scheme to large storage rings leads to very small bending angles, and so to a very small maximum dispersion function. As a consequence, the chromaticity correction needs very strong sextupoles. Apart from problems in magnet technology, this makes it difficult to achieve a large dynamic aperture, needed for efficient injection and acceptable beam lifetime.

To mitigate these difficulties, the new lattice is based on a variation of the standard multi-bend achromat: instead of distributing the seven dipoles equally along the arc, more space is left between dipoles 1 and 2, and 6 and 7. In this space, the beta-functions and dispersion are allowed to grow to high values, which makes the

sextupoles more efficient. This layout is referred to as the hybrid multi-bend achromat lattice.

In the central part four high-gradient horizontally-focusing quadrupoles and three high- gradient bending magnets which also provide vertical focusing are placed alternately. At each end of the cell, two dipoles encompass the regions with large beta-functions and dispersion. Their longitudinally varying bending field helps to reduce the emittance and to increase the dispersion. The lattice has been optimised to achieve the minimum emittance with the following constraints:

The straight section must be long enough to accommodate the present low-gap, 5 m-long insertion device vacuum chamber, which leaves 5.30 m between BPMs.

The quadrupole strengths must be compatible with state of the art magnet design and vacuum chamber requirements. The lattice comprises 30 identical standard cells and two special cells that provide a special straight section for injection. The optical functions are the same in all standard straight sections, thus disposing of the alternating high and low-beta straight sections found in the present lattice.

The insertion device source points will be kept the same as in the present lattice, this implies a reduction of the ring circumference by 413 mm and a corresponding increase of the RF frequency by 172 kHz.

The natural equilibrium emittance is 132 pm and the target vertical emittance is 5 pm, corresponding to a coupling value of 3.9%. With a set of insertion devices giving an energy loss of 0.5 MeV, which is the present average value, the operation emittance values are 110 pm in horizontal and 5 pm in vertical.

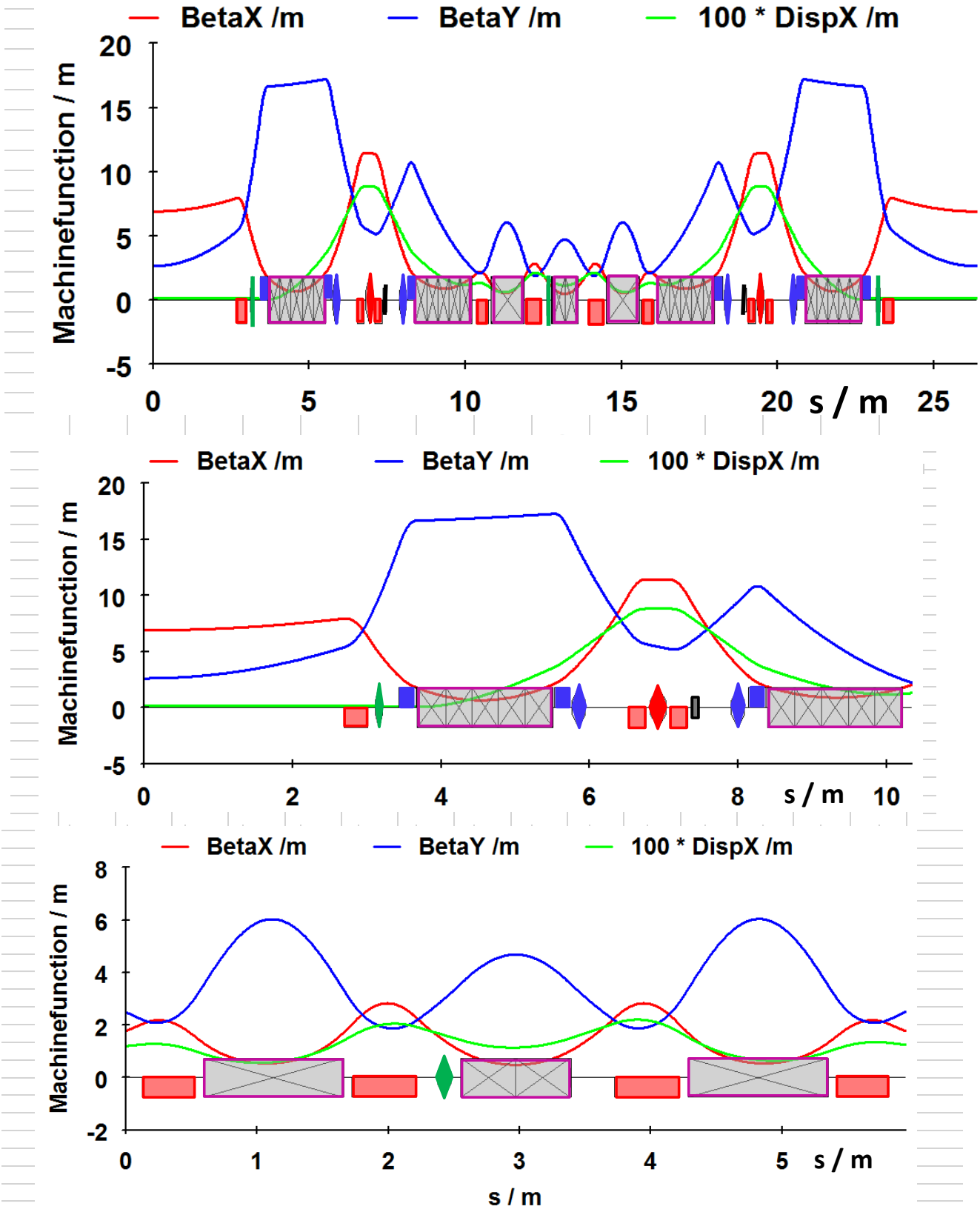


Figure 1.1: Machine functions of the standard cell (above). In more detail the first part (middle) and the middle part (below).

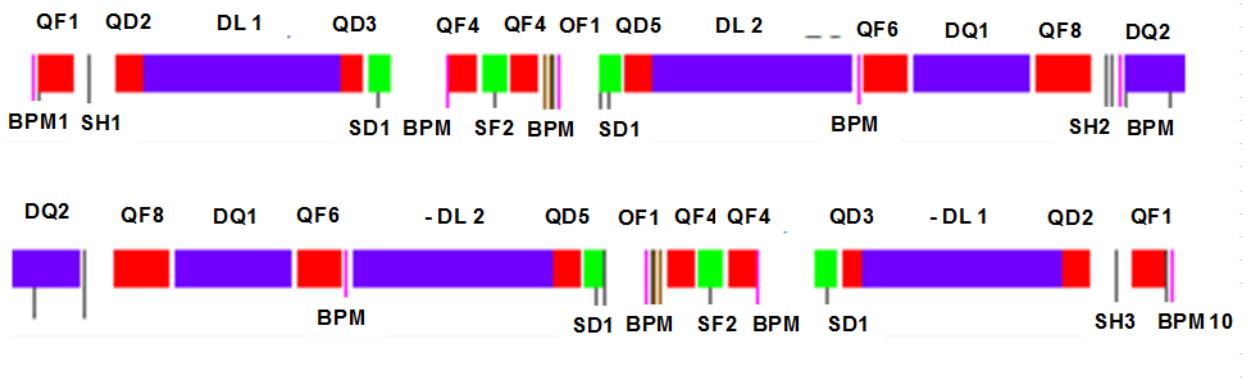


Figure 1.2: Distribution of magnets and BPMs in the standard cell.

The nominal tunes are set to 76.21 / 27.34.

Table 1.1. shows the corresponding quadrupole settings.

Table 1.1: Parameters of the quadrupole families.

| | $L_{iron}$ [m] | $l_{mag}$ [m] | K [$m^{-2}$] | K.l [$m^{-1}$] | G [T/m] | G.l [T] | I [A] |
|---|---|---|---|---|---|---|---|
| **QF1** | 0.295 | 0.31204 | 2.538262 | 0.792047 | 50.8004 | 15.8519 | 86.751 |
| **QD2** | 0.212 | 0.22796 | -2.668802 | -0.608385 | -53.4130 | -12.1761 | -93.642 |
| **QD3** | 0.162 | 0.17891 | -2.400415 | -0.429448 | -48.0415 | -8.5949 | -82.371 |
| **QF4** | 0.212 | 0.22873 | 2.418855 | 0.553276 | 48.4106 | 11.0732 | 82.320 |
| **QD5** | 0.212 | 0.22785 | -2.702544 | -0.615780 | -54.0883 | -12.3241 | -95.650 |
| **QF6** | 0.388 | 0.39709 | 4.482166 | 1.779816 | 89.7054 | 35.6210 | 97.696 |
| **DQ1** | 1.028 | 1.04999 | -1.829095 | -1.920528 | -36.6072 | -38.4372 | -87.041 |
| **QF8** | 0.484 | 0.49216 | 4.429800 | 2.180149 | 88.6573 | 43.6332 | 93.914 |
| **DQ2** | 0.800 | 0.82335 | -1.532351 | -1.261665 | -30.6682 | -25.2508 | -91.225 |

## 1.2 Beam stay-clear

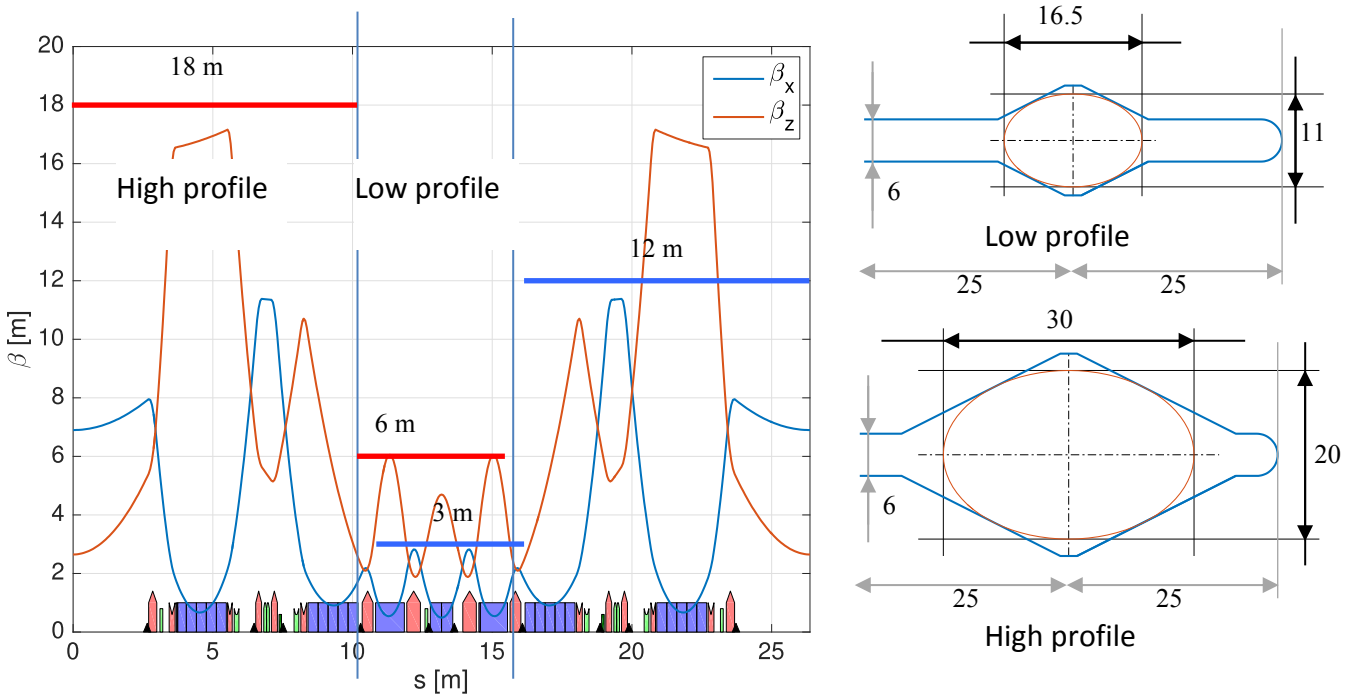


Figure 1.3: Beam stay-clear.

Three regions have been considered for specifying the beam stay-clear: the end regions where the β-values are large, and the central region with low-β.

## 1.3 Non-linear dynamics

The three sextupole families and the octupole family are tuned using a multi-objective genetic algorithm (NSGA II). The optimization target is a combination of dynamic aperture and Touschek lifetime, computed on 10 different error seeds. Tune shifts for the nominal tunes 76.21 / 27.34 and for chromaticities of 6/4 are shown on Figure **1.4** and Figure **1.5**.

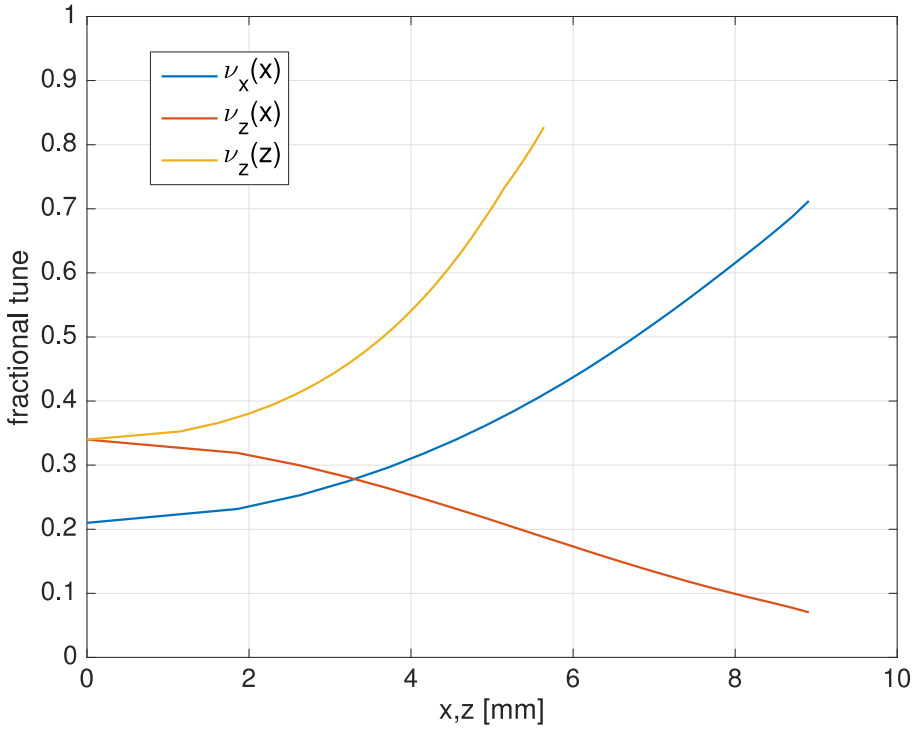


**Figure 1.4: Tune shifts with amplitude.**

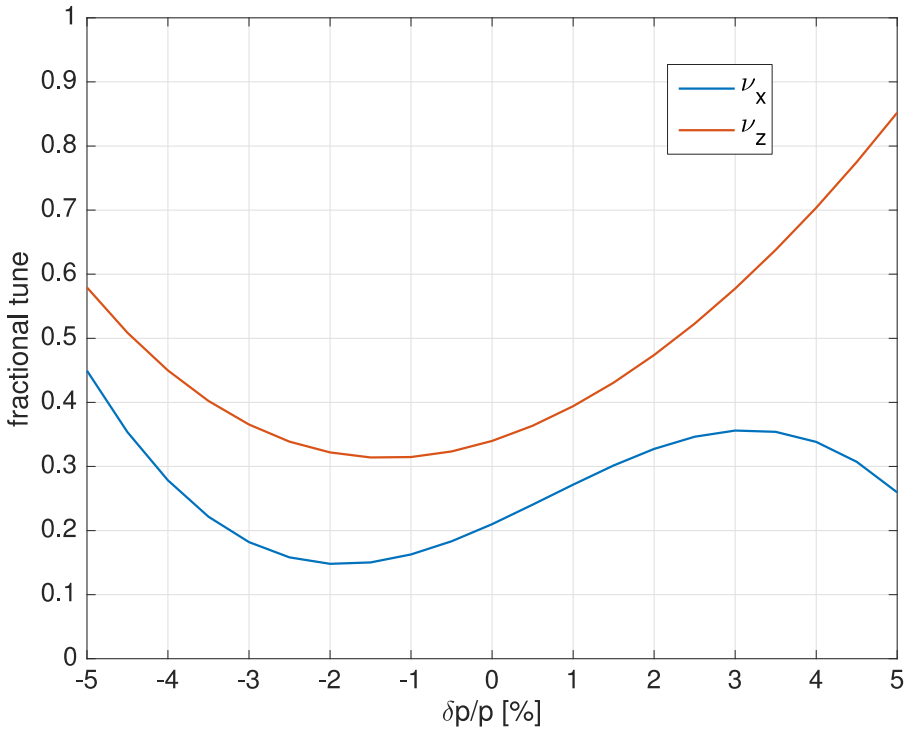


**Figure 1.5: Tune shift with momentum.**

## 1.4 Dynamic aperture

The dynamic aperture at the injection point (see Figure 1.6) is computed in three different conditions: a perfect machine with no errors and no longitudinal motion, the same machine with longitudinal motion (6-D tracking) and finally with all errors and corrections (10 samples). The acceptance reduction with longitudinal motion comes from the path lengthening appearing at large transverse amplitudes.

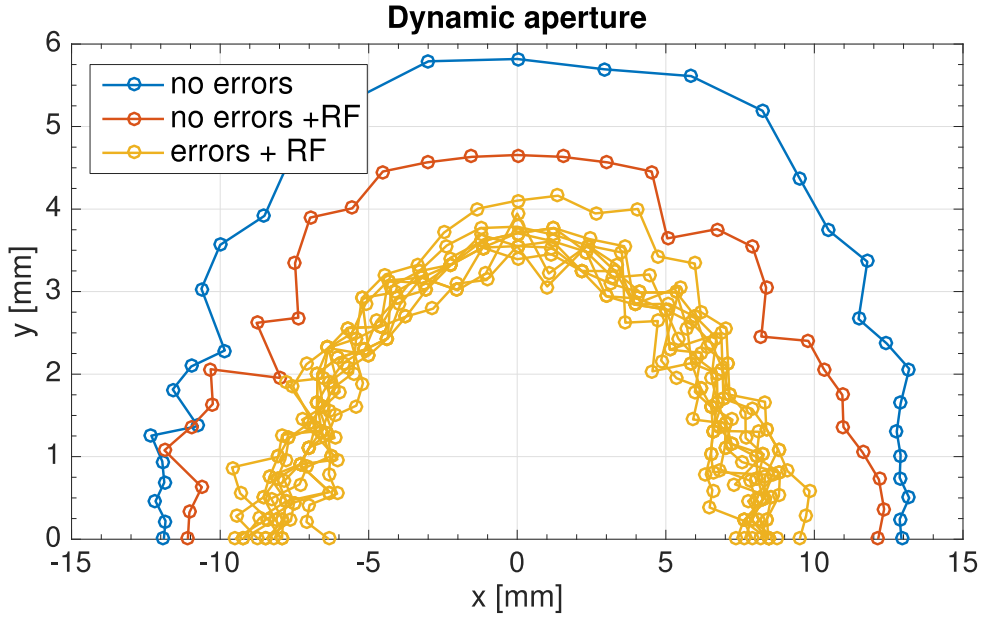


Figure 1.6: Dynamic aperture at the injection point.

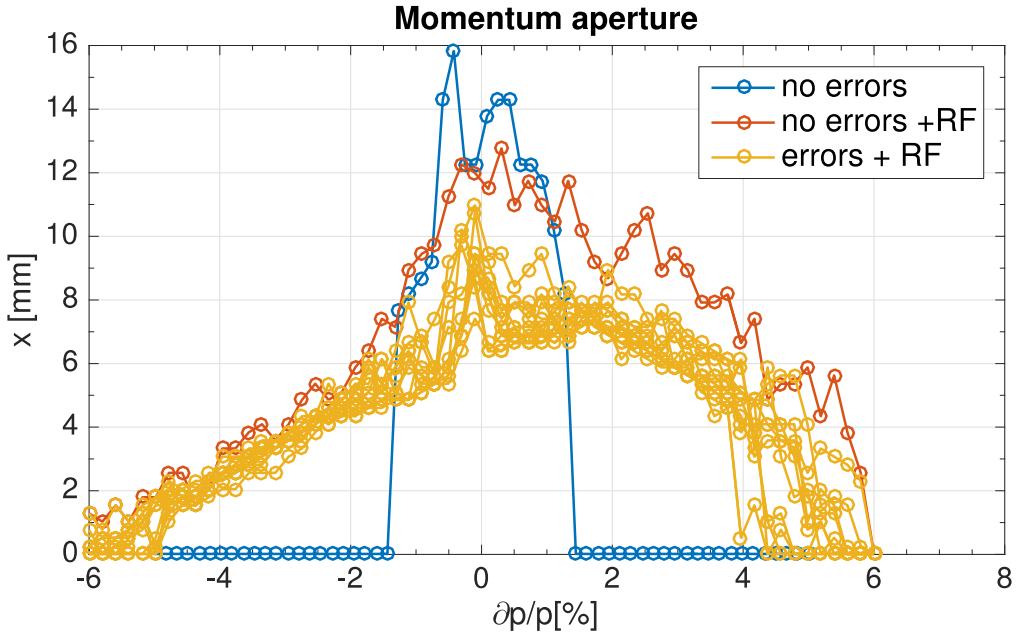


Figure 1.7: Momentum aperture.

On the injection side (x<0), the aperture reaches -8.2 ± 0.4 mm.

The chromaticities can be tuned between 0/0 and 15/15 or more. The corresponding sextupole settings are listed below.

**Table 1.2: Parameters of the sextupole families.**

### Chromaticity (X/Y): 6/4

| | $L_{iron}$ [m] | $l_{mag}$ [m] | H [$m^{-3}$] | H.l [$m^{-2}$] | B'' [$T/m^2$] | B''.l [T/m] | I [A] |
|---|---|---|---|---|---|---|---|
| **SD1A** | 0.166 | 0.17870 | -79.5333 | -14.2126 | -3183.80 | -568.898 | 56.791 |
| **SF2A** | 0.200 | 0.21283 | 77.4146 | 16.4765 | 3099.00 | 659.516 | 55.167 |
| **SD1B** | 0.166 | 0.17885 | -74.7334 | -13.3658 | -2991.67 | -535.002 | 53.215 |

### Chromaticity (X/Y): 10/10

| | $L_{iron}$ [m] | $l_{mag}$ [m] | H [$m^{-3}$] | H.l [$m^{-2}$] | B'' [$T/m^2$] | B''.l [T/m] | I [A] |
|---|---|---|---|---|---|---|---|
| **SD1A** | 0.166 | -0.17857 | -83.8548 | -14.9738 | -3356.51 | -599.367 | 60.007 |
| **SF2A** | 0.200 | 0.21273 | 80.6850 | 17.1642 | 3229.84 | 687.043 | 57.580 |
| **SD1B** | 0.166 | -0.17871 | -79.3217 | -14.1753 | -3175.34 | -567.405 | 56.634 |

### Chromaticity (X/Y): 15/15

| | $L_{iron}$ [m] | $l_{mag}$ [m] | H [$m^{-3}$] | H.l [$m^{-2}$] | B'' [$T/m^2$] | B''.l [T/m] | I [A] |
|---|---|---|---|---|---|---|---|
| **SD1A** | 0.166 | -0.17832 | -89.5788 | -15.9735 | -3585.95 | -639.384 | 65.027 |
| **SF2A** | 0.200 | 0.21262 | 84.1796 | 17.8980 | 3369.54 | 716.416 | 60.177 |
| **SD1B** | 0.166 | -0.17866 | -80.9550 | -14.4632 | -3240.65 | -578.927 | 57.849 |

## 1.5 Path lengthening with amplitude

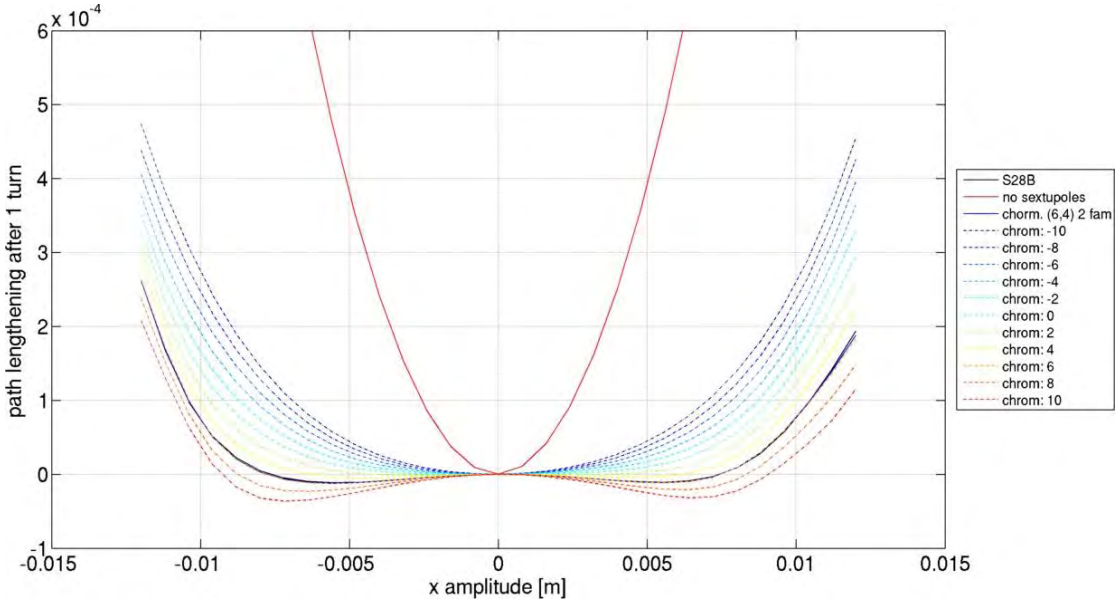


**Figure 1.8: Path lengthening with amplitude for different horizontal chromaticities.**

The path length at large horizontal amplitude is longer that nominal. So a particle thrown on energy at large amplitude (injected beam, horizontal kick) will start a longitudinal oscillation. This explains the reduction of dynamic aperture with RF on. This lengthening depends on the sextupole tuning and may explain that a better lifetime is obtained for positive chromaticity.

## 1.6 Beam losses and collimation

Two sets of horizontal collimators are located upstream the DL1E dipole (last DL dipole of the cell) in cells 13 and 24. Their aperture is set on a compromise between re-localization of losses and lifetime reduction, resulting in 8.4 mm internal and 7.6 mm external. The distribution of the total losses along the cell (with all cells added up) is shown on **Figure 1.9**, with and without collimators (average over 10 error seeds). With the collimators closed, 78% of Touschek losses are located on the collimators and the lifetime is reduced by 5%.

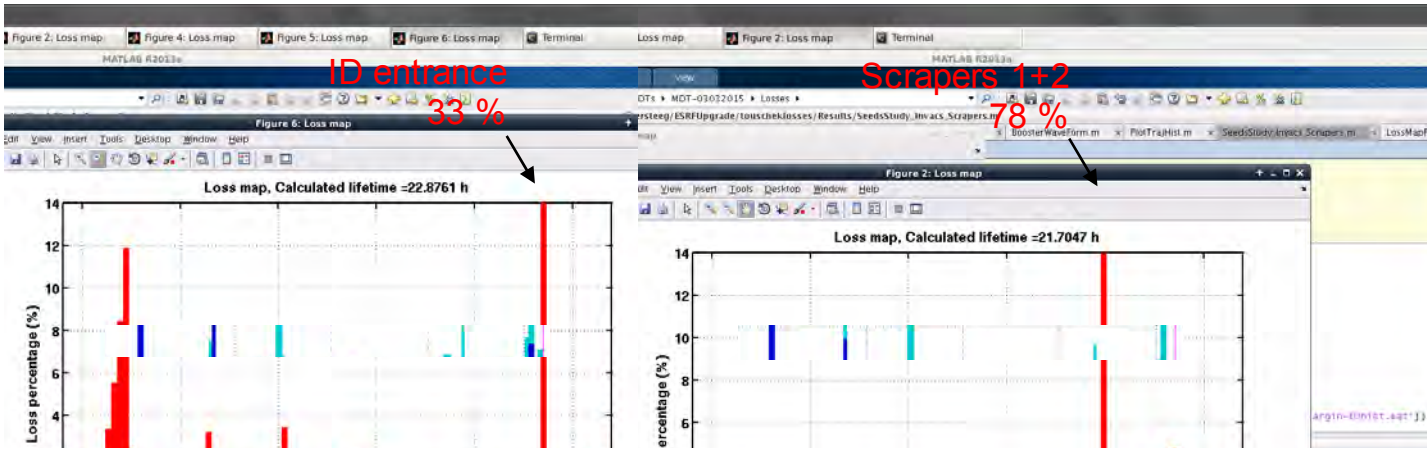


**Figure 1.9: distribution of losses with collimator (left) and without collimator (right), 32 cells superimposed.**

## 1.7 Errors and tolerances

### Correction scheme

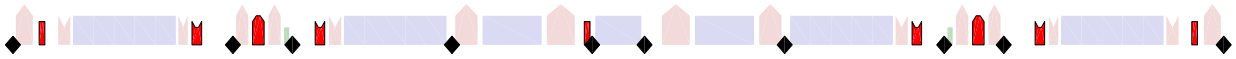

Slow corrections will be performed using:

- 10 BPMs ◆
- 9 combined function correctors (6 sextupoles + 3 dedicated magnets ) providing:
  - Horizontal orbit correction
  - Vertical orbit correction
  - Skew quadrupole
- Individually powered quadrupoles and sextupoles

The correction strategy is:

- 1st turn steering to get stored beam,
- Orbit correction using the theoretical response matrix
- Measurement of the Orbit Response Matrix (simulated at the moment)
- Computation of an error model fitting the measured ORM
- Simultaneous correction of RDTs and dispersions with quadrupoles and skew quadrupoles
- Sextupole correction with a lifetime optimizer
- Iterate

### Tolerances

In the study, the girders are positioned along the shape of the present storage ring, with an accuracy estimated by the alignment group. The tolerance values shown in Table 1.3 are therefore for the positioning of the magnets of their girder.

Table 1.3: Tolerance specifications.

| | Δx [µm] | Δz [µm] | Δs [µm] | Δψ [µrad] | ΔL/L |
|---|---|---|---|---|---|
| **Long. Varying field dipoles** | >100 | >100 | 1000 | 500 | $10^{-3}$ |
| **High gradient quadrupoles, Combined function dipoles** | 60 | 60 | 500 | 200 | $5\ 10^{-4}$ |
| **Medium gradient quads** | 100 | 85 | 500 | 500 | $5\ 10^{-4}$ |
| **Sextupoles** | 70 | 50 | 500 | 1000 | $3.5\ 10^{-3}$ |
| **Octupoles** | 100 | 100 | 500 | 1000 | $5\ 10^{-3}$ |

## 1.8 Failure of a single magnet

The consequences of the failure of a single magnet power supply have been studied in order to specify a back-up system avoiding a beam loss.

Sextupoles: Switching off a sextupole does not cause a beam loss.

Quadrupoles: The constraints are as follows:

Focusing quad : $\Delta I/I < 15\%$ to 20%

Defocusing quad: $\Delta I/I < 30\%$ to 50%

DQs: The allowed variation is 0.15%

## 1.9 Injection cell

Two special injection cells (mirror symmetry around cell 4 straight section) are necessary to reach a higher horizontal beta for injection. A 2.8 m long free space is available in the middle of the straight section for the injection elements (septum magnets).

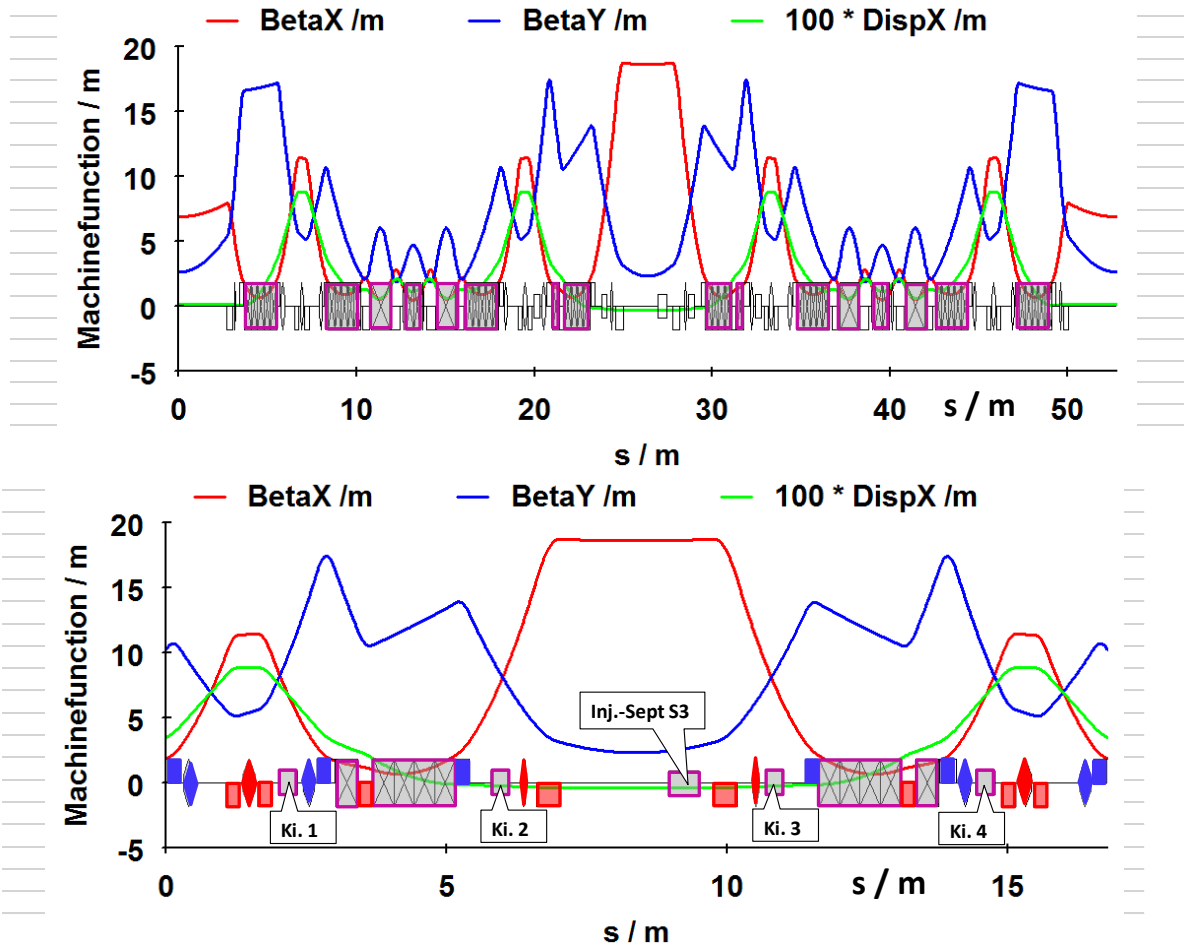


Figure 1.10: Machine functions within the injection area.

The QF1 magnets (QF1J) need a larger aperture, an additional quadrupole family (QF2J) is necessary and the QD3J magnets are longer than in standard cells. The horizontal β-value is 18.64 m

**Table 1.4: Quadrupolea settings in cells 3 and 4**

| | $L_{iron}$ [m] | $l_{mag}$ [m] | K [$m^{-2}$] | K.l [$m^{-1}$] | G [T/m] | G.l [T] | I [A] |
|---|---|---|---|---|---|---|---|
| **QF1J** | 0.370 | 0.40300 | 1.090291 | 0.439387 | 21.8209 | 8.7938 | 119.55 |
| **QD2J** | 0.212 | 0.22942 | -1.913756 | -0.439062 | -38.3016 | -8.7873 | -64.020 |
| **QF2J** | 0.212 | 0.22872 | 2.424378 | 0.554498 | 48.5211 | 11.0976 | 82.563 |
| **QD3J** | 0.295 | 0.31199 | -2.551799 | -0.796134 | -51.0713 | -15.9337 | -87.304 |
| **QF4J** | 0.212 | 0.22872 | 2.480123 | 0.567248 | 49.6368 | 11.3528 | 82.563 |

The injection efficiency depends on the booster emittance and on the tuning of the collimators. Three different operating modes are being considered for the booster:

- Present conditions

- Increase of the horizontal tune leading to a reduction of the equilibrium emittance and off-momentum operation giving a further reduction,
- Same working point as before plus going to full H/V coupling at extraction.

Table 1.4 summarises the injection tuning for each booster configuration.

Table 1.4: Injection efficiency.

| Booster setting | Present configuration | Optimized optics, off-momentum | Full H/V coupling |
|---|---|---|---|
| **Emittances H/V [pm]** | 120/5 | 60/5 | 30/30 |
| **Injected beam offset [mm]** | 6.9 | 6.0 | 5.3 |
| **Optimum β [m]** | 8.0 | 7.4 | 6.7 |
| **Efficiency without collimator** | 62% | 84% | 94% |
| **Efficiency with collimator** | 46% | 72% | 90% |

## 1.10 Impedance and collective effects

An estimate of the longitudinal impedance is given in Figure 1.11 (the contribution of collimators is still not included). Apart from the narrow-band contribution of RF cavities, the impedance is inductive up to 30 GHz. The effective impedance of 0.344 Ω is about half of the estimated value for the present storage ring.

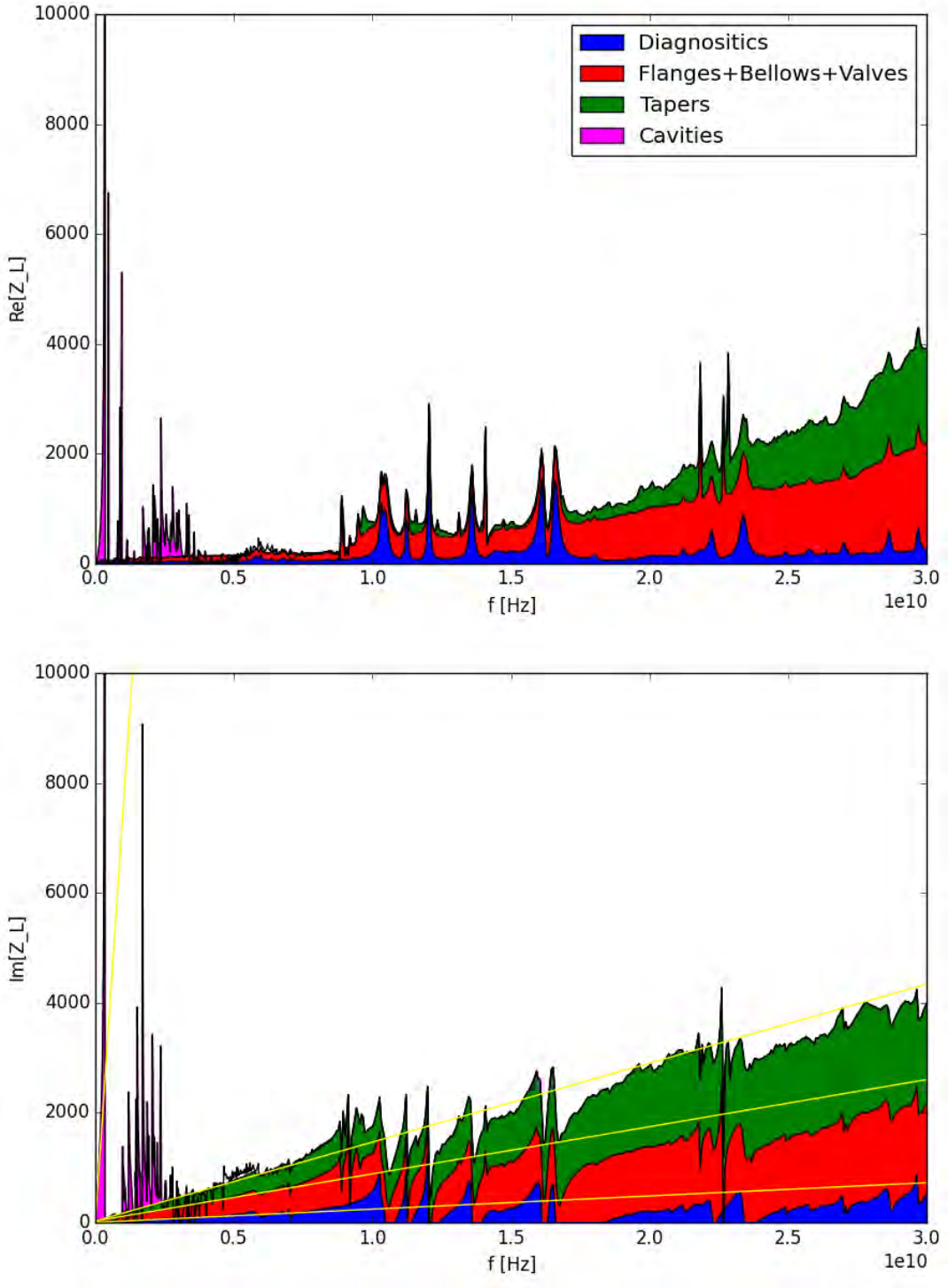


Figure 1.11: Longitudinal impedance.

Table 1.5: Longitudinal impedance budget.

| | $K_{loss}$ [V/pC] | $Z/n_{eff}$ [Ω] |
|---|---|---|
| **Diagnostics** | 4.02 | $8.4\ 10^{-3}$ |
| **Flanges+bellows** | 9.27 | $25\ 10^{-3}$ |
| **Scrapers** | ? | ? |
| **Tapers** | 3.2 | $20\ 10^{-3}$ |
| **Cavities** | 6.66 | $69\ 10^{-3}$ |
| **Resistive wall** | 38.7 | 0.222 |
| **Total** | 51.85 | 0.344 |

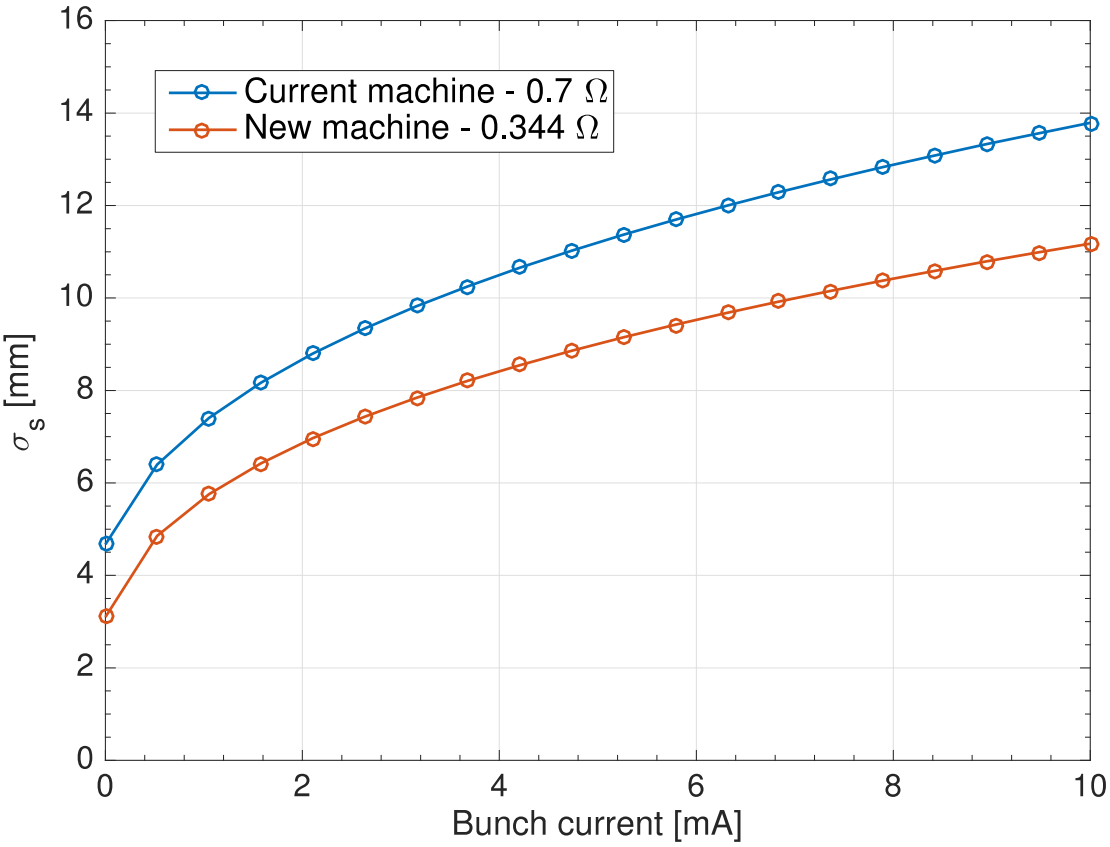


Figure 1.12: Bunch lengthening with intensity.

## 1.11 Influence of a 3rd harmonic RF cavity

For improving the Touschek lifetime, we looked at the effect of a 3rd harmonic cavity. The study was performed by tracking 100000 electrons over 10000 turns. Figure 1.12 shows the bunch length without harmonic cavity (solid lines) and with harmonic cavity (dashed lines) for different impedance values. For the estimated impedance of 0.35 Ω, the lengthening varies from a factor 4.1 (200 mA uniform filling) to 2.3 (4-bunch mode, 40 mA). The bunch profile is shown on Figure 1.13.

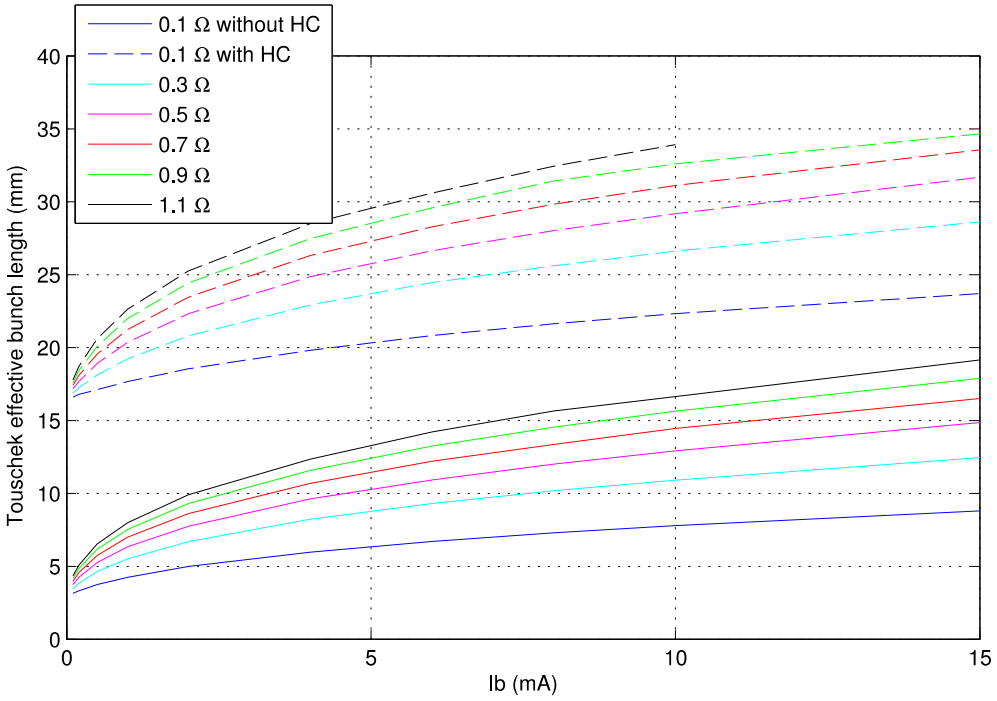


**Figure 1.13: Bunch lengthening with intensity.**

$I_{bunch}$=0.01 mA

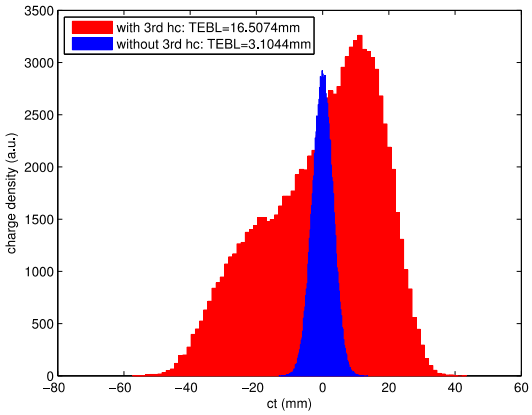


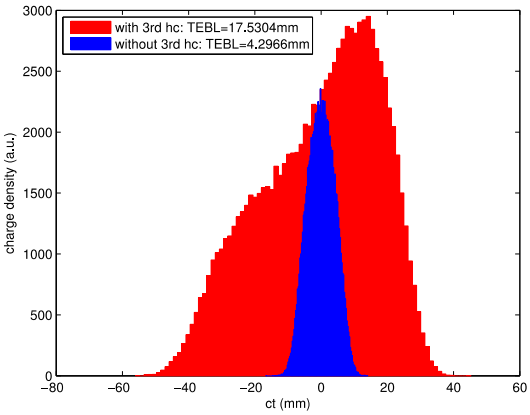


$I_{bunch}$=0.2 mA

200 mA uniform

$I_{bunch}$=6 mA

16-bunch

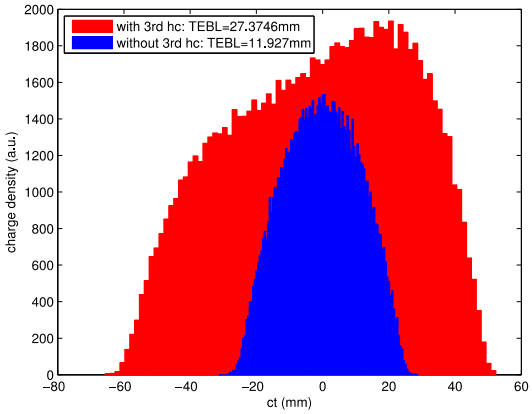


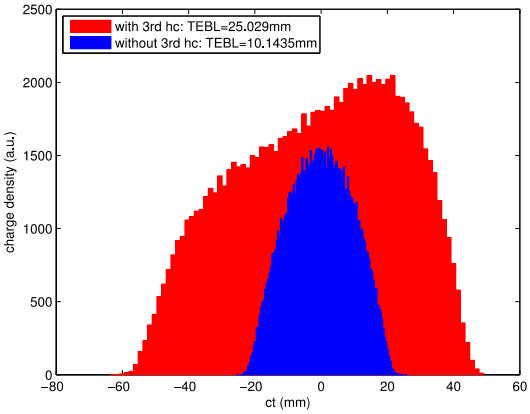


$I_{bunch}$=10mA

4-bunch

Figure 1.14: Bunch profiles.

## 1.12 Parameters

### Storage ring

| | ESRF | ESRF-EBS |
|---|---|---|
| **Energy [GeV]** | 6.03 | 6 |
| **Circumference [m]** | 844.391 | 843.977 |
| **Beam current [mA]** | 200 | 200 |
| **Natural emittance [pm]** | 4000 | 132 |
| **Damping time (H/V/L) [ms]** | 7.1/7.0/3.5 | 8.8/13/9.1 |
| **Bunch length (mm)** | 4.28 | 2.91 |
| **Energy spread** | $1.06\ 10^{-3}$ | $0.93\ 10^{-3}$ |
| **$E_{loss}$/turn [MeV]** | 4.90 | 2.52 |
| **RF voltage [MV]** | 9 | 6 |
| **Synchrotron frequency [kHz]** | 2.10 | 1.30 |
| **Momentum compaction** | $1.78\ 10^{-4}$ | $0.85\ 10^{-4}$ |
| **Tunes (H/V)** | 36.44/13.39 | 76.21/27.34 |
| **Natural chromaticity (H/V)** | -130/-58 | -109/-82 |
| **Operation chroma. (H/V)** | 10/10 | 6/4 |
| **Oper. Emittance (H/V) [pm]** | 4000/5 | 110/5 |
| **Multibunch lifetime [h]** | | 19.3 |
| **16-bunch lifetime [h]** | | 1.8 |
| **4-bunch lifetime [h]** | | 1.2 |

### ID source point

| | ESRF high | ESRF low | ESRF-EBS |
|---|---|---|---|
| **H β [m]** | 37.6 | 0.35 | 6.90 |
| **H η [mm]** | 134 | 31 | 1.73 |
| **H beam size [µm]** | 387.8 | 37.4 | 30.2 |
| **H beam divergence [µrad]** | 10.3 | 106.9 | 4.37 |
| **V β [m]** | 3 | 3 | 2.645 |
| **V beam size [µm]** | 3.46 | 3.46 | 3.64 |
| **V beam divergence [µrad]** | 1.15 | 1.15 | 1.37 |

## BM source point

| | ESRF high | ESRF low | ESRF-EBS |
|---|---|---|---|
| **H β [m]** | 1.06 | 1.61 | 1.82 |
| **H η [mm]** | 51 | 75 | 18.3 |
| **H beam size [µm]** | 77.9 | 112 | 23 |
| **H beam divergence [µrad]** | 111 | 98.5 | 24 |
| **V β [m]** | 42.0 | 32.2 | 2.57 |
| **V beam size [µm]** | 12.9 | 11.3 | 3.6 |
| **V beam divergence [µrad]** | 0.5 | 0.4 | 3.1 |

# 2 Magnet System

## 2.1 Introduction

The magnet system exists of bendings, quadrupoles, sextupoles, octupoles and correctors. The principle layout of these magnets are given in Figures 2.1 to 2.3. For the quadrupoles there are 2 types: medium gradient with a gradient of around 50 T/m and different lengths as well high gradient with gradients up to 90 T/m and different lengths too. The bending magnets with a longitudinal gradient are build up with 5 modules of permanent magnets. The combined bending magnets DQ have fields up to 0.56 T and a gradient up to 1.83 T/m. The required specifications according to the lattice file are given in Table 2.1.

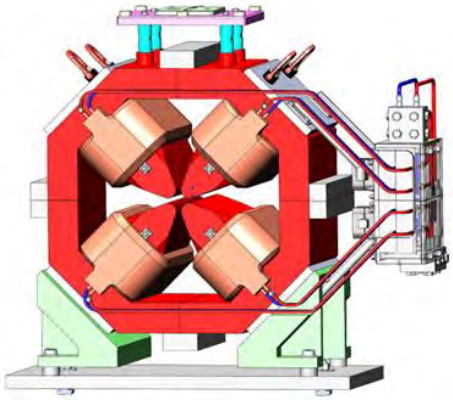

Layout of the medium gradient quadrupoles QF1, QD2, QD3, QF4 and QD5

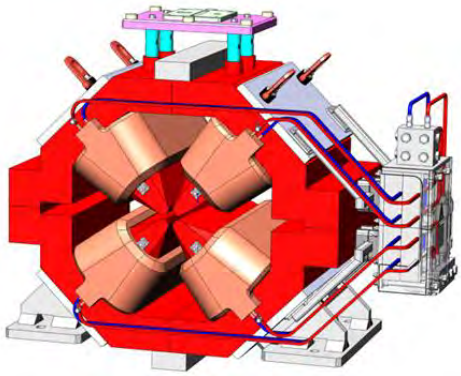

Layout of the high gradient quadrupoles QF6 and QF8

Figure 2.1: Layout of the medium and high gradient quadrupoles.

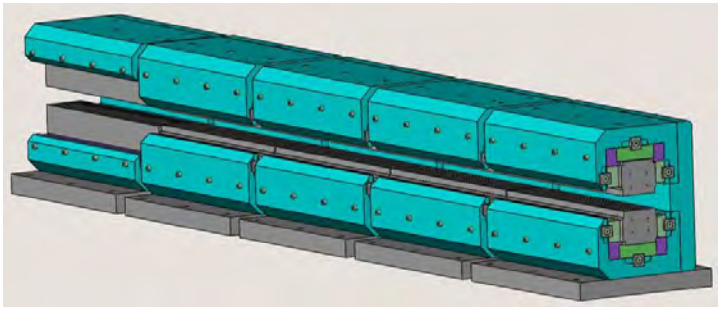

Layout of the permanent bending magnets DL, existing of 5 moduls

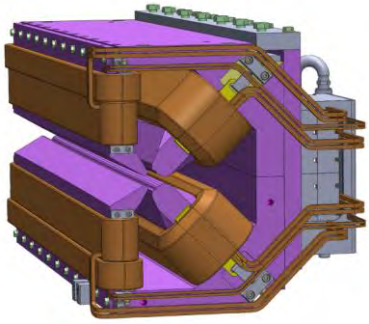

Layout of the combined bending magnets DQ

Figure 2.2: Layout of the bending magnet (DL) and the combined quadr.-bend (DQ).

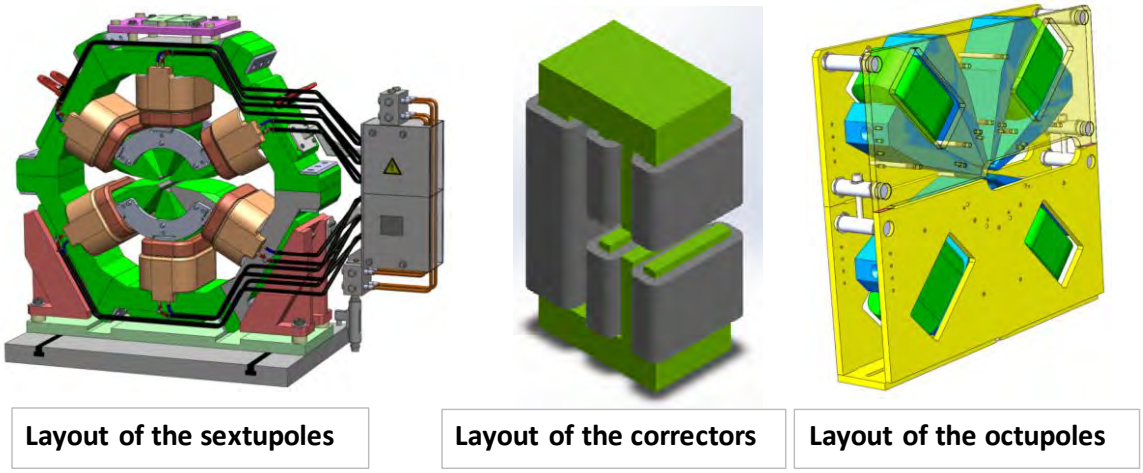


Figure 2.3: Layout of the sextupole (SD&SF), the corrector (SH) and the octupole (OF).

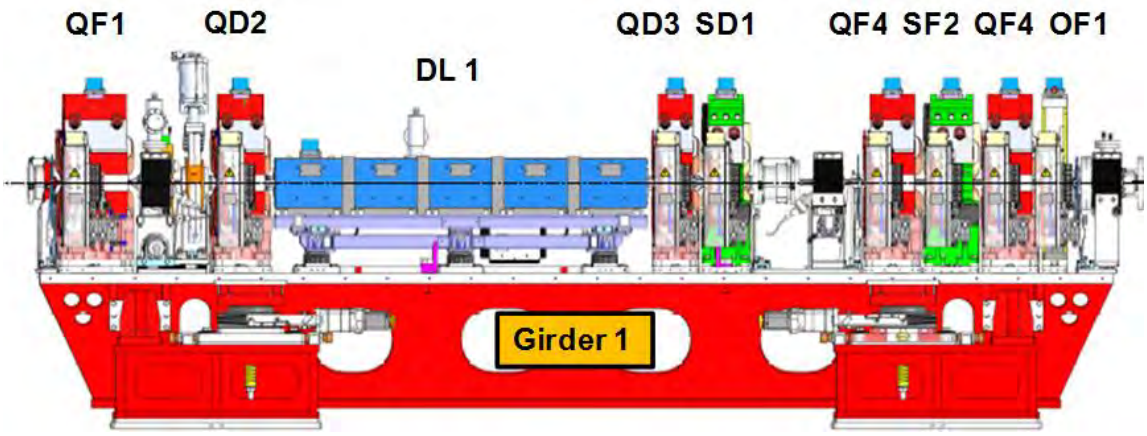


Figure 2.4: Location of the magnets on girder 1.

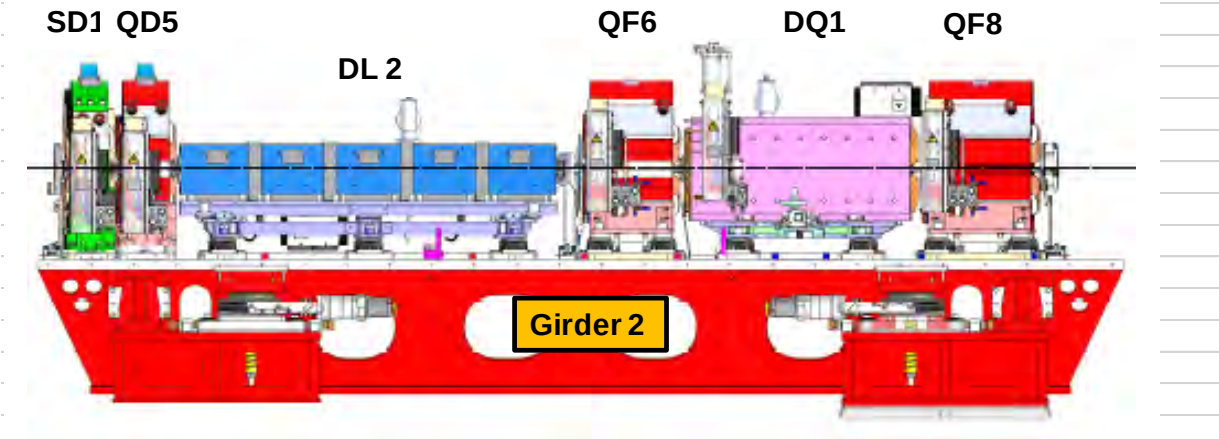


Figure 2.5: Location of the magnets on girder 2.

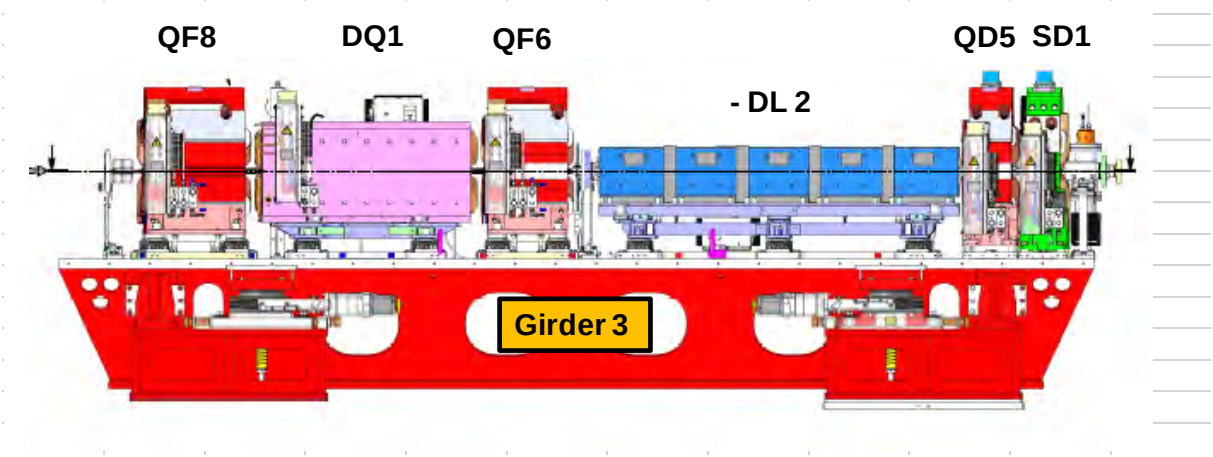


Figure 2.6: Location of the magnets on girder 3.

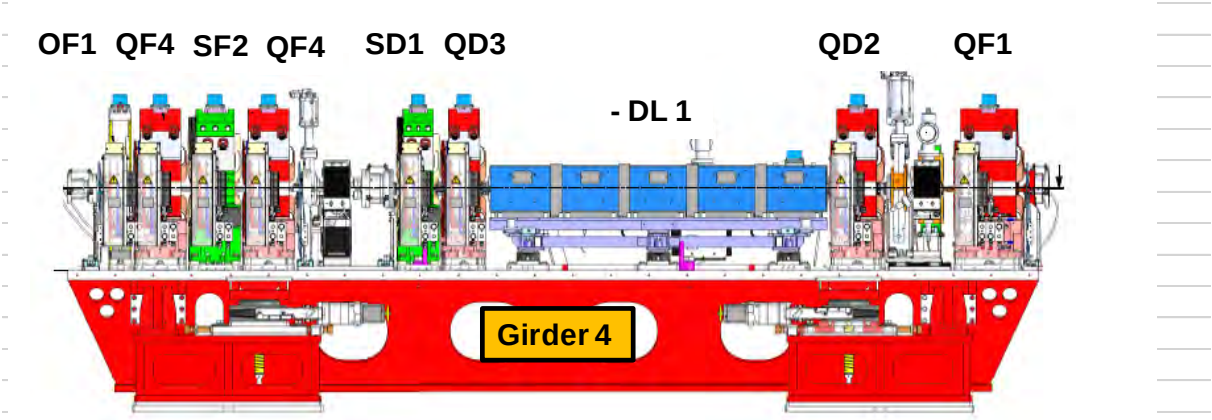


Figure 2.7: Location of the magnets on girder 4.

## 2.2 Quadrupole Design Parameters

The main parameters of the quadrupoles according to the lattice parameters are given in Table 2.1. QF1, QD2, QD3, QF4, QD5 are the medium gradient quadrupoles (MGQ) and QF6 as well as QF8 are the high gradient ones (HGQ). QD2, QF4 and QD5 have the same Iron length, the highest excitation current has QD5 with 95.29 A. In the following tables only the data of the QD5 are mentioned. The excitation current of the different quadrupoles have been determined by the fitting the integrated quadrupole strength (see the figures below).

Table 2.1: Lattice specifications of the quadrupoles.

| Lattice S28-D: Specification of the Quadrupoles | | | | | | | |
|---|---|---|---|---|---|---|---|
| Element | Numb. | L-Latt. (m) | k-value m^-2 | Grad. (T/m) | R(0) (mm) | B(pole) (T) | G*L-Latt. (T) |
| QF1 | 64 | 0.3119 | 2.539460 | 50.8244 | 0.0164 | 0.8335 | 15.8519 |
| QD2 | 64 | 0.22769 | -2.672503 | -53.4871 | 0.0164 | -0.8772 | 12.1783 |
| QD3 | 64 | 0.17862 | -2.404265 | -48.1186 | 0.0164 | -0.7891 | 8.5949 |
| QF4 | 128 | 0.22769 | 2.429985 | 48.6334 | 0.0164 | 0.7976 | 11.0732 |
| QD5 | 64 | 0.22769 | -2.704500 | -54.1275 | 0.0164 | -0.8877 | 12.3241 |
| QF6 | 64 | 0.39866 | 4.464519 | 89.3522 | 0.0127 | 1.1348 | 35.6208 |
| QF8 | 64 | 0.49264 | 4.425445 | 88.5702 | 0.0126 | 1.1160 | 43.6330 |

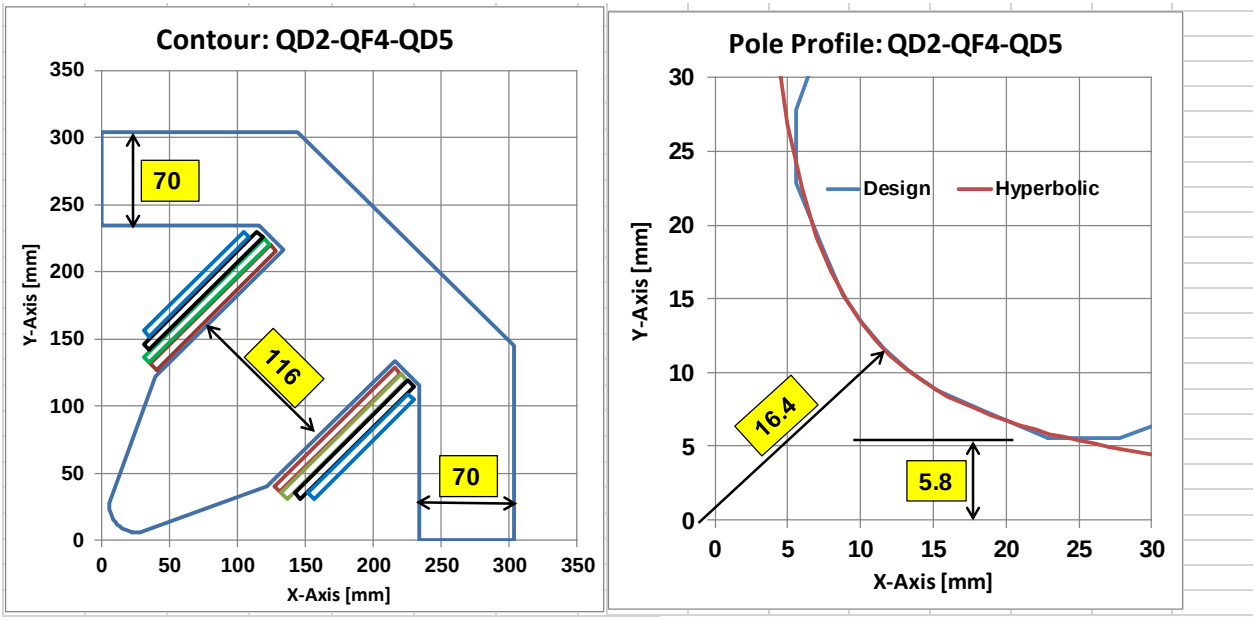


Figure 2.8: Lamination and pole profile for the medium gradient quadrupoles (MGQ).

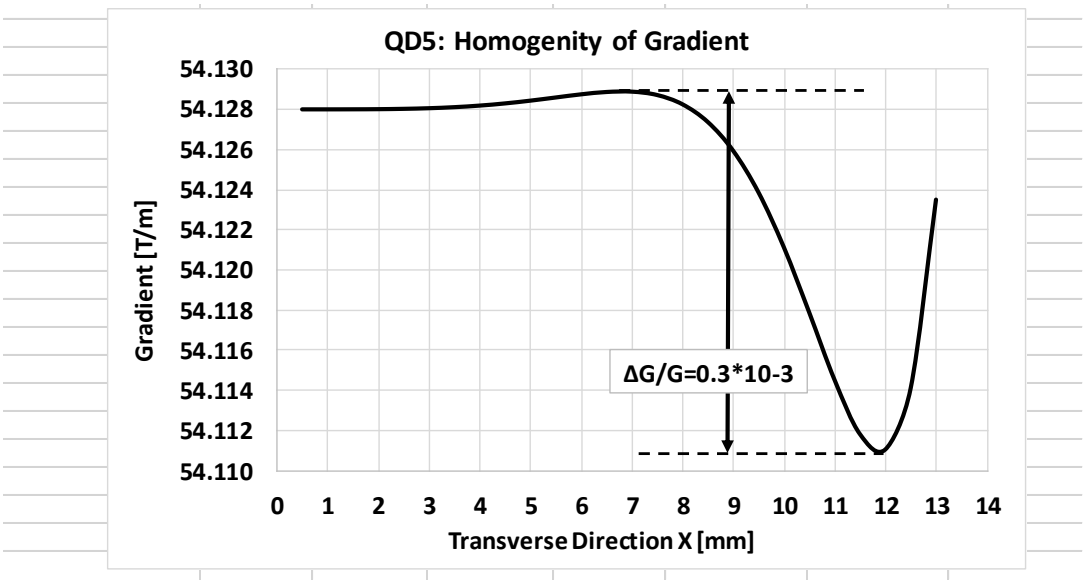


Figure 2.9: The change of the gradient within the good field region (GFR) for the MGQs as a function of the transverse direction. The requirement for the GFR is ΔG/G <1*10-3.

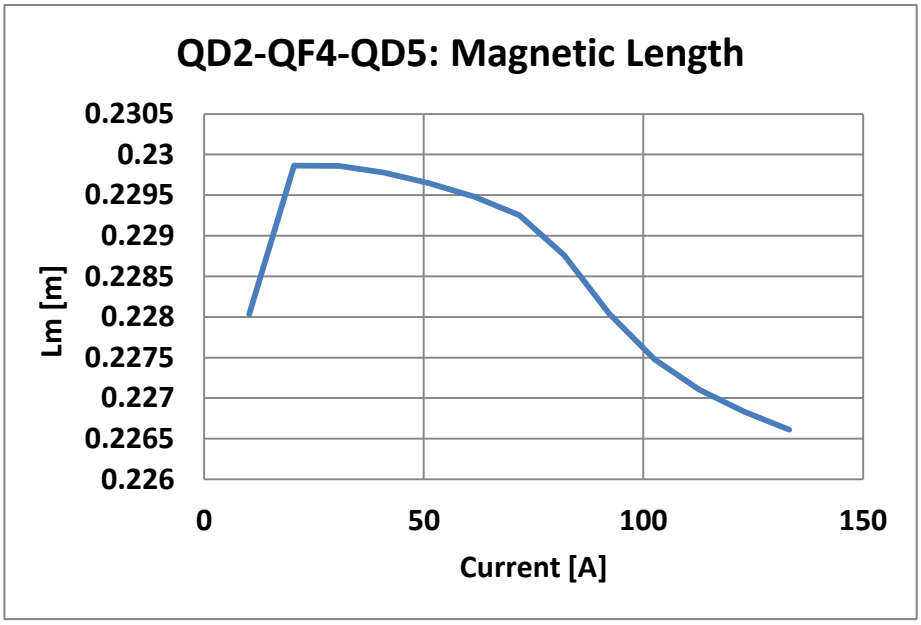


Figure 2.10: The magnetic length of the MGQ as a function of the excitation current.

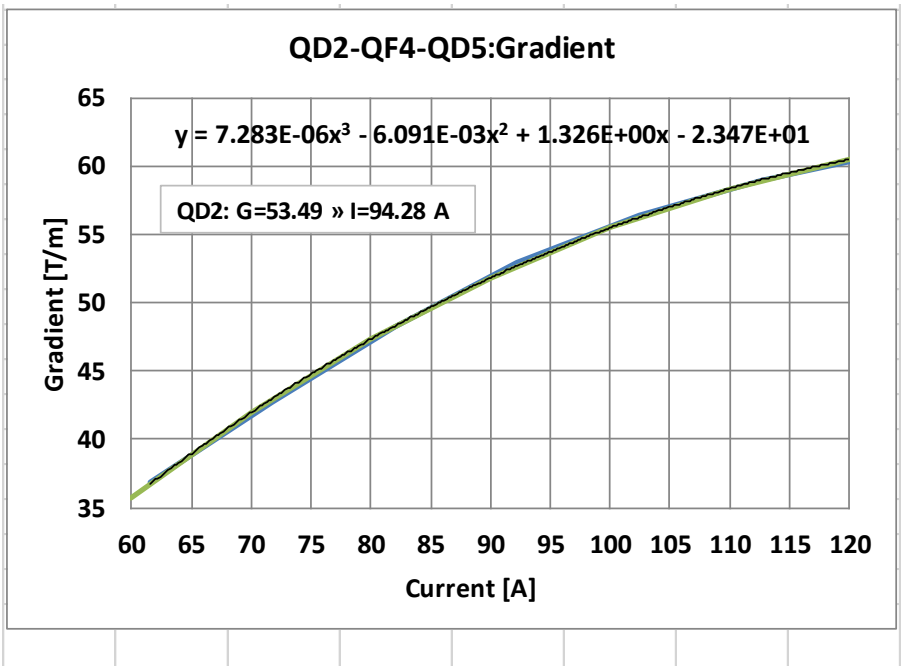


Figure 2.11: The gradient of the MGQ as a function of the excitation current. To get the nominal gradient of 53.49 T/m an excitation current of 94.28 A is required. Important is the value of the integrated gradient as a function of the excitation current, which can be calculated from the values given in Figures 2.10 and 2.11. The corresponding result is given in the following plot (see Figure 2.12).

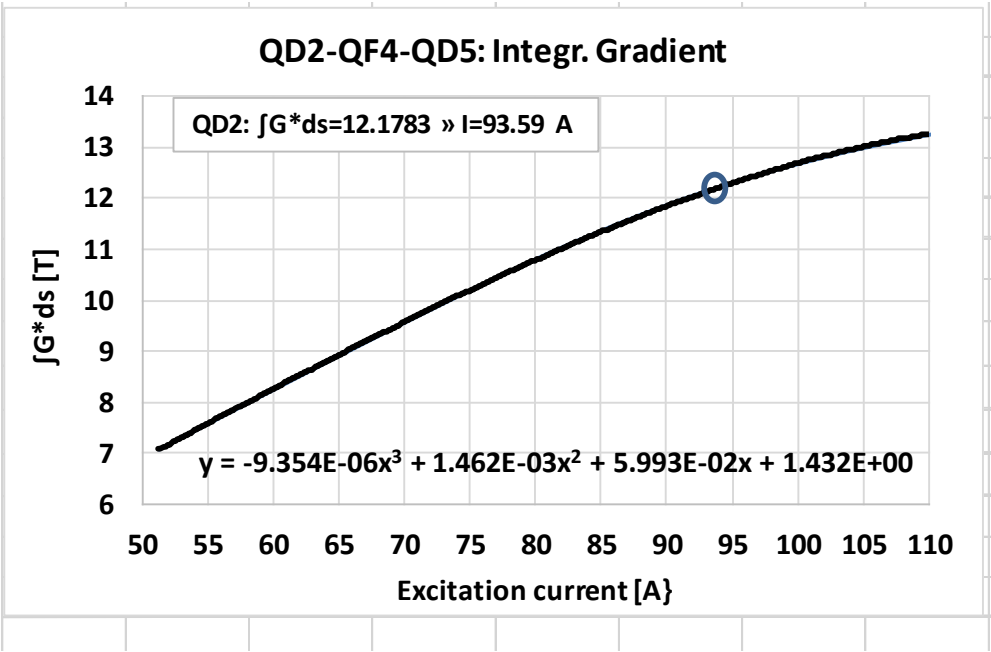


Figure 2.12: The excitation curve for the integrated gradient. For the required value of 12.1783 T a current of 93.59 A is required. The fitting has been done with a 3rd-degree polynomial.

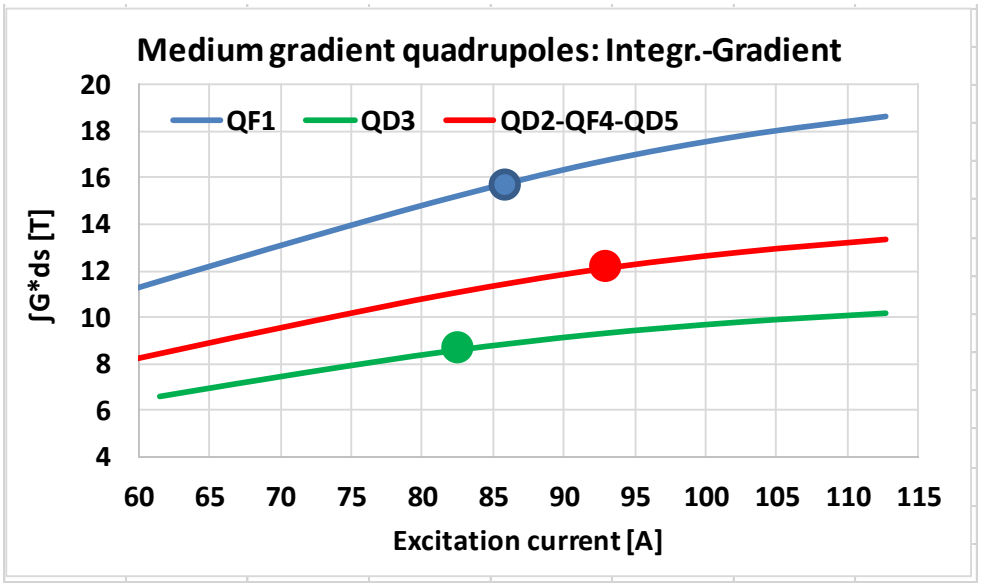


Figure 2.13: The excitation curve for the integrated gradient of the MGQ. The nominal values according to Table 2.1 are marked with filled cycles. The corresponding currents are: I(QF1) = 86.67 A, I(QD2) = 93.59 A, I(QD3) = 82.48 A, I(QF4) = 82.49 A, I(QD5) = 95.29 A.

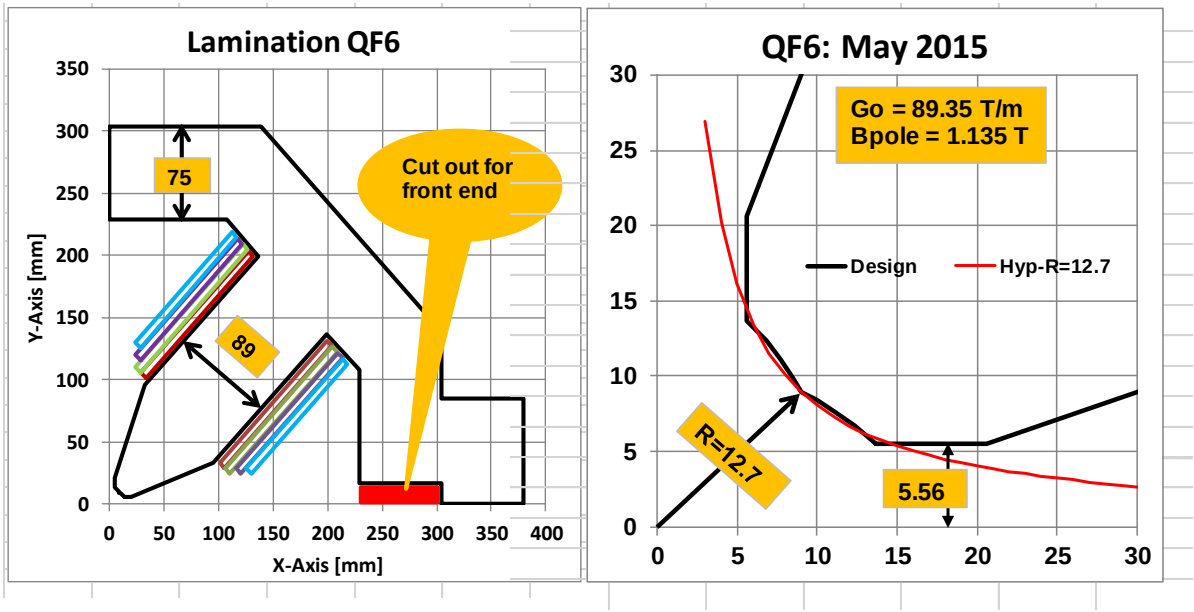


Figure 2.14: Lamination and pole profile for the high gradient quadrupoles (HGQ).

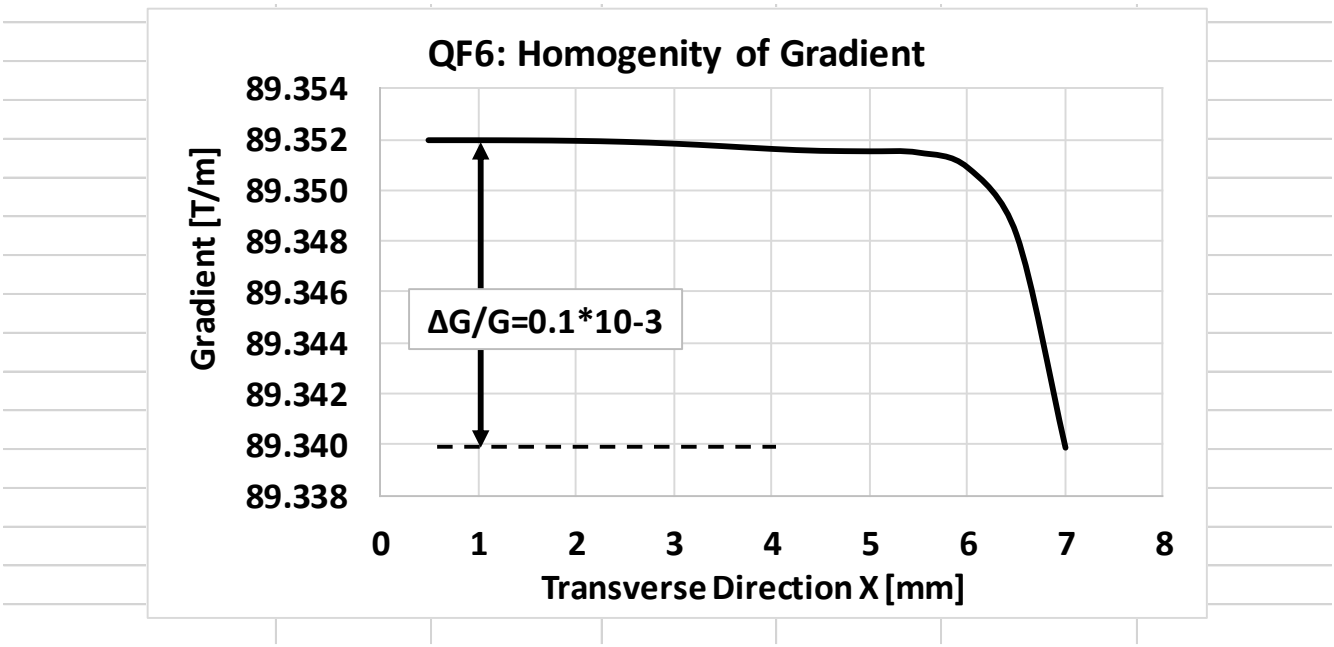


Figure 2.15: The change of the gradient within the good field region (GFR) for the HGQs as a function of the transverse direction. The requirement for the GFR is $\Delta G/G < 1*10^{-3}$.

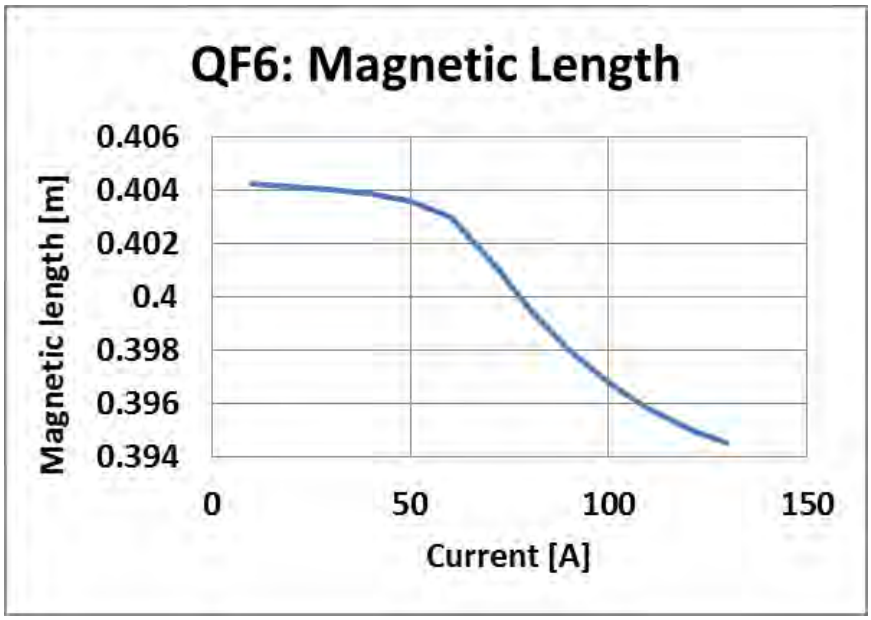


Figure 2.16: The magnetic length of the HGQ as a function of the excitation current.

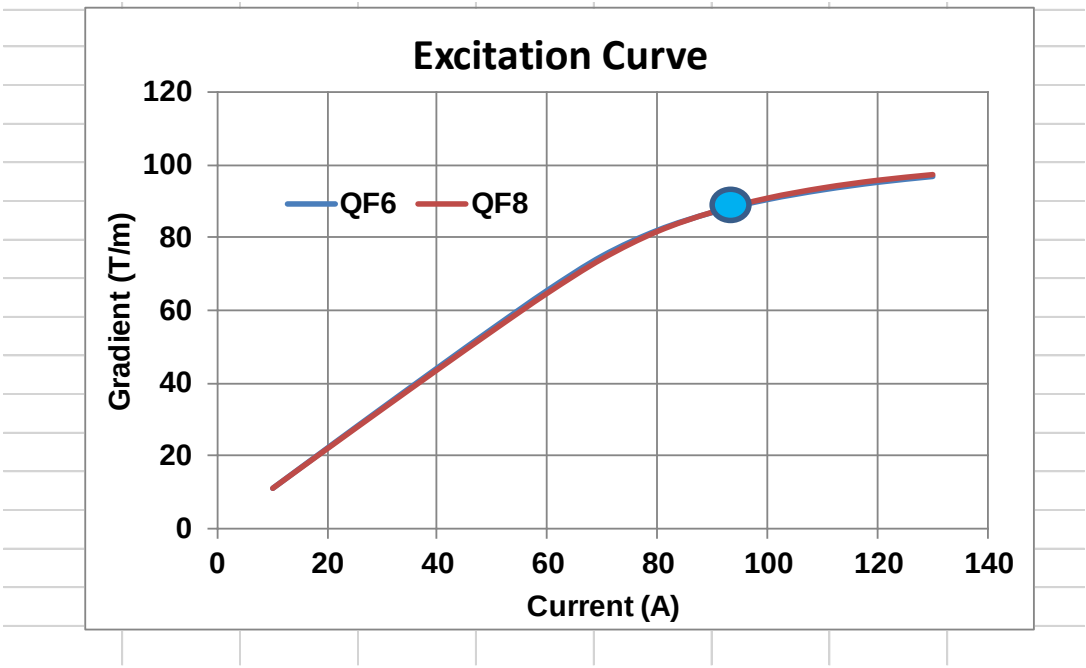


Figure 2.17: The gradient of the HGQ as a function of the excitation current. To get a gradient of around 90 T/m an excitation current of around 95 A is required. Important is the value of the integrated gradient as a function of the excitation current, which can be calculated from the values given in Figures 2.16 and 2.17. The corresponding result is given in the following plot (see Figure 2.18).

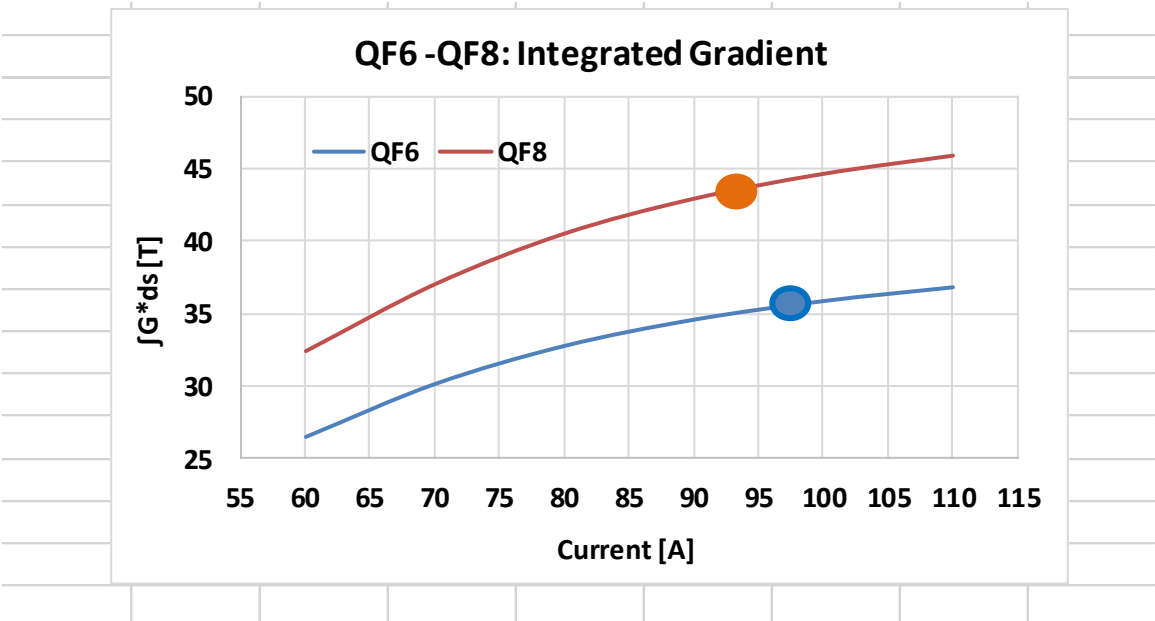


Figure 2.18: The excitation curve for the integrated gradient of the HGQ. The nominal values according to Table 2.1 are marked with filled cycles. The corresponding currents are: I(QF6) = 79.44 A, I(QF8) = 93.233 A.

Table 2.2: Conductor parameters and material which are the same for all quadrupoles.

| Section | 6 x 6 | mm |
|---|---|---|
| Pipe diameter | 3 | mm |
| Copper resistivity | $1.78*10^{-8}$ | Ohm m |
| Insulation | 0.5 | mm |
| Conductor area | 28.0674 | $mm^2$ |
| Material | 1300-100 | |
| Stacking factor | 0.98 | |

Table 2.3: Electrical and winding parameters of the quadrupoles.

| Quadrupoles | QF1 | QD2 | QD3 | QF4 | QD5 | QF6 | QF8 |
|---|---|---|---|---|---|---|---|
| Current [A] | 86.67 | 93.59 | 82.48 | 82.49 | 95.29 | 97.44 | 93.23 |
| Turns | 68 | 68 | 68 | 68 | 68 | 77 | 77 |
| Amp turns [kA turns] | 5.89 | 6.36 | 5.61 | 5.61 | 6.48 | 7.50 | 7.18 |
| Cond. length [m] | 248.5 | 203.5 | 176.3 | 203.5 | 203.5 | 322.0 | 381.1 |
| Resistance [mΩ] | 157.6 | 129.1 | 110.6 | 129.1 | 129.1 | 204.2 | 241.7 |
| Voltage [V] | 13.66 | 12.08 | 9.12 | 10.65 | 12.30 | 19.91 | 22.53 |
| Power [kW] | 1.18 | 1.13 | 0.752 | 0.878 | 1.172 | 1.94 | 2.10 |
| Current density [A/mm2] | 3.09 | 3.34 | 2.94 | 2.94 | 3.40 | 3.47 | 3.32 |
| Magnet inductance [mH] | 130 | 107 | 80 | 107 | 107 | 179 | 211 |
| Time constant [s] | 0.86 | 0.86 | 0.74 | 0.86 | 0.86 | 0.89 | 0.89 |

Table 2.4: Mechanical parameters.

| Quadrupole | QF1 | QD5 | QD3 | QF6 | QF8 | |
|---|---|---|---|---|---|---|
| **Bore radius** | 16.4 | 16.4 | 16.4 | 12.7 | 12.6 | mm |
| **Vertical gap** | 11.1 | 11.2 | 11.2 | 11.1 | 11.2 | mm |
| **Iron length** | 295 | 212 | 162 | 388 | 484 | mm |
| **Magnet length** | 356 | 276 | 223 | 449 | 545 | mm |
| **Magnet height** | 608 | 608 | 608 | 608 | 608 | mm |
| **Magnet mass** | 555 | 405 | 315 | 690 | 855 | kg |

**Table 2.5: Water cooling parameters for each cooling circuit.**

| | QF1 | QD2 | QD3 | QF4 | QD5 | QF6 | QF8 | |
|---|---|---|---|---|---|---|---|---|
| **Coils in series** | 1 | 2 | 1 | 2 | 2 | 1 | 1 | |
| **Cooling circuits** | 4 | 2 | 4 | 2 | 2 | 4 | 4 | |
| **Pressure drop** | 7.2 | 7.2 | 7.2 | 7.2 | 7.2 | 7.2 | 7.2 | bar |
| **Water flow** | 0.528 | 0.4 | 0.64 | 0.4 | 0.4 | 0.46 | 0.43 | l/min |
| **Water velocity** | 1.244 | 0.94 | 1.51 | 0.94 | 0.94 | 1.07 | 1.01 | m/s |
| **Temperature rise** | 8.04 | 20.35 | 4.2 | 15.8 | 21.1 | 15.3 | 17.6 | K |
| **Reynold number** | 3730 | 2820 | 4540 | 2820 | 2820 | 3220 | 3030 | |

**Table 2.6: Systematic multipoles $b_n$ at 13 mm radius.**

| n | QF1 | QD2-QF4-QD5 | QD3 | QF6 | QF8 |
|---|---|---|---|---|---|
| **2** | 10000 | 10000 | 10000 | 10000 | 10000 |
| **6** | 1.11 | 1.06 | 0.21 | -0.14 | -0.03 |
| **10** | -5.18 | -5.06 | -5.38 | 0.37 | 0.51 |
| **14** | 4.46 | 4.30 | 4.25 | -0.41 | -0.52 |
| **18** | -0.92 | -0.90 | -0.87 | 0.03 | 0.05 |
| **22** | -0.03 | -0.03 | -0.04 | 0.0 | 0.0 |
| **26** | 0.04 | 0.04 | 0.048 | 0.0 | 0.0 |
| **30** | -0.00 | -0.00 | -0.00 | 0.0 | 0.0 |

**Table 2.7: Standard deviation of multipoles in units of 104 bn , for the medium gradient (above) and the high gradient quadrupoles (below), expressed at 13 mm, for ±0.040 mm mechanical tolerances (including profile and assembly errors). These values are for all moderate gradient quadrupoles, since the pole shapes are identical.**

| **n:** | **1** | **2** | **3** | **4** | **5** | **6** | **7** | **8** | **9** | **10** | **11** | **12** | **13** | **14** |
|---|---|---|---|---|---|---|---|---|---|---|---|---|---|---|
| **σ(bn)** | 4.9 | 4.2 | 3.1 | 2.5 | 2.2 | 1.8 | 1.5 | 1.2 | 1.0 | 0.86 | 0.72 | 0.54 | 0.47 | 0.37 |
| | | | | | | | | | | | | | | |
| **n:** | 1 | 2 | 3 | 4 | 5 | 6 | 7 | 8 | 9 | 10 | 11 | 12 | 13 | 14 |
| **σ(bn)** | 17 | 10 | 5.2 | 2.6 | 1.3 | 0.7 | 0.4 | 0.2 | 0.1 | 0.06 | 0.04 | 0.02 | 0.01 | 0.01 |

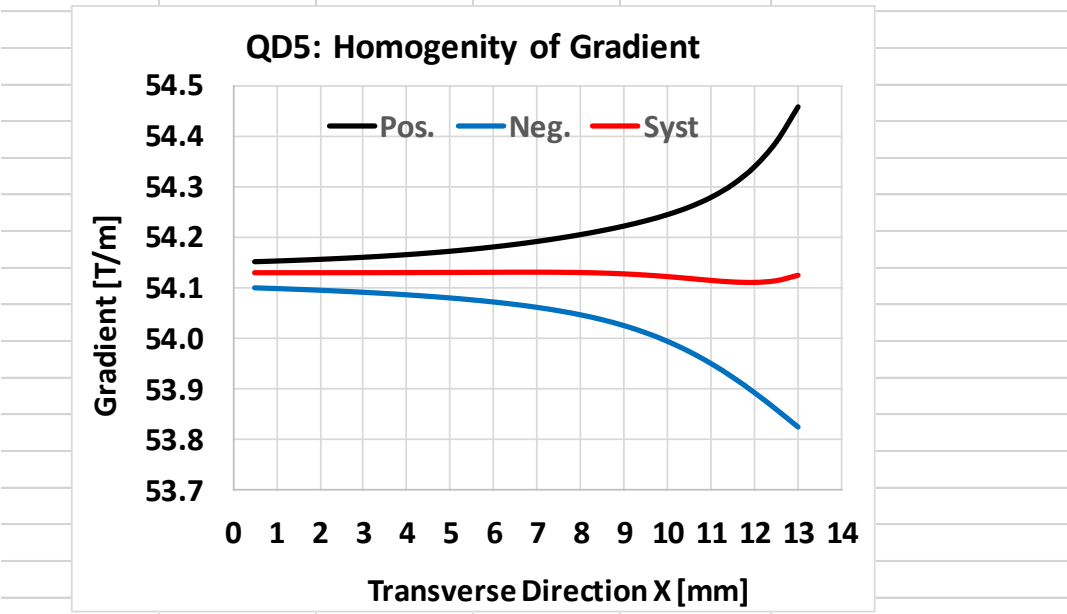


Figure 2.19: Change of the gradient of the MG-quadrupoles according to the multipoles given in Table 7. Pos. means taking the positive values and Nev. negative ones of all multipoles. The maximum deviation at x=13 mm is ΔG/G = +/- 5.5E-03.

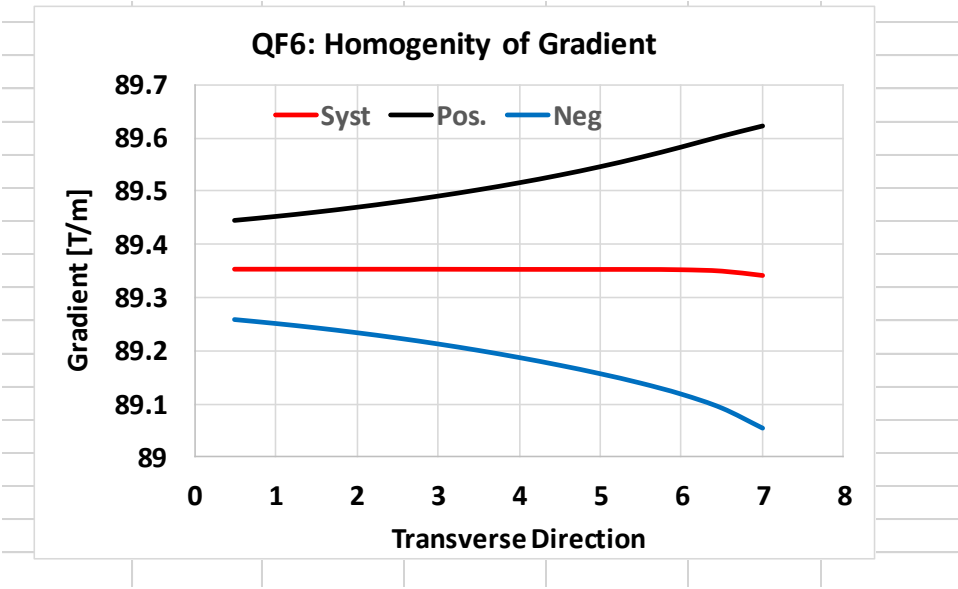


Figure 2.20: Change of the gradient of the MG-quadrupoles according to the values presented in table 7. Pos means taking a the positive values and Nev. negative ones of all multipoles. The maximum deviation at x = 7 mm is ΔG/G = +/- 2.9E-03.

## 2.3 Drawings of the QD5 quadrupoles

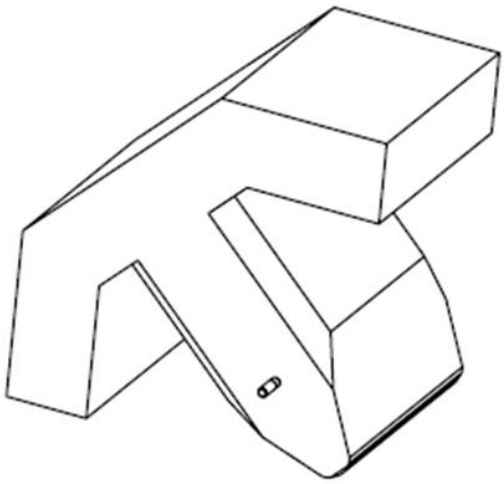

Figure 2.21: The shape of one quadrant (isometric view).

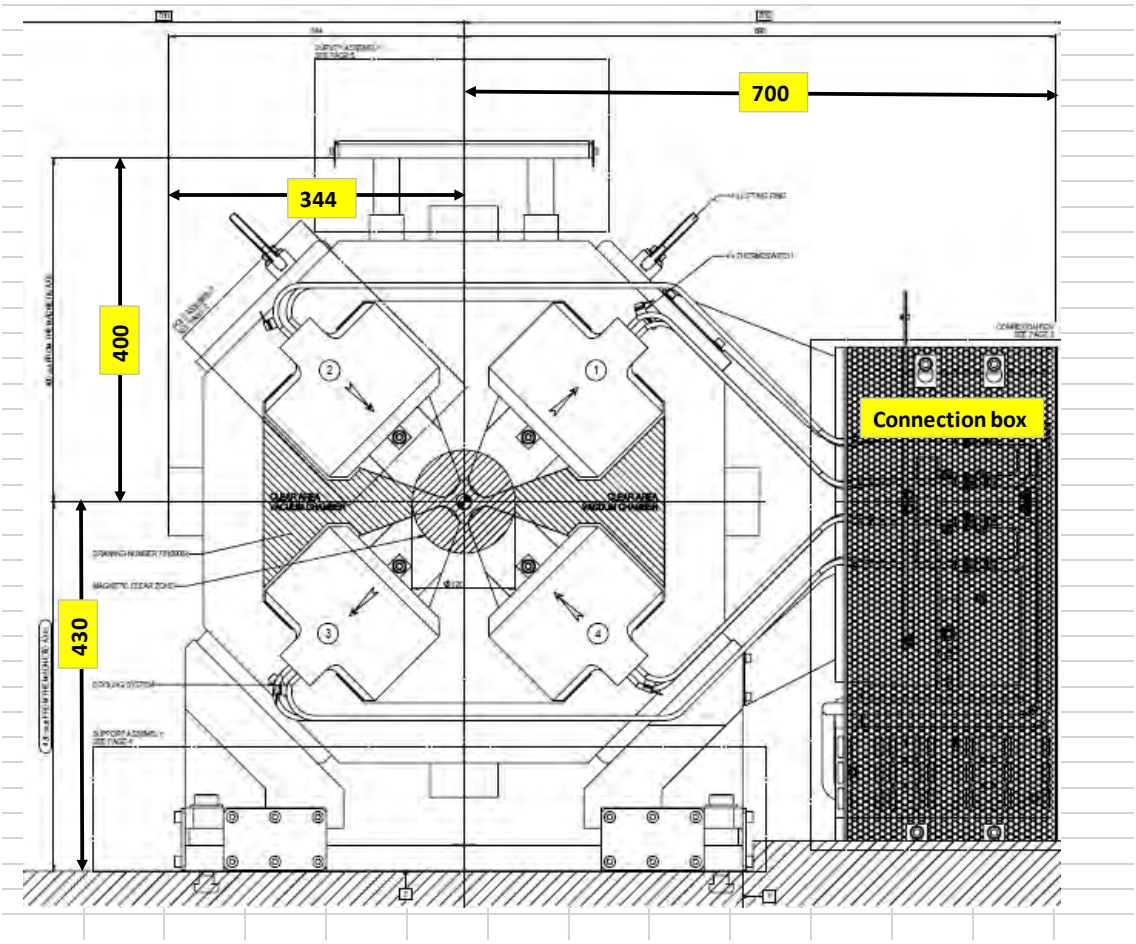

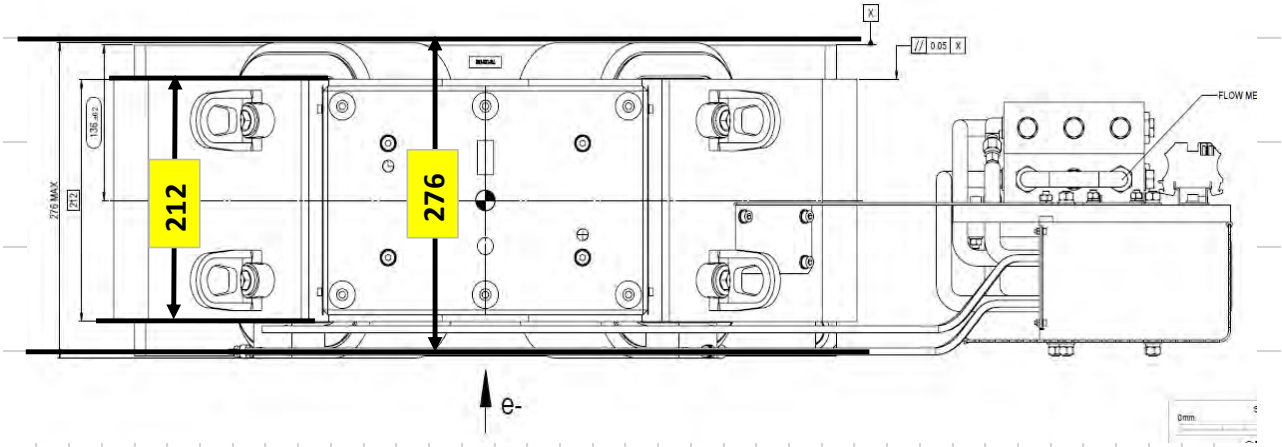


## 2.4 Drawings of the quadrupoles QF6 and QF8

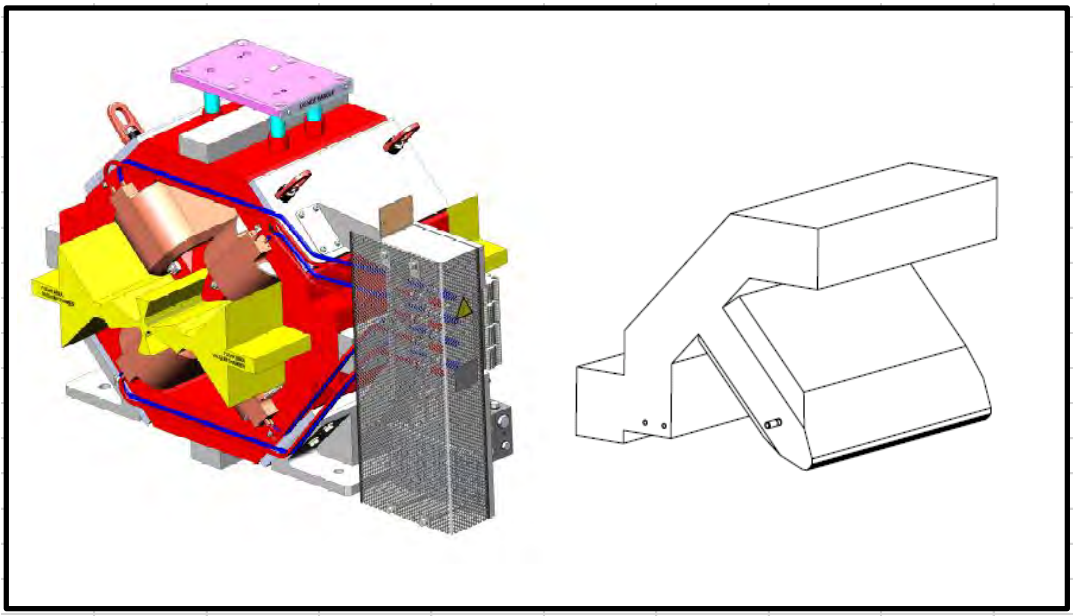

**Figure 2.24: A 3-D view of the QF6 quadrupole and the shape of one quadrant (isometric view) of QF6.**

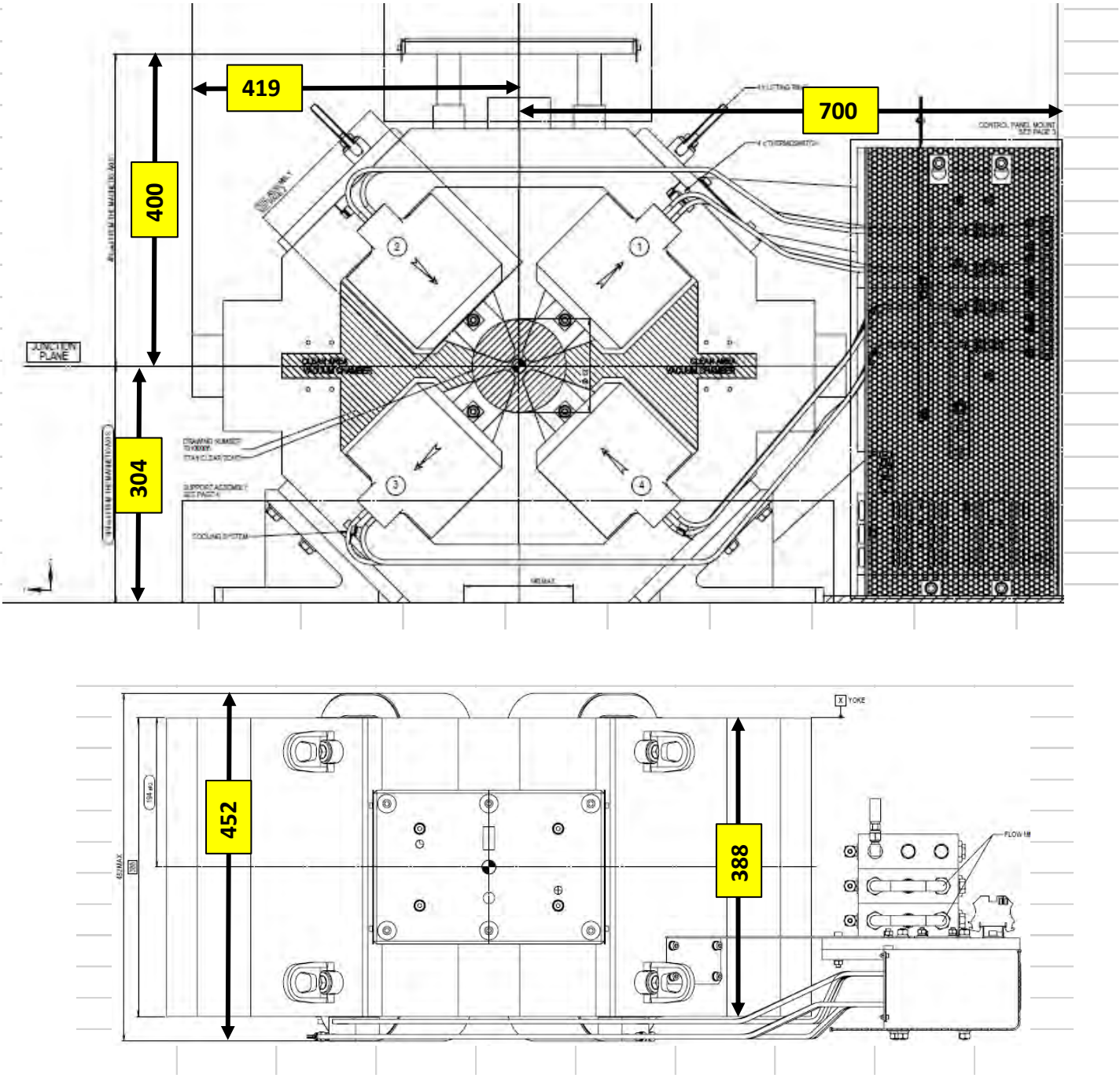


Figure 2.25: Front and top view of the QF6 quadrupole.

## 2.5 Sextupole magnets

### Description of the components and their function

The sextupoles at the ESRF are of two types; the short sextupole (SD1) and the long sextupole (SF2) with mechanical lengths of 166 mm and 200 mm respectively.

The sextupole strength S (B=S*r2) for both is 1700 Tm-2 and the bore radius is 19.2 mm. The field will be generated by cooled water copper coils excited by steady state current density. The yoke of the sextupole is solid using low carbon steel.

In addition to their main function, the sextupoles must be able to produce correction magnetic fields, which are created by a set of additional correction coils.

These correction magnetic fields are:

- a horizontal dipole
- a vertical dipole
- a skew quadrupole

The six main sextupolar coils consist of multiple wire layers of a standard manufactured conductor with a 3 mm diameter cooling hole and of dimensions 6 mm × 6 mm. The correction coils will be made of plain copper wire.

Mechanical shims will be installed on the magnet supports to ensure the positioning of the sextupoles on the magnet girder. The machining, the adjustment and the installation of these shims will be done by the contractor.

**Table 2.8: Lattice specification of the sextupoles.**

| Lattice S28-D-(13-05-2016) | | | | | | |
|---|---|---|---|---|---|---|
| Element | L-Latt. (m) | m(OPA) m^-3 | B'' (T/m^2) | R(0) (m) | B(pole) (T) | B''*L-Latt T/m |
| | | | | | | |
| SD1A | 0.18 | -78.96 | -3159.7 | 0.0192 | -0.58 | -568.4 |
| SF2A | 0.214 | 77.04 | 3082.8 | 0.0192 | 0.57 | 659.4 |
| SD1B | 0.18 | -74.19 | -2968.8 | 0.0192 | -0.55 | -534.1 |
| SD1D | 0.18 | -74.19 | -2968.8 | 0.0192 | -0.55 | -534.1 |
| SF2E | 0.214 | 77.04 | 3082.8 | 0.0192 | 0.57 | 659.4 |
| SD1E | 0.18 | -78.96 | -3159.7 | 0.0192 | -0.58 | -568.4 |

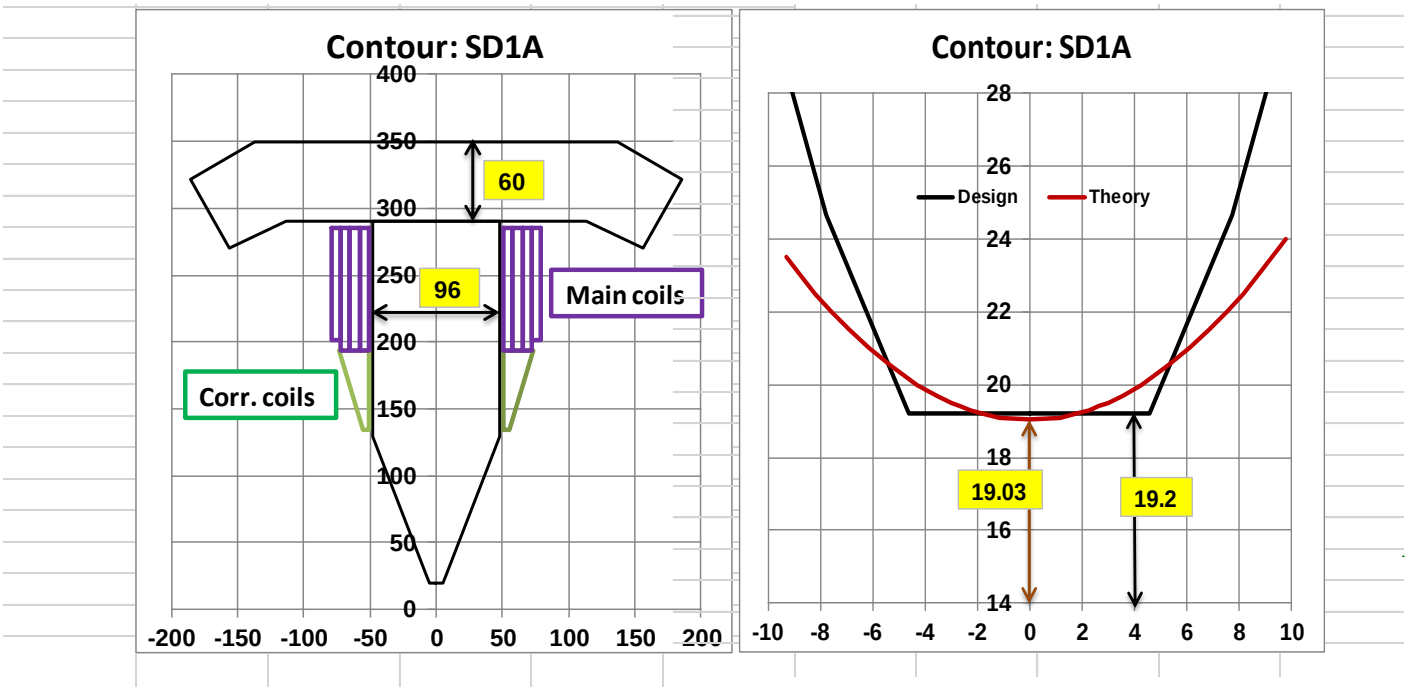


Figure 2.27: Lamination and pole profile for the sextupoles SD1 and SF2.

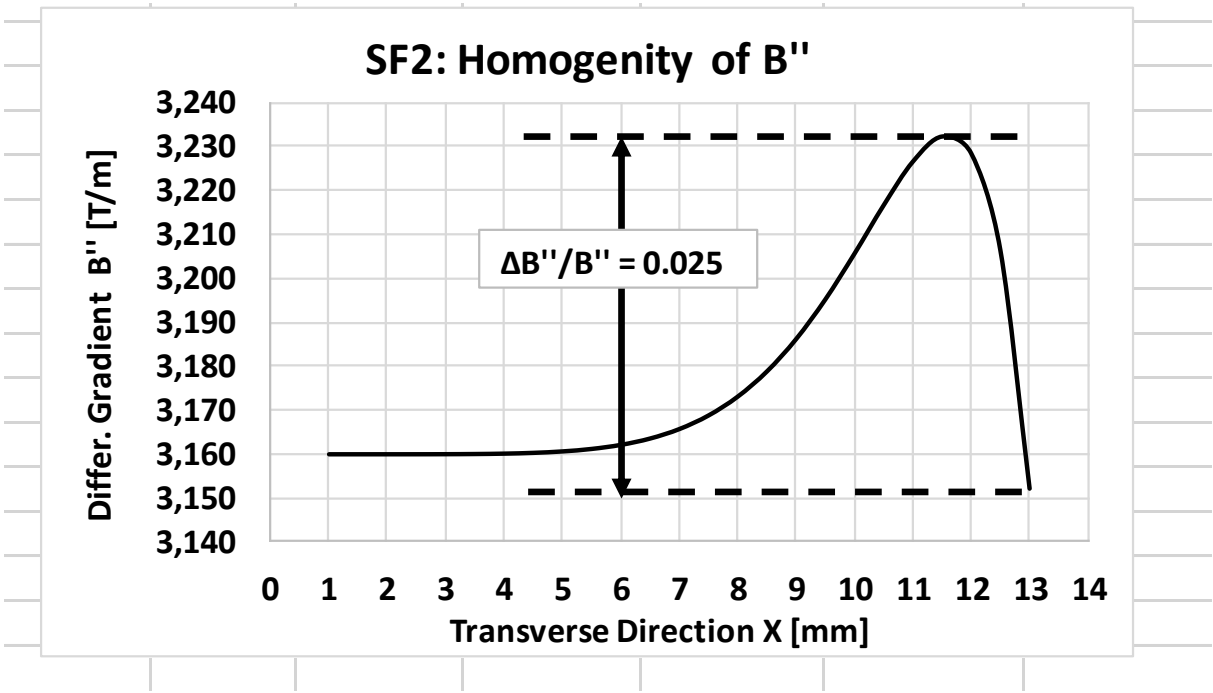


Figure 2.28: The change of the gradient within the good field region (GFR) for the sextupoles as a function of the transverse direction. The systematic multipoles are: n=9: 42*1E-04, n=15: -16*1E-04 and n=22: -0.3*1E-04. The requirement for the GFR is $\Delta G/G < 1*10^{-2}$ over a distance of 13 mm.

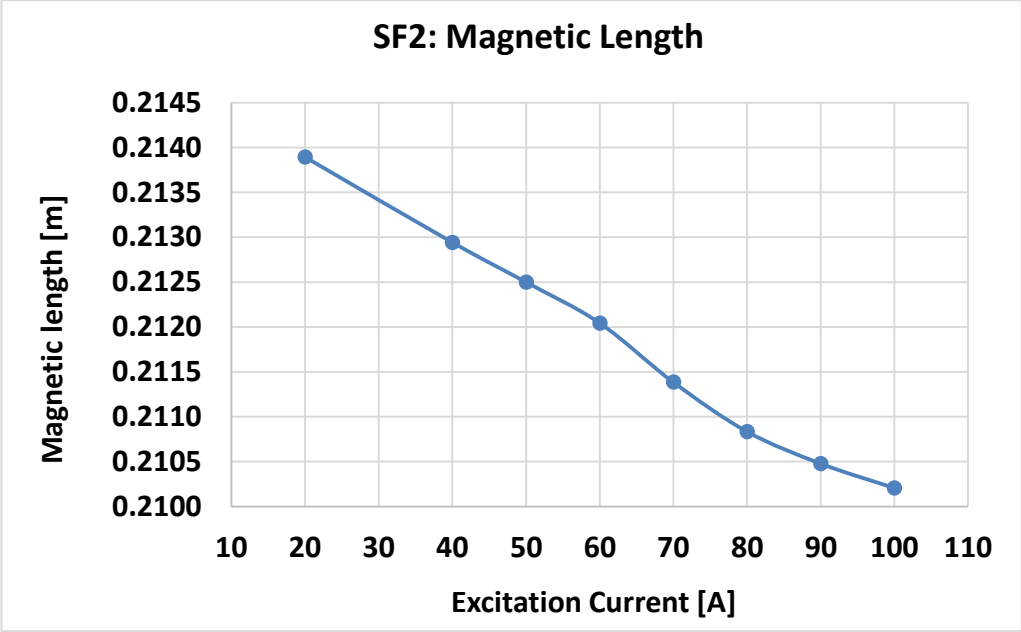


Figure 2.29: The magnetic length of the sextupole SF2 as a function of the excitation current.

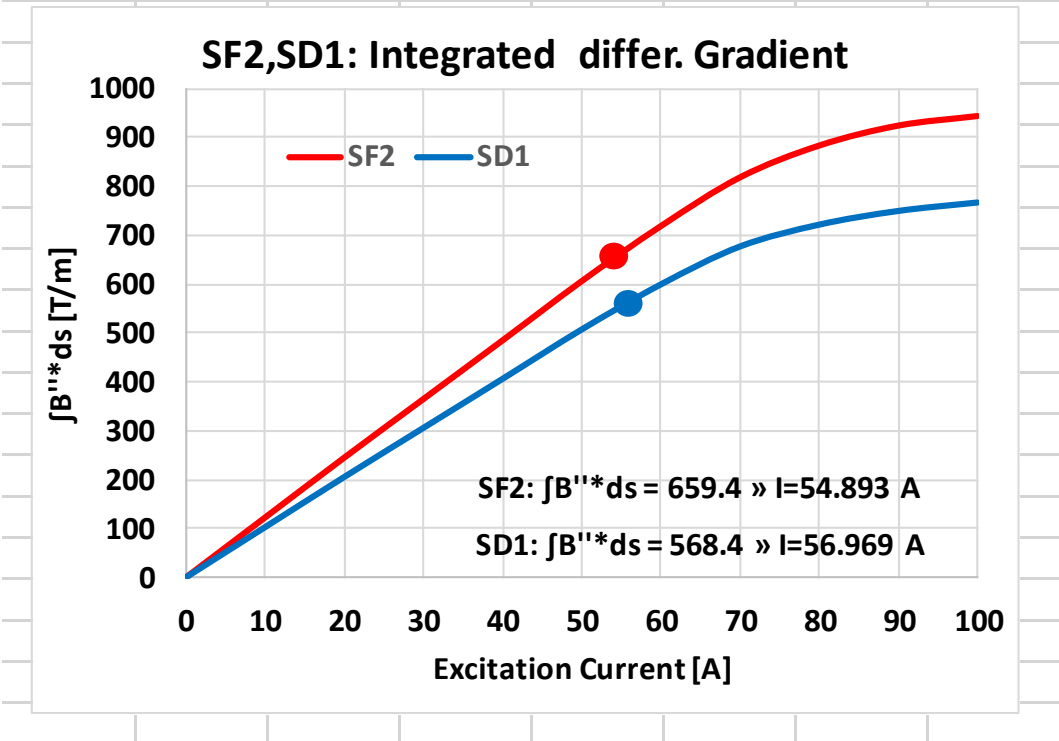


Figure 2.30: The excitation curve for the integrated differential gradient B''. For the required value of 659.4 T/m (SF2) a current of 54.893 A is required; for a value of 568.4 (SD1) a current of 56.969 is required. The fitting has been done with a 3rd-degree polynomial.

Table 2.9: Conductor parameters and material, which is the same for all sextupoles.

| Section | 6 x 6 | mm |
|---|---|---|
| Pipe diameter | 3 | mm |
| Copper resistivity | $1.78*10^{-8}$ | Ohm m |
| Insulation | 0.5 | mm |
| Conductor area | 28.0674 | $mm^2$ |
| Material | AISI 1006 | |
| Type of magnet | SOLID | |
| Stacking factor | 0.98 | |

Table 2.10: Electrical and winding parameters of the sextupoles.

| Sextupole | SD1 | SF2 |
|---|---|---|
| Current [A] | 56.97 | 54.89 |
| Turns | 51 | 51 |
| Amp turns [kA turns] | 2.905 | 2.800 |
| Cond. length [m] | 193.6 | 213.4 |
| Resistance [mΩ] | 122 | 135 |
| Voltage [V] | 7.0 | 7.5 |
| Power [kW] | 0.40 | 0.41 |
| Current density [A/mm2] | 2.03 | 1.96 |
| Magnet inductance [mH] | 60.5 | 72.9 |
| Time constant [s] | 0.5 | 0.5 |

Table 2.11: Mechanical parameters.

| Sextupole | SD1 | SF2 | |
|---|---|---|---|
| **Bore radius** | 19.2 | 19.2 | mm |
| **Vertical gap** | 11.2 | 11.2 | mm |
| **Iron length** | 166 | 200 | mm |
| **Overall length** | 232 | 266 | mm |
| **Magnet height** | 830 | 830 | mm |
| **Magnet mass** | - | - | kg |

Table 2.12: Water cooling parameters for each cooling circuit.

| | SD1 | SF2 | |
|---|---|---|---|
| **Coils in series** | 3 | 3 | |
| **Cooling circuits** | 2 | 2 | |
| **Pressure drop** | 7.2 | 7.2 | bar |
| **Water flow** | 0.42 | 0.41 | l/min |
| **Water velocity** | 0.99 | 0.96 | m/s |
| **Temperature rise** | 6.8 | 7.2 | K |
| **Reynold number** | 1480 | 2860 | |

Table 2.13: Systematic multipoles $b_n$ at 13 mm radius.

| n | SF2 | SD1 |
|---|---|---|
| **3** | 10000 | 10000 |
| **9** | 42 | 42 |
| **15** | -16 | -16 |
| **22** | -0.3 | -0.3 |

**Table 2.14: Standard deviation of multipoles in units of $10^4$ $b_n$, expressed at 13 mm, for ±0.040 mm mechanical tolerances (including profile and assembly errors).**

| n: | 1 | 2 | 3 | 4 | 5 | 6 | 7 | 8 | 9 | 10 | 11 | 12 | 13 | 14 |
|---|---|---|---|---|---|---|---|---|---|---|---|---|---|---|
| **σ(bn)** | 4.9 | 4.2 | 3.1 | 2.5 | 2.2 | 1.8 | 1.5 | 1.2 | 1.0 | 0.86 | 0.72 | 0.54 | 0.47 | 0.37 |

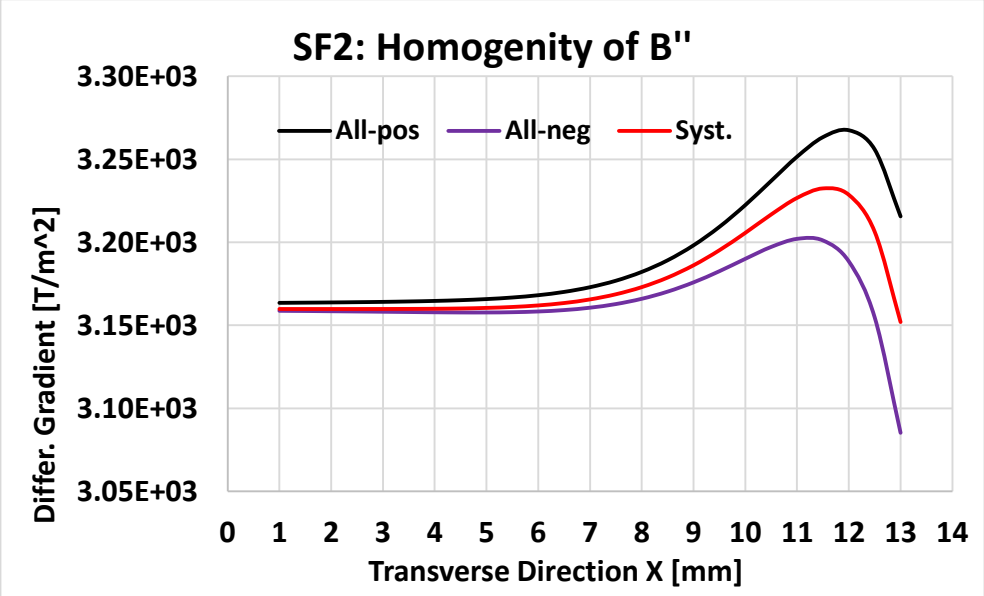


**Figure 2.31: Change of the differential gradient of the sextupoles according to the values presented in Table 2.11. Pos. means taking the positive values and Nev.the negative ones of all multipoles. The maximum deviation at x = 13 mm is ΔG/G = +/- 2.9E-03.**

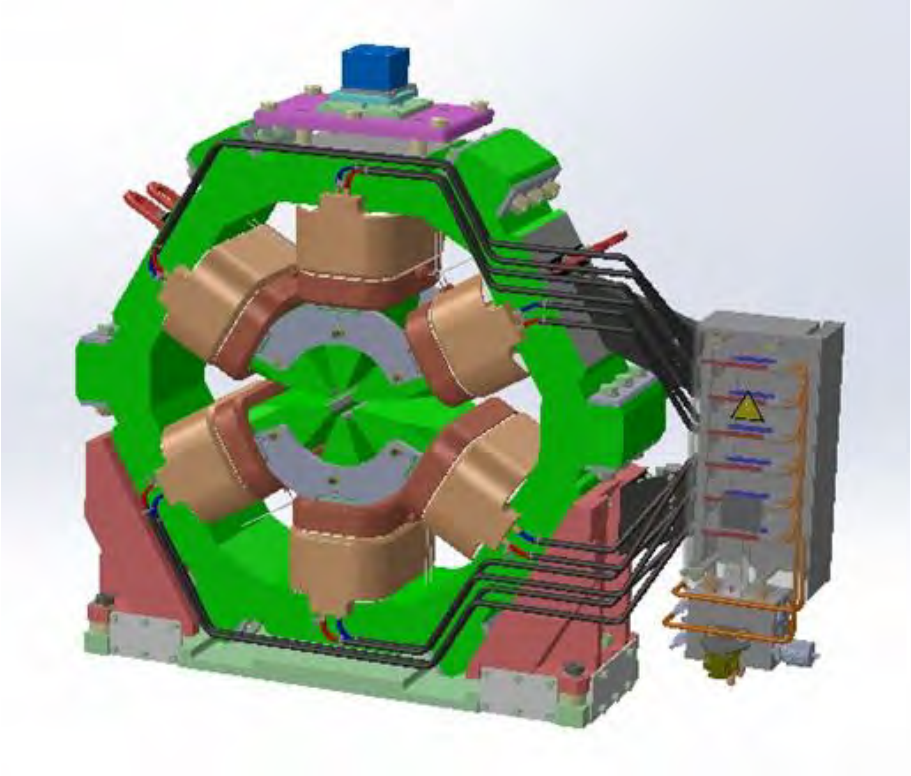

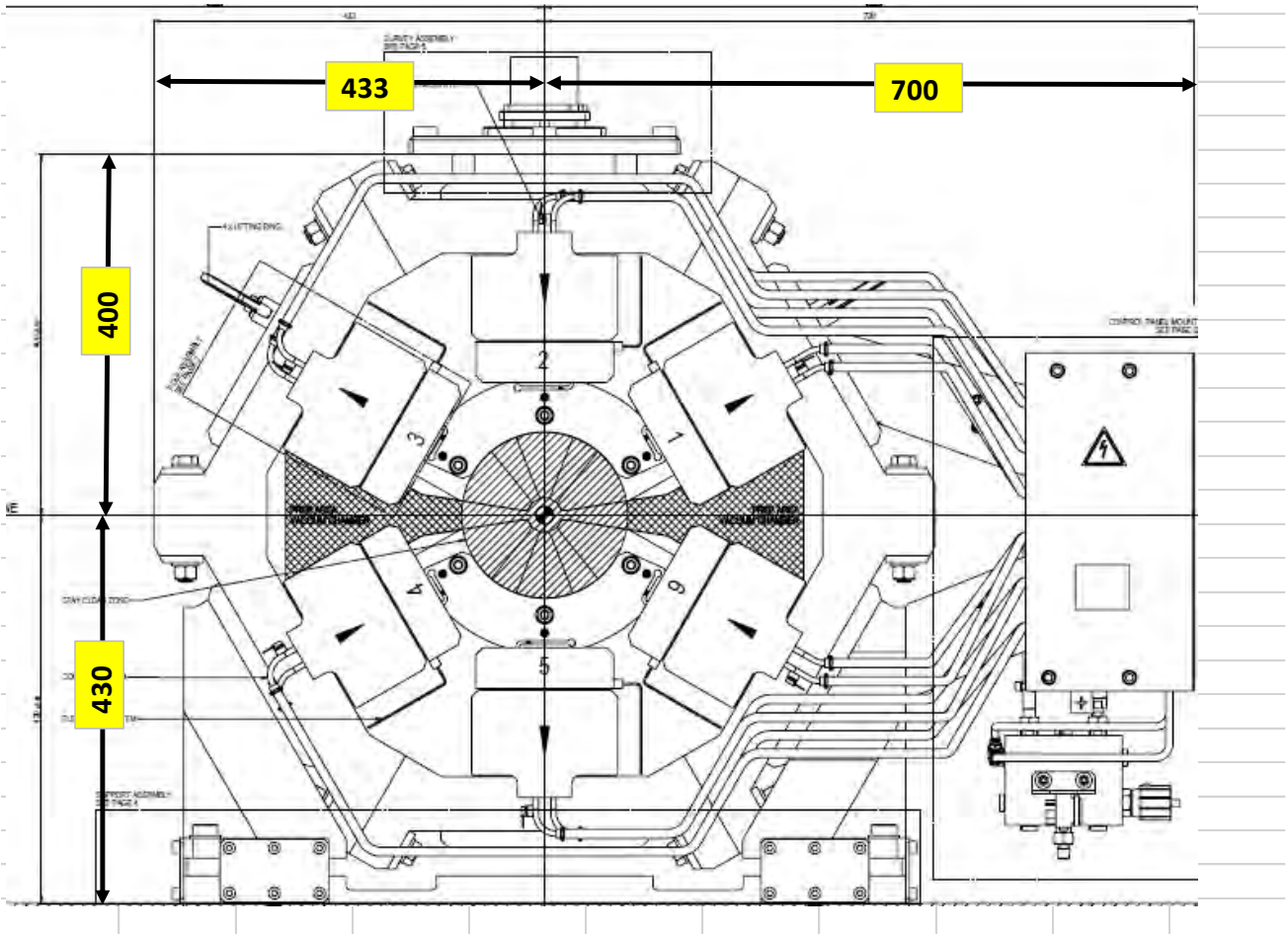
433
700
400
430
1
2
3
4
5
6

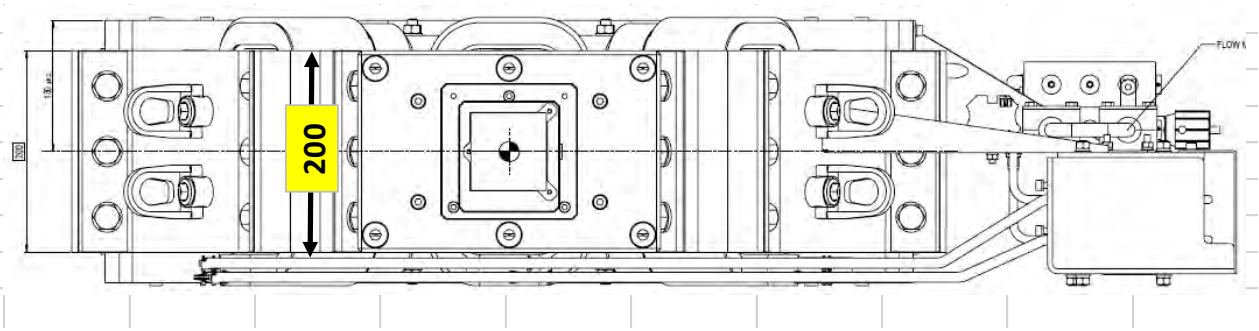


Figure 2.32: Front and top view of the SF2 sextupole.

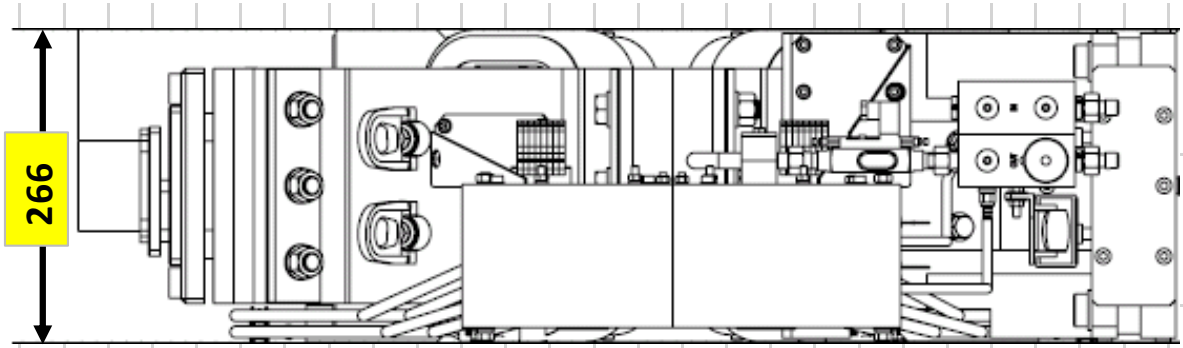


Figure 2.33: Side view of the SF2sextupole.

## 2.6 Combined DQ bending magnets

Table 2.15: Lattice specifications of the combined bending magnets DQ1 and DQ2.

| Lattice S28-D: Specifications of Combined Bending Magnet | | | | | | | | |
|---|---|---|---|---|---|---|---|---|
| Element | Length (m) | Angle (degr.) | Radius (m) | Field (T) | k-value m^-2 | Gradient (T/m) | B*L (T*m) | G*L (T) |
| | | | | | | | | |
| ML_DQ1 | 0.008506 | 0.01334 | 36.54179 | 0.54754 | | | 0.004657 | |
| DQ1 | 1.049988 | 1.64636 | 36.54106 | 0.54755 | -1.82908 | -36.6069 | 0.574919 | -38.4368 |
| ML_DQ1 | 0.008506 | 0.01334 | 36.54179 | 0.54754 | | | 0.004657 | |
| SUM= | 1.067000 | 1.673038 | | | | | 0.584234 | -38.4368 |
| ML_DQ2C_1 | 0.004237 | 0.00454 | 53.53081 | 0.37377 | | | 0.001584 | |
| ML_DQ2C_2 | 0.004237 | 0.00454 | 53.53081 | 0.37377 | | | 0.001584 | |
| DQ2 | 0.823352 | 0.8814 | 53.52222 | 0.37383 | -1.53235 | -30.6681 | 0.307790 | -25.2507 |
| ML_DQ2C_2 | 0.004237 | 0.00454 | 53.53081 | 0.37377 | | | 0.001584 | |
| ML_DQ2C_1 | 0.004237 | 0.00454 | 53.53081 | 0.37377 | | | 0.001584 | |
| SUM= | 0.840300 | 0.899542 | | | | | 0.314125 | -25.2507 |

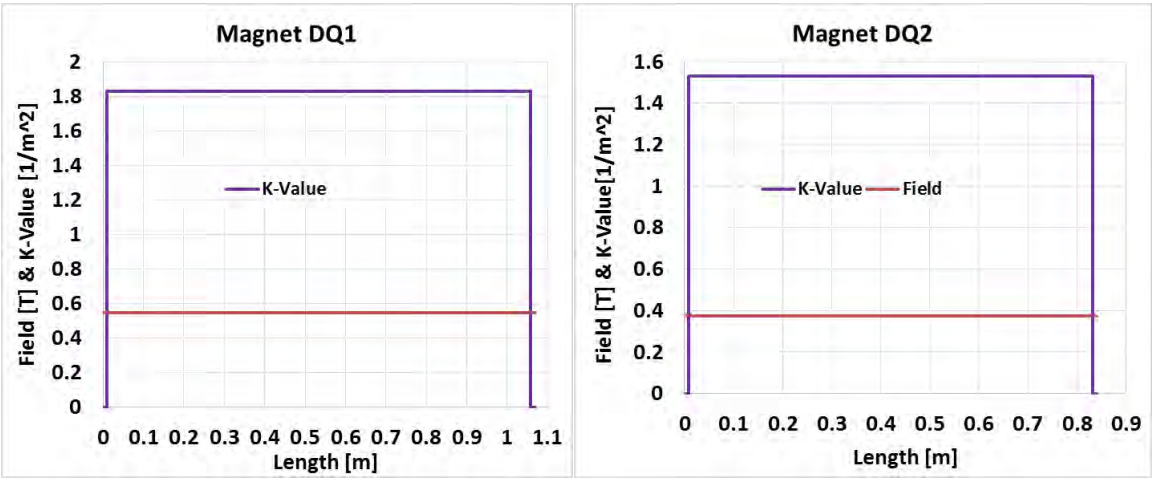


Figure 2.34: The magnetic flux density B as well the quadrupole strength k of the combined bending magnets as a function of the longitudinal direction. At the beginning and the end of the magnets the gradient is over a length of 8mm zero (see Table 2.15).

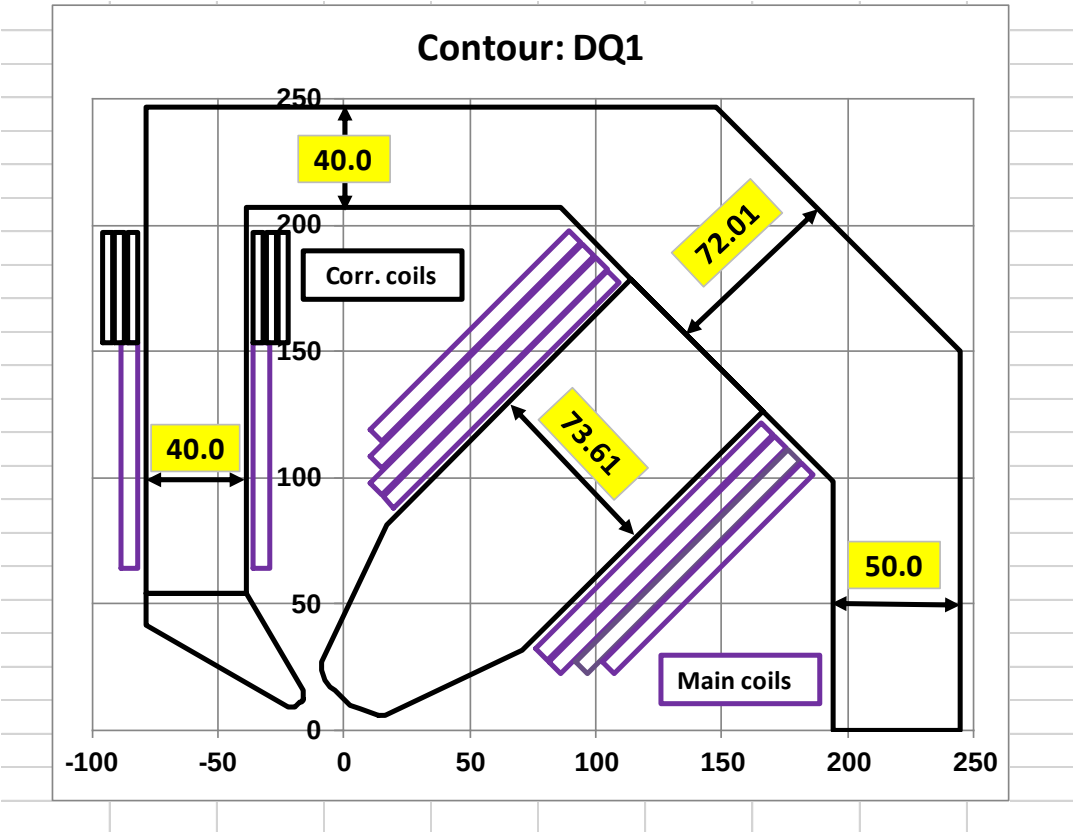


Figure 2.35: Profile of the combined bending magnets DQ1 with the main as well the correction coils.

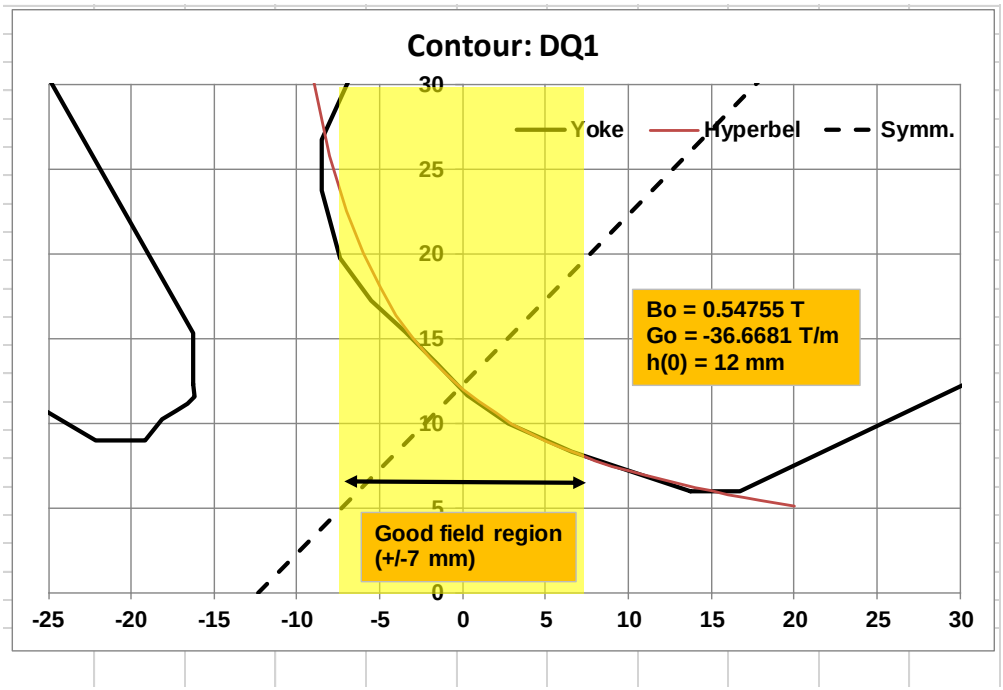


Figure 2.36: Detailed contour of the DQ1 and DQ2 poles. In comparison the hyperbolic contour is given too. The good field region is +/- 7 mm.

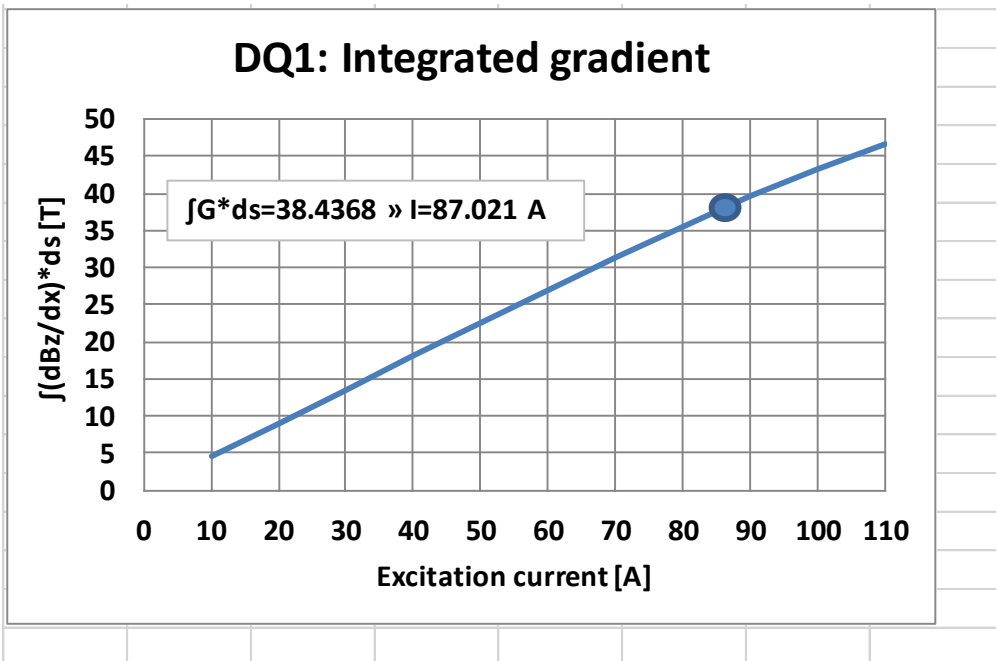


Figure 2.37: The integrated gradient as a function of the excitation current. According to the lattice an integrated gradient of 38.4368 is required. With the design value of I = 85.46 A, the corresponding integrated gradient is 37.8 T. The ration between both values is: I(Latt.)/I(Design) = 87.0211 / 85.46 = 1.0183.

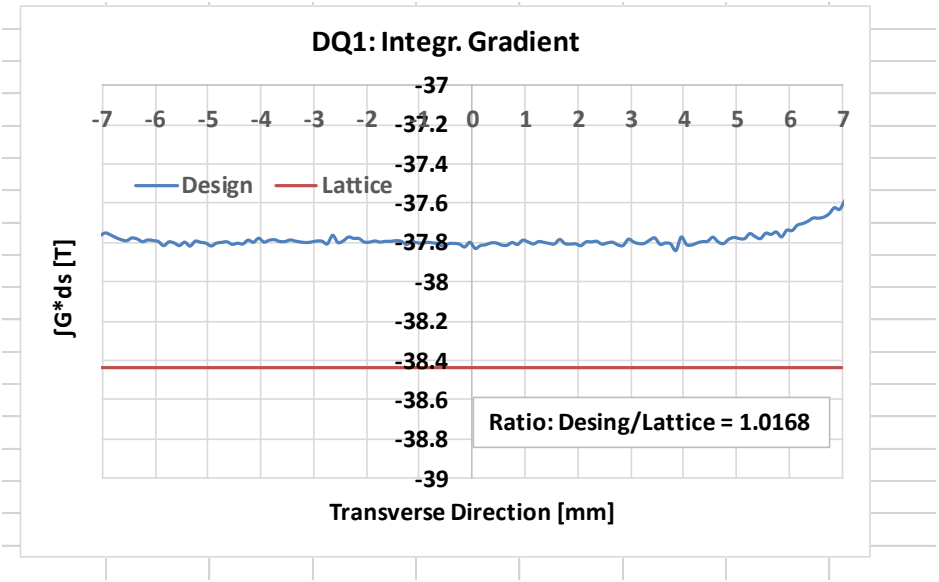


**Figure 2.38: The integrated gradient of DQ1 as a function of the transverse direction according to the design (-37.8 T) and the lattice values (-38.4368 T). In order to get the required lattice the current has to be increased by a factor of 38.4368/37.8 = 1.01685. This is roughly the same value as found in Figure 35.**

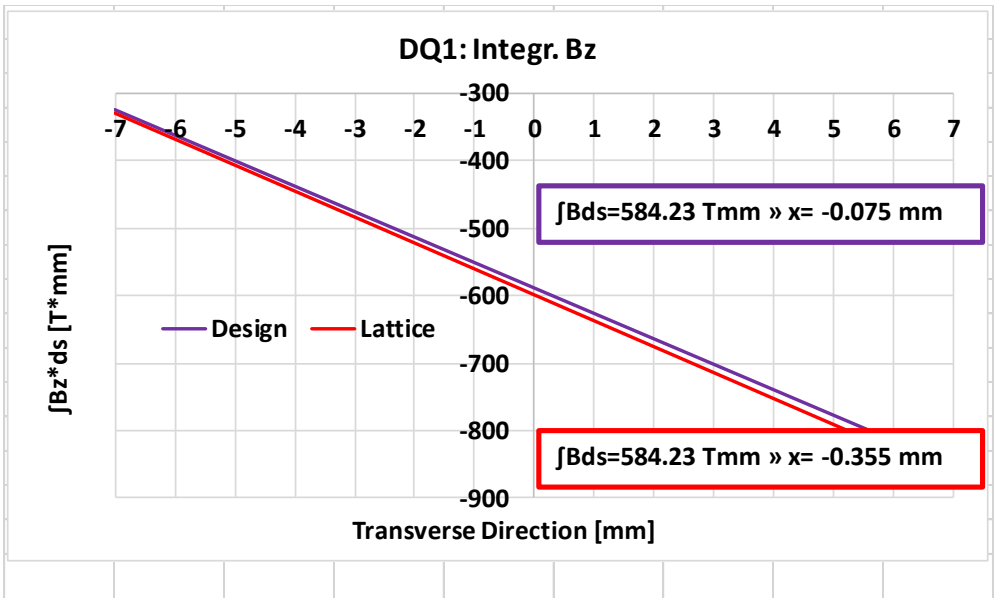


**Figure 2.39: The integrated field of DQ1 as a function of the transverse direction according for the design as well for the lattice values. In order to reach the required values given by the lattice, the magnet has to be moved by -0.355 mm.**

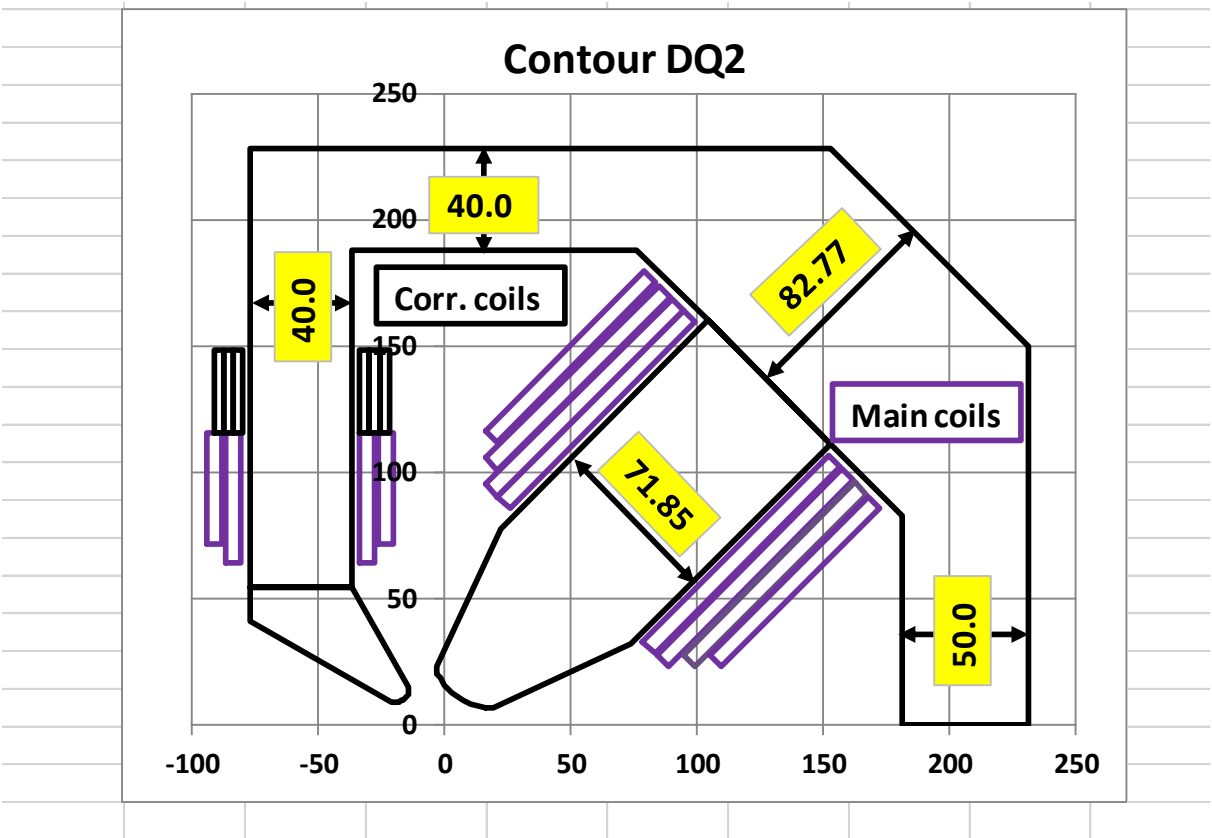


Figure 2.40: Profile of the combined bending magnets DQ2 with the main as well the correction coils.

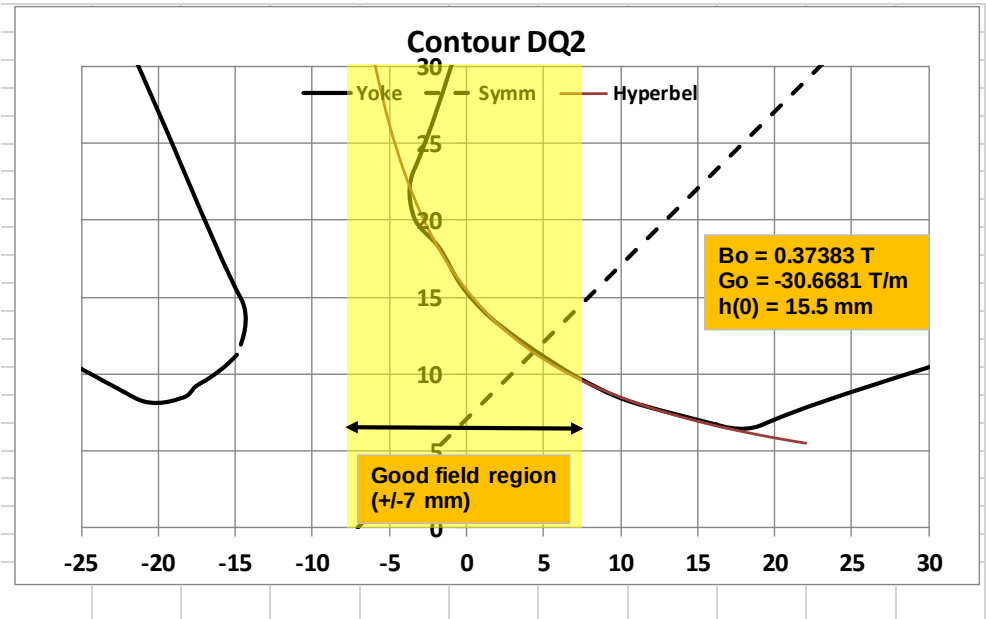


Figure 2.41: Detailed contour of the DQ2. In comparison the hyperbolic contour is given too. The good field region is +/- 7 mm.

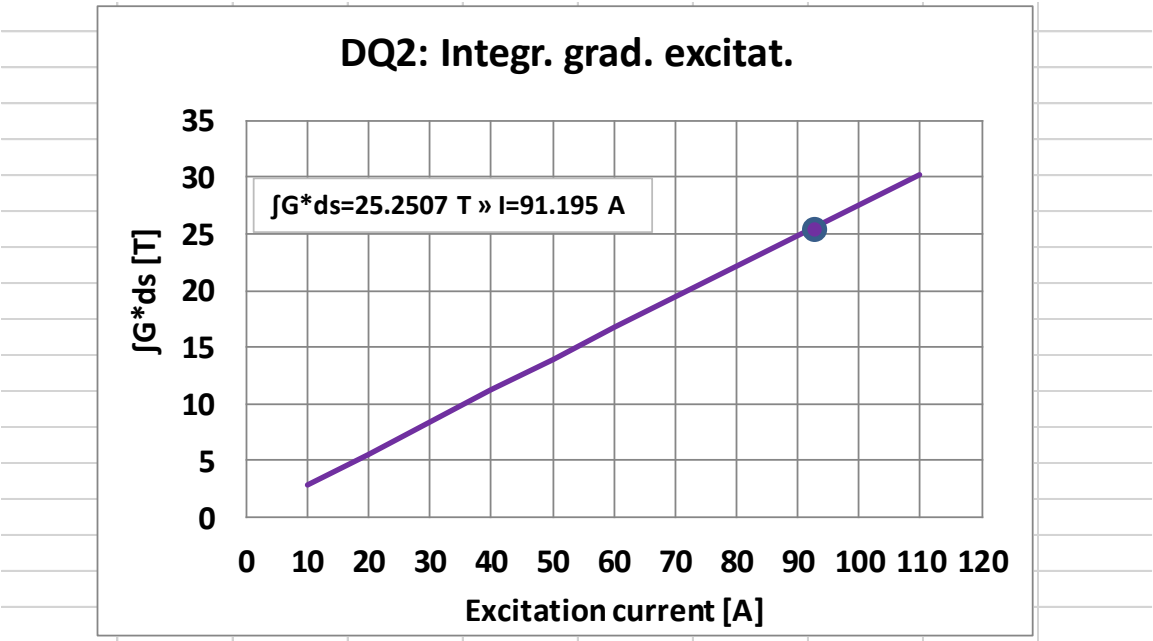


Figure 2.43: The integrated gradient as a function of the excitation current. According to the lattice an integrated gradient of 25.2507 T is required, for which an excitation current of 91.195 A is required. With the design value of I = 89.8805 A, the corresponding integrated gradient is 24.8911 T. The ration between both values is: I(Latt.)/I(Design) = 91.195 / 89.8805 = 1.0146 and 25.2507/24.8911 = 1.0144.

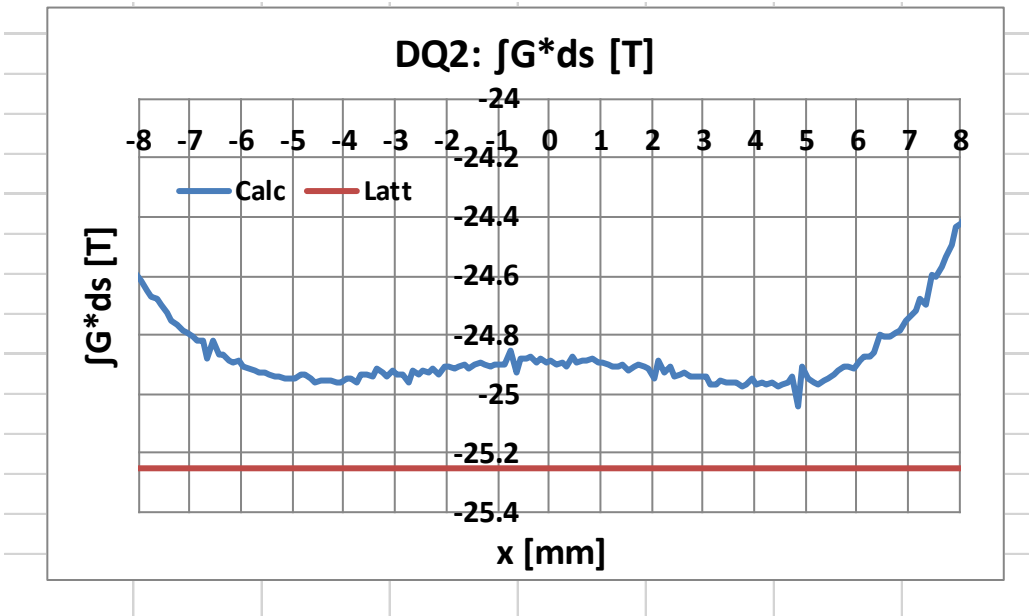


Figure 2.44: The integrated gradient of DQ2 as a function of the transverse direction. The design (Calc.) gives over a range of +/- 1mm a value of -24.8912 T and the lattice value is 25.2507 T. In order to get the required lattice, the current has to be increased by a factor of 25.2507/24.8912 = 1.0144. This is the same value as found in Figure 2.43.

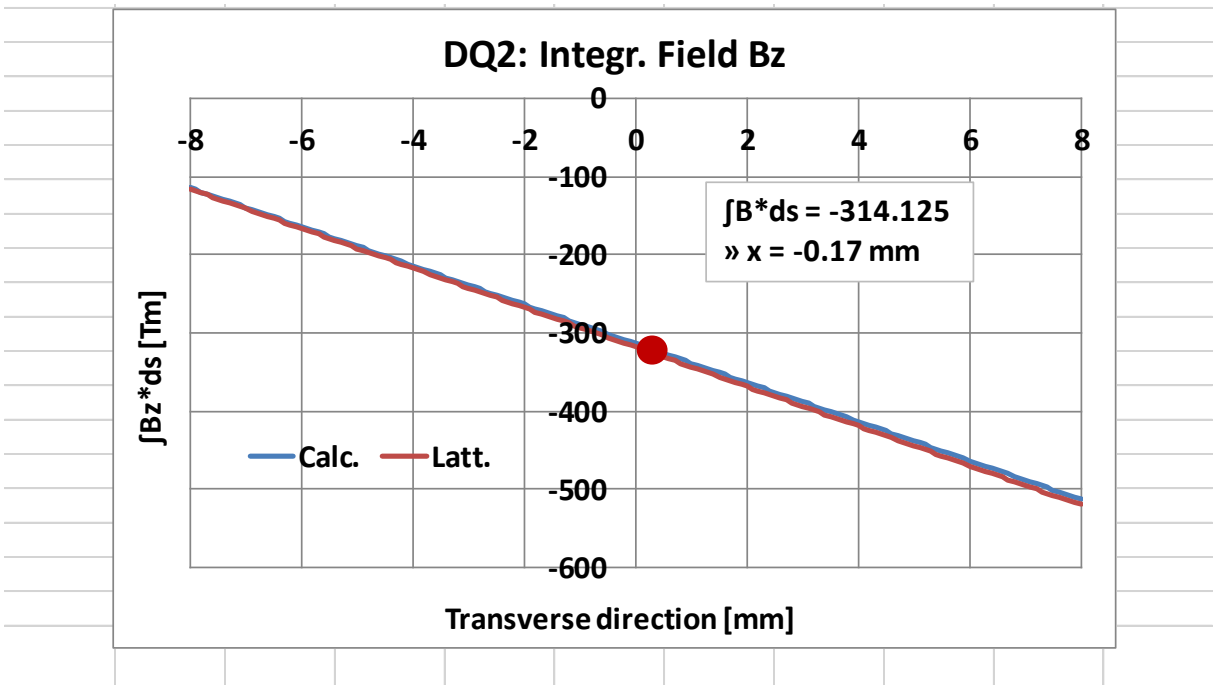


Figure 2.45: The integrated field of DQ2 as a function of the transverse direction for the design as well for the lattice values. In order to reach the required values given by the lattice, the magnet has to be moved by -0.17 mm.

Table 2.16: Conductor parameters for the combined bending magnets DQ1 and DQ2.

| **Section** | **6.5 x 6.5** | **mm** |
|---|---|---|
| **Pipe diameter** | 4 | mm |
| **Copper resistivity** | $1.78*10^{-8}$ | Ohm m |
| **Insulation** | 0.5 | mm |
| **Conductor area** | 28.67 | $mm^2$ |
| **Material** | AISI 1006 | |
| **Type of magnet** | SOLID | |
| **Stacking factor** | 1 | |

Table 2.17: Electrical and winding parameters of DQ1 and DQ2.

| Magnet | DQ1 | DQ2 |
|---|---|---|
| **Current [A]** | 87.021 | 91.195 |
| **Turns (main)** | 65 | 53 |
| **Turns (aux. )** | 12 | 13 |
| **Amp turns [kA turns]** | 6.7 | 6.02 |
| **Cond. length [m]** | 351.5 | 253.3 |
| **Resistance [mΩ]** | 221 | 160 |
| **Voltage [V]** | 19.2 | 14.6 |
| **Power [kW]** | 1.67 | 1.31 |
| **Current density [A/mm2]** | 3.04 | 3.33 |

Table 2.18: Mechanical parameters of DQ2 and DQ2.

| Magnet | DQ1 | DQ2 | |
|---|---|---|---|
| **Radius of curvature** | 36.541 | 53.522 | m |
| **Vertical gap (outside)** | 18.06 | 16.81 | mm |
| **Vertical gap (inside)** | 11.96 | 13.35 | mm |
| **Iron length** | 1028 | 800 | mm |
| **Magnetic length (field)** | 1067 | 840.3 | mm |
| **Magnetic length (gradient)** | 1050 | 823.35 | |
| **Overall length** | 1097 | 869 | mm |
| **Magnet height** | 494 | 456 | mm |
| **Magnet mass** | 900 | 640 | kg |

Table 2.19. Water cooling parameters for each cooling circuit.

| | DQ1 | DQ2 | |
|---|---|---|---|
| **Coils in series** | 1 | 1 | |
| **Cooling circuits** | 2 | 2 | |
| **Pressure drop** | 7.2 | 7.2 | bar |
| **Water flow** | 0.63 | 0.76 | l/min |
| **Water velocity** | 0.84 | 1.01 | m/s |
| **Temperature rise** | 18.95 | 12.5 | K |
| **Reynold number** | 3350 | 4070 | |

Table 2.20: Standard deviation of systematic multipoles expressed at 7 mm.

DQ1

| **n:** | **1** | **2** | **3** | **4** | **5** | **6** | **7** | **8** | **9** | **10** |
|---|---|---|---|---|---|---|---|---|---|---|
| **σ(bn)** | 10000 | 4499.22 | 1.32 | -3.52 | -1.38 | 9.24 | 1.06 | -10.15 | -3.14 | 2.66 |
| **n:** | 11 | 12 | 13 | 14 | 15 | 16 | 17 | 18 | 19 | 20 |
| **σ(bn)** | 2.21 | -0.08 | -1.00 | -0.53 | 0.1 | 0.23 | 0.1 | -0.03 | -0.04 | -0.01 |

DQ2

| **n:** | **1** | **2** | **3** | **4** | **5** | **6** | **7** | **8** |
|---|---|---|---|---|---|---|---|---|
| **σ(bn)** | 10000 | 5532.12 | -0.64 | 25.81 | 5.20 | -17.26 | -5.61 | -3.14 |
| **n:** | 9 | 10 | 11 | 12 | 13 | 14 | 15 | 16 |
| **σ(bn)** | 0.70 | 0.59 | -0.02 | -0.09 | -0.1 | 0.13 | 0.1 | 0.07 |

Table 2.21: Standard deviation of random multipoles expressed at 7 mm for +/- 0.05 mm tolerances. DQ1

| n: | 1 | 2 | 3 | 4 | 5 | 6 | 7 | 8 | 9 | 10 |
|---|---|---|---|---|---|---|---|---|---|---|
| σ(bn) | 90.18 | 43.36 | 17.0 | 8.91 | 4.57 | 3.55 | 2.43 | 1.13 | 0.94 | 0.55 |

| n: | 11 | 12 | 13 | 14 |
|---|---|---|---|---|
| σ(bn) | 0.30 | 0.21 | 0.1 | 0.07 |

DQ2

| n: | 1 | 2 | 3 | 4 | 5 | 6 | 7 | 8 |
|---|---|---|---|---|---|---|---|---|
| σ(bn) | 52.16 | 33.79 | 11.46 | 4.18 | 2.53 | 1.42 | 0.77 | 0.42 |

| n: | 9 | 10 | 11 | 12 | 13 | 14 |
|---|---|---|---|---|---|---|
| σ(bn) | 0.25 | 0.16 | 0.08 | 0.05 | 0.04 | 0.05 |

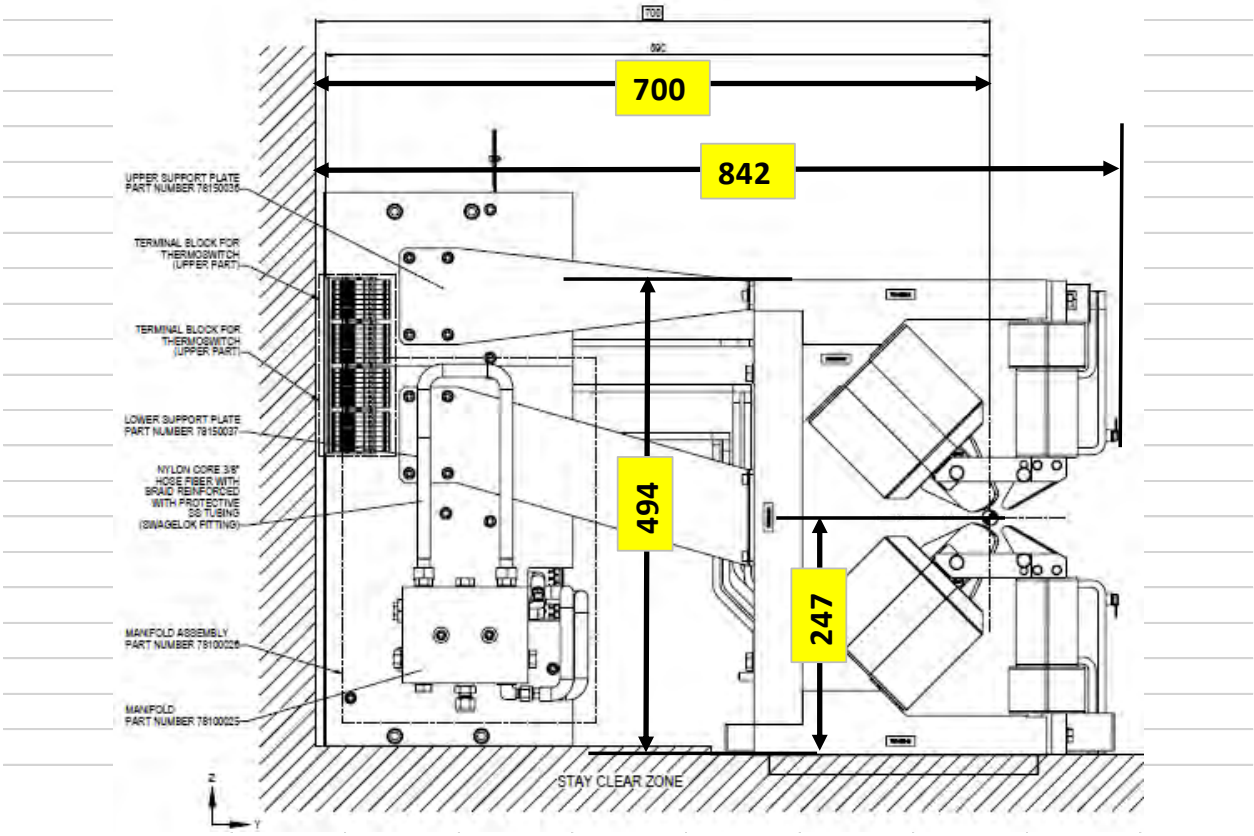


Figure 2.46: Front view of the combined bending magnet DQ1. The dimensions for the DQ2 are the same.

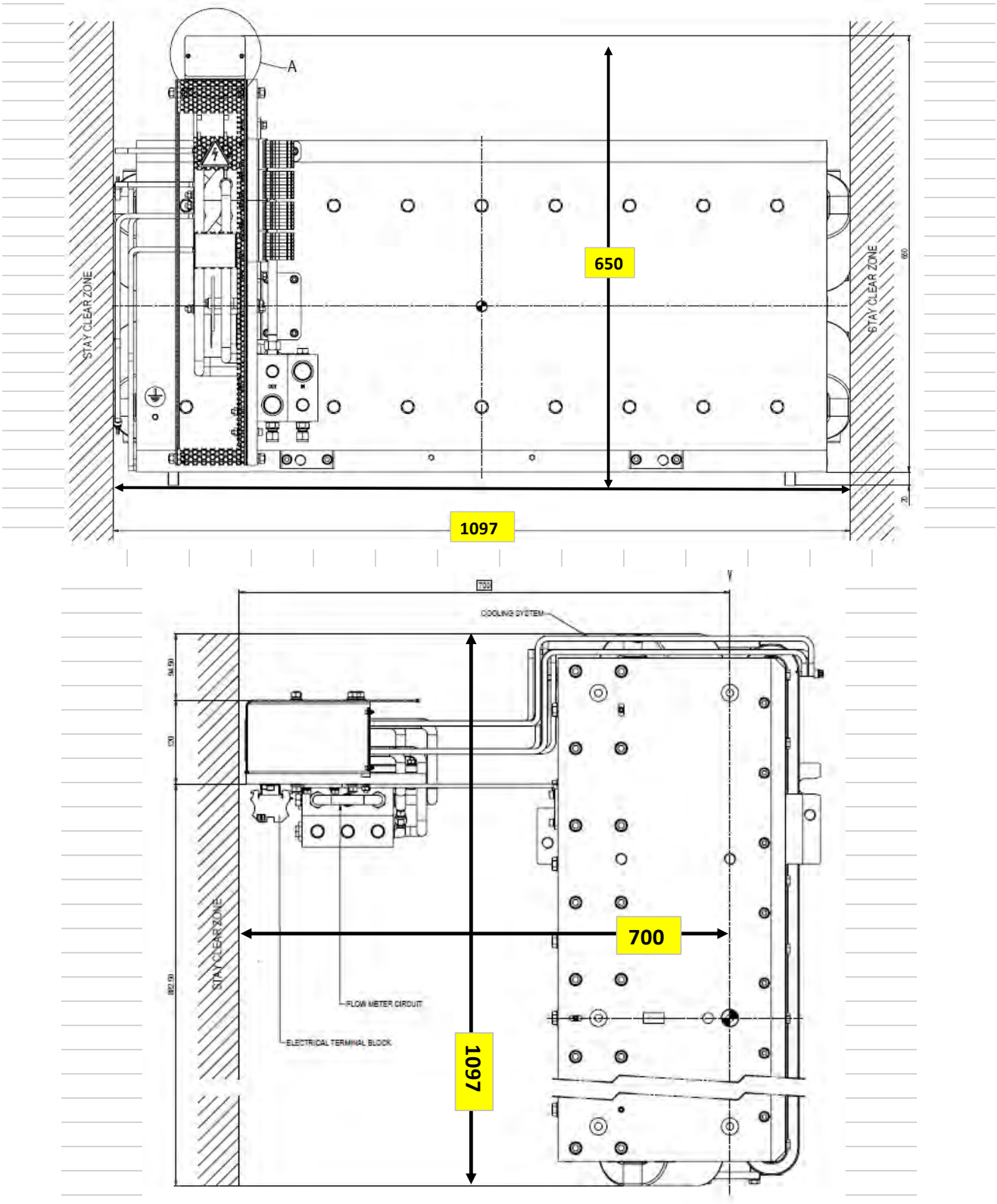


**Figure 2.47: Side and top view of the combined bending magnet DQ1. The dimensions for the DQ2 are the same; the length is different**

## 2.7 Octupoles

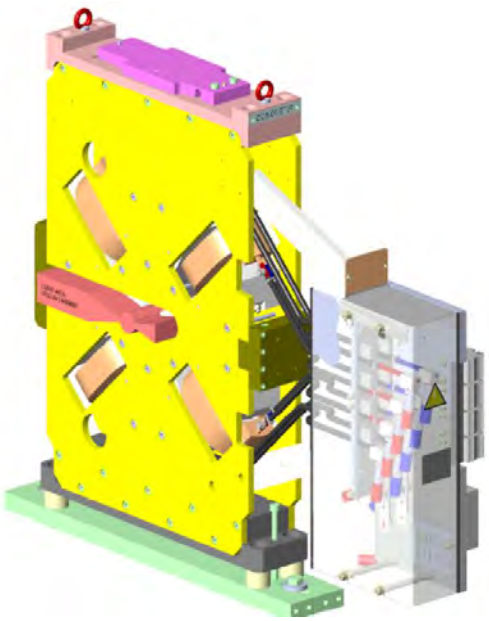

Figure 2.48: 3D view of the octupole.

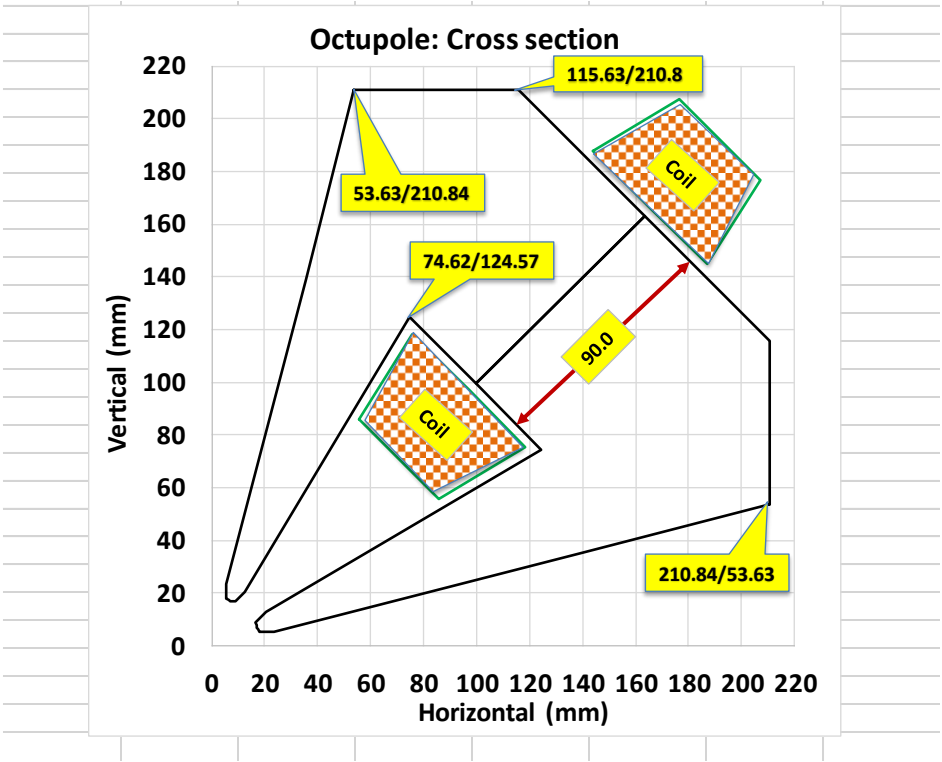


Figure 2.49: Cross section of the octupole (1 quarter) with the coordinates of the different points given in x/y.

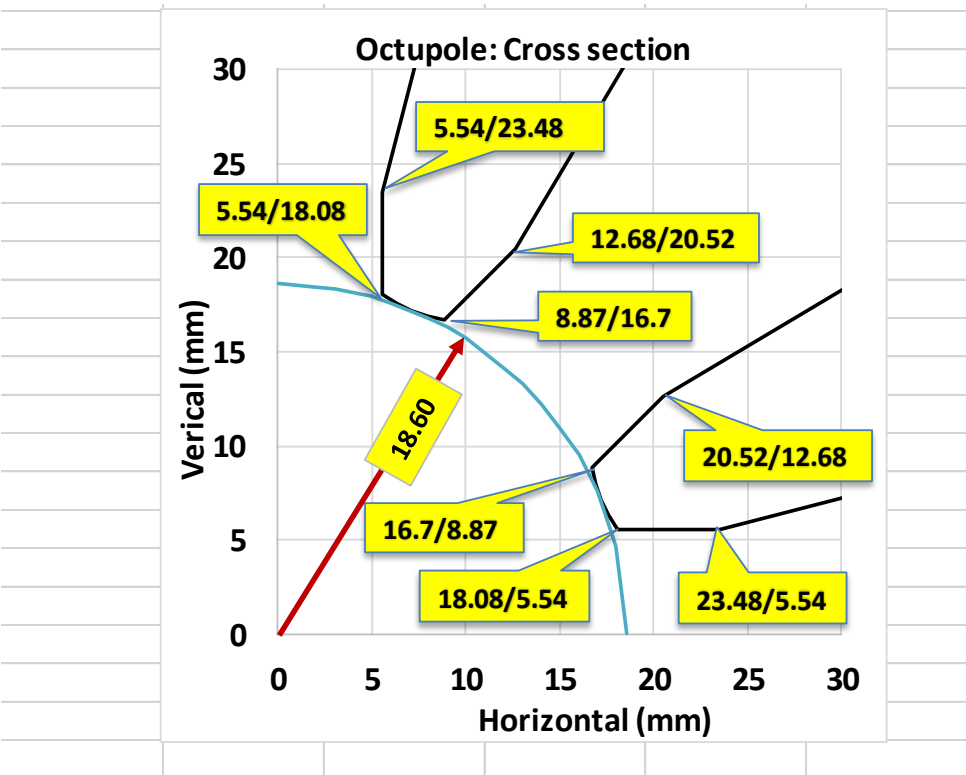


Figure 2.50: The pole coordinates of the octupole given in x/y.

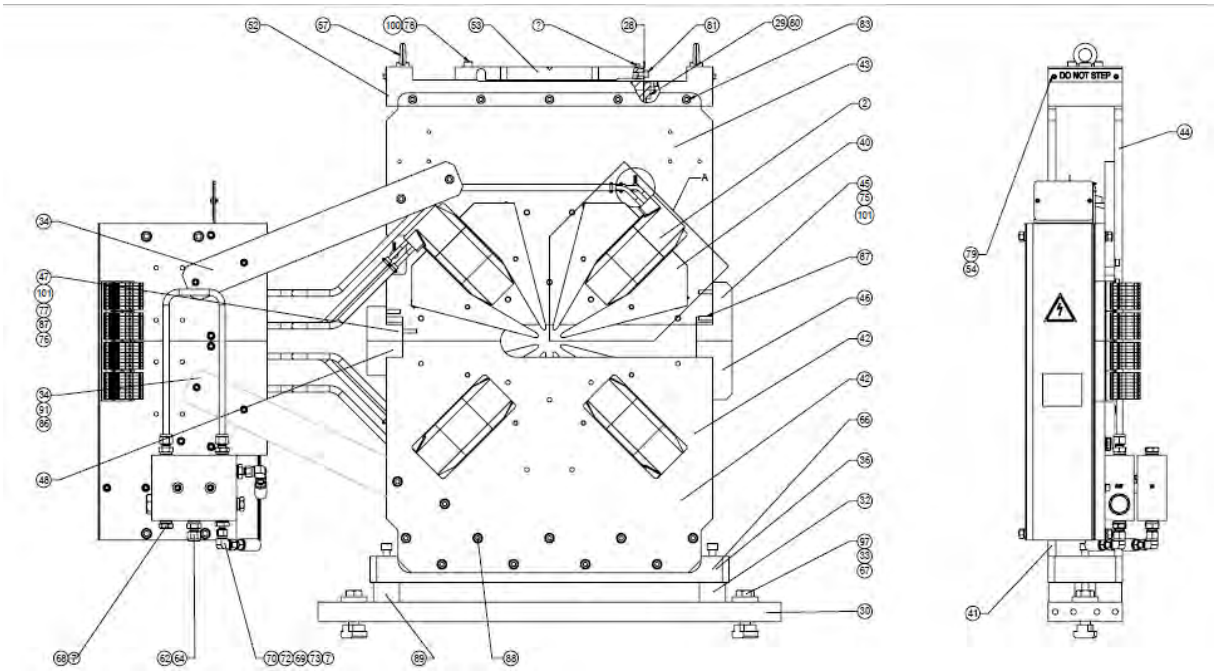

Figure 2.51: The front view of the octupole.

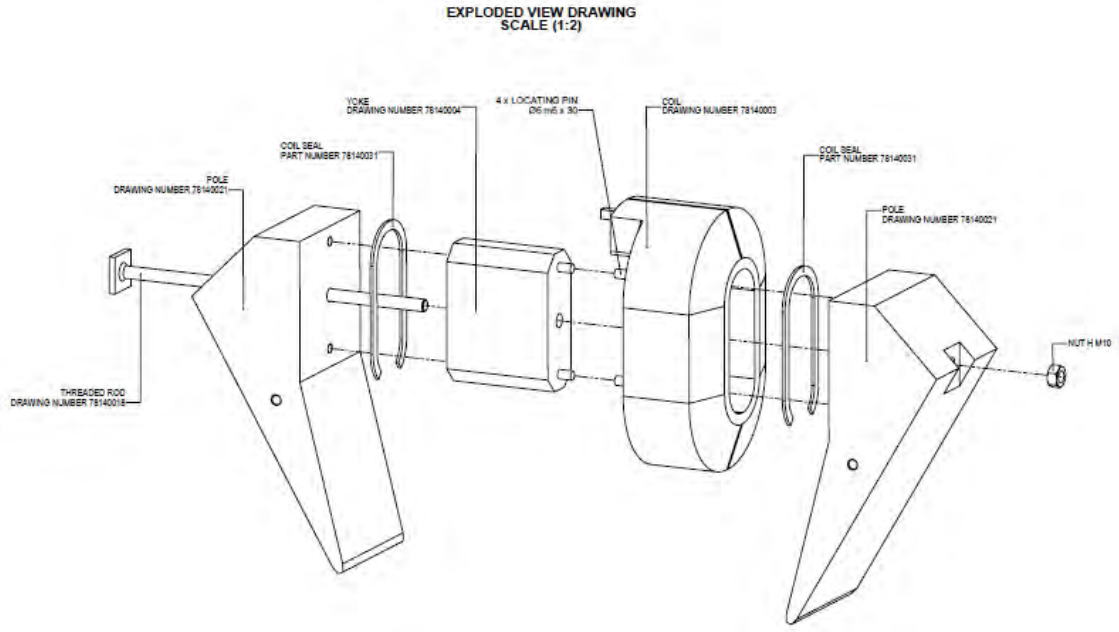


**Figure 2.52: The assembly procedure for the 2 poles and the coil of the octupole.**

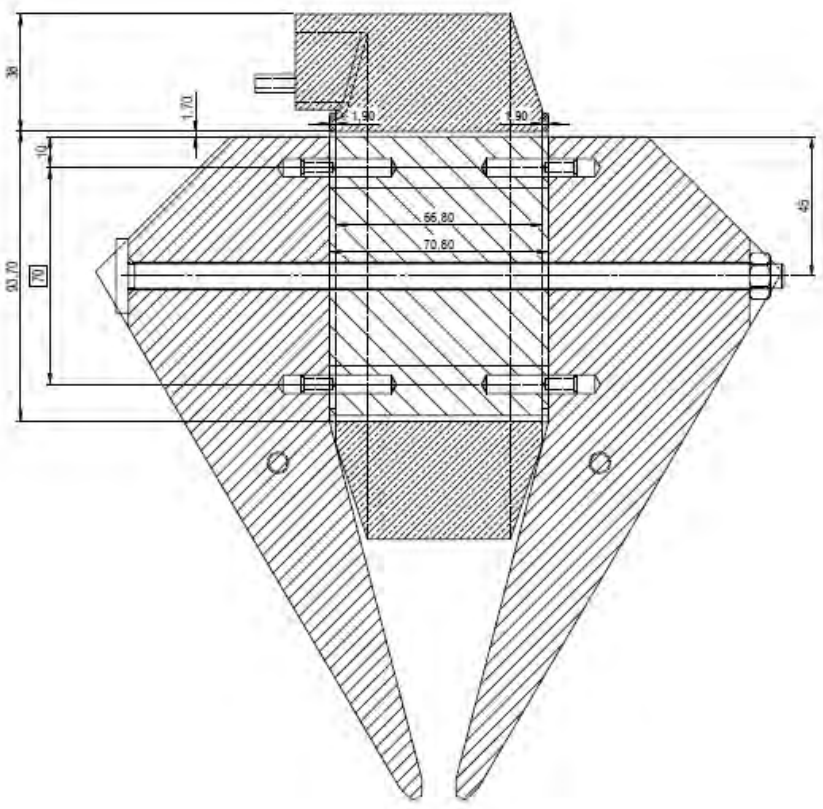


**Figure 2.53: The dimensions of the intersection between the poles.**

**Table 2.22: The parameters of the octupole.**

| List of parameters | Max.-Curr. | Nom.- Curr. |
|---|---|---|
| Bore radius [mm] | 18.6 | 18.6 |
| Yoke length [mm] | 90 | 90 |
| Totale Length [mm] | 114 | 114 |
| Current [A] | 104 | 53.4 |
| Integrated B'' [T/m^2] | 7013.5 | 3598 |
| Center field gradient B'' [T/m^3] | 71795 | 36868 |
| Magnetic length [mm] | 97.69 | 97.59 |
| Gap between poles [mm] | 11.08 | 11.08 |
| Number of A.turns/coil | 3744 | 1922.4 |
| Number of turns/coil | 36 | 36 |
| Conductor length/coil [m] | 12.8 | 12.8 |
| Total electrical resistance [mOhm] | 31.04 | 31.04 |
| Total Inductance [mH] | 21.61 | 11.11 |
| Input Voltage [V] | 3.23 | 1.66 |
| Power [W] | 335.73 | 88.51 |
| Current density in copper [A/mm^2 | 3.70 | 1.90 |
| Conductor width [mm] | 6 | 6 |
| Conductor height [mm] | 6 | 6 |
| Hole diameter [mm] | 3 | 3 |
| Corner radius [mm] | 1 | 1 |
| Copper cross section [mm^2] | 28.07 | 28.07 |
| Pressure drop [bar] | 7.2 | 7.2 |
| Number of coils in serie [] | 4 | 4 |
| Water speed [m/s] | 1.57 | 1.57 |
| Water flow /circuit [l/mn] | 0.7 | 0.7 |
| Water flow/magnet [l/mn] | 0.7 | 0.7 |
| Temperature elevation/circuit [K] | 7.4 | 1.9 |

Table 2.23: The higher multipoles of the octupole.

| Hamonic analysis (refer.-rad. 13 mm) | |
|---|---|
| | |
| n | (Bn/B4)*10000 |
| 4 | 10000 |
| 12 | -165.52 |
| 20 | 1.96 |
| 28 | 0.05 |
| 36 | -0.009 |

## 2.8 Corrector magnets

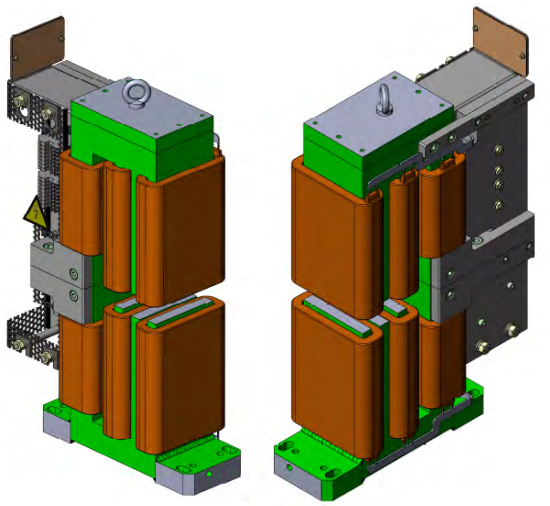

Figure 2.54: 3D view of the corrector.

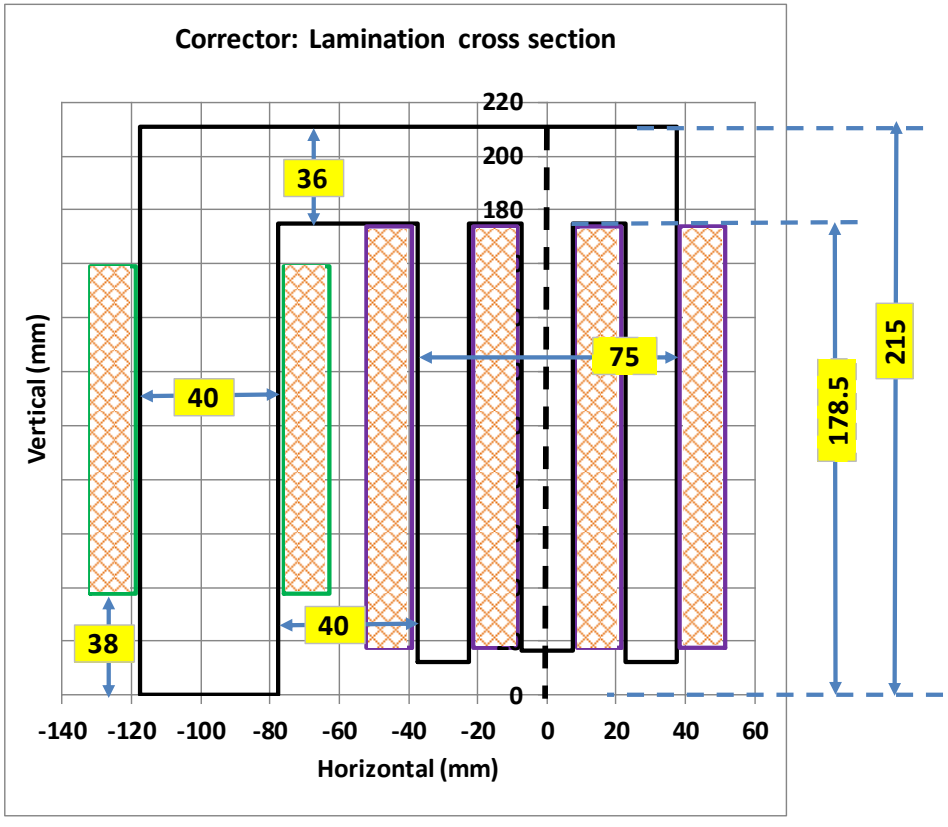


Figure 2.55: The cross section of the corrector with the main dimensions.

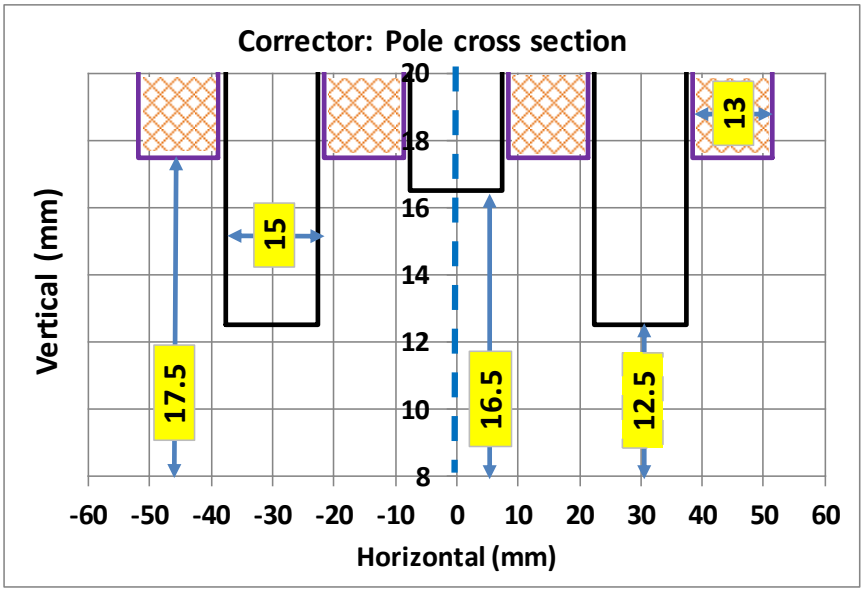


Figure 2.56: The pole dimensions of the corrector.

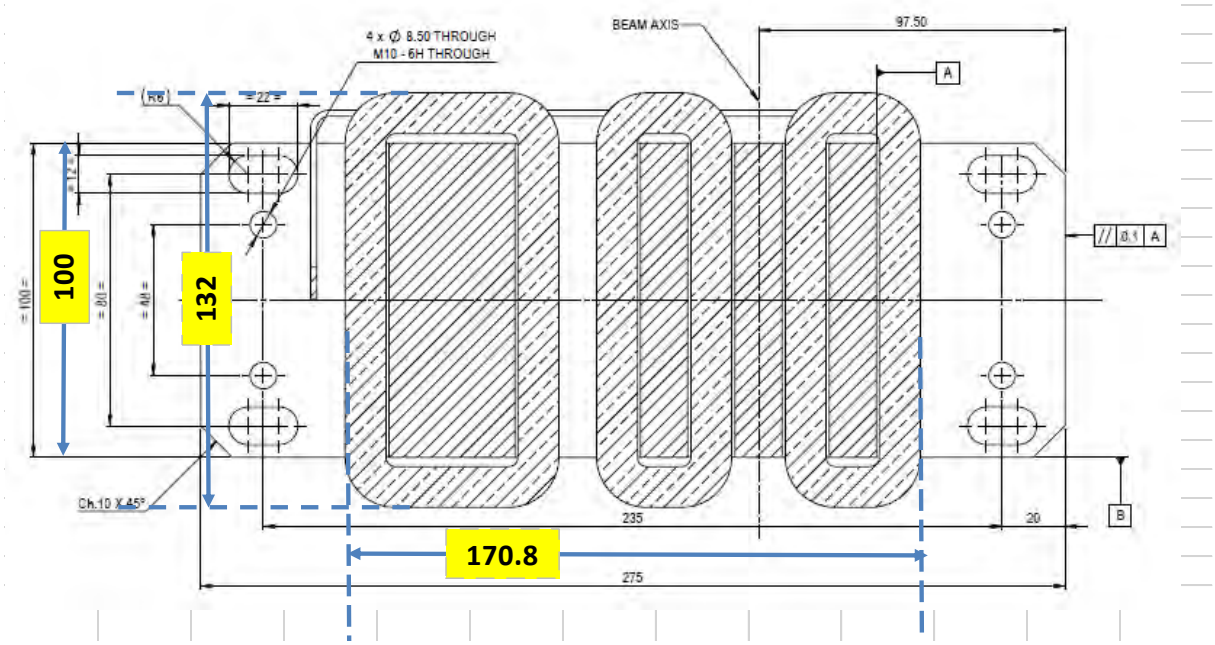


Figure 2.57: The overall dimensions of the corrector.

Table 2.24: The parameters of the corrector.

| Parameter | Correct. | |
|---|---|---|
| Vertical integrated dipole | 10 | T.mm |
| Horizontal integrated dipole | 10 | T.mm |
| Skew integrated quadrupole | 0.12 | T |
| Mechanical length | 100 | mm |
| Gap | 25 | mm |
| Overall width | 450 | mm |
| Overall height | 523.2 | mm |
| Overall length | 150 | mm |
| Nominal current | 2 | A |
| Electrical resistance coil1 | 2,5 | Ω |
| Voltage coil1 | 5 | V |
| Inductance coil1 | 0.98 | H |
| Electrical resistance coil2 | 2 | Ω |
| Voltage coil2 | 4 | V |
| Inductance coil2 | 0.94 | H |
| Power loss per coil1 | 10 | W |
| Power loss per coil2 | 8 | W |
| Copper conductor size | 2x0.9 | $mm^2$ |
| Corner radius | 2 | mm |
| Number of turns for coil1 | 900 | turns |
| Number of turns per coil2 | 620 | turns |
| Number of pre-series magnets | 2 | |
| Number of series magnets | 96 | |

## 2.9 Permanent magnets

In order to decrease the emittance there is a longitudinal gradient introduced in the bending magnets and to reduce the electricity consumption permanent magnet will be used. The ESRF-EBS is the first light source using a longitudinal gradients for the bending magnets and build it up with permanent magnets. The longitudinal gradient will be made in steps, which means the magnet has to be build up in modules, per magnet 5 modules will be used. For the permanent magnets the material Sm2Co17 will be used and the field varies between 0.16 T and 0.65 T. A model of the permanent magnet is presented in Figure 2.58. The field parameters according to the lattice S-28D are given in Table 2.25 and in Figure 2.58.

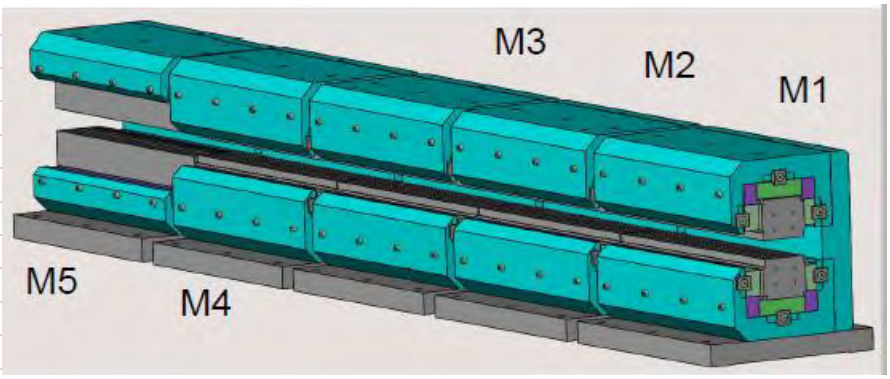


Figure 2.58: 3D view of the permanent bending magnet DL buildup with the 5 modules M1 to M5. As shown in the figure, the module M5 is different from the other ones.

Table 2.25: The parameters of the different modules of the permanent magnet. The location of DL1 and DL2 is given in Figures 2.24 to 2.27.

| Lattice S28-D | | | | |
|---|---|---|---|---|
| Element | L-Latt. (m) | Defl.-Angle (degrees) | Radius (m) | Field (T) |
| | | | | |
| DL1A_5 | 0.380438 | 0.680507 | 32.0313 | 0.62481 |
| DL1A_4 | 0.350447 | 0.412651 | 48.6589 | 0.41130 |
| DL1A_3 | 0.357397 | 0.308684 | 66.3375 | 0.30169 |
| DL1A_2 | 0.365037 | 0.236859 | 88.3018 | 0.22665 |
| DL1A_1 | 0.372210 | 0.178285 | 119.6178 | 0.16731 |
| | | | | |
| DL2B_1 | 0.371770 | 0.186417 | 114.2645 | 0.17515 |
| DL2B_2 | 0.365930 | 0.238128 | 88.0461 | 0.22731 |
| DL2B_3 | 0.356152 | 0.303794 | 67.1705 | 0.29795 |
| DL2B_4 | 0.348205 | 0.381945 | 52.2344 | 0.38315 |
| DL2B_5 | 0.383772 | 0.574921 | 38.2462 | 0.52328 |

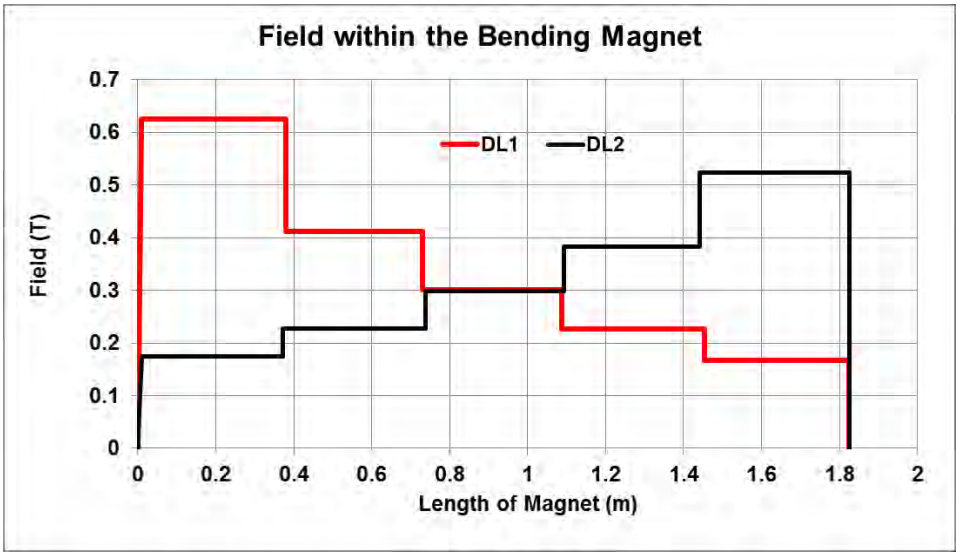


**Figure 2.59: Field distribution within the bending magnets DL1 and DL2 according to the data given in Table 2.25.**

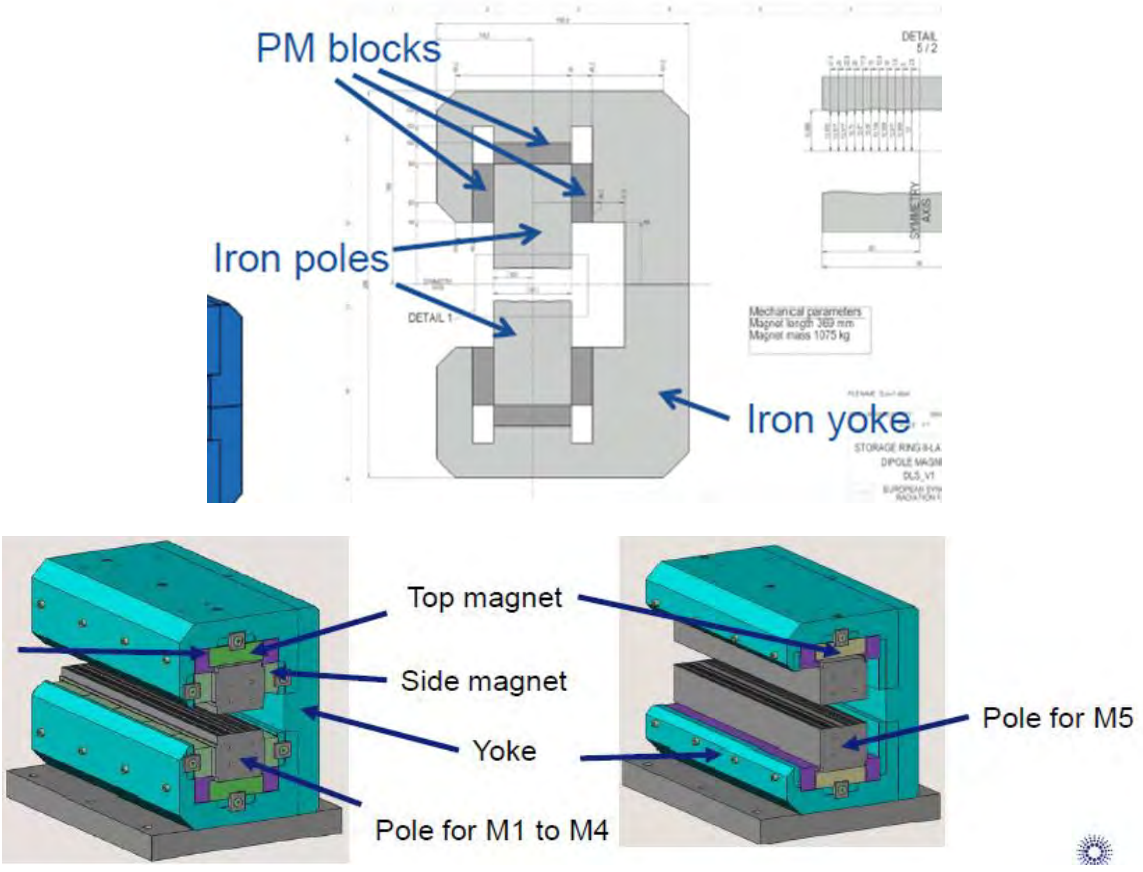


**Figure 2.60: The different components used for the modules M1 to M4 and M5.**

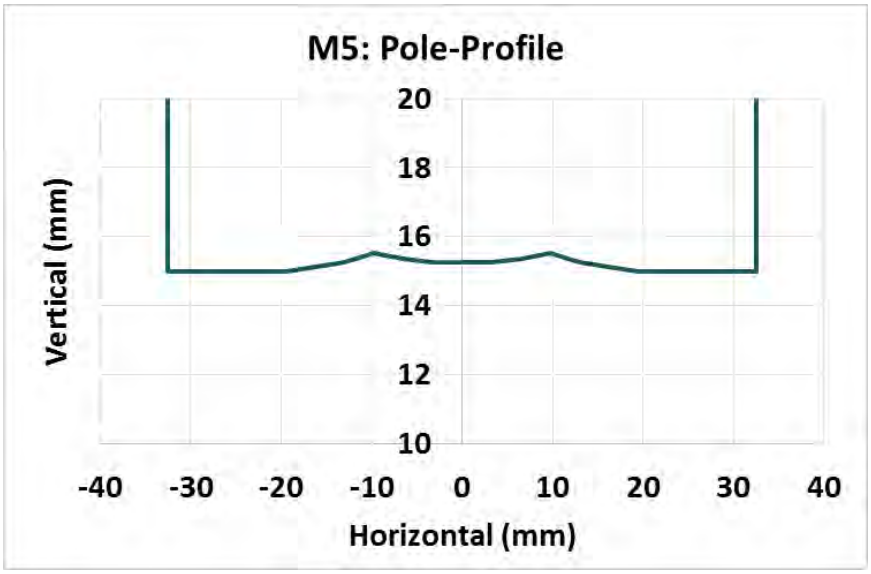


Figure 2.61: The profile of the poles for the module M5.

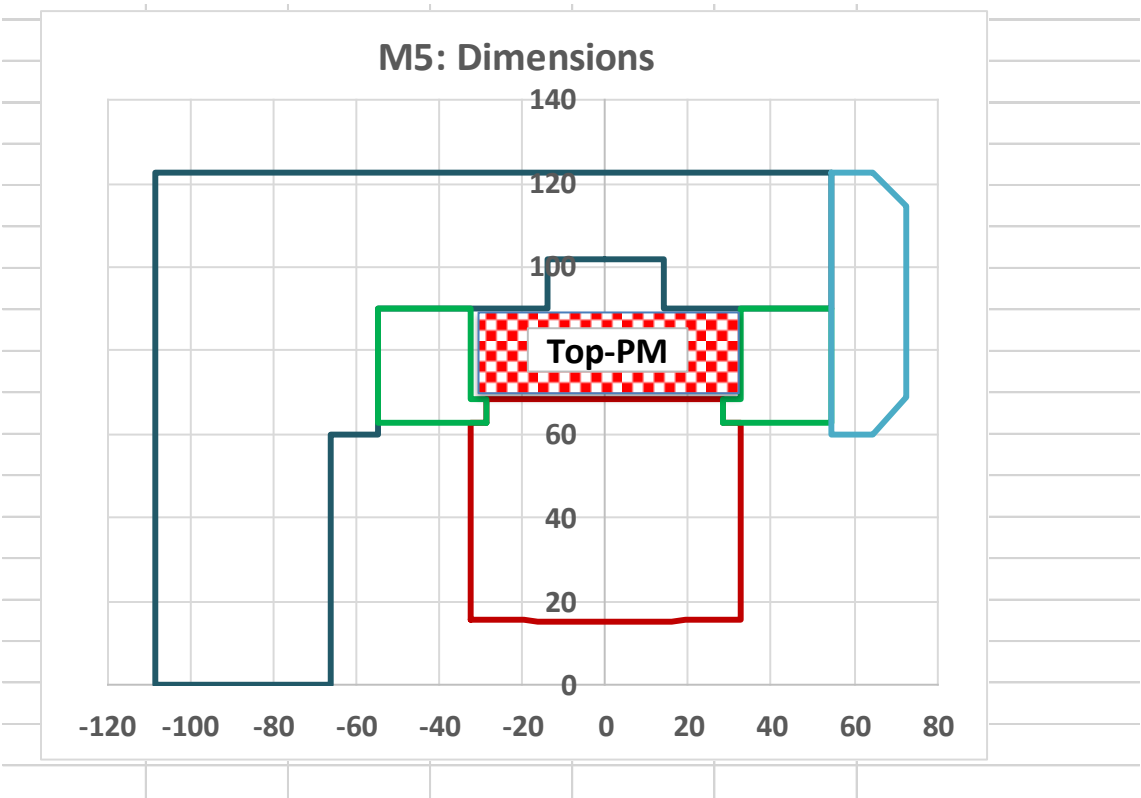


Figure 2.62: Dimensions of the module M5 with the location of the 'top permanent magnet'. The surroundings of the pole are given by a brown line.

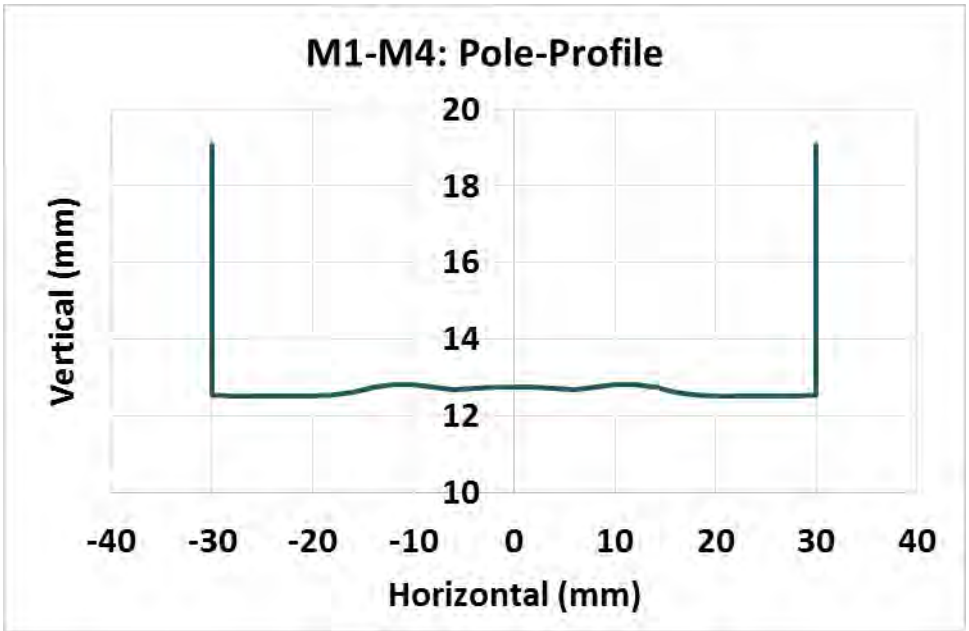


Figure 2.63: The profile of the poles for the module M1 – M4.

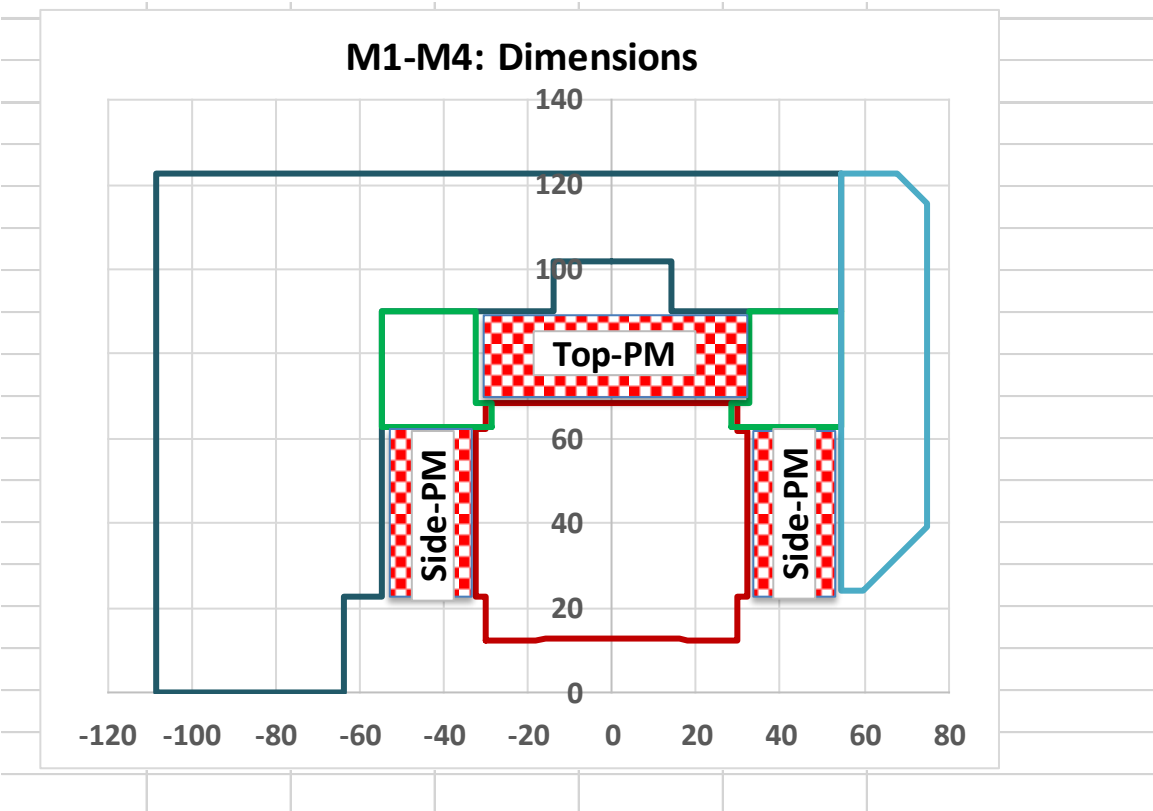


Figure 2.64: Dimensions of the module M1 – M4 with the location of the 'top and side permanent magnets'. The surroundings of the pole are given by a brown line.

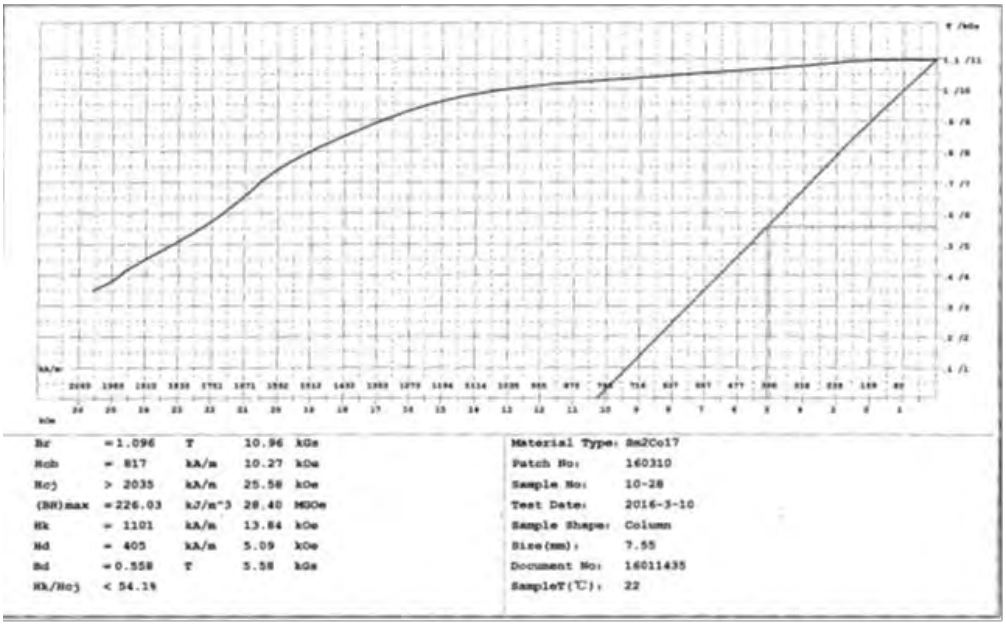


Figure 2.65: The hysteresis curve of $Sm_2Co_{17}$.

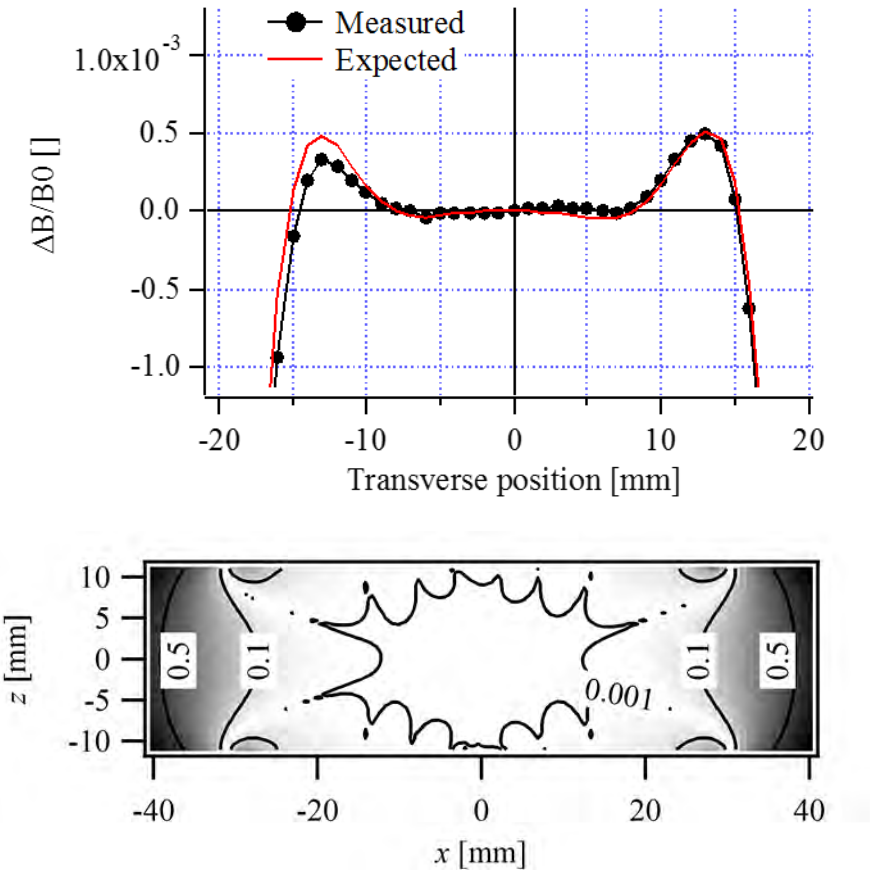


Figure 2.66: The field homogeneity (above) and the integrated field homogeneity for 2 modules (below).

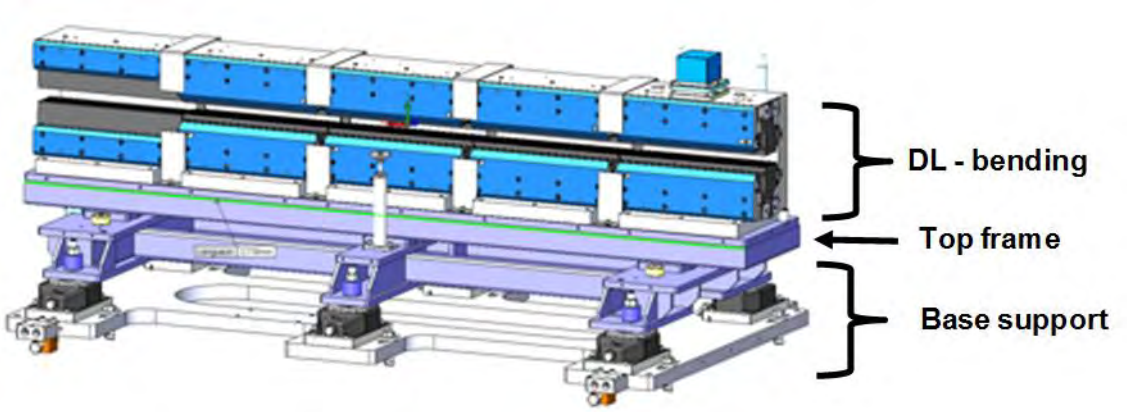


Figure 2.67: The bending magnet Dl with the top plate and its support.

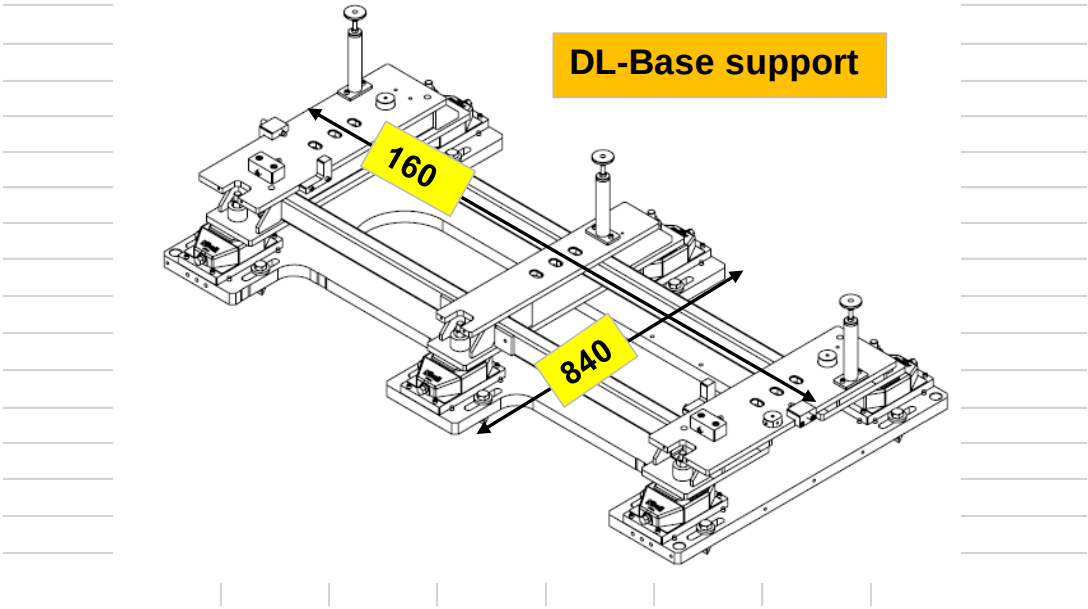


Figure 2.68: The DL base support on which the DL-magnet with the top plate is mounted.

# 3 Accelerator Engineering

## 3.1 Girders

### Design input specifications

The support of the storage ring magnets and vacuum chambers rely on 129 girders (128+1 for injection straight section), 4 girders for each of the 32 storage ring cells. Each girder supports 7 to 9 magnets with a layout which copes with the space constraints and the necessity to have flanges and bellows between vacuum chambers supported by adjacent girders. The girders are all identical with a length about 5.1m.

The intra-girder and inter-girders alignment requirements are 50 micrometres, both in the vertical and transverse directions and, to respect the inter-girders alignment tolerances, a re-alignment of the girders in the vertical direction will be necessary every six months because of the medium-term displacements of the storage ring floor. For this purpose, each girder should be equipped with a ± 5 mm motorised vertical adjustment and a ± 5 mm manual transverse adjustment with 5 micrometres resolution.

Efforts have been made in the first place to develop a motorised girder system with optimum stability for the new girder systems:

- Vibrations amplification factor (over 1-100 Hz) < 1.1.
- First natural frequency f1 > 35 Hz

### General design

The girder we designed to meet the requirements is based on the concept of the orthogonal heptapod, derived from the orthogonal hexapod. A body in the space has six degree of freedom. If we put it on six supports, blocking each of them the movement of a point of it in only one direction and no rotations we obtain an isostatic system easy to adjust.

It is the concept used in the commercial hexapods on six articulated jacks and the cam system of Diamond, SLS, Petra three, and our old machine. Unfortunately, this system isn't enough stiff to meet our stability requirement. So, we decided to modify it introducing a supplementary leg in the vertical direction, losing the perfect isostaticity but increasing a lot the stiffness. Four motorized supports in the vertical direction instead of three, permitting the adjustment of height, pitch and roll.

We have 2 jacks in the transversal direction allowing the translation in Y and the yaw and one jack longitudinal for the longitudinal adjustment. The hyperstaticity of the system must be managed by adjusting carefully the 4 vertical legs to ensure each of them carry correctly its load. The girder itself is made with normal carbon steel. A special attention is given to the welding, that are continuous and nearly full penetration type.

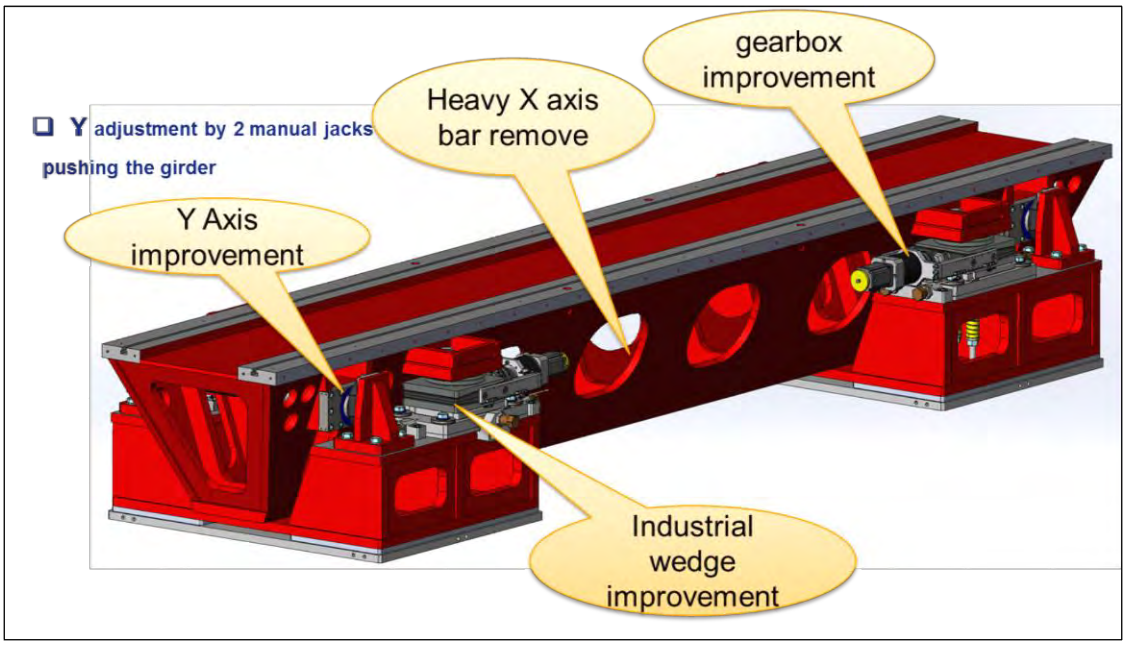


Figure 3.1: Girder general design.

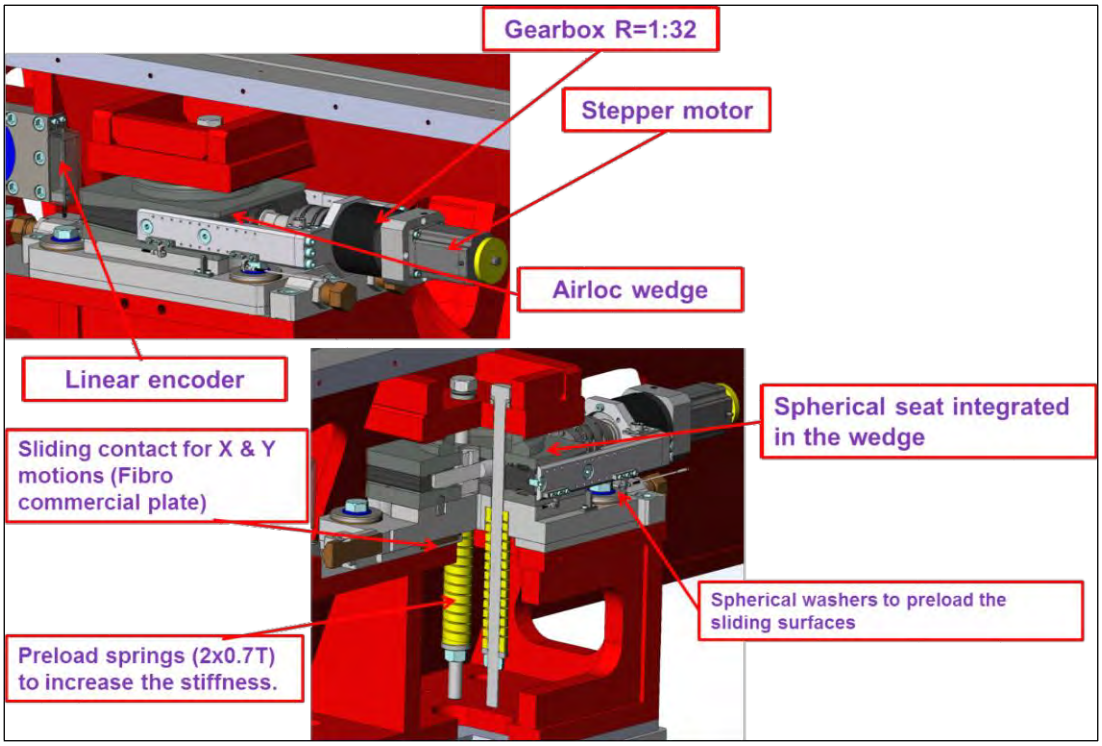


Figure 3.2: Vertical foot design.

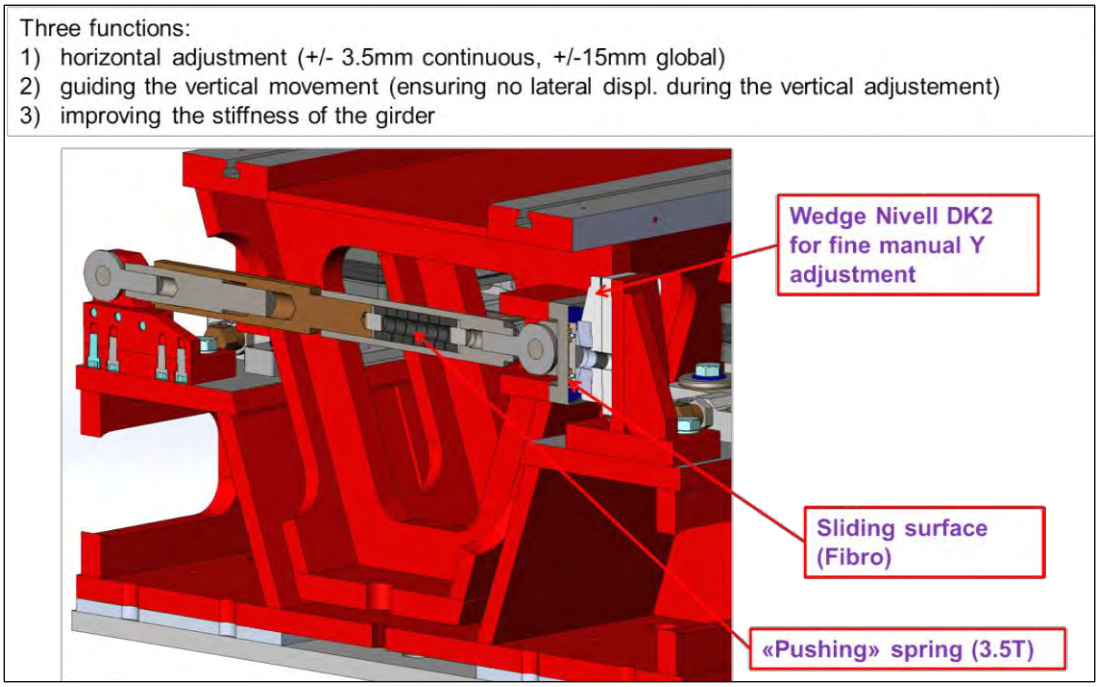


Figure 3.3: Horizontal foot design.

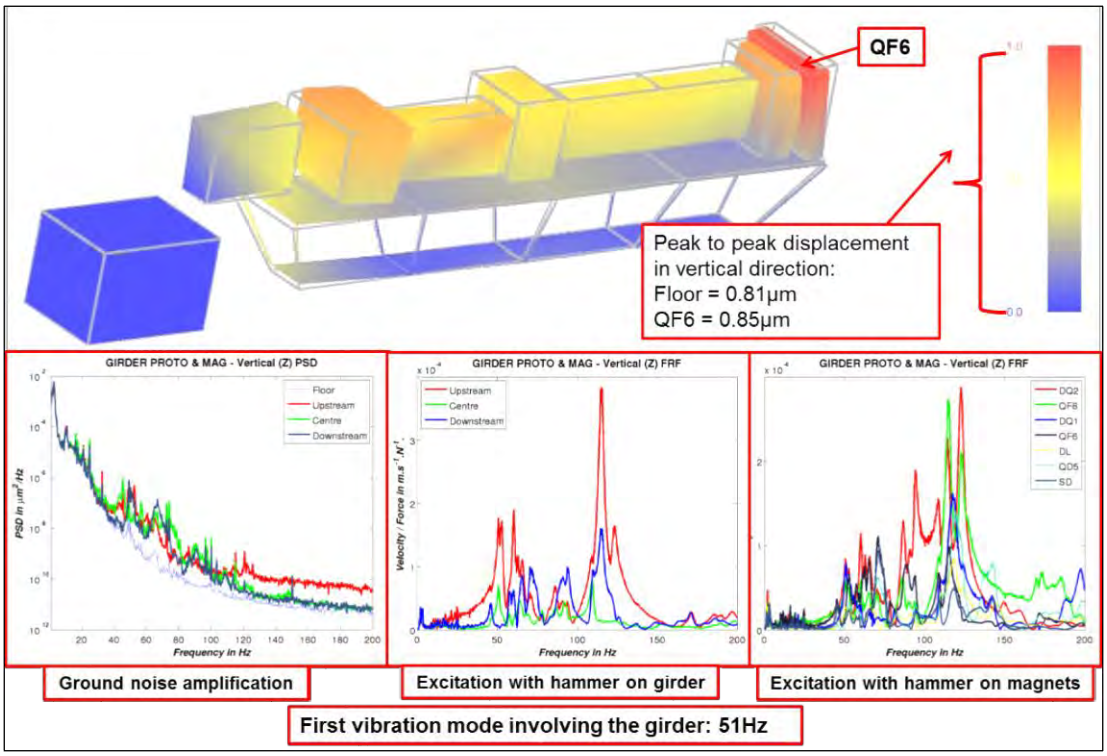


Figure 3.4: Prototype girder vibration analysis results.

### Girder performances

Vibration measurements and analysis were undertaken on a prototype girder installed on Chartreuse EX2 slab. The initial test was performed on 4 feet without magnets. Since the results obtained were satisfactory, i.e.: 1st horizontal mode at 80Hz, the tests carried on with measurements on the girder with dummy magnets. In this configuration, the 1st magnet mode, was found at 42Hz while, the more global 1st girder mode, dropped to 51Hz. The amplification with respect to floor vibration level is weak and does not exceed 1µm peak to peak. Therefore, the prototype girder's behaviour complies with the vibration specifications.

## 3.2 Vacuum chamber engineering

### Design constraints

A conservative approach has been chosen for the vacuum system layout. Vacuum chambers with antechamber provide space and access for discrete ultra-high vacuum (UHV) pumps and lumped absorbers. The vacuum chamber design must comply with the beam stay-clear requirements, overall ring impedance budget, acceptable vacuum levels and synchrotron radiation handling. This is directly translated into a design which includes a chamber that is as large as possible within the magnets, antechambers almost everywhere and lump absorbers to collect the synchrotron radiation. The limited available space restricts the locations where vacuum chamber hardware such as flanges, bellows, pumps and the diagnostic equipment can be installed.

The design and distribution of vacuum chambers is therefore more complex than in the present storage ring. In addition, the vacuum chamber distribution should facilitate the preparation of preassembled girders with magnets, vacuum chambers and vacuum equipment. The circumference of the synchrotron ring is segmented into 32 cells. Each cell type requires identical vacuum chambers, except for the injection section.

### Vacuum chamber families

Beam stay clear requirements imply two types of profile: a low profile with small cross section and a high profile with larger cross section. The vacuum chambers have been classified in three main families:

- High profile aluminium chambers (dipole magnets + other)
- High profile stainless steel chambers (quadrupoles, sextupoles, octupoles)
- Low profile stainless steel chambers (inside combined dipole-quadrupoles + HF quadrupoles)

The insertion device chambers consist of a 5 m long aluminium extruded profile vacuum chamber already installed and conditioned in the existing storage ring.

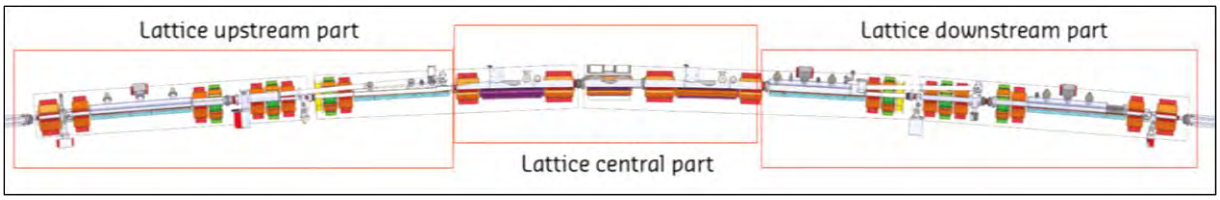


**Figure 3.5: Lattice S28d beam stay clear: large aperture upstream & downstream parts, small aperture central part.**

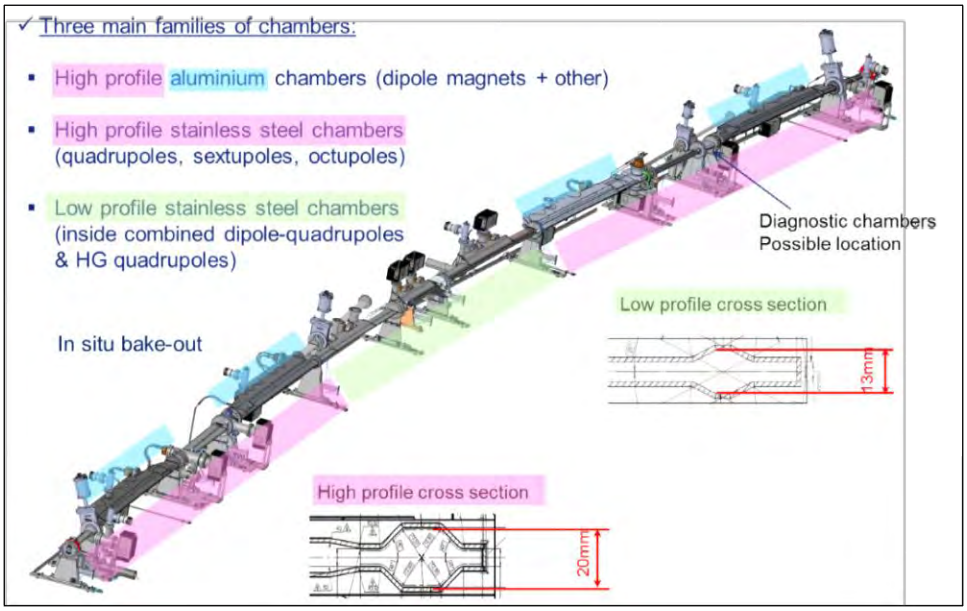


**Figure 3.6 : Repartition of vacuum chamber families.**

## Materials

The vacuum chamber cross section should be as thin as possible. Stainless steel (316LN) is suitable for this, and would also provide the required stiffness. However, it has been possible to use aluminium (2219 T87) for dipole chambers.

The RF-Fingers blades are made in Copper Beryllium alloy (CuBe2, CW101C).

The RF fingers flange side parts are made in Aluminum alloy (AlCu4MgSi, EN AW 2017).

### High profile aluminium chambers

High profile aluminium chambers represent chambers CH2, CH5, CH9 and CH1:

| Family name | Name | Reference drawing N° |
|---|---|---|
| **CH2** | Standard | 88.41.0304**(*)** |
| | Canted small angle | 88.41.0304**(*)** |
| | Canted big angle | 88.41.0304**(*)** |
| | Circular polarization | 88.41.0304 |
| **CH5** | Standard | 88.41.0307 |
| **CH9** | Standard | 88.41.0310 |
| **CH13** | Standard | 88.41.0313 |
| | Canted small angle | 88.41.0313**(*)** |
| | Canted big angle | 88.41.0313**(*)** |

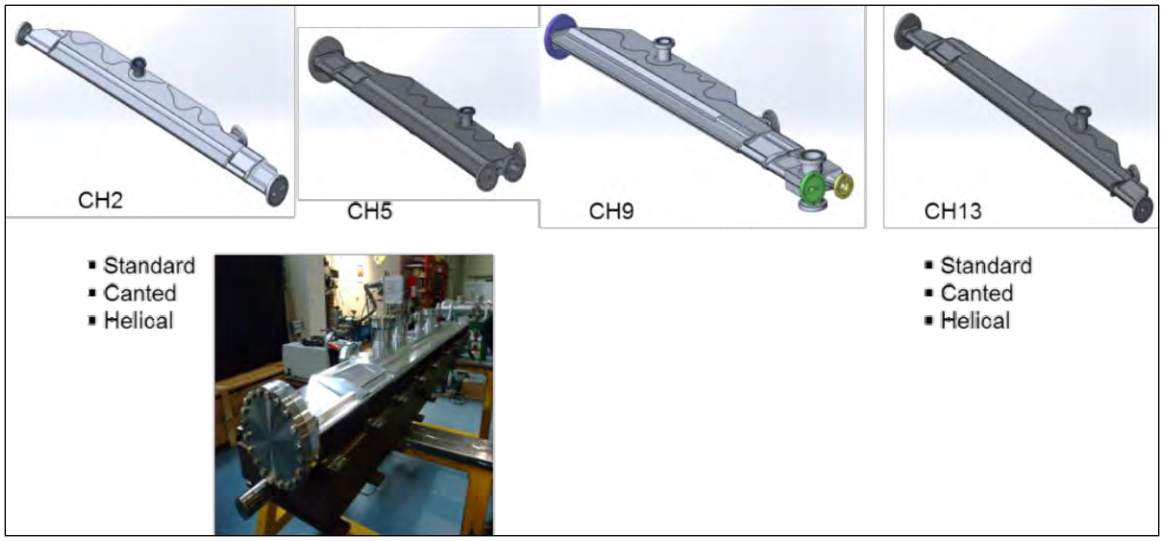


**Figure 3.7: High profile aluminium chambers.**

### High profile stainless steel chambers

High profile stainless steel chambers represent chambers CH1, CH3, CH4, CH11, CH12, CH14 and bellows chambers.

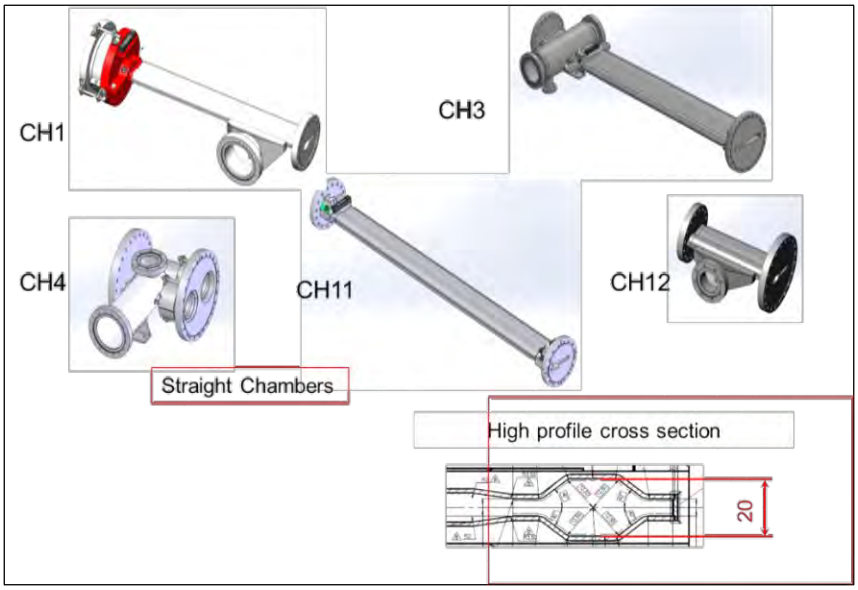


**Figure 3.8 : High profile stainless steel chambers.**

| Name | Reference drawing number |
|---|---|
| **CH1** | 88.41.0425 |
| **CH3** | 88.41.0475 |
| **CH4** | 88.41.0463 |
| **CH11** | 88.41.0170 |
| **CH12** | 88.41.0190 |
| **CH14** | 88.41.0785 |
| **Cross chamber for CH1/CH14** | 88.41.0016 |
| **Bellow CH2-CH3** | 88.41.0567 |
| **Bellow CH9-CH11** | 88.41.0577 |
| **Bellow CH12-CH13** | 88.41.0587 |

### Low profile stainless steel chambers

Low profile stainless steel chambers represent chambers CH6, CH7 and CH8.

| Name | Reference drawing number |
|---|---|
| **CH6** | 88.41.0090 |
| **CH7** | 88.41.0110 |
| **CH8** | 88.41.0130 |

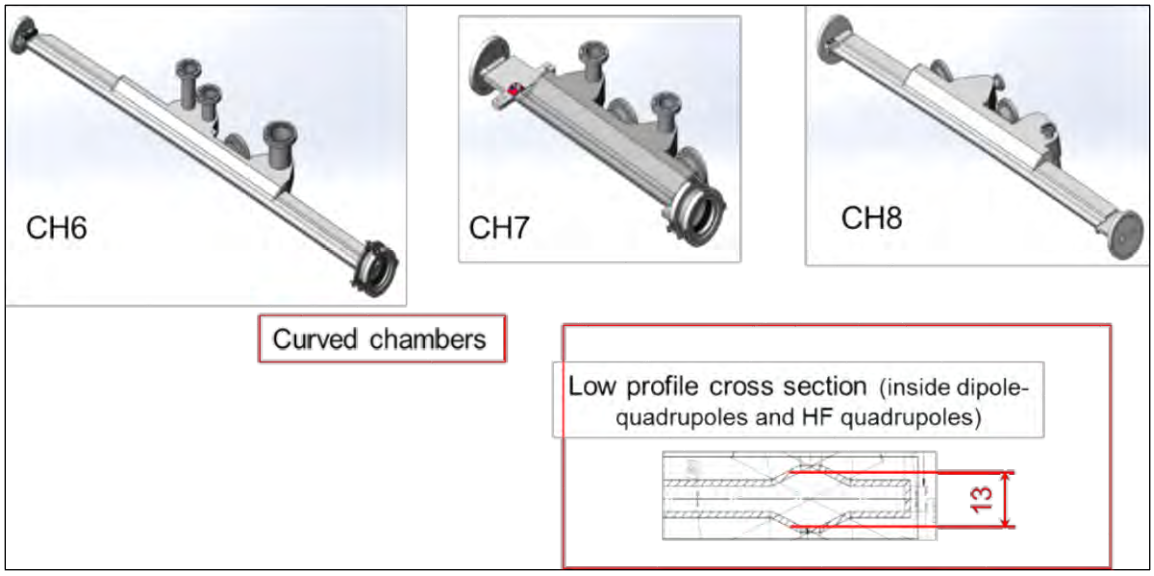


**Figure 3.9 Low profile stainless steel chambers.**

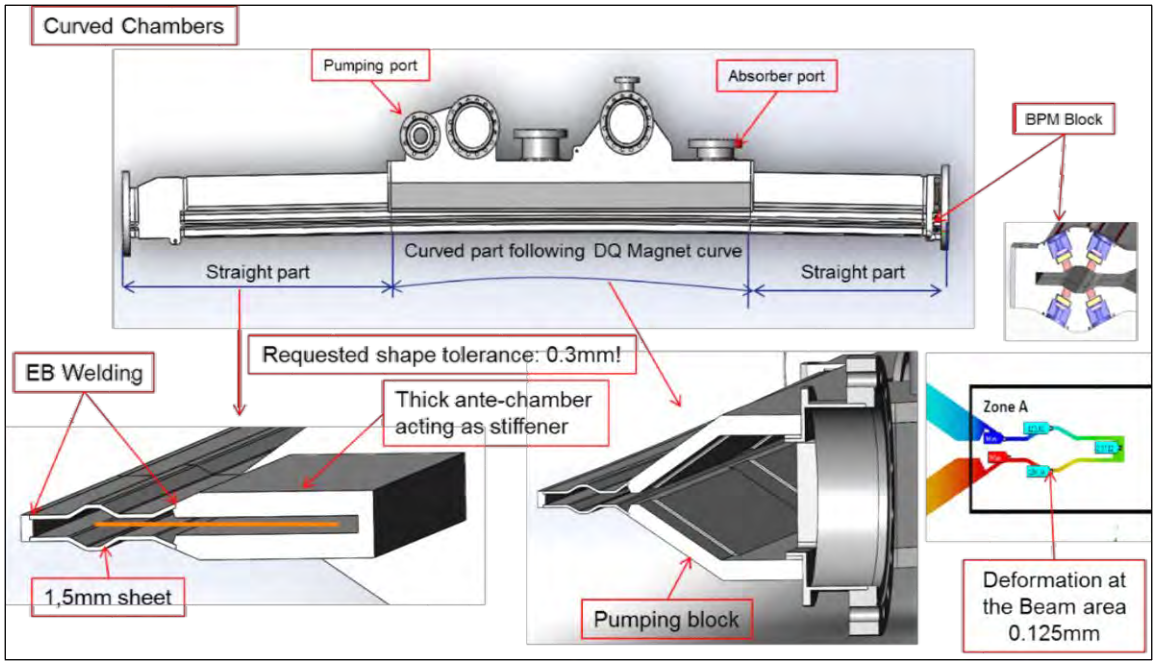


Figure 3.10: Low profile stainless steel chamber CH6 detailed view.

## RF gaskets

RF gaskets have been designed to offer a smooth transition between flanges.

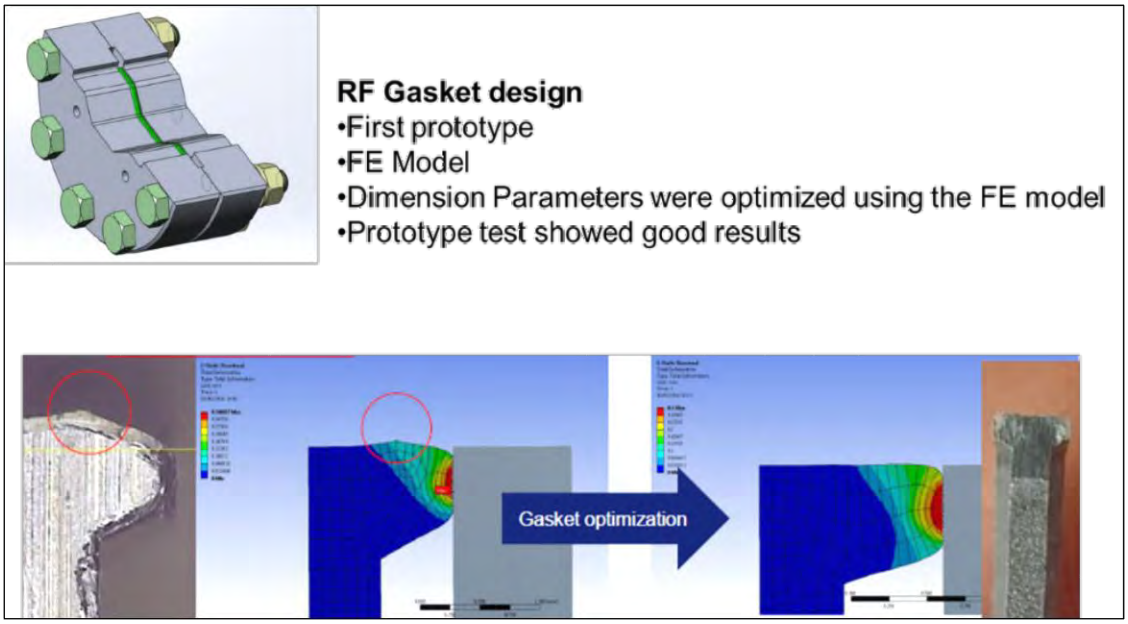


Figure 3.11 RF gasket design and tests.

### RF fingers

The internal shape of vacuum chambers required a new RF finger design.

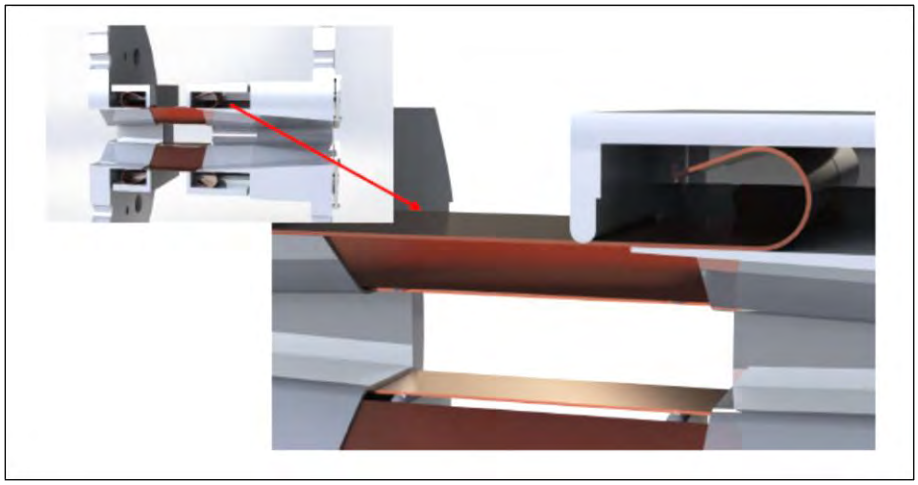

Figure 3.12: RF finger assembly.

The RF fingers are part of the bellow assemblies. The bellows permit limited dilatations of the storage ring cells on both sides of its flanges during periods of heating and re-cooling while guaranteeing the tightness regarding outside air for the whole lifecycle usage. Inside of the bellows the RF fingers guarantee the geometrical and, most importantly, electrical continuity to assure the proper propagation of radio waves in the vacuum chambers. To assure the proper functionality of the RF fingers, they are geometrically blocked in their mounting (see Figure 3.9) on the bellow structure. At the same time the upper flange side part of the bellow pushes the RF finger blade spring-like on the lower part to maintain the working conditions (geometrical/electrical continuity) as good as possible. The blades are extremely thin to fulfil their task properly. Since the blades are mounted directly to the bellow structure they face the same deformations during heating and re-cooling as well as further small displacements expected during the real machine assembly.

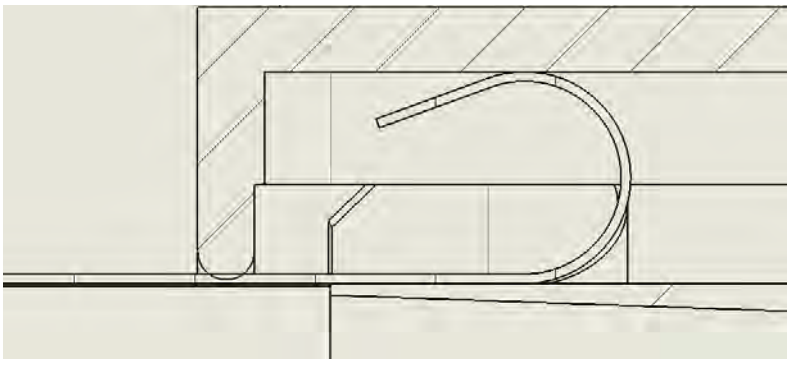

Figure 3.13: RF finger blade in its mounting.

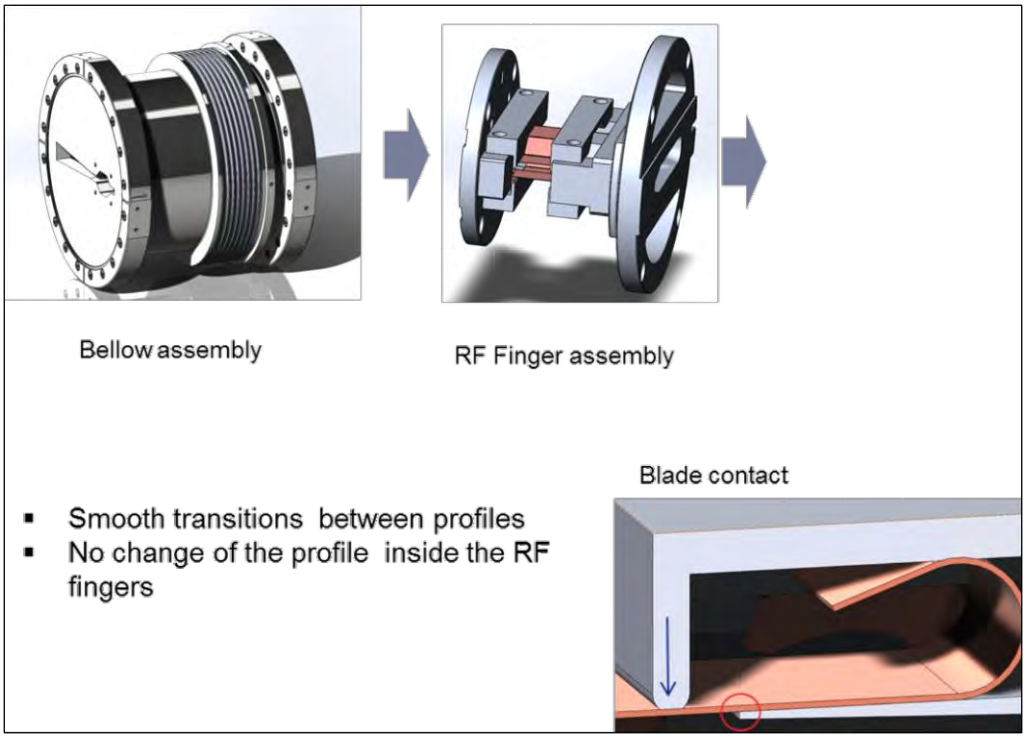


Figure 3.14: RF finger bellow assembly.

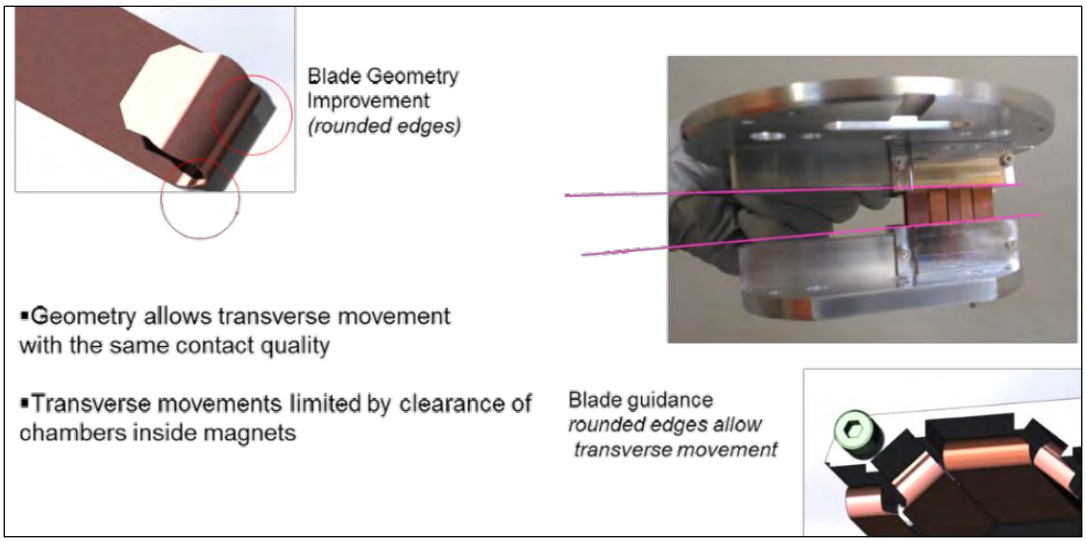


Figure 3.15: RF finger blade geometry.

## 3.3 Supports

### Magnet supports

Girders are used to support the magnets and BPMs with high precision positioning. The interface between each magnet and the girder must be stiff to avoid amplification of vibration and must provide adjustment capabilities for the alignment of the magnetic centre of each magnet within the required tolerance of 50 micrometres.

To reach this positioning precision, each magnet will be aligned and adjusted on the girder. The horizontal adjustment will be done with a mobile adjustment system which will be removed after adjustment.

The vertical adjustment will rely on fine “wedge” adjustment systems for the high gradient quadrupoles, longitudinal gradient dipoles and dipoles quadrupoles. Other magnets will rely on stiff shims on which the magnet will be clamped after horizontal and longitudinal adjustments.

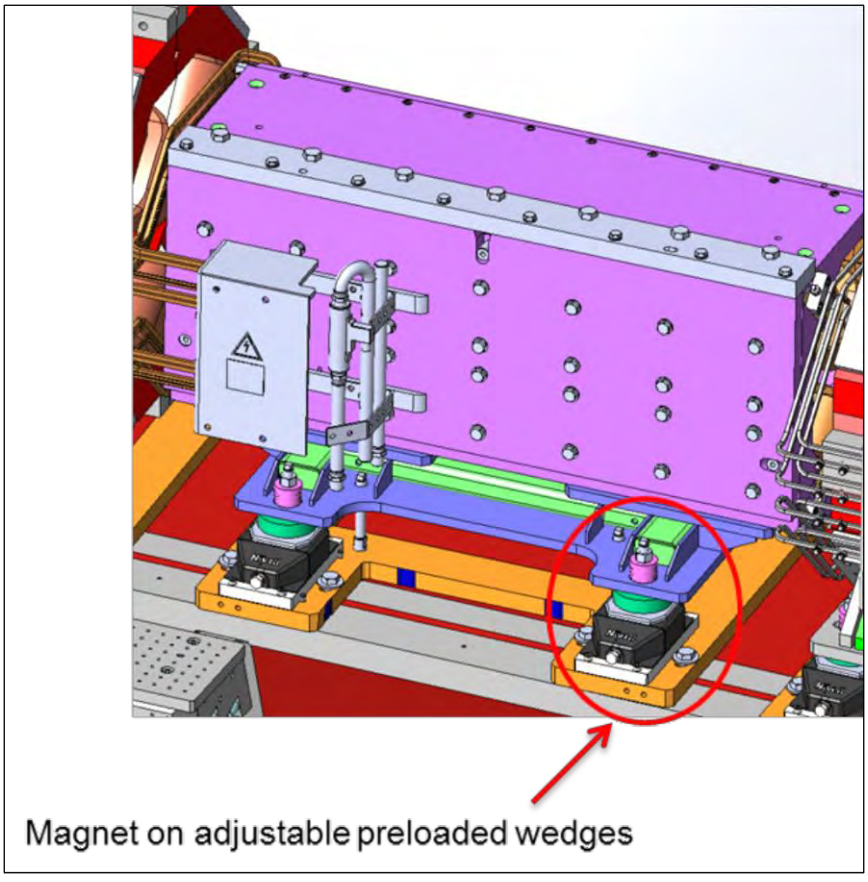


**Figure 3.16: Dipole quadrupole magnet support: preloaded adjustable wedge system.**

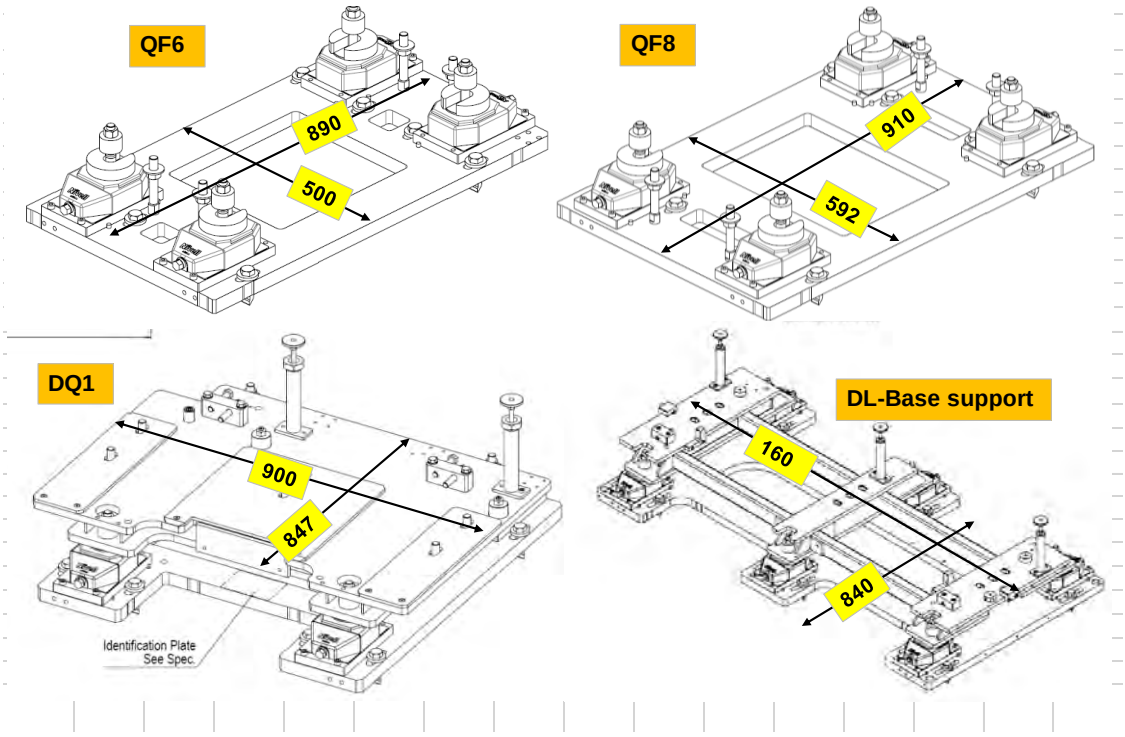


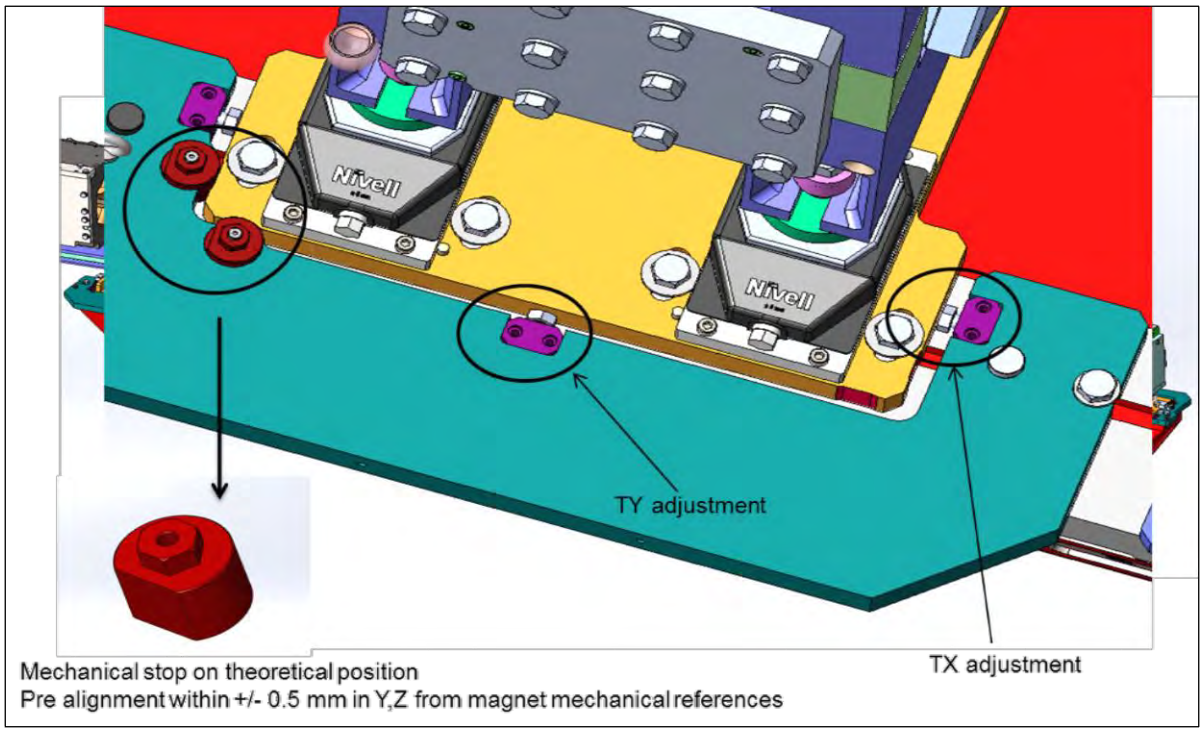


Figure 3.17: Magnet pre-alignment tool.

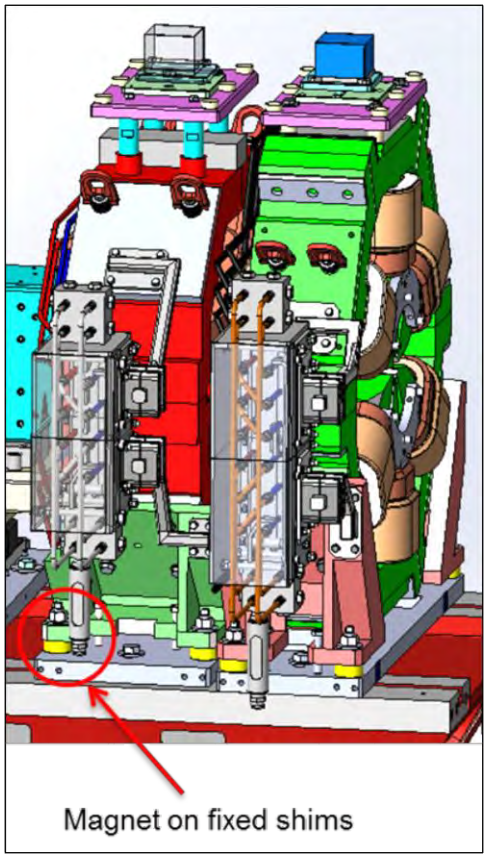


Figure 3.18: Magnet with shims; no vertical adjustment.

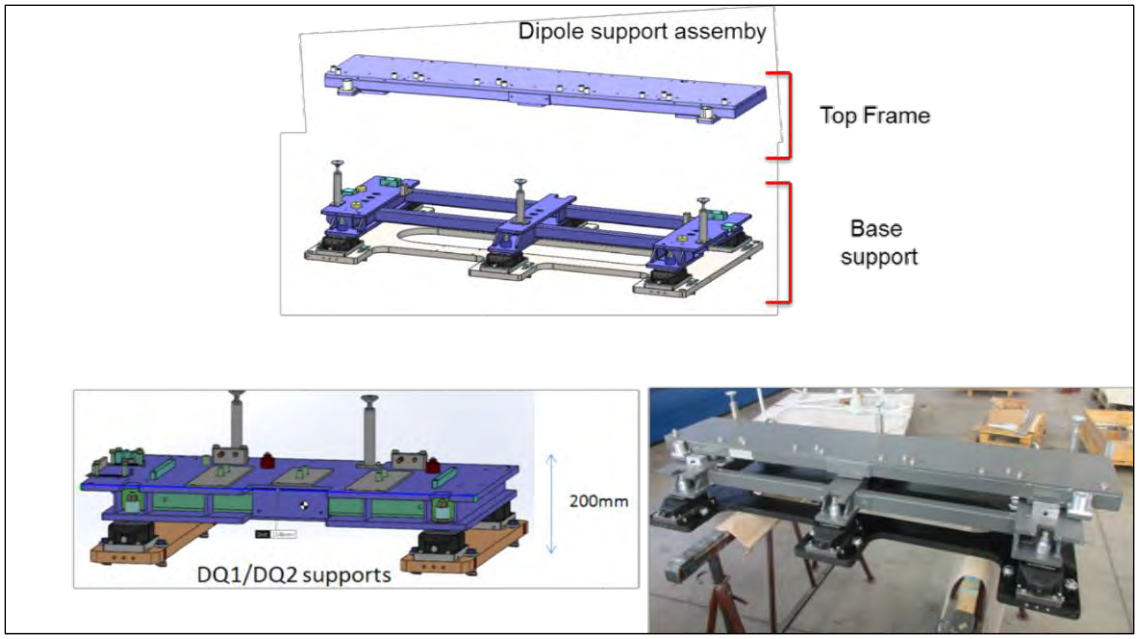


Figure 3.19: Longitudinal gradient dipole 1 DQ supports.

## Vacuum chamber supports

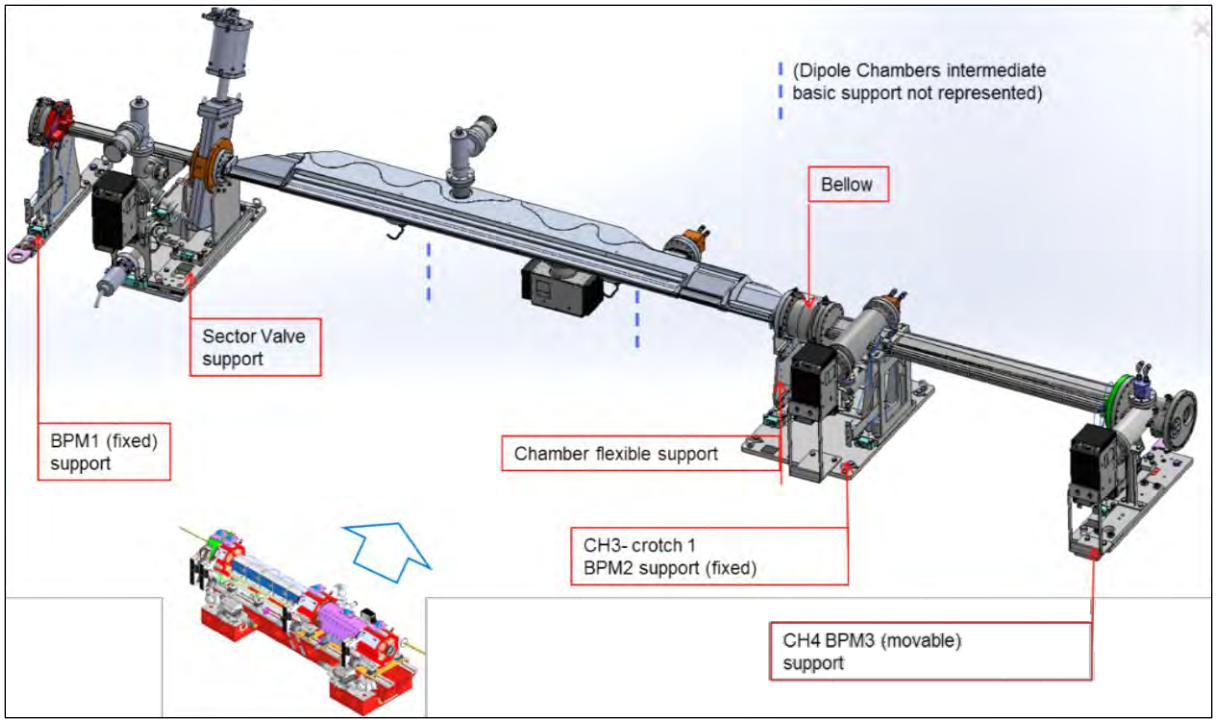


Figure 3.20: Vacuum chamber supports for girder 1.

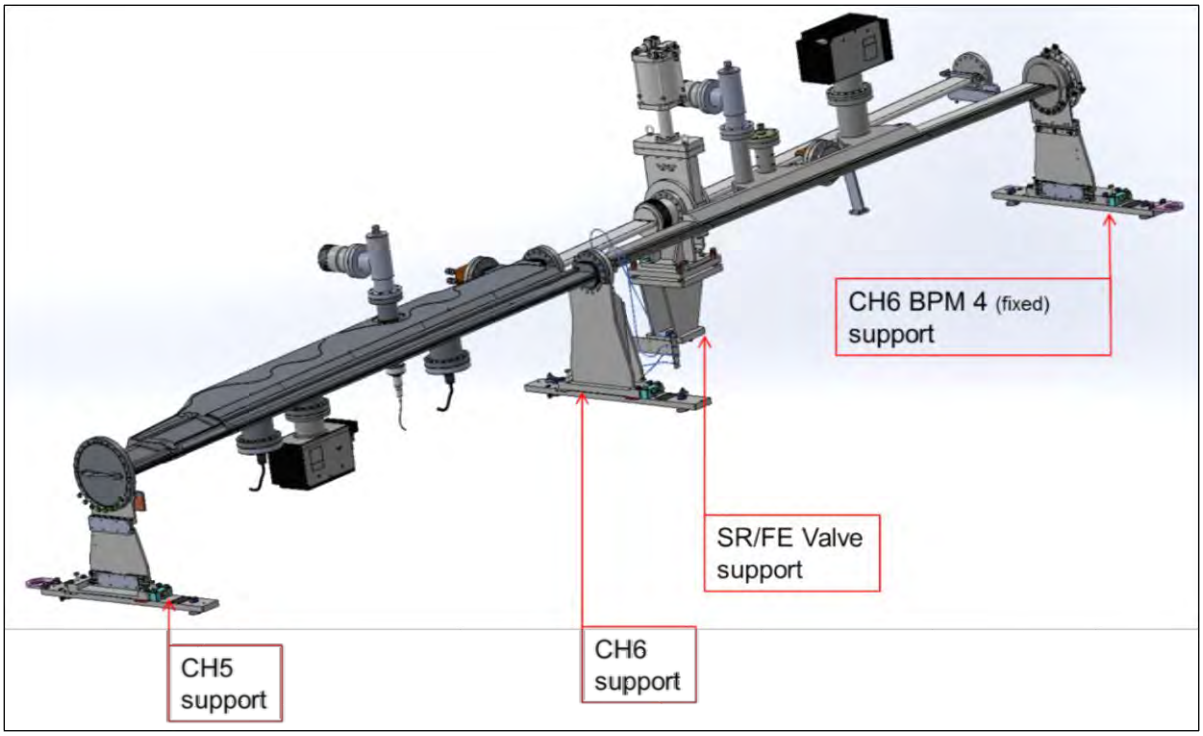


Figure 3.21: Vacuum chamber supports for girder 2.

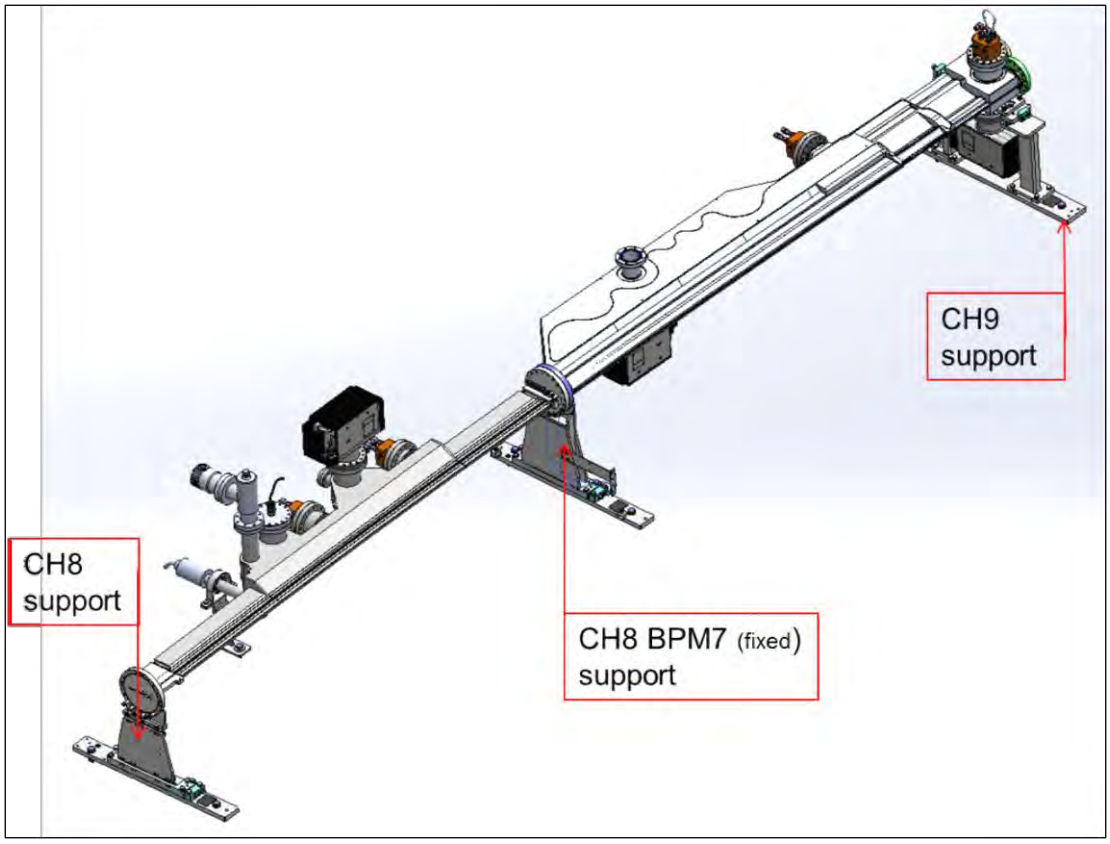


Figure 3.22: Vacuum chamber supports for girder 3.

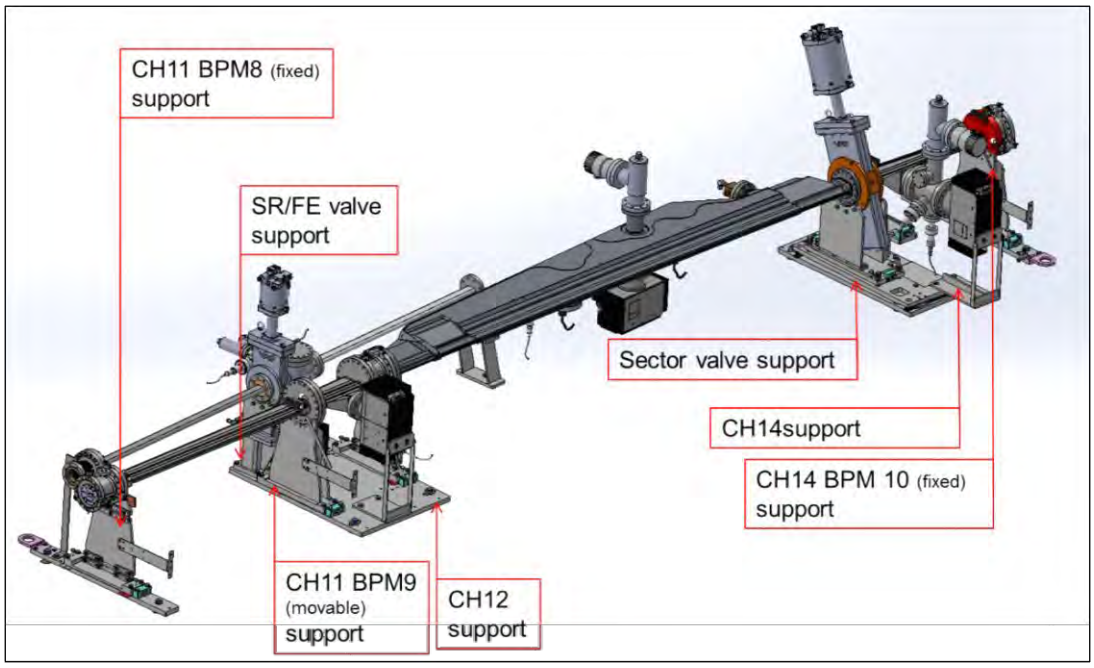


Figure 3.23: Vacuum chamber supports for girder 4.

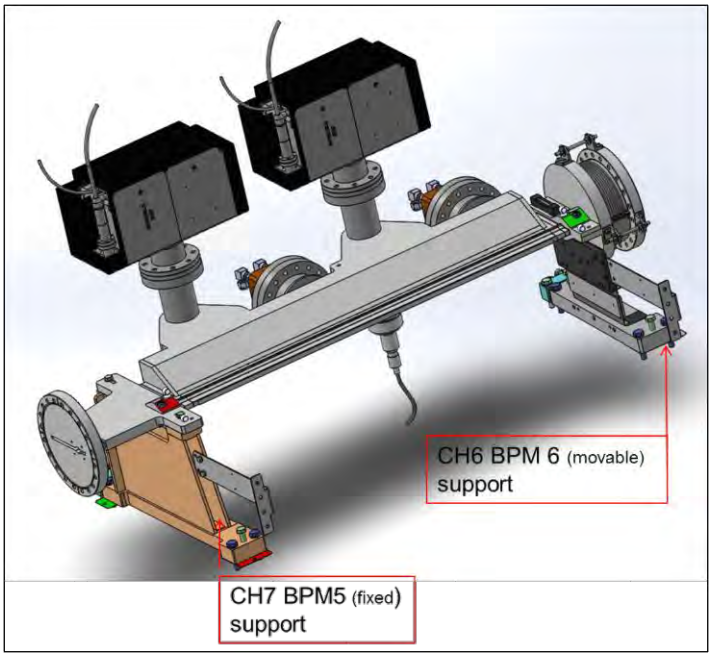


Figure 3.24: Vacuum chamber CH7 support between girder 2 & 3.

## BPM supports

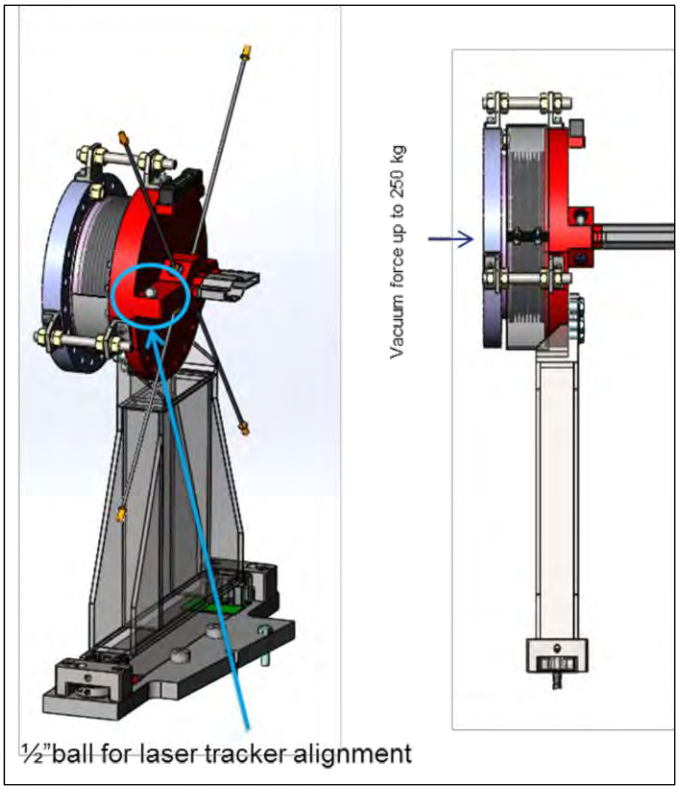


Figure 3.25 BPM fixed support.

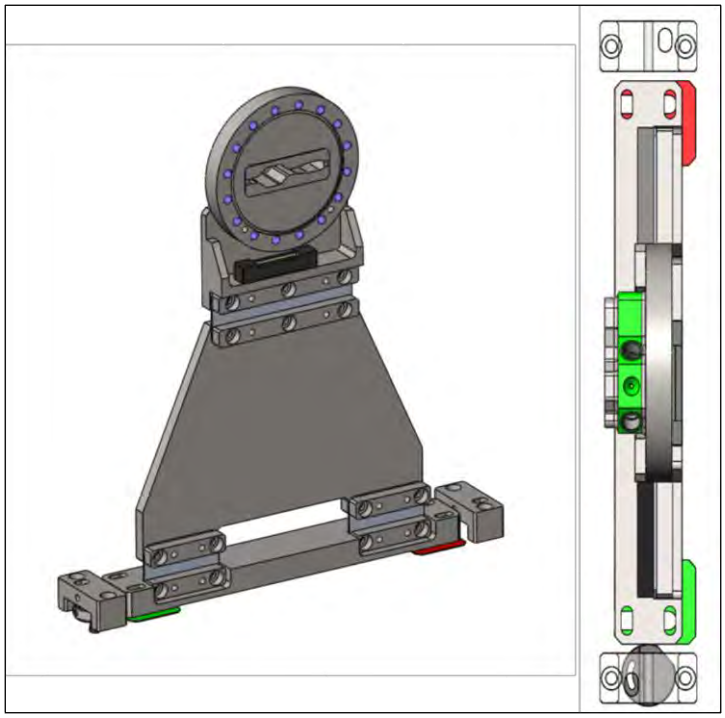

Figure 3.26: BPM flexible support.

Flexible supports have been calculated to:

- Analyze stress during deformation.
- Determine the reaction forces of the original flexible support (flexor) design during chamber dilatations.
- Analyze effects of support forces on chamber.
- Optimize flexor to lower reaction forces but avoid buckling.
- Determine the well positioning of the support regarding curved chamb

## 3.4 Photon absorbers

### Photon absorber design

The thermal photon absorbers used to protect the vacuum chambers can be classified as two major types (toothed and frontal families) and some specials absorbers for the special regions. All these absorbers will be totally made of Copper Chromium Zirconium alloy (CuCr1Zr), water-cooled, and designed such that there is no water-to-vacuum joint and no brazing. The CF flange knife edge is machined in the absorber body.

The difficulty at the design stage is to reduce the maximum temperature and stress on the absorbers to avoid the use of special dispersion strengthened copper (Glidcop™) material which is difficult to braze.

Table 3.1: Material properties.

| | | Glidcop Al-25 | CuCr1Zr | Cu-OFE |
|---|---|---|---|---|
| MECHANICAL PROPERTIES | Young's modulus E (GPa) | 130 | 128 | 115 |
| | Yield Strength (MPa) | 330 | 280 | 75 |
| | Ultimate limit (MPa) | 380 | 380 | 200 |
| | Elongation at break (A%) | 12 | 8 | 45 |
| | Hardness (Brinell) | 120 | 130 | 100 |
| THERMAL PROPERTIES | Thermal expansion at 20°C (1/K) | 16.6 | 17.5 | 16.8 |
| | Conductivity at 20°C ($w.m^{-2}.K^{-1}$) | 365 | 320 | 393 |
| | Typical max. Heat load ($W/mm^2$) | 70 | 50 | 20 |
| DESIGN PROPERTIES | CF Knife edge possible | Yes | Yes | No |
| | Price (€/Kg) for rods > Ø100mm | ~50 | 20-30 | |

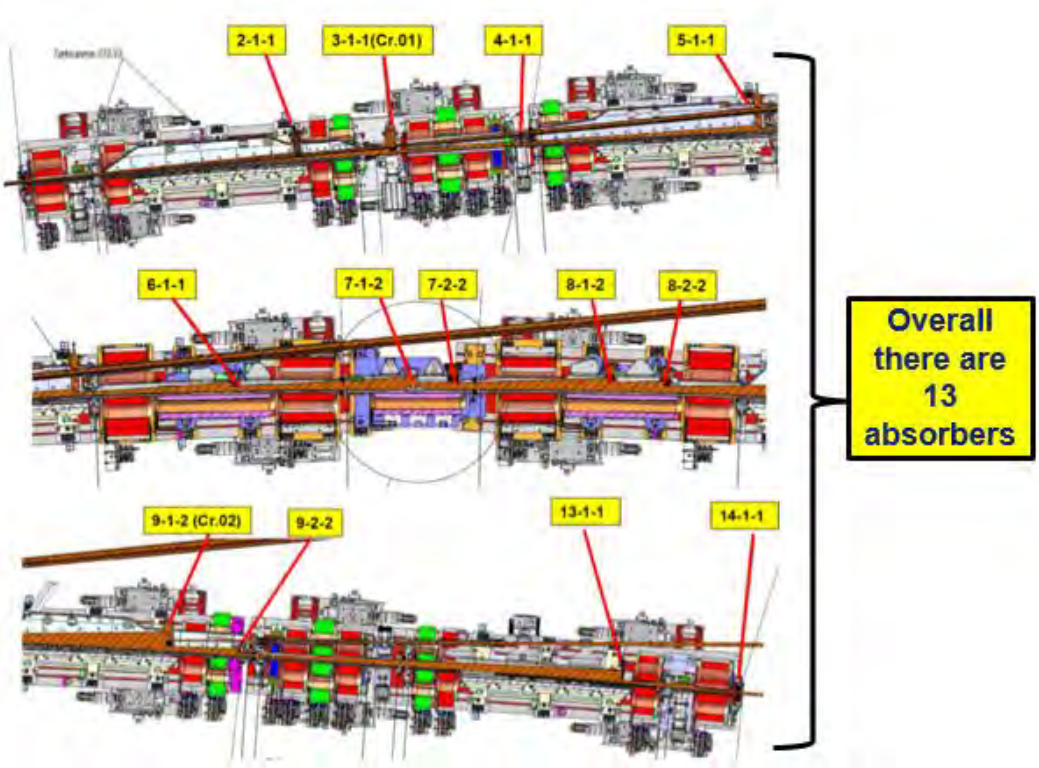


Figure 3.27: Repartition of photon absorbers.

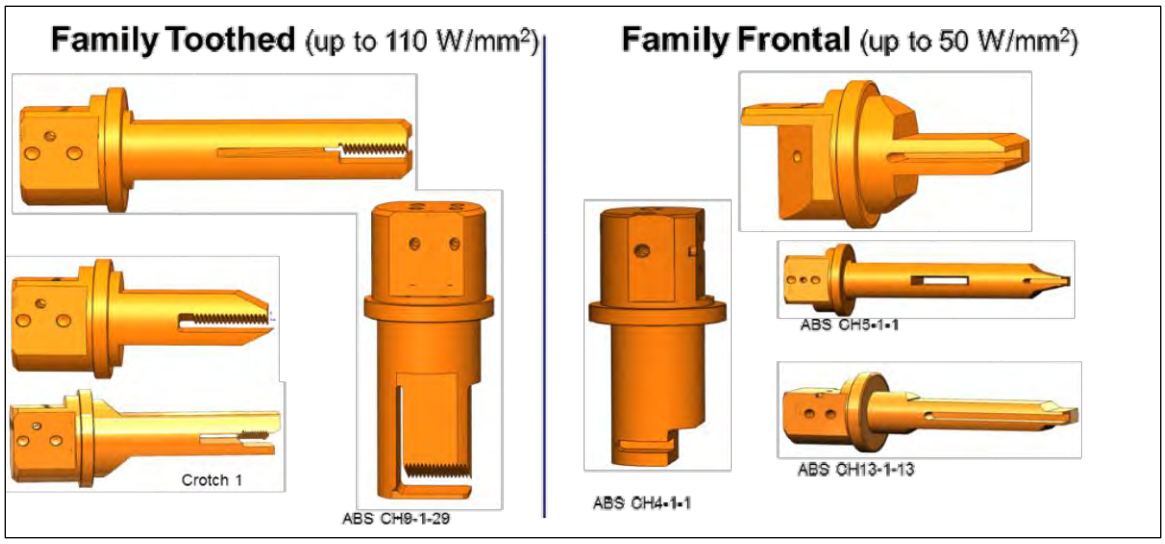


Figure 3.28: Photon absorber families.

About 391 absorbers (including crotch absorbers, without injection cell specials) will be necessary to absorb a total power of 504.5 kW (30 x 15.795 kW + 2x 15.314) kW.

The power density (normal to beam) is moderate compare to current ESRF (10 to 110W:mm$^2$).

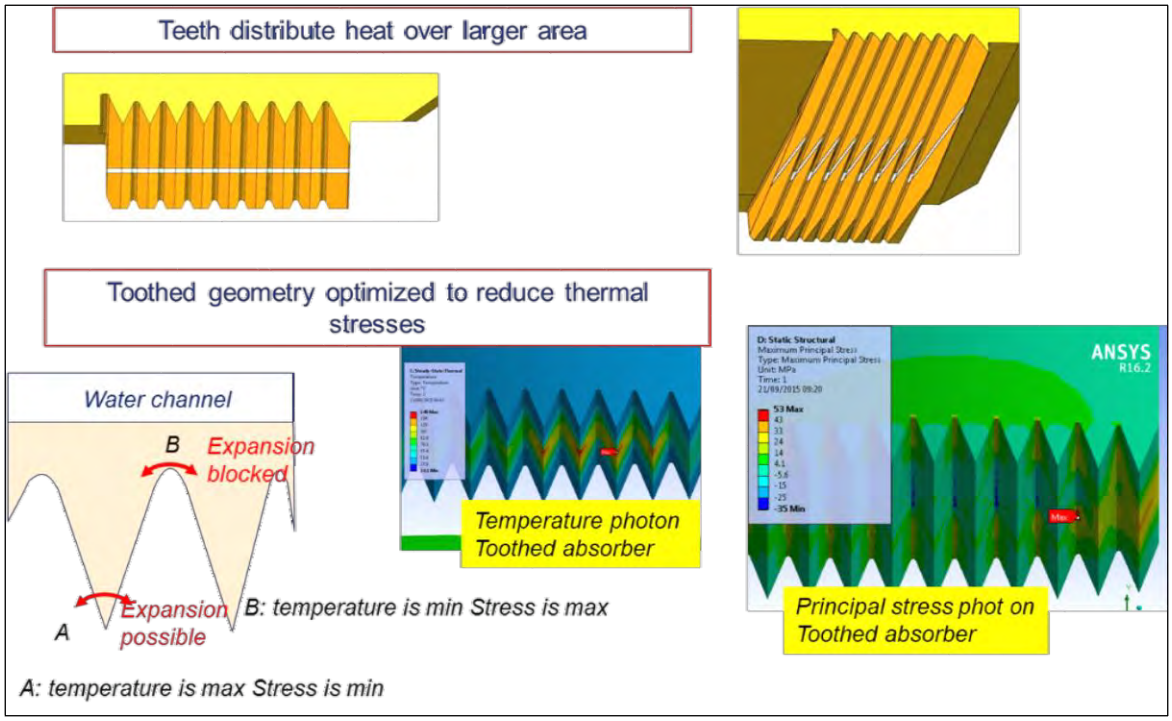


Figure 3.29: Teeth optimization.

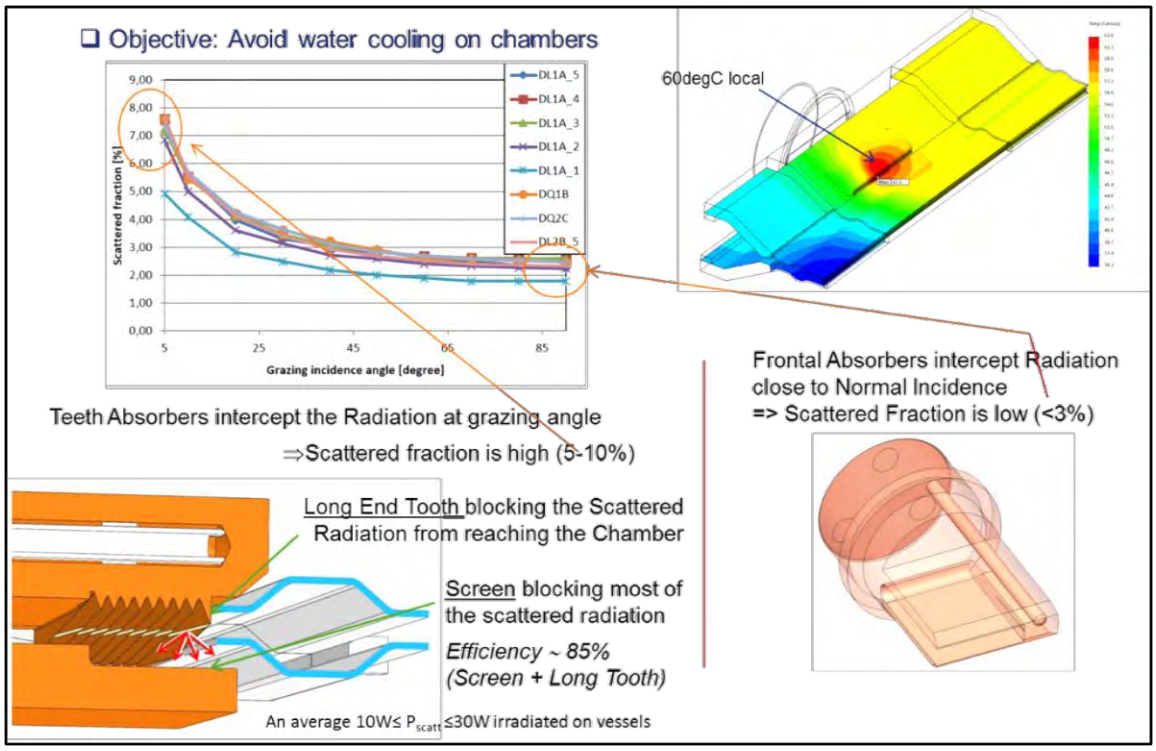


**Figure 3.30: Scattered radiation optimization: scattered radiation blocked as much as possible in the absorber to avoid chamber cooling.**

## Ray tracing

The photon absorbers have been designed taking in account electron beam offset and absorber position offset:

- e-beam lateral offset : 1mm
- Absorber n-1 offset : 1mm

**Table 3.2: Absorber ray tracing – safety margin.**

| Upstream absorber | | Absorber | | [b]/[a] [m] | Abs transverse margin [mm] | [1] e-beam lateral deviation [mm] | [2] absorber offset [mm] | Abs & beam offset [1]&[2] [mm] | Abs remaining margin [mm] |
|---|---|---|---|---|---|---|---|---|---|
| Name | distance to source [a] [m] | Name | distance to source [b] [m] | | | | | | |
| End CV AL chamber | 6.397 | Absorber CH2-1-1pt: H1 | 9.215 | 1.4 | 12 | 1 | 1 | 1.89/6.2 | 10.1/5.8 |
| Absorber CH2-1-1pt: H2 | 9.197 | Absorber CH3-1-1 Crotch 1pt: H3 | 10.154 | 1.1 | 5 | 1 | 1 | 1.86 | 3.1 |
| Absorber CH3-1-1 Crotch 1pt: H6 | 2.182 | Absorber CH4-1-1pt: H7 | 3.444 | 1.6 | 6 | 1 | 1 | 2.26 | 3.7 |
| Absorber CH4-1-1pt: H8 | 3.111 | Absorber CH5-1-1pt: H13 | 5.463 | 1.8 | 7 | 1 | 1 | 1.61 | 5.4 |
| Absorber CH5-1-1pt: H14 | 4.923 | Absorber CH6-1-1pt: H15 | 6.303 | 1.3 | 5 | 1 | 1 | 1.68 | 3.3 |
| Absorber CH6-1-1pt: H16 | 2.227 | Absorber CH7-1-2pt: H17 | 3.749 | 1.7 | 7 | 1 | 1 | 2.48 | 4.5 |
| Absorber CH7-1-2pt: H18 | 3.017 | Absorber CH7-2-2pt: H19 | 3.359 | 1.1 | 5 | 1 | 1 | 1.26 | 3.7 |
| Absorber CH7-2-2pt: H20 | 2.606 | Absorber CH8-1-2pt: H21 | 3.993 | 1.5 | 7 | 1 | 1 | 2.11 | 4.9 |
| Absorber CH8-1-2pt: H22 | 3.648 | Absorber CH8-2-2pt: H23 | 4.119 | 1.1 | 5 | 1 | 1 | 1.28 | 3.7 |
| Absorber CH8-2-2pt: H24 | 3.708 | Absorber CH9-1-2 Crotch 2pt: H25 | 6.038 | 1.6 | 7 | 1 | 1 | 2.28 | 4.7 |
| Absorber CH9-1-2 Crotch 2pt: H28 | 2.633 | Absorber CH9-2-2 pt: H29 | 3.344 | 1.3 | 5 | 1 | 1 | 1.58 | 3.4 |
| Absorber CH9-2-2 pt: H30 | 2.126 | Absorber CH13-1-1 pt: H31 | 6.108 | 2.9 | 10 | 1 | 1 | 4.87 | 5.1 |
| Absorber CH13-1-1 pt: H32 | 4.845 | Absorber CH14-1-1 pt: H33 | 5.426 | 1.1 | 5 | 1 | 1 | 1.26 | 3.7 |
| Absorber CH14-1-1 pt: H35 | 1.787 | CVALpt: H36 | 2.087 | 1.2 | 3.5 | 1 | 1 | 0.89 | 2.6 |

## 3.5 Front Ends

### Insertion device front ends

Insertion device front ends at the ESRF are of two types: undulator (in air, in vacuum, helical) and wiggler (multi-pole). Insertion devices can produce powerful synchrotron radiation with a power density of about 400 kW mrad-2 and a total power up to 25kW. The modular design of the front end in its high power configuration allows horizontal apertures from ±0.08 mrad to ±0.24 mrad. Insertion device front ends are further subdivided into single insertion device and canted insertion device types. Canting allows two insertion devices in one straight section to produce two beams. For existing beamlines the beams are separated by ±0.75 mrad for ID23, ±2.3 mrad for ID30 and ±2.7 mrad for ID16. All insertion device front ends will be kept and adapted to the new lattice. All sources including those in the canted configuration have been taken into account in the design of the storage ring vacuum chambers. The front end can be split into three parts.

Module 1 refers to the first part of the front end nearest to the storage ring and to the second part composed of a series of connecting chambers, called the transition module. Module 2 refers to the third part, upstream of the port end wall that separates the storage ring from the corresponding beamline optics hutch.

The main components of front end module 1 are:

- Photon XBPM: Photon beam position monitor.
- Dipole absorber: This absorber protects the vacuum chambers from parasitical photons produced in upstream dipoles.
- Horizontal slit: Defines the horizontal aperture of the photon beam.
- Photon shutter: A water-cooled Glidcop™ copper shutter that stops the X-ray beam from reaching the optics hutch when in the closed position, or enables the beam to enter the optics hutch when in the open position
- Pneumatic valve: This is an all-metal gate valve that serves to isolate the front end from the storage ring.
- Fast shutter: The fast shutter is a rapid closing valve that stops an air inrush in case of a fast vacuum-to-air leak.

The transition module consists of several vacuum chambers including one acoustic delay line (ADL). The ADL is a segmented vacuum chamber. The different segments are divided by baffles that let the synchrotron radiation pass through. In the event of a vacuum incident on the beamline, the pressure wave coming from the beamline is damped and the level of vacuum inside the storage ring is protected.

The main components of front end module 2 are:

- Vertical slit: The vertical slit defines the vertical aperture of the photon beam. It is made from water cooled OFHC – Cu (oxygen free high conductivity copper).
- Trigger gauges: Two vacuum sensor gauges close the fast shutter of module

1 in just a few milliseconds to protect the vacuum of the storage ring in the event of a vacuum accident on the beamline. These gauges work in association with the acoustic delay line in the transition module.

- Pneumatic valve: This ultra-high vacuum valve isolates the front end from the beamline on windowless front ends.
- Diamond window: This window filters the X-rays and separates the storage ring vacuum from the vacuum of the optics hutch.
- Radiation shutter: This shutter is a block of lead that stops the radiation from the storage ring from entering the optics hutch when in the closed position.

All insertion device beamlines front end module 1 will have to be refurbished due to the compactness of the S28d lattice:

- The XBPM has been removed.
- The dipole absorbers have been designed for the new lattice.

Nevertheless, most individual components have been be reused. The horizontal slit and photon shutter have been moved downstream by approximately 1.6 m to allow the installation of the storage ring DQ2 vacuum chambers and their associated girder. The horizontal slit and photon shutter have been motorized for fine adjustment of their position (half of the insertion device front-end will be upgraded before end 2018). Downstream, the photon shutter dedicated space has been reserved for the installation of new equipment such as compound refractive lenses.

The present front end power and power density configurations are compatible with the new lattice.

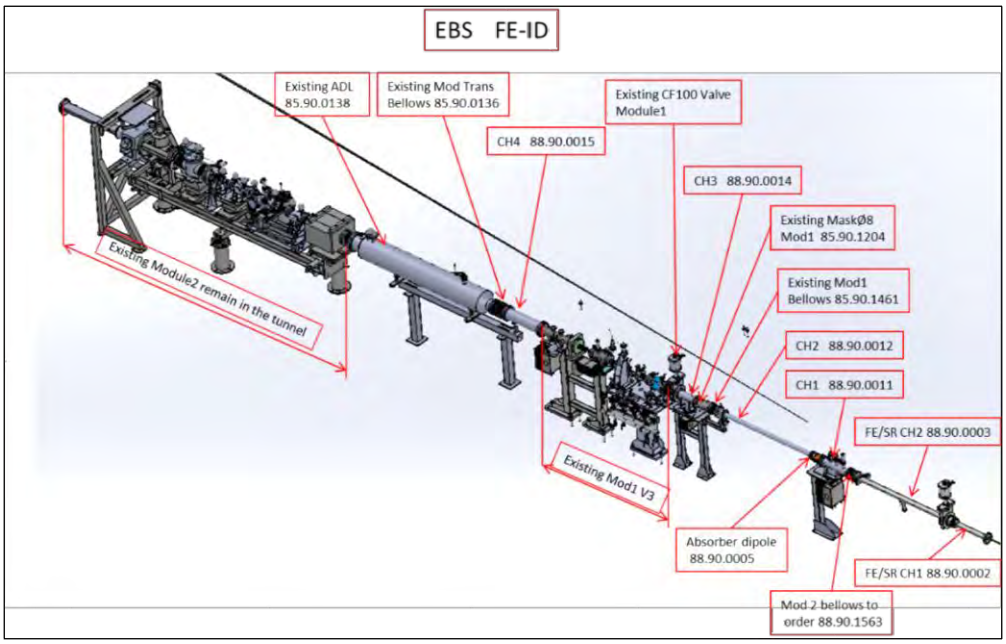


**Figure 3.31: Front-End Insertion Device layout.**

### Bending magnet front ends

Similarly to insertion devices, bending magnet front ends can be split into three parts grouped in two modules. All bending magnet beamlines front end module 1 have been re-designed due to the compactness of the new lattice and the change in source parameters. Further

calculations will be necessary to verify that the beryllium window can operate in safe conditions regarding the increased heat-load. The front ends will need to be re-aligned. The water cooled horizontal aperture has been modified to better match the new radiation fan.

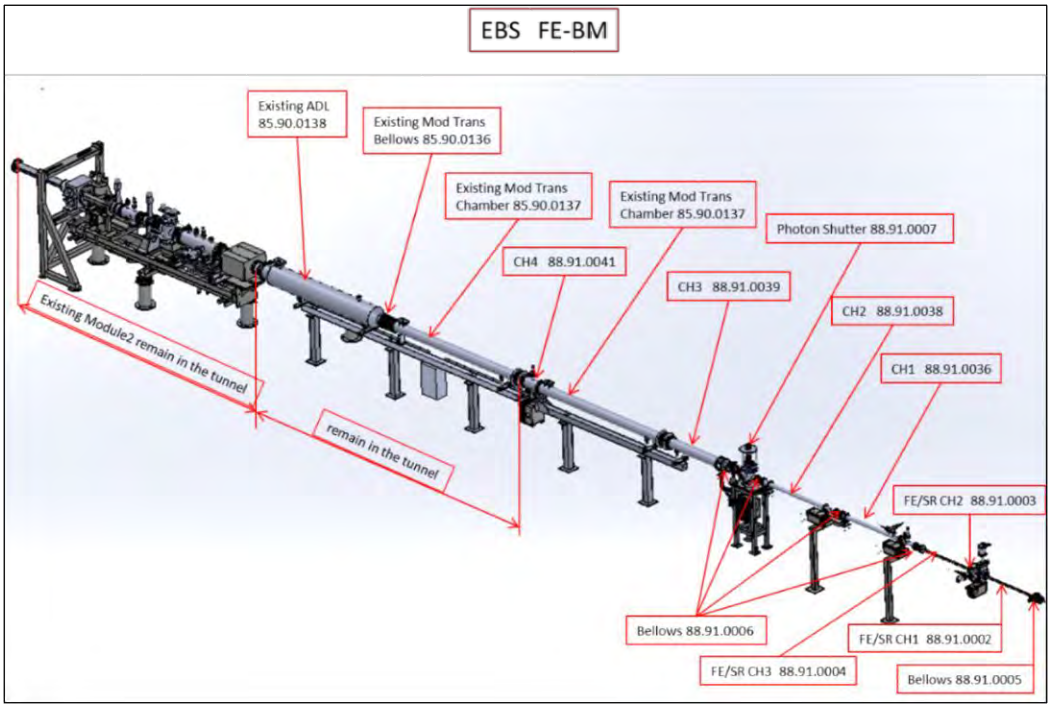


**Figure 3.23 Front-End Bending Magnet layout.**

## 3.6 Annexes

### Arc cell schematic view

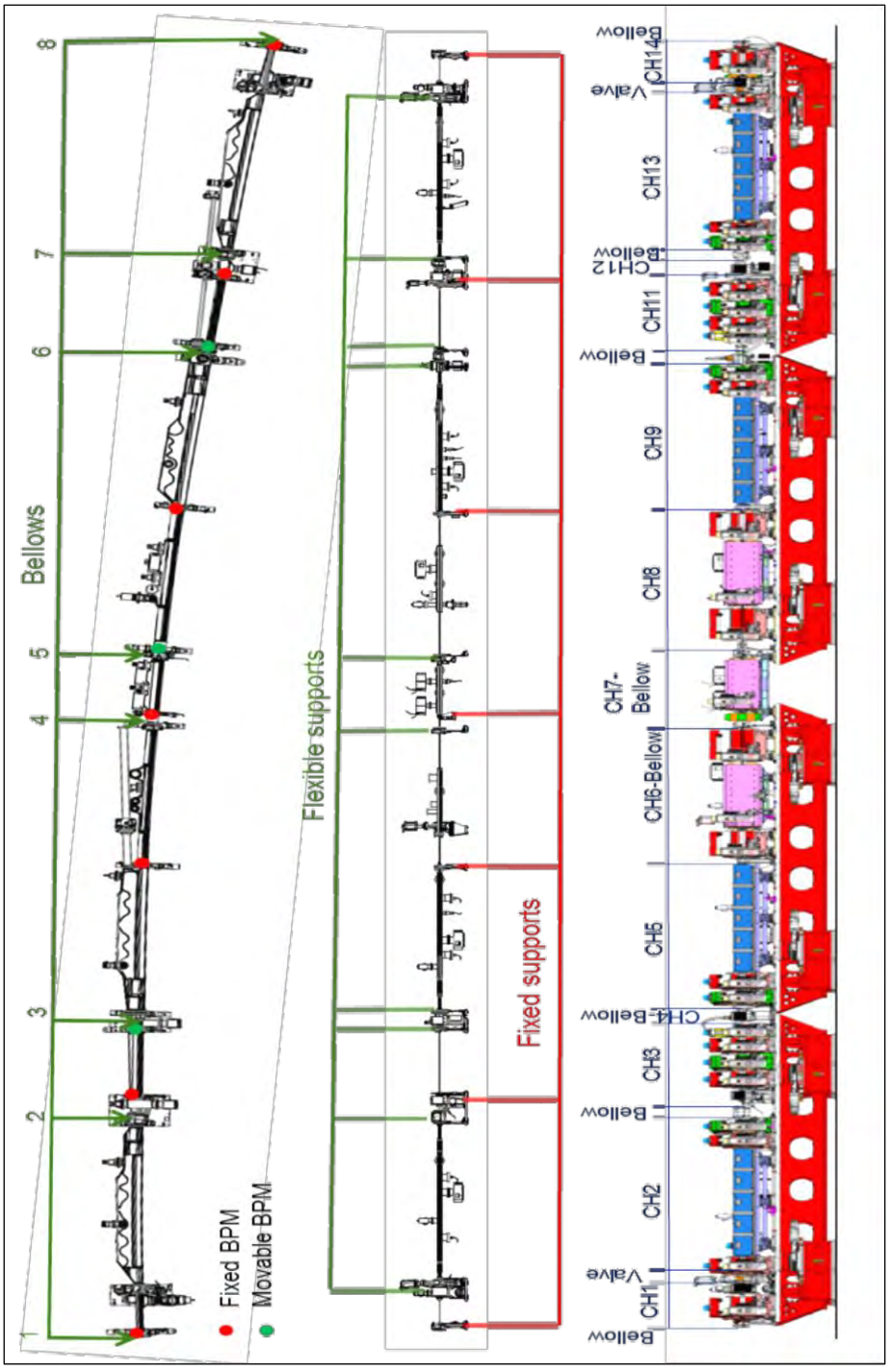


Figure 3.33: Arc cell supports & chamber repartition.

### Photon absorbers

The photon absorbers are distributed over the four girders and chamber 7 as shown in the following **Figure 3.34.**

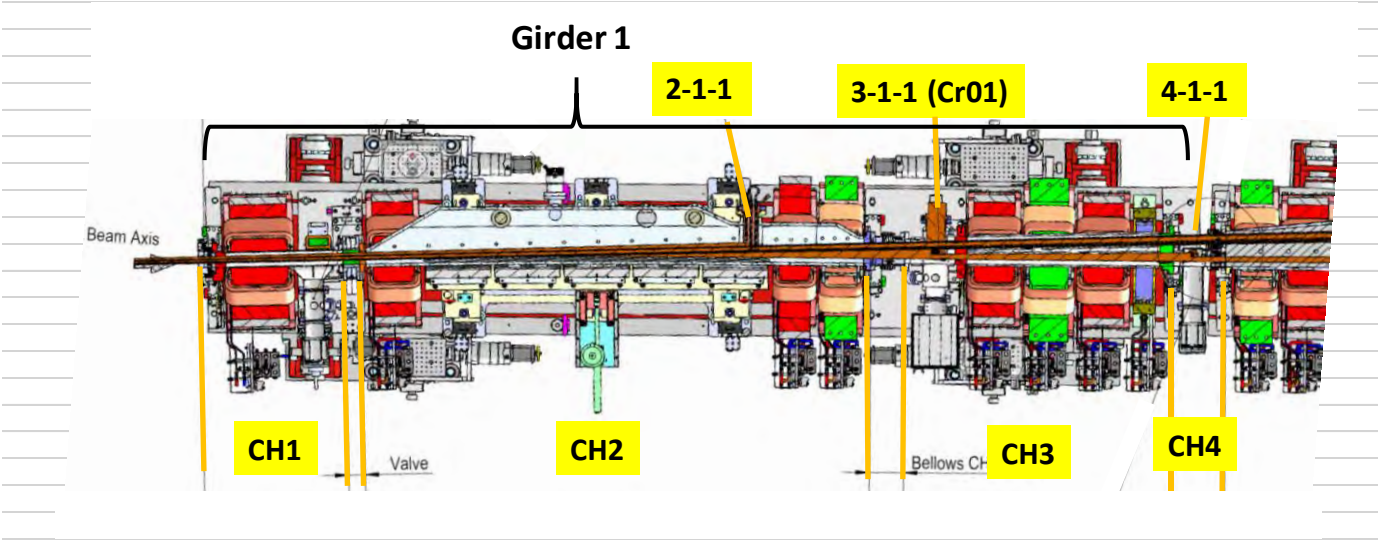


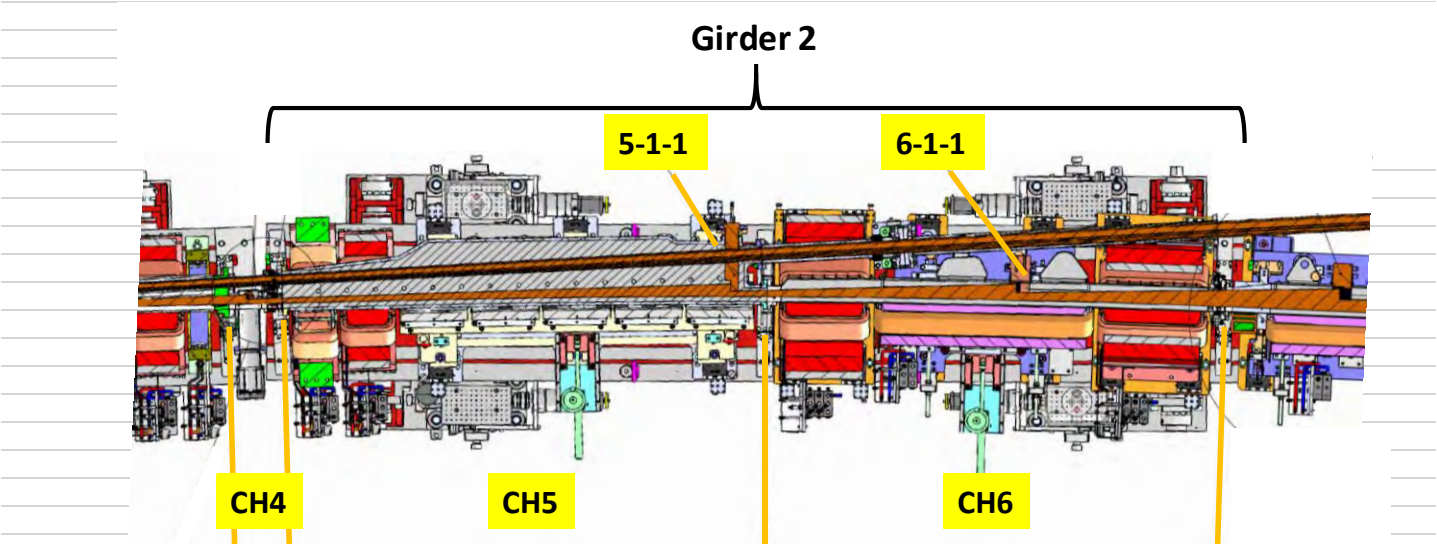

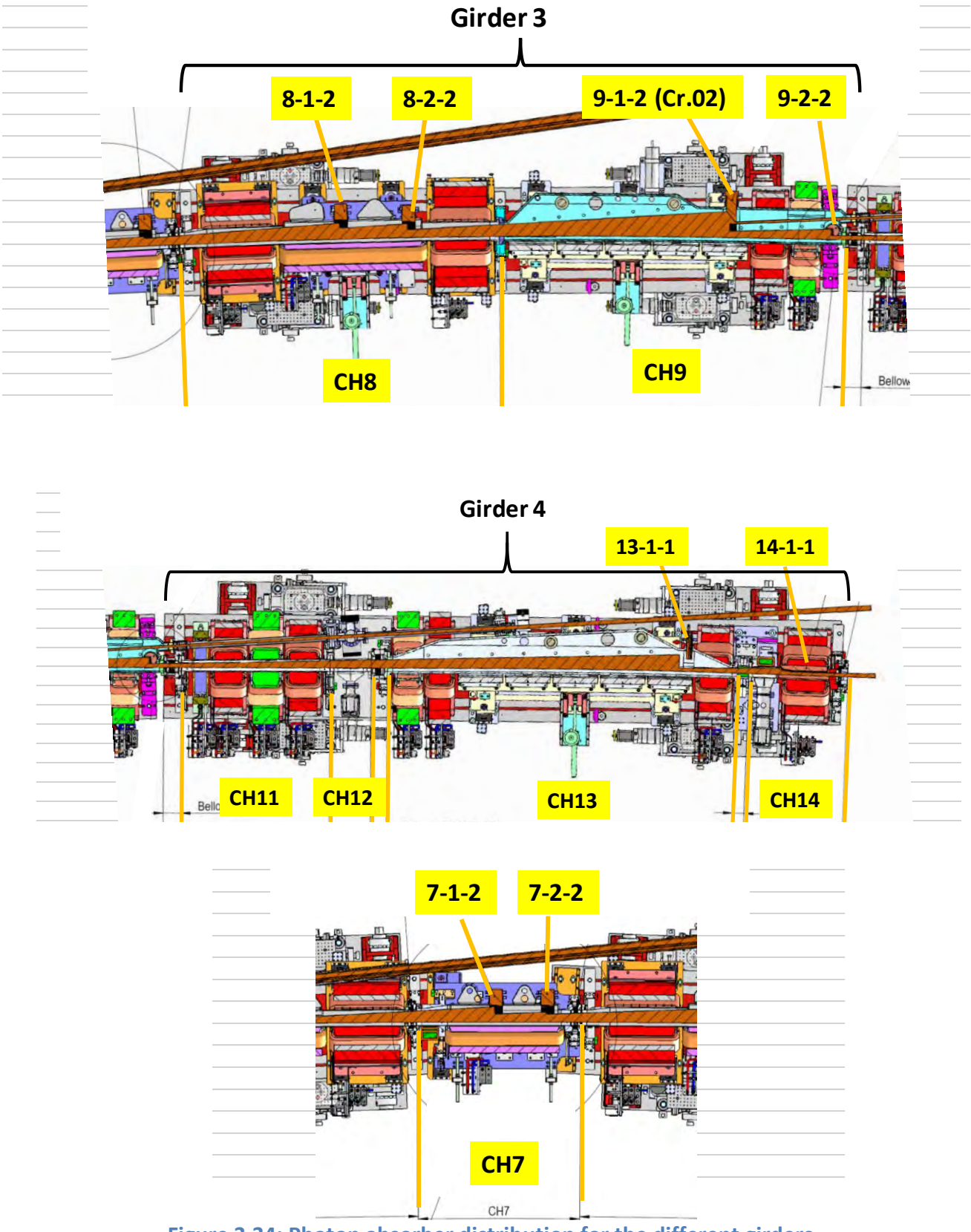


Figure 3.34: Photon absorber distribution for the different girders.

Table 3.2: Photon absorber power distribution.

| Pt n° | Src | D ebeam mm | d m | α degree | σ mm | $V_{beam}$ mm | Pl normal inc. W/mm | Pa W/mm2 | Ptot W | Absorber name |
|---|---|---|---|---|---|---|---|---|---|---|
| H1 | Cell-1_DL1E_5 | 78,68 | 9,21 | 2,11 | 0,78 | 1,967 | 12,37 | 6,29 | 212,6 | Absorber CH2-1-1 |
| H2 | Cell-1_DL1E_5 | 63,33 | 9,21 | 2,00 | 0,78 | 1,966 | 12,38 | 6,30 | | |
| H3 | Cell-1_DL1E_5 | 96,44 | 10,16 | 2,00 | 0,86 | 2,168 | 11,22 | 5,18 | 1163,4 | Absorber CH3-1-1 Crotch 1 |
| H4 | Cell-1_DL1E_5 | 96,27 | 10,17 | 2,00 | 0,87 | 2,171 | 11,21 | 5,16 | | |
| H5 | DL1A_5 | 52,50 | 2,53 | 1,59 | 0,22 | 0,541 | 45,00 | 83,15 | | |
| Src end | DL1A_5 | | 2,28 | 0,96 | 0,19 | 0,487 | 49,99 | 102,62 | | |
| H6 | DL1A_4 | 26,00 | 2,11 | 0,94 | 0,18 | 0,452 | 35,50 | 78,60 | | |
| H7 | DL1A_4 | 47,85 | 3,44 | 0,94 | 0,29 | 0,736 | 21,78 | 29,62 | 461,2 | Absorber CH4-1-1 |
| Src end | DL1A_4 | | 3,26 | 0,72 | 0,28 | 0,696 | 23,01 | 33,04 | | |
| H8 | DL1A_3 | 25,00 | 3,05 | 0,54 | 0,26 | 0,651 | 18,07 | 27,77 | | |
| H9 | Cell-1_DL1E_5 | 242,96 | 13,87 | 3,68 | 1,18 | 2,962 | 8,22 | 2,77 | 326,4 | Absorber CH5-1-1 |
| H10 | Cell-1_DL1E_5 | 242,50 | 13,88 | 3,68 | 1,18 | 2,964 | 8,21 | 2,77 | | |
| H11 | DL1A_5 | 180,33 | 6,27 | 4,95 | 0,53 | 1,339 | 18,18 | 13,58 | | |
| H12 | DL1A_5 | 184,99 | 6,31 | 4,98 | 0,54 | 1,347 | 18,06 | 13,41 | | |
| H13 | DL1A_3 | 165,78 | 5,45 | 3,90 | 0,46 | 1,164 | 10,09 | 8,67 | | |
| Src start | DL1A_2 | | 5,31 | 0,42 | 0,45 | 1,134 | 7,79 | 6,87 | | |
| Src end | DL1A_2 | | 4,94 | 0,18 | 0,42 | 1,056 | 8,36 | 7,92 | | |
| H14 | DL1A_1 | 130,00 | 4,84 | 3,49 | 0,41 | 1,034 | 6,31 | 6,10 | | |
| H15 | DL1A_1 | 93,52 | 6,30 | 4,39 | 0,54 | 1,345 | 4,85 | 3,60 | 562,2 | Absorber CH6-1-1 |
| Src start | DL2B_1 | | 3,14 | 3,36 | 0,27 | 0,671 | 10,17 | 15,16 | | |
| Src end | DL2B_1 | | 2,77 | 3,17 | 0,24 | 0,591 | 11,54 | 19,51 | | |
| Src start | DL2B_2 | | 2,77 | 3,17 | 0,24 | 0,591 | 14,97 | 25,31 | | |
| Src end | DL2B_2 | | 2,40 | 2,93 | 0,20 | 0,513 | 17,25 | 33,62 | | |
| H16 | DL2B_3 | 50,17 | 2,13 | 3,60 | 0,18 | 0,456 | 25,46 | 55,86 | | |
| H17 | DL2B_3 | 113,41 | 3,75 | 3,60 | 0,32 | 0,801 | 14,50 | 18,11 | 1364,5 | Absorber CH7-1-2 |
| Src start | DL2B_4 | | 3,66 | 3,53 | 0,31 | 0,782 | 19,09 | 24,42 | | |
| Src end | DL2B_4 | | 3,31 | 3,15 | 0,28 | 0,707 | 21,10 | 29,84 | | |
| H18 | DL2B_5 | 58,00 | 2,98 | 2,65 | 0,25 | 0,636 | 32,04 | 50,37 | | |
| H19 | DL2B_5 | 86,65 | 3,36 | 4,32 | 0,29 | 0,717 | 28,42 | 39,61 | 549,0 | Absorber CH7-2-2 |
| H20 | DQ1B | 71,03 | 2,56 | 4,01 | 0,22 | 0,547 | 38,98 | 71,21 | | |
| H21 | DQ1B | 118,86 | 3,99 | 4,01 | 0,34 | 0,853 | 25,02 | 29,35 | 1019,2 | Absorber CH8-1-2 |
| H22 | DQ1B | 80,00 | 3,62 | 3,42 | 0,31 | 0,773 | 27,61 | 35,74 | | |
| H23 | DQ1B | 151,36 | 4,12 | 3,42 | 0,35 | 0,880 | 24,25 | 27,58 | 1198,9 | Absorber CH8-2-2 |
| H24 | DQ1B | 86,23 | 3,68 | 2,73 | 0,31 | 0,785 | 27,16 | 34,58 | | |
| H25 | DQ1B | 197,70 | 6,04 | 4,42 | 0,51 | 1,289 | 16,55 | 12,84 | 3036,6 | Absorber CH9-1-2 Crotch 2 |
| H26 | DQ2C | 120,50 | 4,37 | 3,47 | 0,37 | 0,932 | 15,62 | 16,75 | | |
| H27 | DQ1D | 103,39 | 3,26 | 3,24 | 0,28 | 0,696 | 30,65 | 44,03 | | |
| H28 | DQ1D | 50,00 | 2,59 | 2,20 | 0,22 | 0,553 | 38,55 | 69,67 | | |
| H29 | DQ1D | 79,05 | 3,35 | 2,20 | 0,29 | 0,716 | 29,82 | 41,67 | 1782,9 | Absorber CH9-2-2 |
| H30 | DL2D_5 | 29,50 | 2,08 | 1,15 | 0,18 | 0,443 | 45,97 | 103,67 | | |
| H31 | DL2D_5 | 129,65 | 6,11 | 2,97 | 0,52 | 1,304 | 15,64 | 12,00 | 1061,3 | Absorber CH13-1-1 |
| Src start | DL2D_4 | 0,00 | 6,08 | 2,93 | 0,52 | 1,297 | 11,50 | 8,87 | | |
| Src end | DL2D_4 | 0,00 | 5,73 | 2,55 | 0,49 | 1,223 | 12,21 | 9,98 | | |
| Src start | DL2D_3 | 0,00 | 5,73 | 2,55 | 0,49 | 1,223 | 9,49 | 7,76 | | |
| Src end | DL2D_3 | 0,00 | 5,37 | 2,24 | 0,46 | 1,146 | 10,12 | 8,83 | | |
| Src start | DL2D_2 | 0,00 | 5,37 | 2,24 | 0,46 | 1,146 | 7,72 | 6,74 | | |
| Src end | DL2D_2 | 0,00 | 5,00 | 2,00 | 0,43 | 1,068 | 8,29 | 7,76 | | |
| H32 | DL2D_1 | 25,00 | 4,78 | 1,89 | 0,41 | 1,020 | 6,69 | 6,56 | | |
| H33 | DL2D_1 | 87,59 | 5,43 | 1,89 | 0,46 | 1,158 | 5,89 | 5,08 | 611,9 | Absorber CH14-1-1 |
| Src start | DL1E_1 | 0,00 | 2,47 | 1,82 | 0,21 | 0,527 | 12,37 | 23,47 | | |
| Src end | DL1E_1 | 0,00 | 2,17 | 1,64 | 0,19 | 0,464 | 14,05 | 30,25 | | |
| Src start | DL1E_2 | 0,00 | 2,17 | 1,64 | 0,19 | 0,464 | 19,03 | 40,98 | | |
| Src end | DL1E_2 | 0,00 | 1,90 | 1,40 | 0,16 | 0,407 | 21,73 | 53,41 | | |
| Src start | DL1E_3 | 0,00 | 1,90 | 1,40 | 0,16 | 0,407 | 28,92 | 71,09 | | |
| H34 | DL1E_1 | 38,13 | 2,25 | 1,68 | 0,19 | 0,480 | 13,60 | 28,34 | | |
| Src end | DL1E_1 | 0,00 | 2,18 | 1,64 | 0,19 | 0,465 | 14,02 | 30,13 | | |
| Src start | DL1E_4 | 0,00 | 1,72 | 1,09 | 0,15 | 0,368 | 43,61 | 118,53 | | |
| H35 | DL1E_4 | 25,00 | 1,72 | 1,09 | 0,15 | 0,367 | 43,67 | 118,89 | | |
| H36 | DL1E_4 | 32,00 | 2,09 | 1,09 | 0,18 | 0,446 | 35,95 | 80,59 | 1303,8 | CVAL |
| H37 | DL1E_5 | 32,00 | 6,35 | 0,29 | 0,54 | 1,357 | 17,94 | 13,22 | | |

| | | | |
|---|---|---|---|
| | | Power SR absorbers | 14653,8 [W] |
| **Pt nº** | Abs points, marked in the drawings | Power FE BM | 336,26 [W] |
| **Src** | synchrotron radiation source type | Power ID FE | 813,68 [W] |
| **D e-beam** | distance Abs point to e-beam | Total Power | 15803,72 [W] |
| **d (mm)** | distance from source point to Absorber Pt | Total Power Theo. | 15795,8 [W] |
| **α(degree º)** | angle between X-ray and e-beam orbit | | |
| **σ (mm)** | Gaussian vertical height of X-ray | error | 7,92 [W] |
| **Pl (W/mm)** | linear power density @normal inc. on the absorber in the horizontal plan | | |
| **Pa (W/mm2)** | surface power density on the absorber | | |
| **Ptot (W)** | total power on the absorber | | |
| **Name** | name of the photon absorber | | |

## Girder assembly

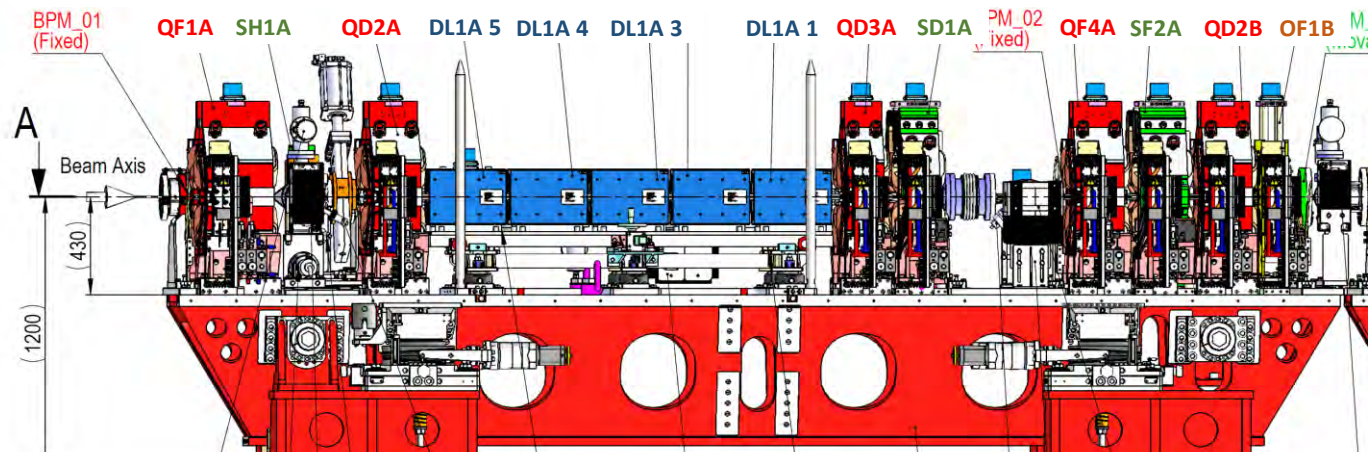


Figure 3.35: Girder 1 front view.

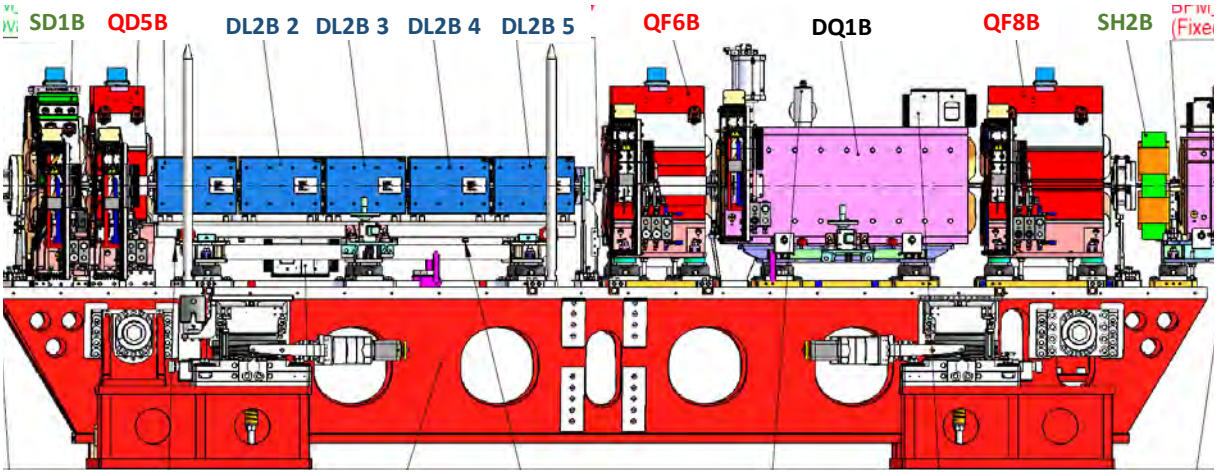


Figure 3.36: Girder 2 front view.

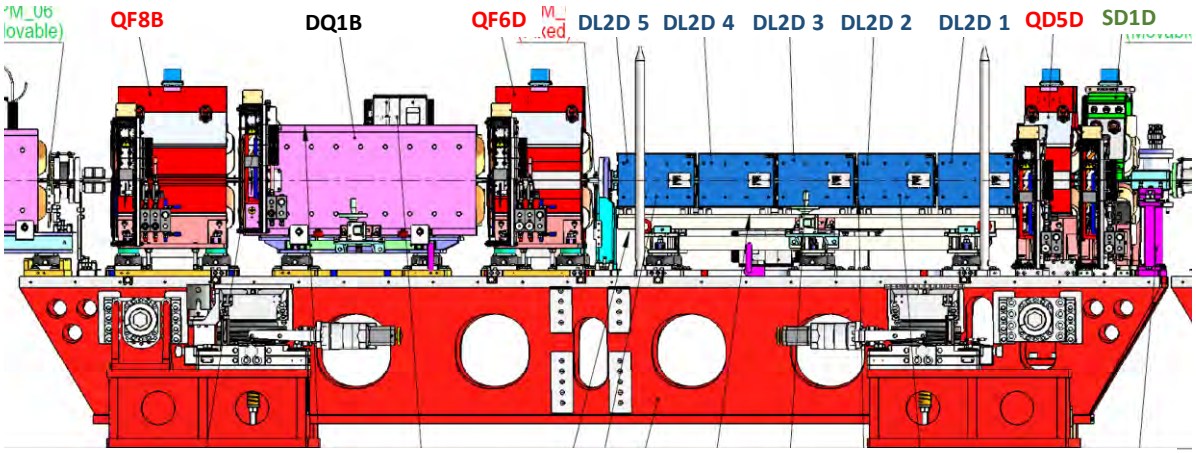


Figure 3.37: Girder 3 front view.

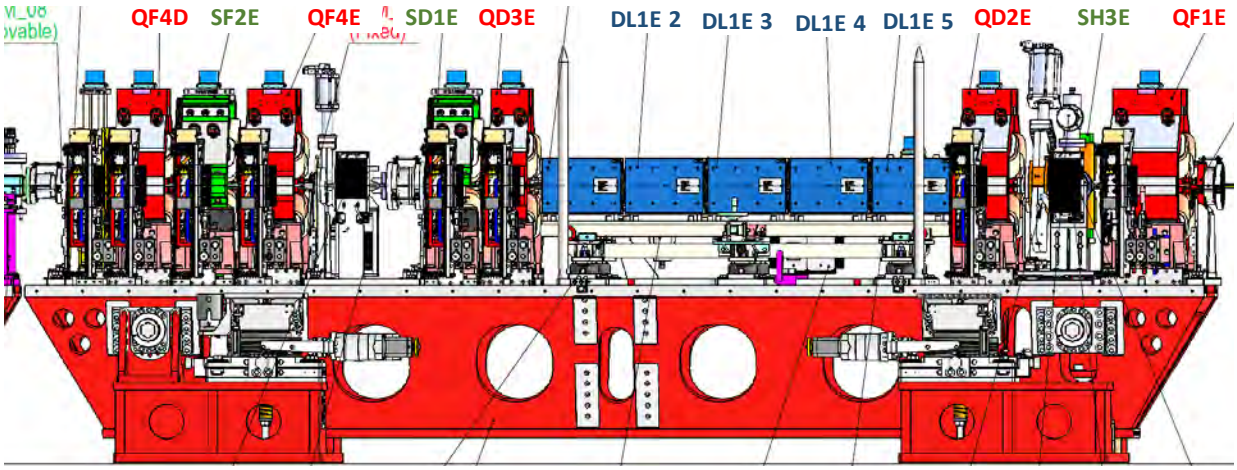


Figure 3.38: Girder 4 front view

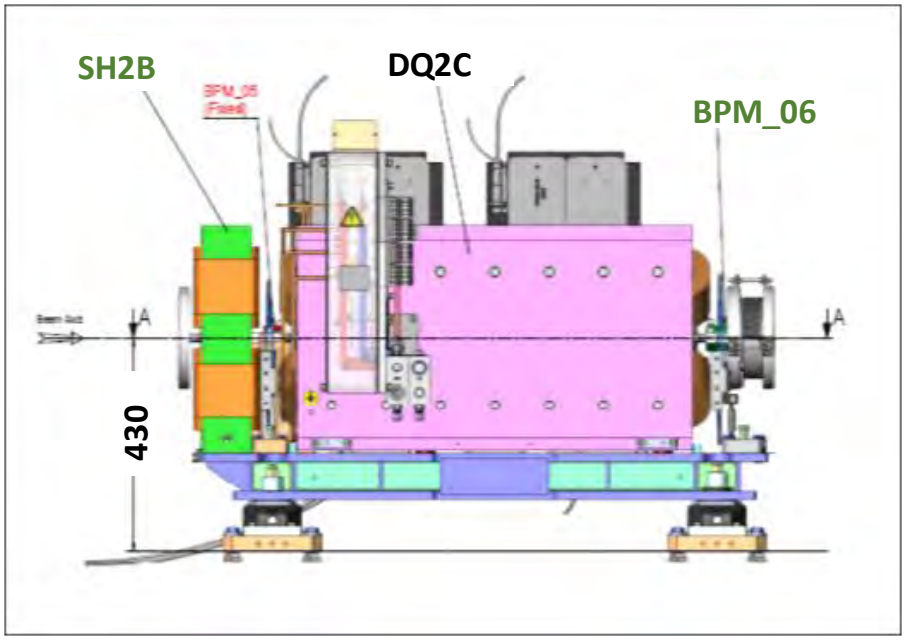


Figure 3.39: DQ2C assembly (between girder 2 & 3).

## Girder magnets: section views

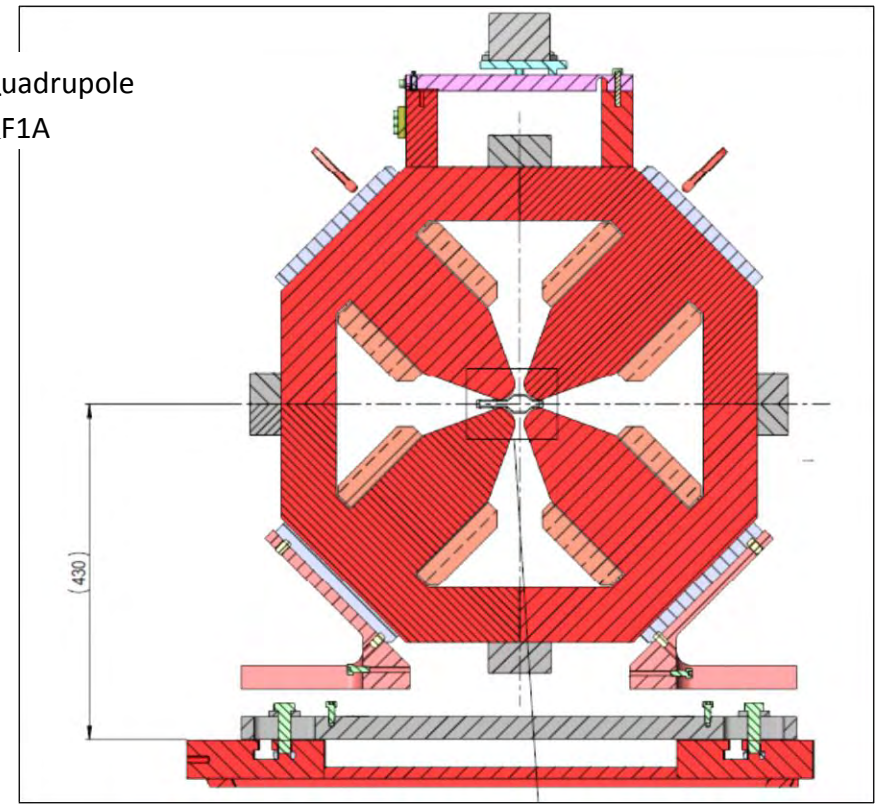


Detail (1:1)

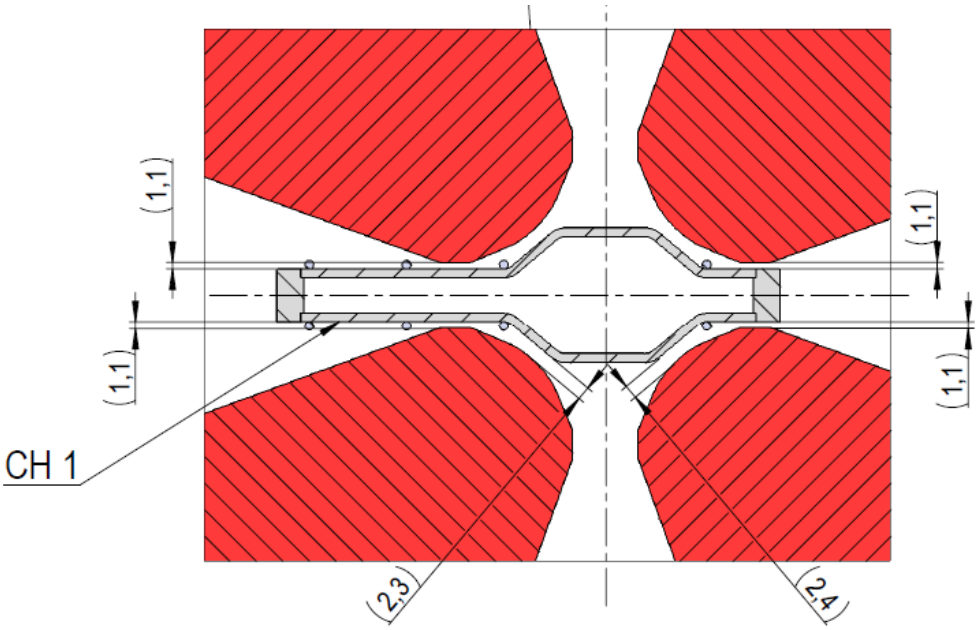


Figure 3.40: Girder 1 QF1A section view.

Corrector
SH1A

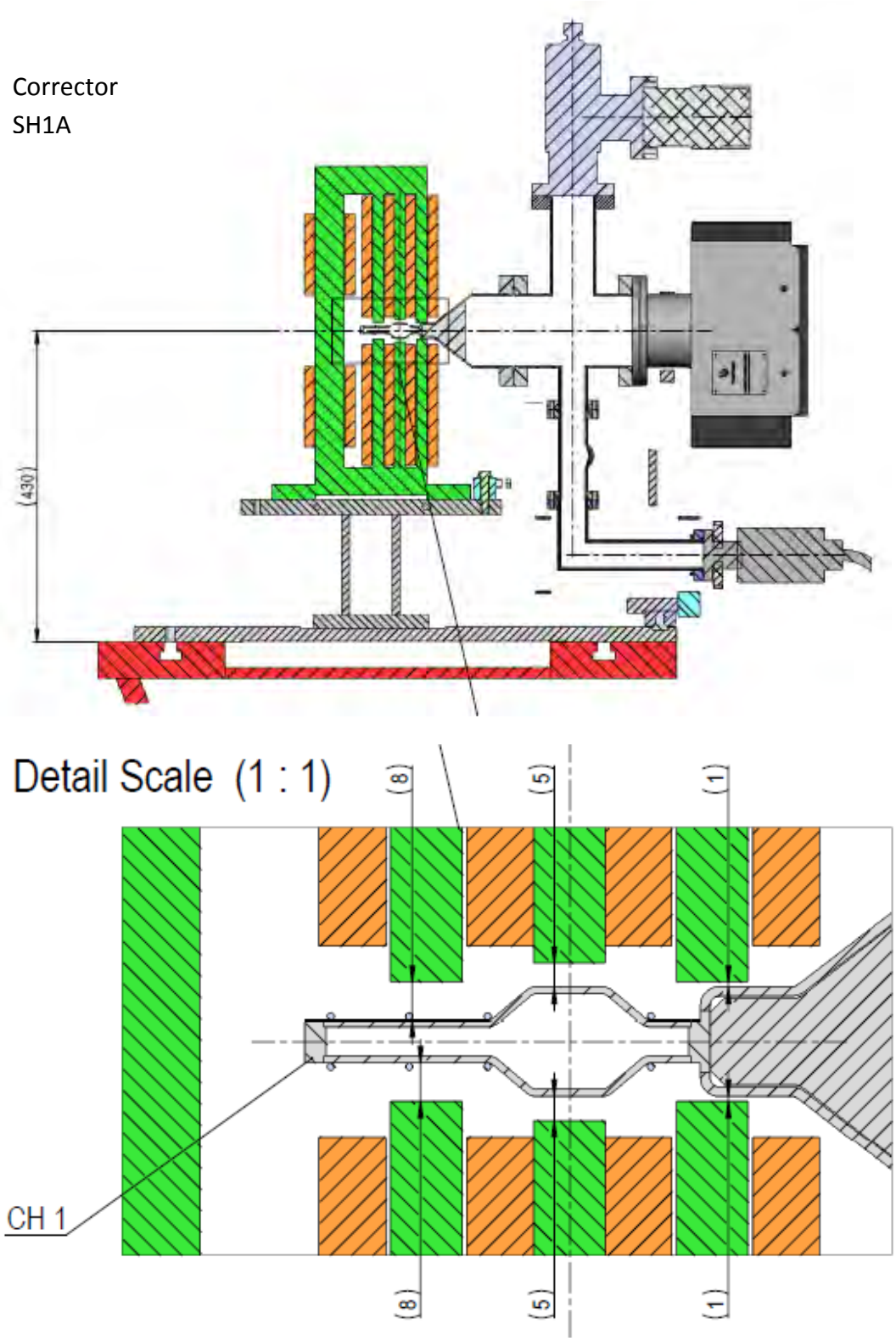


Figure 3.41: Girder 1 SH1A section view.

Quadrupole
QD2A

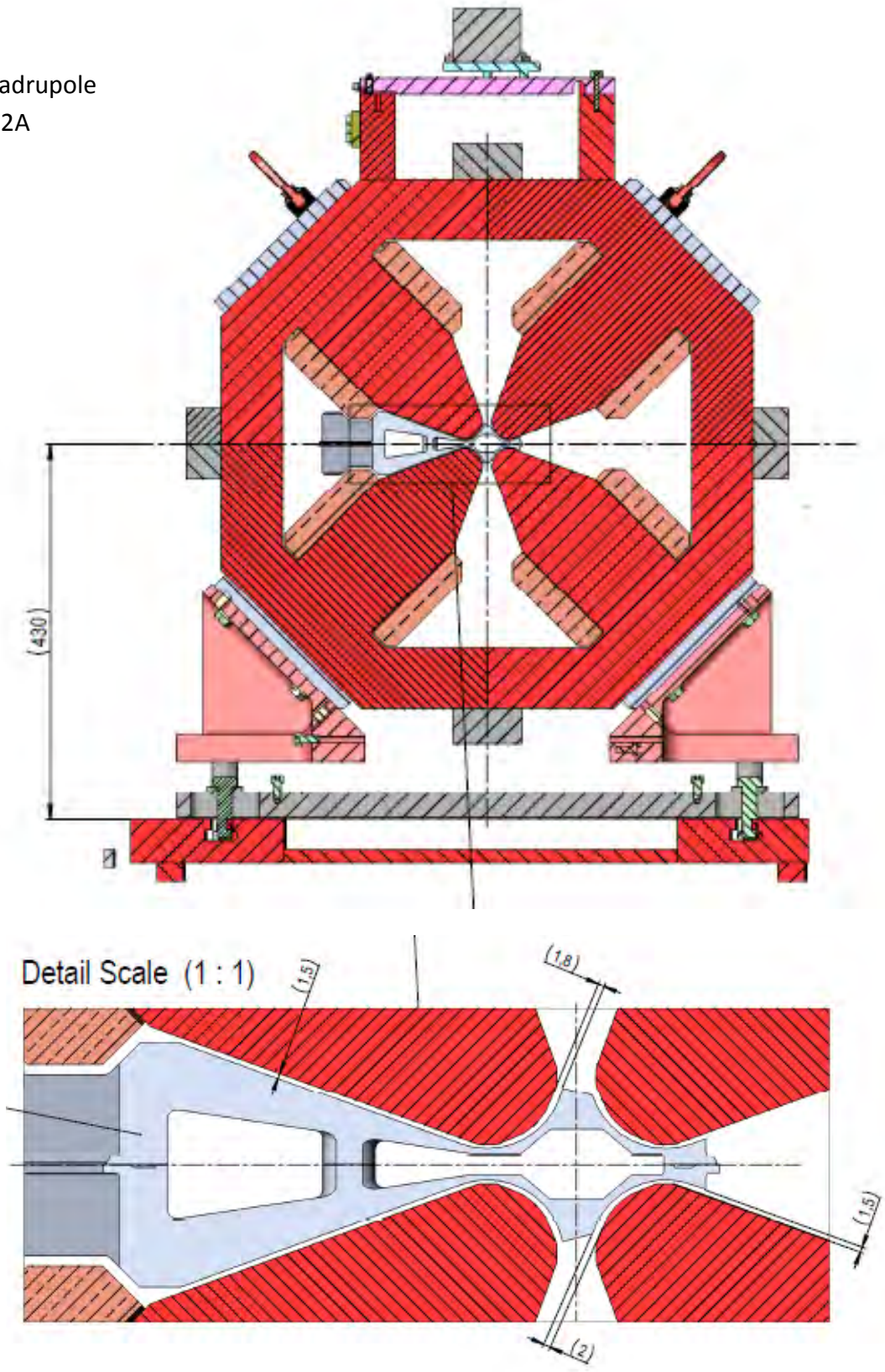


Figure 3.42: Girder 1 QD2A magnet section view.

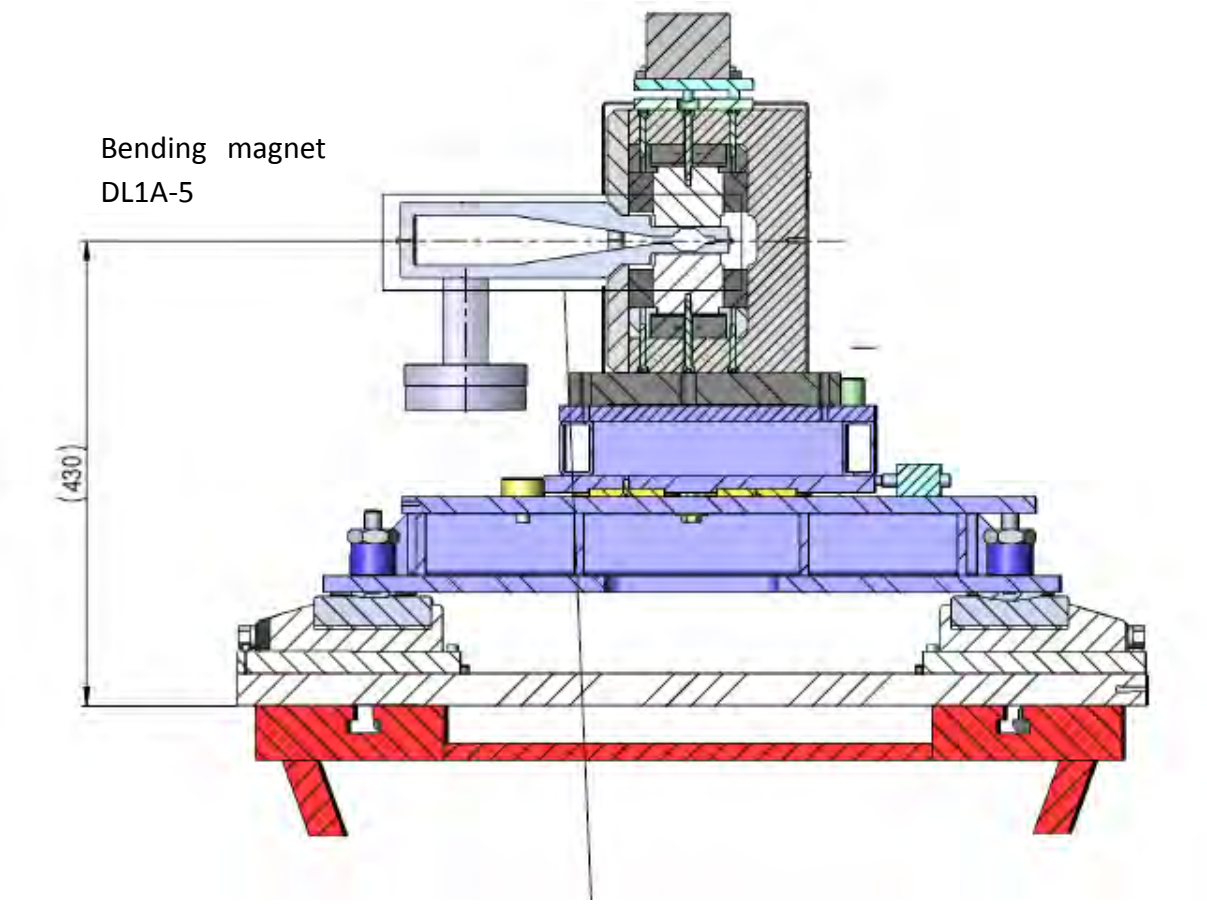


Detail (1:1)

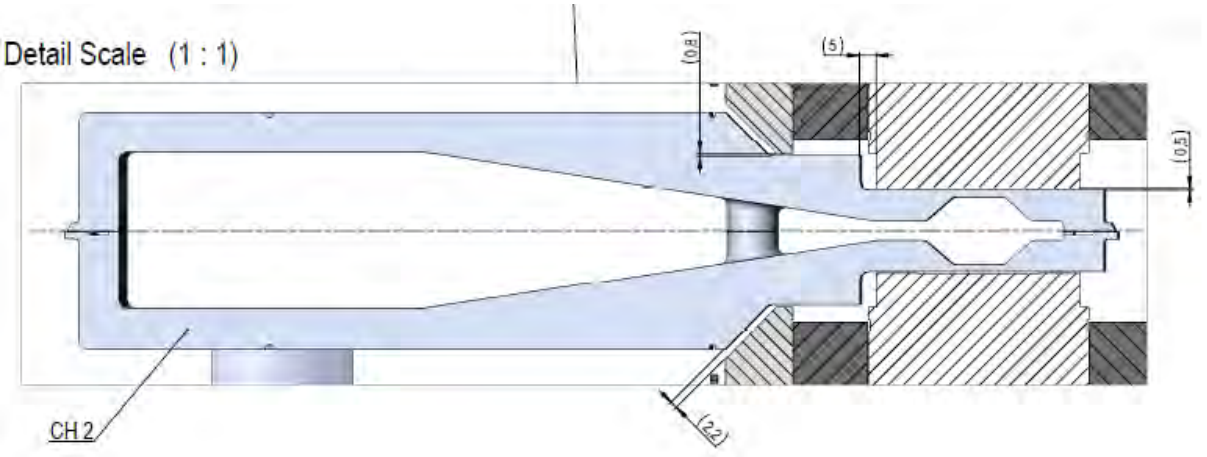


**Figure 3.43: Girder 1 DL1A_5 magnet section view.**

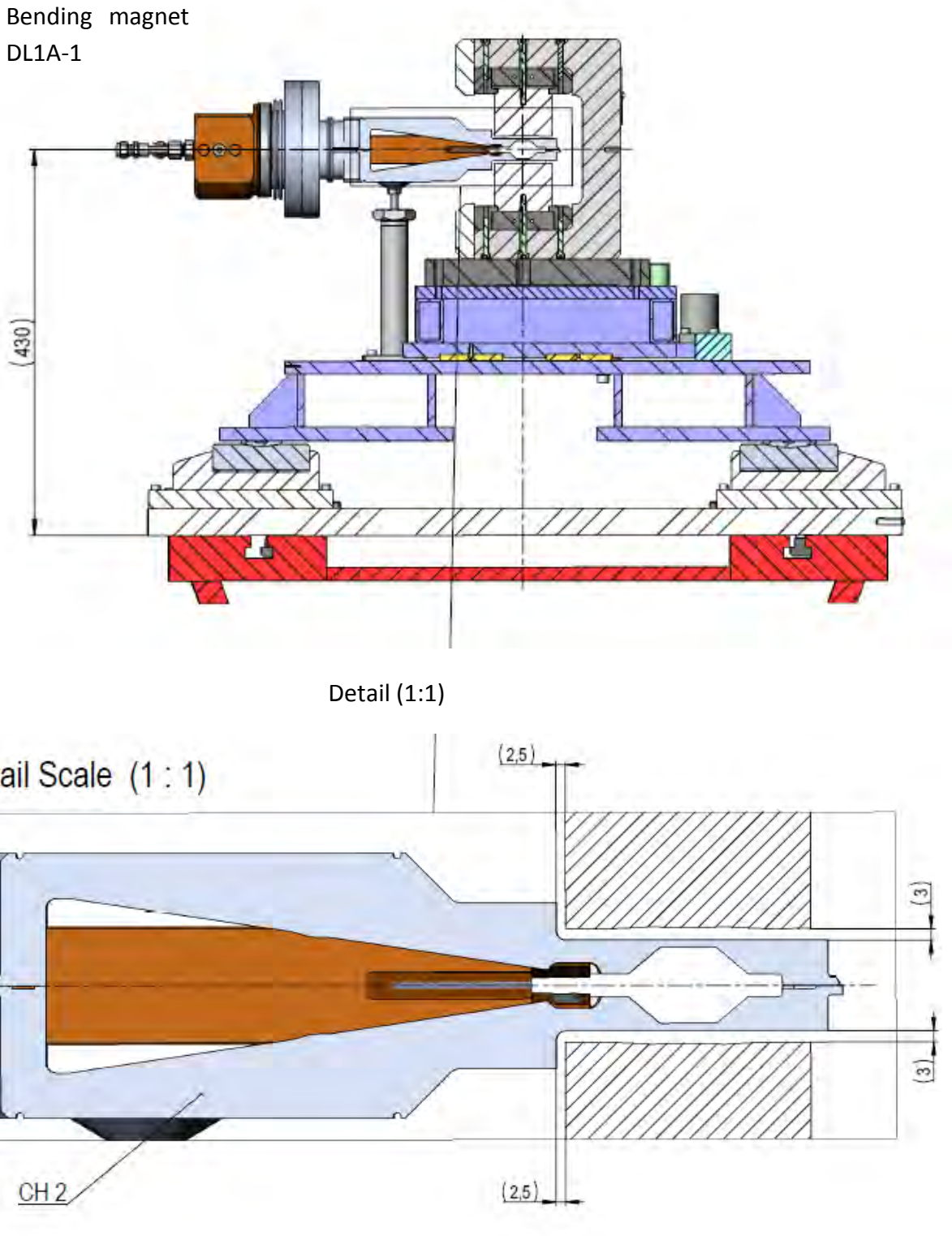


Figure 3.44: Girder 1 DL1A_1 magnet section view.

Quadrupole
QD3A

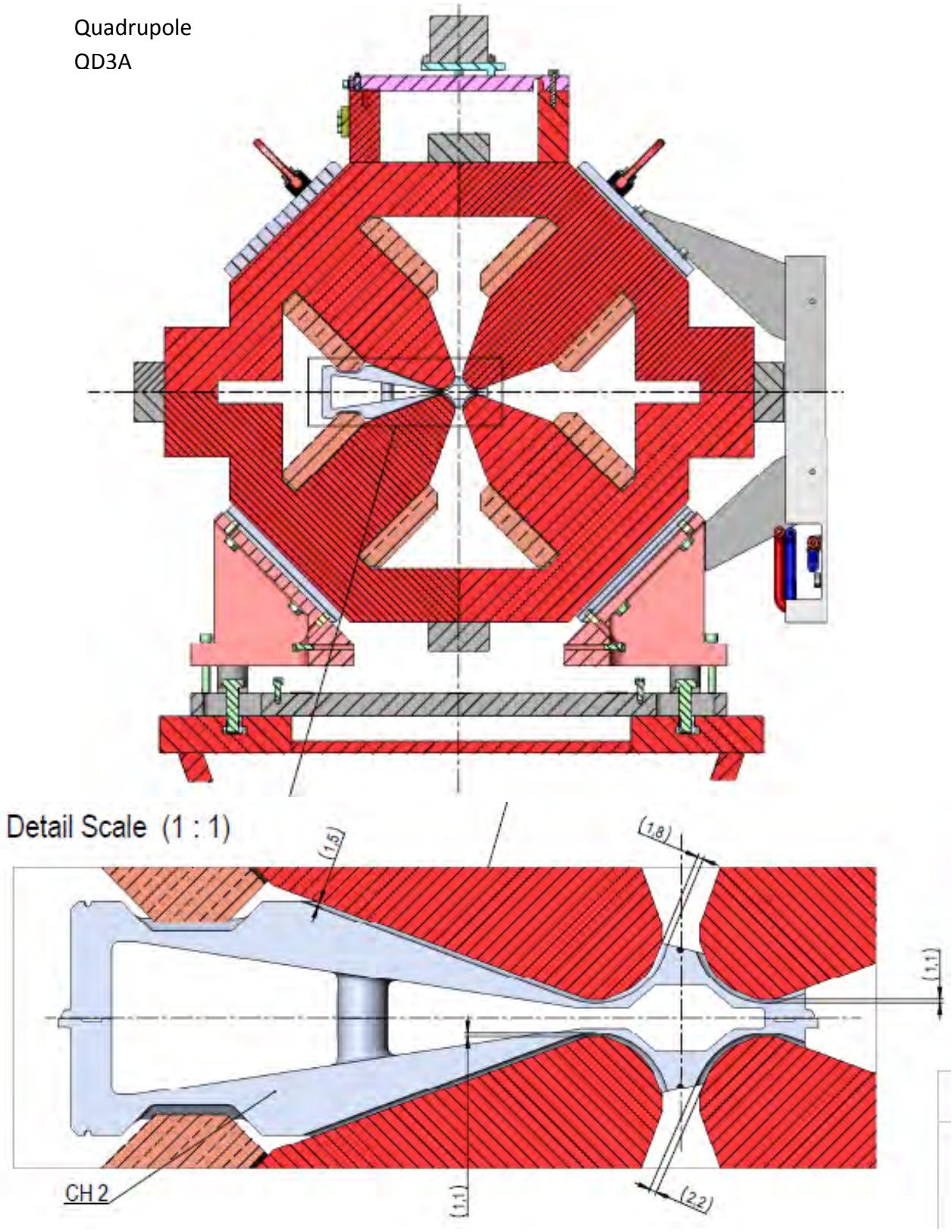


Figure 3.45: Girder 1 QD3A magnet section view.

Sextupole
SD1A

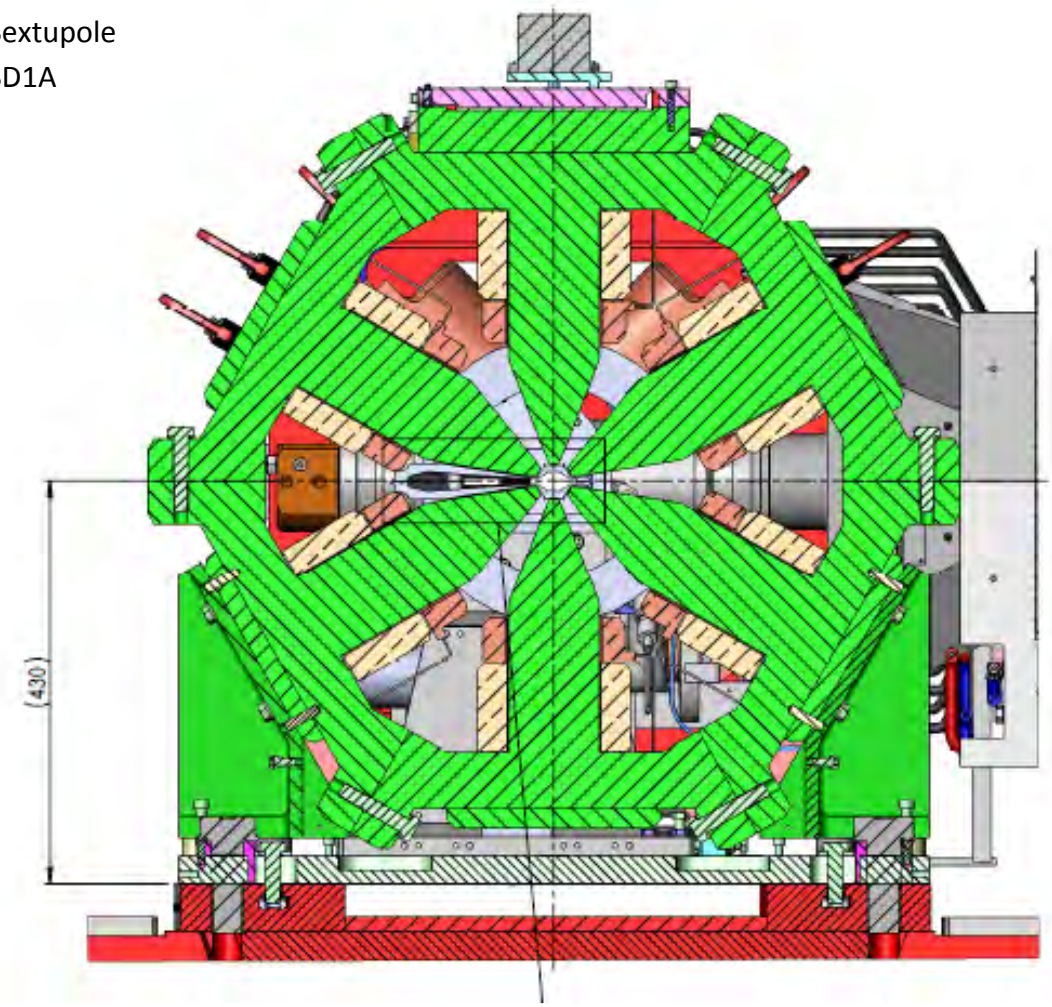


Detail (1:1)

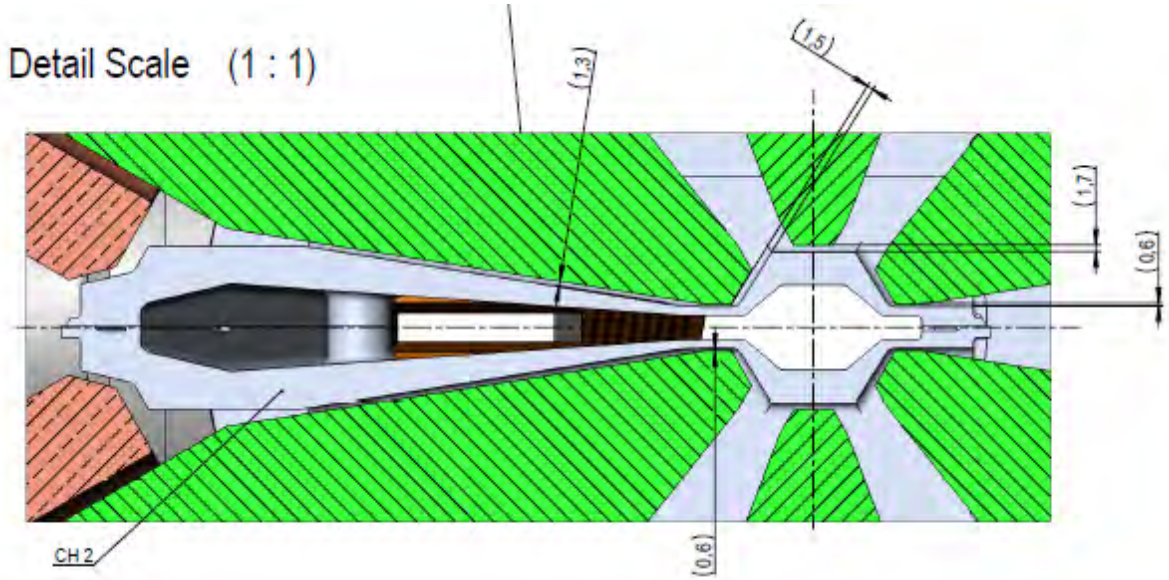


Figure 3.46: Girder 1 SD1A magnet section view.

Absorber
CH3-1-1

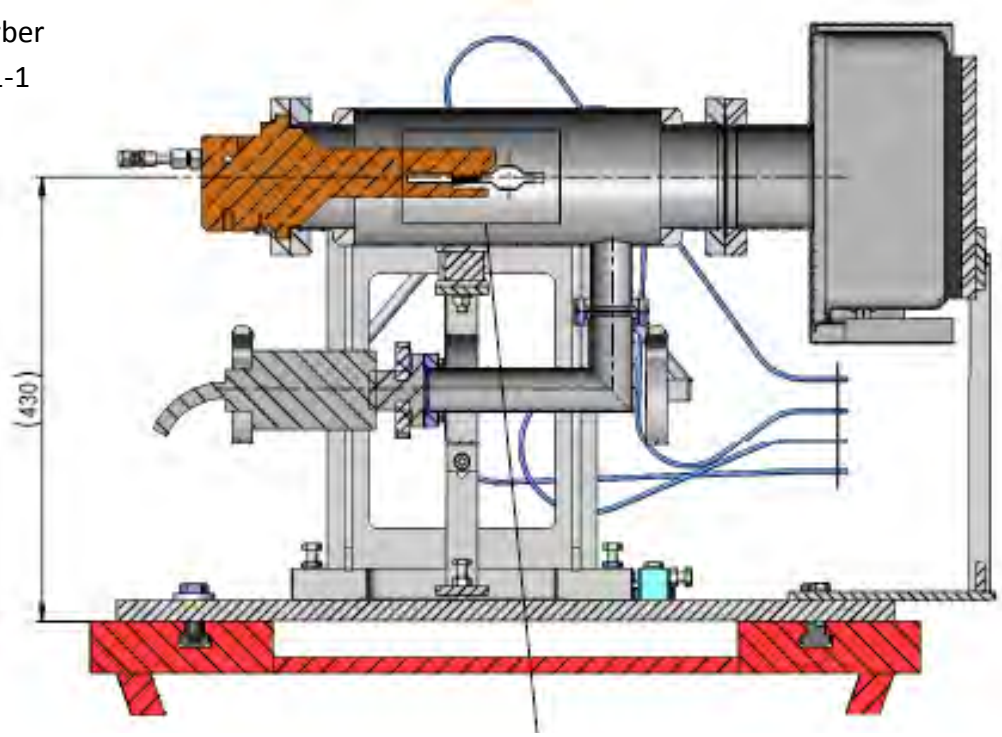


Detail (1:1)

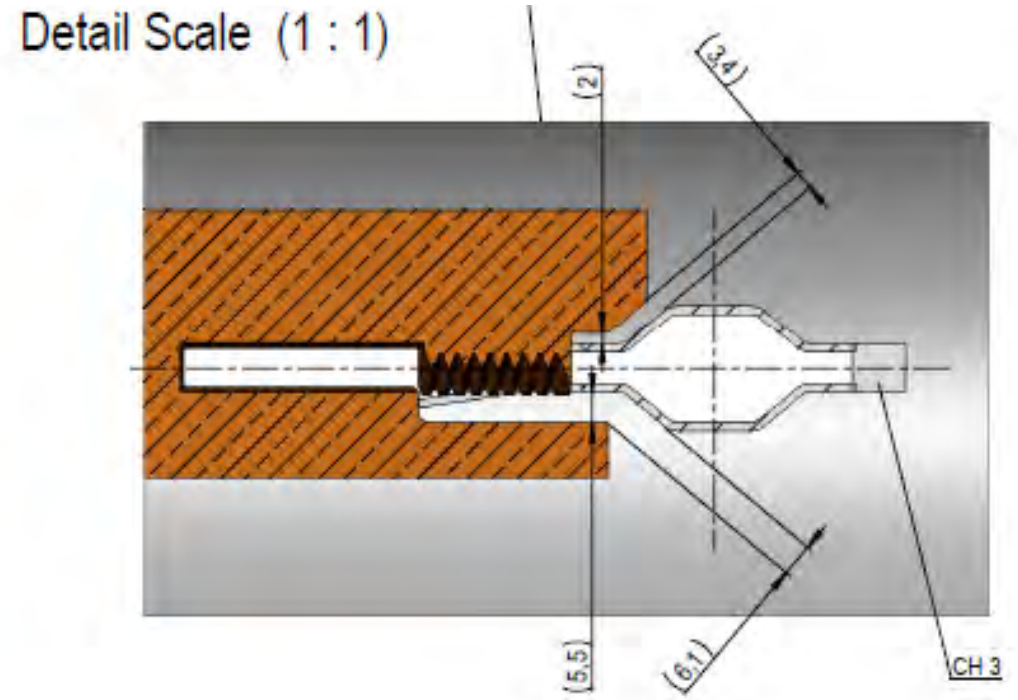


**Figure 3.47: Girder 1 absorber CH3-1-1 section view.**

Quadrupole
QF4A

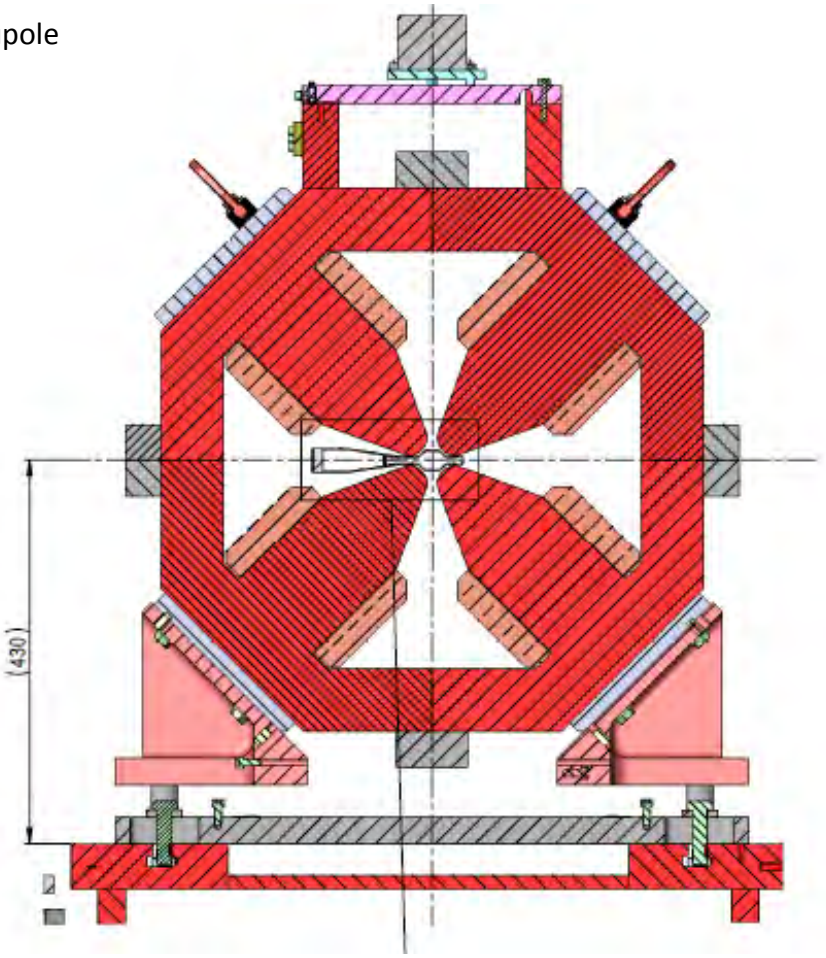


Detail (1:1)

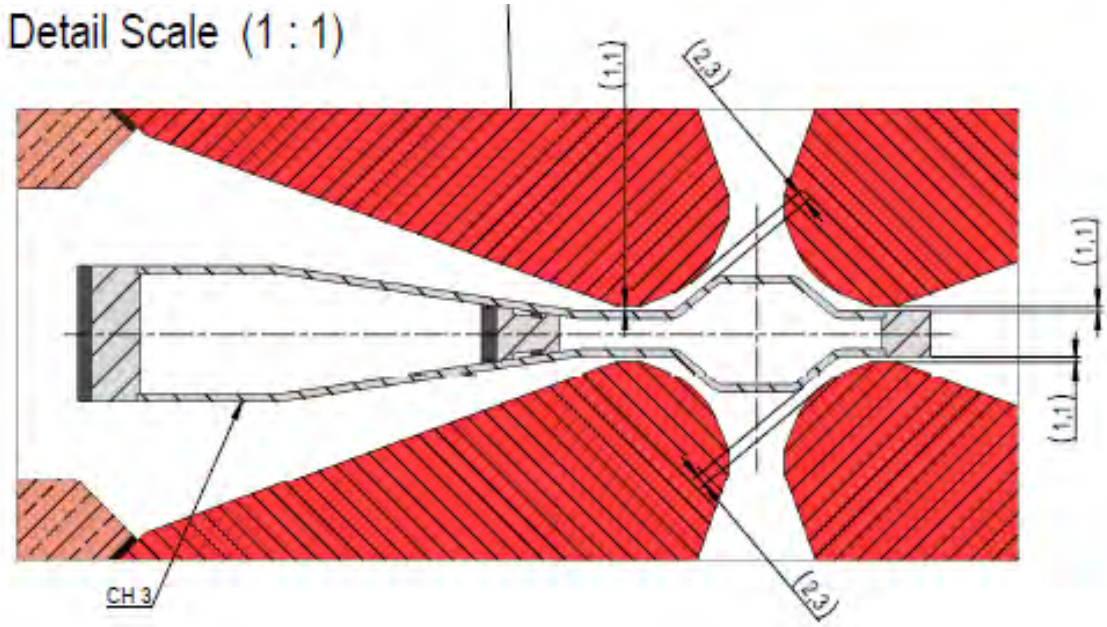


**Figure 3.48: Girder 1 QF4A magnet section view.**

Sextupole
SF2A

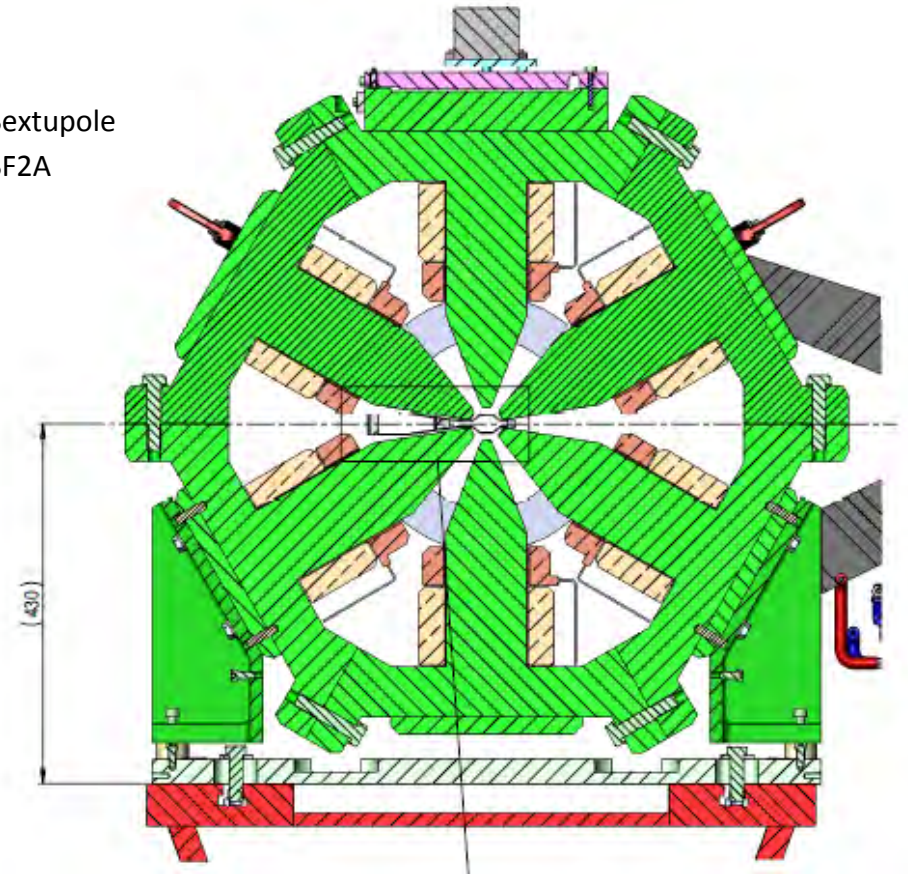


Detail (1:1)

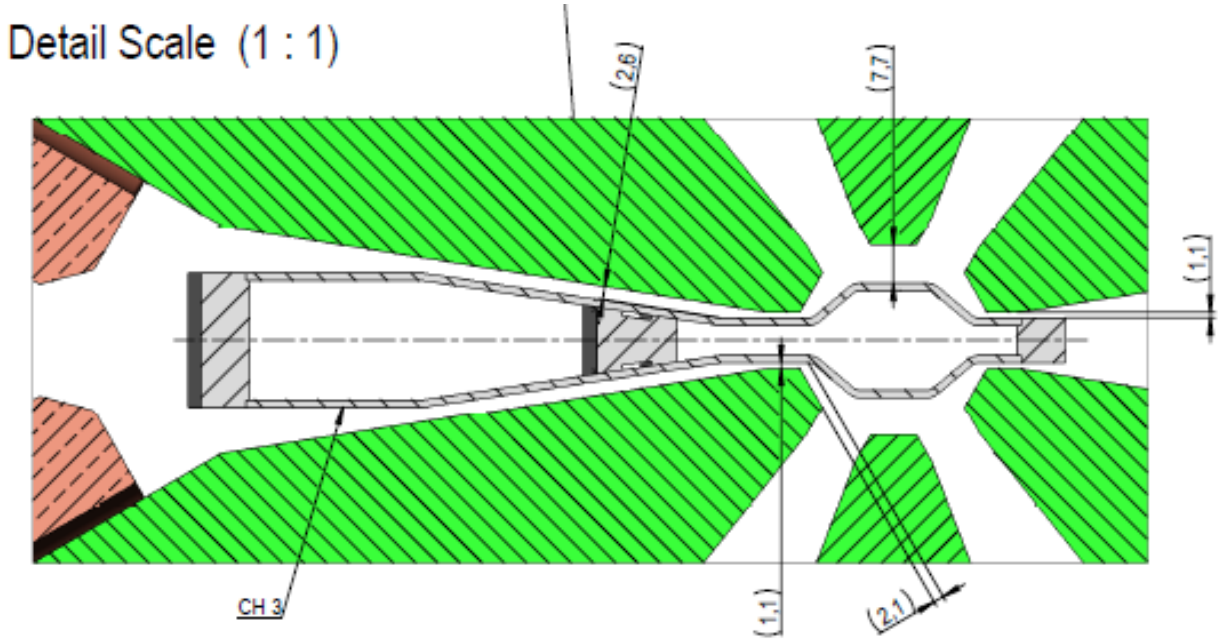


**Figure 3.49: Girder 1 SF2A magnet section view.**

Quadrupole
QF4B

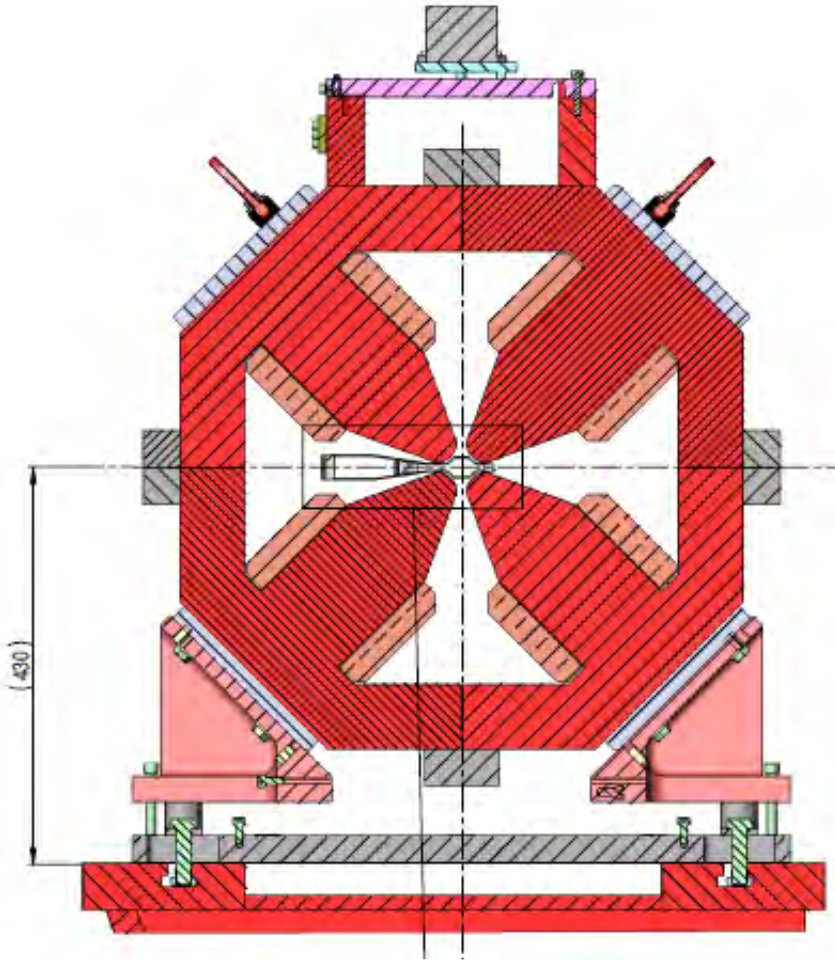


Detail (1:1)

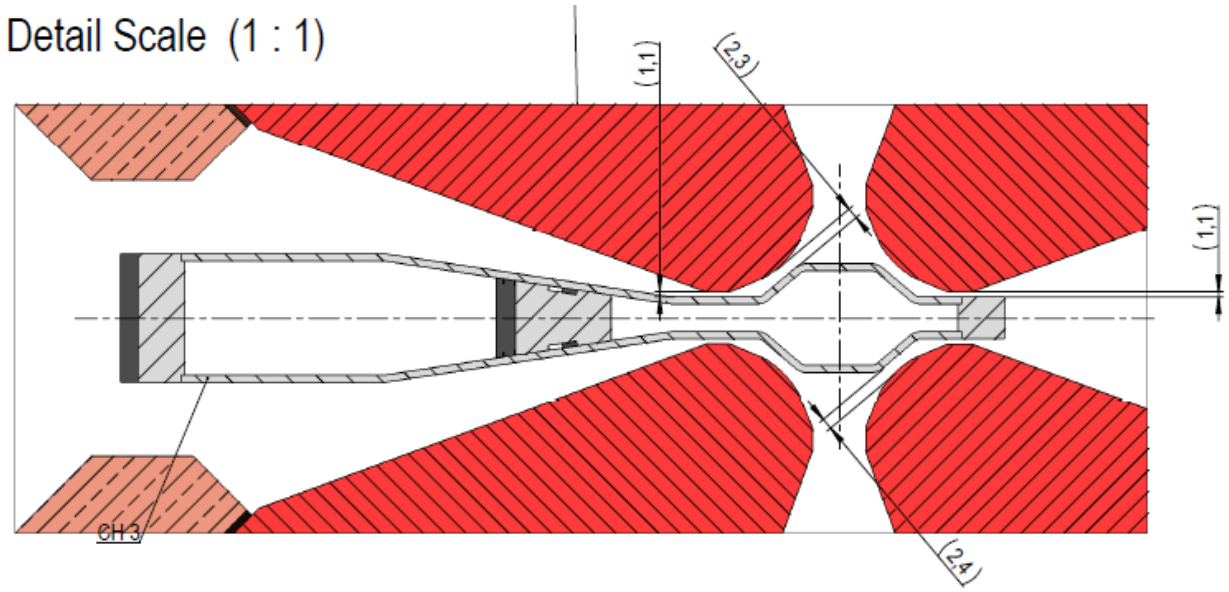


Figure 3.50: Girder 1 QF4B magnet section view.

Octupole
OF1B

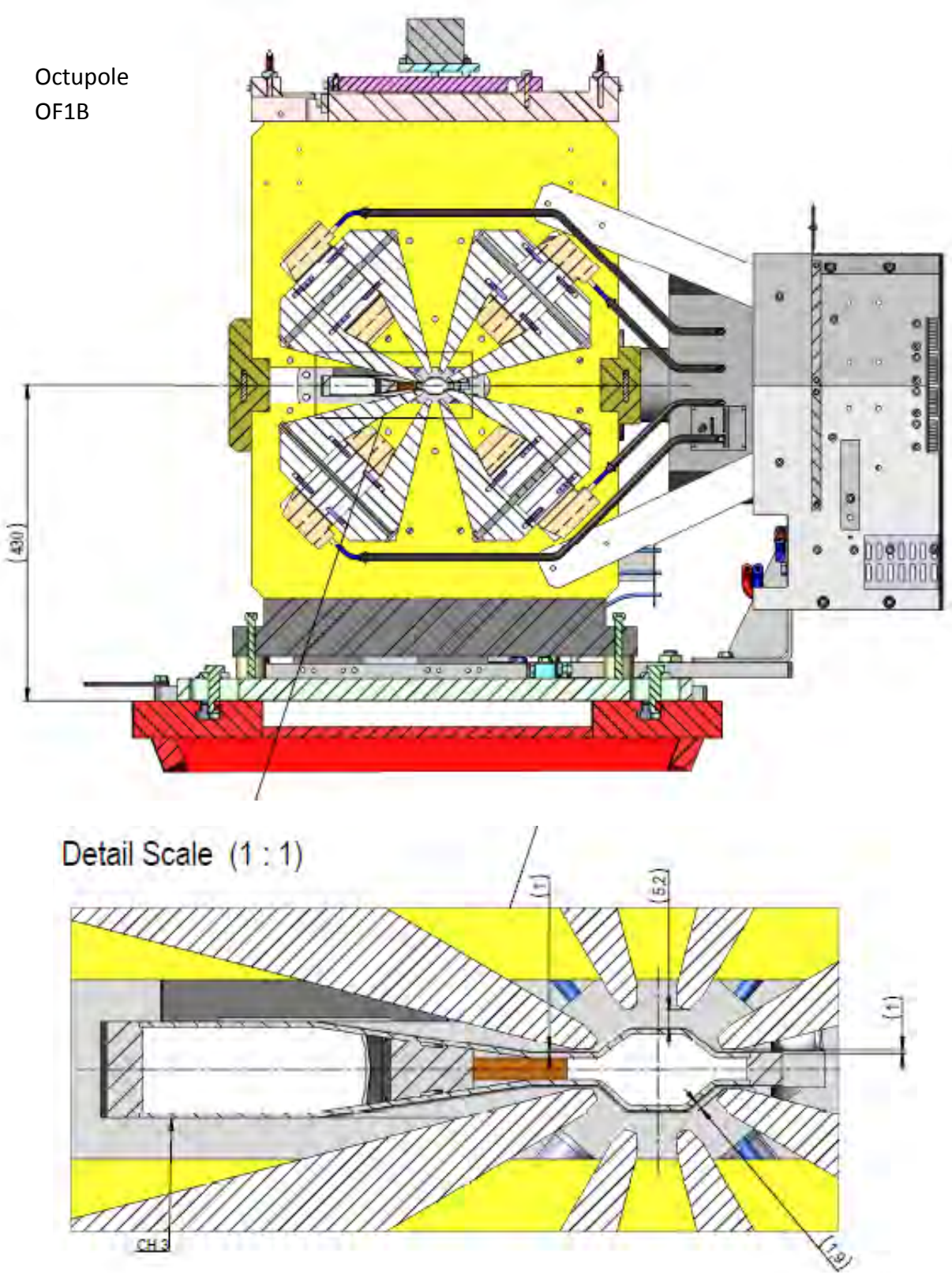


**Figure 3.51: Girder 1 OF1B magnet section view.**

Sextupole
SD1B

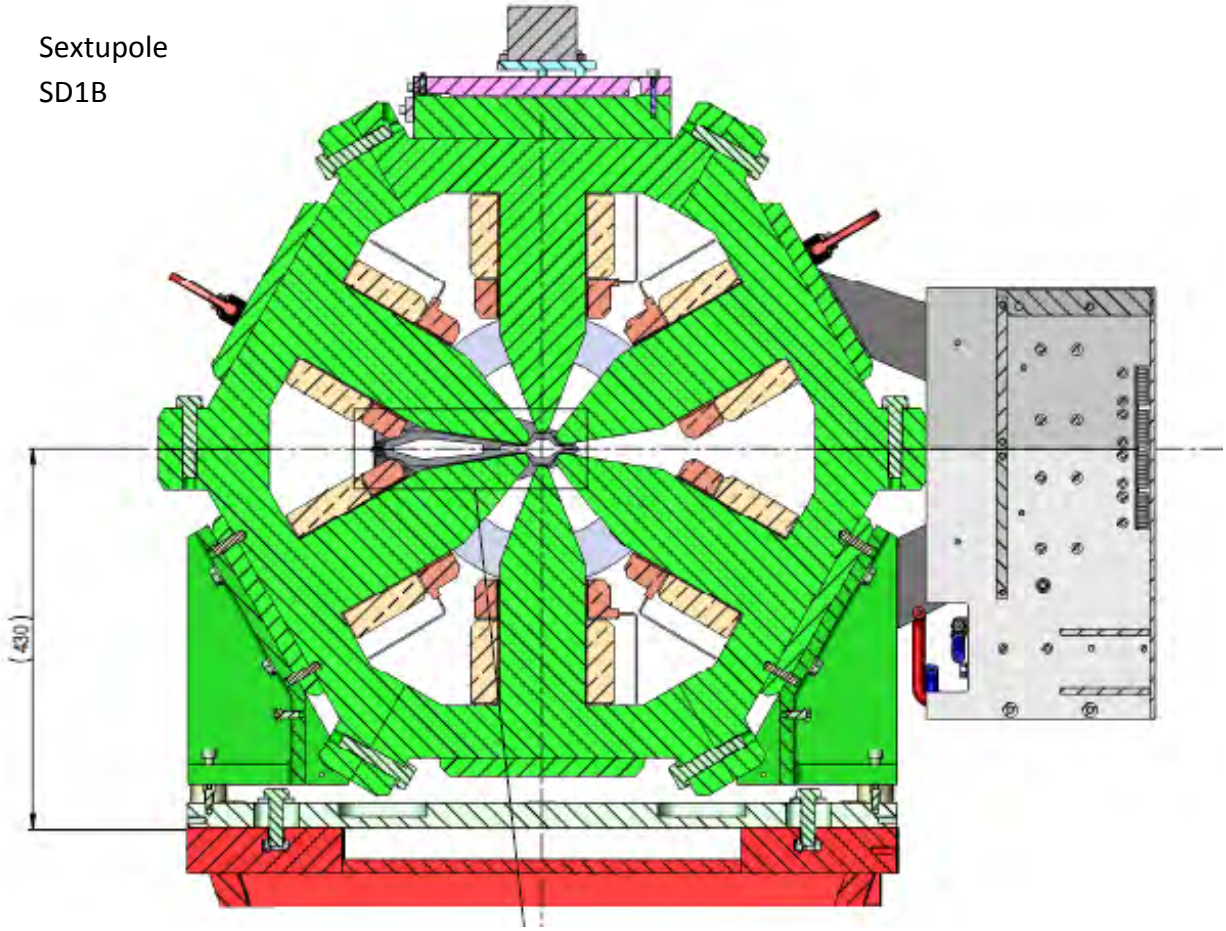


Detail (1:1)

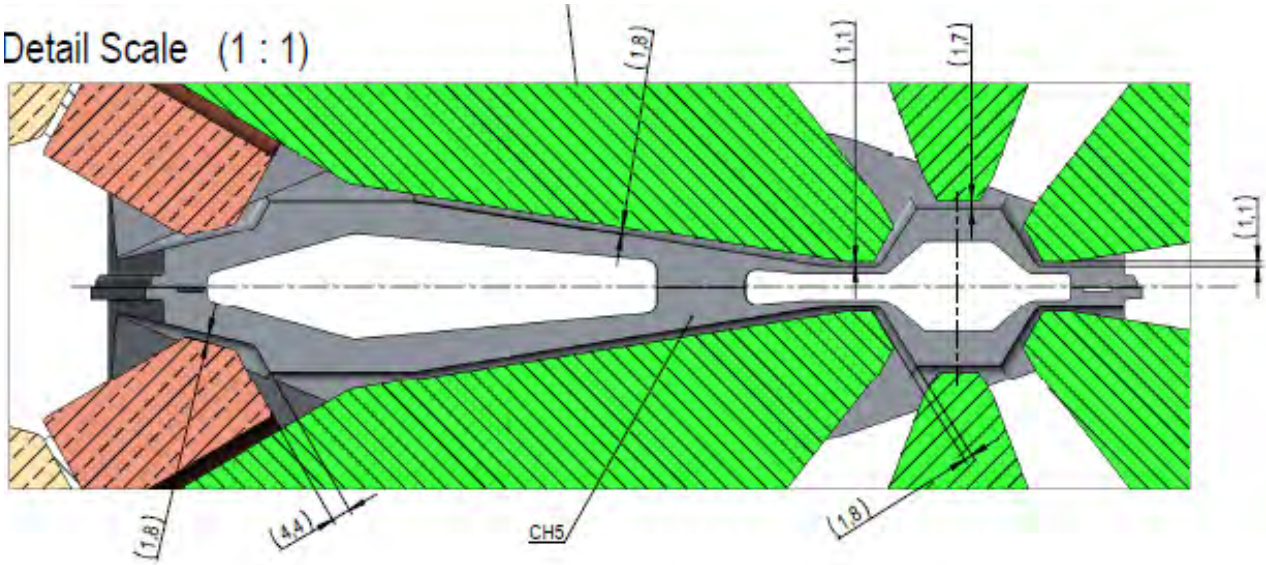


Figure 3.52: Girder 2 SD1B magnet section view.

Quadrupole
QD5B

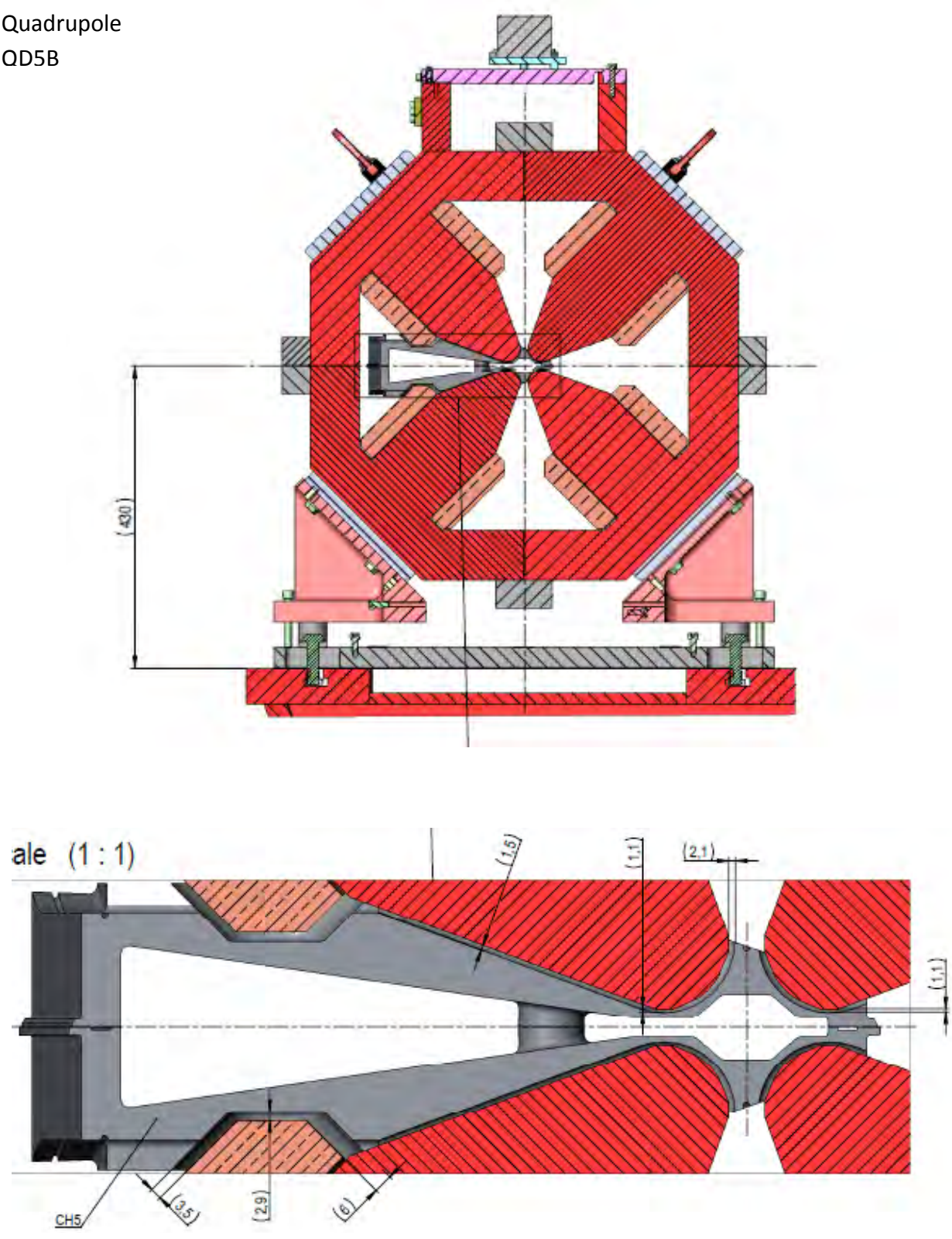


Figure 3.53: Girder 2 QD5B magnet section view.

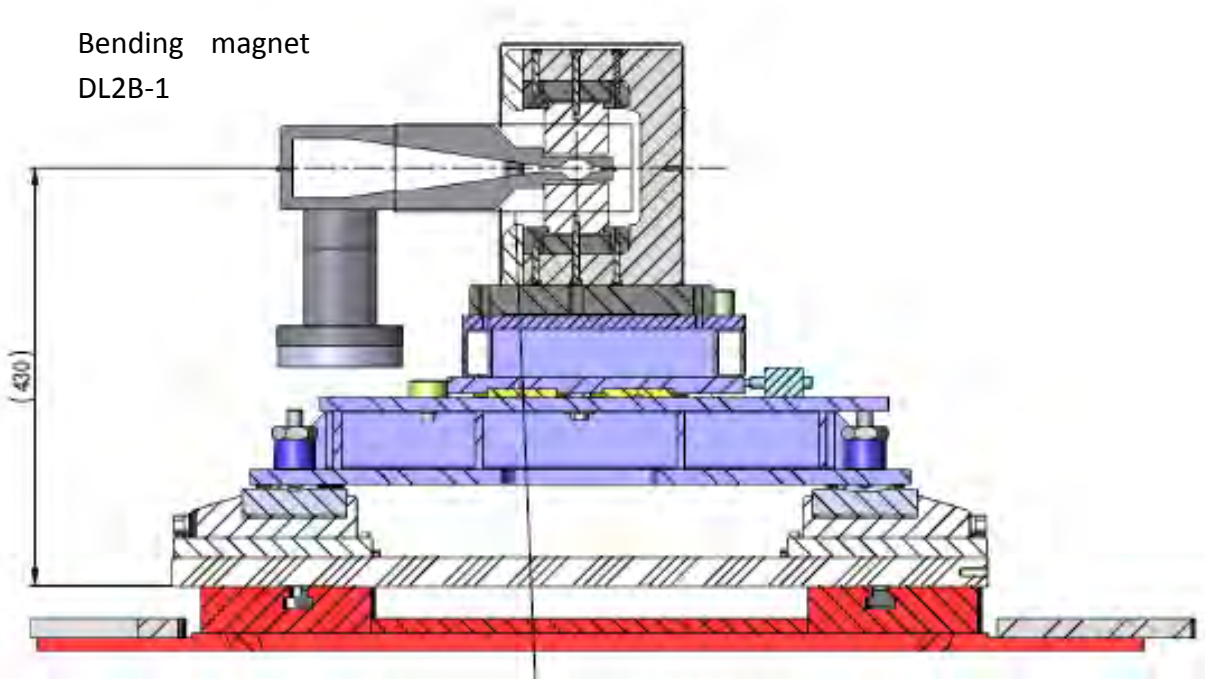


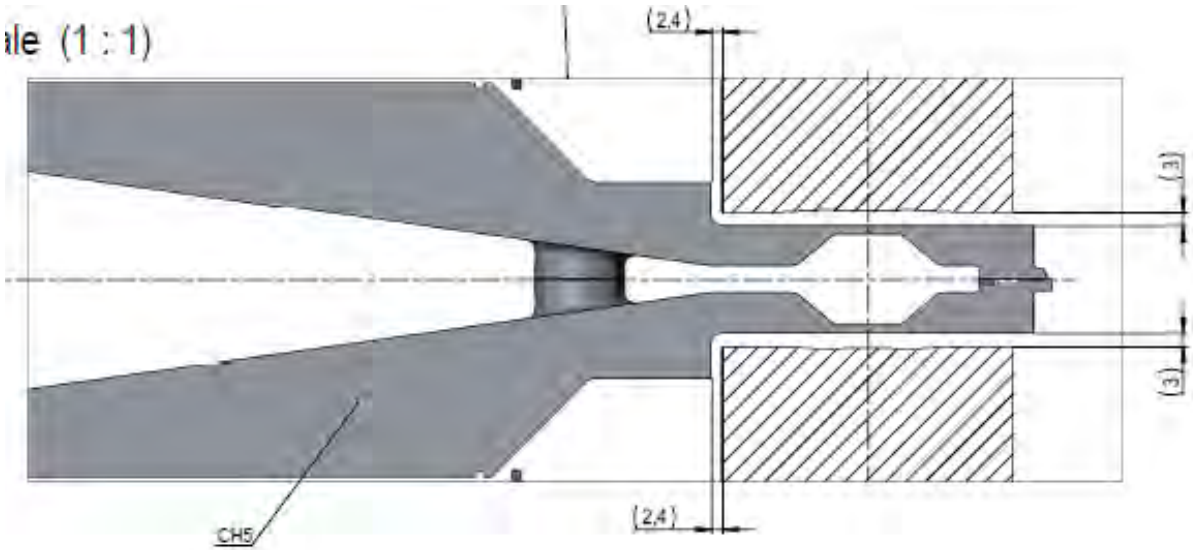


Figure 3.54: Girder 2 DL2B_1 magnet section view.

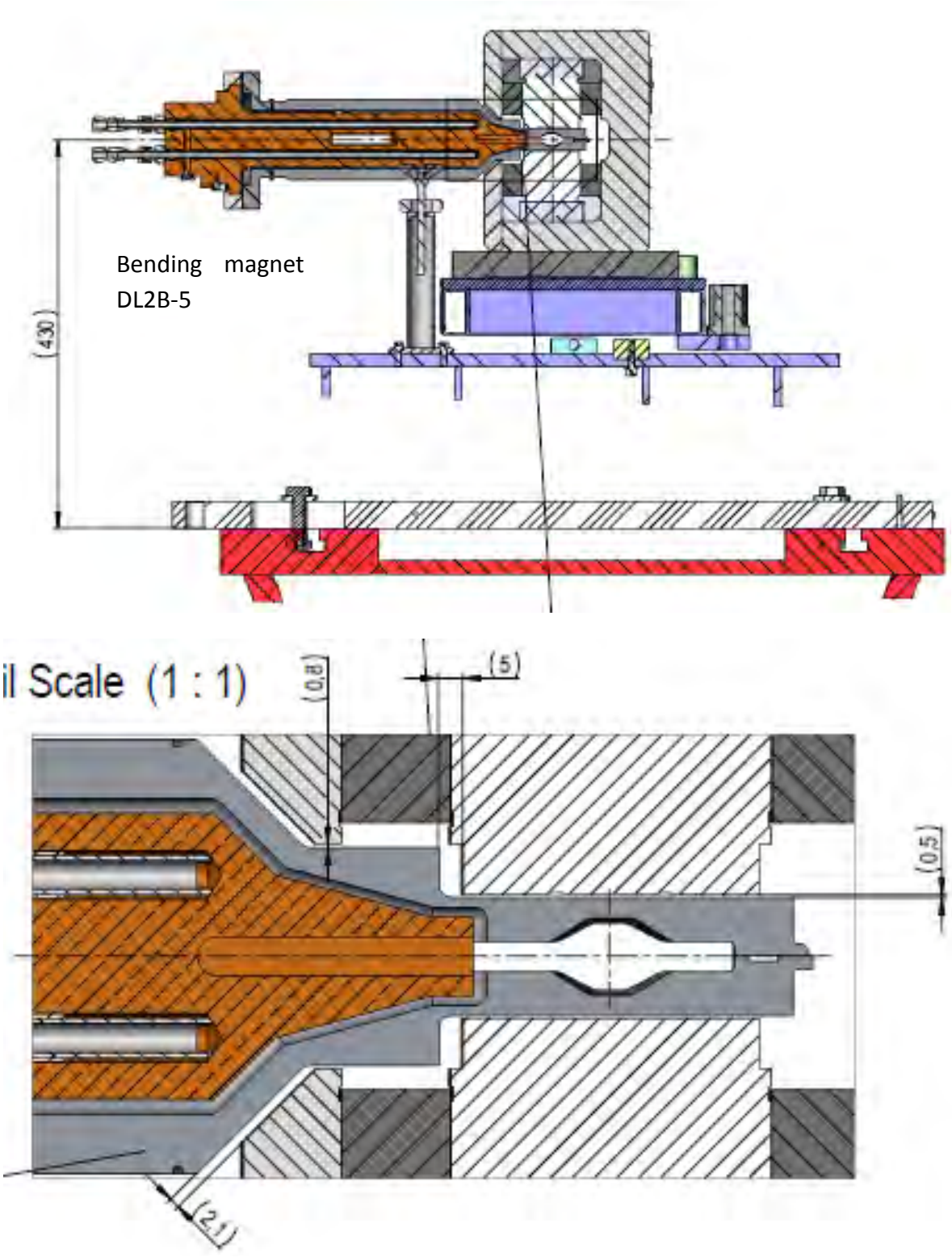


Figure 3.55: Girder 2 DL2B_5 magnet section view.

Quadrupole
QF6B

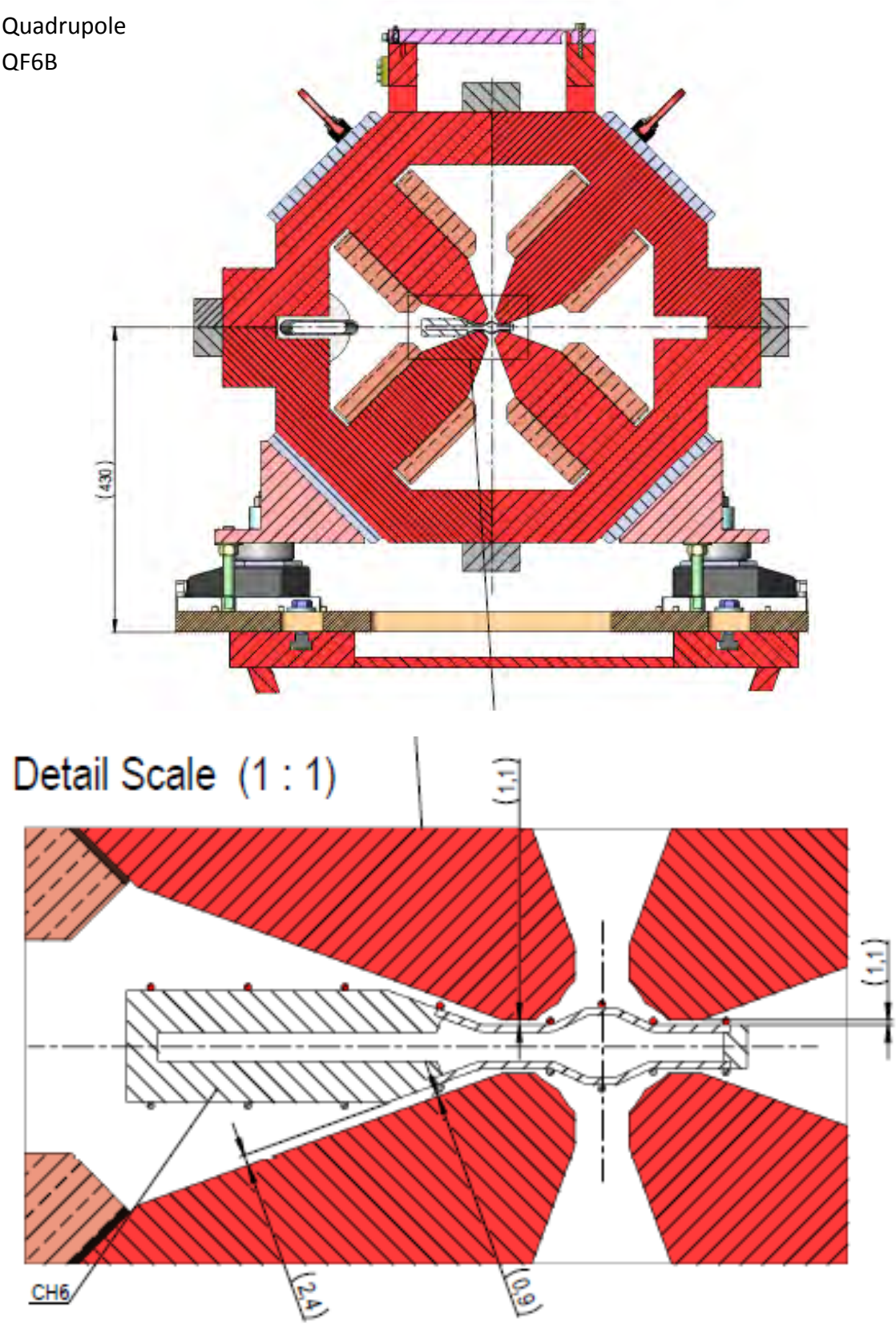


Figure 3.56: Girder 2 QF6B magnet section view.

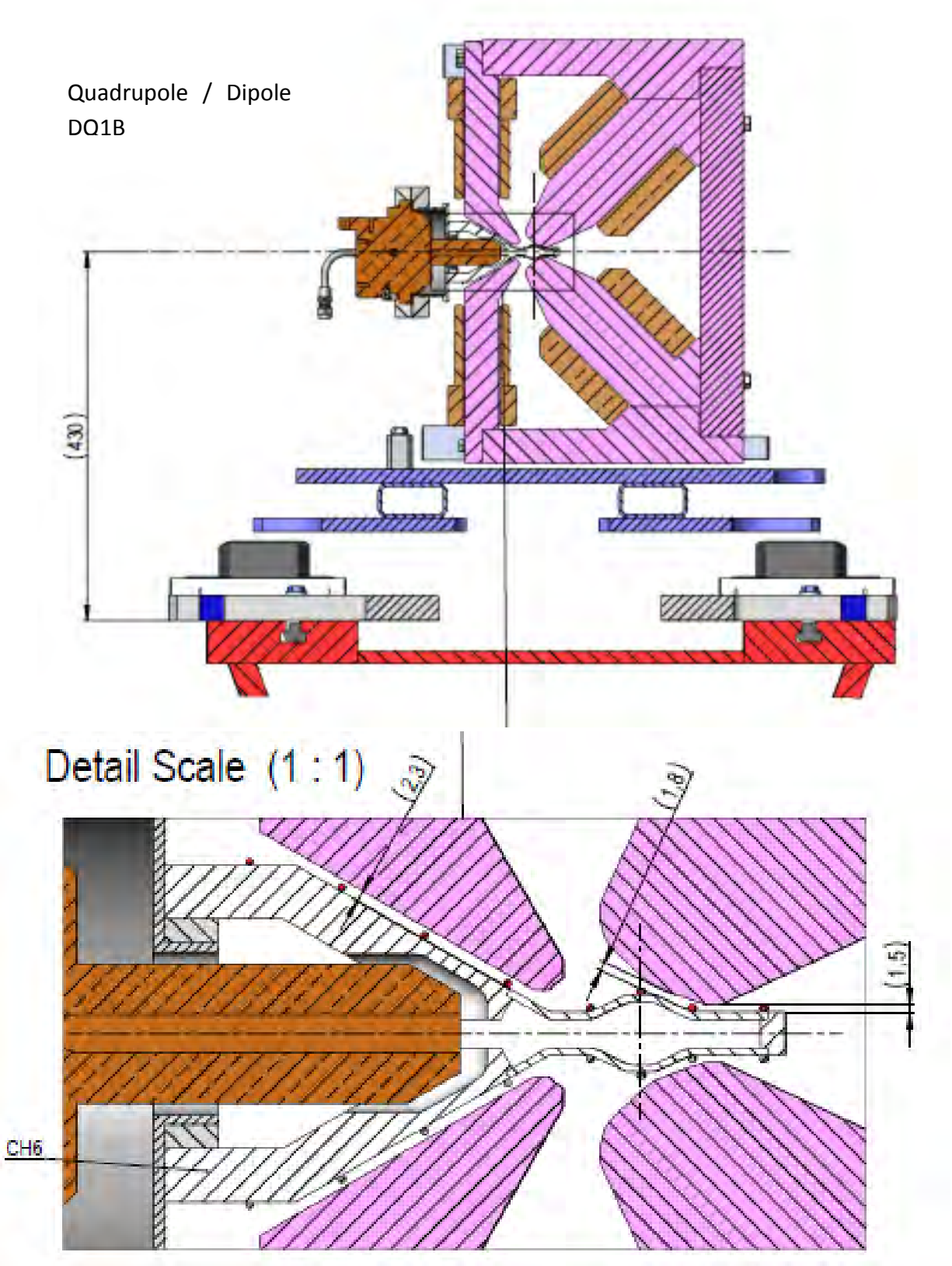


Figure 3.57: Girder 2 DQ1B magnet section view.

Quadrupole
QF8B

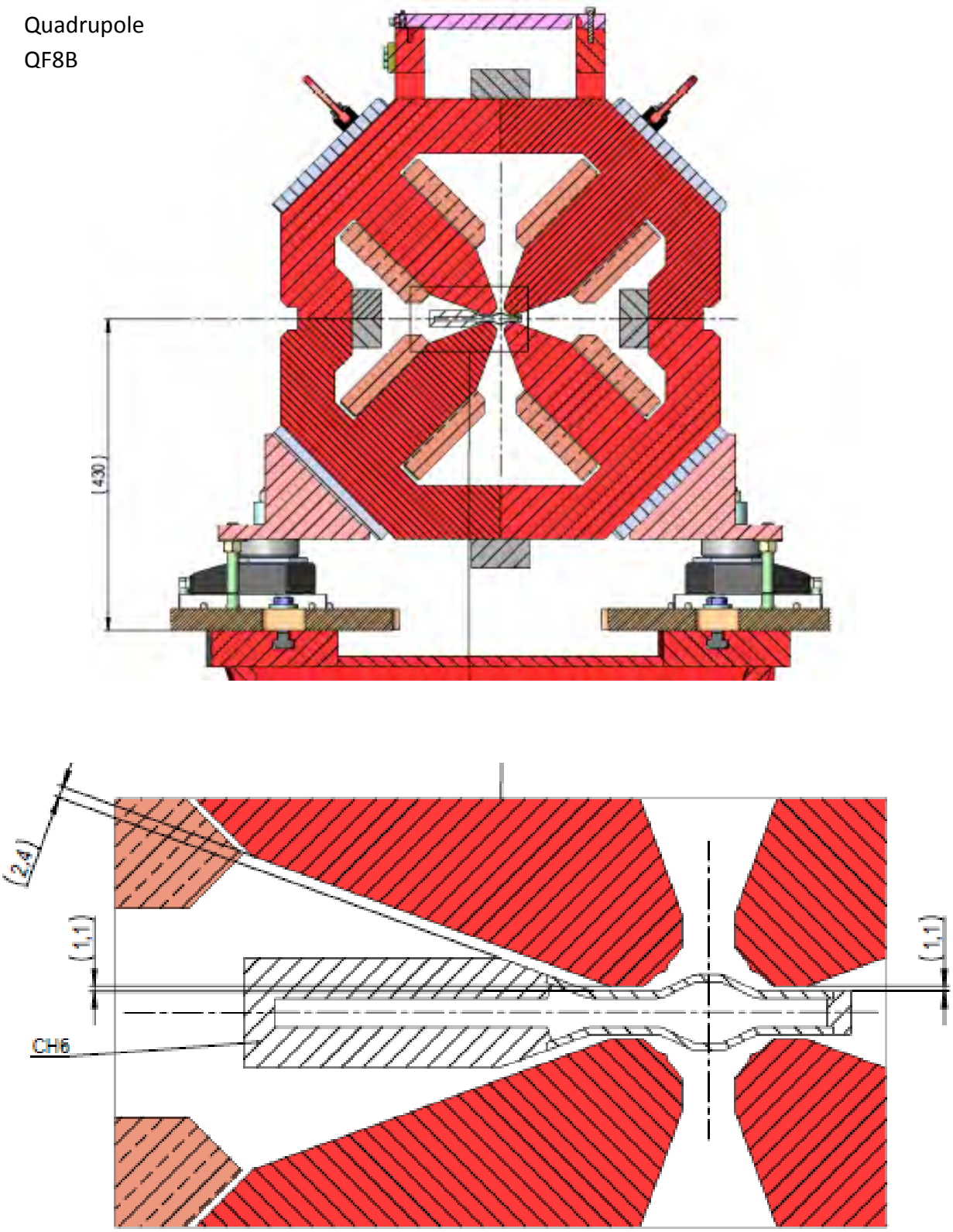


Figure 3.58: Girder 2 QF8B magnet section view.

Quadrupole
QF8D

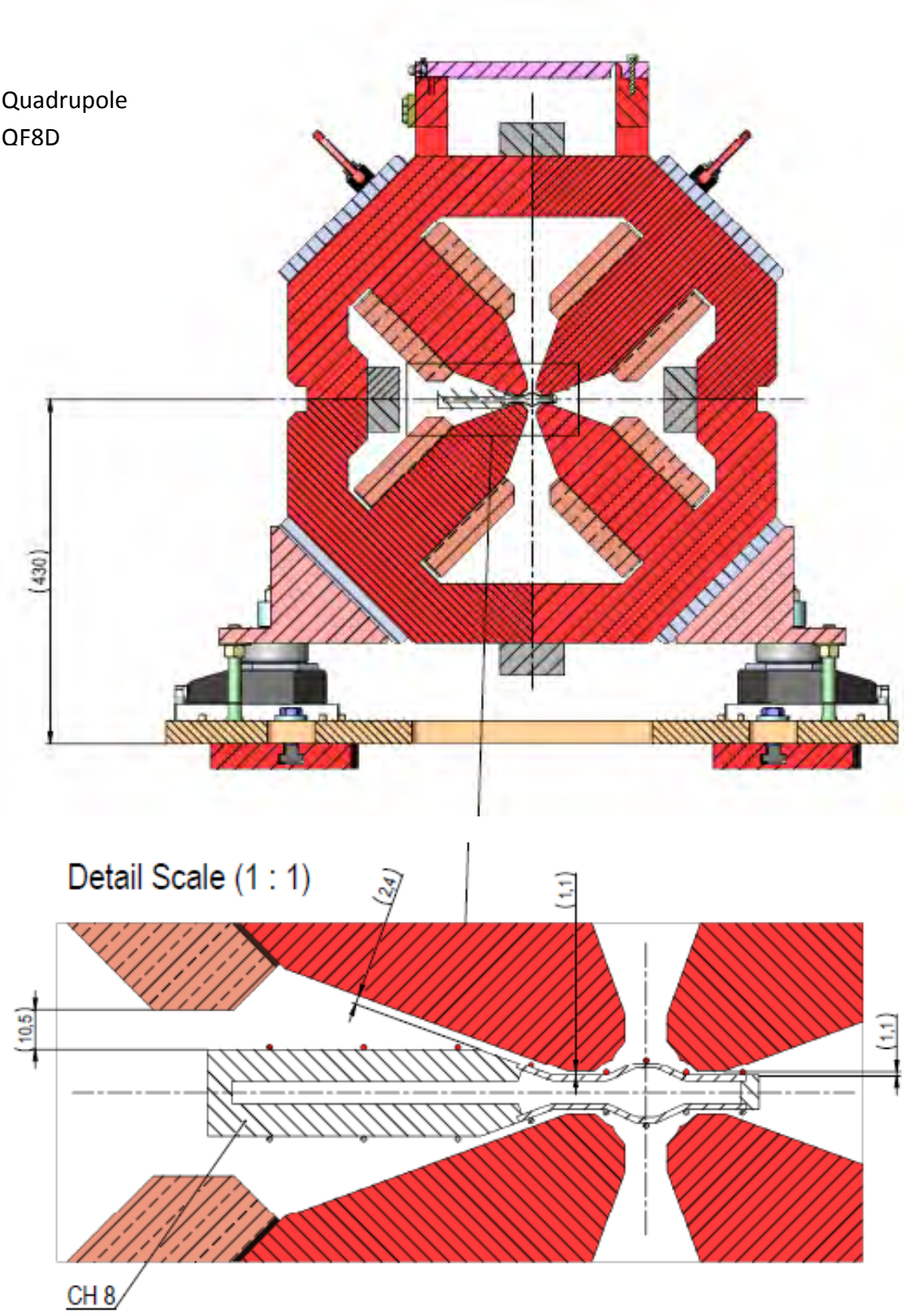


Figure 3.59: Girder 3 QF8D magnet section view.

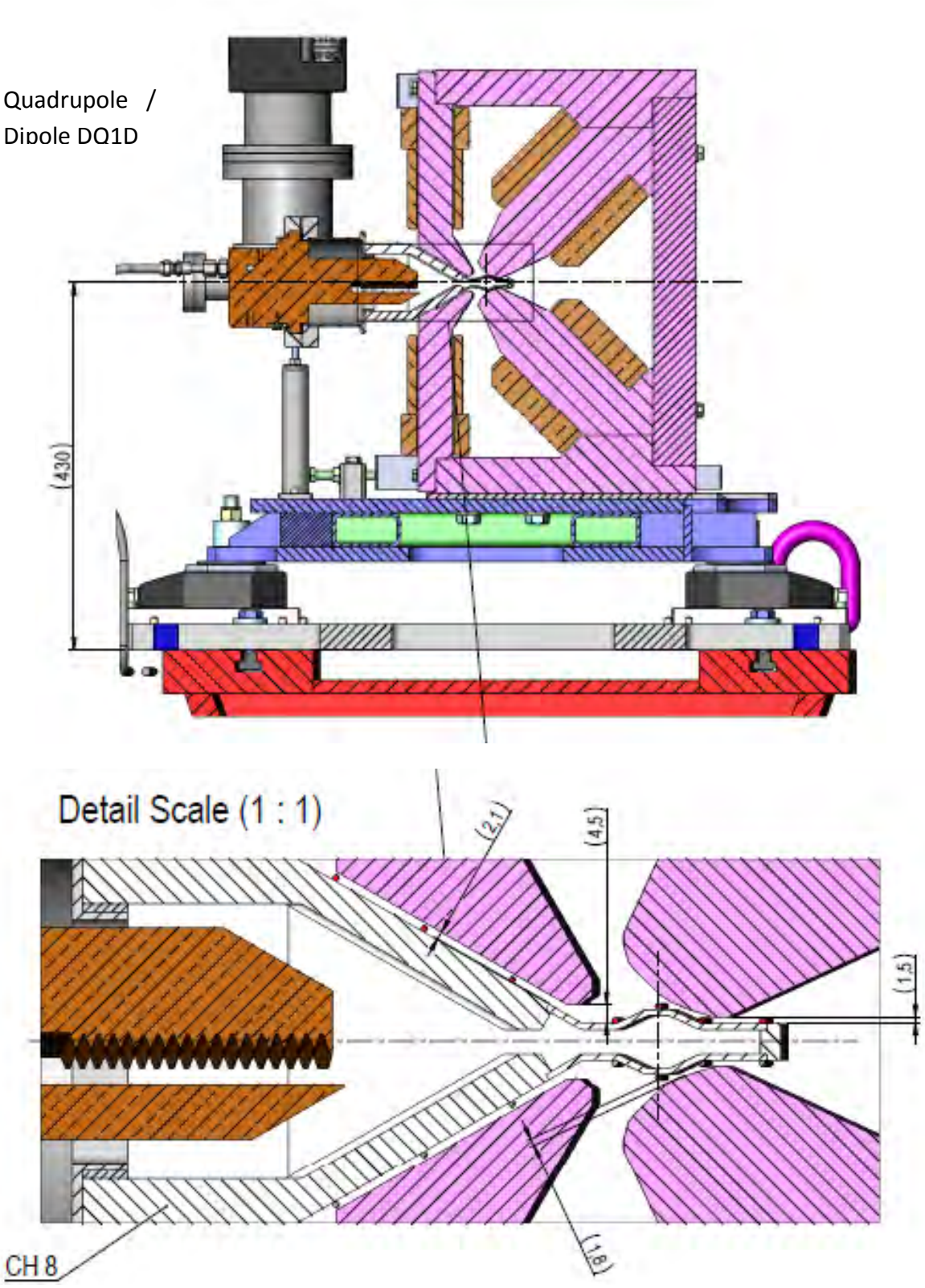


Figure 3.60: Girder 3 DQ1D magnet section view.

Quadrupole
QF6D

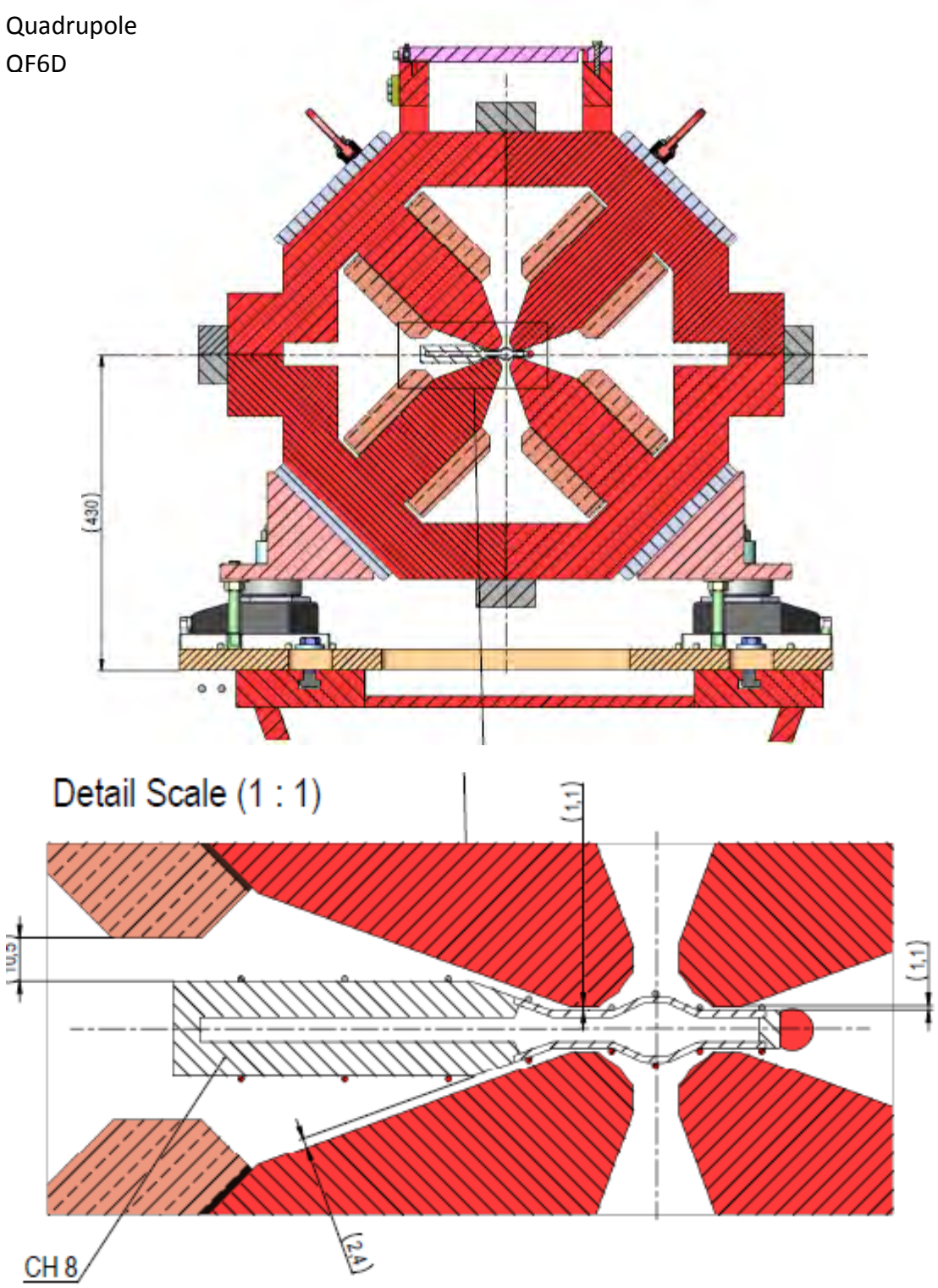


**Figure 3.61: Girder 3 QF6D magnet section view.**

Quadrupole /
Dipole DL2D-5

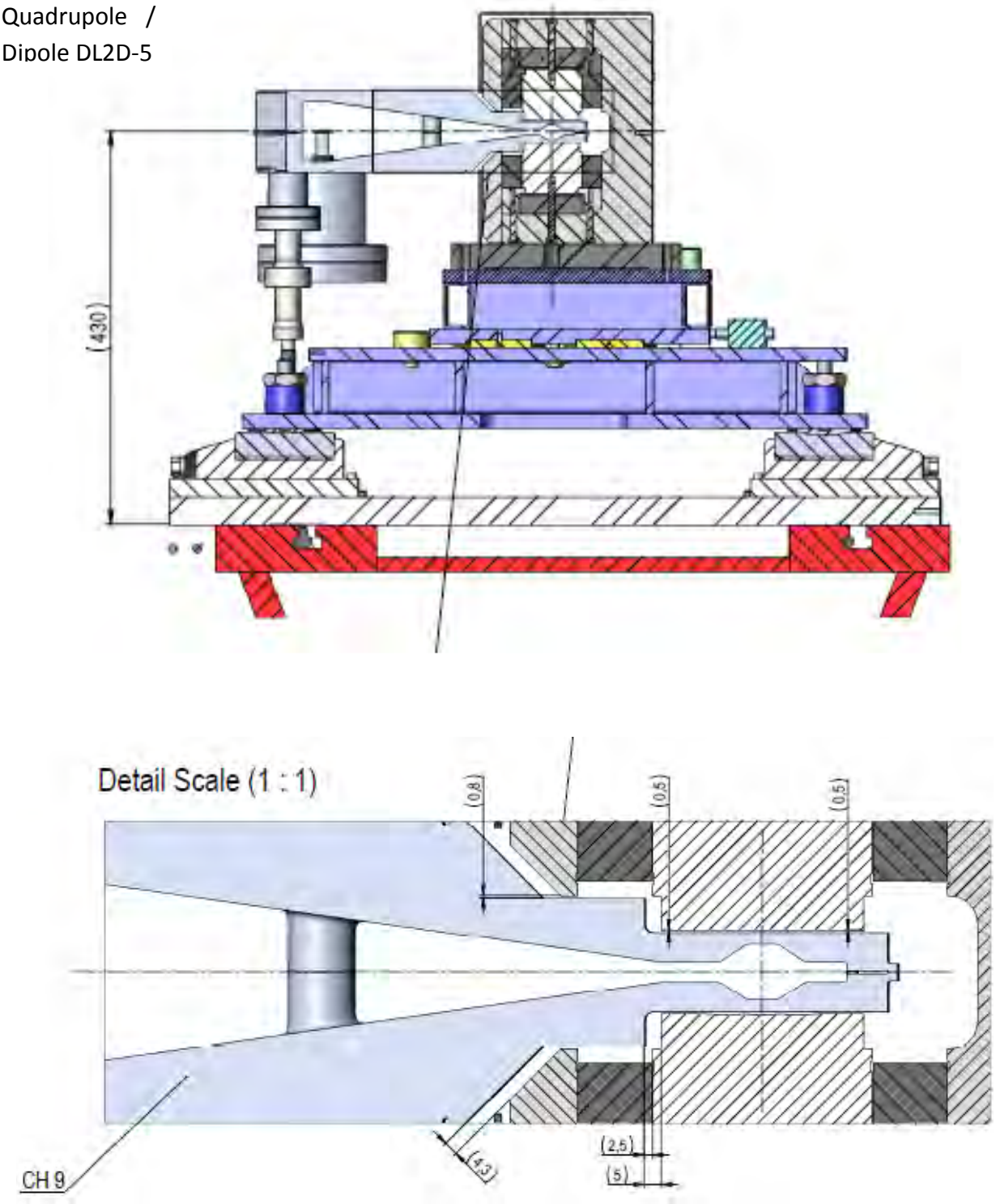


Figure 3.62: Girder 3 DL2D_5 magnet section view.

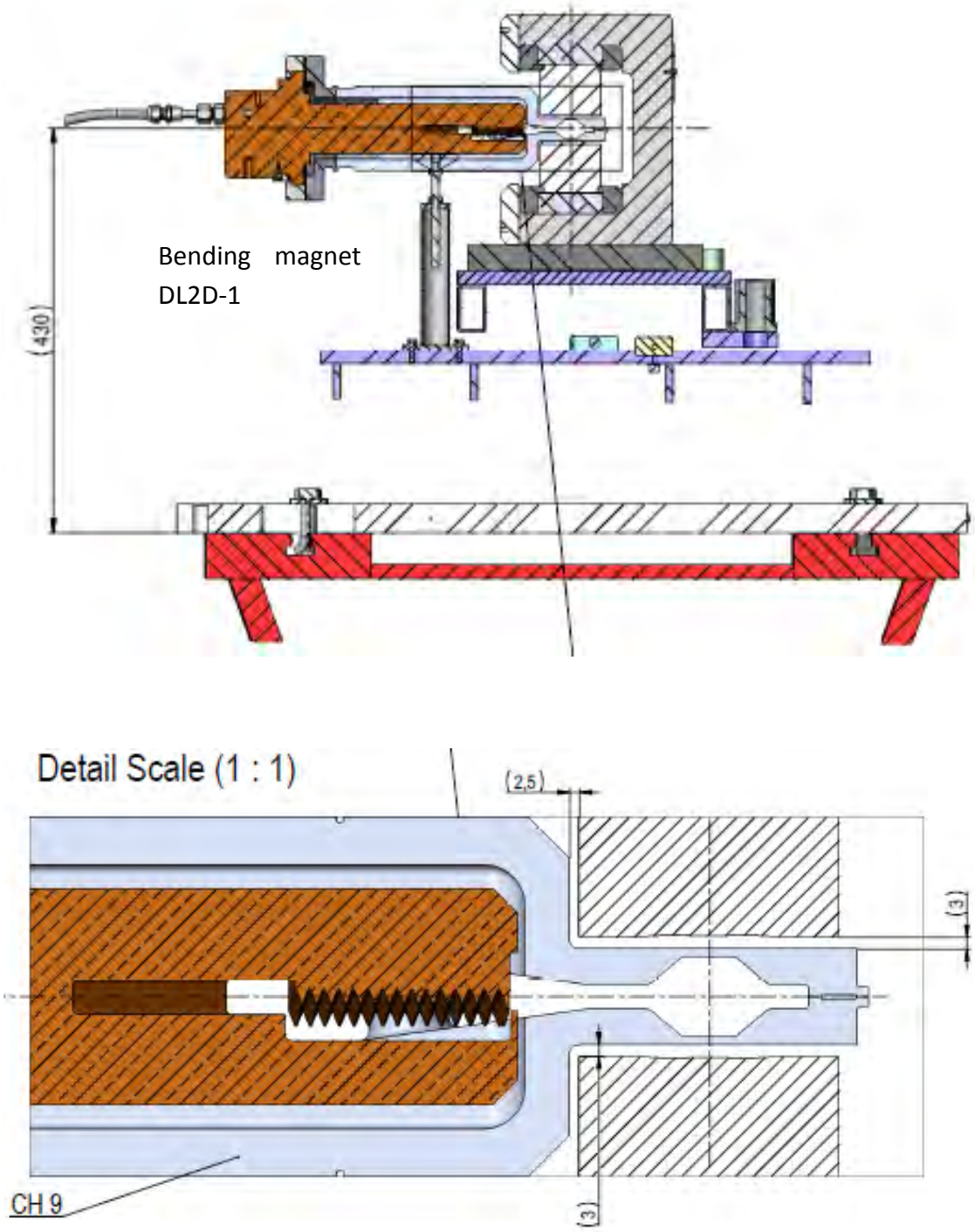


Figure 3.63: Girder 3 DL2D_1 magnet section view.

Quadrupole
QD5D

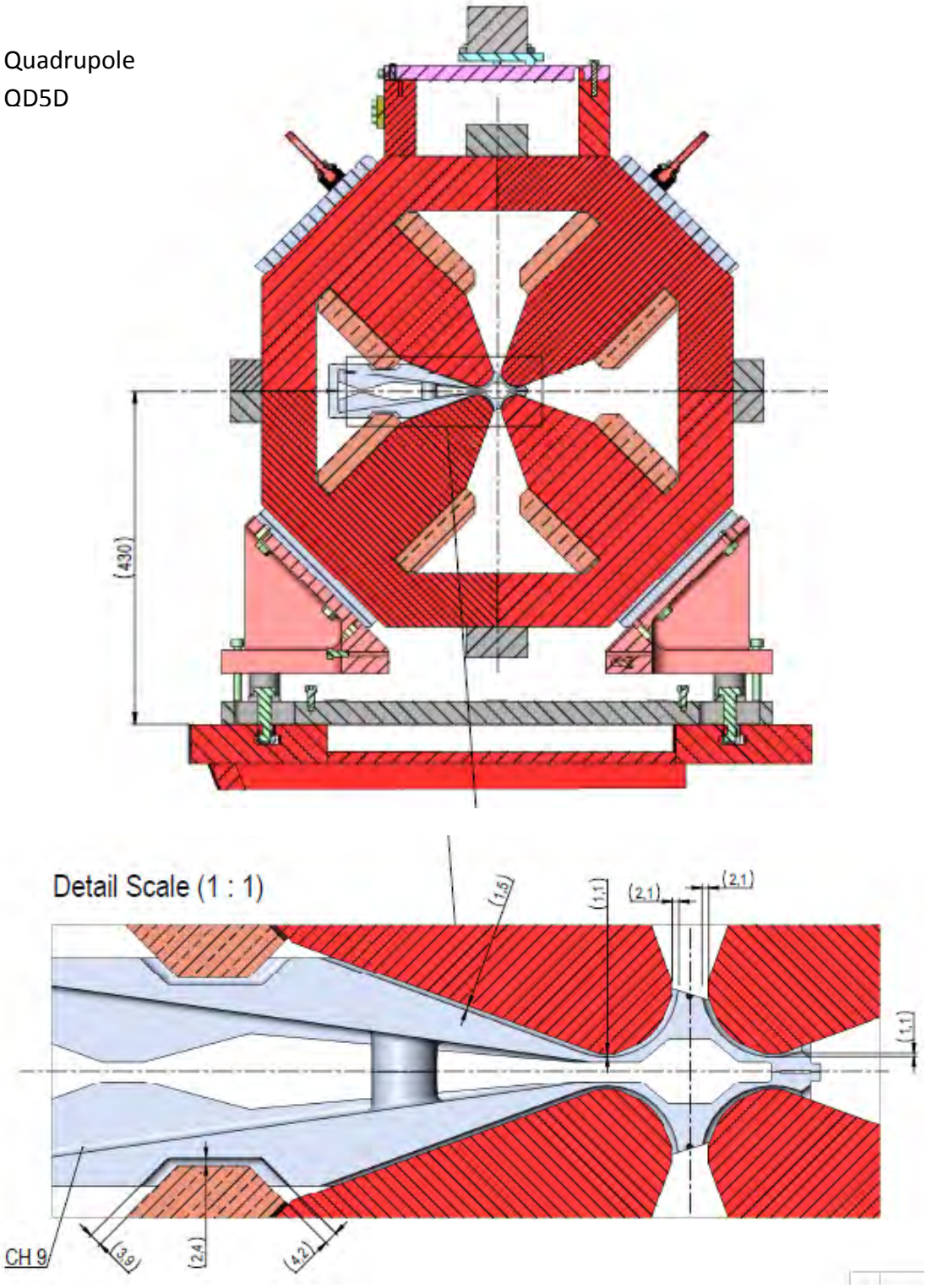


Figure 3.64: Girder 3 QD5D magnet section view.

Sextupole
SD1D

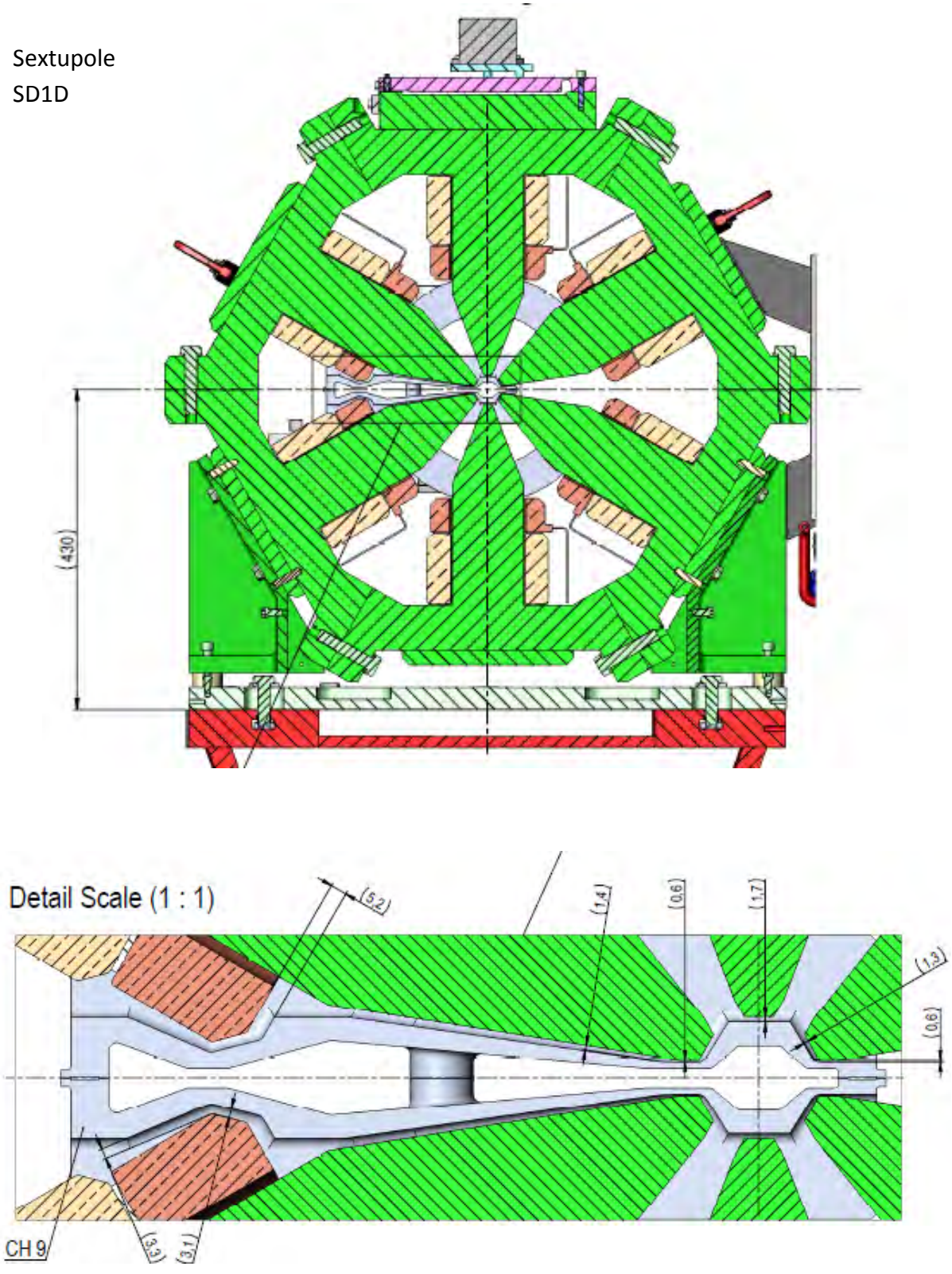


Figure 3.65: Girder 3 SD1D magnet section view.

Octupole
OF1D

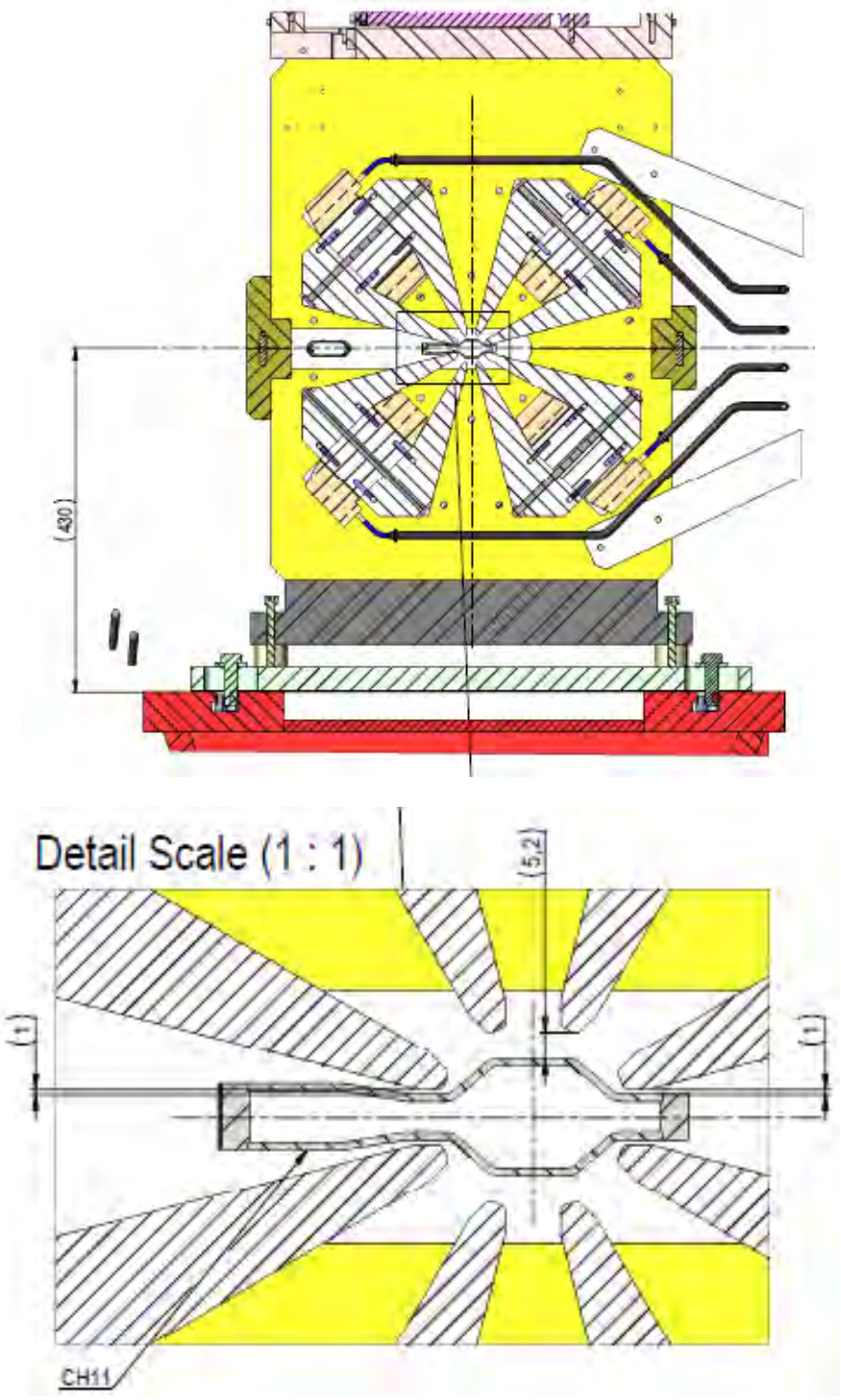


Figure 3.66: Girder 4 OF1D magnet section view.

Quadrupole
QF4D

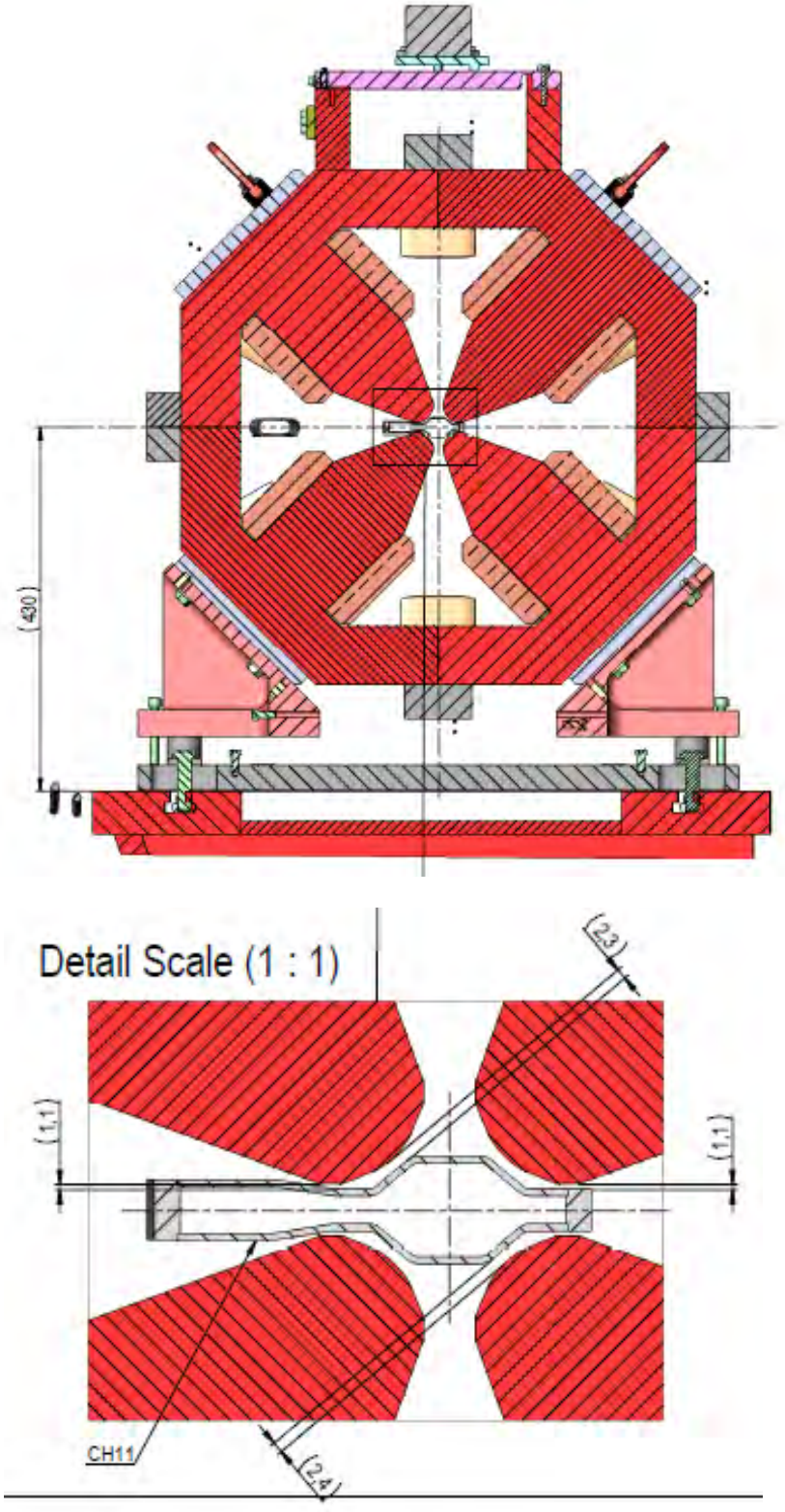


**Figure 3.67: Girder 4 QF4D magnet section view.**

Sextupole
SF2E

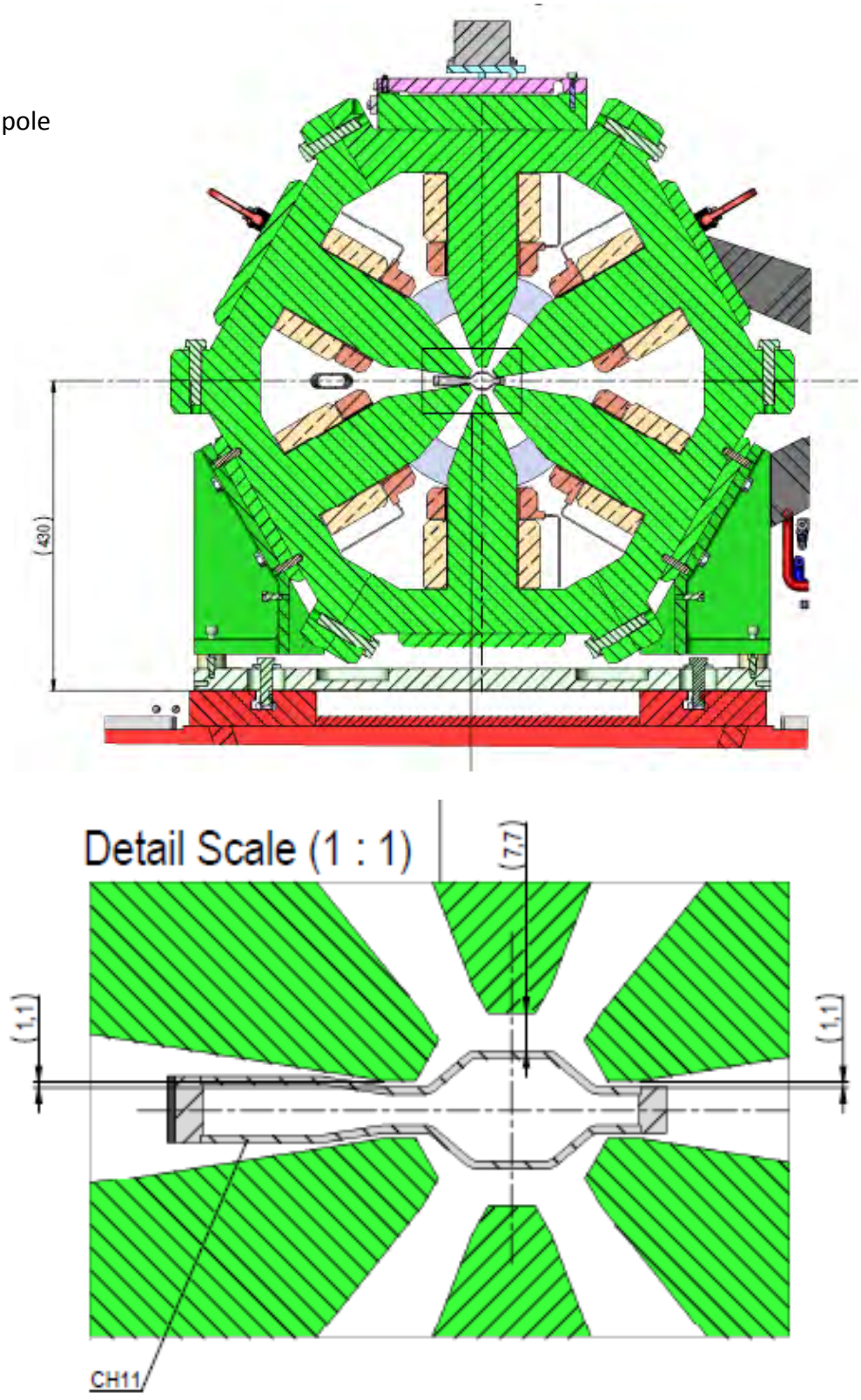


Figure 3.68: Girder 4 SF2E magnet section view.

Quadrupole
QF4E

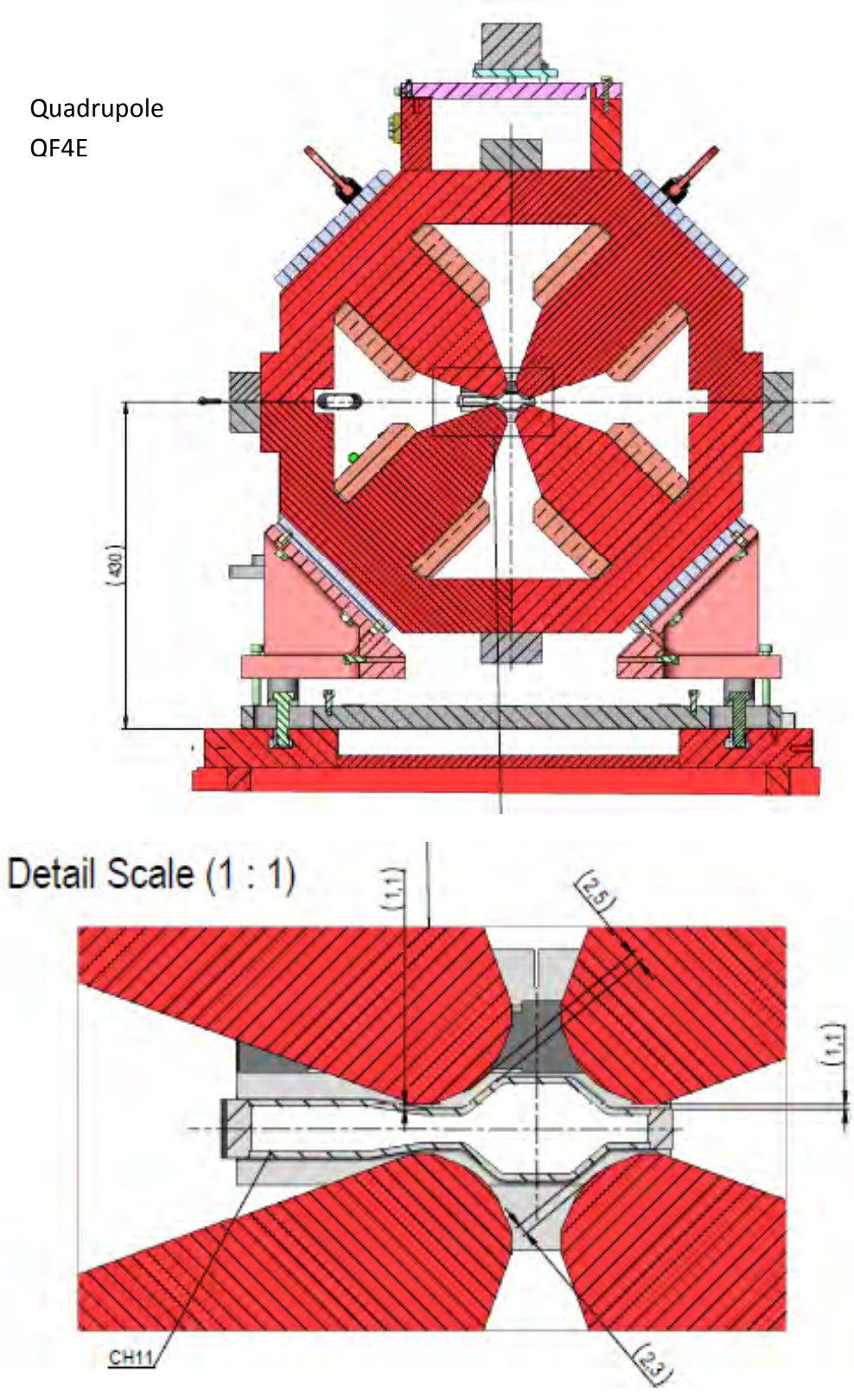


Figure 3.69: Girder 4 QF4E magnet section view.

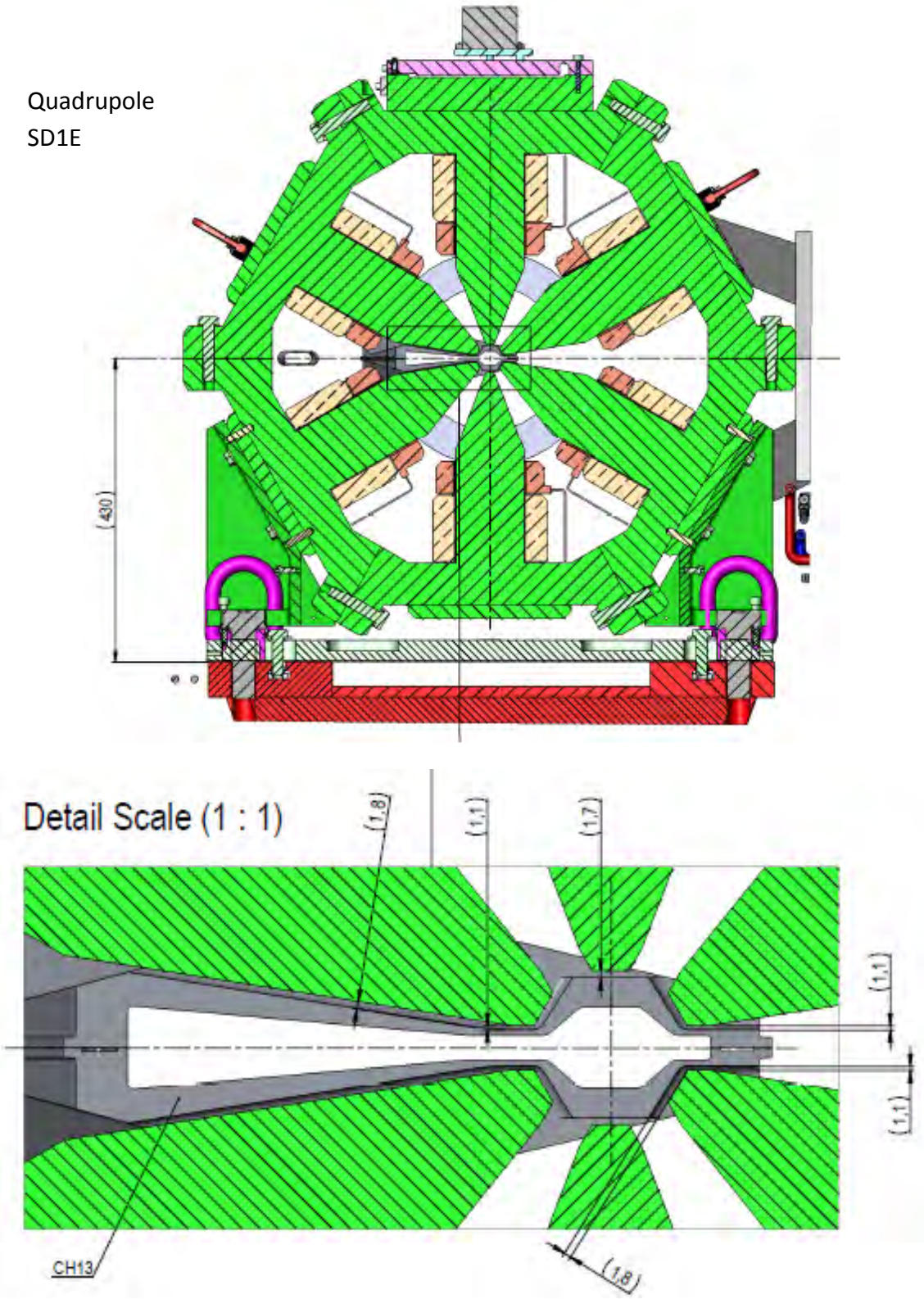


Figure 3.70: Girder 4 SD1E magnet section view.

Quadrupole
QD3E

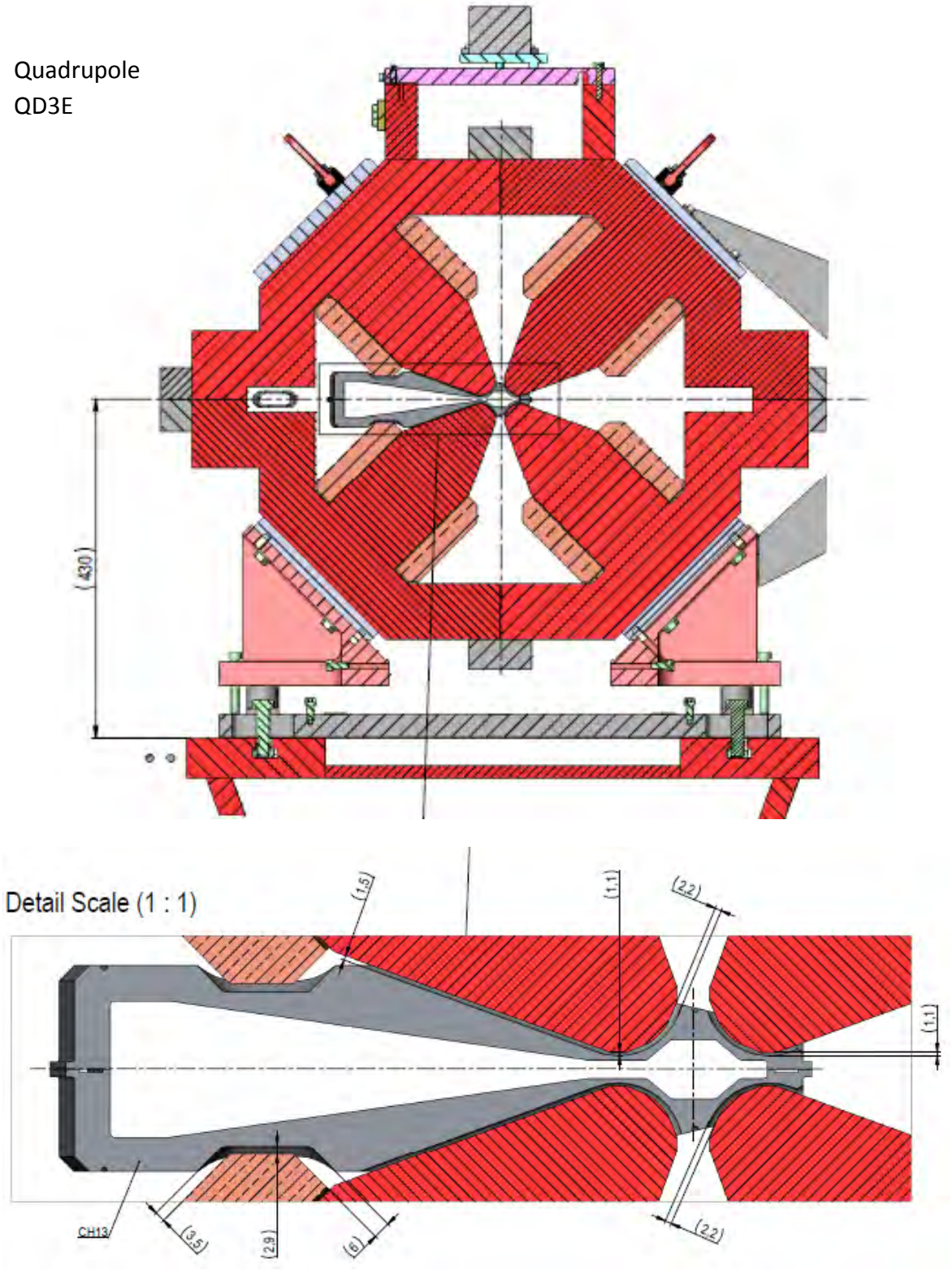


Figure 3.71: Girder 4 QD3E magnet section view.

Bending magnet DL1E-1

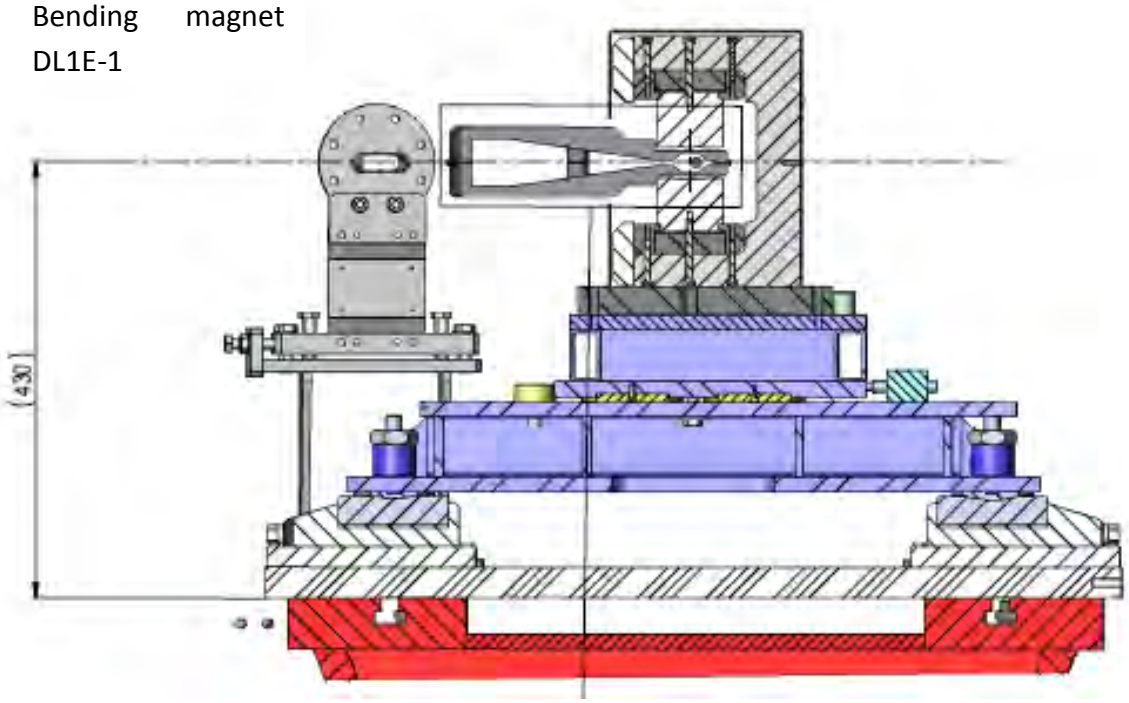


Detail (1:1)

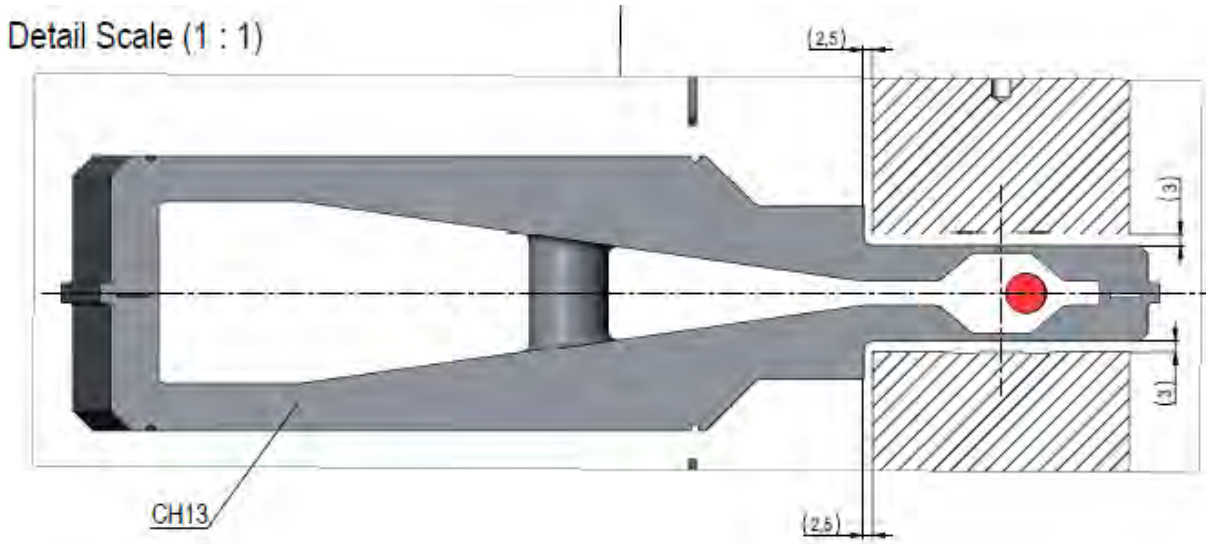


Figure 3.72: Girder 4 DL1E_1 magnet section view.

Bending magnet DL1E-5

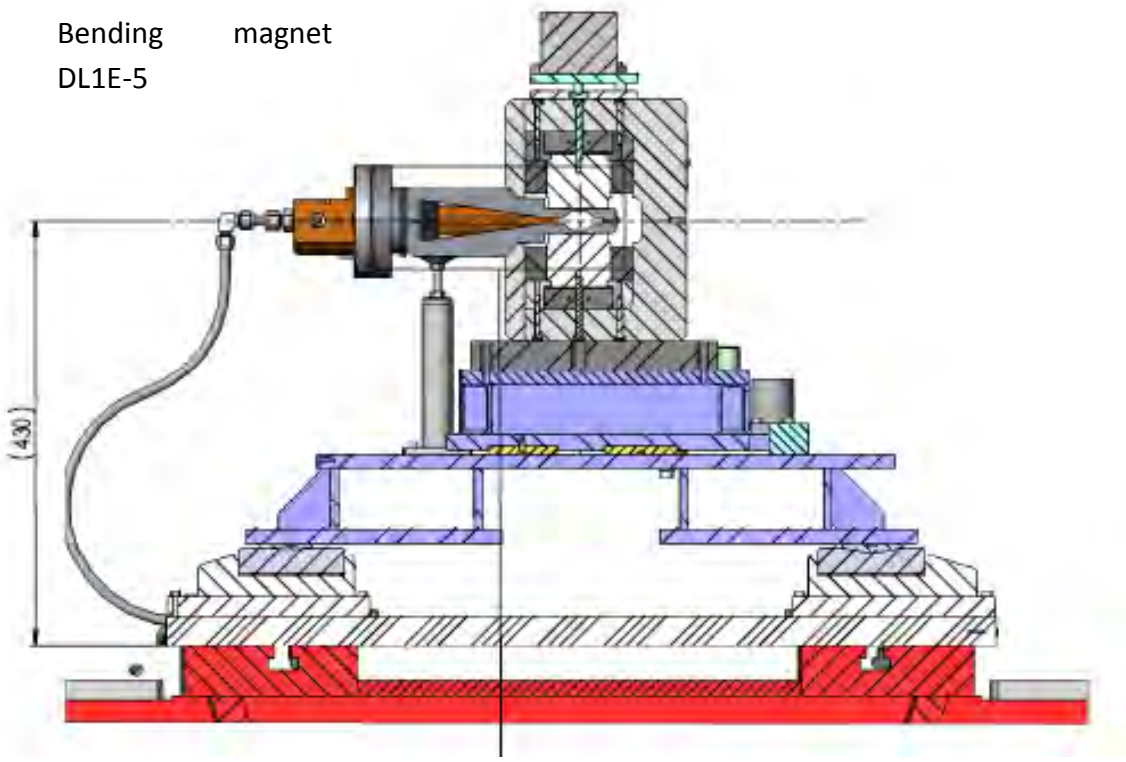


Detail (1:1)

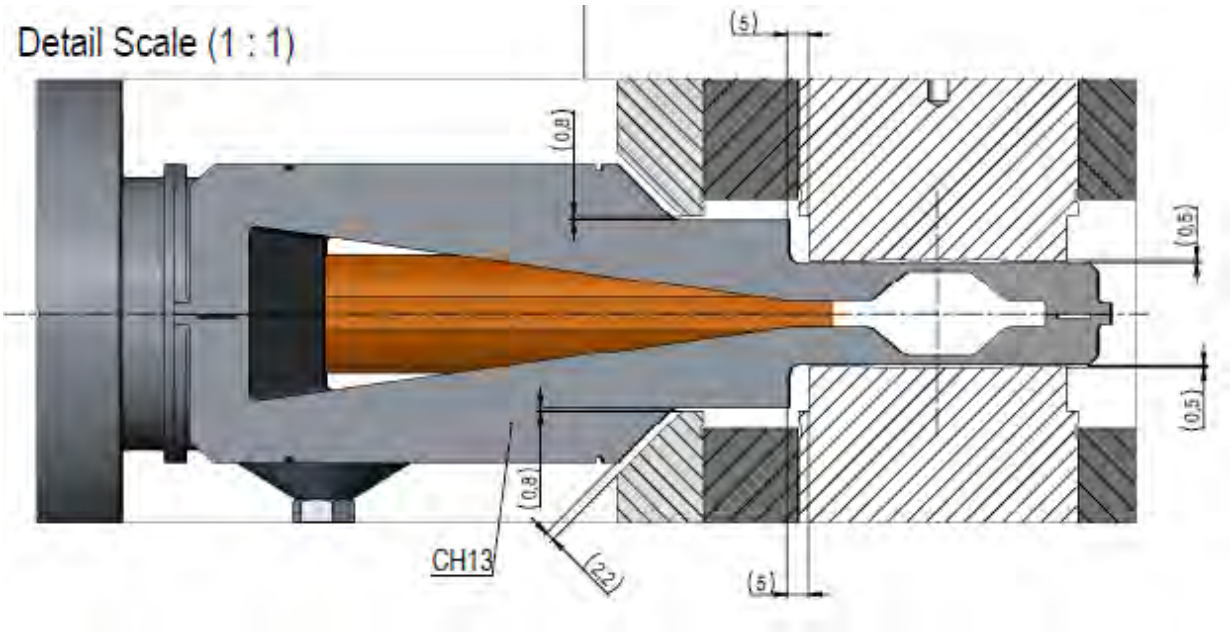


**Figure 3.73: Girder 4 DL1E_5 magnet section view.**

Quadrupole
QD2E

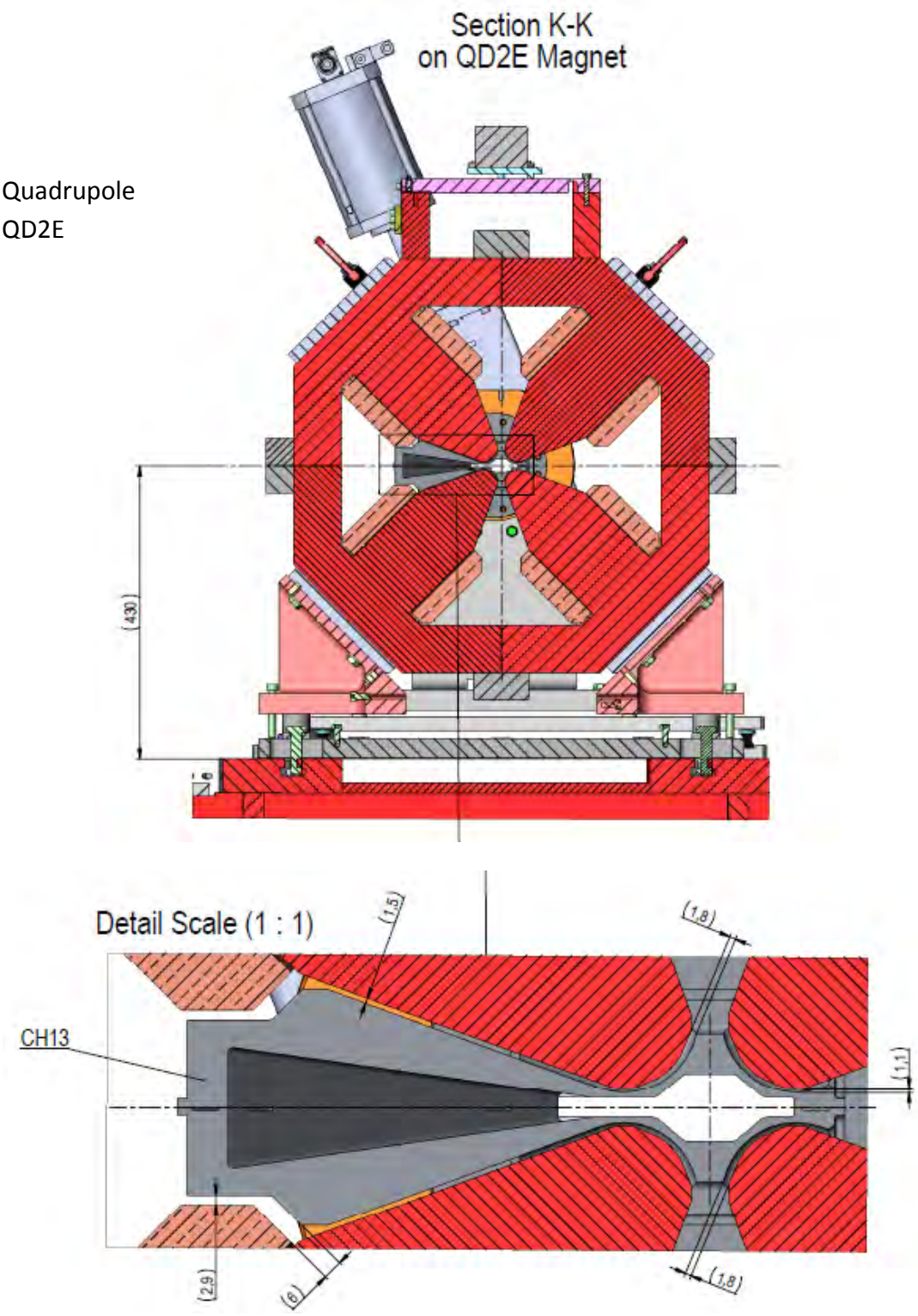


Figure 3.74: Girder 4 QD2E magnet section view.

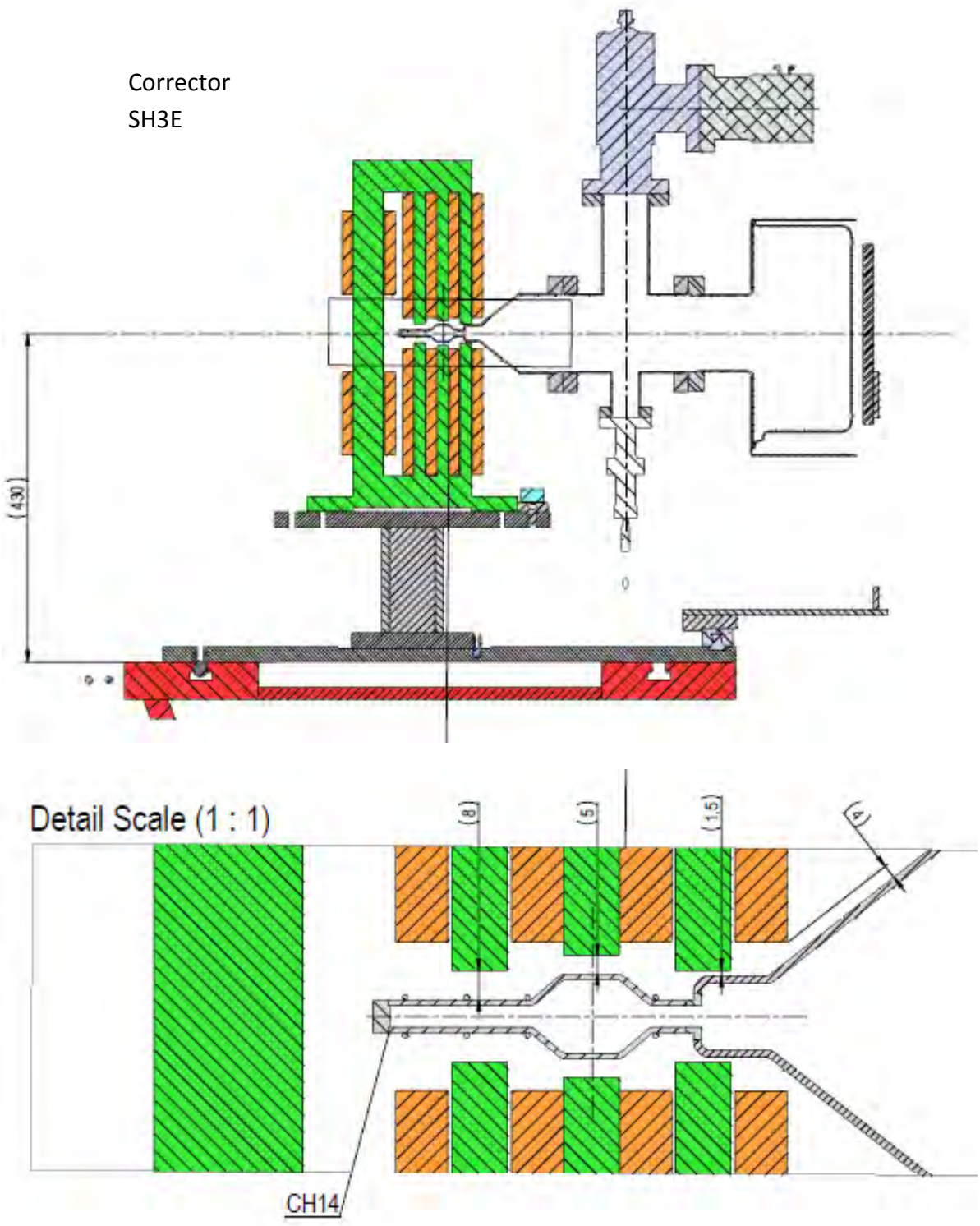


Figure 3.75: Girder 4 SH3E magnet section view.

Quadrupole
QF1E

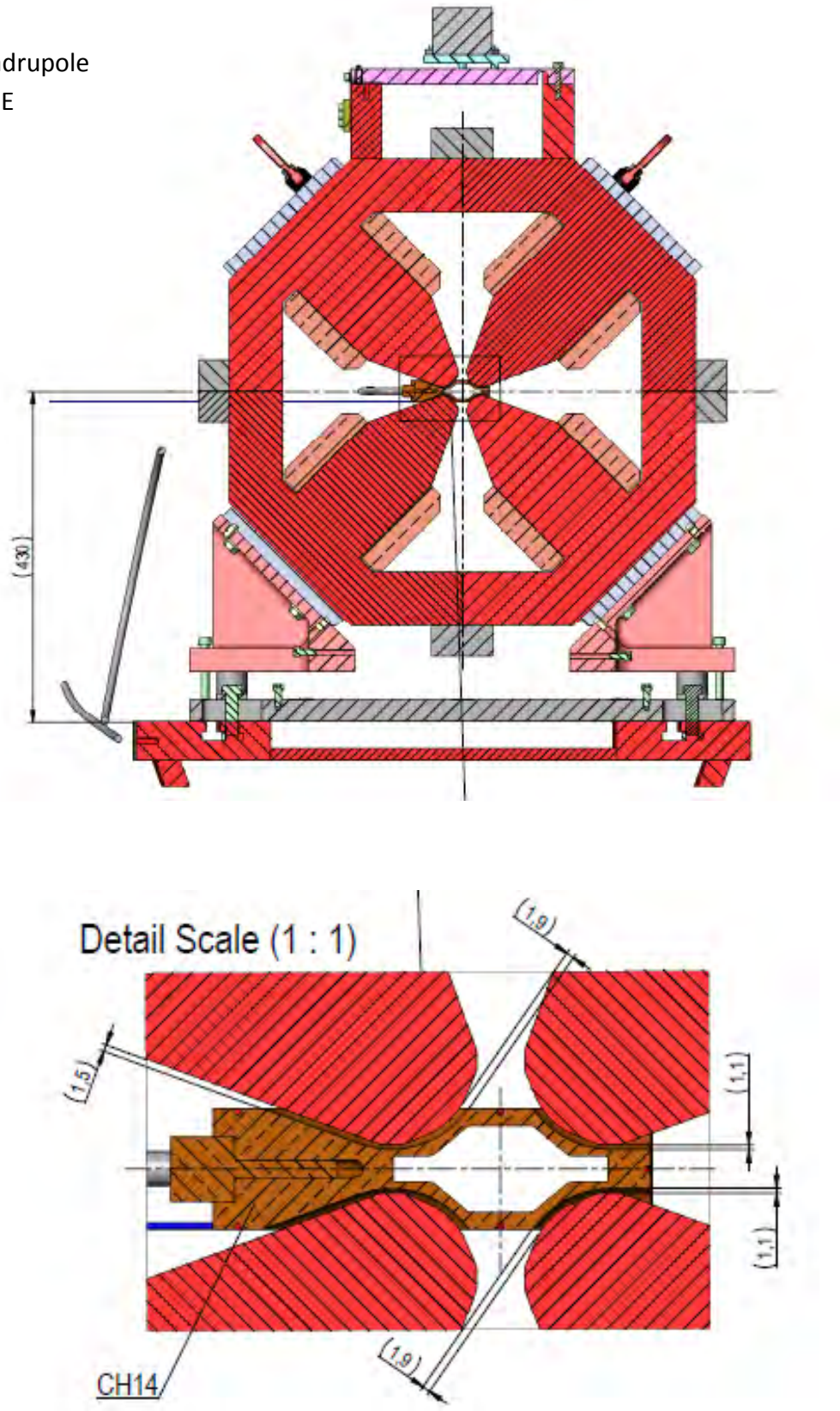


Figure 3.76: Girder 4 QF1E magnet section view.

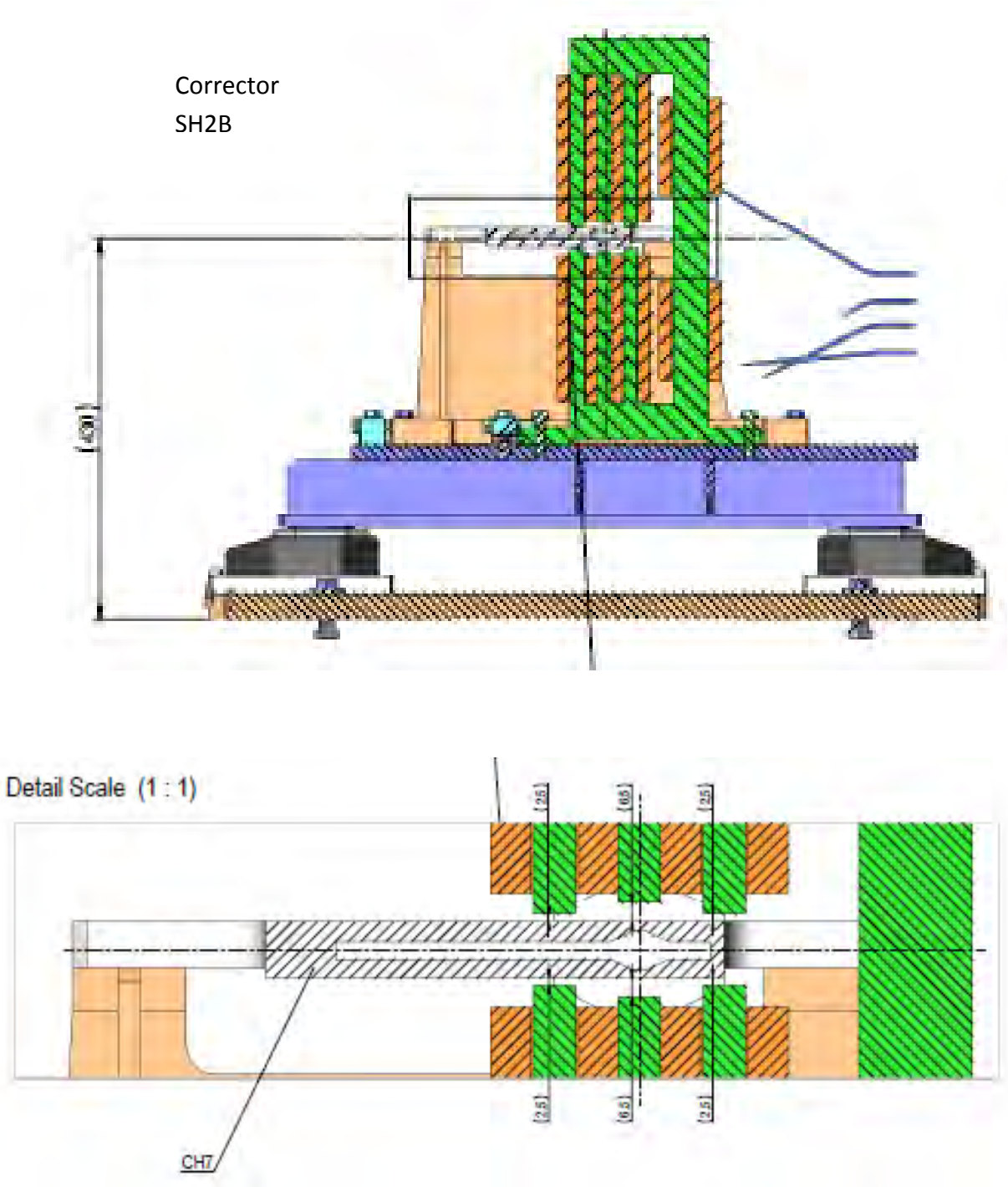


Figure 3.77: Between girder 2 & 3 SH2B magnet section view.

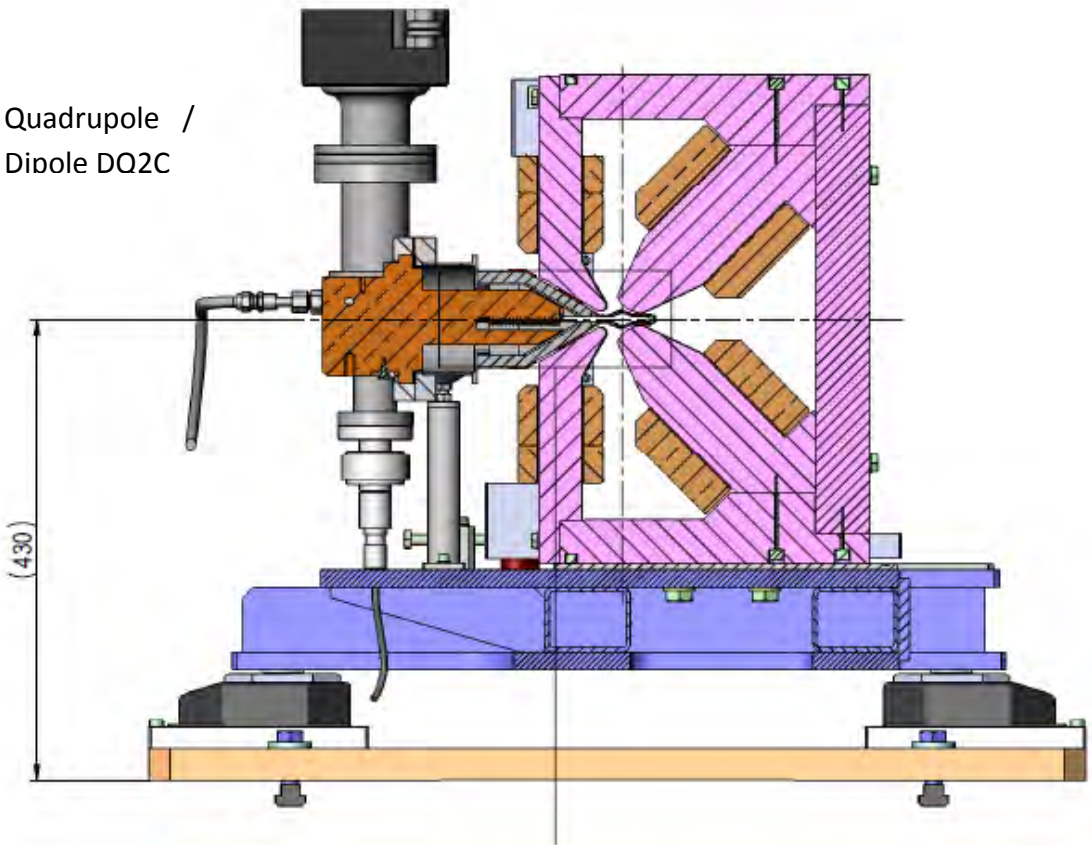


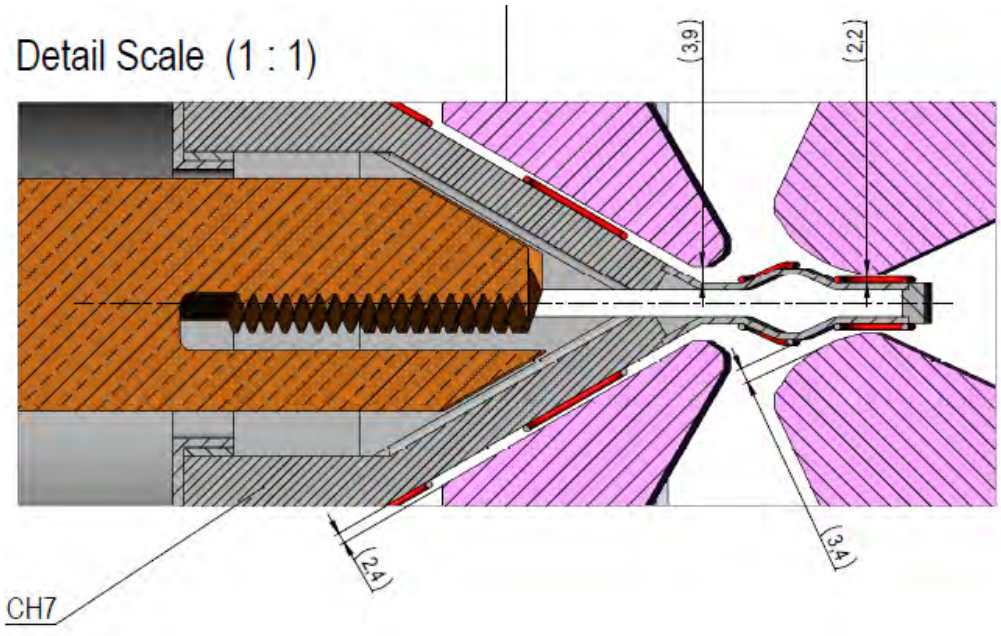


Figure 3.78: Between girder 2 & 3 DQ2C magnet section view.

# 4 Power Supplies and Electrical Engineering

## 4.6 Requirements for the power supplies

The requirements and specifications of the different power supplies for the magnets described in chapter 2 are given in Table 4.1.

In order to power all magnets in a cell individually, 27 power supplies are needed for 1 cell, with 32 cells: this makes overall 864 current regulated channels. Adding some spares and the supplies needed for the Hot-Swapping the number of channels per cell is 36 bringing 1152 channels overall.

The maximum current for all power supplies is 110 A, the nominal values are 10 to 20% lower. The accuracy requested varies from 10ppm to 50ppm peak to peak, according to Beam-Dynamic-Group calculations.

The total quantity of different currents including correctors to control is in the order of 1600, which is 7 to 8 times more than for the present machine.

To keep the same Mean Time Between Failure (MTBF) as the running machine, this is transferred to a request of 3000 hours of MTBF for the power supply group equipment. Transferred to single power converter this represents more than 4.5 million hours of MTBF on average!

**Table 4.1: The specifications of the power supplies for the magnets in 1 cell.**

| Name | quantity per cell | coil temp elevation | Electrical design | | | PS | | | Nom Power cables included | | | |
|---|---|---|---|---|---|---|---|---|---|---|---|---|
| | | | ohmic coils | Voltage | Current | design | cycling current | cycling voltage | | cycling Power | Nom power | cycling Power |
| | | | mohms | [V] | [A] | OVfactor | [A] | [V] | [W] | [W] | cell | Cell |
| **QF1** | 2 | 19.3 | 145 | 13.0 | 86.2 | 1.28 | 110.0 | 16.9 | 1145 | 1864 | 2289 | 3728 |
| **QD2** | 2 | 16 | 117 | 11.1 | 92.3 | 1.19 | 110.0 | 13.6 | 1057 | 1501 | 2114 | 3002 |
| **QD3** | 2 | 10 | 100 | 8.4 | 82.0 | 1.34 | 110.0 | 11.6 | 710 | 1278 | 1420 | 2556 |

| | | | | | | | | | | | | |
|---|---|---|---|---|---|---|---|---|---|---|---|---|
| **QF4** | 4 | 12.7 | 117 | 9.8 | 82.0 | 1.34 | 110.0 | 13.6 | 829 | 1493 | 3318 | 5971 |
| **QD5** | 2 | 17.1 | 117 | 11.5 | 95.3 | 1.15 | 110.0 | 13.6 | 1127 | 1501 | 2253 | 3002 |
| **QF6** | 2 | 12.1 | 188 | 18.4 | 95.4 | 1.15 | 110.0 | 21.5 | 1776 | 2362 | 3553 | 4724 |
| **QF8** | 2 | 14.7 | 224 | 21.2 | 91.8 | 1.20 | 110.0 | 25.6 | 1963 | 2819 | 3926 | 5637 |
| | 16 | | | | | | | | | | 18873 | 28619 |
| **DQ1** | 2 | 15 | 200 | 17.6 | 85.5 | 1.29 | 110.0 | 23.0 | 1523 | 2531 | 3046 | 5063 |
| **DQ2** | 1 | 9.1 | 140 | 12.8 | 90.0 | 1.22 | 110.0 | 16.0 | 1174 | 1757 | 1174 | 1757 |
| | 3 | | | | | | | | | | 4220 | 6820 |
| **SD** | 4 | 7.22 | 125 | 7.9 | 62.0 | 1.77 | 110.0 | 14.5 | 501 | 1599 | 2004 | 6397 |
| **SF** | 2 | 8.55 | 135 | 8.5 | 62.0 | 1.77 | 110.0 | 15.6 | 541 | 1719 | 1081 | 3438 |
| | 6 | | | | | | | | | | 3086 | 9835 |
| **OF1-2** | 2 | 8 | 7.6 | 3.4 | 107.3 | 1.03 | 110.0 | 3.7 | 398 | 407 | 796 | 813 |
| | 2 | | | | | | | | | | 796 | 813 |
| | 27 | | Total PS power for one cell for main electromagnets | | | | | | | | 27.0 | 46.1 |
| | | | | | | | | | | | kW | kVA |

## 4.7 Power distribution

For the power architecture it has been decided to use DC/DC converters, feeded by an AC / DC rectifier (see Figure 4.1). The main advantages of the DC distribution scheme is the reuse of the present 20kV efficient harmonic filtering, the reuse of the centralized space and the material for the AC/DC rectifiers. This solution avoids to distribute, protect the large number of 50Hz AC distribution cables, plugs and cupboards which would be traditionally needed. This enable a better control of the voltage input of the power to convert.

In general 5 cells will be powered by one AC/DC rectifier. For the cells 1 and 2 smaller AC / DC rectifiers will be reused. All the DC/DC converters for one cell will be housed in 1 cubicle as presented in Figure 4.2. The power distribution between the AC/DC rectifier and the DC/DC converters for each cell is presented in Figure 4.3. The power connections between the DC/DC converters and the magnets is given in Figure 4.4.

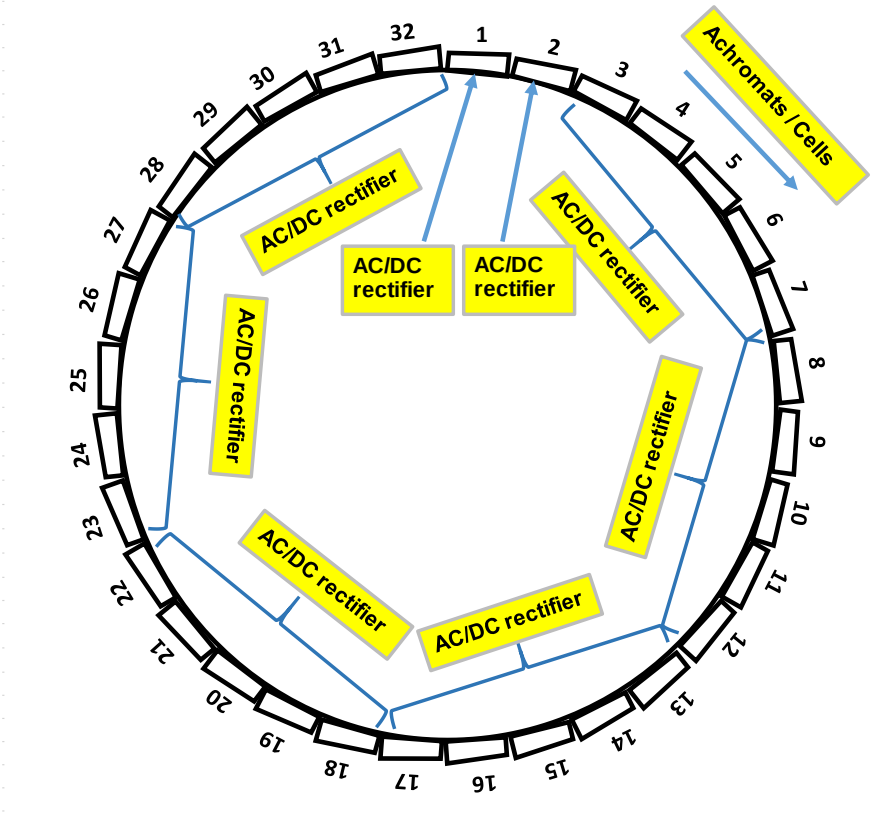


Figure 4.1: The AC/DC power distribution for the ESRF-EBS.

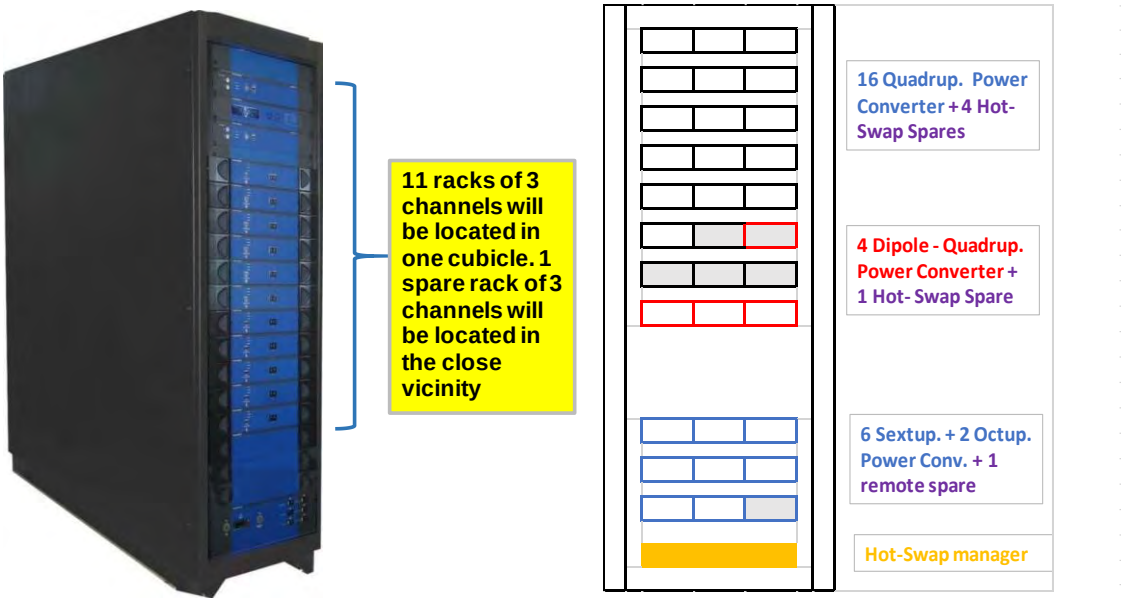


Figure 4.2: The layout of 1 cubicle with 11 DC/DC power supplies.

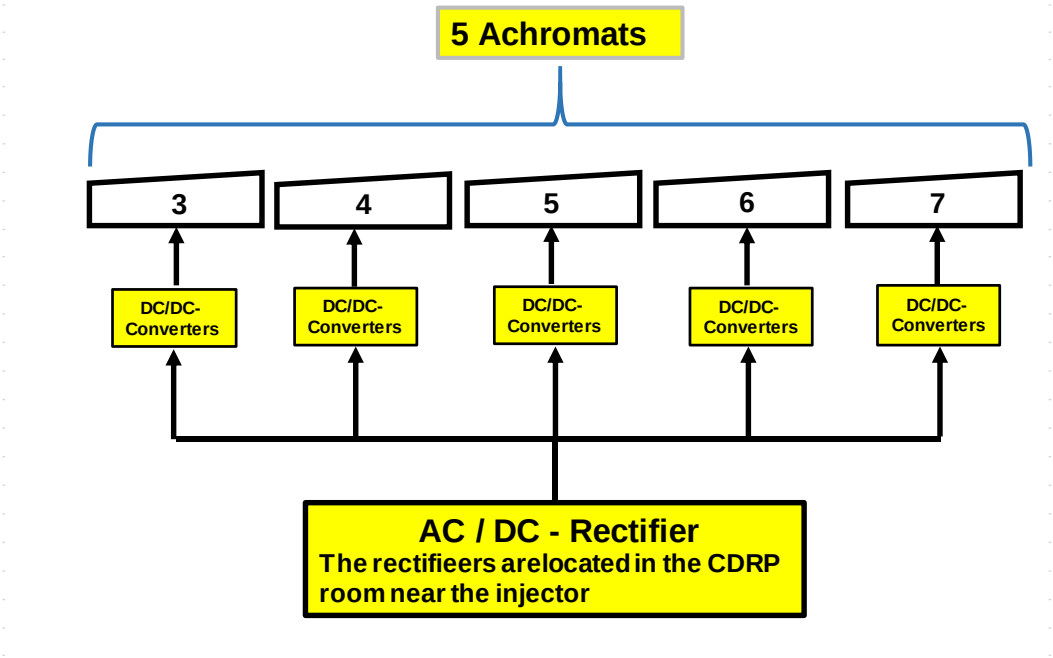


Figure 4.3: The power distribution between the AC/DC rectifier and the 27 DC/DC converters for each cell/achromat.

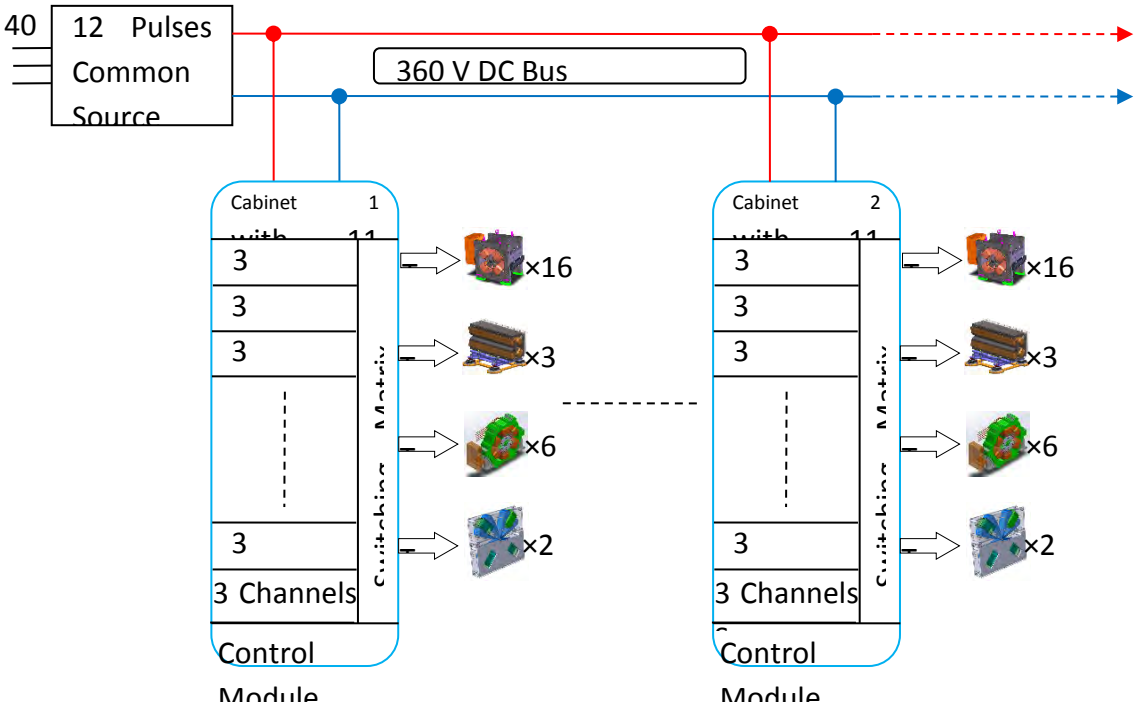


**Figure 4.4: The connections of the DC/DC converters to the different magnets in two cells.**

## 4.8 AC / DC – Rectifier

The modification and reuse of the common sources is based on the power conversion of the 50Hz to a stable DC bus distributed all along the technical gallery. The running converters for family connected magnets will be the base of the reused material. Figure 4.7 is a photo of the SRDC room where they are located.

The goal of these rectifiers is to procure a stable voltage at the input of the DC-DC converters. The output DC voltage level is the result of a multi criteria analysis including the evaluation of the prototypes, availability of the common source park, optimization of the losses of the DC bus transport infrastructure, among the most important ones. The first analysis proposed in the prototype DC-DC enquiry and presented in the MAC was from 50V to 200V and was based on the APS design. In order to better reuse the present park of power converters the second analysis indicates that the voltage 360VDC is optimizing the reuse of the family power converter in operation for the present machine, and the reuse of the matrix connection board which lower the MTRR in case of fault of one common source.

The number of these common sources will be 8 (6 large + 2 smaller + 1 spare) from most of the 6 family quadrupole power supplies and the 3 large sextupoles family power supplies. This includes the matrix connection which will be refurbished with interface renewed and possible reuse dipole and superspare units.

All the reused power supplies will need a refreshing of the interface to the control room in close collaboration with WP6 and a reinforcement of the thyristor control unit with failure robustness capacity. The change of a few number of 50Hz transformers is not excluded

but will be avoided at maximum due the limited time to perform such an operation.

## 4.9 DC / DC converter

The goal of these power converters is to regulate the output current from a DC voltage bus delivered from the set of centralized AC-DC rectifiers. The minimum quantity of DC-DC power converters is 27 per cell and will fit in a standard cubicle of 42 U hosting all electrical input and output links together with control network, magnet interlock and water cooling hoses.

In order to reach an affordable Mean Time Before Failure of 3000h for the complete power supply equipment, the study of similar large instruments like APS and the result of the WP12 validate the idea presented at the first MAC to procure a system able to replace a faulty converter while keeping the beam within the vacuum chamber.

The set of 33 DC-DC converters are grouped per cell and located in one single cubicle. A Hot Swap matrix will connect 27 outputs from the 33 converters and the Hot Swap Manager will survey the output current of the Quadrupole and Dipole quads. This will enable a fast swap out of the current source before the beam is lost. This has been patented under the name Hot-Swap system. The sextupole and octupole will be remotely swappable by operator decision to restore one failing channel which is not critical.

The procurement of this multi-technological concept is distributed among several calls for tender to optimize the technical outmost competences of ESRF staff:

DC-DC converters grouped by 3 in a 2U rack, Hot-swap Cubicle, Hot Swap Manager, cabling links, AC-DC rectifiers, switching matrix, etc., are subject to crossed linked call for tenders.

The technology chosen is a full digital control of each channel adapted to the Hot Swap capacity. The use of a standard DCCT will be controlled externally by another current sensor to trigger the time to exchange the faulty channel.

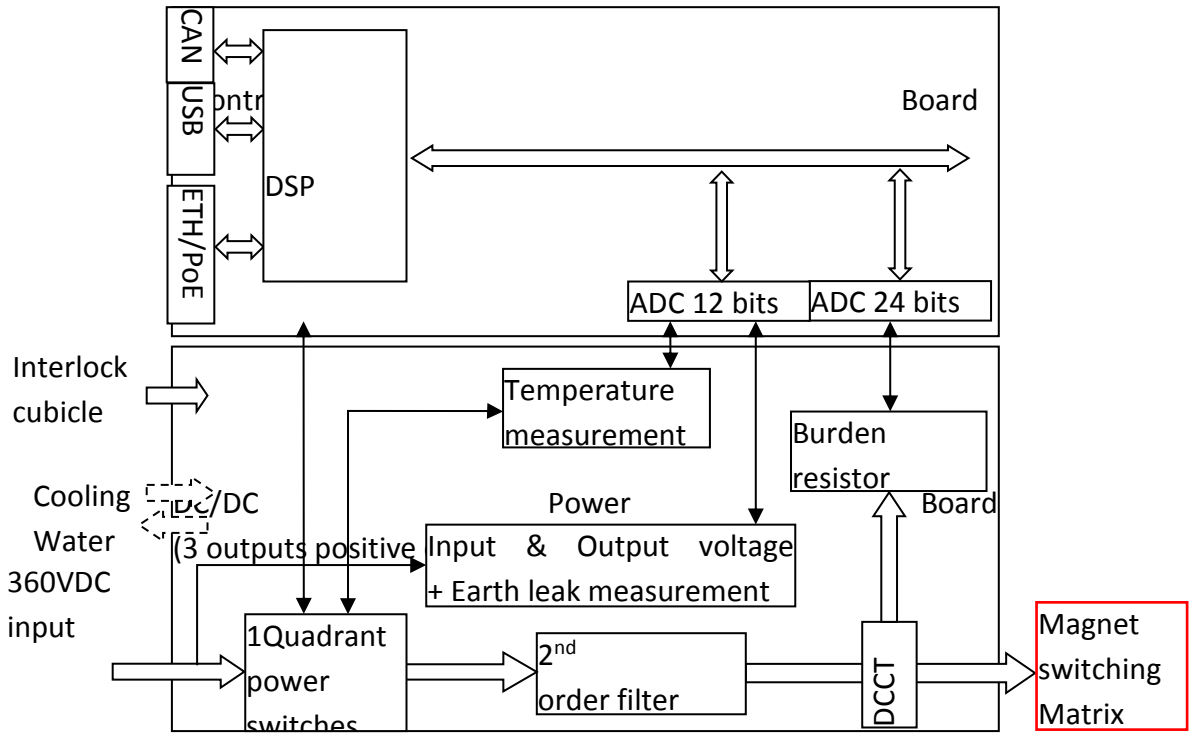


Figure 4.5: Bloc Diagram of the digital control of the power converter.

For the injection cell equipped with 2 recuperated QD6HG from cell 23, they will come with their existing power supplies.

In order to take advantage of the present architecture we will refurbish and adapt the Switching matrix serving the Family power supplies.

This will enable for Main DC distribution (360V) to be ready in less than half an hour in case of breakdown of one of the 8 AC-DC rectifiers.

Figure 4.6: SRDC room with future refurbished AC/DC rectifiers.


Figure 4.7: Switching Matrix serving the family power supplies.

## 4.10 Hot-Swap-Capability

### Introduction of the concept

It has been requested to have a contribution to the operation performance better than one fault per 3000 hours for the power supplies feeding the electromagnets. The consequence of this high performance request when excluding any other Power Supplies failure, is an individual MTBF per channel better than many million hours. If the same failure rate is applicable to the correctors then the individual MTBF has to be greater than 6 million hours. The WP12 has studied this difficulty and validated the enhancement performed by the proposed solution hereafter.

### Proposed solution to the challenge

The solution proposed is to replace a faulty converter before the beam is lost.

The goal of this feature is to detect a discrepancy on a current feeding an electromagnet and take the proper decision to disconnect the faulty power electronics and connect a spare unit while keeping the beam in the storage ring.

The limits of the current excursion has been computed by the theory group under WP1 for the quadrupole magnets and Table 4.1 has been used to prepare the constraints linked to this concept. The values of Table 4.1 are such that it releases the need of high precision DCCTs for Quadrupole magnets. Although the DQ case may request the use of higher accuracy equipment, the study for these 3 magnets per cell needs careful analysis especially due to the presence of correcting coils for the "small poles". The electrical and magnetic coupling may render the problem more tricky. The oscillations of magnetic field is easy to produce and will be seen on the electron beam. A demonstration setup has to show that this could be achieved and applied.

Table 4.1 indicates that the resulting tolerance, in DeltaK/K, or DeltaI/I has to be guaranteed during the transfer from the initial converter to the spare one. The magnetic hysteresis field as a result of the change of power source has to be quantified. A possible action from the control room after the change may be requested. The WP1 and WP6 will tackle this corrective action.

It is supposed that the above maximum current excursion will last more than 100 eBeam turns and therefore more than 300 microseconds, without any beam dynamic effect considered.

This has to be compared with the time constant of the magnets which is forecasted from 500 to 700ms. The time scale for the swap and recovery we are looking for is less than 10ms for the complete replacement after the programmed threshold has been crossed. The use of a freewheeling diode downstream the hot swapping switches is of course necessary to benefit from the energy stored in the gap of the electromagnet while the replacement converter has reach the regulated value. This time has to be adjusted and lowered to 1 ms for the DQ1 and 2 ms for the DQ2.

**Table 4.2: Tolerances of the different quadrupoles until the beam is lost.**

| quadrupole | QF1A | QD2A | QD3A | QF4A | QF4B | QD5B | QF6B | QF8B | DQ1 | DQ2 |
|---|---|---|---|---|---|---|---|---|---|---|
| Tolerance [%] | 18.0 | 13.1 | 17.5 | 20.8 | 20.9 | 19.4 | 30.8 | 22.3 | 0.15 | 0.3 |

### Steps of the Hot-Swapping technical issue.

To cover the majority of the faults encountered since many years of operation of power supplies at ESRF, the main parameter to survey, able to initiate the decision to kick out a converter channel and replace it by a spare one is the deviation of current (set – read).

When the surveying system detects a mis-positioning current of a few percents for Quadrupole only, then the decision is taken to validate the hot swapping action by verifying that the magnet is healthy and that the main DC bus is within its tolerances. Effectively if the magnet is faulty or the main DC bus is outside the tolerance, the hot swapping decision is canceled or will have no effect on keeping the beam in the storage ring. Appropriately the

decision to kick out the faulty converter is then taken and launched. The spare channel (if ready) will be programmed to the correct current with the correct and adapted feedback parameters and connected to the corresponding magnet. The time of switching is very fast compared to the time of the decision to be taken, much shorter than a few microseconds. Precise values depends on the final power design and is a consequence of the thermal efficiency of the system.

## 4.11 Spare power supplies

This issue is to optimize the number of redundant spares and how they will be connected to operated with the highest global expected MTBF. Several solutions has been looked at and the work package in charge of the reliability WP12 has definitively oriented the appropriate configuration.

The initial approach is to validate how many of the 27 channels are needing a spare channel. The sextupole and octupole magnet are not necessarily concerned by the computer assisted hot swapping solution. This is of major importance for the 6 sextupole main coils due to the coupling factor existing with the corrector channels attached on the iron poles of the magnets. The theory group indicates also as a first estimation to be confirmed that a loss of one sextupole magnet doesn't kill the beam. Only the chromaticity is modified and could be partially compensated. As a consequence a solution with maximum 19 channels per cell, equipped with hot swapping solution is the first case under evaluation. The second item is the number of spare channels to implement. This question is governed by the reliability study and also by the minimum availability of standalone channels. This is governed by the final electrical, mechanical and connectivity implementation. The target is to have an independent Ethernet rack driving the redundant channels, the mechanical has to be identical to the "normal channel" 2, 3, or 4 channels per racks and on the same external DC bus. For example if the power converter rack has 4 channels built in, we need 7 racks to power 27 channels and one 4 channels rack could serve as redundant units for the 19 critical ones. If a rack has 3 channels built in, we need 9 racks to power 27 channels per cell and one or two additional racks housing 3 or 6 channels could serve as redundant channels for the 19 critical channels.

### Minimum implementation

The solution having 16 quadrupole magnet power converters backed-up by 4 spares produces a very high MTBF and allow the standby team to exchange the first faulty channel the next morning, nor waiting the next MDT maintenance period one week after. This is only valid if the channels are grouped by 2 maximum in one enclosure. The case with 3 channels per enclosure push us to have 2 rack as

spares to be able to wait until the next MDT to exchange the faulty one.

The non computer assisted faulty replacement will be implemented in a form of 1 spare for the 3 DQ's and 1 spare for the 6 Sextupole and 2 Octupole DC-DC converters. The possibility to exchange remotely one channel could be launched from the control room with a procedure to be worked out. With this minimum implementation the quantity of channel to order will be 33 per cell ( 16+4, 3+1, 8+1) for a total of 1056 converters in operation, the spare units will be added to this value according to the philosophy adopted at the contract placement.

## 4.12 The AC+DC correctors power supplies driven by the Fast Orbit Feed Back

For the AC steerers, it is planned to fully reuse the Bilt power supplies connected to the Fast Orbit Feed Back and the Liberas in operation see **Figure 4.5** of the running power supplies. Only the location of the cubicles will be subject to discussion to optimize the technical gallery space and control cabling issues.

These power supplies are today the one in operation linked with the Libera units and the computer preparing the set points at 10KHz for the 288 channels. Today there is no change foreseen to this system and the Itest (Bilt) power supplies will be connected to the special steerers designed to this function.

The electrical compatibility in term of AC coupling and bandwidth is to be verified but this could not be performed before the first magnet prototype is delivered.

**Figure 4.9: One quarter of the Bilt power supplies for AC steerers driven by the Fast Orbit Feed Back.**

## 4.13 DC corrector power supplies feeding sextupole auxiliary coils

Some magnets are equipped with auxiliary coils like the sextupole magnets and the Dipole-Quadrupole magnets, and will be powered separately.

The six coils wound around the 6 sextupole magnet poles per cell, will perform vertical, horizontal and skew adjustments and will consequently need 4 circuits x 6 sextupole per cell x 32 cells = 768 channels. The present electrical ratings are 2A 11V per channel leading to some 22Watts and the reuse of the actual 250W corrector power supplies (180 units) is not chosen due to poor reliability, non-supported anymore interface to the control room and insufficient number for the new lattice. A specific survey is foreseen to evaluate if a standard commercial industry product is affordable or if some neighbor institute is willing to sell the appropriate design and realization.

Concerning the corrector PS procurement, as soon as the RIPS start to be operational we will start the technical specification writing and the recruitment of the engineer in charge of the contract.

This same DC distribution scheme will also apply for the corrector DC distribution (45V). The switching matrix will be split with more buses to accommodate such a strategy

A DC bus distribution at 45V will be refurbished from 3 of the 5 flexibility power supplies used for High Focusing Optic configuration. This will be the input power for 24 channels (4 x 6 sextupoles/cell) times 32 cells = 768 DC-DC corrector channels.

A RFQ could be needed for the cabinets.

## 4.14 The 96 auxiliary windings of the DQs to adjust the ratio D/Q.

The last document from the WP2 doesn't give any electrical value for these correctors. The cross-section is 8mm2, the number of turn is 45 and the resistance is 200milliohms.

These values indicates that a special design will be necessary to match these correcting coils.

A CFT will be necessary when this function will be settled.

## 4.15 Earth Magnetic Field compensation power supplies

The present lattice is equipped with 2 types of field compensation. One for compensating the algebraic sum of the family current passing in the straight section. One big loop is fed by the Flex 1 on request during all runs except for 16 bunch mode. The second type of compensation is performed under a chosen set of straight section at the request of the WP8 and fed by individual power supplies connected to a 4 wire cable laid just under the insertion devices, with

return outside the tunnel. According to the WP8 the new lattice will require that all straight section are equipped with compensating loops but furthermore the 2 planes need to be adjusted for earth field. The maximum total quantity is therefore 54 = (2 x (32-5)) in operation with some spare to repair in case of failure.

The present solution using low grade power supplies could be extended, reusing the 12 units on operation today. A RFQ will therefore necessary when the power size will be known. We are also looking to power them with the DC correctors (2A 26W) solutions adding the 54 requested to the 768 in view.

Soon, we will get the magnetic earth field correction current request. This should complete the variety of the power supplies to procure.

# 5 Radio Frequency

## 5.6 RF Requirements

Table 5.1 gives the main parameters for the RF system of the new EBS source in comparison with the existing machine:

**Table 5.1: RF parameters of existing machine and EBS machine.**

| **RF parameters** | | **Existing machine** | **New EBS source** | | |
|---|---|---|---|---|---|
| Electron Energy | $E$ | 6 | 6 | | GeV |
| Nominal/maximum stored current | $I_{beam}$ | 200 | 200 | 220 | mA |
| Dipole radiation losses | $U_{dipole}$ | 4.88 | 2.5 | | MeV/turn |
| Maximum ID radiation losses | $U_{ID}$ | 0.50 | 0.50 | | MeV/turn |
| Maximum total radiation losses | $U_{max}$ | 5.40 | 3.00 | | MeV/turn |
| Longitudinal damping time | $\tau_s$ | 3.5 | 9.13 | | ms |
| Momentum compaction factor | $\alpha$ | 1.78E-04 | 8.50E-05 | | |
| Energy spread (low bunch current) | $\sigma_E/E$ | 1.06E-03 | 9.30E-04 | | |
| RF Frequency | $f_{rf}$ | 352.202 | 352.372 | | MHz |
| Harmonic Number | $h$ | 992 | 992 | | |
| Nominal / Maximum RF Voltage | $V_c$ | 8.0 | 6.5 | 6.6 | MV |
| RF Energy acceptance for $V_{c\text{-}nom}$ (for $U_{max}$) | $(\Delta E/E)$ | 3.60% | 5.6% | 5.7% | |
| Synchrotron frequency (for $U_{max}$) | $f_s$ | 1.86 | 1.28 | 1.29 | kHz |
| Compared Instability thresholds for HOM driven instabilities (LCBI), for one given HOM | *ratio* | 1.9 to 1.0 | | | |
| HOM control | | by temperature tuning to less than ± 0.1 deg C | by strong HOM damping | | |
| Number of cavities | *Ncav* | 5 five-cell cav's | 14 mono-cell cav's | | |
| Cavity shunt resistance | *R/Q* | 696 | 145 | | Ω/cavity |
| Quality factor | $Q_0$ | 38500 | 32500 | | |
| Cavity shunt resistance | $R_s$ | 26.8 | 4.71 | | MΩ/cavity |
| Coupling factor | $\beta$ | 4.4 | 2.8 | | |
| Copper losses per cavity | $P_{Cu}/N_{cav}$ | 48 | 22.9 | 23.6 | kW |
| RF power per cavity incl. transmission losses (existing SR: 10%, EBS: 15 % at worst, for $U_{max}$) | $P_{tot}/N_{cav}$ | 292 | 75.6 | 81.4 | kW |

The following parameters and constraints for the EBS machine are given:

- The synchrotron radiation loss is 2.5 MeV/turn from dipole radiation and can reach 3.0 MeV/turn with up to additional 0.5 MeV from Insertion Devices.
- Specified maximum RF accelerating voltage of 6.6 MV (providing an RF energy acceptance of $\Delta E/E = 5.7$ %)
- Maximum stored beam current of 220 mA.
- Higher Order Mode damping for unconditional stability up to 1000 mA. (According to the experience with the existing machine where 300 mA were only obtained with the help of the longitudinal bunch by bunch feedback, temperature tuning of five-cell cavities would not allow operating the EBS machine up to 200 mA. HOM damped cavities are therefore required for the EBS.)
- The RF frequency is increased by 170 kHz from 352.202 MHz in the existing machine to 352.372 MHz for the new EBS lattice.

The EBS will suffer from higher Touschek scattering leading to much lower beam lifetime, so the RF system will provide an option for a harmonic RF system in bunch lengthening mode to improve the lifetime by typically a factor 3 for operation at 200 mA in uniform filling or for the multibunch train of the 7/8+1 filling, and by a factor 2 in 4 x 10 mA or 16 bunch operation at 90 mA as well as for the single bunch in the 7/8+1 filling.

## 5.7 RF system configuration and working points

During ESRF upgrade phase 1, mono-cell HOM damped cavities were developed at the ESRF and three prototypes built and tested on the existing storage ring. These cavities fulfil the stability requirements of the EBS with respect to HOM driven LCBI and 12 additional cavities are in fabrication for the new machine, so that we will dispose of 15 such cavities: up to 14 on the ring plus one spare.

Seven 150 kW solid state amplifiers (SSA) were installed during ESRF upgrade phase 1: four on the booster and three on the storage ring to power the prototype HOM damped cavities in cell 23. A compact SSA using a cavity combiner was developed in house that can provide 85 kW nominal RF power (tested up to 90 kW).

More and more small and medium size accelerators, such as typically synchrotron light sources will or are now planning to implement SSAs rather than vacuum tubes. It was also envisaged to replace all the klystrons with SSAs for EBS. However, in order to limit the required resources for EBS, it was decided to start the new machine with the existing RF amplifiers, including two klystron transmitters.

**Figure 5.1** shows the schematic RF configuration for the EBS upgrade of the storage ring.

The base line configuration consists of 13 cavities on the ring: 10 cavities powered by

existing klystron transmitters TRA1 and/or TRA2, and 3 cavities by the 3 existing ELTA-SSAs. When not used as back up for operation, TRA2 will be available for the RF teststand. (The SSAs will be transferred from cell 23 to cell 25, the existing klystron transmitter TRA3 of cell 25 will be dismounted.)

- Option: as far as possible a 14th cavity will be installed on cell 25 during the long shut down as 14th cavity to be available even faster in case of need, by quick connection to a neighbouring ELTA SSA.

- Extended option: if the in house SSA is validated in time as assumed today, it will be connected to the 14th cavity. It is essential to validate this SSA concept on a cavity in normal operation with beam. Base line operation conditions can be set any time with the 14th cavity in passive mode in order to avoid interference with the start up of the new machine. (The installation of the 14th cavity and its connection to the in house SSA are foreseen within the RF project and will be scheduled accordingly, but shall not be integrated into any critical path. In case of difficulties, these options will be dropped.)

The development of a 3rd harmonic RF system operated in bunch lengthening mode for increased Touschek lifetime is included in the EBS project. However, the time needed for the development and implementation of the harmonic RF system will extend well beyond the commissioning of the new machine.

- Recent beam dynamics simulations indicate that a passive superconducting pair of cavities like Super3HC in Elettra or SLS could give rise to AC Robinson instabilities when tuned to operate at currents below 70 mA. Therefore, the alternative use of active normal conducting cavities is under study. Also the use of active superconducting cavities is investigated.

- Note that the beam stay clear of normal conducting cavities could be a limiting factor due to possible interception of photons. Superconducting cavities have a much larger beam tube and would therefore be easier to integrate into a straight section.

- If the harmonic cavity system is not too long, it will be installed on cell 25 behind the 3 cavities #11, #12 and #13, meaning that the 14th cavity will have to be removed at that time.

- In case the gap left by two missing accelerating cavities is too short for harmonic cavities, they will be installed on cell 14.

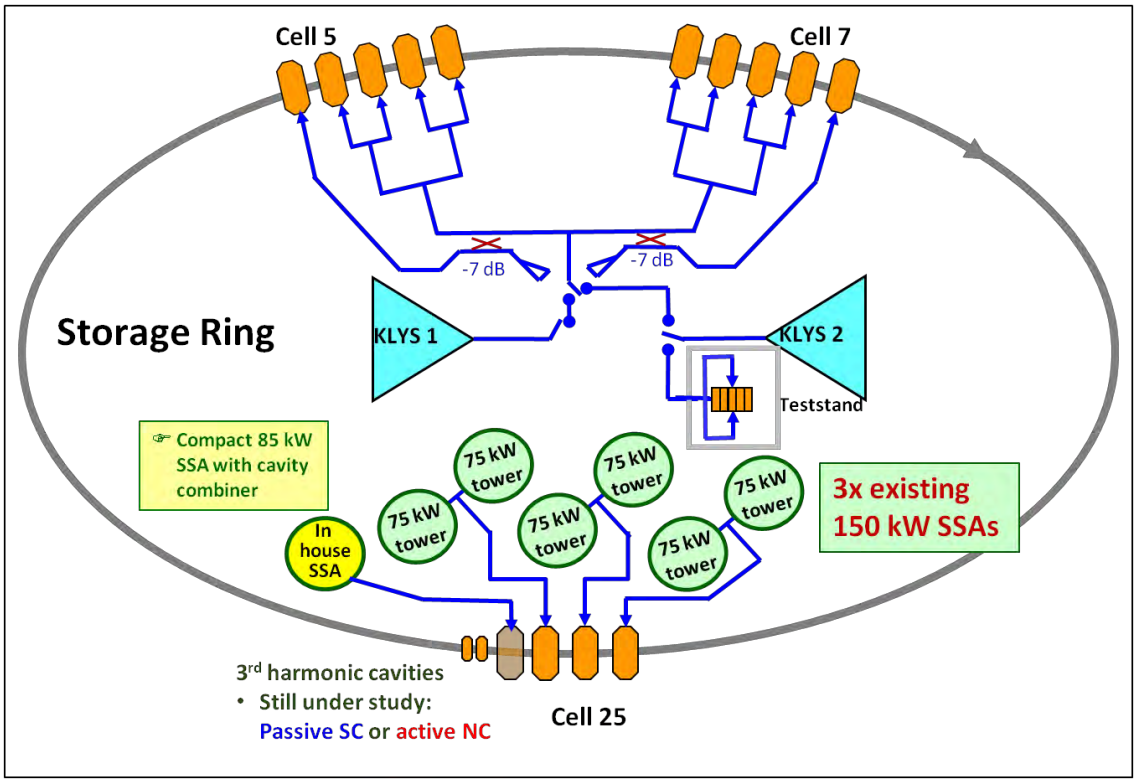


**Figure 5.1: Layout of the RF system for EBS. Cavities are numbered 1 to 14 clockwise from the first cavity in cell 5 to the last cavity in cell 25.**

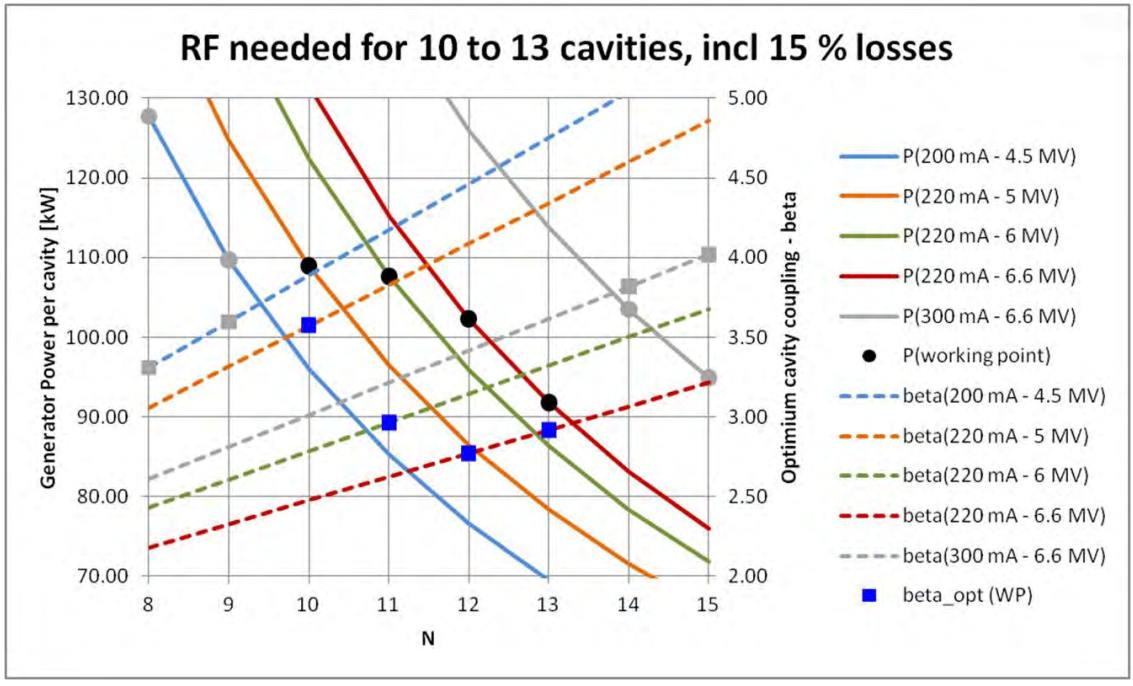


**Figure 5.2: Power per cavity and optimum coupling for various RF configurations for the EBS machine, N being the number of cavities in operation (graph computed for a previous lattice version with $U_{max}$ = 3.1 MeV).**

Figure 5.2 shows the power requirements as a function of the number of cavities in operation. We will still dispose of sufficient operational margin to store up to 220 mA with some missing cavities. Even in case a full string of 5 cavities in cell 5 or cell 7 would be out of order, it would still be possible to store 200 mA at 4.5 MV. Ultimately a performance upgrade, for instance to 300 mA, could be envisaged with 13 cavities on the ring, still keeping a margin of one missing cavity.

The coupling of the cavities delivered by RI is set to $\beta = 2.8$, which gives nearly optimum matching for 11 to 13 cavities in operation, the optimum values being given by the blue squares in Figure 5.2. As shown in Figure 5.3, also with 14 cavities in operation only little reflected power is generated over a large current range. Note that fs-Rob gives the beam loading or Robinson effect on the synchrotron frequency for the coupled bunch mode n = 0, which corresponds to in phase synchrotron oscillations of all the bunches. Vanishing fs-Rob corresponds to the threshold for the fast DC Robinson instability, which occurs well beyond 300 mA, i.e. outside the graph of Figure 5.3.

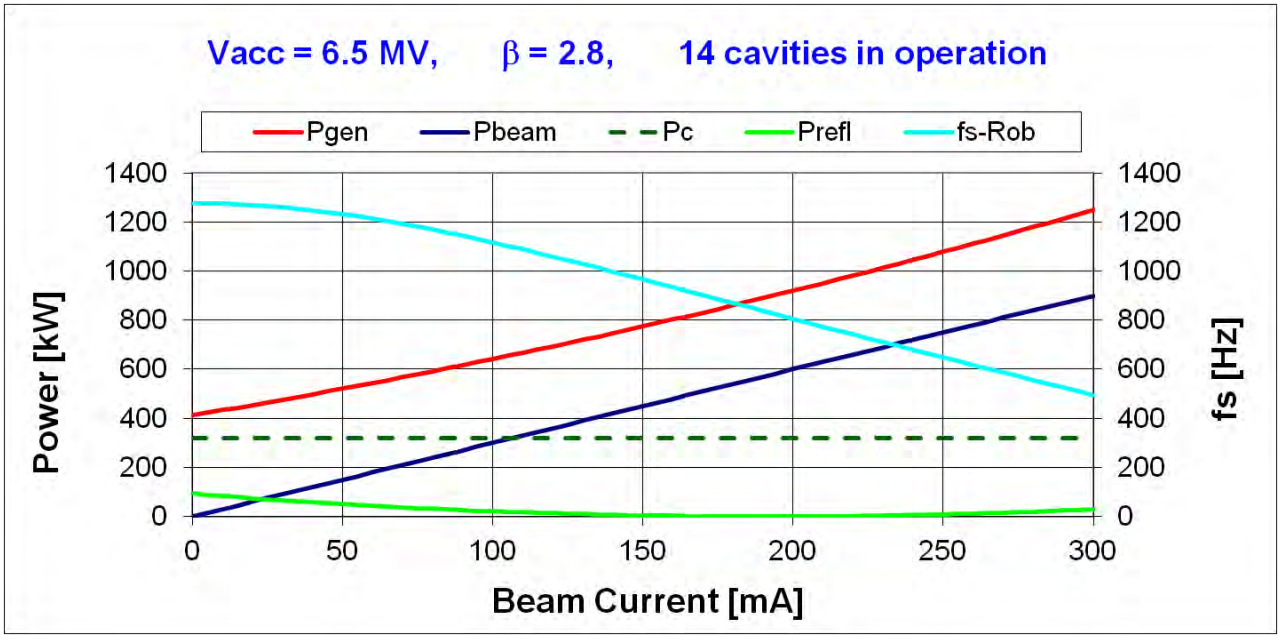


**Figure 5.3: Generator power Pgen, beam power Pbeam, total cavity dissipation Pc, total reflected power Prefl and synchrotron frequency due to Robinson effect fs-Rob as a function of beam current in the EBS machine [seen from the cavities, i.e. not including transmission losses].**

## 5.8 RF layout & buildings (SRTU, transmitter rooms, new RF teststand, ID8 space)

### Cavities in SRTU, cells 5, 7, 25

As depicted in Figure 5.4, the layout for the integration of the cavities in the straight sections of cells 5, 7 and 25 is finalised. It allowed designing the cavity girder system as well as the waveguide connections between the transmitter rooms and SRTU. These details are described hereunder.

### 3D view

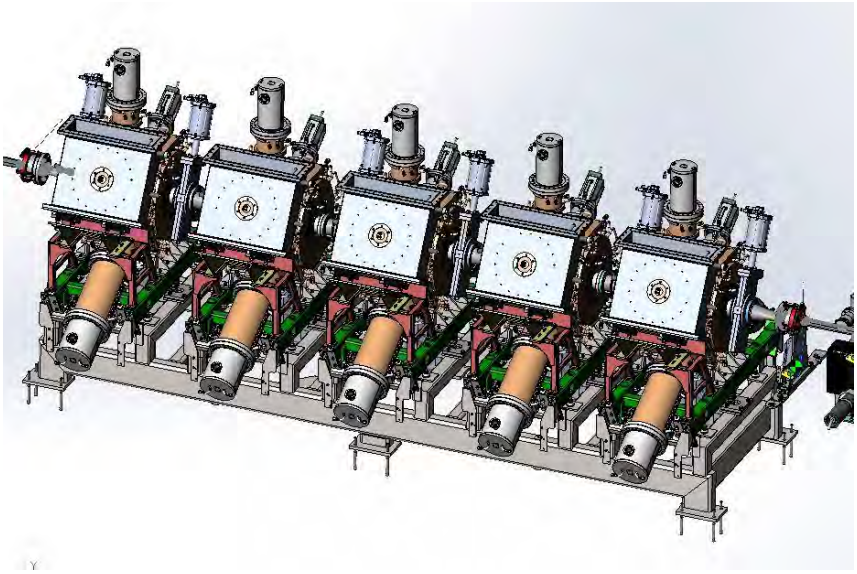

### 2D view

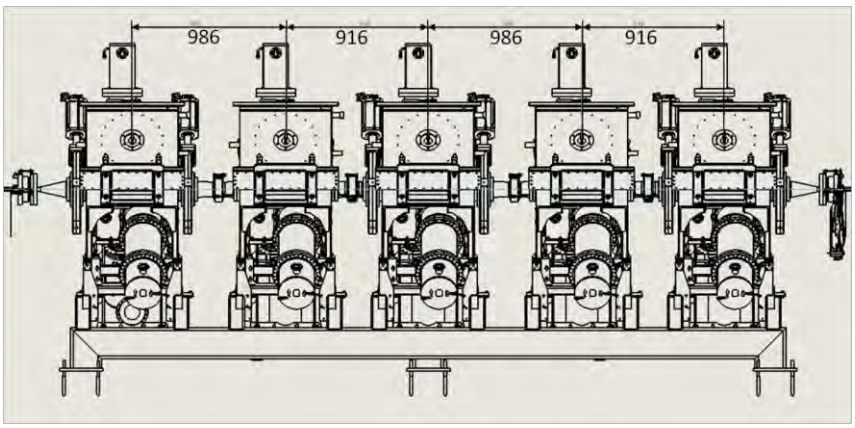


Figure 5.4: SRTU - RF straight section with 5 cavities: example of cell 5.

### Transmitter rooms, waveguide distribution, services

The existing switching system that allows connecting the cavities of cells 5 to TRA1 and those of cell 7 to TRA2, or to connect them all to TRA1 or all to TRA2 will be kept. The nominal configuration will remain as today with TRA1 feeding all 10 cavities of cells 5 & 7 and TRA2 remaining available for the teststand. However, the distribution of power will have to be modified as sketched in Figure 5.5 for the example of cell 5. Instead of splitting the incoming power by 4 to feed two five-cell cavities with two power couplers each, a splitting by five will be required for EBS. Waveguide trombone sections are needed for each of the cavities 2 to 5 in order adjust their phases such that all cavity voltages combine in phase as seen by the beam. For this the trombone lengths can be varied within ± λ/4 (quarter waveguide wavelength). Fine tuning is achieved by means of the shown waveguide phase shifters. Each leg will also be equipped with waveguide directional couplers to monitor the amplitudes and phases of the incident waves as well as the amplitudes of the reflected waves.

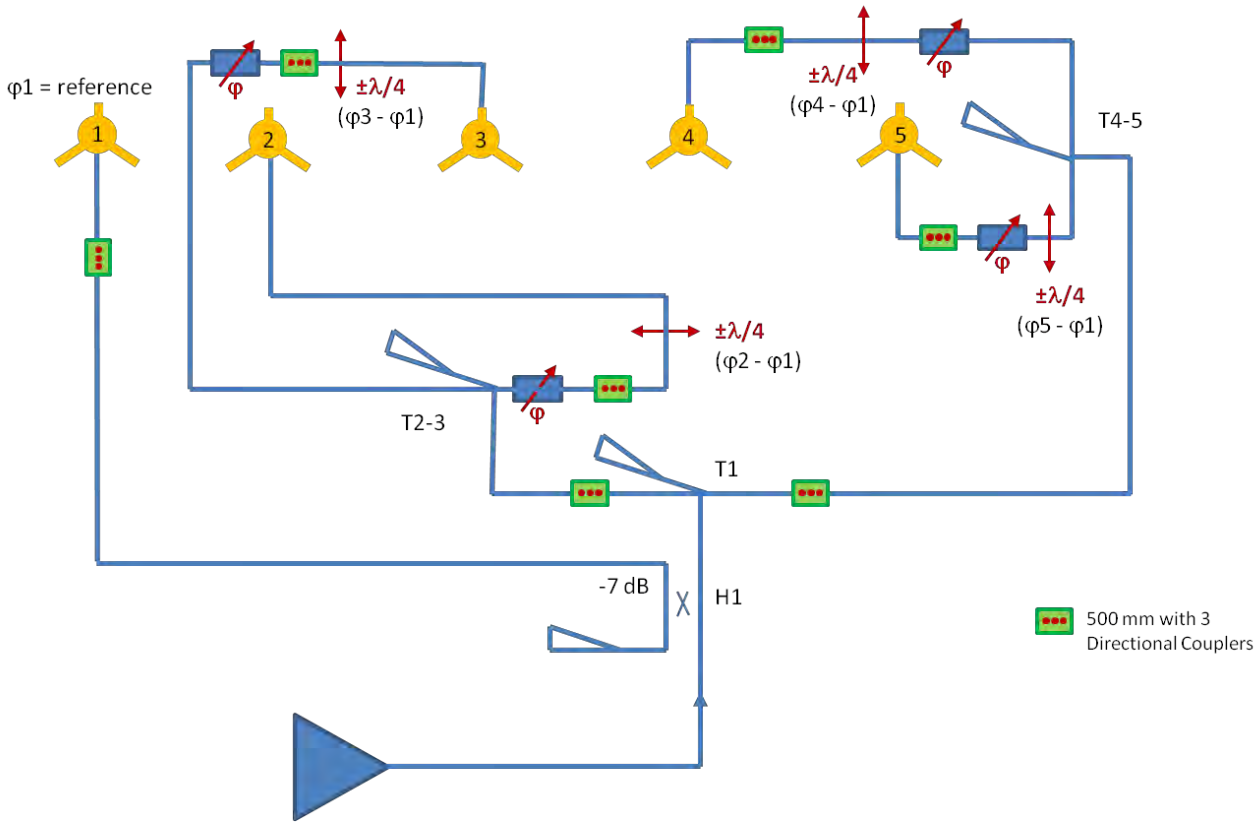


Figure 5.5: Schematic of the waveguide distribution of cell 5 (similar schematic for cell 7).

Figure 5.5 gives the specification for the waveguide distribution system in cell 5, which is similar to cell 7. First, 1/5 of the incident power is coupled by means of a -7 dB hybrid coupler (already in house) and the subsequent splitting by four is achieved with the existing magic T splitters in use today. For matching reasons, the fourth arms of all the splitters are connected to 300 kW water loads: this requires one more water load on each cell as compared to today. The phase shift from cavity to cavity is determined by their respective centre-to-centre distances according to Figure 5.4 and the following table.

| **Cavity** | **Lcav** | **Lvalve** | **Lbellow** | Total | | **Delta Phi** | Delta Phi |
|---|---|---|---|---|---|---|---|
| **distances** | [mm] | [mm] | [mm] | **[mm]** | | [rd] | **[deg]** |
| | | | | | PhiCav1 | 0 | **0** |
| d12 = | 630 | 85 | 271 | **986** | PhiCav2 | 0.9987 | **57.2** |
| d23 = | 630 | 85 | 201 | **916** | PhiCav3 | 0.4817 | **27.6** |
| d34 = | 630 | 85 | 271 | **986** | PhiCav4 | 0.9987 | **57.2** |
| d45 = | 630 | 85 | 201 | **916** | PhiCav5 | 0.4817 | **27.6** |

**Table 5.2: Distances between cavities in SRTU, valid for cells 5, 7 and 25. Every second bellow section includes a photon absorber and is therefore longer by 70 mm than the other two bellow sections.**

In cell 25 the waveguide system is much simpler with one feeder per cavity/SSA as presently on cell 23, including the possibility to operate with a cavity in passive and connect it and its SSA to power loads (2 kW air cooled loads for the cavities, 300 kW coaxial water cooled loads for the SSAs).

A draft 2D layout of the RF transmitters including the waveguide feeders has been designed for cell 25 (Klystron TRA3 replaced with 3 + 1 SSA) and cells 5 & 7 (keeping klystron transmitters TRA1 and TRA2 where they are). It has been handed over for detailed 3D drafting of the waveguide run, the cabling and water piping by a subcontractor of MEG, including a detailed survey of the existing buildings and infrastructures. The drawings are expected early 2017. This will allow issuing a CFT or RFQ for missing waveguide components.

Project: drafting of RF waveguides, water pipes and cables/trays including positioning of the SSAs, location: transmitter rooms of cells 5, 7 and 25. This project involves mainly MEG, RF, BIG, Safety Group. Delivery of drawings: April 2017, checking by Safety Group, followed by possible modifications and then CFT's / RFQ's: RF waveguides: mid 2017 for delivery early to mid 2018**.**

### SRRF extension – New RF teststand and RF storage space

In conjunction with EBS, a new RF building will be implemented close to SRRF to house the future new RF teststand and create dedicated storage space for large RF spares: klystrons, cavities, waveguide components. Figure 5.6 shows the result of the pre-study carried out in June 2016.

Project: SRRF extension & new teststand, "BP 3377 – Extension of MTBS". Project involving mainly BIG, RF, Safety Group. Delivery of drawings: December 2016. This project is already taken into account in the new waveguide distribution in SRRF.


**Figure 5.6: SRRF extension for a new RF power teststand and RF storage space – Pre-study June 2016-08-02.**

## Cavity assembly and storage zone – EXPH / ID08

A dedicated zone has been created in 2015 to receive and prepare the RF cavities. The cavities are equipped with all their ancillary components (tuners, couplers, field probes, vacuum instrumentation and pumps, bake out equipment, sensors, cabling, connection boxes, girders, etc). They are baked in the ID8 assembly area, transferred to the RF power teststand for RF conditioning and brought back to ID08 where they are stored until their installation in SRTU in 2019. Figures 5.7 and 5.8 show this ID8 assembly area. It is essential that all the vacuum interventions are carried out under clean room conditions, obtained under a laminar flow canopy. This allowed reaching base pressures in the $10^{-11}$ mbar range and RF conditioning to 750 kV within less than two weeks.

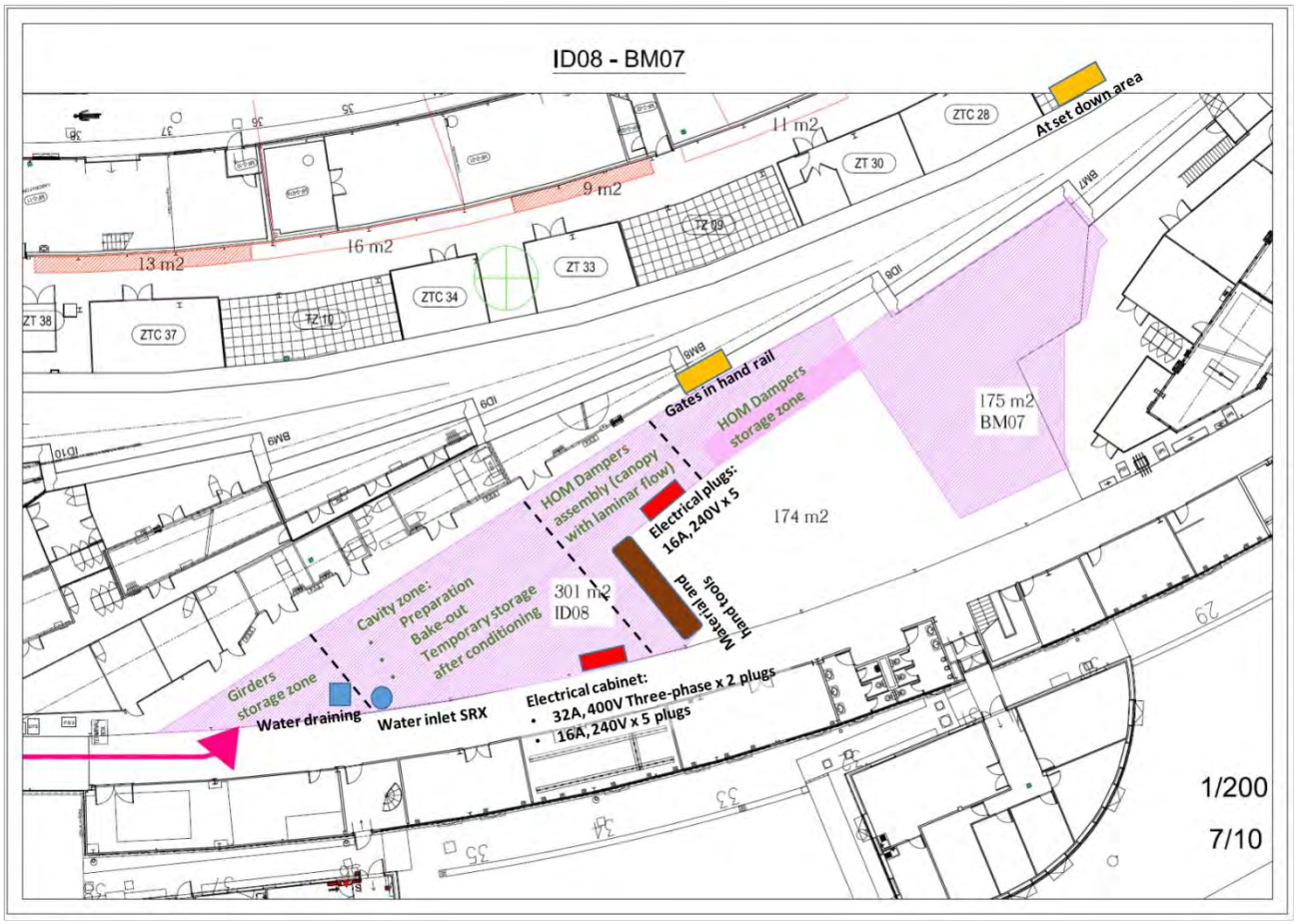


Figure 5.7: RF cavity assembly area in the EXPH / ID08 zone.

**Figure 5.8: The cavity assembly area on ID08. In the foreground, the local clean room area for all UHV works, in the background, RF conditioned cavities and still empty girders.**

## 5.9 RF system components – Specs / Procurement / Upgrades

### Cavities

In 2005 an R&D project was started to develop a 352.2 MHz normal conducting HOM damped cavity for the ESRF, based on the 500 MHz BESSY design of the EU cavity, that is now in operation at ALBA, MLS, BESSY, and soon at DIAMOND. The ESRF design sketched in Figure 5.9 has brought many improvements with respect to the BESSY/ALBA design:

The impedance R/Q has been increased from 117 Ω to 145 Ω.

Comparably much more compact design with much shorter HOM dampers (scaling of BESSY cavity would never fit into ESRF tunnel).

Three ridge waveguides terminated with ferrite loaded tapered absorbers constitute the HOM dampers of the cavity. The ridges are used both to lower the cut off frequencies of the circular waveguide modes and obtain a good coupling to the cavity HOMs. The cutoff frequency of the fundamental mode of the two large HOM

absorbers is set well above the fundamenental accelerating cavity mode frequency of 352.37 MHz and below the lowest HOM frequency, such as to propagate the HOM power to the HOM absorbers and keep the accelerating cavity mode uneffected. The third HOM damper on top provides additional damping for a few higher frequency HOMs. It's length fits into the existing storage ring tunnel. The lengths of the HOM dampers are dimensioned such that the non propating, aperiodically decaying fields at 352.73 MHz are sufficiently low at the HOM absorbers not to affect the quality factor of the accelerating mode.

In the ESRF design, the first ridge waveguide HOM damper section, called coupling section, is directly welded or brazed to the cavity, thereby avoiding a gap between the ridge and the cylindrical port of the cavity. This allowed suppressing flange overheating and subsequent development of leaks as experienced on the MLS and ALBA cavities. It also allowed suppressing a residual HOM observed in the ALBA cavity. This design improvement has been taken over by BESSY for the fabrication of the BESSY and DIAMOND cavities.

Further intermediate HOM damper sections and the HOM absorbers are then flanged head on and a sound electrical contact is achieved by means of a well dimensioned RF finger. The flange connections are sufficiently far from the cavity, where the fields from the main accelerating mode are already decayed in the HOM waveguide under cut off, such that the RF contact fingers are not overloaded.

In the HOM absorbers the water cooled ridges are tapered and loaded with lossy C48 ferrite plates that absorb the incoming HOM power with only minimum reflection.

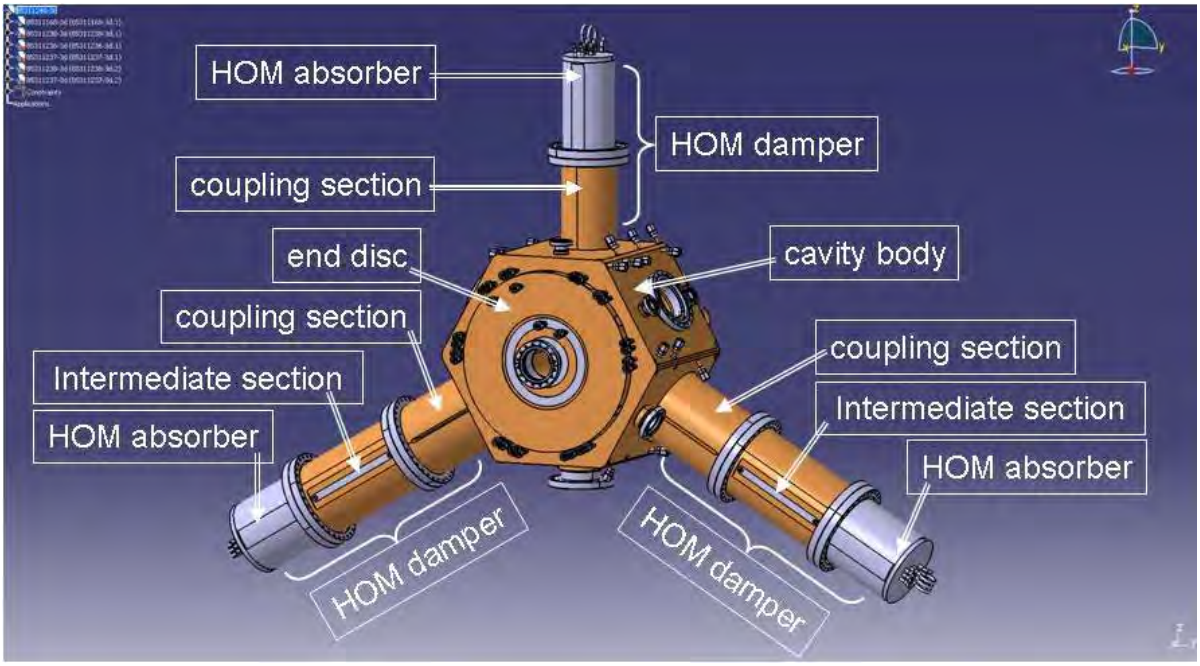

**Figure 5.9: 3D drawing of the cavity assembly showing the cavity body and the attached HOM dampers.**

Three prototype cavities and their sets of HOM absorbers were built between 2009 and 2011, one by RI (D), one by CINEL (I) and one by SDMS (F). They were successfully tested on the existing ESRF ring in cell 23 and conformed to the expected parameters. **Table 5.3** gives the parameters measured on the prototypes and the first four cavities from the series production for EBS.

**Table 5.3: Cavity parameters (the given Q0 was measured on the prototypes and the value in parentheses was measured on the first 3 cavities from the RI series production).**

| **Geometrical impedance of fundamental accelerating mode** | **R/Q** | **145 Ω** |
|---|---|---|
| **Quality factor of accelerating mode** | $Q_0$ | 32500 (prototypes)<br>35000 (series prod.) |
| **Shunt impedance** | $R_s = Q_0 \times R/Q$ | 4.7 MΩ (prototypes)<br>5.1 MΩ (series prod.) |
| **Nominal accelerating voltage** | $V_{c\text{-}nom}$ | 500 kV |
| **Maximum accelerating voltage** | $V_{c\text{-}max}$ | 750 kV |
| **Longitudinal HOM impedances**<br>**(LCBI threshold at 200 mA with 15 cavities and $R_{HOM} \times f_{HOM}$ = 16 kΩ x GHz)** | $R_{HOM} \times f_{HOM}$ | < 3 kΩ x GHz |
| **Cavity dissipation at $V_{c\text{-}nom}$** | $P_{c\text{-}nom}$ | 26.5 kW (prototypes)<br>24.6 kW (series prod.) |
| **Cavity dissipation at $V_{c\text{-}max}$** | $P_{c\text{-}max}$ | 59.7 kW (prototypes)<br>55.4 kW (series prod.) |
| **Length** | $L_{cav}$ | 630 mm |

As shown in **Figure 5.10**, the HOMs are sufficiently damped not to drive longitudinal coupled bunch instabilities (LCBI) below 1 A of stored current in the EBS ring for as much as 14 cavities on the ring (1 A corresponds to the specified margin with respect to the maximum stored current in EBS).

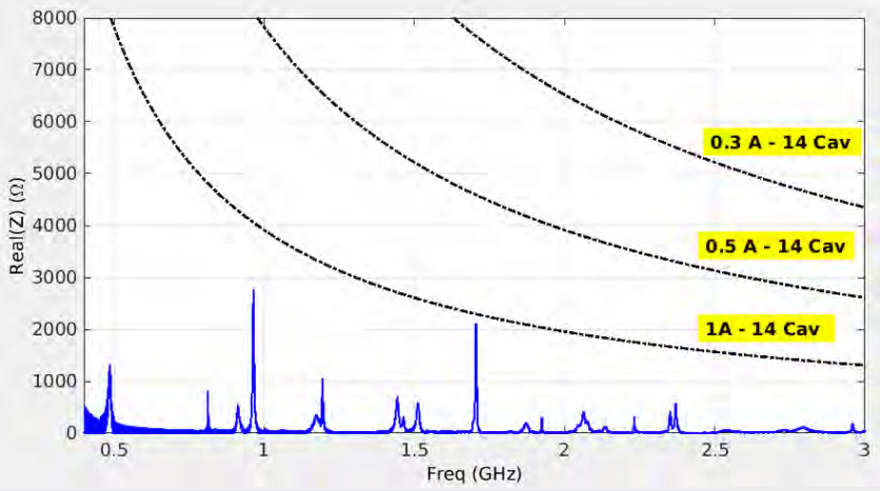


**Figure 5.10: Longitudinal HOM impedances of the EBS cavities compared to LCBI thresholds for 14 installed cavities at various stored currents (GdfidL simulation, confirmed by measurements).**

A small leak developed on a RF pickup port on the CINEL prototype and the cavity was removed from the machine in December 2014. The leak has been varnished and the cavity reconditioned with RF power, however, with a pressure above $10^{-9}$ mbar at nominal RF voltage. In 2013 the CFT 2110 was launched for the series production for EBS: 12 cavity bodies were ordered from RI and 14 sets of HOM absorbers from another company. Due to problems of this company with the production, in December 2016 a contract has been signed with RI for the fabrication of the HOM absorbers with a scheduled delivery between end of 2017 and mid 2018. As a consequence of this late delivery, the RF cavities are currently RF conditioned without HOM absorbers, which will be installed just before installation of the cavities on EBS.

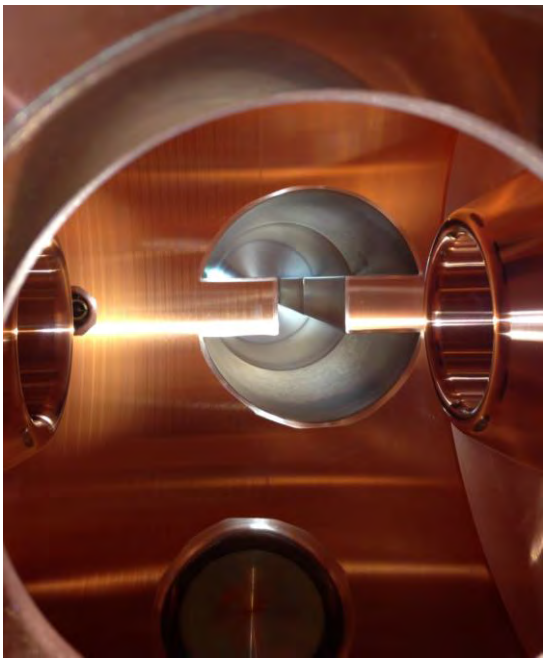

**Figure 5.11: View inside the cavity. Left and right in the photo: beam tubes with nose cones to maximize the fundamental mode impedance. Centre: ridge waveguide of a large HOM damper.**

## Cavity bodies

Two design options were proposed in CFT 2110:

- Design option 1: with vacuum brazing junctions on the cavity body, borings for cooling channels, as applied by RI on their prototype: Drawings: 85.36.1000 to 85.36.1074.

- Design option 2: essentially e-beam welding, with water boxes for cooling (machined cooling channels and electron beam welded lids), as applied by CINEL and SDMS on their prototypes: Drawings: 85.37.1000 to 85.37.1093.

RI retained the design option 1 for the series fabrication of the remaining 12 cavities for EBS. The connection of the HOM coupling sections and the end discs on the body by e-beam welding was replaced with a further brazing step. As a consequence, 3 brazing steps, staggered in temperature are required.

## Brazing in 3 steps

The first cavity was built by using the following three brazing alloys: PalCuSil10, PalCuSil5 and CuSil eutectic. Despite good experience with this for 500 MHz cavities, this sequence didn't work for the slightly more bulky 352.37 MHz cavities for the ESRF. The high copper mass necessitated longer temperature cycles, such that the 2$^{nd}$ step deteriorated the brazing joints from the 1$^{st}$ step which then developed leaks. RI managed to terminate this 1$^{st}$ cavity by rebrazing it several times with additional brazing materials. A new sequence with AuCu (≈ 1000 deg C !), PalCuSil and finally CuSil was implemented by RI for the subsequent 11 cavities. It is at the limit of not melting the copper, but the result is very satisfactory.

## Excellent Q0

The cavities delivered so far by RI exhibit unloaded quality factors $Q_0$ in the range of 34500 to 35500, well above the 32500 to 33000 measured on the prototypes. The main difference is that now all the electron beam welds in the assembly of the cavity bodies are

replaced with high temperature vacuum brazing.

### Repair of a leaky flange

On cavity #5 a leak was detected at the FAT on the pumping port at the brazing interface between the stainless steel flange and the copper sleeve. This was successfully repaired by removing the flange with a part of the copper sleeve and electron-beam-weld a new assembly.

### HOM absorbers

Initially for the three prototype cavities, the HOM absorbers were designed with bodies completely machined from bulk stainless steel 316 LN. The ferrite tiles were to be brazed on copper plates which had then to be brazed on the tapered ridges machined in the bodies. One supplier proposed to braze the ferrite tiles directly on the stainless ridges, which worked out very well. As a result of the CFT 2110, a contract was placed in December 2013 with this supplier for the series production of the HOM absorbers. Unfortunately, it did not reproduce the process parameters needed for an acceptable brazing quality so that the ferrite tiles didn't stick to the ridges. Three years after the order, the contract was finally terminated and new HOM absorbers were ordered in December 2016 from RI. They proposed a modified fabrication process derived from the method applied successfully for many HOM absorbers for BESSY and ALBA.

The series HOM absorbers will be built from copper. The tapered ridges are made of water cooled copper wedges, on which the ferrite tiles are brazed prior to screwing them into the absorber bodies. The design is given in: Drawings: 88.31.0072 to 88.31.0123.

14 sets of 3 HOM absorbers will be delivered from October 2017 until May 2018. So, despite the three years lost with the former contract, the HOM absorbers should arrive in time to be installed on the cavities before their transfer into the storage ring tunnel in 2019. The main consequence of the late delivery is that the cavities are RF power conditioned without the HOM absorbers. Seen that the absorbers do by design not see significant power from the main accelerating mode, this will have no impact on the commissioning of the RF system on the EBS machine.

### Girders

As can be seen in **Figures 5.4** and **5.8**, the cavities are installed on individual "upper" girders including the auxiliary equipments: power coupler with the coaxial to waveguide transition (doorknob transformer), field probes, movable tuner, ion pump, gauges, RGA, water pipes, hoses and manifolds, temperature sensors, flow controllers, as well as electrical distributions boxes for control signals and baking heaters. Each fully equipped cavity ensemble can then be lifted with a crane as a whole and dropped on so called "lower" girders, which consist essentially of simple support frames. Special lower girders equipped with wheels are used for individual cavity ensembles in the RF power teststand and for easy handling in the preparation area. For the future installation in the tunnel, lower girders for cells 5 and 7 will receive 5 cavity ensembles. For cell 25, they are split in 3 and 2 cavities per girder, in view of the possible later removal of cavity #14 to free space for a harmonic cavity. All girders are in house.

The girder design will allow very efficient and fast installation on the EBS machine:

1) Easy installation and alignment of empty lower girders using the crane,
2) Drop of the cavity ensembles one by one with the crane and fine alignment,
3) Installation of intermediate vacuum chambers, including pneumatic valves (in house), photon absorbers and bellows (designed, still to be ordered),
4) Insitu bakeout: easy connection of the boilers and the few additional electrical heaters to the "plug and play" baking system, as already done in the ID8 preparation zone,
5) Fast connection of all control cables to the distribution boxes,
6) Simple connection to the cooling water supply by means of only one input and one output hose per cavity,
7) Easy connection to the waveguide feeders.

### Power couplers

The HOM damped cavities for EBS are equipped with the same power couplers as the existing ESRF five-cell cavities (CERN/LEP design). They are currently operated with up to 170 kW in CW, whereas even under the worst assumptions in **Figure 5.2**, they will never see more than 110 kW on EBS. Thanks to a sufficient stock of spare couplers, no additional units had to be procured for EBS. The 10 couplers currently in operation on the storage ring will add to the spare stock for EBS.

### Tuners

The existing movable tuners (also a CERN/LEP design) can be used on the EBS cavities. However, in order to be able to pre-condition the cavities on the RF power teststand, it was necessary to procure new tuners. The engineering office (MEG) proposed a modification for substantially a shorter and more compact design as shown in Figure 5.12.

In May 2015 a contract was placed with the company CECOM for the fabrication of 17 tuners (1 prototype followed by a series of 16 units). The prototype foreseen in August 2015 was delivered almost one year too late, in July 2016. It was immediately installed on a cavity in the teststand in order to check the compact design at high RF power, in particular that the missing ventilation will not lead to overheating of the bellow. Following successful tests, CECOM received green light to launch the series fabrication according to the new compact design.

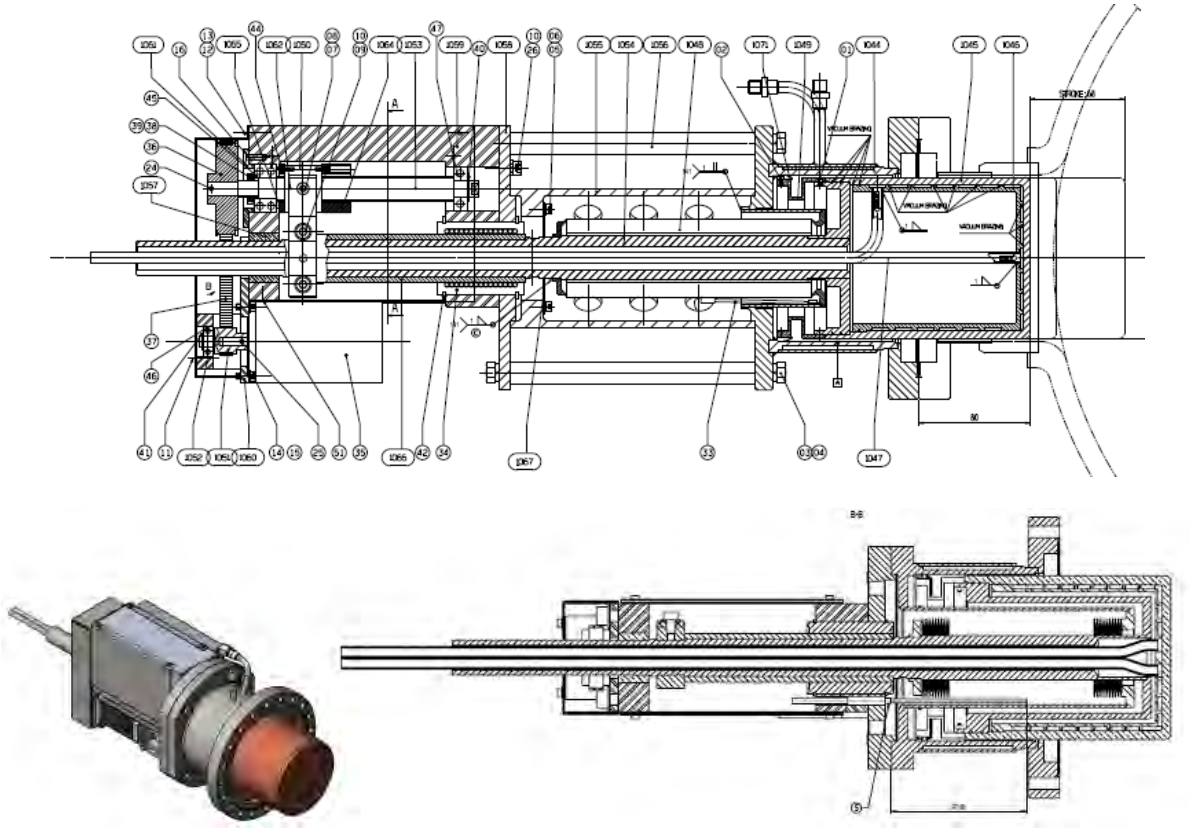

Figure 5.12: Movable piston tuner. Top: CERN/LEP design. Bottom: new compact design for EBS.

Unfortunately, for several reasons linked to the supplier's internal organisation and problems with subcontractors (for vacuum brazing and copper coating of stainless steel), the series production was again delayed. These problems seem now to be solved and the delivery of the series of 16 tuners should start beginning of April 2017. This will allow resuming the RF conditioning of the cavities, that had to be

interrupted after cavity #5 due to missing tuners.

### Field probes

The LEP design has been kept and adapted in length to the HOM damped cavities. It consists of a housing that contains the vacuum and which is made of a flanged stainless steel tube ending with a brazed-on ceramic cap. The loop of the coaxial field probe is in air and couples to the azimuthal magnetic field of the accelerating cavity mode through the ceramic window.

All field probes needed for the EBS cavities are in house.

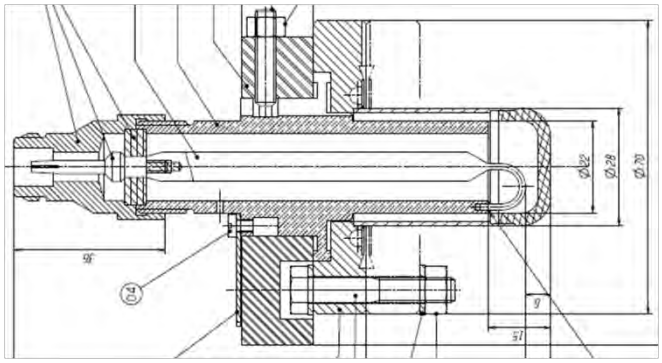

Figure 5.13: LEP type field probe, also used for EBS cavities.

A number of non treated ceramic caps developed leaks when conditioned above 500 kV. This was cured by applying a Titanium coating on the vacuum side of the ceramics. The process is performed in house by the vacuum group. No further leak developed with cavities conditioned up to 750 kV.

### Instrumentation

The cavities are equipped with:

- 1 Pirani gauge, 2 Penning gauges and 1 RGA head on the body,
- 1 Penning gauge on each HOM absorber,
- Temperature sensors at the main in and output water supplies, and a precision Vortex flow meter outside the tunnel,
- Temperature and flow controllers on tuner and coupler cooling circuits
- A temperature sensor on tuner bellow
- Coupler window air cooling: in and output air temperature, pressure interlocks to check presence of air flow
- Coupler window IR temperature measurement and CCD camera to detect glow discharges on the vacuum side
- Tuner position control (step motor) with encoder and potentiometer position measurements, as well as limit switches.

## 5.10 Special waveguides

### Coaxial SRTU roof feed through

With 5 cavities installed close by in a straight section as shown in Figure 5.4, it is not possible to simply prolong the waveguides through the tunnel roof. The 600 mm broad waveguides would not leave enough space for the design of corresponding roof beams. It was therefore decided to design coaxial feedthroughs of diameter $\phi_{ext}$ = 152 mm as shown in Figure 5.14, which need only $\phi \approx 250$ mm holes in the roof beams. The dimensions of the waveguide to coaxial transitions were designed for perfect matching. To withstand the maximum power and worst mismatch conditions of the cavities, the coaxial line element and the waveguide transitions are air cooled. A prototype of the assembly of Figure 5.14 was successfully tested in the lab and is currently checked under real operation conditions on the HOM damped cavity C23-2 in cell 23, with two air cooling configurations.

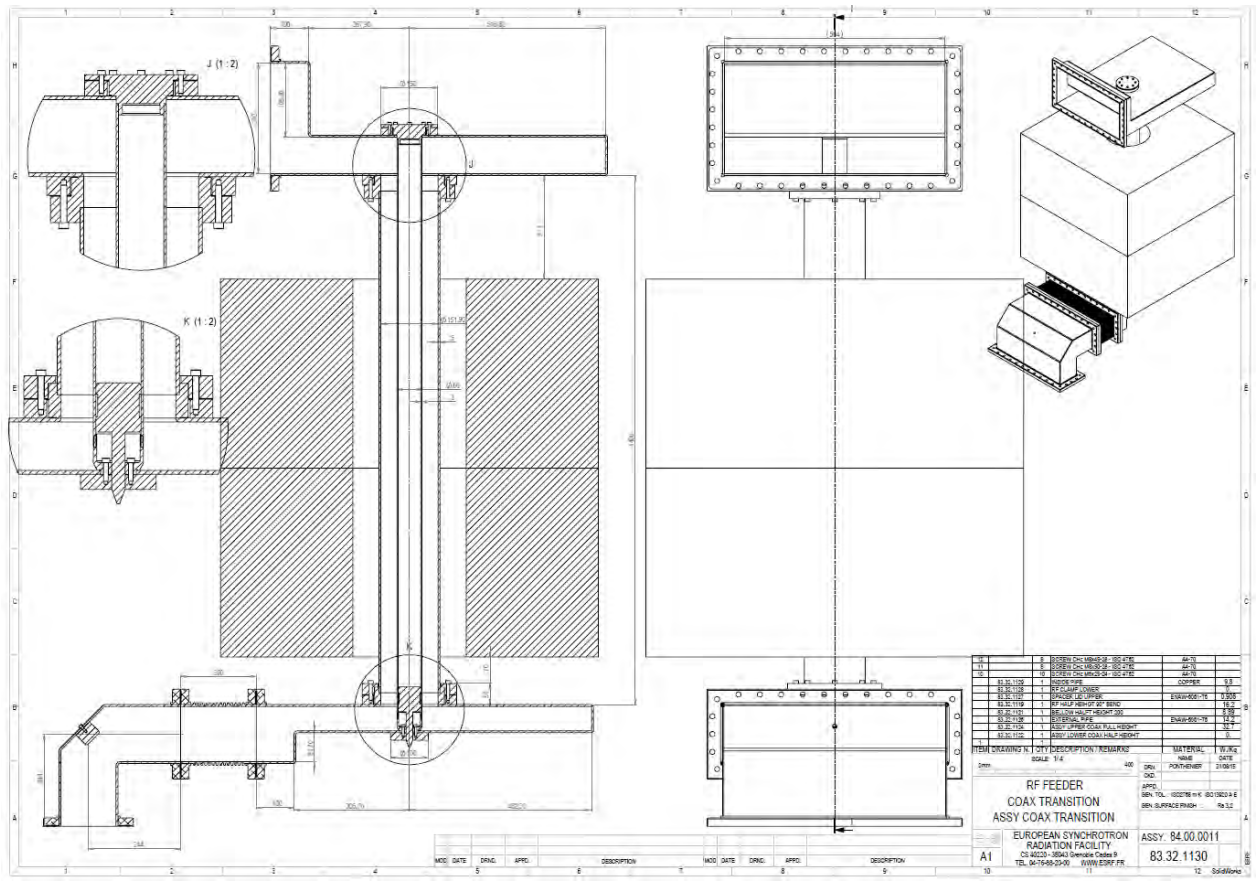


Figure 5.14: Coaxial SRTU roof feed through.

In the first configuration, the SRTU air blown on the window of the power coupler is forced through the coaxial line to an exit chimney mounted on the first full height waveguide on the SRTU roof (for this purpose the output air chimney in SRTU was closed). The air is not allowed to flow further upwards in the waveguide by insertion of an RF window. The alternative configuration, that still needs to be tested, consists of placing an air blower on the tunnel roof. Instead of an overpressure, this blower creates a depression in the waveguide to draw the air from SRTU. In both cases, the air is filtered to prevent dust from contaminating the coupler ceramic. For the alternative configuration, all the elements, including the filter, the hoses and the air chimneys, are designed to minimize the flow resistance and thereby limit the depression and the required power of the air blower.

In both configurations, the warm air is evacuated from the tunnel, which helps limiting the heat load in the tunnel. The alternative configuration with the air blower outside the tunnel further reduces this heat load.

### Waveguide phase shifters

Additional waveguide phase shifters are needed to fine tune the individual cavity phases with respect to the beam phase at the arbitrary positions of the cavities. To ease the tuning at the commissioning of EBS, they will be equipped with step motors. However, as experienced on the existing machine, once correctly tuned, the positions of these phase shifters will presumably not be modified anymore. Therefore the step motor control will be provisional and will not be integrated it into the RF control system.

### 7 dB hybrid and magic Tee splitters

In order to power a fifth cavity in each of cells 5 and 7, as shown in **Figure 5.5**, three 7 dB hybrid couplers have been procured (2 for operation and 1 spare). The remaining splitting by 4 will be done by means of magic T splitters, as in the present system.

### Power loads

The additional splitters require additional power loads to match the loaded arms. For this and for the update of the spare stock, 5 new coaxial 300 kW water loads are being procured.

## 5.11 Klystron transmitters

Mainly one klystron transmitter, namely TRA1, will be in operation on the EBS machine, powering the cavities #1 to #10 in cells 5 and 7. TRA2 will be used more occasionally to feed the RF power teststand and essentially work as hot spare to safeguard operation in case of problems with TRA1. The third transmitter TRA3 will be dismounted in 2019 and replaced by existing solid state amplifiers. Reminding the replacement of the booster klystron transmitter with SSAs in 2012, the number of klystron transmitters in operation on the machine will have been reduced from 3 to 1 during this decade, keeping always one hot spare transmitter to safeguard operation.

### Spare klystrons – expected total lifetime

Table 5.4 gives the list of available klystrons in house in February 2017, along with their accumulated operating hours (HV time). According to our experience, the end of life of klystrons can have several causes. Barium evaporation from the cathode sometimes leads to pollution of the ceramic HV gaps. This can in some cases be recovered by HV spot knocking of the cathode-anode and anode-body gaps as was successfully done on the TRA1-EEV4 klystron in March 2017. In some cases break downs can have an avalanche effect and lead to an unrecoverable deterioration: this end of life scenario has for instance been observed in 2015/16 on the EEV2-2 tube after less than 22000 hours of HV time. One Thales tube experienced a leak on the collector which opened only above a few 100 kW of RF thereby making it useless for operation. After some problems in the early nineties, a number of spare tubes were procured to safeguard operation. Thanks also to careful operation with for instance the implementation of low cathode heating when the HV is off, only little serious klystron failures have been experienced since the early 2000's and we still dispose of a comfortable stock of operational tubes as shown in Table 5.4.

Even if our oldest klystron EEV4 has already more than 70000 hours of HV time, the statistics are too small to allow defining a precise life time expectation of a klystron. Under the reasonable assumption to reach 40000 hours of lifetime per tube, after deduction of the present ESRF operation time until end of 2018, the spare stock of table 4 would still allow operating EBS more than 9 years. Note that this time is continuously prolonged while keeping the EEV4 klystron in operation.

| Transmitter: | TRA1 (1.2 MW) | TRA2 (1.2 MW) | TRA3 (0.4 MW) |
|---|---|---|---|
| Installed tube | EEV4 | EEV1 | Philips |
| HV time [hours] | 71523 | 35614 | 27377 |
| Replacement tube | EEV3 | TH89022-2 | TH89018-2 |
| HV time [hours] | 8374 | 18428 | 36340 |
| Other replacement tube | EEV5 | | |
| HV time [hours] | 10631 | | |

**Table 5.4: Available klystrons at the ESRF in February 2017 and nominal positions of spares.**

## Transmitter control upgrade project

Control hardware and software is evolving fast. So, despite a full control upgrade carried out on all transmitters around the year 2000, the obsolescence of the VME controllers now requires another upgrade for the transmitters that will be kept for EBS. The new control architecture will be adopted that was already implemented for the recently installed SSAs and HOM damped cavities in cell 23 of the existing storage ring is as follows:

- Analog and slow digital signals through WAGO PLC's with Modbus/Ethernet couplers (instead of VME)
- Device servers on a PCI
- WAGO's / PCI dialog via Ethernet
- Fast digital signals (fast interlocks): still old HIS (Hardware Interlock System)
- A new generation HIS of SSA-type is under development and will be retrofitted later
- The former VME feedback loops and higher level control will run in the PCI

The control upgrade of the klystron transmitter TRA2 was completed in 2016 in an almost transparent way. It required rebuilding and re-cabling the interfaces for the numerous signals. It was carried out step by step and interfered only very little with the heavy test program on the RF power teststand for EBS. TRA2 was unavailable only as back up for the storage ring operation from August to October 2016 for necessary software developments. It is, since, fully operational and has already replaced TRA1 as back up for user operation of the facility.

The upgrade of the transmitter TRA1 is planned for the December 2017 shut down. Also the control system to be implemented for the new cavities will based on this upgrade.

## Status of klystron High Voltage Power Supplies (HVPS)

The 100 kV – 20 A High Voltage Power Supplies (HVPS) of the klystron transmitters, initially delivered by Siemens, are extremely reliable. Except for the replacement of compressed air hoses that had become brittle in the HV cages, there hasn't been any fault nor any trip due to the HVPS for many years. Some upgrades were implemented in the codes and some hardware details retrofitted following the in house installation of the 3$^{rd}$ transmitter TRA3 in 1997.

Also some improvements had been implemented in the HV cages on EMC aspects in the late 90's, which allowed suppressing spurious crowbar firings. However, most of the high power electronics, analogue circuit boards, PLC controllers have been kept unchanged. Fortunately, following the dismantling of the booster klystron transmitter TRA0 in 2011, the HVPS parts were added to the existing spare stock that protects us considerably against

problems of obsolescence of certain components, like for instance the old Siematic S5 PLCs. The situation will even improve with the shutdown of the klystron transmitter TRA3 end of 2018. There is thus no need to upgrade the HVPS's.

Apart from swapping some boards with spare ones in order to check them in operation, no HVPS upgrade is planned until after the EBS commissioning. However, the thorough maintenance and operation follow up of the HVPS's that are the key of their outstanding reliability will be pursued.

## 5.12 ELTA SSAs

In 2013, three 150 kW solid state amplifiers (SSAs) were connected to three HOM damped cavity prototypes in cell 23. Together with four such amplifiers installed on 2012 on the booster, this gives more than 1 MW of RF from SSAs. The SSAs shown in **Figure 5.15** result from a transfer of technology from SOLEIL to ELTA-AREVA. Each SSA consists of two 80 kW towers that are built around a three stage $\lambda/4$ coaxial combiner tree. The 650 W RF modules and their individual 280V to 50V DC/DC supply converters are mounted on 8 water cooled plates at the periphery of the towers. The smaller $9^{th}$ cooled plate supports the pre-driver and two 650 W drive amplifiers. On top of the towers are fixed the communication boxes which condition and transmit temperature, water flow and RF signals and receive control signals. Each box communicates with the remote control PCI via a RS 485 serial line though a serial line rocket port concentrator. The power is supplied by a 300 kW / 400 V to 280 V AC/DC converter. After some early faults essentially due to faulty DC filters at the 50 V DC inputs of the 650 W RF modules, the SSA's have been responsible in average for only half a beam trip per year each. So far not a single transistor has failed. Note that the operation remains unaffected as long as less than 6 RF transistor modules are in fault. Below nominal output power, the SSAs would remain operational with even more unpowered RF modules.

For EBS, during the 2019 shut down these three SSAs will be moved from cell 23 to cell 25 as shown in **Figure 5.1**.

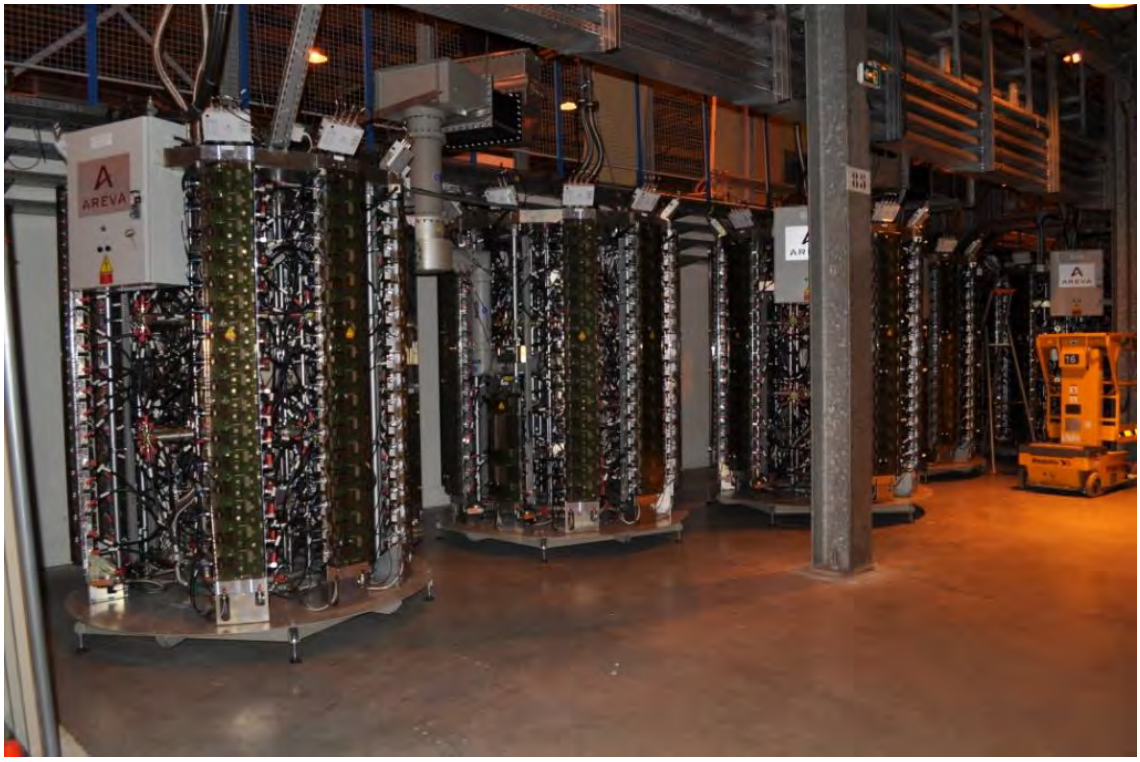


**Figure 5.15: Three 150 kW – 352 MHz SSAs in cell 23 of the existing storage ring – ELTA-AREVA / SOLEIL design.**

## 5.13 In-house SSA

In parallel to the procurement of the ELTA SSAs, an internal SSA R&D programme was launched in order to deepen in-house expertise and to sufficiently master this new technology to be able to operate and maintain it in a most reliable and sustainable way.

In the frame of the EU project FP7/ESFRI/CRISP, the ESRF developed a compact and low cost 352 MHz SSA shown in Figure 5.16. The power from 132 fully planar SSA modules, suited for mass production and requiring only little tuning, is combined by means of a compact cavity combiner. It delivers a nominal power of 85 kW with as much as 62 % DC to RF conversion efficiency. Six amplifier modules are installed on each of the 22 water cooled wings that constitute the outer cylindrical wall of the combiner cavity. The wings also support the antenna loops that couple inductively to the magnetic field of the fundamental cavity mode.

The output waveguide is capacitively coupled to the eclectic field. The coupling factors are adjusted for fully matched power transmission from the RF modules to the output waveguide. This in house SSA will be installed in cell 25 to power the 14$^{th}$ cavity of Figure 5.1.

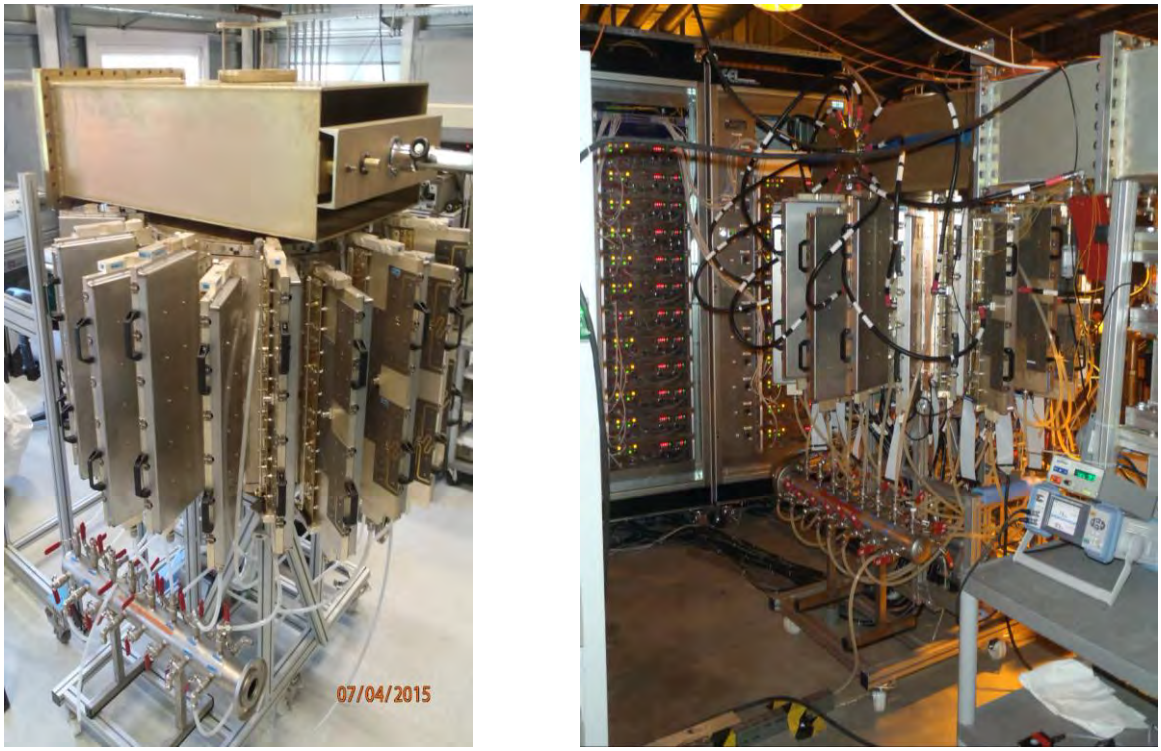


**Figure 5.16: In-house 85 kW SSA. Left: during assembly in the lab. Right: during power tests.**

## 5.14 Longer term power requirements

Including the booster, for EBS the 352 MHz RF power will roughly be generated half with SSAs and half with klystrons. Today, the ESRF disposes of sufficient spare klystrons to operate EBS this way for about a decade. There being only one manufacturer left, it is however uncertain whether 1 MW klystrons will still be available on the market in 10 years from now. In any case, the price will probably be very high: today already about 800 k€ per tube. Acquiring experience with SSA technology and becoming prepared for an alternative solution in case of obsolescence of klystrons was therefore one of the objectives that were met when implementing 1 MW of SSAs at the ESRF.

The in house development of SSAs also allowed gaining experience with their design and contributing to the further development of this technology towards building more compact and less costly SSAs. For instance, in the frame of the European FP7/ESFRI/CRISP project, the ESRF had dimensioned a cavity combiner for a 150 kW 200 MHz SSA for CERN. In a subsequent call for tender exercise open to all possible technologies at this frequency, Thales was selected with a SSA solution based on a cavity combiner to obtain 2 MW at 200 MHz for the CERN/SPS-LIU upgrade: 1 transmitter being composed of 16 x 144 kW amplifiers, each amplifier using a cavity combiner to combine the power from 80 x 2 kW modules, with 2 transistors per module.

Once the EBS will come into user operation, the longer term evolution of the RF system will be re-addressed taking into account the state of the art for high power amplifiers at 352 MHz. The following solutions will then be evaluated:

- either purchasing new klystrons to refresh the spare stock,
- or procure additional SSAs to replace the klystron transmitters,
- or implement other technologies that may come up, like for instance high efficiency IOTs, etc.

## 5.15 3rd harmonic RF system

The implementation of a 3rd harmonic RF system for bunch lengthening that will allow increasing the Touschek lifetime in the EBS machine is still under study. Its operation is essentially based on the cancelation of the RF voltage slope at the synchronous phase by properly phasing the harmonic voltage as sketched in Figure 5.17.

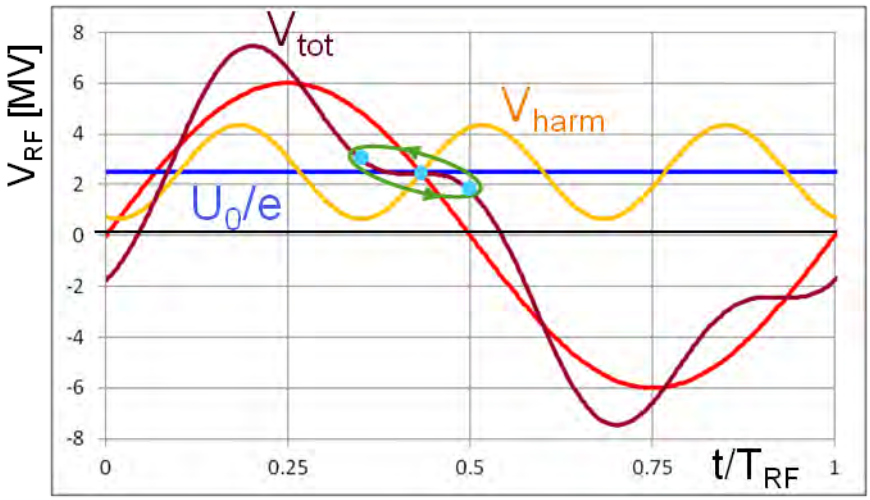


**Figure 5.17: 3rd harmonic voltage for bunch lengthening.**

For a given amplitude the slope of the harmonic voltage $V_{harm}$ is proportional to the harmonic number $n$ and the maximum achievable lengthening scales with $1/n$. The 3rd harmonic has been chosen as a good compromise to cancel the slope of the total RF voltage with a reasonable harmonic voltage. For optimum tuning a bunch elongation factor up to 4 could theoretically be obtained. Practically one should expect a maximum an elongation factor of about 3.

## 5.16 Superconducting passive harmonic cavity

The harmonic voltage can be obtained by means of a passive superconducting (SC) cavity, as e.g. Super3HC at SLS or Elettra, which is operated below resonance ($\Delta f < 0$) where its beam impedance is almost purely inductive:

$$Z_{harm} \approx \frac{R_{harm}}{1 + jQ\frac{2\Delta f}{f_{res}}} \xrightarrow[\Delta f >> \frac{f_{res}}{2Q}]{} Z_{harm} \approx -j\left(\frac{R_{harm}}{Q}\right)\frac{f_{res}}{2\Delta f},$$

$f_{res}$, $R_{harm}$, $Q$, $\Delta f$ being respectively the resonance frequency, the shunt resistance, the quality factor and the detuning of the cavity. Note that $R_{harm}/Q$ depends only on the geometry and the inductance is thus independent from the cavity losses.

The voltage induced by the beam in this inductive impedance has therefore always nearly the optimum phase with respect to the beam to provide the right slope in Fig. 17. The optimum amplitude of the voltage $V_{harm}$ being proportional to $I_{beam}/\Delta f$ , is easily controlled via the resonant frequency of the cavity for a given current $I_{beam}$ in the machine.

First simulations performed for a scaling in frequency of one Super3HC module from 1500 MHz to the 1057 MHz (3rd harmonic at the ESRF) indicate that such a cavity could be operated at optimum voltage from 200 mA down to about 70 mA beam current. For lower beam currents, the optimum detuning would become too small and the cavity would drive an AC Robinson instability. This would unfortunately not allow operating the harmonic system in 4 x 10 mA filling, where the Touschek scattering and lifetime reduction are the worst. Further simulations are foreseen to confirm this result.

In case the ESRF would opt for a SC cavity, the CEA Saclay would be ready to launch a collaboration contract for the design and fabrication of the cavity and for the specification of the required 4 K cryogenic system.

## 5.17 Normal conducting active harmonic cavity

Alternatively, normal conducting (NC) harmonic cavities could be used. In order to obtain optimum voltage and phase conditions with a reasonable number of cavities, they would have to be operated actively, i.e. powered with third harmonic RF generators.

Assuming a scaling of the ESRF HOM damped cavity to the third harmonic frequency at 1057 MHz, first calculations indicate that with 5 such cavities on the machine, the conditions for optimum bunch lengthening could be achieved with about 30 kW of generator power per cavity. The correct phasing of the harmonic voltage is no longer “automatic” as for a passive SC cavity and would necessitate carefully designed amplitude and phase regulations. Simulations to check the stability for various beam filling patterns are under way.

Thanks to the existing expertise at the ESRF, designing a HOM damped NC cavity would be straight forward. Also the operation of a NC cavity system would not require many additional resources, as opposed to a SC system, for which a sophisticated cryogenic system would have to be designed, built, operated and

maintained. A prototype transistor module for a 3rd harmonic SSA is already under development.

## 5.18 Bunch lengthening for standard ESRF filling modes

The bunches are already substantially elongated for high current per bunch.

The bunches are already increasingly elongated with raising current per bunch due to the interaction with the broadband impedance of the EBS machine of 0.67 Ω (conservative estimate).

A harmonic RF system still provides additional bunch lengthening, which reduces for higher current per bunches.

Table 5.5 gives the expected lifetime improvements [N. Carmignani, B. Nash, J. Jacob]. Except for the multibunch filling, one can expect a lifetime improvement from harmonic RF system by about a factor 2.

| Mode | I / bunch [mA] | σz [mm] | Lifetime [h] | Lifetime improvement factor |
|---|---|---|---|---|
| **Multibunch** | 0.23 | 17 | 72 | 3.6 |
| **Single bunch** | 8 | 26 | 3.2 | 2.0 |
| **16 bunch** | 5.75 | 25 | 4.0 | 2.1 |
| **4 bunch** | 10 | 27 | 2.5 | 1.9 |

**Table 5.5: Lifetime improvement factor thanks to a harmonic RF system for standard ESRF modes.**

## 5.19 Transient beam loading for partially filled storage ring

For a non symmetric fill pattern with a gap of unpopulated bunches as in the standard 7/8+1 filling, the high beam loading of the cavities at 200 mA can lead to substantial amplitude and phase modulations. These transients alter the amplitude and phase conditions for maximum bunch lengthening. They are proportional to the R/Q of the main and of the harmonic RF systems, and are therefore stronger for NC than for SC harmonic cavities, as NC cavities exhibit in total a 8 times higher R/Q.

First simulations for NC cavities indicate that the maximum achievable bunch lengthening factor would be around 2 for a 7/8 +1 filling. Further investigations are under way to compare the SC

and the NC solutions with respect to transient beam loading. The situation could be improved if the 7/8+1 was replaced by a more symmetric pattern, as for instance a 2 x 3/8 + 2 filling, with two symmetric gaps around the circumference. This too is subject of ongoing investigations.

# 6 Control System

## 6.6 Introduction

The Accelerator Control System (ACS) is the interface between the accelerator and the operators, physicists and beamlines users. It controls the entire accelerator complex. Its most important roles are interfacing, configuring and controlling the equipment, and monitoring and archiving machine parameters for offline analysis.

When replacing the former Storage Ring by the new EBS, The ACS will continue controlling the linac, the transfer lines the booster and the new EBS in an unified manner. Therefore the same standards will be used for controlling the new storage ring and all the injector equipments.

The new EBS lattice places new requirements on the control system. It has many new pieces of equipment to control and is more sensitive and delicate to tune. The ACS's job is to make it easy to diagnose problems when they happen and ideally even before they happen. The control system for the EBS needs to sample data at much higher rates and archive them for as long as possible (decades). We will continue the permanent program of renewal of the control system to ensure it stays modern and serves the users in the best possible way.

One of the main challenges is to keep the current system operational and continue its permanent upgrade while preparing to integrate the new needs of the EBS.

## 6.7 TANGO control system software framework

### Objectives

Continue the maintenance and development of Tango control system. Ensure the long term sustainability of TANGO for the lifetime of the EBS (20 years at least).

### Status

The TANGO control system, originally developed at the ESRF in 1999, has been adopted by the majority of light sources in Europe. Since then TANGO has continued to be developed and improved collaboratively and became the de-facto standard control system for European light sources. This large community guarantees the long term sustainability of the control system and allows fruitful exchanges between the different control teams and industrial partners sharing the same technology. Thanks to the continuous development effort of these last years, the present system is ready to satisfy the requirements for the control of the EBS accelerator with no critical challenges in term of software characteristics. TANGO is based on the

concept of distributed objects and services which is today still considered as state-of-the art for distributed systems.

### Planned

Develop the next major version of TANGO V10 which will be able to use a different binary protocol than CORBA. TANGO currently depends on 2 protocols (CORBA and ZMQ). CORBA is over 20 years old now and although not an issue today could be an issue in the long term (decades). The aim of TANGO V10 is to address this before it becomes an issue. TANGO V10 will also push the web interface protocol (REST api) further to make it a standard protocol for user interfaces. Thanks to the presence of a team of kernel developers at the ESRF and the Tango Collaboration new features will be added as necessary e.g. integration of nanosecond timestamps. The Tango Collaboration is financed by a number of institutes (currently 8 but growing each year) who rely on Tango for their operations.

We have to refactor all pieces of software which are still using the obsolete protocol named Taco to convert them to Tango. This is particularly important where old pieces of hardware are planned to be re-used for EBS.

- Radio-frequency klystron control system are being refurbished to remove any dependence on VME and Taco.
- Linac, and Injection/extraction elements need some hardware interface refurbishment.

A number of industrial partners have trained TANGO developers and can used as sub-contractors to develop device servers in case we experience a peak in the development and the local developers are not sufficient.

## 6.8 Electronic interfaces to the accelerator hardware (injector + EBS)

### Objectives

Define standards for electronic interfaces with the Electronics Unit and provide support for the ASD adopt and follow these standards. Keep mastering the different hardware interfaces to avoid developing and maintaining duplicate solutions.

### Status

The EBS will replace the entire storage ring hardware (excluding a few exceptions like the insertion devices, and diagnostics equipment) and will therefore introduce a lot of new equipment to be controlled. The procurement of these equipments is under the responsibility of the different work packages. However we should guarantee the new equipment is compatible with the ESRF control system standards and well interfaced to the control system. For example the new Beam Position Monitors (BPMs) need to be integrated in the orbit correction alongside the existing BPMs.

### Planned

WP6 has issued a set of standard requirements concerning the control interfaces in the form of a document (**Annex 6.1**) to attach to each procurement procedure (CFT, RFQ or simple purchase) for any new equipment.

We are pushing for finishing the modernization of the existing hardware interfaces and eliminating the obsolete parts that show signs of age:

Radio Frequency klystron control systems, still using obsolete VME cards, are being refurbished with new electronic interfaces. SRRF1 has already been converted.

Linac Control System is also using obsolete VME cards and needs to be refurbished

Transfer line control system still uses the obsolete FBus powersupplies which forces to use obsolete VME. This VME will be replaced as soon as new power supplies are installed on TL2. These powersupplies will be replaced by more modern ones before end 2018, therefore we delay the removal of this VME until then.

HQPS system interface has also to be refurbished for the same reason. The old G64 based Analog HLS systems will continue to be used to measure the level drift over the tunnel roof and other places. A ModbusG64 board should be installed in each technical zone to drive these systems.

Insertion Device motor controllers are planned to be used for the new IDs. The new controllers will be Ethernet based.

## 6.9 Control infrastructure

The Ethernet network protocol is used for communicating between any equipment, the control system software and control room. Therefore particular attention should be applied to guarantee high reliability and bandwidth for the control system Ethernet network infrastructure. EBS plans to install thousands of new Ethernet connected devices for the new individual magnet power supplies, BPMs, various diagnostics, gigabit Ethernet cameras etc.

### Ethernet network infrastructure

#### Objectives

Prepare the connection of all new equipment via Ethernet and keep the connection of all existing equipment. Ensure the performance of the Ethernet network infrastructure is adequate in terms of performance, reliability and security.

Status

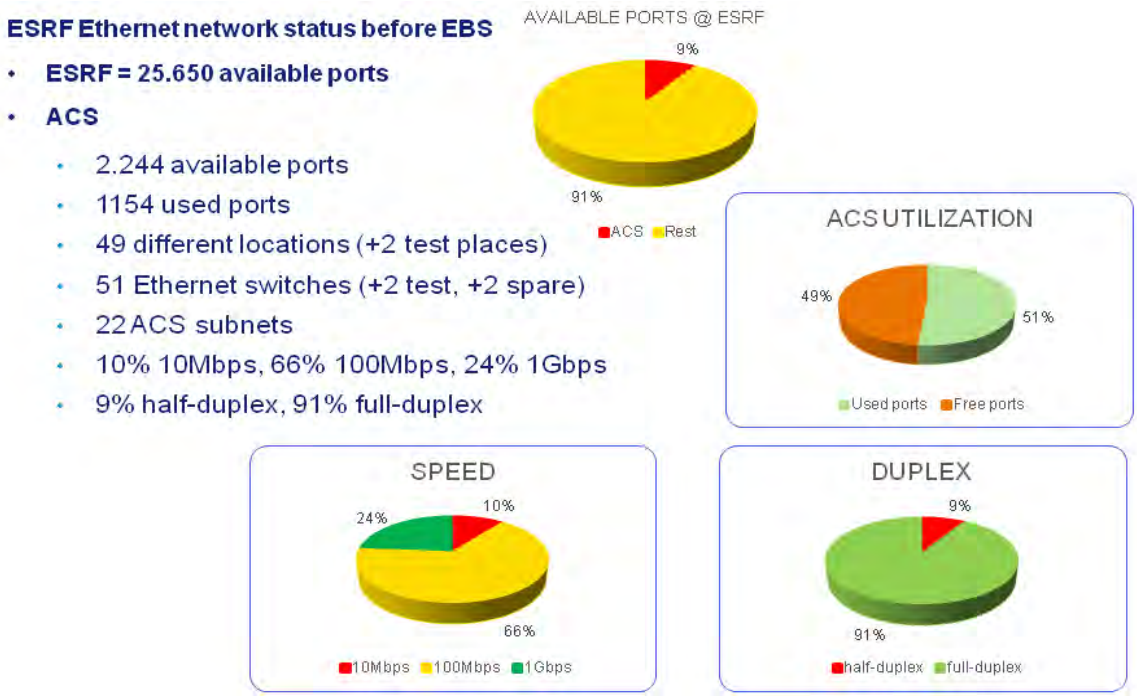


**Figure 6.1: The current status of the ESRF Ethernet network.**

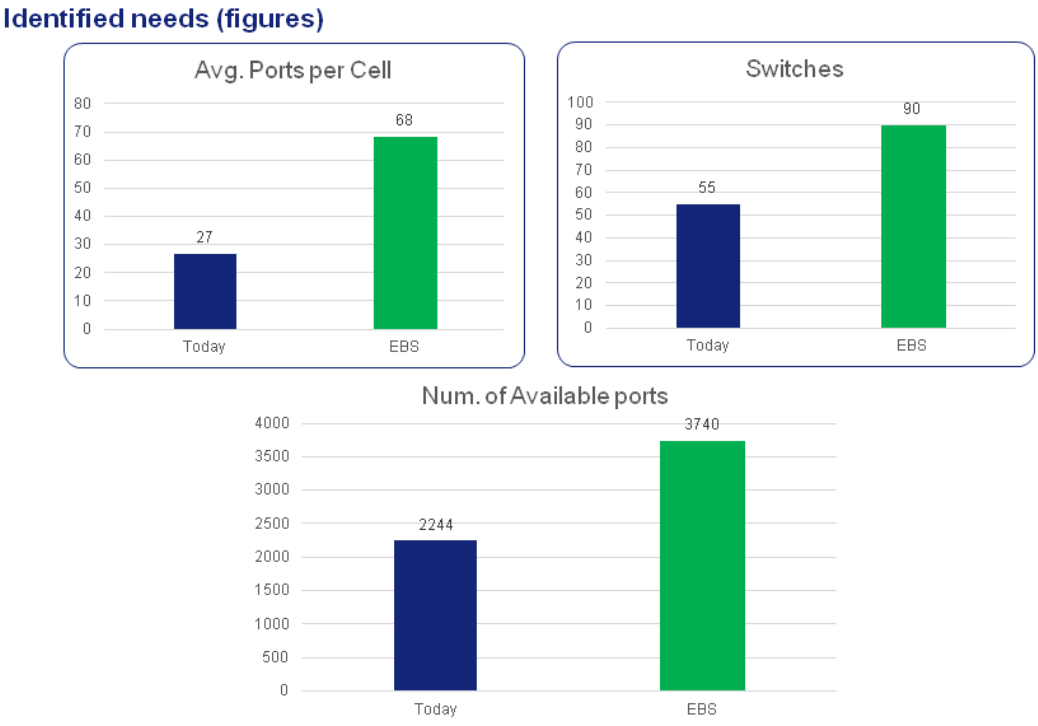


**Figure 6.2: The needs identified for ESRF-EBS.**

## Planned

The network installation will be renewed before the long shutdown of 2019 to be able to tackle the connection of all the equipment during the shutdown. Work has already started in cells XYZ.

The recabling of the Ethernet network will facilitate the unmounting of the existing storage ring cables and save time when mounting the EBS. At the same time the new network will increase the number of connections available for the EBS. The new network installation is distributed over 60 different physical locations over the all accelerator site and should accept between 40 and 80 connections per location.

## Computer infrastructure

### Objectives

Maintain a distributed computer infrastructure which is adapted to the needs of the control system. Ensure the historical database has sufficient storage and computational capacity to provide an efficient and powerful user experience. Optimise the maintenance and reliability of the distributed computer infrastructure to ensure the system remains modern + up-to-date e.g. by using virtualisation, diskless embedded systems, regular updating of operating systems etc. Ensure the control room provides a modern control experience for operators by providing large screens, voice output, voice recognition, modern user interfaces, touch screens etc.

### Status

The control system is composed of a set of 90 rackable PCs distributed all over the site and around 30 server computers located in the control room computer room. The rackable PCs are used for electronic hardware interfaces. Such as serial lines, IEEE 1394or PCI IO interface boards. The server computers host the control software for the Ethernet connected hardware and the main processes of the control systems. A set of 12 Linux workstations are currently used as operator interface in the control room.

The majority (90%) of the computers are running under Debian Linux, 10% are running Microsoft Windows (XP or W7). All the computers are managed in collaboration with the Systems and Communication team of the TID. The control system software is installed in a central file server which is mounted as a Network File System on every computer. This configuration eases the management of the infrastructure because the software has not to be installed on each computer and the backup has only to be done on the central file server.

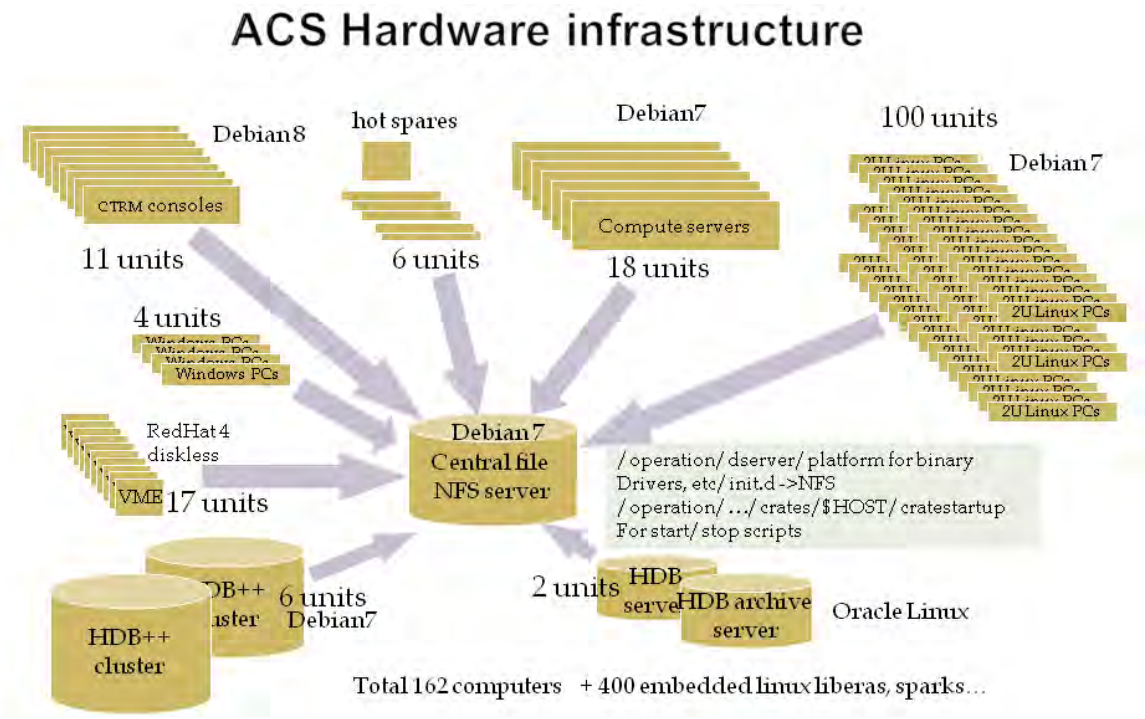


**Figure 6.3: The accelerator control system hardware infrastructure.**

### Planned

No systematic upgrade of the installed computers is foreseen. As during standard operation period, we will continue upgrading the computers when they become too old or too weak. However we will generalize the use of a virtualisation solution for computing servers in CTRM. This solution allows a simple and intelligent management of the operating system evolutions and reinforces the general reliability.

## 6.10 Timing and synchronization system

### Objective

Replace the existing accelerator synchronization system to solve hardware obsolescence issues in favour of a new system which implements former performance and:

- Improves the scalability and flexibility of the system
- Proposes high precision time stamping feature

The existing system is still in service, and the implementation of the new one should be performed in an incremental and reversible way.

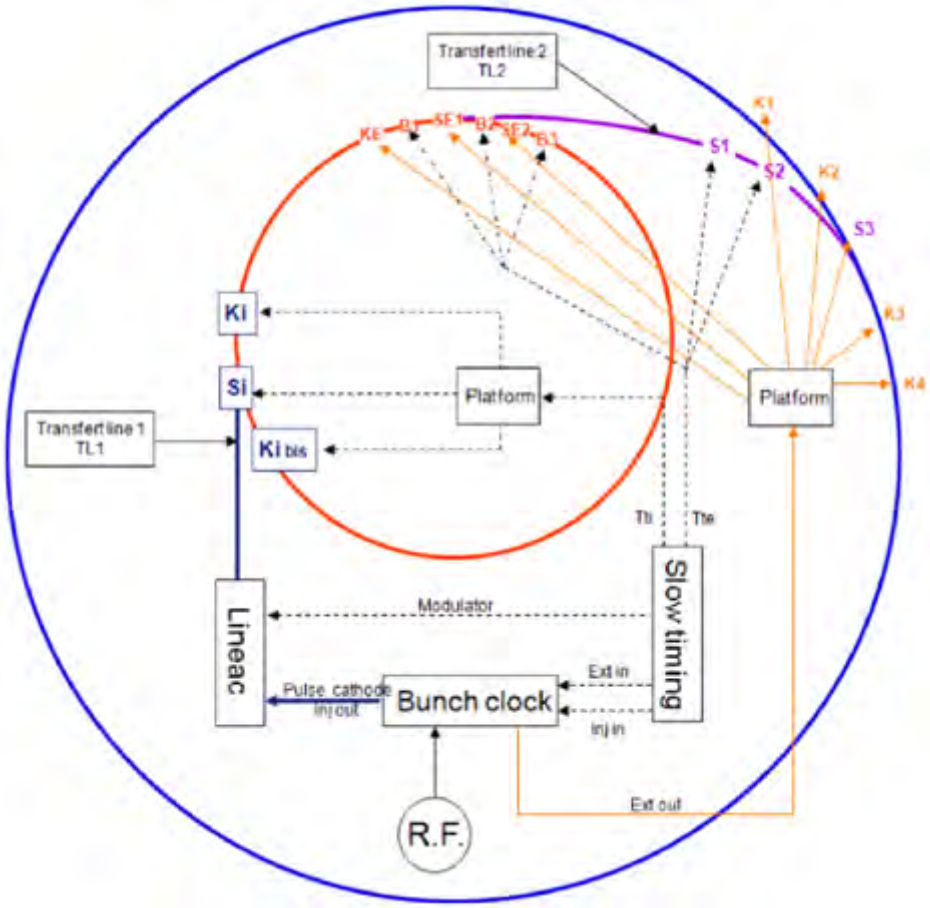


Figure 6.4: Current synchronisation system.

## Status

The synchronization (aka timing) system is a "site wide distributed sequencer". It generates triggers for the following equipment:

- Linac Gun.
- Linac to booster transfer line.
- Booster to Storage ring transfer line.
- Diagnostic equipment.
- Some beamline equipment.

The main parameters are the following:

- RF frequency: 352.2 MHz; RF period: 2.84 ns.
- Booster: 352 buckets; revolution frequency: 1 MHz.
- Storage Ring: 992 buckets; revolution frequency: 355.04 KHz.
- Slow Trigger: (Tied to booster magnets ramping voltage or Ramping injector Power Supply): 4 to 10 Hz.
- Jitter at the Linac gun must be minimized (ideally around 10 psrms).

The current accelerator synchronisation system used at ESRF (Figure 6.4) dates from the early 90s. It is based on two separate systems:

- Bunch clock and fast timing: synchronization at RF resolution.
- The VPDU system: synchronisation at the microsecond resolution.

The synchronisation signals, centrally generated, are distributed across ESRF site (accelerator and beamlines) via coaxial cables.

## Synchronisation project

### Description of the system

The new system will be based on the White Rabbit (WR) timing system developed and promoted by CERN. CERN is involved, for internal needs, in the evolution of White Rabbit toward synchronization uses. White Rabbit is also supported by a large user community. White Rabbit is an open hardware solution which allows several suppliers to provide the Hardware. The main characteristics are:

- High precision sub ns stamping performances
- Open Hardware solution.
- Possibility to customize/upgrade/adapt the functionalities of the system through the programming of a FPGA device
- Built in compensation of Optical Fiber length and temperature drifts.
- Available hardware: PCi-Express form factor (standard at ESRF) and possibility of standalone modules

To allow its use for Accelerator Synchrotron Synchronisation purpose, specific features such as RF-over-Ethernet and Trigger top-down transmission have been developed and validated conjointly with CERN.

The architecture of the new system is described in Figure 6.5.

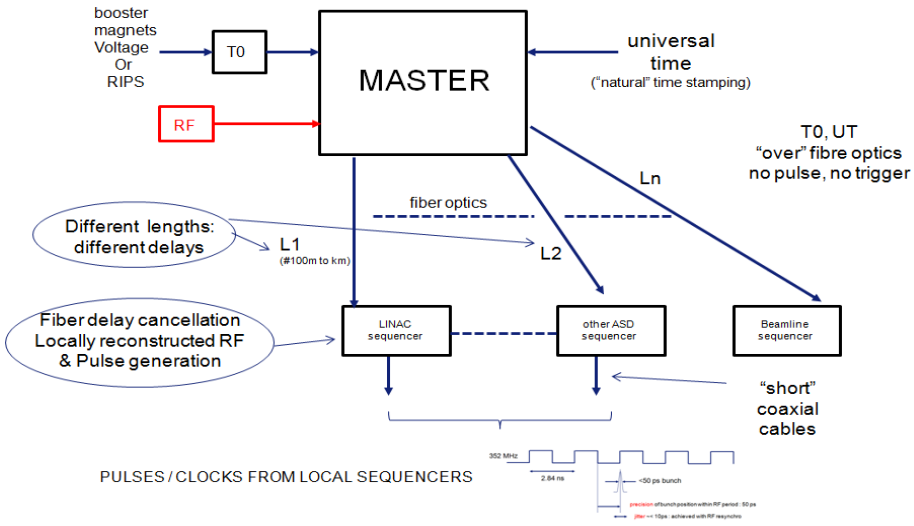


Figure 6.5: Distributed architecture of the new system

The main characteristics of this new system:

A master unit is connected to endpoints through a dedicated network (optical fibers).

The main inputs of the system are: the Radio frequency signal (ie 352MHz at ESRF), a T0 trigger tied to the booster magnets ramping voltage or Ramping injector Power supply that initiates the synchronisation sequences, a "universal time" signal provided by an external GPS module.

The master unit, receives these inputs and distributes on the optical network the following information:

- Information enabling the reconstruction at the end-points of the RF signal (RF over Ethernet feature). The reconstructed RF is constantly synchronized to the incoming original one. The phase is also respected.
- T0 trigger that initiates the synchronisation sequences
- Universal time (ptp) – This is the basic feature of White Rabbit.

The "end points" are standalone modules located close to the equipment that needs to be synchronized. These modules generate local triggers following a predefined sequence.

White Rabbit uses a dedicated network (already in place). The transmission delays due to different physical lengths are automatically compensated by the White Rabbit system.

## Description of the project

The project is organized into four phases:

### Phase 0

Evaluation of different technical solutions. Selection of the most adapted to current and future needs. White Rabbit selected.

### Phase 1

Installation of a test-bench on the existing FO network (between CTRM and Cell 16).

Development of a standalone module, based on White Rabbit SPEC board, dedicated to our needs. This module will act as "end-point" and locally generates triggers, synchronously with RF. The module outputs will be electrically compatible of the existing ESRF hardware.

The first prototypes of WHIST (White Rabbit Synchronisation & Timing) modules have been produced and are being evaluated. The results are promising. A new set of prototypes based on a slightly modified design will be soon produced.

### Phase 2

Implementation of the "Master unit".

This phase aims at replacing the existing Bunch Clock unit in the ESRF control room. In this phase, the new master unit will be interconnected to the current system. This will be then intensively tested. This phase is reversible.

### Phase 3

Completion of the Accelerator complex Synchronization system: including INJPF, PINJ, SRRF, SYRF. At the end of this phase, it is planned to have a new operational system delivering synchronized triggers to the Accelerator

complex: master unit, end points, dedicated optical fiber based network.

Once these phases are completed, it is foreseen to extend the use of the new system to beamlines and accelerator diagnostics.

## 6.11 History database upgrade

### Objective

Develop a system to increase the data rate by an order of magnitude and multiply by 4 the number of archived signals. This imposes a disk space and a data throughput multiplied by 40.

Simplify and lower the cost of the database management by using Open Source database technology.

### Status

The former ESRF History Database had been designed 20 years ago to archive a limited number of signals at a rate which is much lower than the needs of the EBS. The system had been interfaced to TANGO so that currently the majority of data comes from TANGO device servers but both the hardware and the software need to be fully redesigned to fit the new requests.

**Table 6.1: Characteristics of old versus new HDB**

| | **Old HDB** | **New HDB** |
|---|---|---|
| **Time precision** | 1 second | 1 millisecond |
| **Total number of inserts/hour** | 120K | 6M |
| **Filling mode** | Polling/events | events |
| **No. Signals total** | 6K actives/14K total | 24K/56K |
| **Beamline signals** | 2K | 10k |
| **Extraction tools** | C GUI | C++/ Java / Python / Matlab / Web |
| **Database size** | 0.5TB/y | 20TB/y |
| **Online capacity** | 9 months online<br>5 years archive<br>Older data on tape | Unlimited online |

| Database | Oracle | Cassandra |
|---|---|---|

The former HDB has a time resolution of 1 second and stores a few thousands of signals (see Table 6.1). The global bandwidth and disk size does not allow the archiving of all the accelerator parameters simultaneously at 1 Hz. Furthermore, we cannot keep more than 1 year of data online due to limitations in the query response time.

### Planning

In the framework of the TANGO collaboration a new History DataBase project has been started in collaboration with the Elettra synchrotron. We have redesigned the TANGO archiver to increase the bandwidth, the volume of data and the time resolution from a second to a millisecond. Furthermore we take benefit of the new Big Data oriented databases recent technologies used in cloud applications by commercial companies such as Facebook. The data is replicated on multiple servers and therefore the system is, by design, fault tolerant without compromising performance.

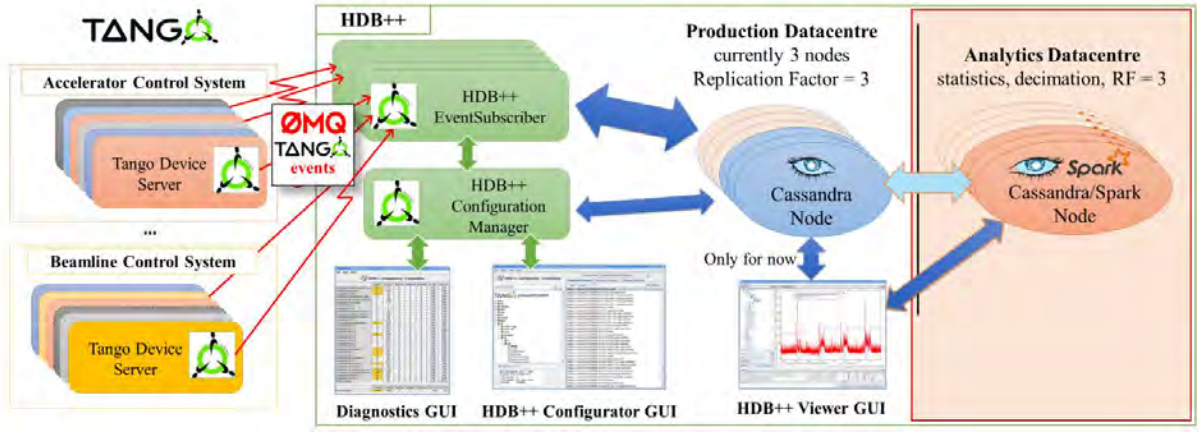


### Software oscilloscope

We will also enhance the use of local polling buffers to build a massively distributed temporary circular buffer history with the last few days of acquisition. These data will be accessible with a software oscilloscope tool (see figure 1) which will enable users to display and do different kinds of common analysis like spectral, FFT, digital correlation etc. to diagnose and detect problems. A similar tool has been developed for the vacuum and insertion devices. This will be extended to other sub-systems of the EBS to include a wider variety of sources e.g. storage ring current, BPM's, and with a much higher frequency (up to 1 kHz). To do that, we will update the TANGO core library with enhanced management of the polling buffer

history. The software oscilloscope will fill the gap between the HDB (10 Hz) and the Fast Data Logger (10 kHz).

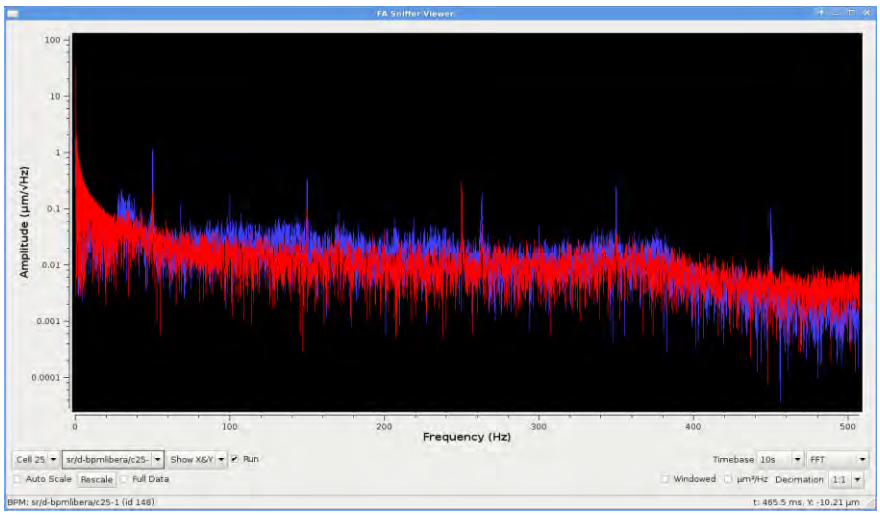


**Figure 6.6: Software oscilloscope application**

## 6.12 High level software

### Objectives

Unify the look and feel between different developer teams (mainly beam dynamics and accelerator control teams) to a higher quality standard and upgrade all the deprecated applications ones to use modern user interface toolkits possibly web based.

### Status

The control room work stations host the graphical user interfaces and a collection of high level interfaces to various software such as Matlab or Labview. There is also a set of old C applications written with the now obsolete Motif toolkit.

### Planning

In order to prepare the control of the EBS while the present Storage Ring is running, we have prepared an EBS simulator. This simulator, integrates the Matlab Accelerator Toolkit in a Tango based simulated EBS. This simulator is actively used to prepare the accelerator physics feedback and control processes. It will also be used to develop and test a set of high level software for controlling the new EBS. i.e. orbit correction, optic tuning, vacuum layout application, naming, etc.

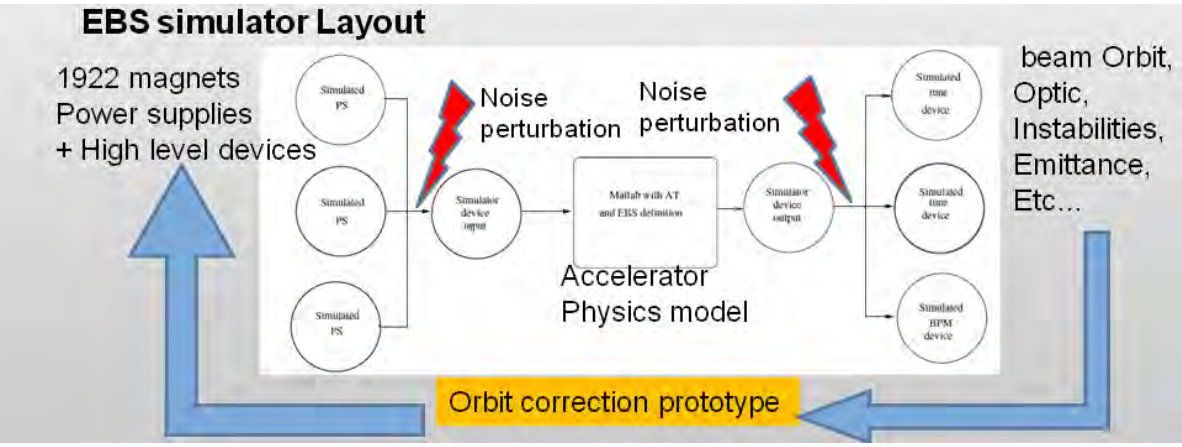


20 graphical user interfaces application are being prepared to be tested on this simulator. The simulator will be completed with a simulated version of all individual device servers and serve as test bench for the new user interfaces and high-level applications.

We are also studying the possibility of using a more modern web based toolkit.

## 6.13 Device servers software/ equipment control

### Objectives

The integration of the new equipment should inter-operate with the existing equipment. Therefore we need to keep a high degree of compatibility and interchangeability between old and new equipment. The high level software and graphical user interfaces should be able to control both old and new equipment. Furthermore, some high level processes, such as the orbit correction systems, radio frequency system application and vacuum application have been already prepared to be able to integrate in the same coherent process, old and new pieces of equipment.

### Status

Many pieces of equipment are already connected via a Tango device server. A large part of them will stay when the EBS will be put in operation. i.e. Linac, injector, booster and also several important parts of the storage ring such as Radio-Frequency systems, Insertion devices, Front-End, Vacuum gauge controllers, Libera beam position monitors, current monitors, HLS systems, motor controllers etc. It is planned to keep several thousands of equipment controllers. Many of these systems have been recently integrated in the control system in the context of the upgrade phase to prepare the EBS operation e.g. new Ramping Injection Powersupply System (RIPS), new control of the injection elements, new booster orbit

measurement and correction systems, new bunch cleaning in the booster, and booster diagnostics.

In addition to the above equipment, we have to include many new different pieces of equipment in the control system. For example thousands of individual magnet power supplies, hot swap manager, new timing and synchronization system, new type of vacuum controllers, new position control for the girders, new RF cavities, new type of beam position monitors, and many others.

## Planning

The various work packages of the present upgrade will define the complete list of new pieces of equipment to control and the list of device servers to develop. A member of the ACU is present in each of the work package to collect the needs and establish a workload forecast. The global compilation of the needs should be carefully and permanently surveyed in order to anticipate the need in man power to perform the development in due time. In parallel with these new developments we have to continue the modernization of hardware interfaces for existing systems and get rid of the old TACO C device servers.

- The main project is the control of the thousands of new magnet power supplies correctors and the hot-swap manager managing their connection on the magnets. This system should guarantee a high level of reliability and fast response time.
- The software for controlling the 128 girders and their 4 motorized axes and various position sensors is in development
- The control of the new radio-frequency cavities and transmitter are in development
- The reconfiguration of the orbit correction systems (fast and slow) is being prepared
- The development of device servers for new vacuum controllers and deployment of a new layout including several hundreds of vacuum elements is in progress.
- The reconfiguration and test of all the insertion devices control system should be anticipated.

## Injector control

Even if the injector is not considered as part of EBS, as far as the control system is concerned, it is. Therefore, important work is underway to control the injection process in the perspective of filling the EBS. The work concerns the following points:

- Ramping Injection Power Supply
- Linac upgrade
- Topping-up management
- Booster diagnostics upgrade
- Booster orbit measurement and correction system upgrade
- Injection/extraction element control for EBS using RIPS
- Booster Quadrupoles motorization systems
- Transfer lines power supplies and steerers power supplies upgrade

A naming convention for the new machine has been established and will be ready before starting the installation of the new accelerator at the latest. See chapter 6.9 for the proposed naming for the EBS.

The Accelerator simulator control system described earlier will be populated step by step with a simulated version of all the new device servers, allowing the development and test of the upper layer software well before the physical installation starts.

## 6.14 Control system EBS devices naming convention

The present document proposes a naming convention for the EBS objects in the control system.

### Generalities

The TANGO control system framework defines objects which are identified by a strict naming architecture. Within a TANGO control system, each device is defined by a name composed of 3 fields separated by slashes.

The first field is named *domain*, the second field is named *family* and the last field is named *member*. A tango device name looks like domain/family/member

It is a hierarchical notation. The member specifies which element within a family. The family specifies which kind of equipment within a domain. The domain groups devices related to which part of the accelerator/experiment they belongs to.

At ESRF, the machine control system domain names are SR for the storage ring, TL1 for the transfer line 1 or SY for the synchrotron booster. For experiment, ID11 is the domain name for all devices belonging to the experiment behind insertion device 11.

Those devices are complex objects that expose a state, a status, a list of commands and a list of attributes.

An attribute is a physical value that can be read or set from the device. Each attribute has a name.

For instance srmag/ps-qd1/c01/current, designs the current of the power supply named srmag/ps-qd1/c01

### Full object name

The device name as above is not enough to cover all Tango usage like device server for multi control systems. With the naming schema, we must also be able to name attribute and property. Therefore, the full naming schema is:

- [protocol://][host:port/]device_name[/attribute]

The protocol, host, port, attribute, property and database fields are optional.

The meaning of these fields are :

- [protocol]: Specifies which protocol is used (Tango or Taco). Tango is the default
- [host:port]: This field has different meaning according to the dbase value. If dbase=yes (the default), the host is the host where the control system database server is running and port is the database server port. It has a higher priority than the value defined by the TANGO_HOST environment variable. If dbase=no, host is the host name where the device server process serving the device is running and port is the device server process port.
- [attribute]: The attribute name

The protocol://host:port field are necessary only when accessing objects managed by another TANGO_HOST.

For instance accessing the storage beam current from a beamline control system, one should read tango://ebs:10000/sr/d-ct/1/current where ebs is the host alias name of the accelerator control system database.

### Domains

The following 21 domains are defined:

**BL**: for devices dedicated to beam lines.

**DSERVER**: reserved for Tango itself. All administration device server process devices are automatically created/removed in this domain. It should not be used for any other devices.

**ELIN**: For all devices belonging to the linear accelerator.

**FE**: For all devices belonging to the Front end part of the accelerator in which particules are photons instead of electrons. There are up to two front-end per cell (one behind the insertion devices and another one behind the bending magnet). The member field specify The X ray source (ID or BM), For instance, vacuum pump in front-end will be named fe/v-ip/bm01-11 or fe/v-ip/id11-11. In the family field, the equipment group sr is supported for this domain

**ID**: Sophiscated use of device naming with 4 domains: ID, ID-CARR, ID-CORR and ID-UND.

**ID-CARR**: the ID carriages.

**ID-CORR**: The ID correction.

**ID-UND**: The ID undulators.

**INFRA**: For all devices belonging to the ESRF infrastructure (like the fluid system, HQPS, mains drop detection,...). In the family field, the equipment group hqps and mains are supported for this domain

**LABS**: For all devices belonging to laboratories like the front-end lab (today MD012), the ID04 lab, the TZ16 lab or the RF test-stand. The distinction between labs is included in the member part of the device name (ie labs/family/id04-xxx or labs/family/tz16-xxx)

**SRDIAG**: For all devices part of diagnostic equipment and belonging to the storage ring.

**SRMAG**: For all devices dedicated to the control of the storage ring magnets.

**SRRF**: For all devices dedicated to the control of the storage ring radio frequency system..

**SRVAC**: For all devices dedicated to the control of all vacuum related equipments in the storage ring. The member device name part include a cell number, a vacuum container family number (vacuum chamber number x) and the equipment number in this container (ex: c01-ch02-1 for first equipment in vacuum chamber 02 in cell 01)

**SR**: For all devices belonging to the storage ring but not part of the SRDIAG, SRMAG, SRRF or SRVAC domains.

**SY**: For all devices belonging to the booster accelerator.

**SYS**: For all devices belonging to the control system itself. In the family field, the equipment group hdb and adm are added for this domain

**TEST**: All devices created in this domain should have a short lifetime.

**TL1**: For all devices belonging to the transfer line 1.

**TL2**: For all devices belonging to the transfer line 2.

**TMP**: This domain is reserved Tango itself. All devices automatically created/removed for the Tango LogViewer application belongs to this domain. It should not be used for any other devices.

### Families

The proposal is to use the same hint than the one used today (family field = <equipment group>-<equipment type>) but to make it a rule. The possible equipment groups are:

- a, d, ps, rf, sa, t, v for alignment, diagnostic, power supply, radio frequency, safety, timing and vacuum
- beam for devices related to beam control and beam measurements (like devices for orbit bump, beam tunes,..)
- itlk for interlock
- modbus for devices controlled using Modbus
- icepap for icepap motor controller
- wago for wago devices

We will also use some equipment groups more specific to some domains:

- hdb and adm for the SYS domain
- hqps and mains for the INFRA domain
- sr for the FE domain
- id for the ID domain

There is no strict rule for the equipment type, however we can define at least the following types:

- mot for motor
- serial for communication device using serial line
- socket for communication device using socket
- pen, pir for penning or piranies gauges
- rga for residual gas analyser
- hls for hydrostatic leveling system
- rv for remote valve

### Members

There are two requirements for the member field:

- When a number is used in the member field and if there are more than 9 instances, this number must be specified using 2 digits (01, 02,...09, 10, 11). This allows computing software to nicely display devices in a ordered list. Ex : c01, c09, c10, id01, id11, bm05, d23
- When cell number or X source (ID or BM) is specified in the member field, it should be at the beginning of the member field followed by the - character: c01-xxx, id12-xxx, bm25-xxx

## 6.15 Changes required for existing devices in the former storage ring

In today's storage ring, there are several devices with names which should be modified. For instance the first vacuum gauge in cell one is named sr/v-pen/c1-1. It should be changed to srvac/v-pen/c01-1. The same is true for several diagnostic devices (sr/d-ccd/c12 should become srdiag/d-ccd/c12). Obviously one utility tool to do DS process devices name re-naming has to be written. Obviously, changing a living device name has some consequences which are:

Application(s) using these devices must be modified in order to connect to devices using their new names. Most of the time, applications take their device(s) name from a kind of configuration file or from a computing language included file. These files have to be updated and applications re-generated. Nevertheless, renaming a device does not change at all anything in the device interface and therefore, these changes at the application level seems reasonable

Device data storage in HDB. Nowadays, the o-cial history database for the ESRF machine control system is HDB. If the renamed device has some data stored in HDB, it should be possible to manage the new device name by doing a SQL update in the HDB SDT table. The device renaming tool has to take this into account.

Device data storage in HDB++. In a coming future, the HDB system will be replaced by HDB++ (new release of HDB). Data are already stored in HDB++ but the system does not yet include a stored device name change. This feature will be added to HDB++ allowing the renaming device tool to do its job.

## 6.16 EBS device naming convention case by case

### Beam control

sr/beam-bump/c01-v2 Second vertical beam orbit bump in storage ring cell 01

sr/beam-bump/all-h All horizontal beam orbit bumps

sr/beam-orbitcor/svd-h Horizontal beam orbit correction using SVD method

sr/beam-orbitcor/svd-auto Automatic beam orbit correction using SVD method

sr/beam-orbitcor/meff-h Horizontal beam orbit correction using Most Effective Steerer method

**Interlocks**

sr/itlk-mach/beam-low One machine interlock

sr/itlk-mag/all Another machine interlock

**In the SRMAG domain**

srmag/ps-qf1/c01-a Power supply for first QF1 quadrupole in storage ring cell 01

srmag/ps-qf1/c01-e Power supply for second QF1 quadrupole in storage ring cell 01

srmag/ps-qf1/all All power supplies for QF1 quadrupole in storage ring

srmag/ps-q/all All power supplies for quadrupoles in storage ring

srmag/vst-sd1/c01-a vertical steerer located in the sextupole sd1a in cell 01

srmag/hst-sh1/c01-a horizontal steerer located in the corrector sh1a in cell 01

**In the SRDIAG domain**

srdiag/d-pct/c15 Parametric current transformer in storage ring cell 15

srdiag/beam-current/total Storage ring current transformer

srdiag/beam-current/single Storage ring current transformer for the single bunch

srdiag/d-bpm/c01-1 First BPM in storage ring cell 01

srdiag/beam-position/all Device for all Libera BPM in storage ring

srdiag/beam-tune/h The storage ring optic horizontal tune

srdiag/d-fuse/c04 The fuse device in cell 04

srdiag/mot-fuse/c04 The motor used by the fuse device in cell 04

srdiag/icepap/c04 The icepap controller used by the fuse device motor

srdiag/itlk-fuse/c05 The fuse interlock (cell 05)

srdiag/wago-fuse/c05 The Wago PLC used by the fuse interlock

srdiag/modbus-fuse/c05 The modbus device used to communicate with the wago PLC

**In the SRVAC domain**

Concerning the families, we can identify the following types (pen,pir,rga,ip,rv)

Concerning the members, we have to identify the cell, then the name of the vacuum chamber, then a number. Therefore, we can give the following examples

srvac/v-pen/c01-ch01-1 First Penning gauge in storage ring cell 01 and vacuum chamber 01

srvac/v-gauges/c01 All Penning gauge in storage ring cell 01

srvac/v-gauges/all All Penning gauges in storage ring

**In SYS domain**

sys/adm-hostinfo/orion The hostinfo device running on the computer named orion

sys/adm-starter/orion The starter device running on the computer named orion

sys/ebs-status/1 For machstat device

### In INFRA domain

infra/fuids/aux The auxiliary uid circuit

infra/mains-harmcor/1 The mains power supply harmonic correction device

### In FE domain

fe/sr-frontend/id11 The storage ring frontend for beam line ID 11

fe/sr-frontend/bm25 The storage ring frontend for beam line on BM 25

### In ID domain

id/id-frontend/id01 The insertion device system front end for beam line ID 01

### Devices for alignment group

The pattern for naming the devices is the following:

- <domain>/a-<device-type>/<cell>-<girder>-<leg>.

Or <domain>/a-<device-type>/<cell>-<other location> or <domain>/a-<device-type>/all (for multichannel vectorized devices).

The domain can be sr, sy, tl2, etc.

The device type can be hls, mot (motor), wps, tap, etc.

The cell is defined by 3 characters: cXX where XX goes from 01 to 32.

The girder is defined by 2 characters: gX (1 to 4) ordered in the direction of the beam. The g1 is the closest to the previous cell g4. The leg: each girder is supported by 4 legs where motors, HLS and other devices are located. We identify longitudinal position by 1 or 2 (in the direction of the beam). We identify the transverse position by "I" for internal side of the SR or "e" for external side of the ring.

Therefore we can give the following example of names;

sr/a-hls/c01-g1-e1 (HLS of cell 01, 1st girder, external pod, upstream)

sr/a-hls/c32-g4-i2 (HLS of cell 32, fourth girder, internal pod , downstream)

sr/a-hls/c01-roof

sr/a-wps/c01-g1-e1 (WPS of cell 01, 1st girder, external pod, upstream)

sr/a-wps/c32-g4-i2 (WPS of cell 32, fourth girder, internal pod , downstream)

sr/a-mot/c01-g2-e1 (motor of cell 01, 2nd girder, external pod, upstream)

sr/a-mot/c32-g3-i2 (motor of cell 32, third girder, internal pod , downstream)

sr/a-hls/all (multichannel device giving a vector of the 512 HLS levels, temperatures and other attributes.)

sr/a-mot/all (multichannel device giving a vector of the 512 motors, allowing reading of positions, coders, etc.. in vector attributes and to start the movement on 512 motors simultaneously)

sr/a-tap/fill, sr/a-tap/purge, sr/a-tap/c02-g3 (tap in cell 2 before girder 3), sr/a-tap/c02-roof

## 6.17 TANGO_HOST environment variable

Within a Tango control system, there is a key data which is the host and port number on which the Tango database server is listening. Most of the time, this is dened using one environment variable named TANGO_HOST. For the EBS, there will be a new TANGO_HOST which should not be the host name where the database server is running but one of its alias name. This will allow a smooth change of this host assuming we give the same alias to the new host. For EBS, the proposed alias name is simply ebs. Therefore the TANGO_HOST environment variable will be (assuming the chosen db port number is 10000) ebs:10000

Other control system like the one which will be set-up for the EBS simulator will use acc-simu as alias name and a value for TANGO_HOST of ebs-simu:10000

## 6.18 Changes schedule

Even if these proposal mainly focus on the EBS control system, it is foreseen to backport these changes in the control system used nowadays to control the ESRF accelerator complex. The proposed schedule to do these changes is:

- Shutdown between run 2016-1 and 2016-2 (March 2016): Remove GLOBAL and ID30 domains.
- Shutdown between run 2016-2 and 2016-3 (May 2016): Renaming device tool ready (including renaming device feature in HDB++).
- Shutdown between run 2016-2 and 2016-3 (May 2016): Renaming devices in domain ID25 and TL1SY.
- Shutdown between run 2016-3 and 2016-4 (August 2016): Create the LABS domain - Renaming devices in domain ID04 - MD012 - RF and TZ16.
- Shutdown between run 2016-4 and 2016-5 (October 2016): Renaming devices from TANGO and HOST domains.
- Shutdown between run 2016-5 and 2017-1 (December 2016): Create the INFRA domain - Renaming devices from SYS to INFRA.
- Shutdown between run 2017-1 and 2017-2 (March 2017): Rename devices in domain BP and EXP.

# 7 Diagnostics

## 7.6 Introduction

In the ESRF-EBS storage ring, there will be the same diagnostic elements as in the present one. Overall there are nine monitors:

- Beam Position Monitors
- Emittance Monitors
- Current Monitors
- Beam Loss Monitors
- Strip Lines
- Scrapers
- Collimators
- Beam – Inhibitor
- Visible Light Monitor

Because of the different sizes of the vacuum chambers a new design of all the nine diagnostics elements has to be made. In the following chapter the design of all diagnostics components will be described.

## 7.7 Beam Position Monitors (BPMs)

### Introduction

There will be 320 BPMs in the EBS, i.e. 10 per cell (See Figure 7.1).

The BPM blocks will have two different internal geometries:

- large for BPMs # 1-2-3 & 8-9-10 and
- small for BPMs # 4-5-6-7.

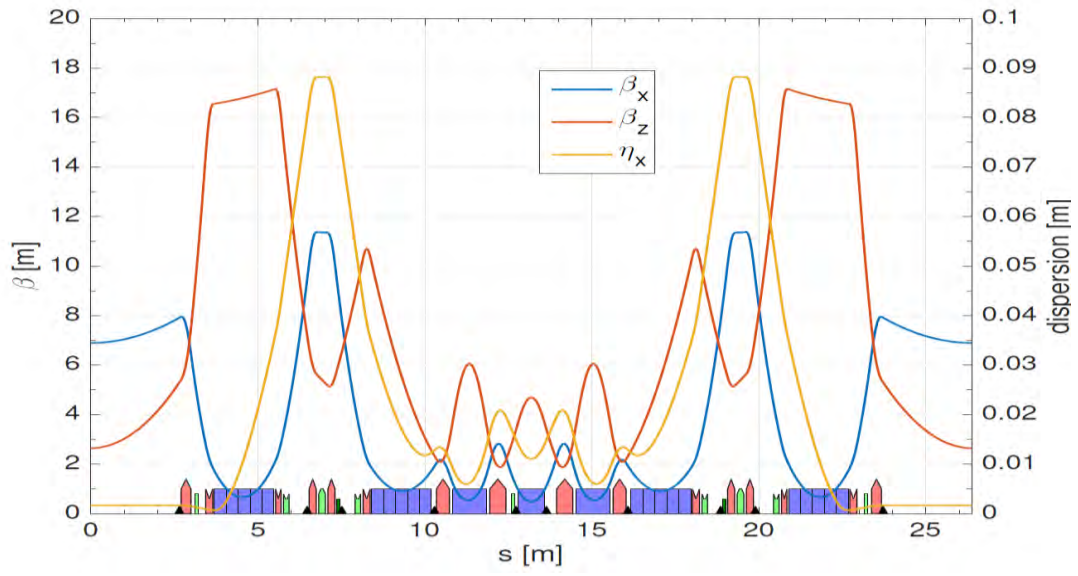


Figure 7.1: The positions of the 10 BPMs shown in black triangles.

Table 7.1: The geometry of the BPM blocks and the type of electronics for the 10 BPMs.

| Name | Geometry | Libera/Spark | S | Beta_X | Beta_Z | Disp. |
|---|---|---|---|---|---|---|
| **BPM_01** | Large | Libera | 2.651 | 7.919 | 5.303 | 0.002 |
| **BPM_02** | Large | Libera | 6.479 | 9.498 | 7.173 | 0.080 |
| **BPM_03** | Large | Spark | 7.515 | 7.824 | 6.543 | 0.073 |
| **BPM_04** | Small | Spark | 10.292 | 1.926 | 2.326 | 0.013 |
| **BPM_05** | Small | Libera | 12.731 | 1.134 | 3.391 | 0.015 |
| **BPM_06** | Small | Libera | 13.643 | 1.134 | 3.391 | 0.015 |
| **BPM_07** | Small | Spark | 16.082 | 1.926 | 2.326 | 0.013 |
| **BPM_08** | Large | Spark | 18.859 | 7.824 | 6.543 | 0.073 |
| **BPM_09** | Large | Libera | 19.895 | 9.498 | 7.173 | 0.080 |
| **BPM_10** | Large | Libera | 23.723 | 7.919 | 5.303 | 0.002 |

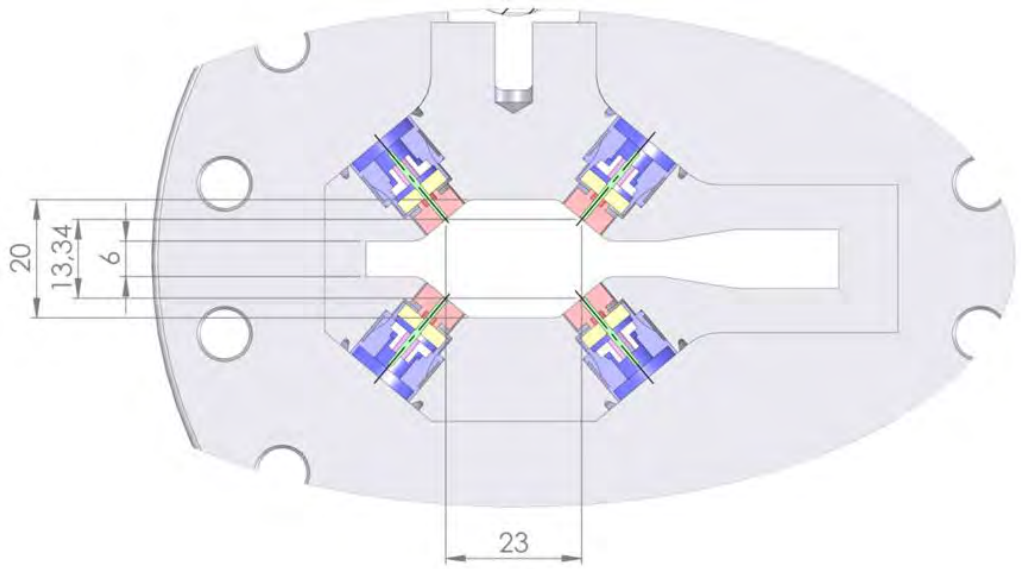


**Figure 7.2a : Geometry of a large BPM block (#8 is shown here), button diameter is 8mm.**

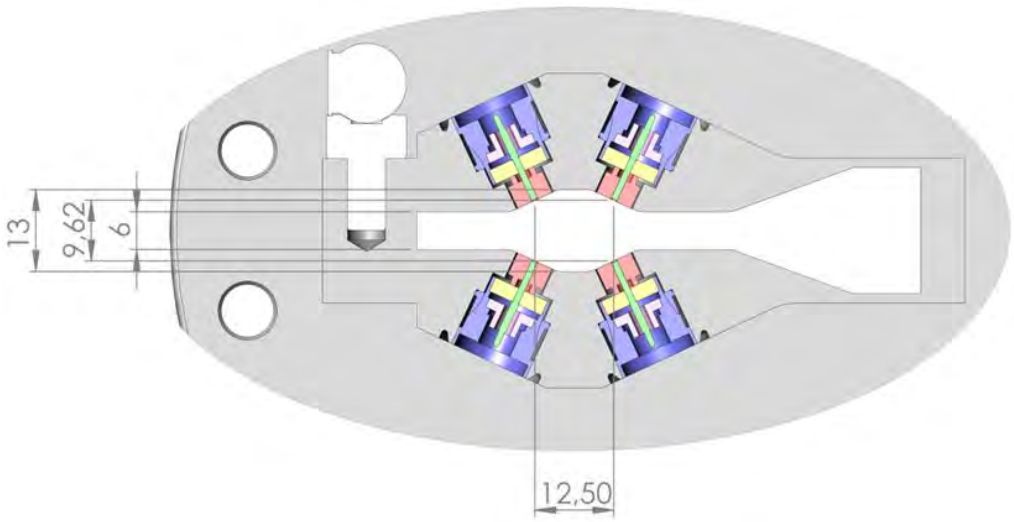


**Figure 7.2b : Geometry of a small BPM block (#4 is shown here), button diameter is 6mm.**

These 10 BPMs (per cell) will have 2 different electronics for signal acquisition & treatment:

- For the (6) BPMs # 1, 2, 5, 6, 9, 10 it will be the existing (since 2009) Libera-Brillance*, and
- For the (4) BPMs # 3, 4, 7 & 8 it will be the new system : Spark-ERXR**.

*Note : names used hereafter : Libera and Spark

** Note : prototypes still under tests, final approval expected end-201

The 6 BPMs with Liberas will (as today) put their position data at 10KHz (FA) rate on a special and independent network. They use dedicated I/O rocket ports on the Liberas for that, and a dedicate software protocol inside (called Communication Controller) in each unit to distribute these data packets in a coordinated and synchronised manner over that network. This system is further described under Fast Orbit Control (FOC).

The Sparks, that equip the 4 other BPMs, will not be part of this network, and thus not contribute to the FOC. However, the Sparks will have the full functionality for position measurements in terms of data-rates like : the ADCs (108MHz), Turn-by-Turn (355KHz), decimated_TbT (5.5KHz) and Slow Acquisition (=SA at 40Hz)

Moreover, between Sparks and Liberas the characteristics of sensitivity, resolution and reproducibility will be very close (see section D).

### Hardware components, trigger & timing, interlocks (BPIs)

Each BPM will have :

- BPM-block, with four BPM-buttons, with SMA-male compatible output connectors
- Four short (approx. 60 cm) RF cables (to an interconnection/support plate),
- The interconnection/support plate
- Long and bundled (4_in_1) RF cables to the cubicle holding the electronics
- Libera or Spark electronics
- Possibly external Bandpass Filters, or not, in front of the electronics (undecided yet)

- SR-clock (355KHz) signal (driving a PPL and thereby keeping all 320 units in step)
- Trigger signal (for suppl. Synchronisation e.g. Turn-by-Turn and FOC/CC)

**Table 7.2: The 10 BPMs with the conversion constants (Kx, Kz) from button signals to X and Z beam position coordinates.**

| Name | Buttom Diameter | Geometry | K_X | K_Z |
|---|---|---|---|---|
| **BPM_01** | 8 | Large | 6.5 | 16.4 |
| **BPM_02** | 8 | Large | 6.5 | 16.4 |
| **BPM_03** | 8 | Large | 6.5 | 16.4 |
| **BPM_04** | 6 | Small | 4.7 | 7.4 |
| **BPM_05** | 6 | Small | 4.7 | 7.4 |
| **BPM_06** | 6 | Small | 4.7 | 7.4 |
| **BPM_07** | 6 | Small | 4.7 | 7.4 |
| **BPM_08** | 8 | Large | 6.5 | 16.4 |
| **BPM_09** | 8 | Large | 6.5 | 16.4 |
| **BPM_10** | 8 | Large | 6.5 | 16.4 |

The BPM blocks have 2 distinct geometries, and the characteristics of these are further described in section E.

The short RF cables will be installed at the time of the installation of the chambers onto the girders. These cables will be submitted to the foreseen bake-out then. These cables will, once the girder installation finished (i.e. with all magnets etc.), be extremely difficult to access at the point of the BPM blocks. The short cables have a female-sma connector on the BPM-block side, and also a similar (but not identical) female-sma connector on the interconnection plate. This interconnection plate will give an easy access for later connection to the long-RF-cables (see **Figure 7.3**).

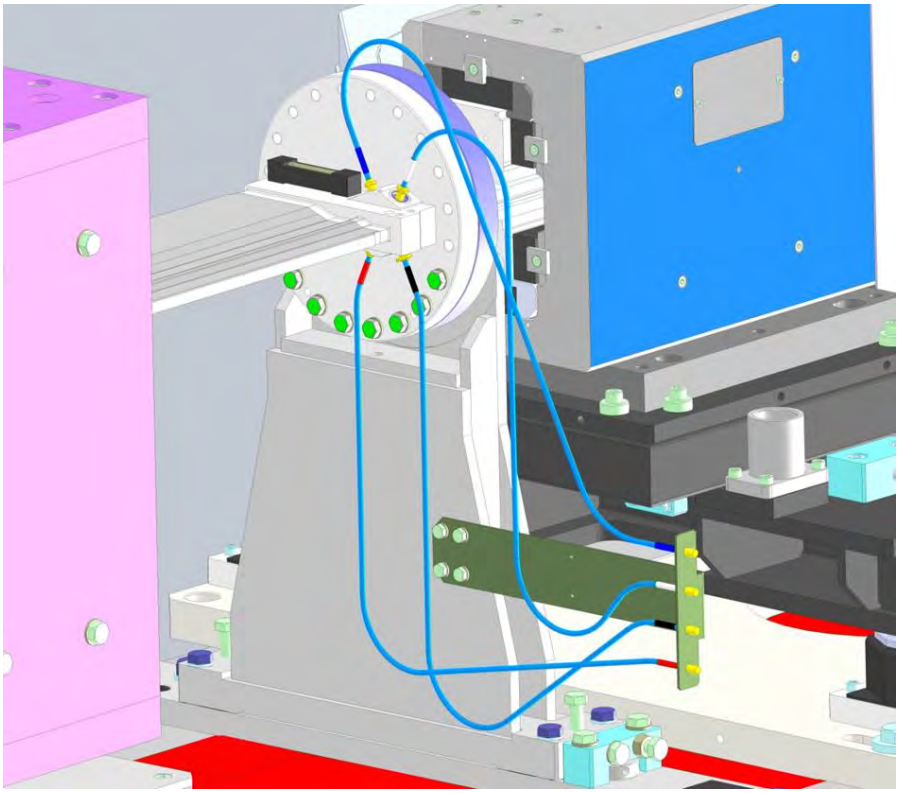

**Figure 7.3: Illustration of the RF-cabling close to the BPM-block, with 60 cm short colour-coded cables (cordons) and interconnection plate. To be noted : One magnet element is omitted from this illustration, in real conditions the connections at the BPM are virtually inaccessible.**

Prior to this connection the so-called button to button RF transmission characteristics will be measured of the BPM block by a dedicated device.

The long and bundled RF cables are of a type with 4 individual RF cables inside one common RF shielding. The diameter of the individual RF cable is 5mm, and that of the whole bundle less then 16mm. These cables offer a lower attenuation of the 352MHz signals (0.201dB/m) and a better shielding (>90dB) against external RF fields then the typical RG-233 RF cable (0.273dB/m attenuation, with >70dB shielding) used in many of the present BPM systems.

These cables will be procured independently (from the global/general cable contractor for the EBS) and will have their SMA connectors of the tunnel side already pre-mounted (in suitable workshop) at the time of delivery. This avoids any tedious mounting of these connectors inside the tunnel.

Their length, to reach precisely their destination inside the cubicles can be estimated within a limited precision of roughly 1m. This is not precise enough to make an optimum routing and connecting of all these numerous RF cables inside the cubicle with a minimum of encumbrance. Therefore the cutting and the final mounting of the SMA connectors on the cubicle side will be done locally, by the same company that produces & delivers these bundles RF cables.

The trigger and timing signals originate from the present timing system, through a clock-card N354. It provides both the SR-clock frequency and a trigger-pulse depending on a selectable

and desired functionality/configuration. These signals are then distributed through an (old and existing) hardware system with cables and conditioning cards (GPulse) to each BPM cubicle. Inside the cubicle a distribution rack further converts these signals (from RS-422 level to PECL levels) and distributes to each Libera unit (PECL cable). Additional convertor cards (to TLL levels) will be needed later to provide the Spark units with TTL signals. In total there are 3 types of timing/trigger signals provided in this (hardware) manner:

- The SR-clock
- The Trigger
- The Post-Mortem Trigger.

Some BPMs (with Liberas only) will have their interlock-outputs wired-up to the general machine interlock. These are typically between 10 and 30 BPMs (to be decided) as is today and with the thresholds of these Beam-Position Interlocks (PBIs) settable. (presently 2mm (hor.) and 0.7mm (vert.)).

### Software & interfacing

The Liberas will use their Tango-device server as today for the control and data-read-out (except FA data stream). In fact, each Libera has an associated device server that runs on a separate computer, and in general a so-called (and single) all-server (handling group-calls & communication) serves as the interface layer for all 192 (today 224) BPM stations. For the Sparks the situation (of device-server and software interface) is not yet defined. The Sparks may be procured with an embedded Tango-device-server (provided by the company), or the ESRF ACU group will make this Tango-server that interfaces to the (MCI) software layer of this device. At a higher level so-called Tango group-servers will be used to gather data from all (128) units in single calls.

### Signal levels and resolution characteristics

The amplitude of the RF-signal for 1mA stored beam, at the end of the long and bundled RF ‘cordons’ (so at entrance of electronics) is given in table 3.

It is also represented in ADC peak values, corresponding to that 1mA beam of a 1uS length (352 buckets) as provided by a roughly 3mA long-pulse from the Booster injector.

This takes into account the complete RF cable attenuation, different for each BPM, and the button-size/block-geometry aspect, and is for regular cells (not injection zone).

The above supposes that the unit with external attenuator & band pass filter, and that causes a total loss of 4.7dB (as used today), is omitted as expected. But this is today not yet decided.

The value of 1mA beam is a suitable example for the early phase of the commissioning where a Booster maximum current (3 to 5mA) long-pulse (352buckets filled) is injected into the Storage

Ring. Table 7.3 indicates ADCs peak values between 1400 and 2100 counts depending on BPM station. With no beam at all these ADCs show a background / offset level of below 200 counts peak. Even if this injected (1mA) beam only makes a fraction of a turn, it will be possible to measure in so-called single Turn mode (i.e. with 355KHz T-b-T data rate) the beam position with a resolution value of about 10 micrometers rms.

At the other extreme, with beam currents close to nominal values (100-200 mA), and using a signal bandwidth of 1 Hz, the resolution of a BPM will be about 20-40 nanometers rms, depending on electronics (Libera/Spark), the exact filling pattern, the BPM geometry, etc.

### Table 7.3: RF signal strengths for 1mA stored beam.

| Name | Geometry | button diam. [mm] | Libera/ /Spark | signal ** at button [dBm] note 1 | total length RF-Cables * [m] note 2 | total Cable_Attn.* [dB] note 2 | signal ** at electronics [dBm] | signal ** at electronics [uV rms] | signal [ADC] ** pk-values note 3 |
|---|---|---|---|---|---|---|---|---|---|
| BPM_01 | Large | 8 | Libera | -55.8 | 17 | 3.4 | -59.2 | 245 | 1716 |
| BPM_02 | Large | 8 | Libera | -55.8 | 16 | 3.2 | -59 | 250 | 1750 |
| BPM_03 | Large | 8 | Spark | -55.8 | 14 | 2.8 | -58.6 | 262 | 1834 |
| BPM_04 | Small | 6 | Spark | -54.7 | 13 | 2.6 | -57.3 | 304 | 2128 |
| BPM_05 | Small | 6 | Libera | -54.7 | 13 | 2.6 | -57.3 | 304 | 2128 |
| BPM_06 | Small | 6 | Libera | -54.7 | 15 | 3.0 | -57.7 | 291 | 2038 |
| BPM_07 | Small | 6 | Spark | -54.7 | 21 | 4.2 | -58.9 | 253 | 1772 |
| BPM_08 | Large | 8 | Spark | -55.8 | 23 | 4.6 | -60.4 | 213 | 1492 |
| BPM_09 | Large | 8 | Libera | -55.8 | 25 | 5.0 | -60.8 | 203 | 1422 |
| BPM_10 | Large | 8 | Libera | -55.8 | 26 | 5.2 | -61 | 199 | 1394 |

* for standard cells, i.e. not cells 32, 1, 2
** for 1mA
note 1 : 6mm button generates 1.1dB more signal then the 8mm (due to geometry of block)
note 2 : including 60 and 80cm of short RF-cables
note 3 : for 1/3 fill, peak values of that 1/3 fill

### Characteristics of the two distinct geometries of the BPM blocks

The diameter of the button is 6mm for the BPMs #4-5-6-7 (small geometry) and 8mm for the BPMs #1-2-3 & 8-9-10 (large geometry).

The k-factors are as follows [mm]:

| Large Geometry | | Small Geometry | |
|---|---|---|---|
| k_X | k_Z | k_X | k_Z |
| 6.5 | 16.4 | 4.7 | 7.4 |

Note: the simplest formula for calculating position is $Z=Kz \cdot (A+B-C-D) / (A+B+C+D)$

This formula suffers from increasing dislinearity for off-centered beam positions. This is illustrated in Figures 7.4, 7.5, 7.6 and 7.7.

Therefore another method, based on a converging iterative process (or alternatively a look-up table), will be used for any precise measurements of the beam coordinates when the beam is not close to the centre.

This will be crucial in the early phases of commissioning (for beam trajectory measurements) and also for special studies of the lattice that implies large orbit deviations.

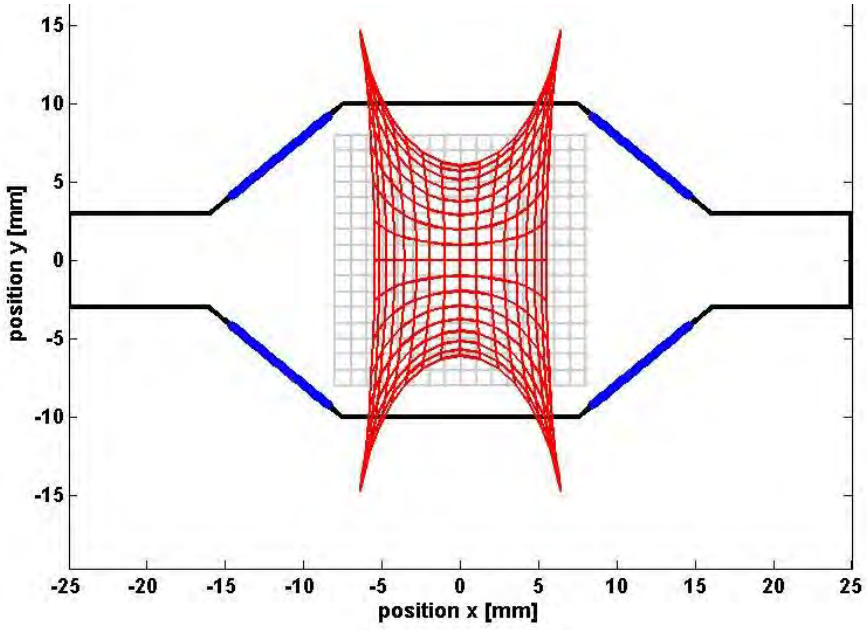


**Figure 7.4: Mapping distortions from the delta/sigma formula, the grey-grid represents the real beam positions (1mm step, 8mm excursion), and the red-grid the corresponding calculated values [BIG geometry].**

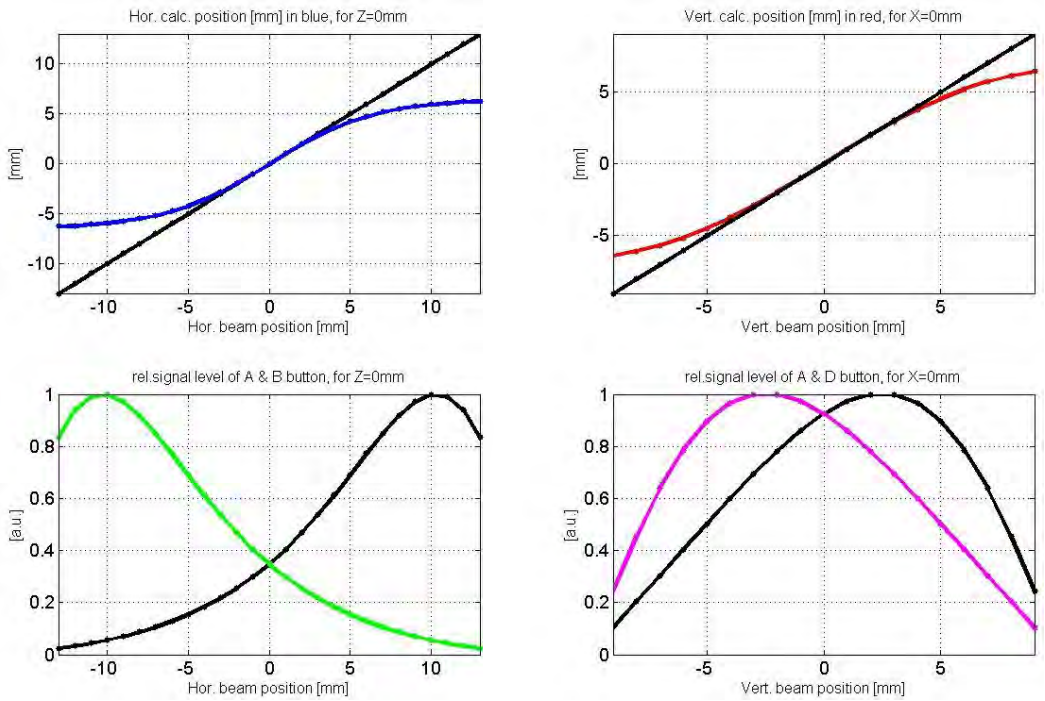


**Figure 7.5: Distortions from the delta/sigma formula for position values (top plots), and the relative signal strength from buttons for beam displacements [BIG geometry].**

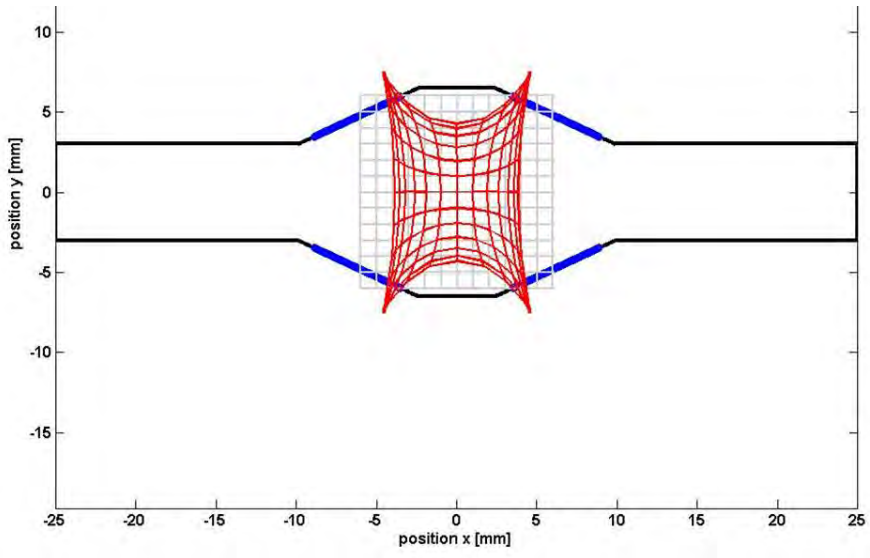


**Figure 7.6: Mapping distortions from the delta/sigma formula, the grey-grid represents the real beam positions (1mm step, 6mm excursion), and the red grid the corresponding calculated values [SMALL geometry].**

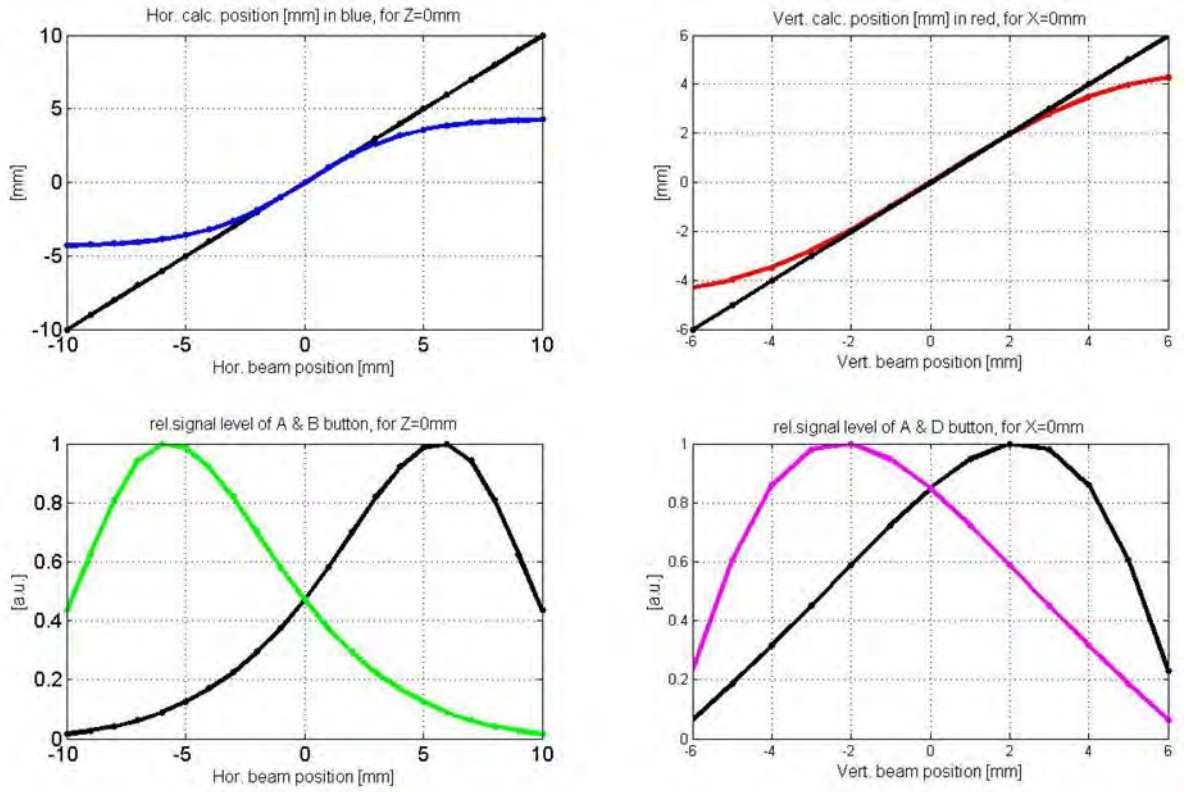


**Figure 7.8: Distortions from the delta/sigma formula for position values (top plots), and the relative signal strength from buttons for beam displacements [SMALL geometry].**

It is to be noted that the k_Z factor of the large blocks at 16.4mm being higher (by a factor 2.5) then the k-X factor (6.5mm) implies that the resolution of the measurement in the vertical plane will be worse (wrt the horizontal plane) by that same factor of 2.5.

**Table 7.5: Beam-based alignment to measure BPM offsets by varying currents in single quadrupoles - list of BPMs and the closest quadrupoles.**

| Name | Type | Length | s | betax | betaz | distance centers of BPM-Qpole |
|---|---|---|---|---|---|---|
| BPM_01 | BPM | 0 | 2.651 | 7.919 | 5.303 | |
| QF1A | Quadrupole | 0.295 | 2.997 | 6.455 | 7.499 | 0.20 |
| BPM_02 | BPM | 0 | 6.479 | 9.498 | 7.173 | |
| QF4A | Quadrupole | 0.212 | 6.747 | 11.383 | 5.646 | 0.16 |
| QF4B | Quadrupole | 0.212 | 7.309 | 10.065 | 5.522 | |
| BPM_03 | BPM | 0 | 7.515 | 7.824 | 6.543 | 0.31 |
| BPM_04 | BPM | 0 | 10.292 | 1.926 | 2.326 | |
| QF6B | Quadrupole | 0.388 | 10.736 | 1.593 | 2.989 | 0.25 |
| QF8B | Quadrupole | 0.484 | 12.428 | 2.283 | 2.172 | |
| BPM_05 | BPM | 0 | 12.731 | 1.134 | 3.391 | 0.54 |
| BPM_06 | BPM | 0 | 13.643 | 1.134 | 3.391 | |
| QF8D | Quadrupole | 0.484 | 14.430 | 2.053 | 2.842 | 0.54 |
| QF6D | Quadrupole | 0.388 | 16.026 | 2.048 | 2.201 | |
| BPM_07 | BPM | 0 | 16.082 | 1.926 | 2.326 | 0.25 |
| BPM_08 | BPM | 0 | 18.859 | 7.824 | 6.543 | |
| QF4D | Quadrupole | 0.212 | 19.277 | 11.350 | 5.170 | 0.31 |
| QF4E | Quadrupole | 0.212 | 19.839 | 10.131 | 6.679 | |
| BPM_09 | BPM | 0 | 19.895 | 9.498 | 7.173 | 0.16 |
| QF1E | Quadrupole | 0.295 | 23.672 | 7.958 | 5.406 | |
| BPM_10 | BPM | 0 | 23.723 | 7.919 | 5.303 | 0.20 |

### Initial offsets and offset calibration with beam

The offset of a BPM is defined as the result value yielded by the BPM with the beam in the centre. It is hereby supposed that the centre of the BPM is also the centre of the adjacent quadrupole. This offset has different contributions:

1: Alignment or fidulisiation errors of the BPM block with respect to the adjacent quadrupole.

2: Electric-mechanical offset of the BPM block due to differences between the 4 buttons.

3: Electric offsets due to the non-equal sensitivity of the electronics.

For 1: the value is estimated at 50 um rms.

For 2: it is caused by mechanical tolerances on the both the BPM-block and the buttons, and the precision limitations in the (button to block) welding process. These mechanical tolerances (typ. 10 to 50um) have been defined at stringent but realistic values. Reducing them to smaller values would have been costly and cumbersome (to verify or check).

The resulting estimation is given according to the block geometry and the plane as follows. It is to be noted that it applies to the case with all variations (in mechanical dimensions) of 100% random nature, and 0% systematic error.

| Offset caused by BPM mechanical tolerances | X-plane [values in um rms] | Z-plane [values in um rms] |
|---|---|---|
| **Small** | 71 | 112 |
| **Big** | 59 | 151 |

For 3: it will be measured and calibrated with a dedicated but simple equipment (stable RF-source), inside the SR-Tunnel, taking into account the full electric signal chain (RF-cables, interconnections, Electronics). It aims (after applying compensation factors derived from the calibration measurements) at an rms value of less than 50 um.

The beam-based alignment method will be applicable as soon as a sufficient stored current and lifetime permit this. Even at low current (i.e. typ. 10mA) and low lifetime (i.e. typ. 1hr) would the BPMs be compatible with this method, in which the current in the most adjacent quadrupole (only) is varied and the resulting effect on the orbit measured. In a reiterative approach the method converge to the point where the quadrupole current change is negligible; at this point the obtained BPM value is defined as the offset of that BPM. It is the sum of all causes of offsets (as detailed above). It aims at 20um resolution/precision in a reasonable duration of the overall method. It is also determined by the precision & reproducibility with which a small variation of the (individual) Q-pole current can be obtained from the power-supplies control.

Table 7.5 shows which BPM is coupled/associated with what quadrupole, and the distances between the centres of each.

### Slow and Fast Orbit Control

The orbit correction of the EBS storage ring will use 10 BPMs and 10 correctors per cell.

Among these BPMs and correctors only 6 BPMs and 3 correctors per cell will have the capability to get position data and apply correction kick at a rate of 10 KHz.

Table 7.6 shows the exact distribution of these 2 types of BPMs and correctors.

The rest of the BPMs and correctors will be operated at a much lower rate. Consequently, the orbit correction will be performed using two systems working in parallel:

- The slow orbit correction system (SRCO) using the full set of 320 fast and slow BPMs and 320 fast and slow correctors operating at a relatively slow rate (less than one correction per second).
- The fast orbit correction (FOC) system using a subset of the full BPMs and correctors set and operating at a rate of 10 KHz.

**Table 7.6: The distribution of BPMs and correctors (steerers) in the cell, with the distinction between those that are only Slow, and those that are both Slow & Fast.**

| Name | Type | Length | s | betax | betaz |
|---|---|---|---|---|---|
| BPM_01 | BPM | 0 | 2.651 | 7.919 | 5.303 |
| SH1A | Fast-Slow-Steerer | 0.1 | 3.207 | 4.503 | 10.540 |
| SD1A | Slow-Steerer in Sextupole | 0.166 | 5.934 | 4.445 | 12.950 |
| BPM_02 | BPM | 0 | 6.479 | 9.498 | 7.173 |
| SF2A | Slow-Steerer in Sextupole | 0.2 | 7.022 | 11.355 | 5.267 |
| BPM_03 | Slow-BPM | 0 | 7.515 | 7.824 | 6.543 |
| SD1B | Slow-Steerer in Sextupole | 0.166 | 8.076 | 3.200 | 9.833 |
| BPM_04 | Slow-BPM | 0 | 10.292 | 1.926 | 2.326 |
| SH2B | Fast-Slow-Steerer | 0.1 | 12.694 | 1.247 | 3.224 |
| BPM_05 | BPM | 0 | 12.731 | 1.134 | 3.391 |
| BPM_06 | BPM | 0 | 13.643 | 1.134 | 3.391 |
| BPM_07 | Slow-BPM | 0 | 16.082 | 1.926 | 2.326 |
| SD1D | Slow-Steerer in Sextupole | 0.166 | 18.464 | 4.344 | 8.782 |
| BPM_08 | Slow-BPM | 0 | 18.859 | 7.824 | 6.543 |
| SF2E | Slow-Steerer in Sextupole | 0.2 | 19.552 | 11.374 | 5.539 |
| BPM_09 | BPM | 0 | 19.895 | 9.498 | 7.173 |
| SD1E | Slow-Steerer in Sextupole | 0.166 | 20.606 | 3.300 | 15.059 |
| SH3E | Fast-Slow-Steerer | 0.1 | 23.267 | 5.387 | 9.026 |
| BPM_10 | BPM | 0 | 23.723 | 7.919 | 5.303 |

| | |
|---|---|
| BPM | is Libera (with Slow & Fast outputs) |
| Slow-BPM | is Spark (with only Slow outputs) |

The future FOC system will be quasi identical to the FOC system of the present storage ring; it will reuse 6 Libera Brillance BPM electronics per cell (instead of 7 now), and the 3 BILGE correctors power supplies of the present system; It will also reuse the 8 correctors power supply controllers boards and the so called Communication Controller network which broadcasts the FOC system position and correction data among the components of the system.

The orbit correction will be applied using auxiliary windings embedded in the sextupoles magnets for the slow corrections and a set of three so called correctors magnets per cell able to apply correction with a larger bandwidth, as required by the fast orbit correction loop.

In order to operate the SRCO and FOC systems in parallel the two systems must be able to communicate: since the position data and correctors set are not the same they would aim at slightly different optimal orbits, so we must have a way to force the FOC to converge toward the same average orbit as the optimal orbit set by SRCO. This feature is achieved by having the possibility to add an offset to the position data used by the FOC to compute the fast correction.

This offset is continuously trimmed according to any drift of orbit correction computed by SRCO; we obtain this result by forcing the average error position signal for every BPMs read by the

FOC to be zero when the orbit set by the FOC is the same as the orbit set by SRCO.

The only non-zero error signal seen and corrected by the FOC will then be the effect of the fast orbit distortion which will be corrected between .01 and 100Hz.

The possibility to add this offset to the position data read on the Communication Controller by the correctors power supply controllers boards required to modify the firmware of the FPGA of these boards. This feature has been implemented and tested.

Expected stability: with a bandwidth of 100 Hz, the FOC will have a significant effect up to 50Hz; the frequency of the main resonance mode of the girders of the new SR will be about 50Hz compared to 7Hz on the present ring, so the damping effect of the FOC for the new ring will be less than for the present one.

However, due to the higher frequency of the girder resonance, we also expect that the amplitude of the un-damped fast orbit distortion will be smaller than on our present ring, so the amplitude of the orbit distortion damped by the FOC will eventually be smaller than on the present ring; this is the situation observed on several storage ring designs using a similar girder design (SOLEIL, ALBA for instance). The main beneficial effect will be to prevent orbit distortion caused by the gap change of un-sufficiently corrected insertion devices spoiling the stability of the Xray beams used by the other beamlines.

## 7.8 Emittance Monitors

### Introduction

The X-Ray Pinhole has proven in the past to be a reliable method for the simultaneous measurement of the electron beam emittance in electron storage rings in both, the vertical and horizontal, planes. Using X-rays emitted from a bending magnet, the working principle of the X-ray pinhole is based on the image formation using a small aperture placed in the photon beam path. As detailed in **Table 7** X-ray pinholes will be installed in 5 locations: ID7, ID25, D11, D17, D27.

**Table 7.7: X-ray source locations for the X-ray pinhole installations. The 'cumulated angle' is the total angle accumulated from the center of the straight section to the source point.**

| Cell | Beamport | Source | Cumulated Angle | Angle with respect to dipole entrance | Solid angle (horizontal) transmitted through absorber | Horizontal absorber opening | Transmitted radiation power |
|---|---|---|---|---|---|---|---|
| | | | [mrad] | [mrad] | [mrad] | [mm] | [W] |
| **7** | ID | DL1A_5 | -2 | -2 | 0.6 | 1.55 | 68 |
| **25** | ID | DL1A_5 | -2 | -2 | 0.6 | 1.55 | 68 |
| **11** | D | DQ1D | -107.525 | -1.5 | 0.5 | 1.7 | 50 |
| **17** | D | DQ1D | -107.525 | -1.5 | 0.5 | 1.7 | 50 |
| **27** | D | DQ1D | -107.525 | -1.5 | 0.5 | 1.7 | 50 |

The ID and D locations differ by the available dipole field strength (influence on X-ray energy and flux) and the □-functions at the source point. The minimum resolvable emittance value depends on the inverse of the □-value at the X-ray source, such that the ID beam ports with their considerably higher □-value are more adapted to ultra low emittance measurements. At the same time the B-field of the DL1A_5 dipole segment is stronger (0.62 T) than the field of DQ1D (0.55T), which means that the X-ray flux from the ID location is higher. Thus both, better resolution and higher X-ray flux are in favour for a pinhole installed on a ID beam port. Nevertheless, D beam port pinholes are important in order to have more measurements for the horizontal beam emittance and in order to deduce the energy spread (see corresponding section below).

Since the theoretically achieveable minimum vertical emittance of the ESRF-EBS lattice is below 0.2 pm, the pinhole measurement will not have sufficient resolution for beam dynamics studies (see below) and it is foreseen, at a later point, to install compound refractive lenses for X-rays replacing (or in parallel to) the pinhole at one ID-beamport, since imaging with X-ray lenses promises higher resolution.

### Mechanical implementation of dedicated ID- and D-type emittance beamports

Each of the X-ray pinhole installations needs a special crotch absorber allowing to extract ⍰⍰ ≈ 0.5mrad of X-rays emerging from the flat part of the bending magnet field profile. Since the pinhole itself and the detection system will be located in air, the X-rays exit into air through a cooled aluminium window.

The corresponding crotch absorbers (CH3 1/1 and CH9 1/2) and the chamber CH4 in cells 7 and 25 are therefore non-standard.

The design for these beam ports as well as the downstream installations of motorisations, pinhole and camera has not yet been started (state of July 2016).

Figure 7.8 sketches the locations of X-ray source and pinhole positions with the corresponding approximate distances and magnification factors. Accurate values will be available only at the end of the design phase of the pinhole front ends.

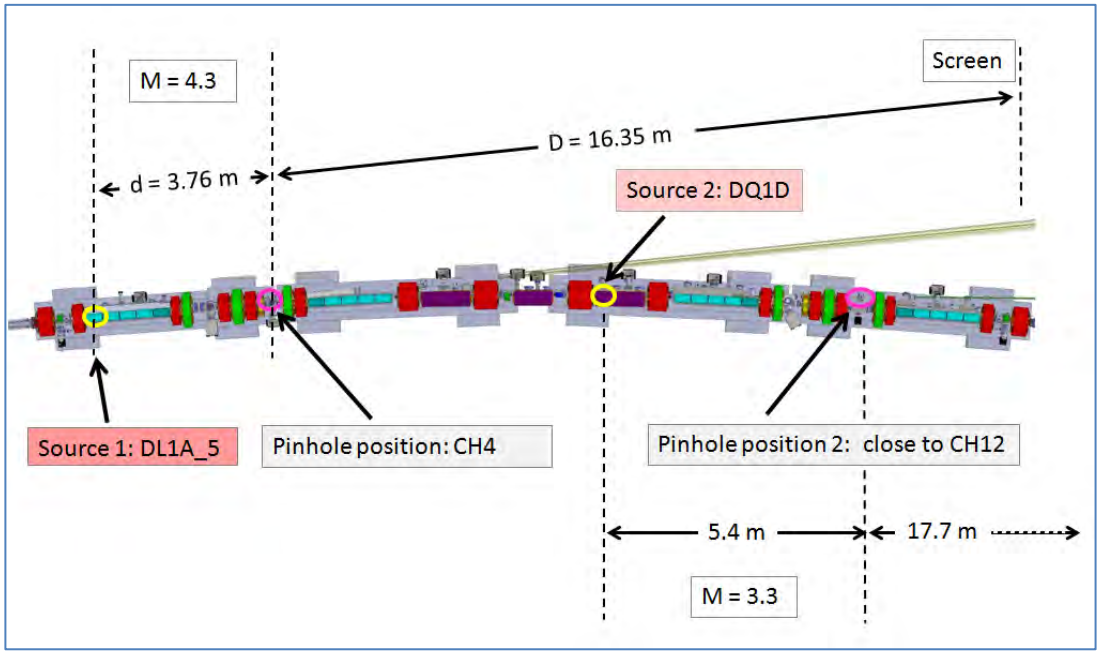


**Figure 7.8: Location of pinhole installation in ID and D sections - schematic overview.**

### Aluminium beamport window

The Al window will be based on the design of the present beam port windows. It consists of a 2 mm thick sheet of pure aluminium cut into a water cooled Al block. This latter is brazed into an explosion bonded stainless steel/aluminium flange. The thickness of the window has been chosen by evaluating the transmitted power against the radiation dose created in the first 10 cm of air behind the window.

The transmission should be kept high enough to allow high photon flux on the detector (scintinllating screen/CCD) and beam detection

with a good contrast ratio even at low beam currents, while the ozon production due to the X-rayse should be limited as much as possible. Comparison with the source powers of DL1A_5 and DQ1D with the existing pinholes D9, D11 and ID25

lead to a ~2 mm thick window as best compromise between peak photon energy, photon flux and expected radiation damage.

Table 7.8 illustrates the X-ray beam properties: peak energy on pinhole, transmitted power through Al-window, radiation dose in the first 10 cm of air behind the window for the ID and D beam ports in comparison with the existing pinhole installations (D9, D11, ID25).

**Table 7.8: X-ray beam energy and radiation power behind aluminium window. ?? is the horizontal solid angle of radiation transmitted by the absorber. (*) Radiation dose deposited in the first 10 cm of air behind the Al window; this distance was chosen because it roughly represents the distance between the aluminium window and the pinhole (behind which the X-ray flux ist drastically reduced).**

| | | D9 | D11 | ID25 | DL1A_5 | DQ1D |
|---|---|---|---|---|---|---|
| **B** | [T] | 0.4 | 0.85 | 0.5 | 0.62 | 0.55 |
| **$d_{Al}$** | [mm] | 3 | 4 | 2 | 2 | 2 |
| **$E_{peak}$** | [keV] | 29 | 38 | 28 | 30 | 29 |
| **$P_{trans}$** | [W/mrad] | 6 | 36 | 15 | 25 | 19 |
| **Rad. Dose / mrad** (*) | [kGy/s/mrad] | 200 | 825 | 550 | 835 | 660 |
| ?? | [mrad] | 1 | 0.3 | 1 | 0.6 | 0.5 |
| **Rad. Dose** | [kGy/s] | 200 | 275 | 550 | 500 | 330 |

### Special Crotch Absorber

The crotch absorber of the two ID beam ports dedicated to emittance measurement is a normal absorber as it will be used for a closed D/ID front end (no beamline), but with a slot in the absorber transmitting 0.5 mrad and 0.6 mrad of radiation respectively, at a center beam angle of -2 mrad for DL1A_5 and -1.5 mrad for DQ1D (angle with respect to the ideal dipole field edge). See Figure 7.9 for illustration of the absorber design.

Ideally the source point should be located on the flat part of the B-field in order to have a well defined photon flux and energy. However, the possible emission angles are limited by the angular acceptance of the front end, i.e. X-ray

beam absorbers and space limitations by the storage ring magnets.

Figure 7.10 and Figure 7.11 illustrate the situation of DQ1D. The case of DL1A_5 is similar with slightly different angles. The source point (i.e. also the position of the absorber opening) should not shift more than +0.5 mrad upstream (towards the magnet entrance) in order to stay on the flat part of the field. In the downstream direction (towards magnet's flat field region) there is no limit given from the point of view of the emittance measurement, and the opening can be shifted as far as the mechanical constraints of the front end layout allow

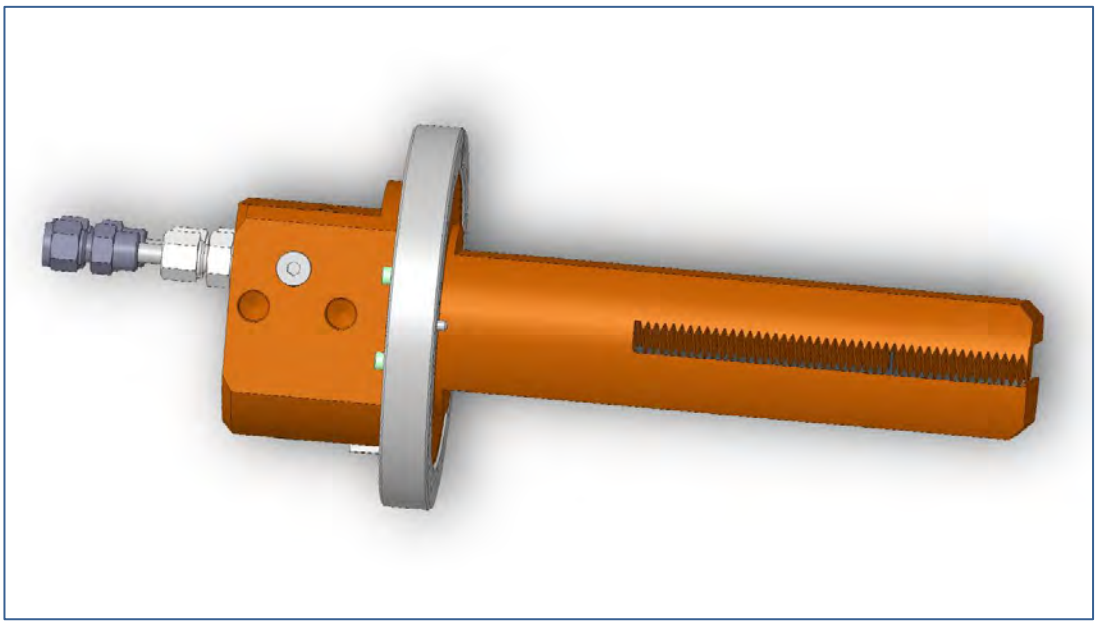

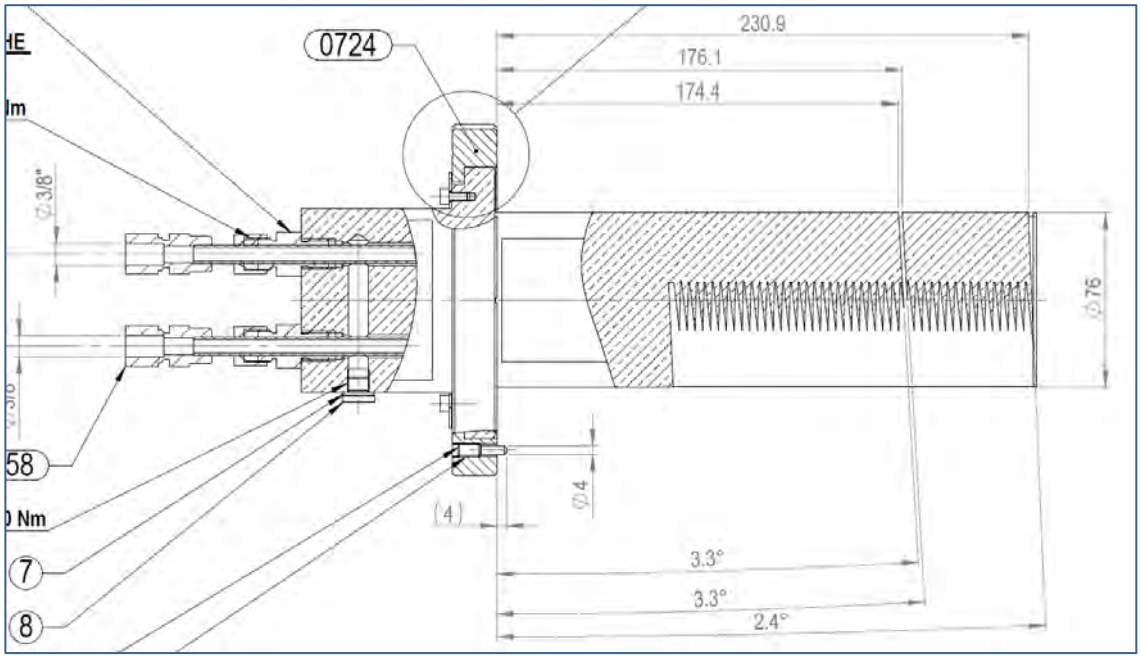


**Figure 7.9: Special crotch absorber for emittance measurement at D beam port. (adapted view. The small slit in the toothed absorber region transmits 0.5 mrad of X-rays originating from DQ1D. The design for the ID emittance crotch absorber is equivalent (special CH3 absorber, part number 88.41.0728).**

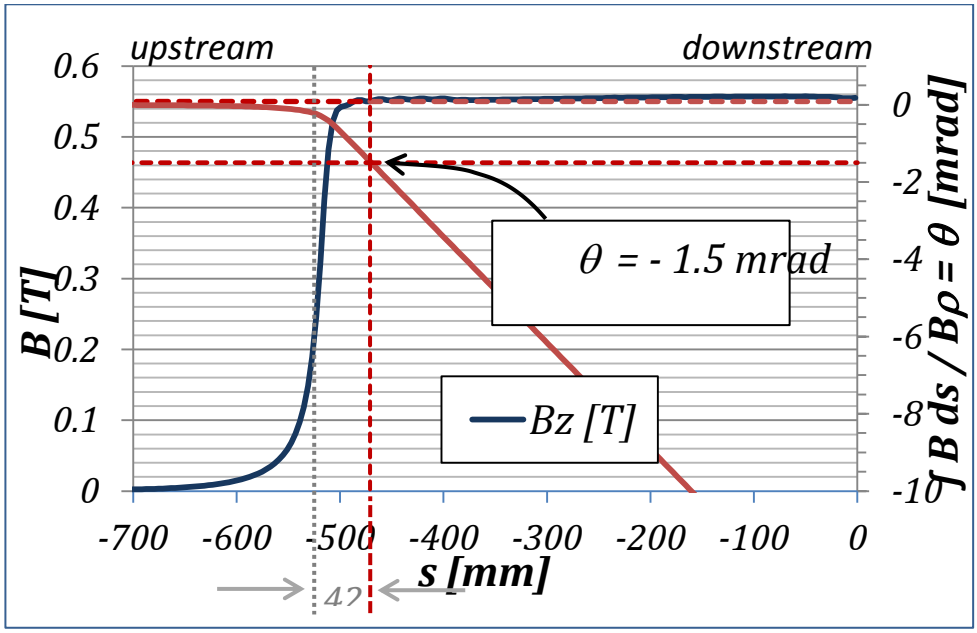


**Figure 7.10: DQ1D: first half of dipolar field component as function of longitudinal positions and beam emission angle □ obtained from integration of B over ds normalised by B□ = 20.15 m. The gray line indicates the field edge for the equivalent ideal B-field. s = 0 mm indicates the center of the dipole.**

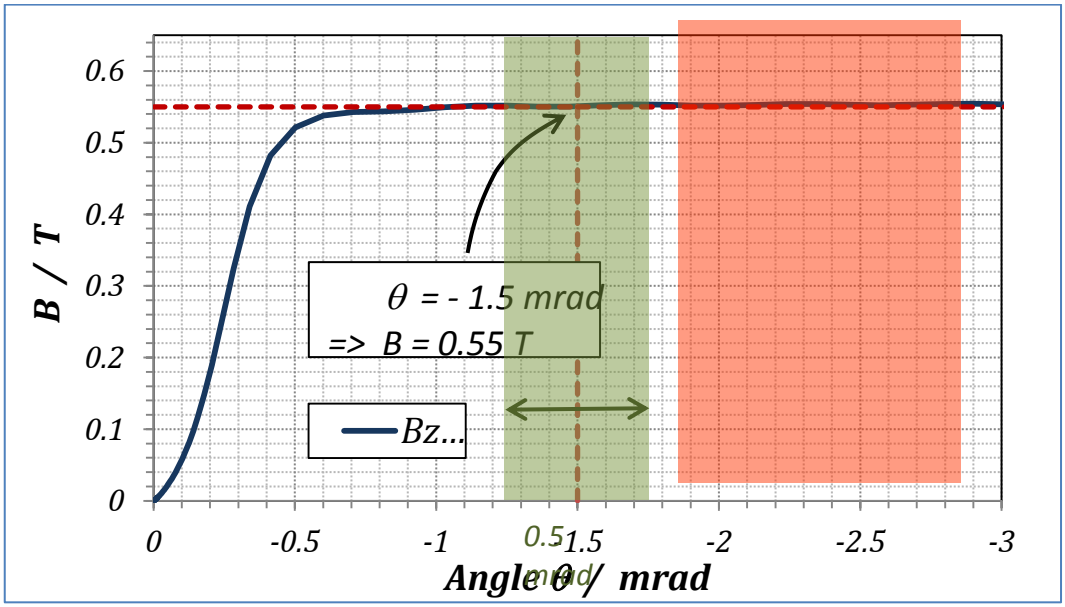


**Figure 7.11: Plot of DQ1D dipolar field component as function of the bending angle, with  = 0 being defined as the angle of the straight section in front of the dipole. The green region represents the angular opening in the absorber, transmitting the beam for the emittance measurement. The red area indicates the limit given by the mechanical layout, i.e. no beam can be extracted into the front end.**

### ID beamport (source DL1A_5)

#### Special CH4 chamber

This vacuum chamber will be modified in order to allow the installation of the X-ray pinhole.

#### Pinhole

The pinhole design will be very close to the current design using crossed slits formed by tungsten bars.

#### Detector

The detector, which is the ensemble of fluorescence screen, visible light optics and CCD camera, will be very similar to the design of the current X-ray pinhole detector.

### D-beamport (source DQ1D)

For the D beam ports no storage ring vacuum chamber needs to be modified.

#### Absorber

The crotch absorber of the two D beam ports dedicated to emittance measurement will be modified such that only 1 mrad of radiation at a

center beam angle of -2mrad will be transmitted into the front end.

### Pinhole

The pinhole design will be very close to the current design using crossed slits formed by tungsten bars.

### Detector

The detector, which is the ensemble of fluorescence screen, visible light optics and CCD camera, will be very similar to the design of the current X-ray pinhole detectors.

### Pinhole Resolution (X-rays only)

The resolution limit of the X-ray pinhole (not involving the optical imaging of the scintillator screen) is given by an optimum pinhole size resulting from the equivalence of the geometrical shadow projected on the screen and the diffraction limit of the X-rays beam. Minimization of the total rms size yields the optimum pinhole aperture, the minimum rms beam size at the source that can be resolved using the above optimum pinhole size, and the minimum resolvable emittance:

$$A_{opt} = \sqrt{\sqrt{3}\,\frac{(\lambda dD)}{D+d}} \quad ; \quad \sigma_{min} = \sqrt{\frac{\lambda d}{2\sqrt{3}}\,\frac{D+d}{D}} \quad ; \quad \varepsilon_{min} = \sigma_{min}^2/\beta$$

### Application to ID-beamport (source DL1A_5) and D-beamport (source DQ1D)

Table 7.9 details the achieveable resolutions at the the ID- and D-beamports, assuming a photon energy of 70 keV. For the presented values the approximate positions of sources, pinholes and screens indicated in Figure 7.8 were used. These values will slightly change in the future depending on the final mechanical beam port design.

**Table 7.9: Achievable minimum resolvable rms beam size □min at the source points at DL1A_5 and DQ1D. B is the bending magnet field strength and □x,z the beta-values at the source points. D and d are the distances pinhole-screen and source-pinhole. M is the X-ray pinhole magnification and □min is the rms source size on the scintillator screen.**

| | B | □z | □x | d | D | M | $A_{opt}$ | □min | □min | □z,min | □x,min |
|---|---|---|---|---|---|---|---|---|---|---|---|
| | [T] | [m] | [m] | [m] | [m] | | [□m] | [□m] | [□m] | [pm rad] | [pm rad] |
| **DL1A_5** | 0.62 | 16.64 | 1.65 | 3.76 | 16.35 | 4.3 | 10 | 5 | 21 | 1.4 | 14 |
| **DQ1D** | 0.55 | 3.81 | 1.46 | 5.4 | 17.7 | 3.3 | 11 | 6 | 20 | 9 | 25 |

From the above it is evident that the better location to resolve small vertical emittances is the source point at DL1A_5. A comparison of these resolution limits with the electron beam

sizes expected for the new lattice is shown in Table 10. Resolving the beam size in the horizontal plane should not present any problem, while in the vertical plane only the DL1A_5 location is adapted, and only if the lowest theoretically achievable coupling values are not reached. Since it is planned to artificially increase the coupling during USM to reach about 5 pm of vertical emittance, the pinhole at DL1A_5 is sufficient for normal operation. For machine studies with lower vertical emittances other techniques that promise better resolution – like X-ray lenses or X-ray diffraction – will be needed.

**Table 7.10: Comparison of expected beam sizes at the two source points within DL1A_5 and DQ1D for different coupling values. The cells marked in green indicate the beam sizes which should be relovable using the pinhole technique.**

| | **Expected for ESRF EBS** | | | | **Pinhole resolution limit** |
|---|---|---|---|---|---|
| | $\sigma_x$ [□m] | $\sigma_z$ [□m] | | | $\sigma_{min}$ [□m] |
| | | coupling 4% ($\sigma_z$ = 5 pm) | coupling 1% ($\sigma_z$ = 1.3 pm ) | coupling 0.1% ($\sigma_z$ = 0.13 pm ) | |
| **DL1A_5** | 15 | 9 | 4.7 | 1.5 | 5 |
| **DQ1D** | 19 | 4 | 2.2 | 0.7 | 6 |

The DQ1D location is only adapted to horizontal emittance measurements, but nevertheless this second source point location is a requirement for energy spread measurements (see section on energy spread below).

Using higher photon energies the resolution limit can be pushed a little bit, but not a lot at the expense of photon flux at the detector:

Example for DQ1D: $E_{ph}$ = 100 keV; □ = 0.1 Ångstrom → $\sigma_{z,min}$ = 6 pm.

### Detector (resolution and sensitivity)

The optimum pinhole size is the same in both planes, horizontal and vertical. In the current situation with a horizontal emittance of 4 nm and a horizontal beam size at the source of about 140 □m it is not very important to force the resolution to the minimum limit in the horizontal plane. The horizontal pinhole size is therefore increased well above the optimum value to 50 □m as compromise between a high photon flux on the screen and sufficient resolution.

In the low emittance lattice, however, also the horizontal pinhole size has to be reduced to the optimum value in order to correctly resolve the small source beam size. This results in an important loss of X-ray flux which will complicate the imaging of the scintillator and contributes to the noise of the overall emittance measurement, especially at low beam currents.

Detailed estimations of available light flux and the choice of all detector components, like scintillator thickness, optics, CDD are still to be done. This is important for optimum light detection without loss of resolution.

## Energy Spread

The real energy spread (increased in case of high bunch current) can be measured by comparison of two horizontal beam size measurements at locations with different dispersion values. The requirement for a correct energy spread measurement is a substantially different dispersion value in each of these two places. The two source points DL1A_5 and DQ1D (as described above) fulfill this requirement as can be read from Table 7.11 which lists the dispersion and its contribution to the total beam size at the source.

**Table 7.11: Contribution of energy spread □ to the horizontal beam size. □ is the horizontal dispersion value at the source.**

| | | DL1A_5 | DQ1D |
|---|---|---|---|
| □ | | 0.001 | 0.001 |
| □□□□□□ | □m□ | 0.0007 | 0.01322 |
| $\sigma_{tot}$ | [□m] | 13.49 | 18.31 |
| $\sigma_{disp}$ | [□m] | 0.7 | 13.22 |
| $\sigma_{disp}/\sigma_{tot}$ | [%] | 5 | 72 |

The energy spread □ and the corresponding dispersion-free emittance $\varepsilon_0$ will be deduced from the two measured beam sizes by:

$$\delta = \sqrt{\frac{\beta_2\sigma_1^2 - \beta_1\sigma_2^2}{\beta_2\eta_1^2 - \beta_1\eta_2^2}} \quad ; \quad \varepsilon_0 = \frac{\sigma_2^2\eta_1^2 + \sigma_1^2\eta_2^2}{\beta_2\eta_1^2 - \beta_1\eta_2^2}$$

## 7.9 Current monitors

### Introduction

For ESRF-EBS three different types of current transformers will be used:

- The DC component of the beam intensity (current) in the storage ring is measured using Parametric Current Transformers (PCTs) – also called DCCTs**.**
- Integrating Current Transformers (ICTs) have the capability to measure the single bunch current in the timing-filling patterns (7/8+1, 16-bunch, 4-bunch, Hybrid).
- A Fast Current Transformer (FCT) can be used (via oscilloscope) to monitor the filling pattern.

Such commercially available current transformers (CTs) are standard equipment at the ESRF as well as in other synchrotron light sources.

For ESRF-EBS we foresee to recuperate the 3 PCT devices installed in the present storage ring as well as the 2 ICTs and one FCT. This concerns all of the toroids and their read-out electronics.

The special vacuum chamber needed for the CT installation is re-designed to fit the new vacuum chamber profile, space requirements and influence on the impedance of the machine.

The 3 CT pairs (PCT+ICT/FCT) will be installed replacing the vacuum chambers CH12 of cells 5, 10 and 15 (see Table 7.12).

**Table 7.12: Future locations of PCTs, ICTs and FCT.**

| Cell | Chamber No. | PCT | ICT | FCT |
|---|---|---|---|---|
| **05** | CH12 | | | |
| **10** | CH12 | | | |
| **15** | CH12 | | | |

Note 1: Since the CTs will be needed in the current storage ring up to its last day of operation, they can not be installed on the girders during the planned assembly phase, but only after having been dismounted from the existing machine.

Note 2: The ferrite material of the transformer torii is not resistant to temperatures higher than 80°C. Bake-out temperatures on the CT-chamber must not exceed this value, failing which the CTs will be irreversibly damaged!

### Mechanical implementation

In order to allow the electromagnetic fields to escape from the electrically conducting vacuum pipe, this latter needs to present a gap in the close vicinity of the CT torii. The gap size and shape is designed to fit two requirements:

As low as possible influence on the overall impedance of the machine and optimisation (attenuation) of the RF power transmitted through the gap into the copper shielding of the ICT to avoid heating of the ICT ferrite torus.

### Explanation of the main elements of the CT-chamber ensemble

**Figures 7.12** and **7.13** show the 3D external view of the CT-chamber ensemble and a vertical cut through the chamber with the details of the gap geometry.

The ICT is located exactly over the electrical gap in the chamber since it needs to collect a wide RF frequency spectrum ( 0 to ~20 MHz). The PCT, not being subject to the same requirement, is placed next to the ICT but not over the gap.

### Electrically isolating gap

The gap consists of two overlapping tubes, where the 1 mm space between the female and male chambers is filled with ceramics. Both, the big surface created by the overlap and the ceramics contribute to the increase of the gap capacity which is beneficial for the impedance budget of the machine and reduces at the same time the power transmitted through the gap into free space.

For details on the impedance simulations see **Figure 7.17**.

### Ceramic pipe

A 10 mm thick ceramic tube around the gap assures the UHV vacuum level in the beam pipe. It is brazed/soldered on either side to the female and male chambers and should be perfectly isolating.

### RF shield around ICT/FCT

The gap presenting an important source of RF radiation outside the vaccum chamber, a copper shield is mounted around the ICT in order to protect other storage ring equipment.

This has however a drawback: the shielding turns into an RF cavity and the ICT torus heats up due to absorption of (a part of) RF-power stored in this cavity.

### Ventilation

To protect the ICT/FCT from overheating a forced air flow is circulating inside the RF-shield.

### Return current blades

Since the vacuum chamber is electrically broken due to the gap, large copper blades assure the flow of the wall current around both of the CTs.

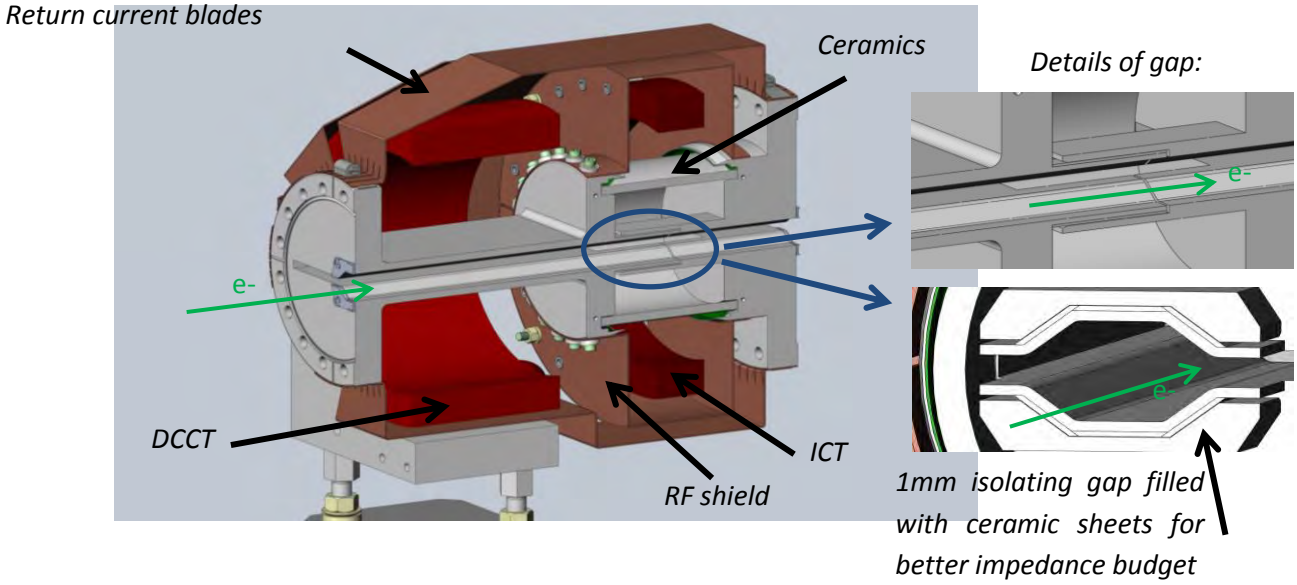


**Figure 7.12: Vertical cut through the CT chamber assembly and zoom to the electrically isolating gap.**

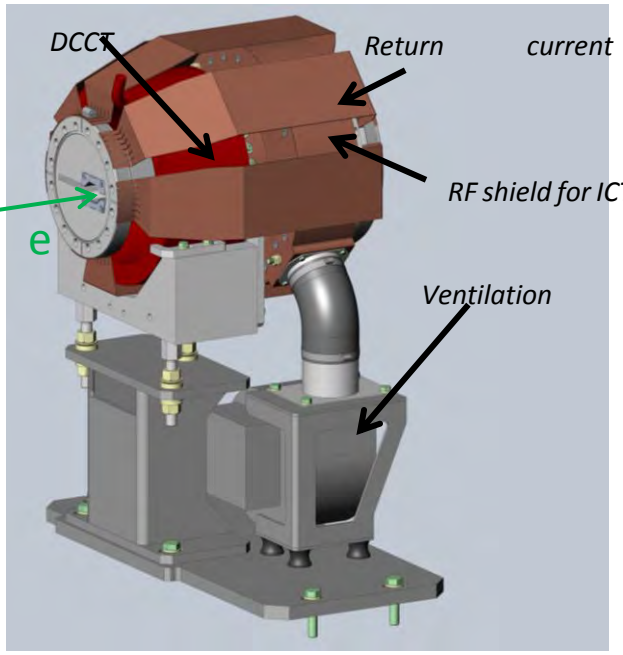


**Figure 7.13: 3D view of the CT chamber with supports, shielding elements and air ventilation.**

### Read-out electronics and software

The cables between the CT hardware (SRTU) and the read-out electronics (TZ) are detailed in Table 13. The cables for the PCTs in cell 5 and 10 as well as for the ICTs and the FCT are standard cables. An exception is the PCT in cell 15 that uses a special cable with special connectors, delivered by Bergoz Instrumentation. This cable has to be removed carefully during the dismantling of the storage ring and be reused upon installation. Cables and connectors must not be damaged!

#### Table 7.13: Cables

| | **PCT C05 / C10** | **PCT 15** | **ICTs / FCT** |
|---|---|---|---|
| **Cable type** | multipoint | Special cable from Bergoz | Air filled coax |
| **Connector type** | standard | Special connectors from Bergoz | SMA |

All of the read-out electronics will be recovered. The software will therefore be unchanged, and the measurement of beam intensity should work immediately and reliably at the restart of the new storage ring.

### Impact of the electric gap on impedance

The beam coupling impedance of the CTchamber ensemble is given by the geometry of the gap. The existing gap design has proven to work with respect to the impact on impedance (beam stability) and with respect to heating of the ICT/FCT torii (**if** ventilation inside the copper shield is respected!). It is therefore taken as reference and adapted to the new beam pipe. The smaller beam pipe aperture leads to higher impedance and to more heating of the ICT torii. The simulations allowed to define a gap design which keeps or even improves the level of impendance and heating.

### Main changes in the design with respect to today

Reduction of the gap dimensions (see **Figure 14**):

- Smaller gap aperture: 8 mm → 1 mm
- Smaller distance between overlapping female and male chamber: 2 mm → 1 mm

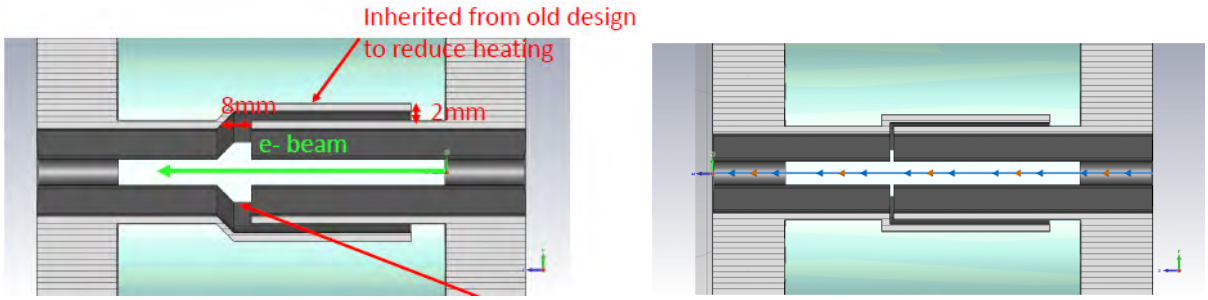


**Figure 7.14: Left: existing gap chamber design; right: both gap dimensions reduced to 1 mm.**

Due to the CT chamber geometry the beam coupling impedance is dominated by a peak centered around ~200 MHz. Higher frequencies between 3 GHz and ~9GHz are present but with much lower amplitude. Frequencies above roughly 9 GHz can not propagate inside the beam pipe.

Figure 15 illustrates the significant improvement (decrease) of impedance of roughly a factor 2 upon reduction of the gap dimensions to 1 mm.

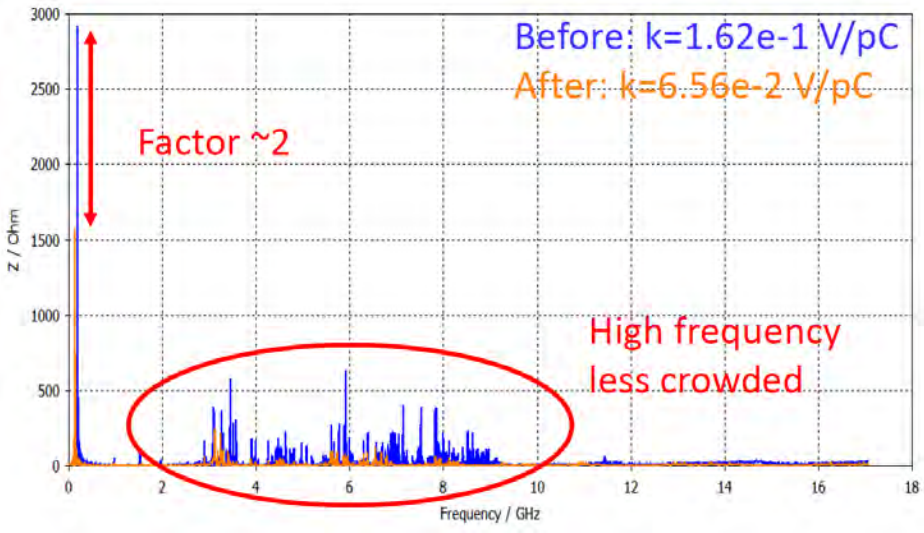


**Figure 7.15: Blue: gap dimensions as for the present machine (8 mm and 2 mm); orange: gap dimensions reduced to 1 mm.**

### Overlap region between female and male chamber filled with ceramics

Filling the gap between the overlapping chamber parts with ceramics should reduce the RF power transmitted into the copper shield and thus reduce heating of the ICT torus. At the same time, as illustrates Figure 7.16, the impedance is reduced by a factor of 4 for the low

frequency mode, while at higher frequencies the overal gain is not so obvious. In any case the introduction of ceramics in the chamber gap is clearly beneficial.

Decreasing the slit width between the overlapping chambers from 2 mm to 1 mm reduces the impedance by a factor of 2 and the resonances excited by the interfaces between ceramics/vacuum/steel are well attenuated (Figure 7.17). The 1mm gap size is therefore chosen.

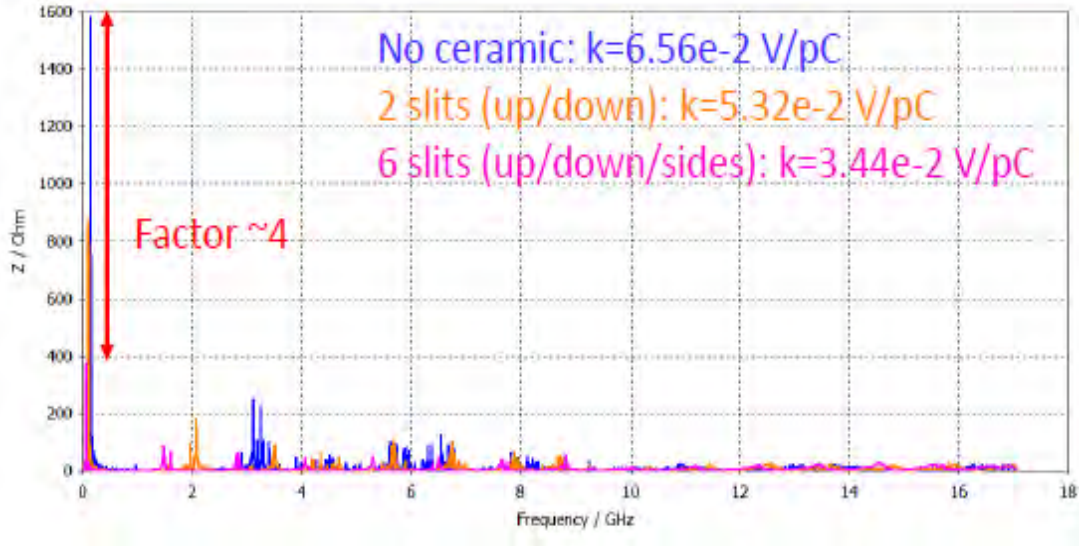


**Figure 7.16: Comparison of gap space empty and filled (partially = orange, totally = magenta).**

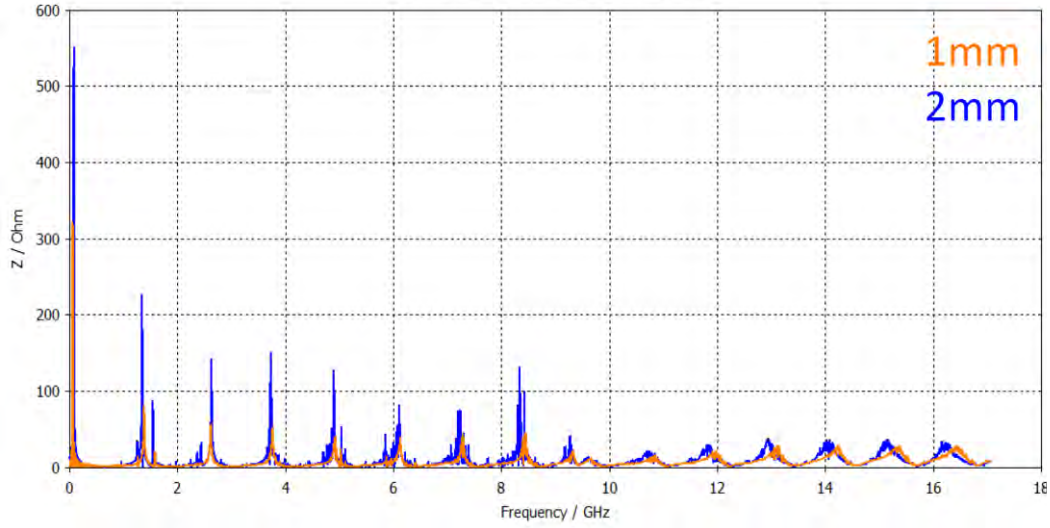


**Figure 7.17: Impedance as function of distance between the 2 overlapping chamber parts (filled with ceramics).**

### Conclusion on impedance simulations:

The optimised gap design with a small 1 mm gap and distance between the overlapping chambers allows to significantly reduce the impact on the beam coupling impedance with respect to the current gap design with bigger gaps. Filling the gap with ceramics improves further the impedance budget and attenuates the low frequency RF signal captured in the copper shield, thus heating of the ICT torus is reduced. In this configuration the impedance is improved by a factor of ~5 compared to the present situation (simulation of existing installation not shown here).

## 7.10 Beam Loss Monitors (BLMs)

### Introduction: different types of beam loss monitors in today's ring

Three different types of detecting systems, sensitive to the loss of the 6 GeV electrons, exist today in the ring.

### The 32 Unidos ionization chambers and their specific electronics module (electro-meter)

One unit is installed per cell in the existing ring with its ionization chamber inside a (big) lead box of 1cm thickness, positioned underneath the 1rst dipole in a cell. The electronics module is (like the ionization chamber) a commercial device (PTW company) and situated in a cubicle. The signal output is carried by a very special cable that needs protection.

### The 32 IG5 ionization chambers and their specific electronics module

One unit is installed per cell in the existing ring with its ionization chamber inside a lead box of 1cm thickness, position underneath the 2nd dipole in a cell. The electronics module is (like the IG5 ionization chamber itself) a rather simple low-cost device (Log-amplifier) and situated in a cubicle in the Technical Zone. The signal output is carried by a simple coaxial cable and the HV supply by another (HV-compatible) coaxial cable.

### BLMs based on Scintilators with PhotoMultiplier Tube (PMT)

A total of 64 units of such Beam Loss Monitors (BLMs) are installed, at each dipole, roughly 1m upstream the crotch absorber. They consists of:

- Perspex scintillator rod of 25mm diameter and 600mm length
- PMT with 25mm input window
- heavy cylindrical Lead shielding (10mm thickness)
- cables for power-supply & gain-control between the PMT and the analogue electronics
- analogue electronics card and a slow (~1Hz) signal digitizer (of the WAGO version)

The functionality of the above Unidos and the IG5 systems is limited to only slow measurements. They do not have a suitable adjustable gain, and their sensitivity is not optimized to detect low levels of electron

losses. Their distribution, of only 1 per cell, does not allow a precise estimation of the position of the electron losses, within a cell.

The volume and weight of these systems is very considerable, also due to the large & heavy Lead boxes in which they are situated (without they would also be sensitive to scattered X-rays). The weight (64Kg) and encumbrance (70x40x35cm) means they can only be put at the floor level, and any available spaces for that are limited.

However, their simplicity and robustness warrants a reliable and permanent survey of any very strong (or excessive) losses, in one or some sectors of the ring.

The PMT-BLMs have a much higher sensitivity than the Ionization chambers but their functionality is also only for slow measurements : They have only slow analogue electronics and no fast digitizer, and in case of fast & strong losses (at injection) the PMTs saturate which make linear measurement losses not possible.

These devices also have a heavy lead shielding (housing) that weighs about 13Kg, and that weight and size also makes them relatively difficult to handle and position.

It is envisaged to replace these existing systems with a new system that consists of:

- 128 BeamLoss Detectors (or Heads or Sensors), referred to BLDs hereafter, installed at 4 specific locations per cell
- 32 signal acquisition & treatment electronics, 1 per cell (in the TZ cubicle) that serves 4 BLDs, referred to as Libera-BLM.

**Figures 7.19a** and **7.19b** in the appendix on BLMs shows the structure of the BLD.

It consists of:

- A specific ( optimized) scintillator material (EJ-200, or BC-408, depending on manufacturer), in the shape/form of a cylindrical rod with typical dimensions of 100mm height and 22mm diameter.
- A PMT (ref. H10720-110 from Hamamatsu) of size of 50x22mm with an 8mm circular size of the photo-cathode window.
- A simple aluminium housing (200x25x25mm), with a standardized RJ-25 connector for the PMT's power-supply and gain-control voltage and a SMA (coaxial) output connector.
- A cylindrical lead shielding that is independent of the above, and that can be simple shifted over the BLD. The thickness is typically 2mm and the total weight is less than 1Kg.

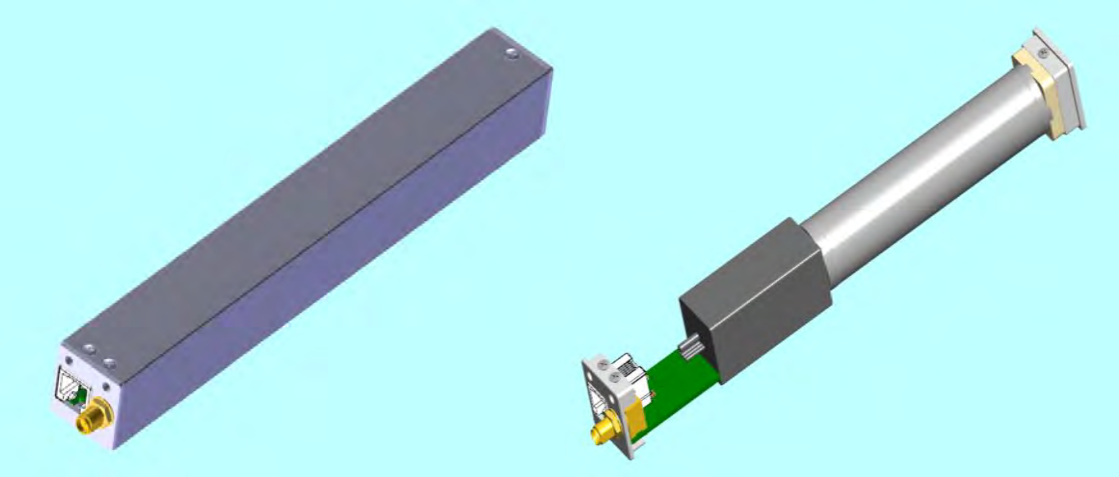

**Figure 7.18 (a and b): a view of the BLD with its 25x200mm aluminium housing and the connectors (left) and a view inside showing the scintilator rod, the photo-multiplier tube (PMT) and an interconnecting printed circuit with connectors (EJ-25 and SMA).**


**Figure 7.19: The electronics for the control and signal acquisition of 4 BLDs (front-view): the Libera BLM of dimensions 210x210x44mm.**

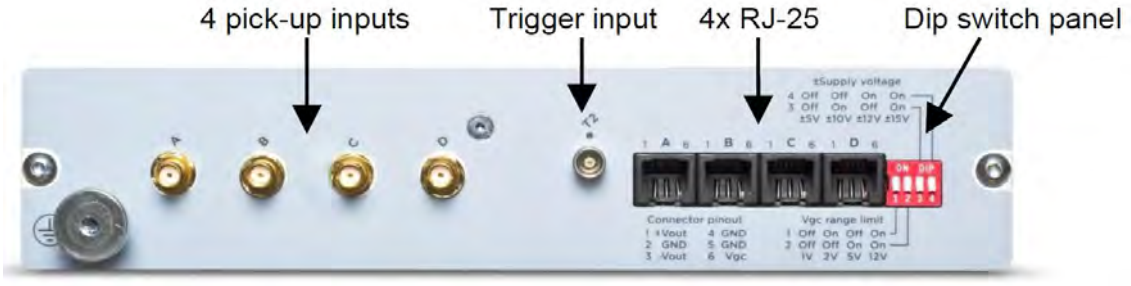


**Figure 7.20 : Rear-view of the Libera BLM with its inputs and connectors.**

The Libera BLM is shown in **Figures 7.19** and **7.20**.

It has a Tango device server that via Ethernet connection allows to fully control the device and to read its different data-buffers.

Each unit has 4 independent inputs (SMA connectors) and 4 (RJ-25) connectors through which power supply and gain control can be provide over standard (and in-expensive) RJ-25 '6p6c' cables.

The 4 ADCs (14bits resolution) inside the unit can operate upto 125MHz. The analogue bandwidth is above 10MHz. The input sensitivity can be set from typically 5V full-scale to less than 150mV.

The device can be triggered by an external trigger signal, and has a large variety of different buffers (configurable in sample-rate and size) to provide the signals from the BLDs in fast time-resolution modes, or (much) slower time-scales, and down to continuous data streams at 40Hz.

This system (both the BLD and the Libera-BLM) is presently under development and tests. It is expected that a final and definitive version will be reached in the 2$^{nd}$ part of 2016.

It is considered to install the full system of the above 128 BLDs and 32 BLMs in the existing Ring, perhaps in early 2017, and to benefit from its data to already detect and understand more electron loss details of this Ring. But also to compare the quality of its data with that of the 3 present existing systems. This comparison should lead to the conclusion that there is no good reason to re-install these old, heavy and volumeous systems in the EBS.

It is important to stress that the BLDs can handle (i.e. measure without strong dislinearities) in the two extreme domains of levels of electrons losses :

- Very strong and fast losses at e.g. the moment of injection,
- Very slowly varying losses of very low intensity, e.g. due to a local change of losses itself due to small variation of UHV conditions.

The BLDs will all be calibrated before their installation, and can if needed be re-calibrated at any time of access to the tunnel, by the use of a small portable radiation source like Cesium-137.

This is a relative calibration, that allows measuring the relative sensitivity of each individual BLD with respect to the others.

The purpose of the BLDs is not to provide an absolute measurement of how many electrons per second were detected. Instead they provide good, reliable and comparative measurements between a sufficiently large number of them, being distributed in an identical manner in each cell.

In addition to the 128 regularly distributed BLD units in the Ring it is foreseen to deploy identical units (with also identical BLM electronics) at some specific positions like in close vicinity to some in-vacuum insertion devices, the TL2 and cell 4 injection zone, the booster extraction zone, and downstream of the scraper collimators (in cells 13 and 24).

## 7.11 Striplines

Three horizontal, two vertical striplines and a longitudinal kicker (1.4GHz low Q cavity) will be installed in the location listed in the table 14. They will be used as the dampers of bunch by bunch feedback systems.

**Table 7.14: Distribution of the different diagnostic components around ESRF-EBS.**

| diagnostic elements and their location (cell & chamber) | | | | | | |
|---|---|---|---|---|---|---|
| | | | | Feb. 2016 | Resp. | designer |
| item / element | quant. | cell(s) | chamber no. | status | | |
| | | | | | | |
| Current Monitor (toroid & ceramic chamber) | 3 | 5, 10, 15 | 12 | study finished | FE | Borrel |
| Pick-Up / Kicker-Stripline Horizontal | 3 | 28, 29, 30 | 12 | study almost finished | EP | Borrel |
| Kicker-Stripline Vertical | 2 | 27, 31 | 12 | study almost finished | EP | Borrel |
| longitudinal kicker cavity | 1 | ID25 ? | straight ? | to be started | EP | ? |
| Shaker (Tune monitor, coupling control) | 2 | 25, 26 | 12 | to be started | EP | Borrel |
| Collimator (hor.scraper+massive shielding) | 2 | 13 & 24 | 12 | pre-study underway | KS | Borrel |
| DL1A_5 ID-Emit. monitor (X-ray beam-port window/absorber) | 2 | 7 & 25 | 4 (? ) | to be started | FE | Pasq. |
| DQ1D BM-Emit. monitor (X-ray beam-port window/absorber) | 2 | 11, 17, 27 | 10 (?) | to be started | FE | Pasq. |
| Beam-Inhibitor (safety interlock) | 1 | 7 | 12 | pre-study underway | KS/NB | Benoist |
| Scrapers (Hor.) behind Septum | 1 | 4 | special | to be started | KS | Mairs |
| Scraper Horizontal | 1 | 11 | | | | |
| Scraper Vertical | 1 | 6 | 12 | to be started | KS | Borrel |
| Visible Light Extraction Mirror | 1 | 5 | 4 (? ) | to be started | KS | Pasq. |
| "Fuse" = Vertical Blow-up Interlock + Purity monitor | 2 | 4, 19 | in Front-End | to be started | KS | Pasq. |
| BPMs with different button geometry for tests | 1 | 12 | 12 | pre-study underway | KS/NB | Benoist |
| | | | | | | |
| to be kept free for a possible ID-9 bump | 2 | 8, 9 | 12 | | EP | |

Each of the striplines used in the feedback will be driven by a set of two 0.1 to 200 MHz bandwidth 100W power amplifiers. The longitudinal kicker will be driven by a 1.2 to 1.4 GHz bandwidth 200W power amplifier.

The new ring will be equipped with three bunch by bunch feedback systems able to damp instabilities in the vertical, horizontal and longitudinal planes; the longitudinal system will be most likely used only as a diagnostic tool since the instability threshold of the longitudinal instabilities is expected to be higher than the intensity stored in operation, thanks to the use of HOM free cavities for the RF system.

These systems will reuse Libera bunch by bunch electronics to perform the signal processing. The input signals will come from dedicated sets of BPM buttons located at the end of the vertical striplines chambers. Illustrations of the vertical stripline are shown in **Figures 7.21** and **7.22**.

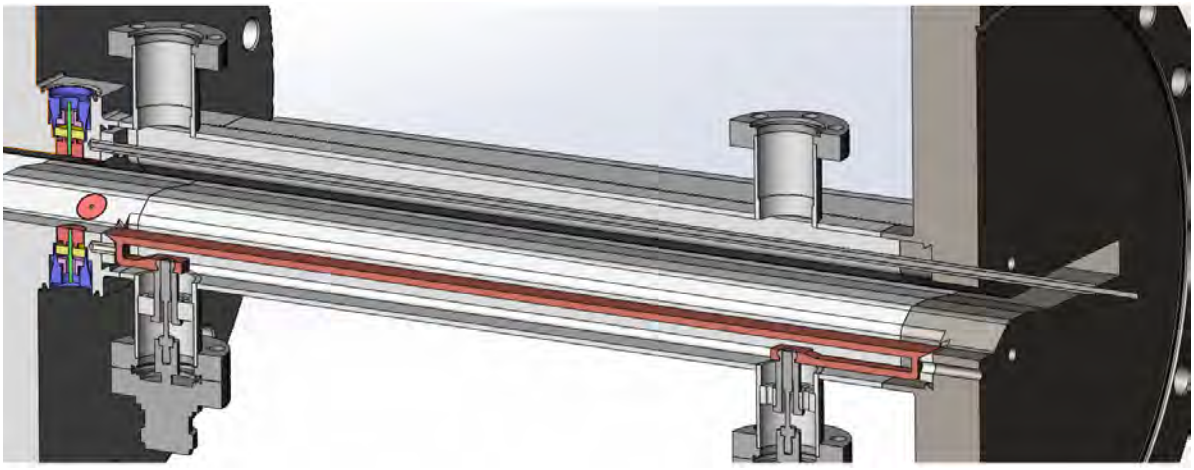

Figure 7.21: View of the vertical stripline.

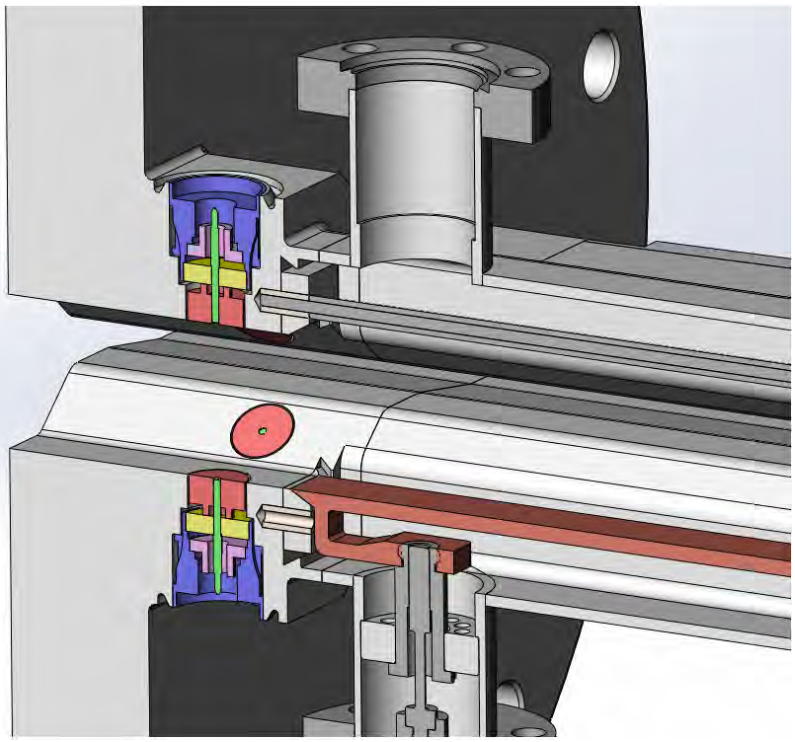

Figure 7.22: Details on the side where also BPM-block with 6 buttons (8mm) are implemented.

## 7.7 Scrapers, collimators and beam inhibitor

The EBS will be equipped with:

- 1 horizontal scraper with both (independent) internal and external jaws, in the cell 4 injection zone, just downstream the quadrupole behind the SE-3 Septum tank.
- 1 horizontal scraper with internal jaw only, in the chamber-12 of cell 11.
- 1 vertical scraper with both (independent) upper and lower jaws in the chamber 12 of cell 6.
- 1 beam-inhibitor (also wrongly called 'beam killer') that consists of 1 horizontal, internal jaw in chamber 12 of cell 7.
- 2 scrapers and collimators in chamber 12 of the cells 13 and 24.

### Scrapers and collimators

This item is by far the most difficult, complex and challenging system. The combined installation and operation of these two devices, with each of them operating at a horizontal aperture of roughly +/- 7.5mm, aims at localizing 80% of all electron losses, while having a limited effect on the lifetime of the stored beam (reduction of about 5%).

The second purpose of these devices is to contain, as much as possible, all the products (i.e. the electro-magnetic shower) of the impinging 6GeV electrons into the jaws of this collimator.

This has entailed both the large dimensions of these 2 horizontal jaws, and their choice of material (Tungsten). The same device also holds two massive vertical jaws, of same material and roughly same dimensions. However, these jaws are not adjustable in position, and the vertical aperture is fixed at 15mm (while the nominal vertical aperture of this vacuum chamber is at 20mm). Both horizontal jaws can be moved independently. The complexity of the external jaw is that it has to absorb and evacuate about 1KW of synchrotron light power coming from the upstream dipole(s). This jaw therefore needs a water cooling circuit inside, and the associated pipes for the water conduction need to go through flanges & bellows as well.This particularly complex component needs a feasibility study and manufacturing first before the global design can be confirmed.

To minimize any impedance issues of the device the currents flowing in walls of the vacuum chamber need to transferred in a smooth manner all along the length of this device. This can be done by so-called RF-fingers. However, due to the overall size, the density of internal components, and the fact that the 2 horizontal jaws can move over >10mm range makes that these RF-fingers will be of complex shape & design, and also difficult to precisely install at the time of assembly.

The feasibility of this assembly needs to be assessed first by manufacturing (nearly) all (dummy) components from plastic material and to verify that the real insertion, positioning, tightening (of screws) of the entire assembly is possible.

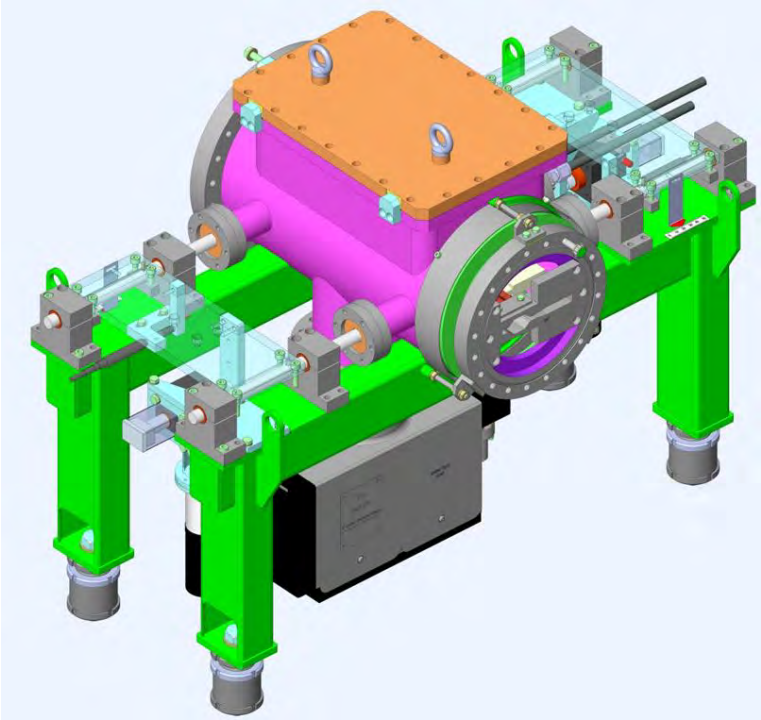

Figure 7.23: Global views of the scraper collimator study (May 2016).

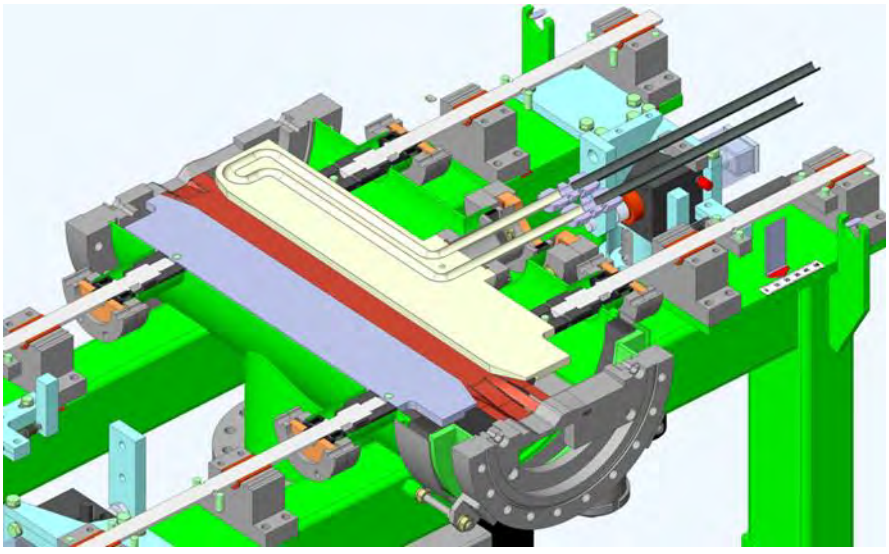

Figure 7.24: View of the scraper collimator study with a detailed inside view.

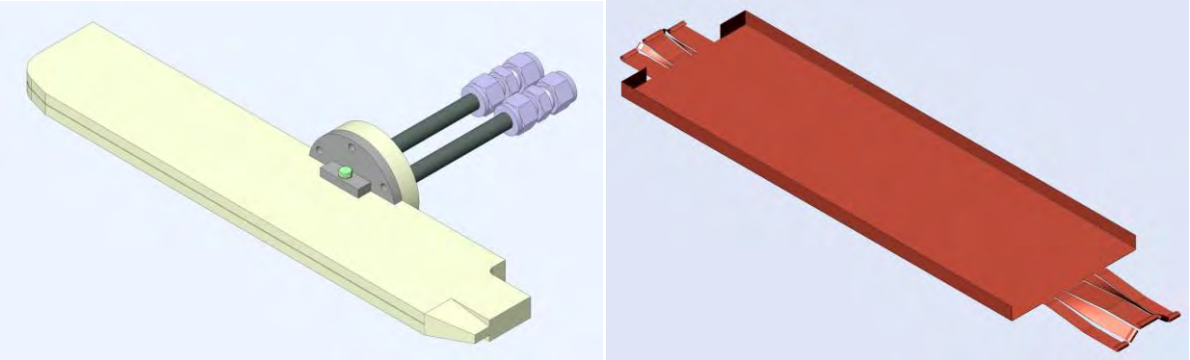

**Figure 7.25: Detailed views of the external jaw (with cooling tubes) and the upper RF finger of the Scraper-Collimator.**

### Beam inhibitor

This item is a requirement from the ESRF Safety system. This inhibitor will be driven into the path of the electron beam when a hardwired safety interlock is received from that safety system. However, that same hardwired safety interlock will also be given to the RF system, making it cut the RF-power typically within a few milliseconds, and thus cause the total loss of the stored beam. The mechanics of the inhibitor will be acting much slower (in fact 0.5 to 1sec) so the jaw of the inhibitor will not touch or feel the electron beam. As such it is to be seen as a back-up safety system: it will assure that the electron beam will be dumped, even if the RF interlock was somehow non-operational (which should in principle never occur).

The inhibitor will have two independent limit-switches, that are wired in series, and that confirm back to the safety interlock system that the jaw is in the inserted position. If the safety interlock system does not obtain this confirmation (within 2 sec from the moment of the original interlock) then it will provide another hardwired interlock to the dipole magnet system.

The beam inhibitor consists of a chamber, with a flange and bellow and a translation mechanism that allows a horizontal jaw to be inserted into the electron beam path, in a simple and reliable way, upon reception of that interlock signal. The translation mechanism is pneumatically driven outwards (extracted): when air pressure is present, and when the safety interlock signal is negative (NO interlock) then the jaw is (first driven and then) maintained in the extracted position.

In case the air pressure fails or the safety interlock signal is positive (that itself cuts the air-pressure on that pneumatic barrel) then the spring-loaded force implemented in that translation mechanism will result in driving the jaw to the inserted position. Some simple adjustments allow to obtain a suitable speed of that movement, i.e. faster than 1sec but not too

fast and not causing any strong mechanical shocks.

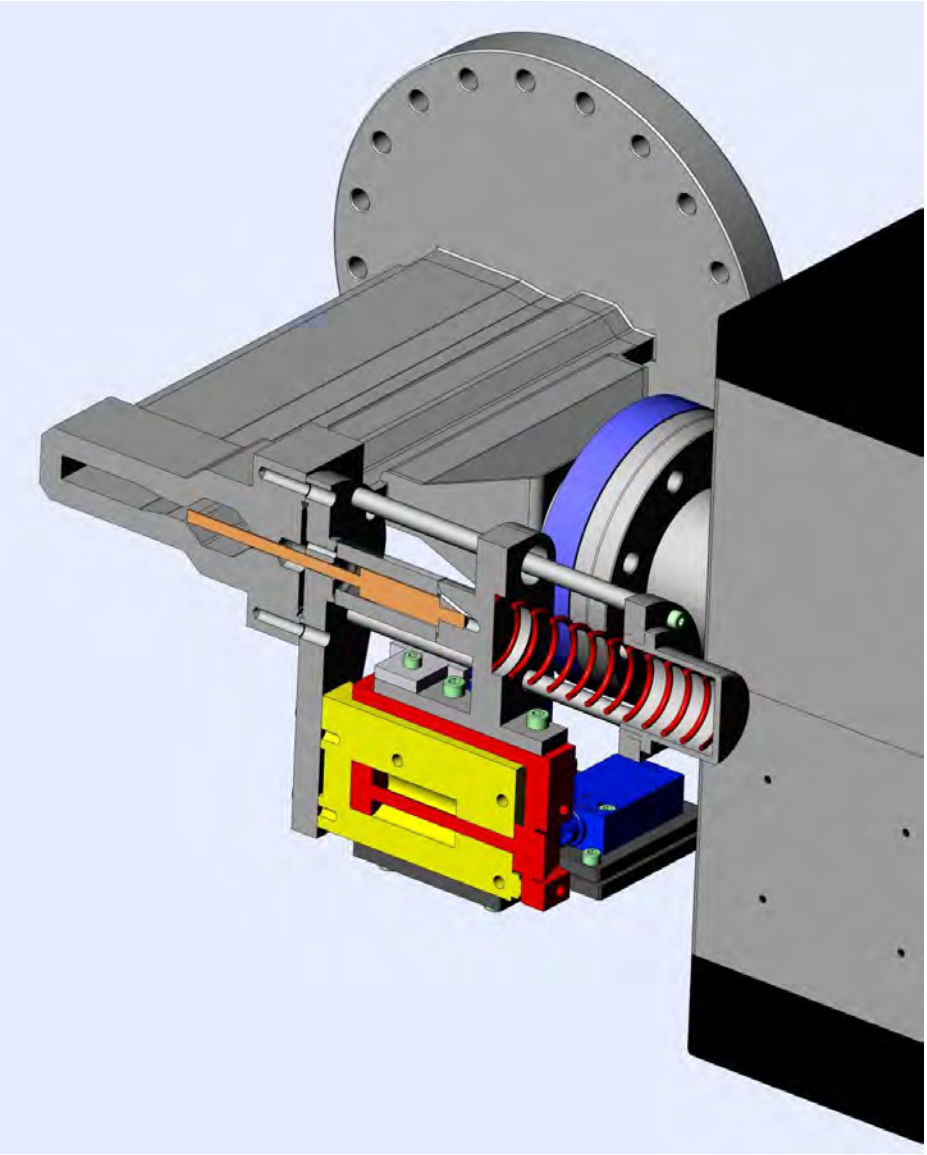

Figure 7.26: View of the beam inhibitor.

Table 7.15: Distribution of various devices & systems in the EBS ring.

| cell | chamber 12 | other-1 | other-2 | other-3 |
|---|---|---|---|---|
| 1 | | | | |
| 2 | | | | |
| 3 | | | | |
| 4 | | purity & fuse | scraper Hor. (I & E) | screen monitor |
| 5 | Current Transf. | VLM | | |
| 6 | Scraper Vert (U & D) | | | |
| 7 | Beam-Inhibitor | ID-emit (DL1A_5) | | |
| 8 | ID-9 bump | | | |
| 9 | ID-9 bump | | | |
| 10 | Current Transf. | | | |
| 11 | Scraper Hor. (I only) | BM-emit (DQ1D) | | |
| 12 | test-BPMs | | | |
| 13 | collimator | | | |
| 14 | | | | |
| 15 | Current Transf. | | | |
| 16 | | | | |
| 17 | | BM-emit (DQ1D) | | |
| 18 | | | | |
| 19 | | purity & fuse | | |
| 20 | | | | |
| 21 | | | | |
| 22 | | | | |
| 23 | | | | |
| 24 | collimator | | | |
| 25 | shaker | ID-emit (DL1A_5) | long. Cavity (?) | |
| 26 | shaker | | | |
| 27 | stripline-V spare | BM-emit (DQ1D) | | |
| 28 | stripline-H spare | | | |
| 29 | stripline-H spare | | | |
| 30 | stripline-H oper. | | | |
| 31 | stripline-V oper. | | | |
| 32 | | | | |

## 7.8 Visible Light Monitor

The visible light of the synchrotron light, generated by a suitable dipole in cell 5 (most probably DL1A_5), is to be transmitted into the existing laboratory in the experimental hall called (confusingly) “ID-4”. This lab exists since long and receives that visible light through a (10cm diameter) hole in the tunnel wall. However, with the EBS the trajectory (or path) of the visible light will be very different, simply due to the different position of the dipole.

In short, a new hole is to be drilled into that wall, most probably about 3m upstream with respect to todays position of the hole. Then a chicane structure is to be put in place that serves to transmit the light path into the lab

while completely shielding against the radiation inside the tunnel. In principle it should be possible to work continuously anywhere inside this lab, independent of the mode of operation of the EBS (injecting, stored beam current etc.).

This chicane structure is (most probably) made of two separate chicanes : one inside the tunnel, and one inside the lab. Each of these chicanes employs a set of mirrors (at least 2) **to** create a beam path shift, similar to a periscope (See Figure 7.27). These mirrors are inside a suitable shielding castle. Obviously the size, thickness, exact structure, materials etc. of this shielding castle can only be determined in close collaboration with and full approval from the radiation protection group. The most logical type of chicane would be vertical, i.e. the beam is shifted upwards by the 1st chicane (from 1.2m beam height to say 1.8m), and shifted downwards by the 2nd chicane inside the lab.

The path of the above described visible light beam is NOT in the SR-UHV environment. The separation from SR-UHV (to atmosphere) is made by a suitable window, typically of Saphire or quartz glass, on typically a CF40 or CF63 sized flange. Such window is most probably a off-the shelf component.

The most essential element in the Visible Light extraction system is the first mirror (called VLM here-after for Visible Light Mirror). It is the most delicate since inside the SR-UHV and also potentially exposed to the heatload from the X-rays (emitted by the same dipole, and on the same path as that of the visible light. It will have a vertical translation for controlling its position, a water-cooling system, and a set of thermo-couples for temperature measurements.

### Installation aspects

- The chamber that holds both the VLM and the window would be a special Chamber 4, assembled in the assembly area.
- The beam transmission part after the window will consist of 2 chicanes, with 4 mirrors inside and these mirrors would be in atmosphere. These mirrors will have (some) motorization controls. The box (or breadboard) that holds these mirrors may need to be pre-aligned by the colleagues of the alignment group. The angle and position of these mirrors need to be fine-adjusted by 2 colleagues of the diagnostics group.

An improved version would use various tubes and windows, not to pump a high-quality vacuum, but to protect (the light beam) against air turbulence and (the mirrors) against accumulation of dust particles.

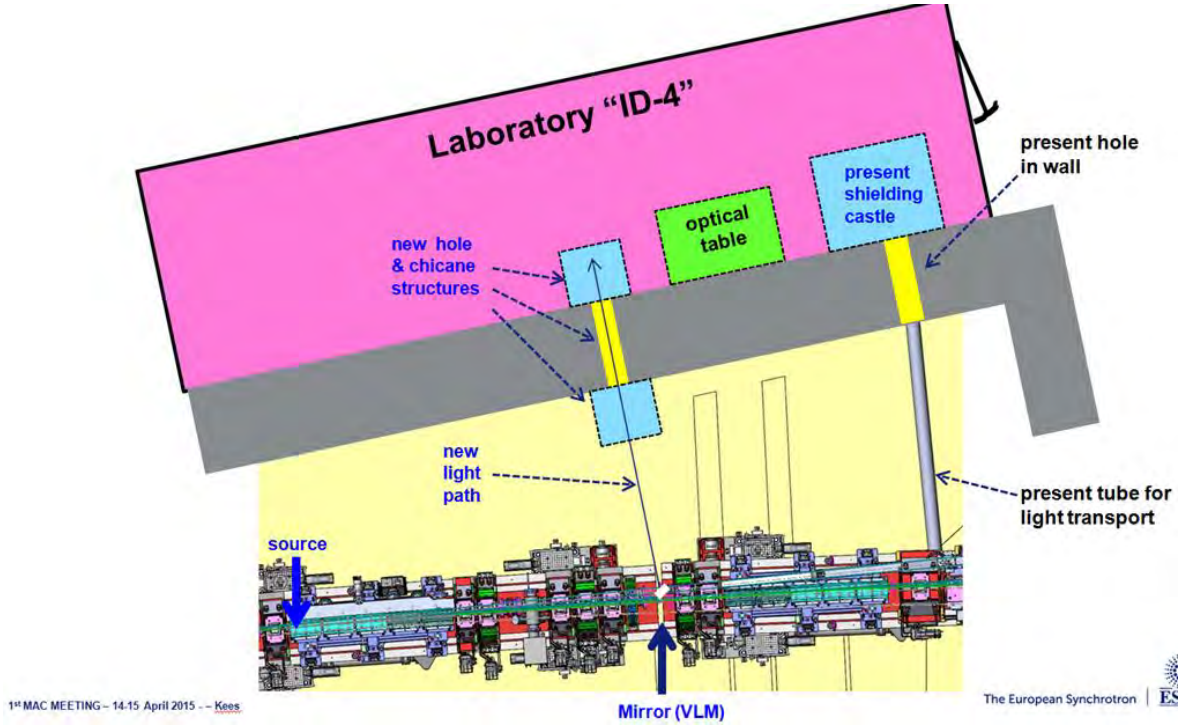


Figure 7.27: Sketch of the implementation of a Visible Light extraction and transmission system to direct that light suitably into the "ID-4" lab.

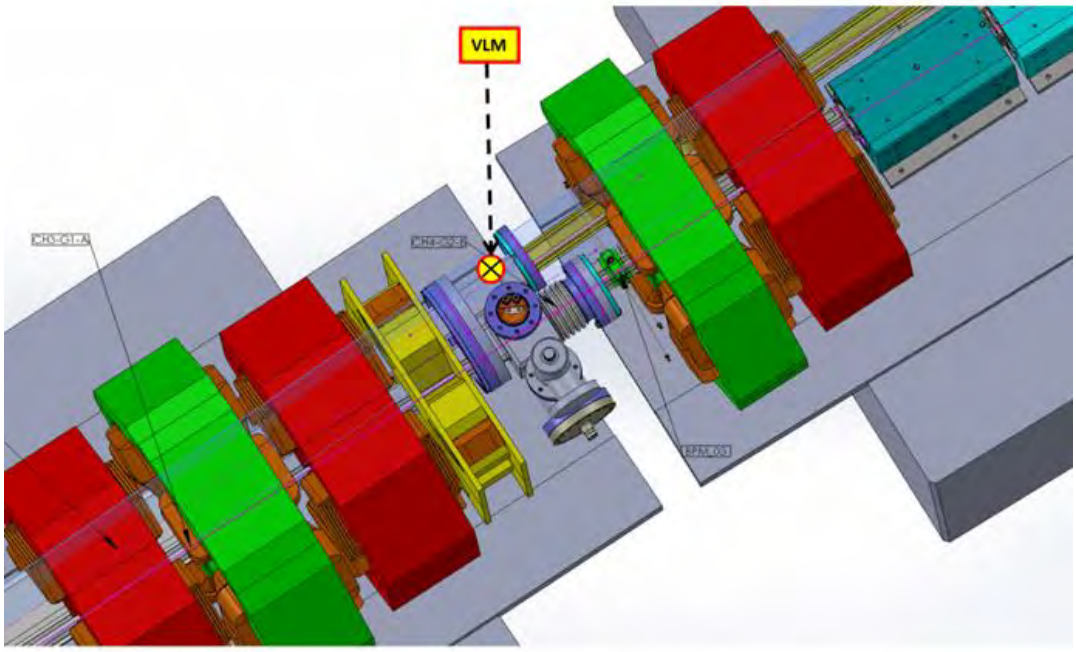


Figure 7.28: Position of VLM in Chamber 4 (cell 5).

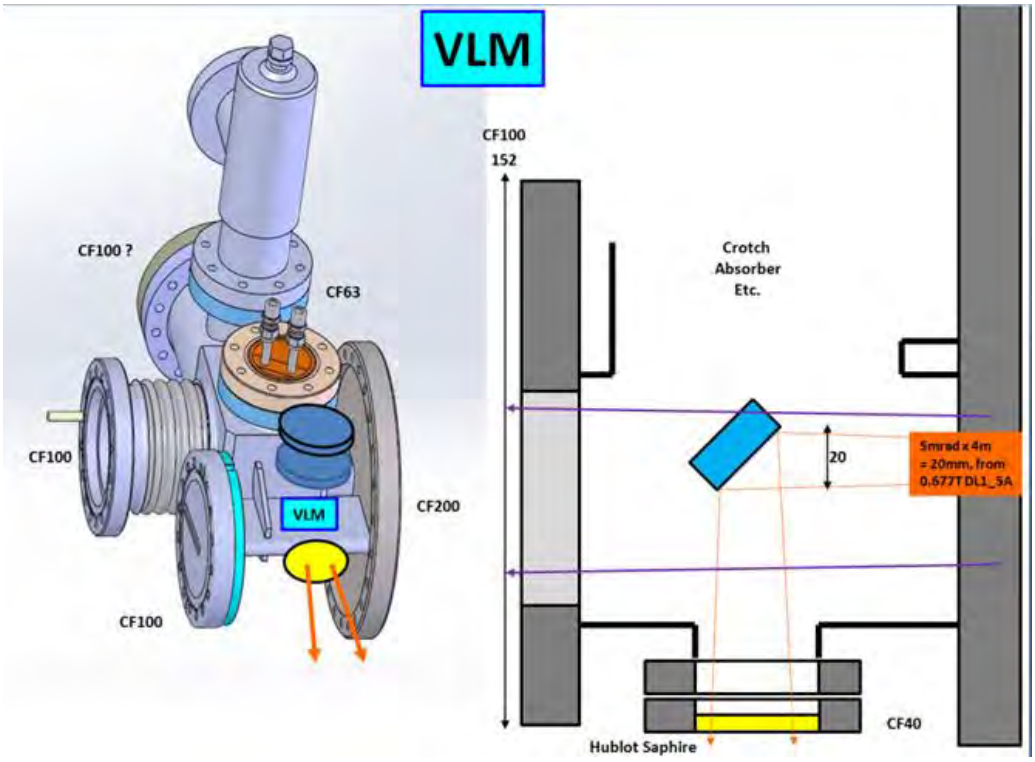


Figure 7.29: 3D and top view of the VLM.

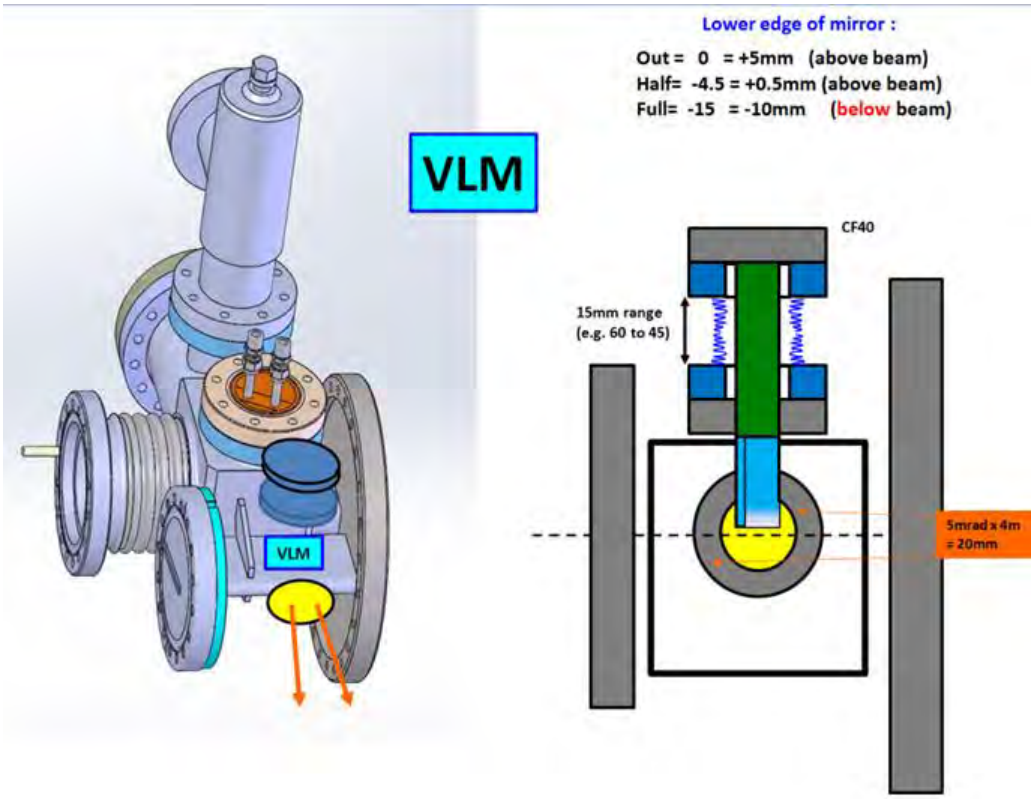


Figure 7.30: 3D and side view of the VLM.

# 8 Photon Sources

## 8.7 Introduction

The main goal of the ESRF-EBS is to reduce the horizontal phase space area of the photon beam produced by different X-ray sources installed in the storage ring. This is primarily achieved through the reduction by a factor of 30 of the 'dominant contributor', namely the horizontal emittance of the electron beam. The brilliance of the different undulator based sources will therefore be increased by a factor of about 30 above 10 keV. Figure 8.1 compares the brilliance of the same sources with the existing lattice (dashed lines) and the future ESRF-EBS lattice (plain lines).

Because the ESRF-EBS will operate at the same electron energy as presently (6 GeV),the majority of existing Insertion Devices (IDs) are directly usable in the new accelerator at least as a starting point. For a number of cases, the length of the straight section (SS) needs to be reduced from 6/7 m down to 5 m: the nominal length of ID straights in the new accelerator. An associated 'reverse engineering' is therefore needed for ID16, ID30, ID20, ID24, ID23 and ID32.

In addition, for the new accelerator, the distribution of the photon beam along the straight sections requires a new layout of absorbers. This new condition is due to the presence of dipoles which are much closer to the ID straights than in the present storage ring. For the existing in-vacuum undulators, this calls for substantial modifications of some mechanical parts inside the vacuum tank of the devices including the implementation of photon absorbers within flexible transitions at either ends of the undulator. All straight sections need to be checked to ensure the proper operation of the insertion devices.

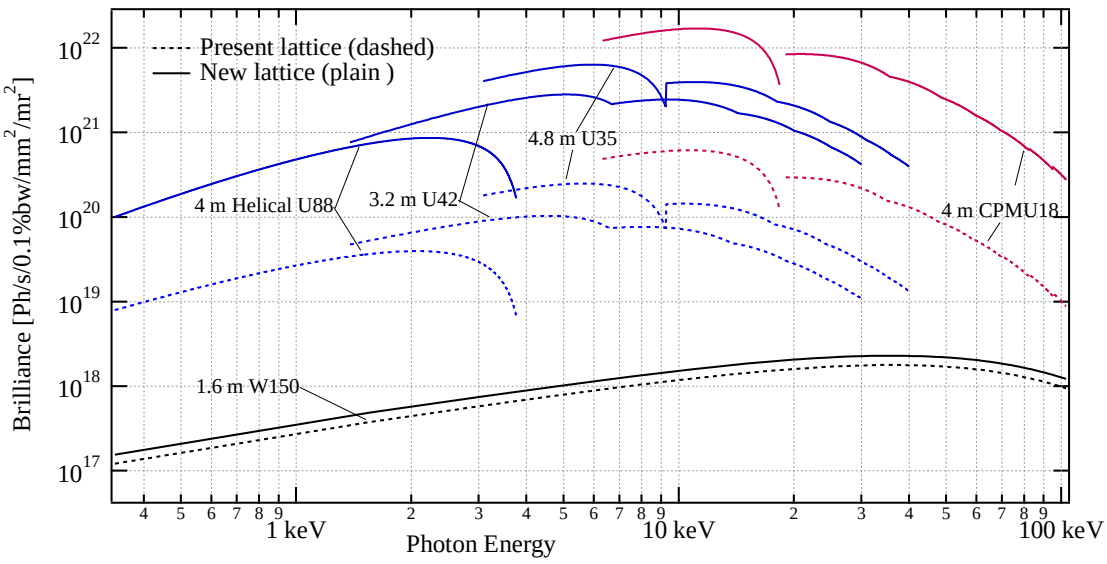


**Figure 8.1: Brilliance presently achieved with typical ID sources in the present lattice (dashed) and with the ESRF-EBS (plain).**

Finally, new engineering designs for undulator support structures are needed for the reverse engineering of the straight sections longer than 5 m including canted undulators. Moreover, these new designs redefine the basis for further upgrade of the IDs in the straights including conventional undulators, revolver undulators and in-vacuum undulators (IVUs) / Cryogenic Permanent Magnet Undulators (CPMUs) as well. This report focuses mainly of the technological efforts to be put on the migration to the new lattice.

A second important topic is the Bending Magnet sources, the main subject (or issue) being connected to the reduction of the magnetic field at the bending magnets in the new magnet lattice. The impact on the photon performance is largely visible above 30 keV with a significant reduction of photon flux. Consequently, a dedicated study on possible alternative based on Short Wigglers or Short high field Bending Magnets is required.

## 8.8 Insertion Device straight sections

For the Insertion Device straight sections the different tasks to be addressed and completed can be listed as follow:

- Reverse engineering of straight sections longer than 5 m.
- Canted straight sections (ID30, ID16, ID23).
- Normal (non-canted) straight sections (ID20, ID32, ID24).
- New ID arrangement in the 5 m long ID15 canted straight section.
- Two short segments in branch B.
- Modification of all existing IVUs/CPMUs to ensure compatibility with new storage ring, including modification of water cooling circuit.
- 10 IVUs.
- Integration of photon beam absorbers in IVUs/CPMUs.
- Modified flexible transitions at end of IVUS/CPMUS.
- New designs for IVUs/CPMUs for the EBS.
- New designs for standard and revolver undulator supports.
- Reverse engineering normal straight sections.

For ID20 and ID24, the 5 m straight section in the new ring will be filled with existing segments and/or existing undulator assemblies mounted on revolver support in order to keep a high flexibility as presently. The ID distribution at present and in the future accelerator for ID20 and ID24 is presented in **Table 8.1** and **Table 8.2**.

Table 8.1: Present and future ID layout in ID20 (U: standard undulator, RVU: revolver undulator).

| **SS length [m]** | **6** | | | | **5** | | |
|---|---|---|---|---|---|---|---|
| **ID type** | U | RVU | RVU | RVU | RVU | RVU | RVU |
| **Period [mm]** | 26 | 26/32 | 26/32 | 26/32 | 26/32 | 26/32 | 26/32 |
| **ID length [m]** | 1.4 | 1.4 | 1.6 | 1.6 | 1.6 | 1.6 | 1.6 |
| **Lattice** | Present | | | | ESRF EBS | | |

Table 8.2: Present and future ID layout in ID24 (U: standard undulator, RVU: revolver undulator).

| **SS length [m]** | **6** | | | | **5** | | |
|---|---|---|---|---|---|---|---|
| **ID type** | U | U | RVU | U | U | RVU | RVU |
| **Period [mm]** | 27 | 27 | 27/32 | 32 | 27 | 27/32 | 27/32 |
| **ID length [m]** | 1.6 | 1.6 | 1.4 | 1.4 | 1.6 | 1.6 | 1.6 |
| **Lattice** | Present | | | | ESRF EBS | | |

### ID24

For ID24, the use of the dependence of the photon energy versus horizontal angle (through dispersive optics) required (a priori) a dedicated study owing to the expected smaller electron beam divergence in the new accelerator. The study suggests that the impact of the smaller horizontal divergence of the electron beam (10 µrad presently versus 5 µrad in the future) is very limited and the beamline should benefit from a much better correlation photon energy-horizontal angle with the new accelerator [1].

### ID32

ID32 makes use of helical undulators of type APPLE II. The present 6 m straight section is fully used with 3 segments of period 88 mm. The migration to 5 m straight section needs the construction of a 2.1 m device.

**Table 8.3: Present and future ID layout in ID32.**

| **SS length [m]** | **6** | | | **5** | |
|---|---|---|---|---|---|
| **ID type** | HU | HU | HU | HU | HU |
| **Period [mm]** | 88 | 88 | 88 | 88 | 88 |
| **ID length [m]** | 1.6 | 1.6 | 2.5 | 2.1 | 2.5 |
| **Lattice** | Present | | | ESRF EBS | |

### Canted straight sections

The preservation of canted straight sections with the same canting angles as presently is a primary strong requirement. The canting angle will be achieved at both sides of the straight section thought a reduction of the deflection angle at the neighbouring DL magnets. More precisely , the high field DL1 module which is the closest to the straight section will be updated with a reduced number of magnet blocks to provide the required canting angle of 2 mrad (ID15), 2.2 mrad (ID30) or 2.7 mrad (ID16). The central deflecting magnet will be the same as used presently ( compact permanent magnet dipole with -4 mrad (ID15), -4.4 mrad (ID30) and -5.4 mrad (ID16). For the ID23 canted straight section the full canting sequence of 0.75 mrad | -1.5 mrad |0.75 mrad can be achieved with the existing narrow permanent assemblies without modifying the neighbouring DL.

### ID30

The present and new ID distribution in the ID30 SS in presented in **Table 8.4**. The proposed layout is based on new standard undulator supports with a nominal length of 2.3 m as shown in **Figure 8.2** (drawing 88.80.0095).

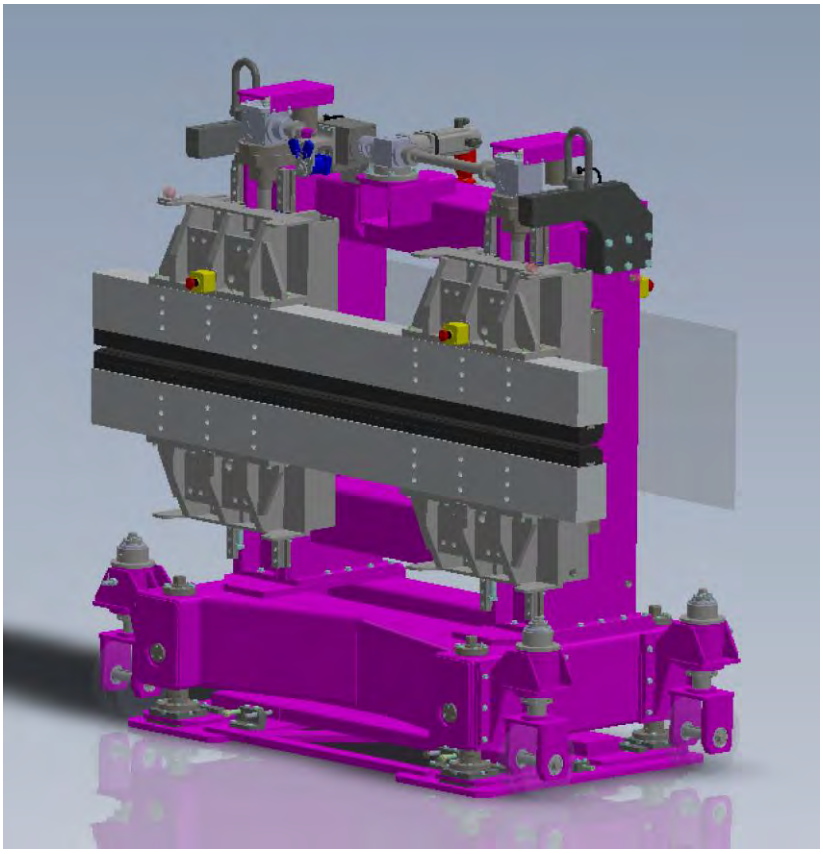

Figure 8.2: 3D view of a 2.3m long standard undulator support.

Table 8.4: Present and future ID layout in the ID30 canted straight section.

| **SS length [m]** | **6** | | | | **5** | |
|---|---|---|---|---|---|---|
| **Canting angle [mrad]** | 2.2 | | -2.2 | | 2.2 | -2.2 |
| | Branch A | | Branch B | | Branch A | Branch B |
| **ID type** | U | U | U | U | U | U |
| **Period [mm]** | 21.2 | 21.2 | 35 | 35 | 21.2 | 21.2 |
| **ID length [m]** | 1.4 | 1.4 | 1.4 | 1.4 | 2.3 | 2.3 |
| **Lattice** | Present | | | | ESRF EBS | |

### ID16

The 2.5 m long IVU in the ID16 branch needs to be replaced with a 2 m long IVU with the same period. For the second branch a 2.3 m long revolver (2 positions, main drawing 88800150) will be used to replace the two short revolvers presently in use (Table 8.5).

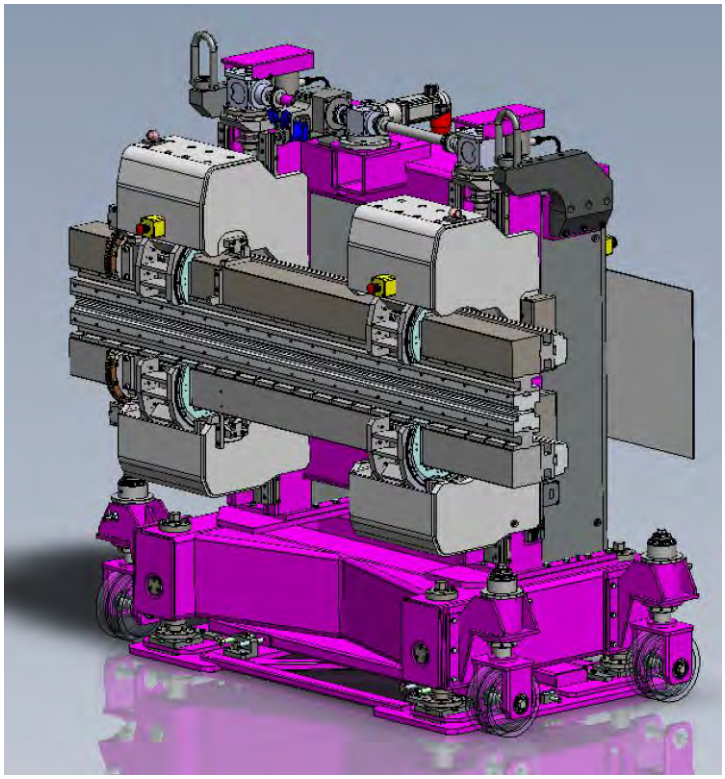

Figure 8.3: 3D view of a 2.3m long revolver undulator support.

Table 8.5: Present and future ID layout for the ID16 canted straight section.

| **SS length [m]** | **6** | | | **5** | |
|---|---|---|---|---|---|
| **Canting angle [mrad]** | 2.7 | -2.7 | | 2.7 | -2.7 |
| | Branch A | Branch B | | Branch A | Branch B |
| **ID type** | IVU | RVU | RVU | IVU/CPMU | RVU |
| **Period [mm]** | 26 | 18.3/22.4 | 18.3/22.4 | 26/20 | 18.3/22.4 |
| **ID length [m]** | 2.5 | 1.4 | 1.4 | 2 | 2.3 |
| **Lattice** | Present | | | ESRF EBS | |

### ID15

The ID segments of the canted ID15 straight section is presented in Table 8.6 for the present configuration and the expected scheme in the new accelerator. The first branch will include a short high field wiggler with a period of 76 mm (length 0.4 m), and a short IVU/CPMU with a magnetic length of 1.5m (Figure 8.4, main drawing 88800390).

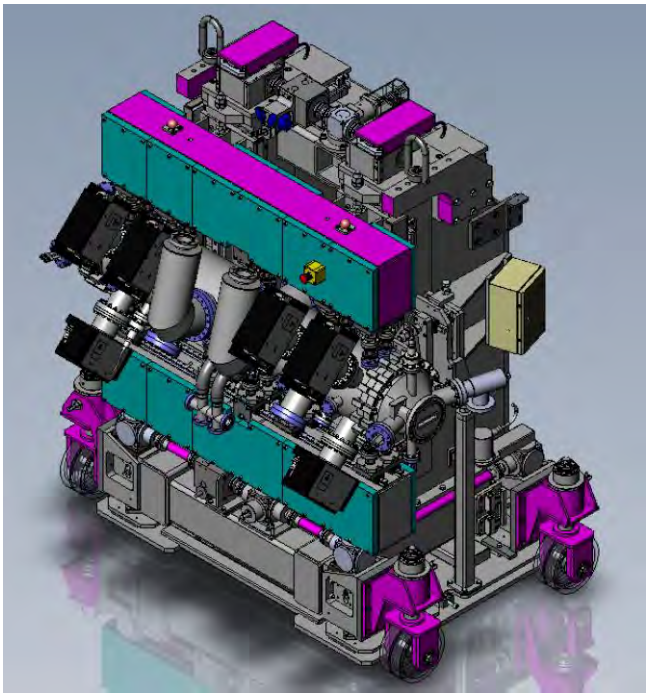

Figure 8.4: 3D view of a 1.5 mm long IVU/CPMU.

Table 8.6: Present and future ID layout for the ID15 canted straight section.

| **SS length [m]** | **5** | | **5** | | |
|---|---|---|---|---|---|
| **Canting angle [mrad]** | 2 | -2 | 2 | | -2 |
| | Branch A | Branch B | Branch A | | Branch B |
| **ID type** | IVU | IVU | CPMU | W | IVU |
| **Period [mm]** | 22 | 20 | 18 | 76 | 20 |
| **ID length [m]** | 2 | 2 | 1.5 | 0.5 | 2 |
| **Lattice** | Present | | ESRF EBS | | |

### ID23

The adaptation of ID23 results only from the removal of the present RF cavities at the middle of the straight section (Table 8.7). The existing canting magnets and IDs will be used in the new accelerator at the starting point.

**Table 8.7: Present and future ID layout in the ID23 canted straight section.**

| **SS length [m]** | **7** | | | **5** | |
|---|---|---|---|---|---|
| **Canting angle [mrad]** | 0.75 | RF cavities | -0.75 | 0.75 | -0.75 |
| | Branch A | | Branch B | Branch A | Branch B |
| **ID type** | U | | U | U | U |
| **Period [mm]** | 20.2 | | 35 | 20.2 | 35 |
| **ID length [m]** | 1.6 | | 1.6 | 1.6 | 1.6 |
| **Lattice** | Present | | | ESRF-EBS | |

## 8.9 Anticipation of future ID demand

### Engineering of support structures

Before the completion of the accelerator construction, the demand for new undulators needs to be anticipated. A prominent topic will be the more intensive use of short period small gap devices such as IVUs or CPMUs. A new design for 2 m long IVU/CPMU has been completed, including the following main new features:

- New arrangement of connecting rods between the outer main girders and inner magnet girders to ensure minimum impact on field quality under magnetic load.
- Possibility to support the vacuum chamber on the ground floor and align vertically the undulator on the beam without constraining the neighbouring bellows and vacuum chambers.
- Remote control of the pitch along the beam direction.
- Improved compatibility between IVU and CPMU versions.
- Parameterized engineering drawings for the magnetic assembly with periods from 10 mm to 21 mm.
- New cooling to ensure higher operation reliability.

It is expected to launch an anticipated construction of 4 IVU/CPMU by end of 2018.

Main drawing for the new 2 m long IVU/CPMU: 88800240.

### ID minimum gaps

The minimum ID gaps reachable in the new accelerator lattice will depends mainly of the performance of the two electron beam collimators to be installed in cells 12 and 24. Indeed, the residual beam loss pattern at each ID straight section will define the required beam stay clear compatible with negligible radiation induced demagnetization of the permanent magnet arrays. Dedicated studies are being done with the present accelerator for the validation of Touschek loss models in view of building a robust model for the new ring.

At the restart of the new accelerator, the minimum ID gap will be the same as presently. Further minimum gap reduction will only be clearly defined after the first experimental optimization of the beam loss pattern.

## 8.10 Bending magnet sources

As a side effect of the reduction of the magnetic field at dipoles the photon performances at bending magnet beamlines are directly affected (reduced) in the hard X-ray region in particular. To overcome the difficulty, three types of alternative sources have been studied, all these magnetic structures are implemented between the combined function magnet DQ2C and the high gradient quadrupole QF8 with a maximum length of 110 mm (see **Figure 8.5**). Considering the different X-ray sciences and associated instrumentation developed in the past at BM beamlines , it becomes obvious that a single type of source cannot be adopted. As a result, the choice of the source has been left at the level of each beamline in order to provide an optimum matching of the source with the existing optics and science carried out.

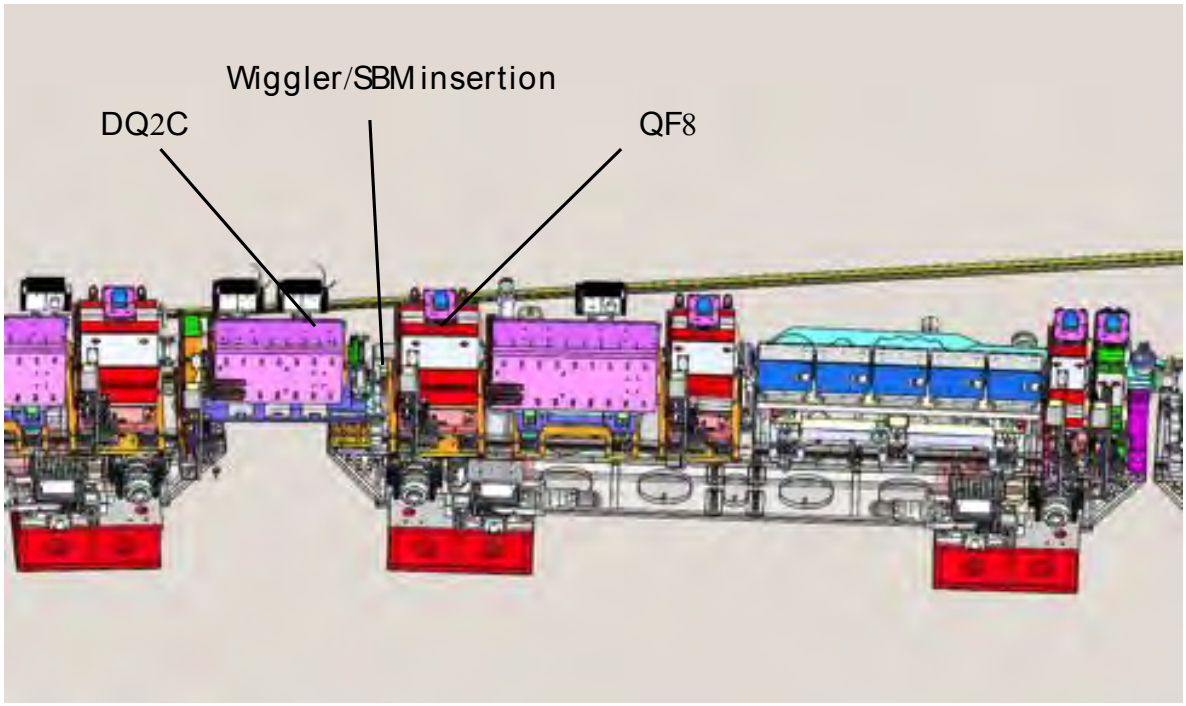


**Figure 8.5: Location for the insertion of short wigglers/bending magnet.**

The proposed structures are the following:

- Short bending magnet (SBM).
- Two pole wiggler (2PW).
- Three pole wiggler (3PW).

All sources will be fixed gap devices with a maximum field of 0.86 T: the same field as in the present high field dipoles to avoid modification of the existing lead shielding at the optics hutches. The only exception will the High field 3PW for BM18 (3PW18) with a peak field of 1.56 T.

The main parameters of the different sources are presented in **Table 8.8**. The fan axis depend on the adopted structure. For the SBM case, the best compensation scheme base on the re-adjustment of the neighbouring DQs lead to a mean axis of -6.96 mrad. For the 2PW case, the choice of the wiggler field polarity change also the mean X-ray axis [2].

Table 8.8: Main parameters of the new sources for the bending magnets.

| Parameter | SBM | 2PW | 3PW | 3PW18 |
|---|---|---|---|---|
| **Maximum field [T]** | 0.86 | 0.86 | 0.86 | 1.56 |
| **Length [mm]** | 63 | 102 | 102 | 109 |
| **X-Ray fan axis [mrad]** | -6.96 | -7/-8.7 | -7.85 | -7.85 |
| **Max. fan angle [mrad]** | 2 | 1.7 | 1.5 | 2 |
| **P.m. Material** | $Sm_2Co_{17}$ | $Sm_2Co_{17}$ | $Sm_2Co_{17}$ | $Sm_2Co_{17}$ |
| **Pole Material** | Pure Iron | Pure Iron | Pure Iron | Pure Iron |

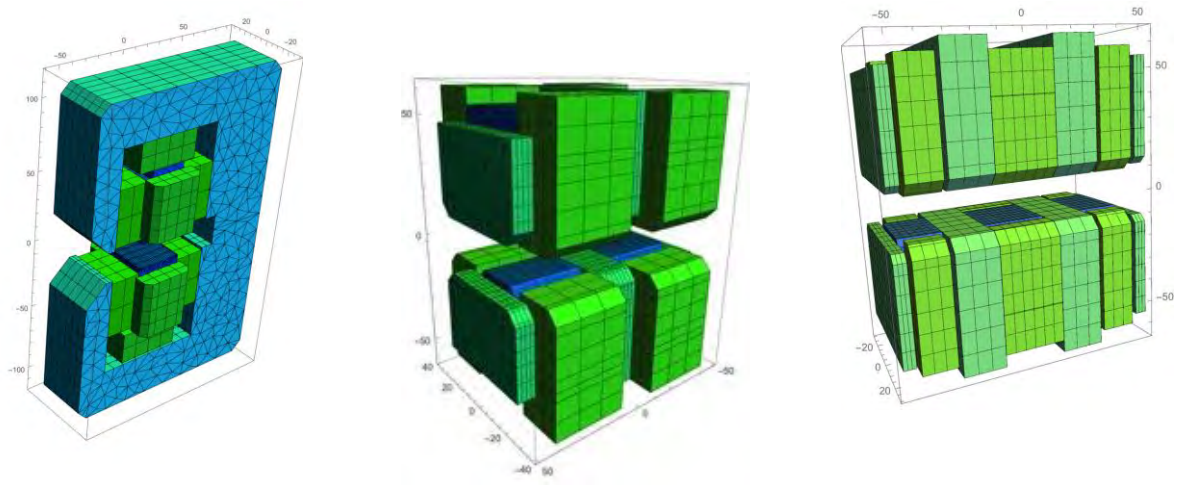

SBM 2PW 3PW

Figure 8.6: 3D view of the proposed magnetic structures.

Table 8.9: Electron beam parameters at the middle of the wiggler / SBM.

| | Horizontal | Vertical |
|---|---|---|
| $\beta$ [m] | 1.8 | 2.57 |
| $\alpha$ [] | -2.02 | 1.93 |
| Dispersion $\eta$ [m] | 0.018 | 0 |
| Dispersion derivative $\eta'$ [] | 0.0154 | 0 |
| R.m.s size $\sigma$[ µm] | 23 | 3.6 |
| R.m.s. Divergence $\sigma'$[µrad] | 24 | 3 |

### Photon flux

The photon flux collected in an aperture of 1 mrad x 0.5 mrad (H x V) from the different sources is presented in Figure 8.7 for an electron beam current of 200 mA. The photon flux is not dependent on the electron beam emittance. Compared to the usual bending magnet type sources the 3PW and 2PW provide higher flux due to the number of poles contributing to the flux. For the 3PW at high energy, the flux is similar to that of a dipole due to the low contribution to the flux from the side poles at high photon energy.

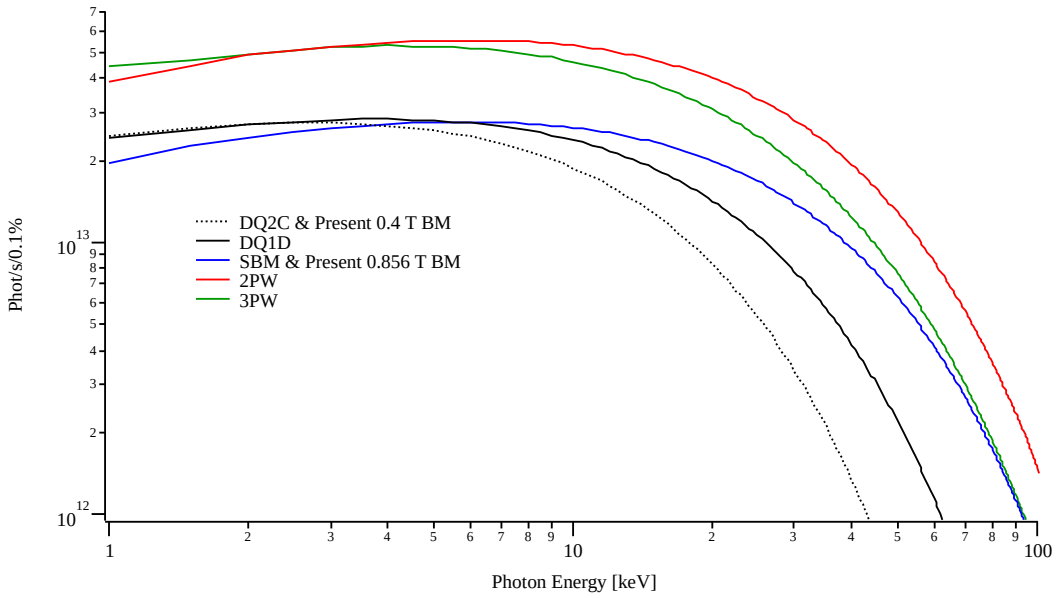


**Figure 8.7: Photon flux collected in an angular aperture of 1 mrad x 0.5 mrad (H x V) for the different possible sources.**

### Brilliance

Compared to the present situation, the increase in brilliance of the different new BM type sources is primarily a consequence of the reduced horizontal of the electron beam and also the reduced beta function in the vertical plane. **Figure 8.** shows the resulting brilliance achieved with the different proposed BM type sources (SBM, 2PW, 3PW and neighbouring DQs, plain lines) and the present 0.86 T bending magnet source (dotted line).The electron beam current is 200 mA in all cases.

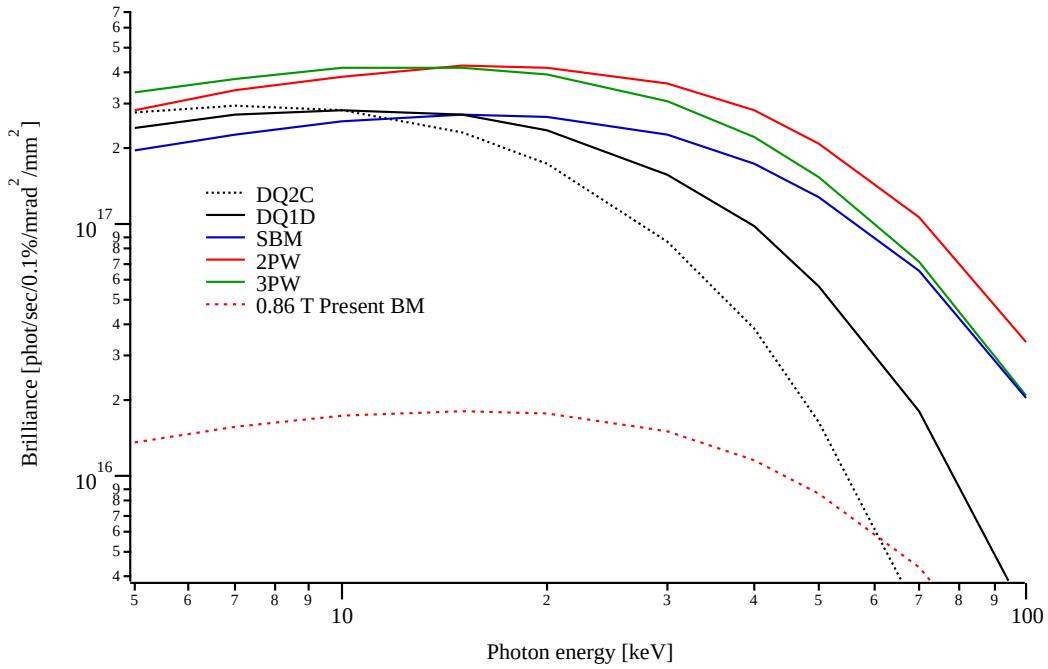


**Figure 8.8: Brilliance of the different possible BM type sources for the ESRF EBS (plain lines) and present high field BM (dotted).**

### Source position

The longitudinal position of the new sources (wigglers or SBM) will not be the same as with the present dipoles, the difference is substantial and needs to be taken into account for the adaptation of the optical elements in the different beamlines (**Table 8.10**). Moreover, at the front end, the horizontal position of X-ray fan will also be slightly different and depends on the source type. In **Table 8.10** the reference is taken with the present high field BM at -9 mrad. Apart for the 2PW in configuration B, the new sources are radially slightly moved further away from the ring.

**Table 8.10: Changes in longitudinal and horizontal position of the new source with respect to the present BM at -9 mrad ( high field).**

| | Present | EBS | | | |
|---|---|---|---|---|---|
| **Source** | BM @ -9 | 3PW | SBM | 2PWA | 2PWB |
| **Distance Front End to source [m]** | 22.5431 | 25.516 | 25.516 | 25.516 | 25.516 |
| **Fan axis [mrad]** | -9.00 | -7.850 | -6.960 | -7.050 | -8.650 |
| **Change in longitudinal source** | 0 | 2.973 | 2.973 | 2.973 | 2.973 |
| **Horizontal position at FE [mm]** | -203.86 | - | - | - | - |
| **Change in horizontal position at FE [mm]** | 0 | 3.43 | 26.13 | 23.84 | -16.99 |

## References

[1] About transverse distribution of undulator beams outside on axis resonance: 02-16-IDM.

[2] Implementation of Short Wigglers as photon sources for the Bending Magnet Beamlines in the new ESRF lattice: 01-15/IDM.

# 9 Booster and Storage Ring Injection

## 9.7 Present Status

The layout of the existing booster synchrotron is given in Figure 9.1. The circumference is 299.16 m and it has a threefold symmetry. The three straight sections are required for the location of the cavities, the injection and the extraction.

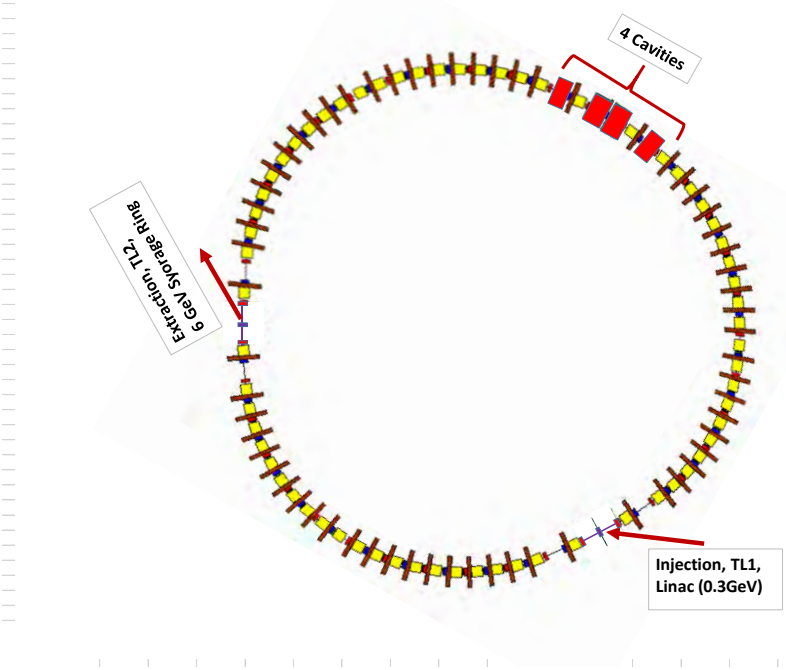


Figure 9.1: General layout of the ESRF booster synchrotron.

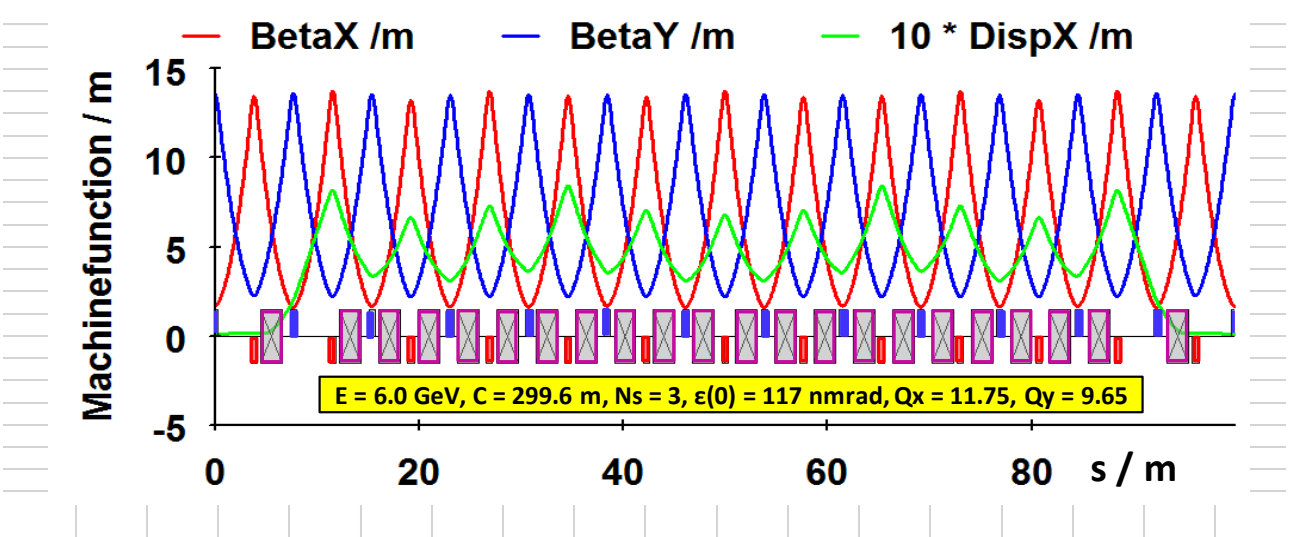


Figure 9.2: Machine functions within an achromat of the booster synchrotron with the main parameters. The explanation of the different components is given in Figure. 9.3.

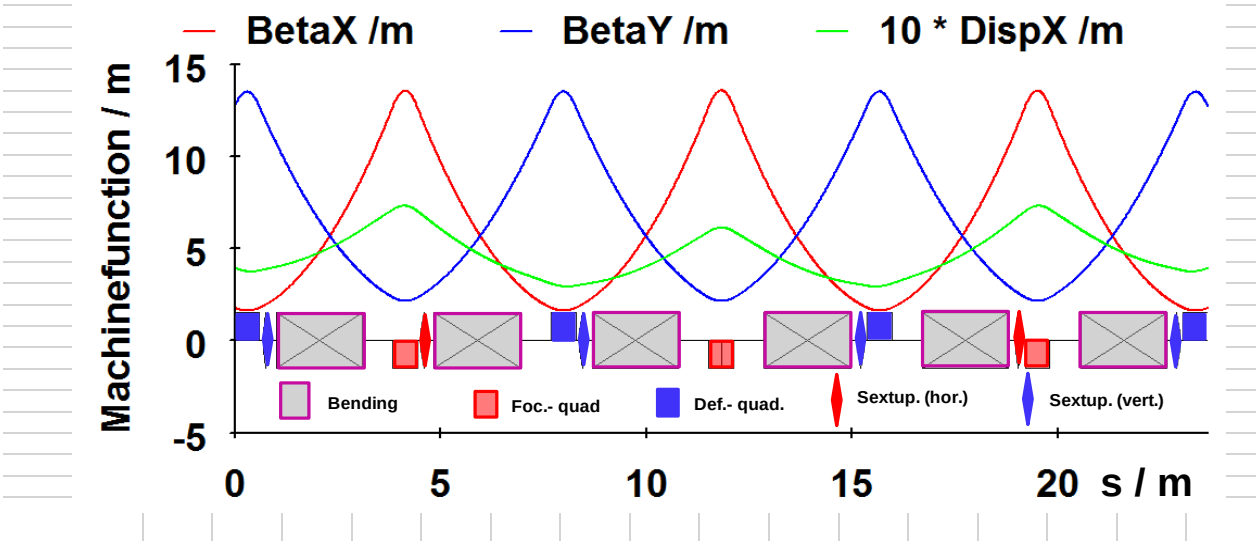


Figure 9.3: The machine function in the middle of the achromat with the symmetry point.

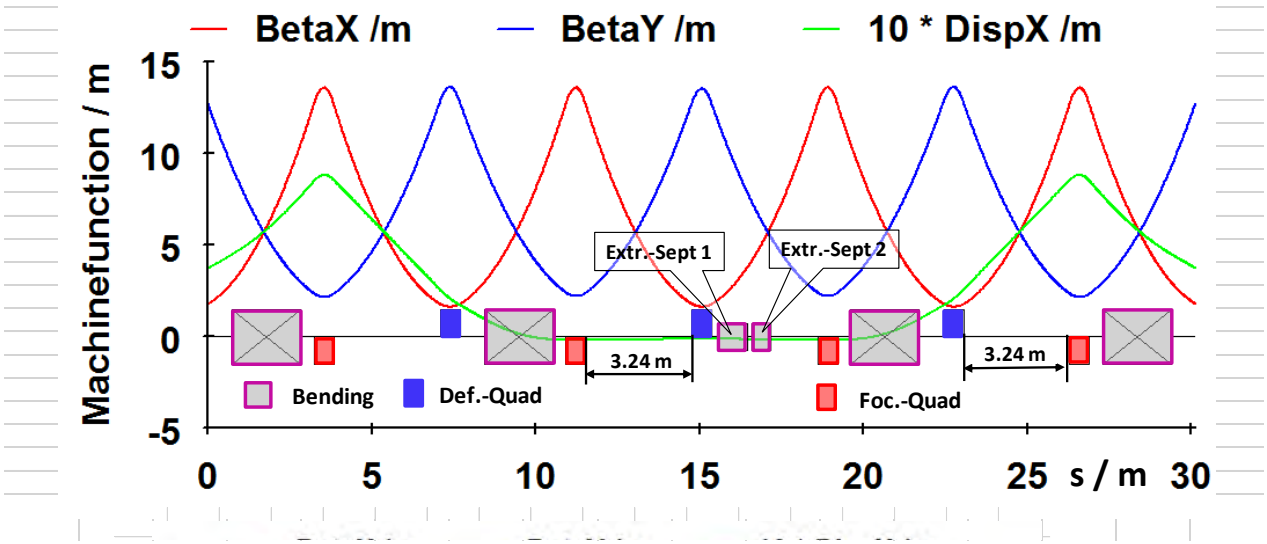


Figure 9.4: The machine functions within the straight areas. The length of the straights for the accommodation of the cavities and the injection as well the extraction elements is 3.24 m. Within this area there aren't any sextupoles. The location of the extraction septums are given.

The machine functions in an achromat (1/3 of the circumference) are given in Figure 9.2. The lattice exist of a FODO-structure with a symmetry point in the middle of the arc (see Figure 9.3). The arrangement of the magnets within the straight sections are presented in Figure 9.4.

The cross section at the end of TL2 is roughly 1.5 mm (1 sigma). This cross section injected to the EBS storage ring is too large and would result in not acceptable electron losses. Hence an upgrade of the booster synchrotron has to be done with the following possibilities:

- Increase of the horizontal tune
- Operating the booster 'off momentum'
- With a fully coupled beam.

## 9.8 Injector upgrade: off-momentum operation

The limited dynamical aperture provided by the SR lattice makes it important to reduce as much as possible the horizontal beam size in order to improve injection efficiency. Transverse emittance can be reduced by working of momentum. If the RF frequency is set above the design value, horizontal emittance is partially transferred to the longitudinal plane, and for the nominal booster optics, this transfer is described in the following Figure 9.5.

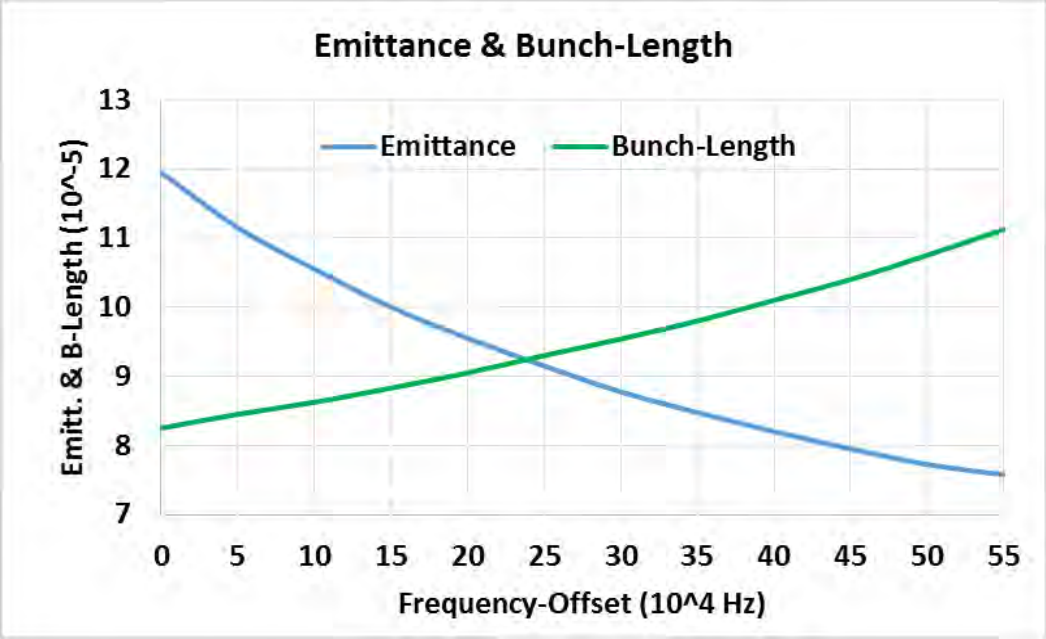


**Figure 9.5: The change of the emittance and bunch length as a function of the RF-frequency.**

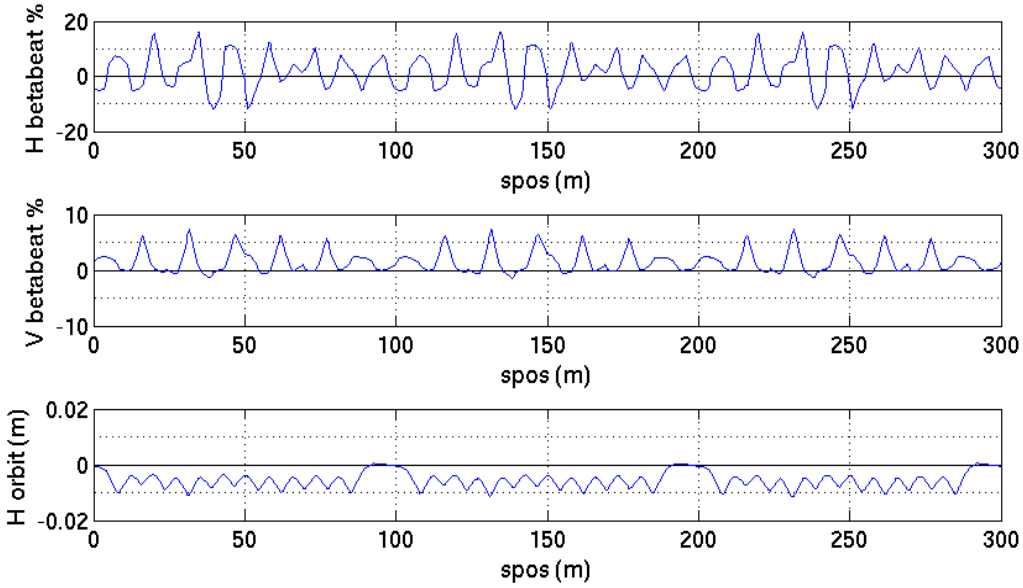


**Figure 9.6: Beta-beat and horizontal orbit induced by a frequency offset of +40kHz.**

The drawback of this method is a substantial bunch lengthening that can be minimised by increasing the RF voltage. Furthermore, as the accelerator is operated off momentum the

closed orbit follows the dispersion function and goes of axe in sextupoles. The resulting beta-beat is then reducing the dynamical aperture. The good compromise between emittance reduction, bunch lengthening, beta-beat increase, and closed orbit deviation, is for a frequency offset of 40kHz resulting in an emittance reduction of 32%.

## 9.9 Injector upgrade: Fully coupled beam

Most efficient to reduce horizontal emittance is to equalise the fractional parts of vertical and horizontal tunes leading to a fully coupled beam. As in normal conditions vertical emittance is much smaller than horizontal one, for the fully coupled beam we get:

$$\epsilon_{Hcoupled} \approx \epsilon_{Vcoupled} \approx \frac{\epsilon_{Huncoupled}}{2}$$

The resulting increase of vertical beam size is not an issue as the beam is injected on axe vertically and the beam size is still much smaller than the vertical dynamical aperture.

The combined effect of these two beam manipulations has been tested and measured by performing beam twiss parameters measurement in the transfer line between the booster and the storage ring. The measurements performed by scanning beam size versus the strength of a given quadrupole is in agreement with theoretical predictions with large error bars on the measurement (see Figure 9.7 and Table 1.)

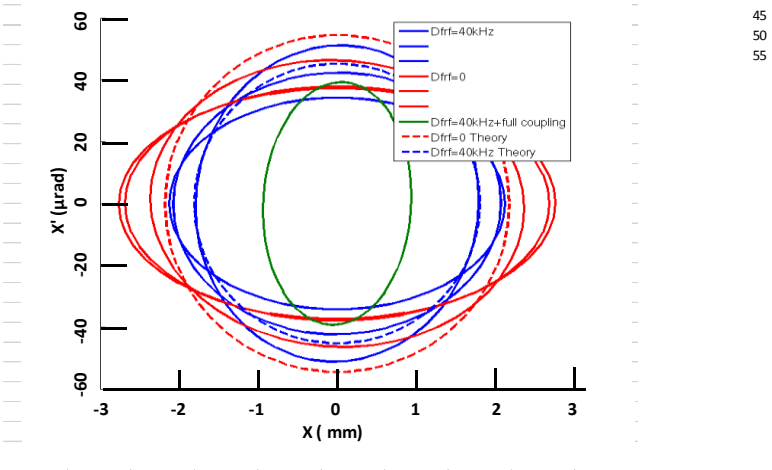


**Figure 9.7: Phase space reconstruction from the measurement compared to tracking results. Three measurements for the case Dfrf=0 and three measurements for the case Dfrf=40kHz are presented. The quality of the measurement can be evaluated considering the dispersion between the three samples and their comparison with theoretical phase space.**

**Table 9.1: Emittance of the booster synchrotron applying an RF frequency offset and full transverse coupling.**

| | Dfrf=0Hz | Dfrf=+40Hz | Dfrf=+40Hz + coupling |
|---|---|---|---|
| ?h measured (nm.rad) | **105** | **86** | **37 (Error bar unknown)** |
| ?h tracking | **120** | **82** | **41** |

## 9.10 Injector upgrade: Increasing the horizontal tune

It is also foreseen to reduce emittance by increasing the horizontal tune by one integer. Simulation showed going from 11.75 to 12.75 for the horizontal tune allows to gain 15% on the emittance. It will nevertheless reduce the dynamical aperture of the Booster significantly meaning it is not sure whether it is possible to combine all the different schemes to reduce emittance keeping the beam losses to a minimum. The twiss functions we expect to operate with are presented on Figure 9.8.

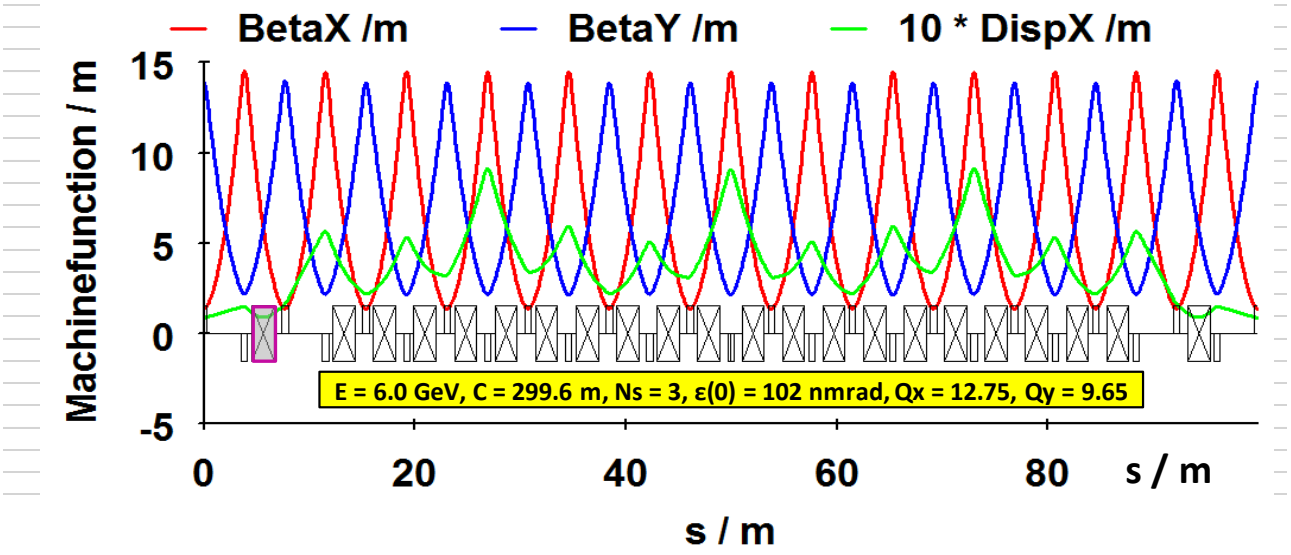


**Figure 9.8: Twiss functions for one of the three super periods of the booster, horizontal tune has been increased by one integer. The QF settings have been changed from (Figure 9.2) k=0.7336 to 0.7738 and for QD from -0.6534 to -0.6601.**

As a result, combining all this emittance reduction schemes we can reduce horizontal emittance down to 0.34nm.rad, if the combination is possible, which has not been proven yet.

## 9.11 Injector Upgrade: Phase space shaping in TL2 using a sextupole

Adding a sextupole in the TL2 transfer line with a +-90Deg phase advance with respect to SR injection septum, can allow to shape the beam and better match phase space available in the injection septum. The triangular deformation induced by the sextupole can better accommodate to the edge defined by the septum blade in phase space as shown in Figure 9.9.

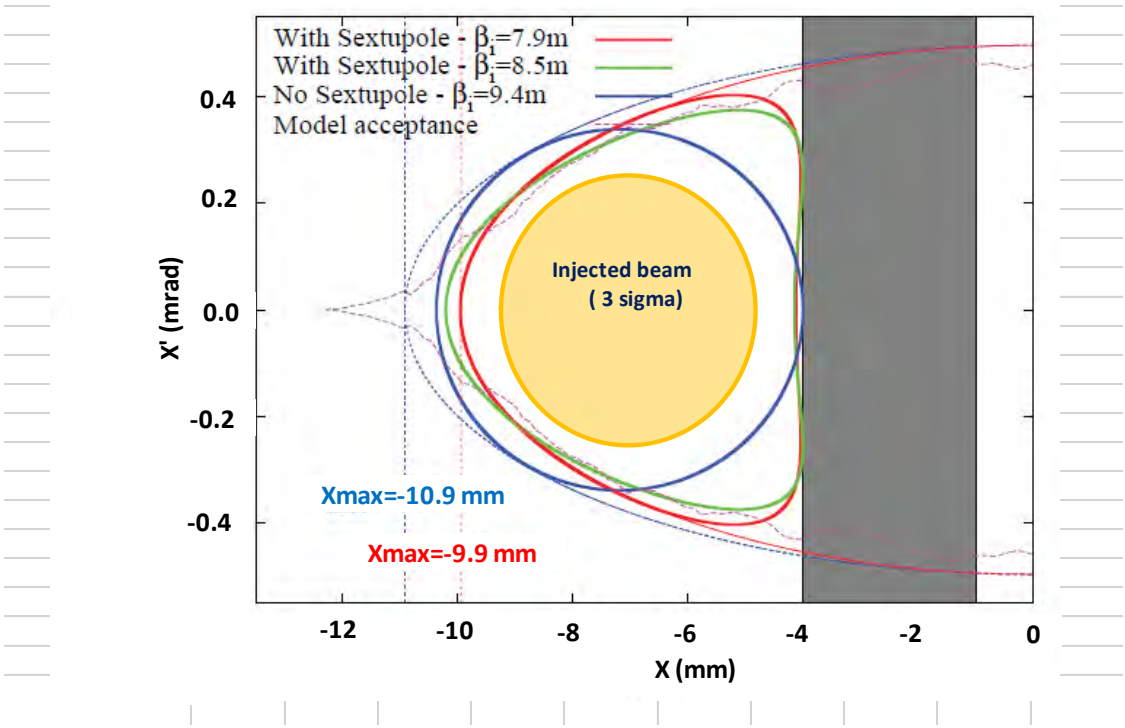


**Figure 9.9: Phase space optimisation at septum location, using a sextupole. Comparison to standard case. A reduction of about 1mm for the maximum oscillation amplitude of injected particles is expected.**

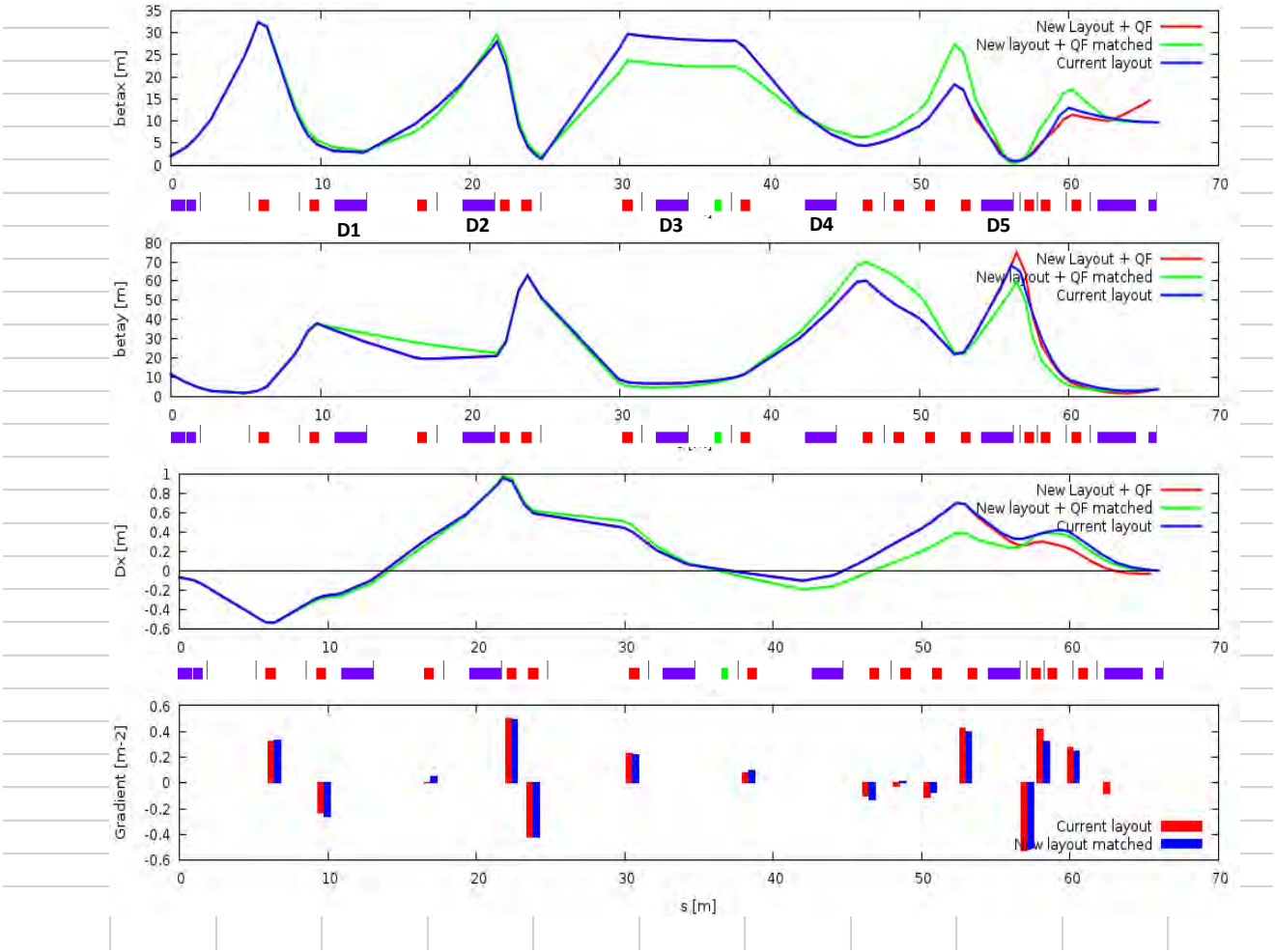


**Figure 9.10: TL2 optics adapted to beam shaping. In this case the normalised integrated sextupolar strength required is $K_2L$=5.35 $m^{-2}$.**

For this phase space shaping to be efficient, the following constrains must be respected regarding matching in the transfer line:

- H phase advance between the sextupole and septum is 90 + n x180 deg.
- H beta as large as possible at sextupole location and beta as small as possible. It allows to limit the sextupolar strength required, and limit the induced distortion in the vertical plane.
- Dispersion should be 0 at the sextupole location.

The resulting optimised optic of the TL2 transfer line, including the sextupole, is presented in Figure 9.10.

## 9.6 Injector upgrade: Booster circumference reduction

SR and SY RF frequency are driven by the same master source and their length in then related true their harmonic number: 992 for the SR and 352 for the Booster. As the SR length is changing the RF frequency must be increased from 352.2000 MHz to 352.372, and therefore the booster circumference must also adapt to this new RF frequency.

As described above, it is foreseen to work off frequency by +40 kHz in order to reduce horizontal emittance. We then want the booster length to be consistent with an RF frequency of 352.372 - 0.04 = 352.332 MHz.

The corresponding length, for an unchanged harmonic number of 352 is 299.5099 m, leading to a change of circumference of -0.1123 m if the theoretical circumference is considered, or -0.1042 if we consider today's measured circumference. We will consider the average of these two numbers -0.1082 as none is more realistic than the other considering the situation in 2018.

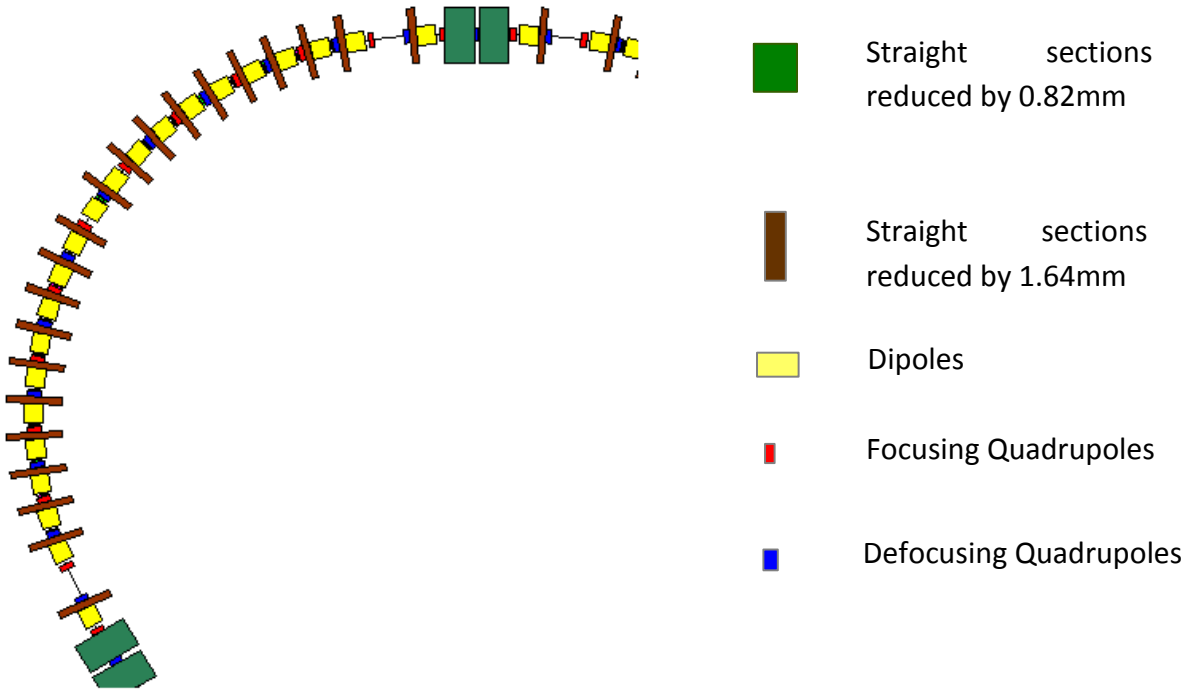


Figure 9.11: Schematic view of about 1/3 of the booster.

### Mechanical aspect

The symmetry of the booster is a threefold symmetry with three arcs and three straight section regions. The arcs are constructed with a unique type of girder, while the straight sections, dedicated to injection, extraction, and RF cavities, are more specific. The reduction can be done by reducing the distance between two consecutive dipoles by 1.64mm as shown on Figure 9.10.

This reduction can also be seen as a movement of 17.22mm of all elements in a direction perpendicular to the beam motion and toward the inside of the ring.

### Adaptation of injection and extraction process to lattice changes and circumference reduction.

Also the change of position of the injection and extraction point goes with modifications of the transfer lines. For the transfer line making the transition between the 200 MeV Linac and the booster, only a slight modification of the tuning of the dipoles, and a realignment of the end of the line, is needed.

For the extraction, from the booster, two modifications have to be taken into account:

- The change of tunes leads to different quads settings and therefore a different beam trajectory for the extracted beam.
- The horizontal shift of -17.22mm.

To recover initial beam trajectory at the exit of TL2 dipole 1, the extraction elements have to be retuned, and part of the TL2 line has to be realigned. For reliability and stability considerations, the power supply and magnet of SE2-1 will be exchanged for new ones, and SE2-2 module will be exchanged for a permanent magnet septum.

Combining new quadrupole settings, tuning of extraction elements, and horizontal shift of extraction point we have the following modifications to perform:

- Part of the horizontal shift is compensated by enhancing the field of Se1 and decreasing the field of Se2. Nevertheless there is still ~12mm to be recovered. A small angle of 1.2mrad is sufficient to recover initial trajectory at the first dipole of TL2. It means the beginning of TL2 has to be realigned on this new trajectory. Deflection of dipole 1 has to be increased by 1.2mrad either by adding an additional magnet or by refurbishing the actual dipole.
- The design of a permanent magnet based septum that will also be suitable for one of the SR injection septums is foreseen.

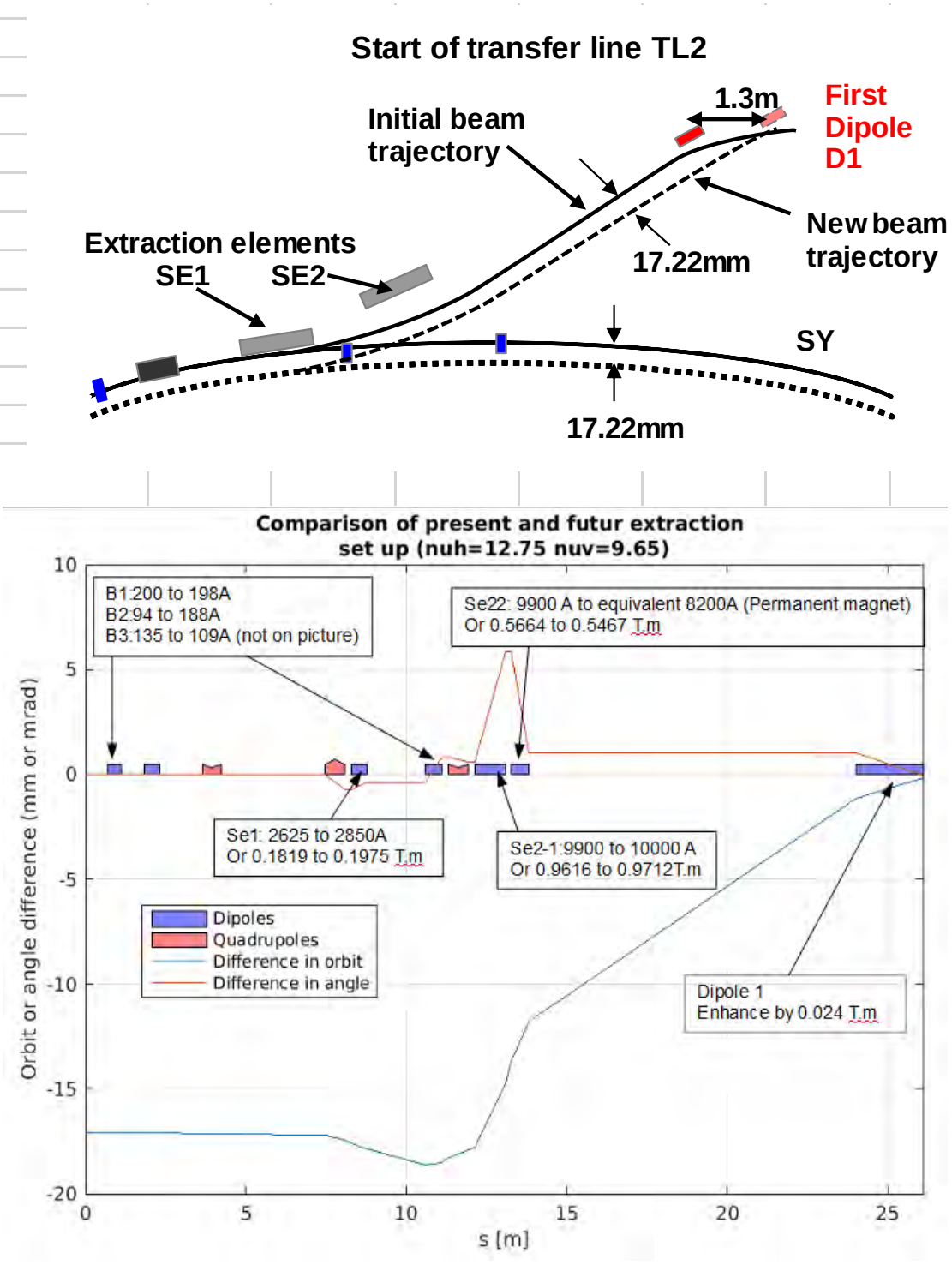


**Figure 9.11: Adaption of the first part of the TL2 transfer line (above) and comparison between H position and angle between future and actual extracted beam trajectory (below).**

## 9.7 Injector upgrade: RF refurbishment

Two RF cavities have been installed in addition to the two existing ones. Each one is fed by its own SSA amplifier able to provide 150kW peak RF power to the cavities. It corresponds to a maximum of 11MV peak accelerating voltage if all cavities are operated. It also allows to operate the booster with only three out of the four systems, in the case one is not operational. The corresponding bunch length VS cavity voltage for the modified optics and an RF frequency offset of 40kHz is presented on Figure 9.12.

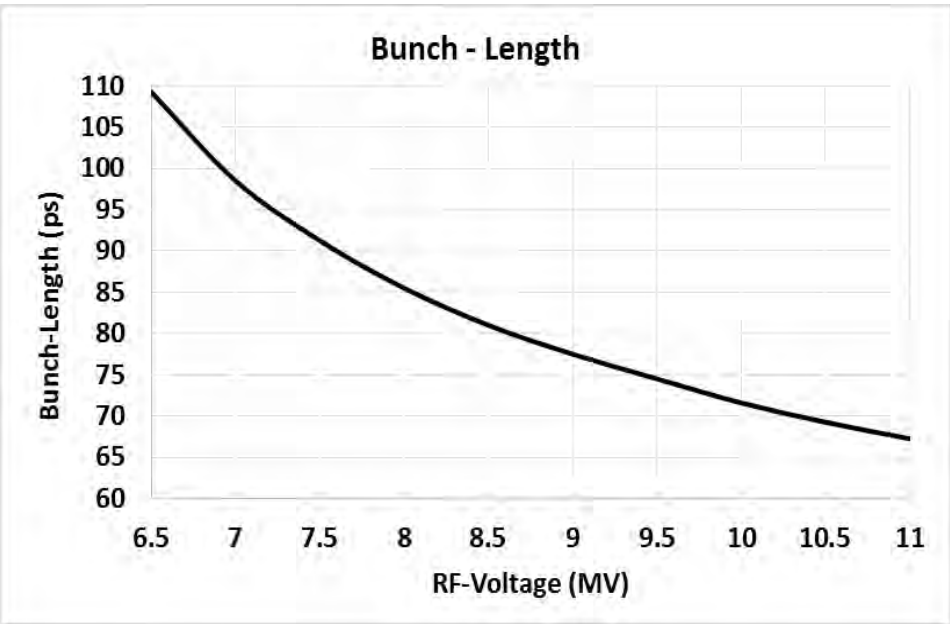


**Figure 9.12: Bunch length versus RF peak voltage for the above presented optic and an RF offset of 40kHz. By raising the RF voltage from 7 to 8.5MV, the nominal bunch length of 82ps can be recovered.**

## 9.8 Magnet power supply upgrade

The booster magnets power supplies based on a 10Hz resonant White circuit is replaced by ramped ones. The design and relies on IGBT's technology. 6 units as the one discribed below provide the current to the three magnet families. One unit for the focusing quads, one unit for the defocussing quads, and two units in paralelle for the dipoles. Two spare units are then available, one for the quads, the other for the dipoles.

To avoid high voltage legal constrains, the maximum voltage at the capacitor should stay below 1500Vdc limiting the maximum

repetition rate to 4Hz. The resulting optimised waveform for the dipoles power supply is plotted on Figure 9.13 as well as the block diagram of the hardware of one unit. DCCT current measurement with a dynamic range of $10^6$ drives a fine regulation of the magnet currents. They will allow a shot to shot stability better than 0,01 units or 10kHz for the tunes, even at injection energy.

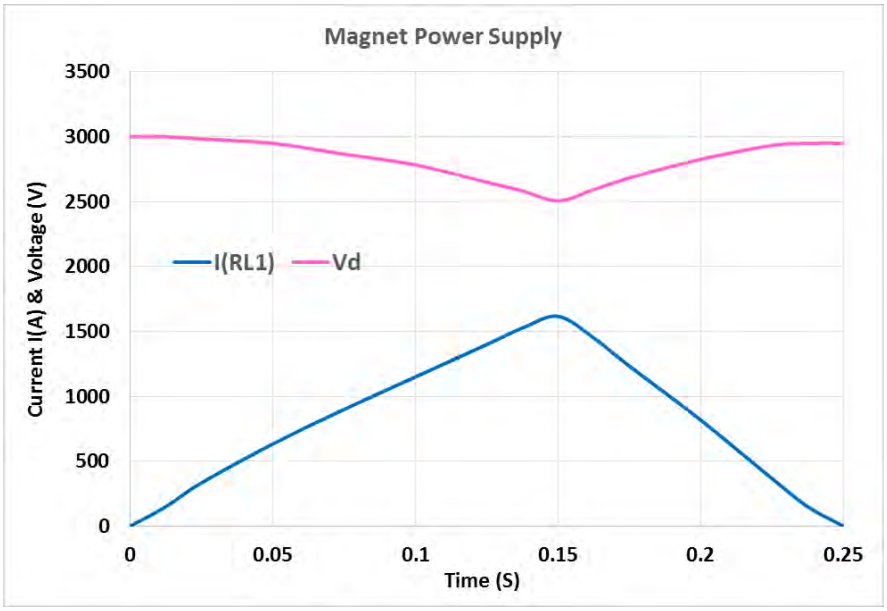


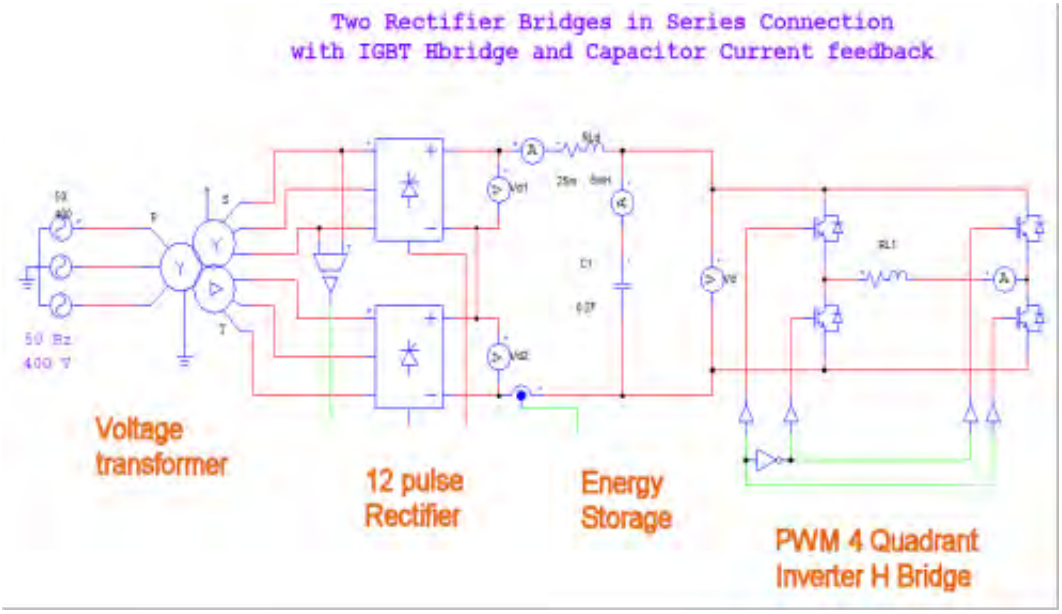


**Figure 9.13: Top: Current (blue) and voltage (pink) waveform for the dipoles magnet family. Bottom: block diagram of a quadrupole Power supply.**

The characteristic of this new power supply is given in the following Table 9.2.

**Table 9.2: Characteristics of the new power supply.**

| | Dipole | Quadrupoles<br>(Focusing & defocusing are same) |
|---|---|---|
| Structure | **2 H Bridges in parallel** | **1 H bridge** |
| Max Voltage on the load. | **3000V** | **925V** |
| Load (as seen by the PS) | **0.56Ω, 0.18 H** | **0.82Ω, 0.125 H** |
| Waveform length | **250ms** | **250ms** |
| Max current | **1600A** | **500A** |

## 9.9 Injector upgrade: Parameter table

**Table 9.3: The main parameters of the upgraded booster.**

| | **Injection (180Mev)** | **Extraction (6Gev)** |
|---|---|---|
| **Machine length (m)** | 299.5099 | |
| **RF Frequency including 40kHz offset (MHz)** | 352.3320 | |
| **Tunes H/V** | 12.75/9.65 | 12.75/9.65 |
| **Peak RF voltage (MV)** | ~0.5 | 8.5 |
| **Transverse emittances H/V (nm.rad)** | Linac dependent | 34 / 34 (full coupling) |
| **Energy spread** | ~1% (Linac dependent) | 1.00E-003 |
| **Bunch Length including RF offset (ps)** | Linac dependent | 82 |
| **Synchrotron frequency (kHz)** | ~38 | 24.9 |
| **Length of cycle (ms)** | 250 | |
| **Loss per turn (Mev)** | ~0 | 4.5 |
| **Momentum compaction** | 9.50E-003 | |
| **Momentum offset induced by 40kH RF frequency offset (% )** | -1.50% | |
| **Damping times (H/V/L ms)** | > $10^4$ | 1.5/2.3/1.6 |

## 9.10 Injection into the storage ring

### Introduction

Injection in the ESRF storage is done following the same principle as for the existing machine. The injection transfer line (TL2) and the storage share a common in-vacuum element, the septum S3, which allows the injected beam to enter the storage ring with zero angle while the stored beam is not perturbed. To minimize the injection oscillations the injected beam is approached as close as possible to the septum blade using a pulsed for magnet bump.

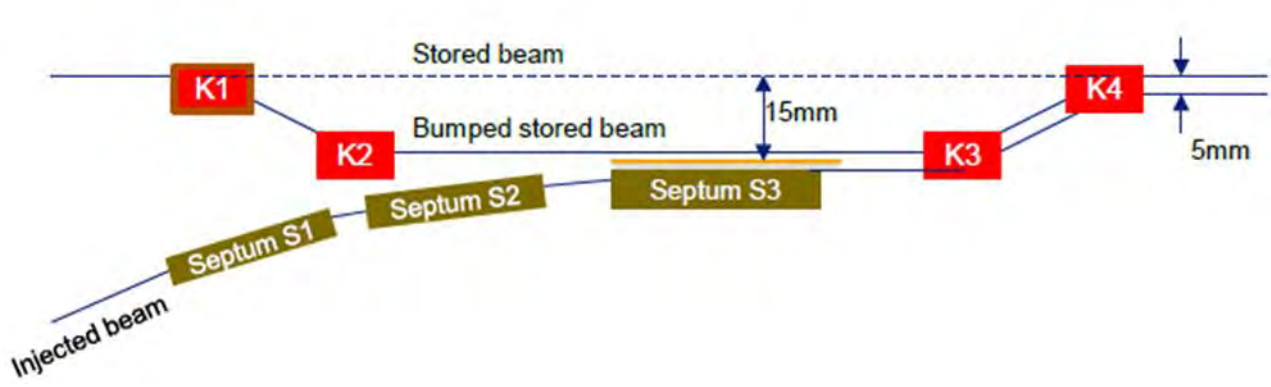


**Figure 9.14: Schematic view of the injection area. K1-4 are pulsed kicker magnets. S1, S2 and S3 are septum magnets.**

Figure 9.14 shows a schematic view of the injection area, the four kickers K1-4 are used to generate the closed orbit bump approaching the stored beam to the septum blade, and the septum S3 is used to kick the injected beam onto the stored beam orbit. Including the septum blade thickness (~3mm) and stay clear margins for both the injected and stored beam. The distance between the stored and injected beams is approximately 5mm, consequently significant injection oscillations will propagate around the ring. The septum blade is located at 15mm from the storage ring beam axis. Concerning the septum magnets S1 and S2 two option are presently considered:

- S1 is a permanent magnet and S2 an electro-magnet (baseline).
- Both modules are electro-magnets.

The baseline scenario should allow to improve the average injection efficiency by minimizing the fluctuations of the injected beam trajectory. However, the radiation hardness of the permanent magnets is not very well known, it was therefore decided to keep the possibility to move back to a fully electro-magnet design open in case the field of the permanent magnets starts degrading. A similar strategy is adopted for the Booster extraction.

## 9.11 Injection cells layout and optics

The storage ring includes 32 cells, two of which are dedicated to injection, cells 3 and 4. The main challenge in designing the injection cells is to increase the horizontal β-function at the injection point to improve injection efficiency while keeping the overall dynamic aperture under control.

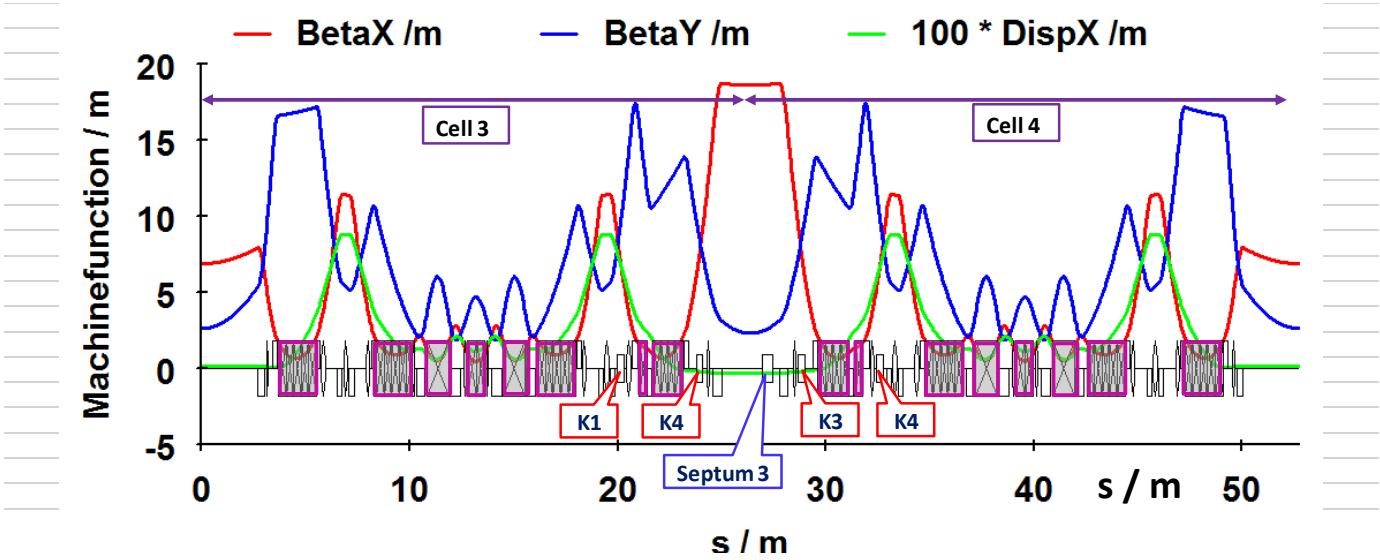


Figure 9.15: Injection cells optics.

Figure 9.15 shows the optics of the injection cell, the horizontal β-function is increased to 18m by using 2 focusing quadrupole (QF1I and QF1J) on each side of the injection point. Both QF1 are the 37cm quadrupoles used in the present 7m straight section in order to accommodate the 15mm bump within the good field region. The change in optics functions at the sextupole locations is minimized in order to avoid breaking the 32 fold symmetry of the storage ring, for optics matching purpose an additional quadrupole was inserted between the 4$^{th}$ and 5$^{th}$ module of the last dipoles before the injection point (QF2I and QF2J). Beyond the quadrupole QF4I and QF4J the injection cells are identical to the standard cell. The kickers K2 and K3 were placed as close as possible the quadrupoles QD2I and QD2J respectively in order to minimize the required field to provide a 15mm orbit bump.

## 9.12 TL2 layout and optics

The design of TL2 is based on some initial considerations in order to minimize the impact on the storage and installation process:

- TL2 layout is to remain unchanged from D1 to D4 (section remaining in tunnel).
- Although this value should be optimized, the distance between the storage ring QF1 quadrupoles on each side of the

injection point is fixed to 2.8m as given by the storage ring initial lattice design.

- Re-use as much as possible the existing hardware.

The TL2 transfer line will be only partly dismantled and taken out of the tunnel, all the magnets located between D1 and D4 will remain in the at their present location. Recent survey measurements are therefore used as reference to constrain the new beam trajectory to these magnets position.

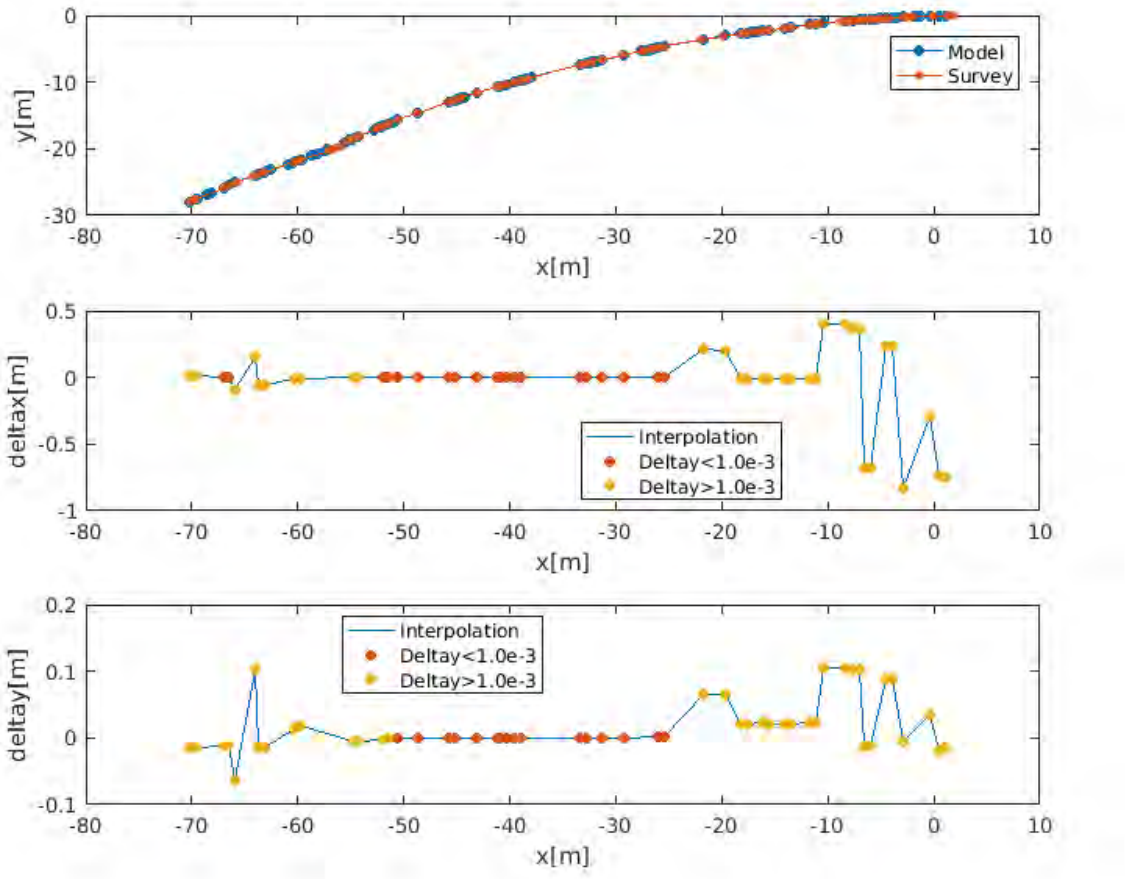


**Figure 9.16: TL2 alignment with respect to the survey.**

Figure 9.16 represents a comparison between the model of TL2 and recent survey measurements. The red dots represent a difference between the model and measurements of less than 1mm. As expected significant difference are observed towards the injection of the storage ring and the extraction of the Booster. However, the central part located between D1 and D4 is consistent with measurements within 1mm. It should be noted that all the TL2 dipoles are assumed to be operated at their nominal field. In reality, the Booster will be operated off-energy to reduce its transverse emittance and the dipole fields will differ by approximately 1% (1 mrad) from their nominal value. Two options are envisaged to reduce the dipole fields by the needed 1%: add shunts or increase the gap between poles. The design effort therefore concentrates towards the entrance and exit of TL2, major changes are

different deflection angles in the septum magnets and a shift in position of the last 2 TL2 dipoles (D4 and D5).

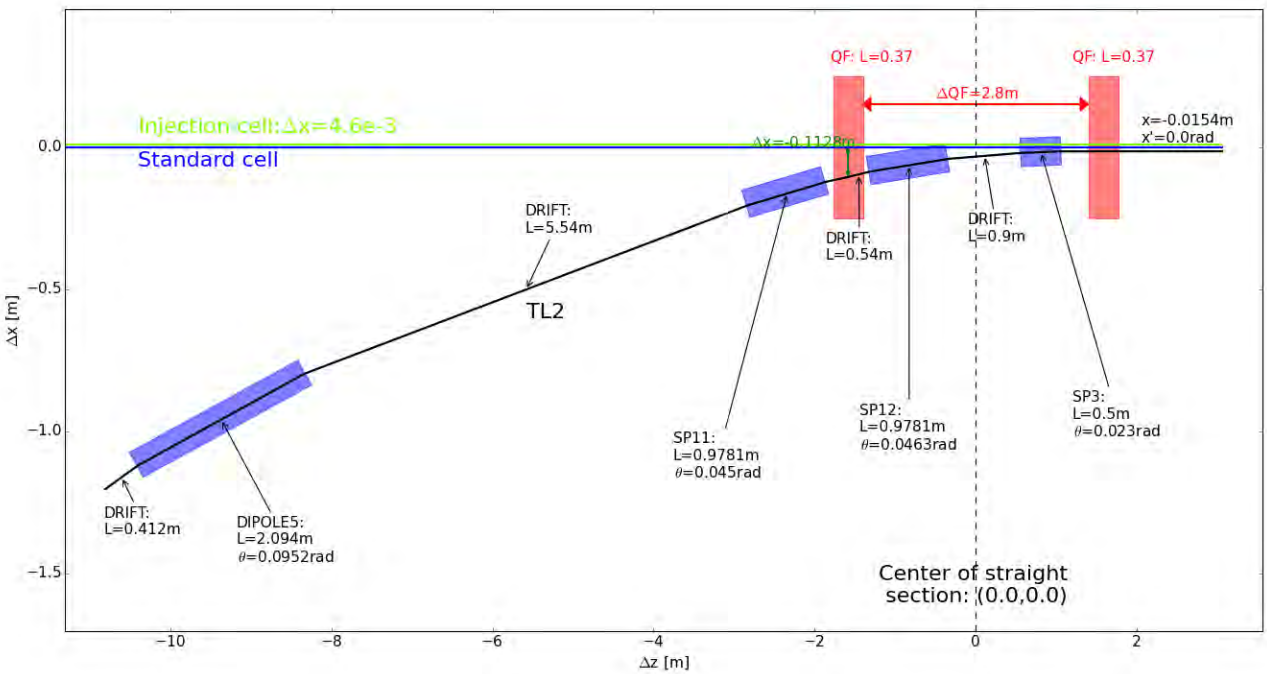


**Figure 9.17: TL2 schematic view from D5 to the injection point. The origin is the center of the standard cell. The magnets transverse dimensions are not to scale.**

Figure 9.17 shows zoom onto the injection zone of the storage ring. The space allocated for all the septum magnets is compatible with the design of the present machine.

However, the S1/2 module needs to be split in two parts each giving approximately the same kick: a single power supply can be used (as is in the present machine) if required. The S3 chamber needs to be rebuilt to accommodate the ESRF-EBS beam pipe profile.

The TL2 D5 dipole magnet operates at nominal field (besides the correction for off-momentum field) and can be kept attached to the Booster power supply system but is shifted by 41cm towards the storage ring along the beam axis with respect to its current position.

The major difference with respect to the available systems is the increase in kick angle for all septum magnets:

- S1 kick angle is fixed to 45mrad which is 2% increase w.r.t to the present angle and allows to insert a permanent magnet or an electro-magnet.
- S2 kick angle is increased by 5%: requires a new power supply.
- S3 kick angle is increased by 5%: requires a new power supply.

In addition, margin of a few percent should be allocated for injection tuning. These increase in

nominal field require new power supplies which are described in the following sections.

The injected beam is going through the QF upstream the injection point with an offset of approximately 10.8cm at the center of the quadrupole. The $b_n$ coefficients introduced by the off-axis field with 11cm offset for a quadrupole operated at maximum current (140A) are shown in Figure 9.18.

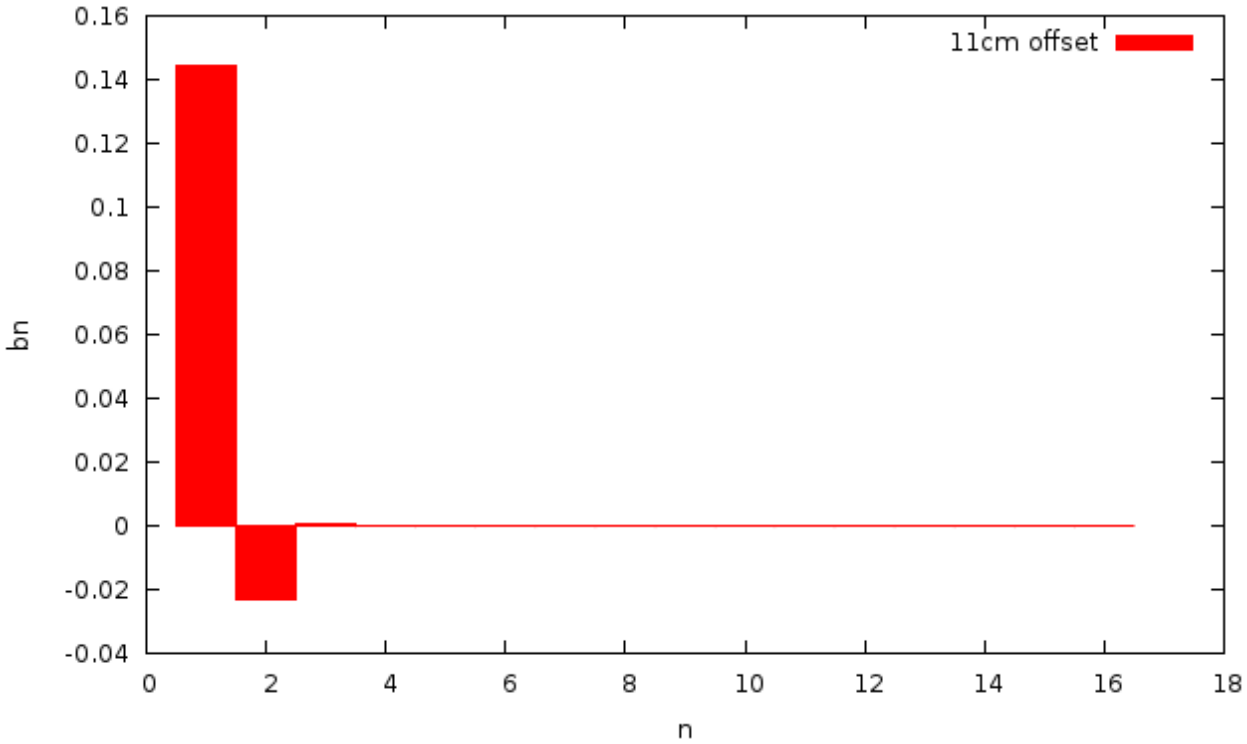


**Figure 9.18: bn coefficients with 11cm offset in the storage ring QF.**

Strong dipole and quadrupole components are still present while the sextupole is very weak and higher order multipoles are negligible. In the following calculations we will therefore consider the dipole and quadrupole contributions only. The dipole component will deflect the injected beam away from the stored beam by:

$$\Delta x' = \frac{b_1}{B\rho} = 7.1 \ mrad$$

which needs to be compensated by other magnets (D5 and septa). On the other hand, the gradient will first give an amplitude dependent kick:

$$\delta x' - \delta x = \frac{b_2}{B\rho} \cdot (r - r_0) = -1.15 \ mrad/cm \cdot x$$

which will make the tuning more complicated, and second, modify the linear optics function at the exit of TL2 which requires to rematch the transfer line. This effects are taken into account into the calculation presented in Figure 9.18 and the following optics design of the TL2 lattice.

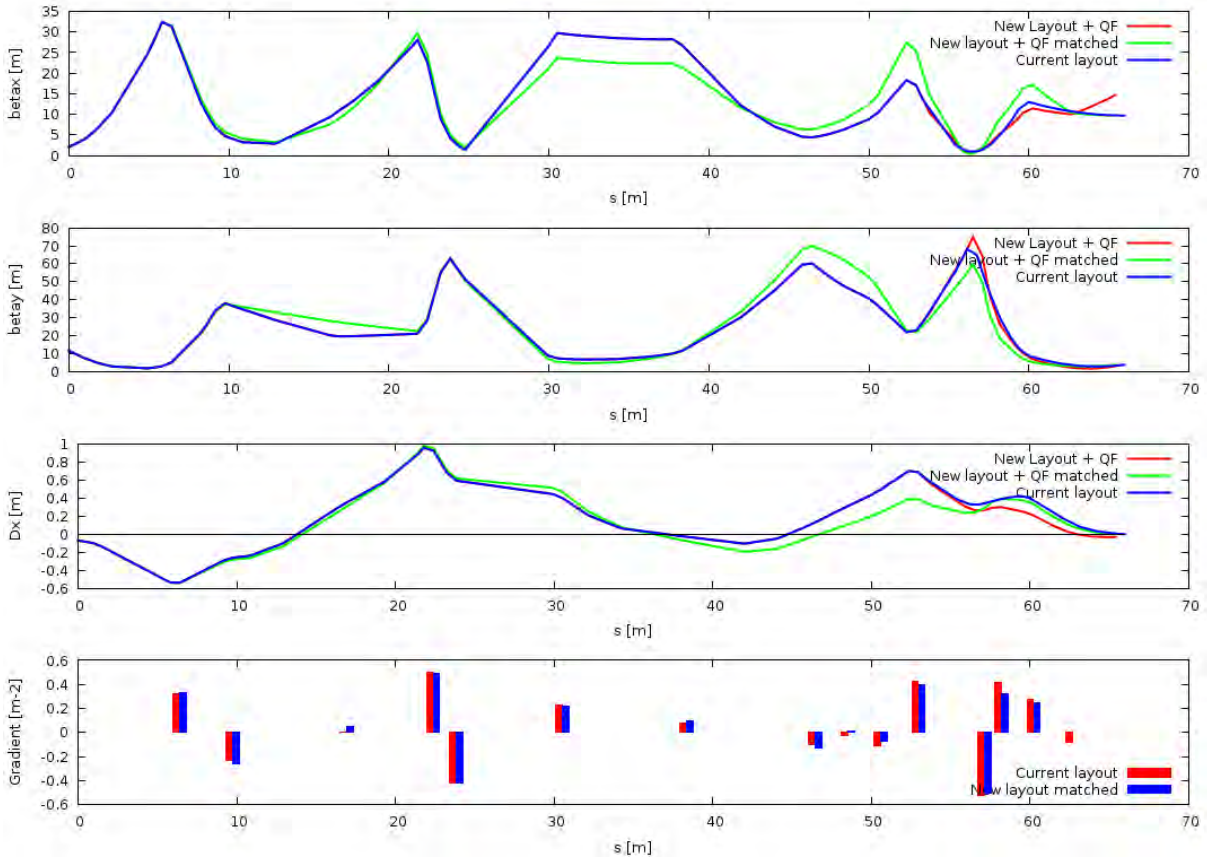


Figure 9.19: Optics matching including QF1 off-axis field.

Figure 9.19 shows the TL2 optics matching including QF off-axis field, in blue is the current TL2 layout, in red the layout including displaced quadrupoles due to mechanical constraint avoiding interference with the storage ring magnets and QF off-axis field without matching and in green the fully matched solution including all changes. A solution is found fulfilling all constraints at the end of the transfer line. Polarity inversions may be required in a few TL2 quadrupoles but this is not an issue, all gradients are within the current limits given by the power supplies.

## 9.13 Injection bump

In order to minimize the injection losses and oscillations the stored beam is brought as close as possible to the S3 septum blade using a four kicker closed orbit bump pulsed at 4Hz. These kickers (K1 to K4) are located in the injection cells 3 and 4. The design is based on a 15mm bump which is the septum blade location which should give sufficient operational margin. In case on axis injection is required for commissioning a static closed orbit bump using the storage ring steerers can be used to bring the stored beam up to 20mm.

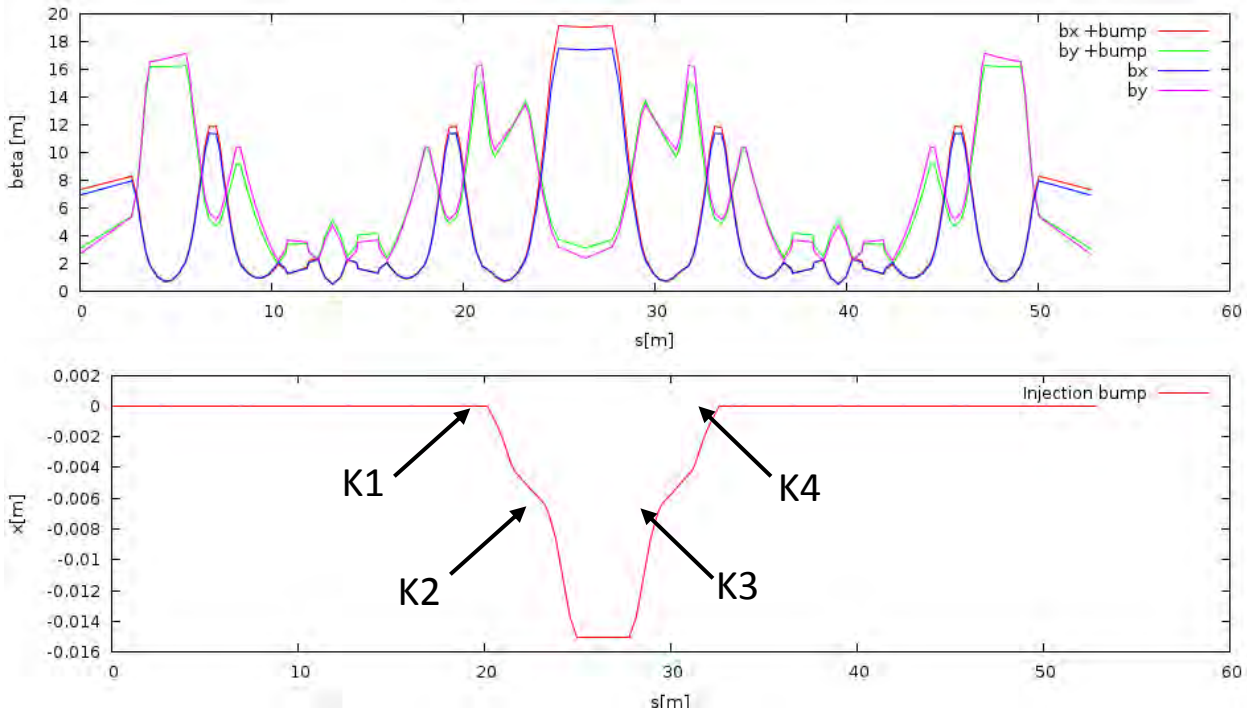


**Figure 9.20: Injection cell optics function and injection closed orbit bump.**

The kick required to generate a 15mm bump at the injection point is 2.36mrad maximum. The existing kickers cannot provide such a strong kick, a new design is therefore required. This could be easily achieved by taking advantage of the smaller beam pipe and reducing the magnet gap. The kickers currently feature a good field region of approximately 40mm, for the new machine the maximum excursion in the kickers is of the order of 7mm, allowing to reduce the good field region down to 10mm.

## 9.14 Current stability

Tracking simulations were performed to evaluate the impact of misteering on injection efficiency. This allows to derive tolerances on current stability of the pulsed elements to achieve a maximum reduction of injection efficiency of 5%. It was for now decided to keep the same pulse shape as for the existing systems, tolerances should therefore be achieve taking into account these constraints.

Figure 9.21 shows the results of the tracking simulations. The criteria of less than 5% reduction in injection efficiency is achieved for

$$-0.5\text{mm} < dx < 0.8\text{mm}$$

$$-0.2\text{mrad} < dx' < 0.2\text{mrad}$$

To derive the tolerances we will assume that the septa introduce only angle distortions and the kickers only position which is not true in reality but should give a rough estimate of the required stability.

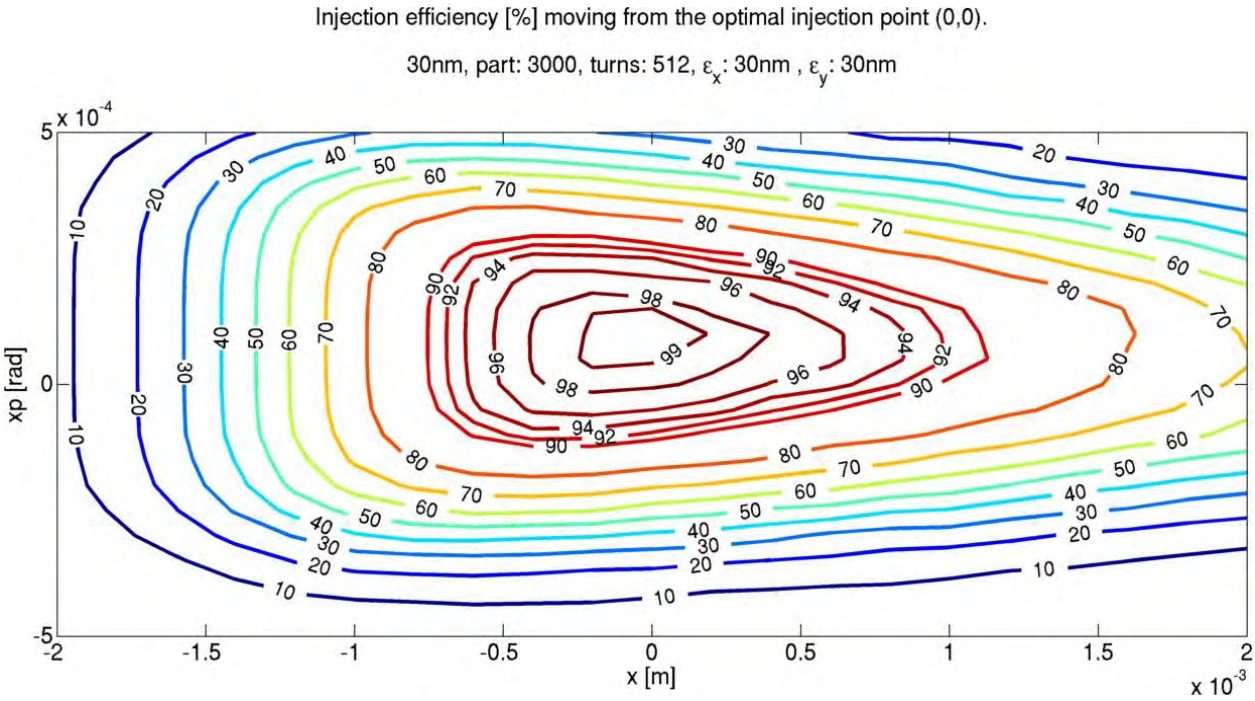


**Figure 9.21: Injection efficiency reduction due to misteering at the end of TL2.**

The stability in this case is a combination of the shot-to-shot stability and ripple on the flat-top which cannot be compensated for by means of feedback systems or manual steering as opposed to long term drifts.

The fluctuations on the total deflection angle given by the Booster and TL2 septa should therefore not exceed +/0.2 mrad. All septa do not contribute by the same amount to the total angle, in order to account for this effect the errors of the septa added in quadrature should not exceed +/-0.2mrad:

$$,-2,\Delta x'\text{-}S1/2\text{-}2.+,\Delta x'\text{-}S3\text{-}2.+,\Delta x'\text{-}SE22\text{-}2.+,\Delta x'\text{-}SE21\text{-}2.+,\Delta x'\text{-}SE1\text{-}2..<0.2\ mrad$$

Several solutions are possible and relaxing the tolerance on one septum will make it tighter for the other. S1, S2 and SE21 being the same magnets powered with the same power supply we assume they are identical. We assume all magnets contributions are un-correlated which will be true for the new machine. We can then try to share the load evenly in terms of percentage of the maximum current as follows:

$$,-3,,,x'\text{-}S1/2.,\Delta,x'\text{-}S1/2.\text{-},x'\text{-}S1/2...\text{-}2.+,,,x'\text{-}S3.,\Delta,x'\text{-}S3.\text{-},x'\text{-}S3...\text{-}2.+,,,x'\text{-}SE22.,\Delta,x'\text{-}SE22.\text{-},x'\text{-}SE22...\text{-}2.+,,,x'\text{-}SE1.,\Delta,x'\text{-}SE1.\text{-},x'\text{-}SE1...\text{-}2..<0.2\ mrad,$$

for

$$,\Delta,x'\text{-}S1/2.\text{-},x'\text{-}S1/2..=,\Delta,x'\text{-}S3.\text{-},x'\text{-}S3..=,\Delta,x'\text{-}SE22.\text{-},x'\text{-}SE22..=,\Delta,x'\text{-}SE1.\text{-},x'\text{-}SE1..,$$

we find a stability of 0.25% for all septa to achieve the desired tolerance on the total angle. However, S1 and S2 contribute for approximately 60% of the total kick, the simulations were done for the ideal case not taking into account possible combinations of position and angles and operational experience with the present machine indicates a safe range of approximately +/-10A (0.1%). Providing these magnets require new power supplies, we request a stability of 0.1% for the new power supplies and relax slightly the requirement on the S3 power supply. This gives a total error on the angle of 0.12 mrad. From tracking simulations, the degradation of injection efficiency would remain below 2% in this case.

Finally, the baseline scenario involves replacing SE22 and one module of S1/2 magnet type by permanents magnets: the error is then brought down to 0.1 mrad which is a factor 2 below the threshold derived from tracking simulation.

Concerning the kickers two criteria have to be accounted for: the injection efficiency and the perturbations on the stored beam. The bump amplitude is 15mm for a desired peak position distortion of 0.8mm at the septum blade, this leads to a tolerance of 5% on the kicker strength which should be easily achievable. However, these fluctuations will also determine how close we will be able to approach the stored beam to the septum blade and hence reduce the injection oscillation amplitude. Any gain would therefore represent a gain on the maximum achievable injection efficiency.

On the other hand, the perturbations to the stored beam are considered transparent for the beam lines when they are smaller than $0.1\sigma$. When the injection bump is ramped up its effect can be approximated by a localized dipole kick. The peak amplitude of the betatron oscillations introduced around the ring is expressed as:

$$,\delta x\text{-}peak.[\sigma]=\theta,\text{-}„\beta\text{-}0.\text{-}\varepsilon…$$

The required stability of the four kickers combined is then 0.02% to achieve $0.1\sigma$ orbit stability all around the ring. This very tight tolerance is due to the very small horizontal emittance and is hardly achievable with the present technology. Transparent injection can therefore not be promised to the beam lines with the present design as we could expect up to several $\sigma$ orbit distortion from the kickers power supply ripples design specification of 1%.

Finally, orbit fluctuations of a few 0.1mm are often observed in TL2 nowadays most likely originating from the Booster extraction, these certainly have a significant impact on the overall performance and will be even more relevant for the new machine due to strong QF off-axis field. For the ESRF-EBS this impact will be partly mitigated by the installation of new septum magnets and power supplies at the Booster extraction which design is presented in the followings sections, but the bumpers, the extraction kicker Ke and the SE1 septum magnet are kept: on the longer term an upgrade of these devices is desirable.

## 9.15 Beam stay clear

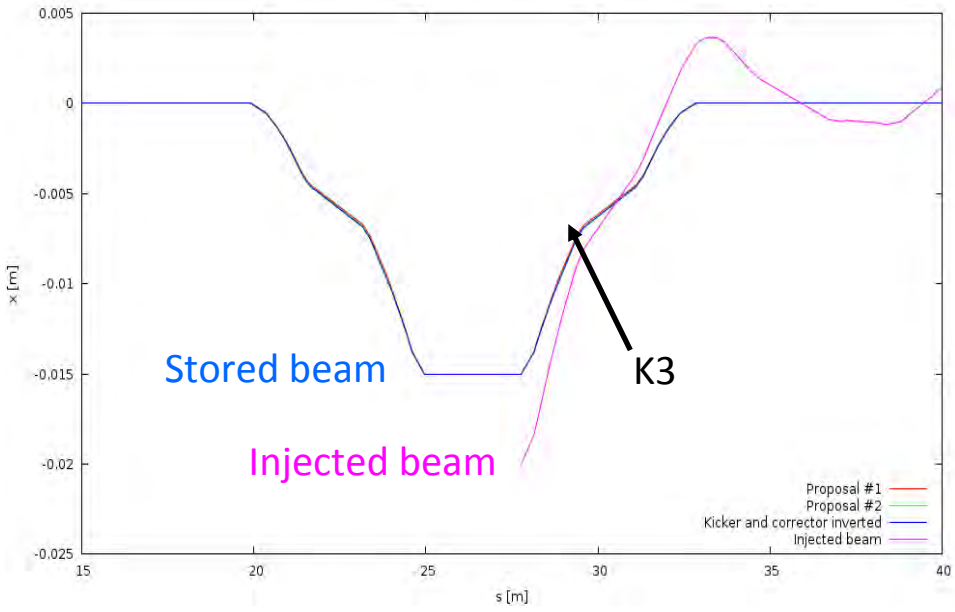


**Figure 9.22: Stored and injected beam trajectories.**

In addition to what was foreseen for the standard cell, the beam stay has to accommodate the injection bump, and the injected beam downstream the injection point. The vacuum chamber should therefore be enlarged towards the inside of the ring over the whole injection bump. In order to minimize impedance effects the transition should be done smoothly, following the bump profile. The hard aperture limit being the septum blade located at 15mm from the beam axis there not point extending the beam pipe beyond this.

On the outgoing side of the septum, additional space should be made available for the injected beam. Figure 9.22 shows the trajectories of the stored and injected beams assuming a 15mm bump. As seen on that figure the trajectories cross approximately at the K3 location and hence a transition from the enlarged profile to the standard profile could be foreseen at that location. Beyond that point the distance between the two trajectories does not exceed 4mm which can be accommodated within the standard vacuum chamber profile.

## 9.16 Summary table

The following table summarizes the requirements for the Booster / TL2 pulsed elements requiring an upgrade and the injection kickers. Stability is defined for electro-magnets.

Table 9.4: Upgrade requirements for booster / TL2 magnets.

| Magnets | **Comments** | **Max. kick (design +1% for beam tuning)** | **Stability (shot-to-shot+flat-top ripple)** |
|---|---|---|---|
| S1 and S2, SE21 | SE21 and S2 are electro-magnets, S1 is a permanent magnet | 45mrad to 48mrad depending on the module | 0.1% max. |
| SE22 | Permanent magnet | 27mrad | 0.1% max. |
| S3 | Present S3 needs to be rebuilt | 26mrad | 0.3% max. |
| K1->K4 | Good field region can be reduced to 10mm. New kickers needed | 2.36mrad max 2.95mrad for on-axis injection | 0.02% to make the injection transparent |

With these specifications the fluctuation of injection efficiency should be kept well below 5% and the perturbations on the stored beam well below the σ level. The present design does not provide such stability from the injection kickers, one can therefore expect several σ orbit perturbation in case the injection kickers system is not upgraded.

## 9.17 Injection efficiency

**Figure 9.23** shows the injection efficiency for different emittance scenarios, the bunch length is assumed to be equal to 20.4mm which correspond to 40 kHz frequency offset in the Booster giving 90pm horizontal emittance. Starting from this conservative (no optics change) baseline scenario we go all the way to the full emittance exchange in the Booster. It appears that full emittance exchange is the only configuration allowing to achieve a theoretical 100% injection efficiency with the present design.

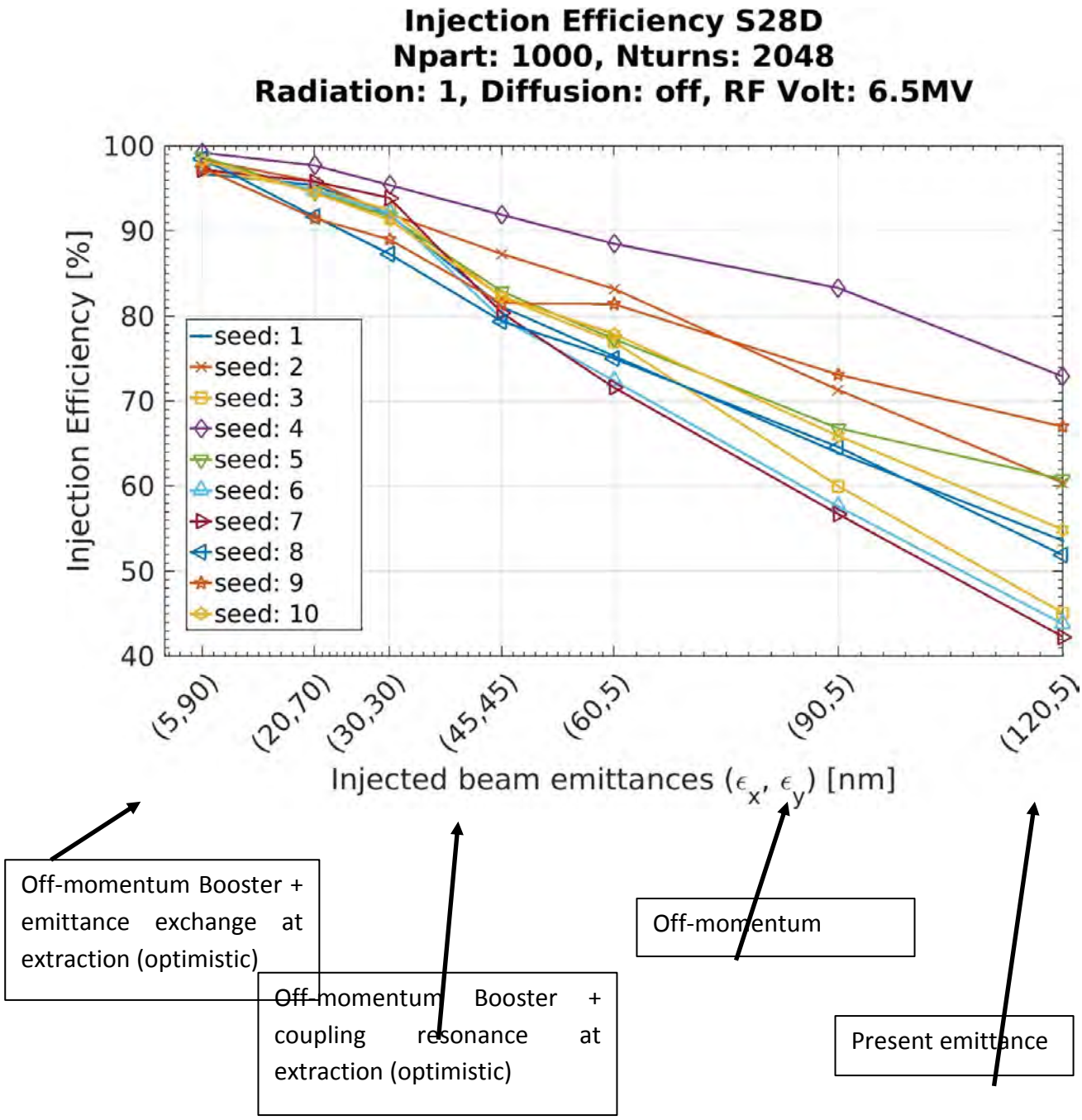


Figure 9.23: Injection efficiency for different emittance scenarios.

## 9.18 Magnet design

### Kicker magnets

Four kicker magnets have been designed for the EBS injection zone. These kickers will be built with a NiZn ferrite yoke and a two turns coil. A typical current waveform is shown in Figure 9.24. The main specifications are given in Table 9.5.

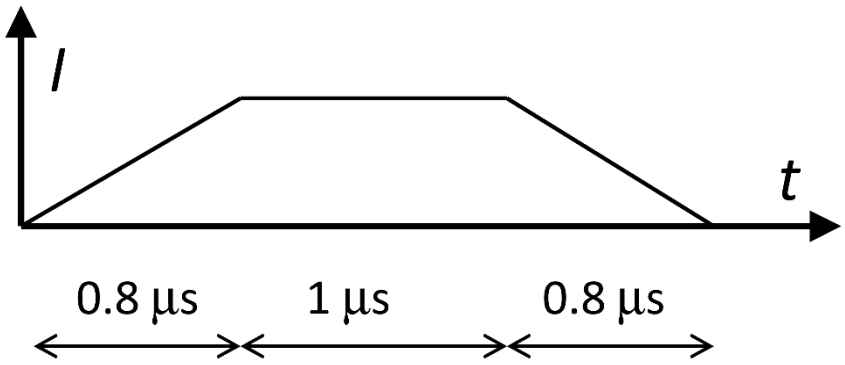


Figure 9.24: Typical current wave form.

Table 9.5: Specifications of the ESRF-EBS kickers.

| | | |
|---|---|---|
| **Nominal current** | 2 | kA |
| **Nominal angle** | 2.35 | mrad |
| **Electron energy** | 6 | GeV |
| **Inductance** | 3.8 | µH |
| **Minimum gap** | 32 | mm |
| **Yoke length** | 285 | mm |
| **Good Field Region** | ±7 | mm |
| **$\Delta B/B$ within GFR** | ±0.001 | |

A preliminary design was done with a simple 2D, DC model (Figure 9.25). The impact of the pole width on the field and its homogeneity is shown in Table 9.6. An approximate value of the field can be computed with the analytical formula $B \approx \mu_0 NI/g \approx 0.167$ T at 30 mm gap: the simulated field is a few percent below, depending on the pole width. The pole width was set to 50 mm to maximize the field. At this stage of the design, the field homogeneity is not within the specifications; this issue will be solved by machining a slot on the pole surface, as shown latter in this report.

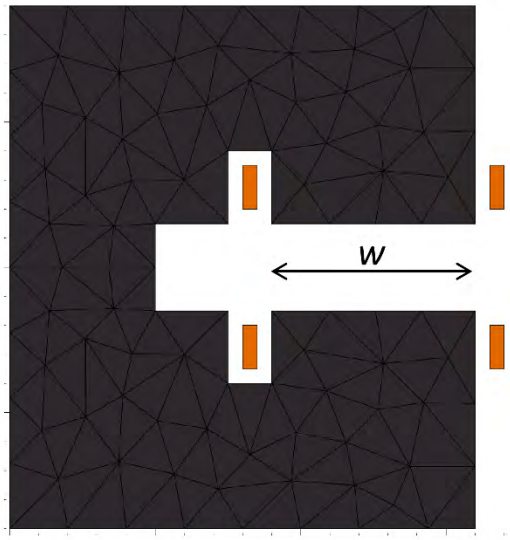


**Figure 9.25: Preliminary model of the kicker magnet (DC simulations with Radia, a 3D magnetostatic code developed at the ESRF).**

**Table 9.6: Impact of the pole width on the field and field homogeneity, at 30 mm gap and 2 kA.**

| | | | | | | |
|---|---|---|---|---|---|---|
| *W* | 40 | 50 | 60 | 70 | 80 | mm |
| $B_0$ | 0.165 | 0.163 | 0.162 | 0.157 | 0.149 | T |
| $\Delta B/B$ | ±0.03 | ±0.006 | ±0.001 | ±0.001 | ±0.001 | 1 |

A 3D model of the kicker magnet has been simulated with the Opera3D/Elektra software (Figure 9.26). The kick angle is 2.36 mrad at 2 kA. A 0.7 mm depth slot has been machined in the pole faces to reach the specified homogeneity (Figure 9.27). The longitudinal profile of the field is shown in Figure 9.28.

The inductance of the magnet has been evaluated to 3.6 µH. The effect of the current leads was neglected and the inductance of the real magnet is expected to be slightly higher.

The four kickers will be assembled and tested in house, the main parts (i.e. the ferrite yokes and the coils) being subcontracted.

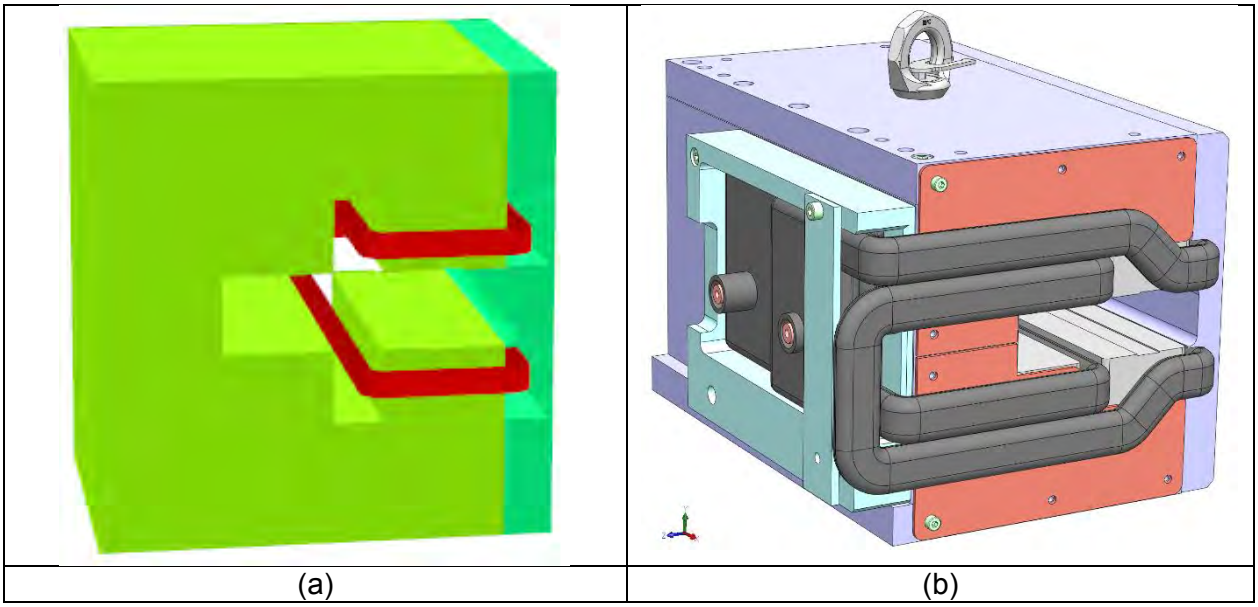


**Figure 9.26: (a): Opera3D model of the ESRF-EBS kicker magnet. The yoke is built in FerroxCube 8c11 NiZn ferrite and the conductive screen on the right is in aluminium. A machined slot is visible on the poles: this slot is used to improve the homogeneity of the field. (b): CAD view (SolidWorks) of the kicker magnet.**

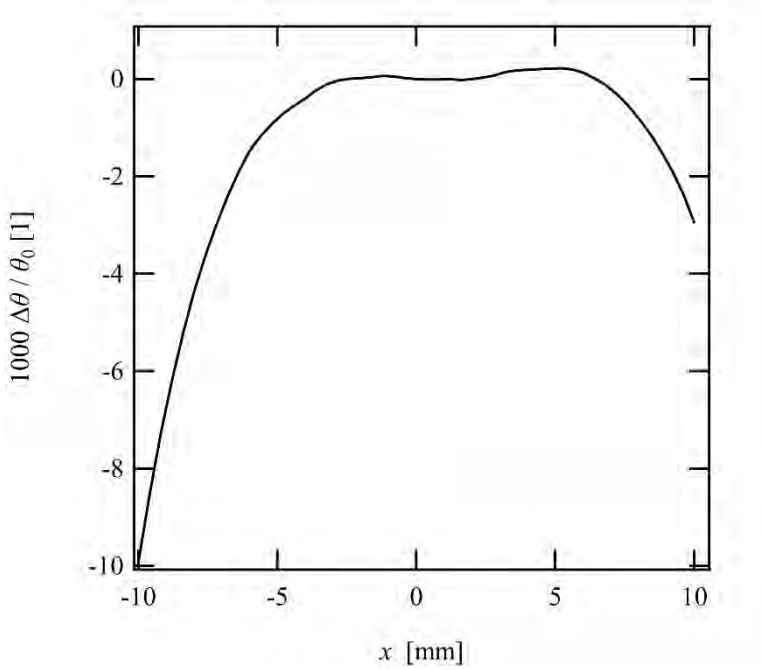


**Figure 9.27: Transverse homogeneity of the kick angle for a 1 MHz, 2 kA excitation current. The kick angle is 2.36 mrad at x = 0 mm. (Opera3D/Elektra simulation.)**

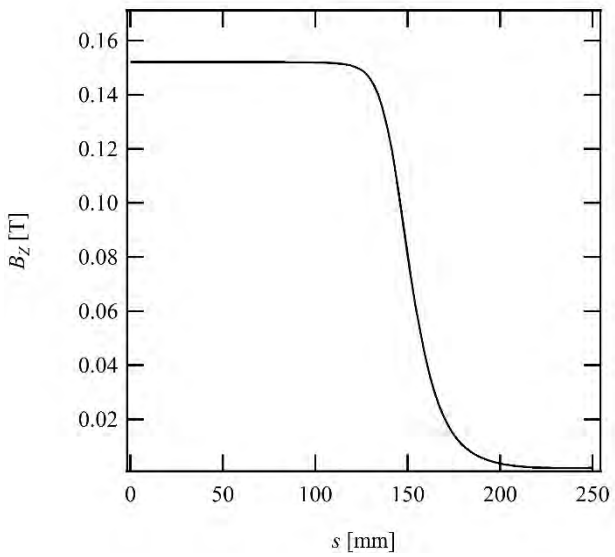


**Figure 9.28: Fringe field of the kicker magnet for a 1 MHz, 2kA excitation current. The ferrite length is 285 mm. (Opera3D/Elektra simulation.)**

### Pulsed septum magnets

Six pulsed septum magnets (including 2 spares) will be built from specifications by a subcontractor. The specifications are similar to those of the present septa (see Table 9.7).

**Table 9.7: Main specifications of the pulsed septa.**

| Septum type | Long | Short | |
|---|---|---|---|
| **Integration length** | 978 | 587 | mm |
| **Integrated Field** | > 1 | > 0.6 | T m |
| **Good Field Region (GFR)** | ±10 x ±4 | ±10 x ±4 | mm x mm |
| **$\Delta B/B$ within the GFR** | < 0.001 | < 0.001 | |
| **Max current** | 12 | 12 | kA |
| **Pulse duration** | 2 | 2 | ms |
| **Repetition rate** | 4 | 4 | Hz |

### Permanent septum magnets

A Permanent Magnet (PM) dipole will be built and installed at the location of the S1 septum. This PM septum is similar to the modules of the Dipoles with Longitudinal gradient (DL) to be installed in the EBS. The main differences between the PM septum and the DL modules are the length (970 mm for the septum, 353 mm for the DL module) and shielding plate installed on the stored beam side of the septum (the DLs are C shaped magnets).

The magnetic design is shown in Figure 9.29. About 28 kg of $Sm_2Co_{17}$ material are needed to magnetize the septum. This material was chosen for its high resistance to radiation damage. The yoke and poles are solid soft iron parts; the pole shape has been optimized to improve the transverse homogeneity of the field. Figure 9.30 shows a design view of the PM septum. Some of the septum parameters are summarized in Table 9.7.

The septum angle is shown in Figure 9.31. The angle will be shimmed to 45 mrad at the center and the residual angle on the stored beam is 3 µrad. A permanent magnet is also foreseen for the short module which will be a scale down of this design.

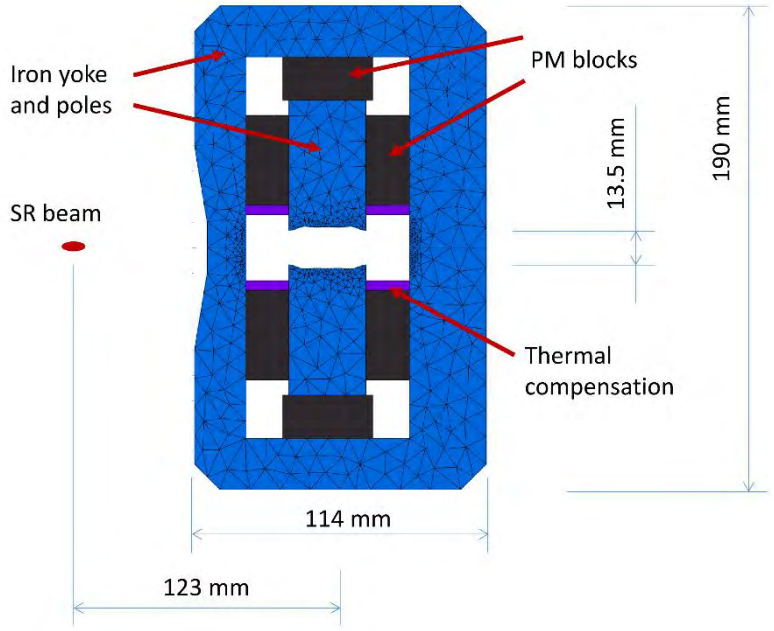


**Figure 9.29: View of the 3D magnetic model (Radia) of the PM septum magnet, with its main dimensions. The PM blocks are in $Sm_2Co_{17}$ material with 1.1 T remanent field. The thermal compensation is done with low Curie temperature FeNi shims. The total length is 970 mm.**

**Table 6.7: PM septum parameters.**

| | | |
|---|---|---|
| **Angle @ 6 GeV** | 45 | mrad |
| **Length** | 970 | mm |
| **Gap** | 13.5 | mm |
| **Transverse dimensions** | 114 x 190 | mm x mm |
| **PM weight** | 28 | kg |
| **Total weight** | 135 | kg |

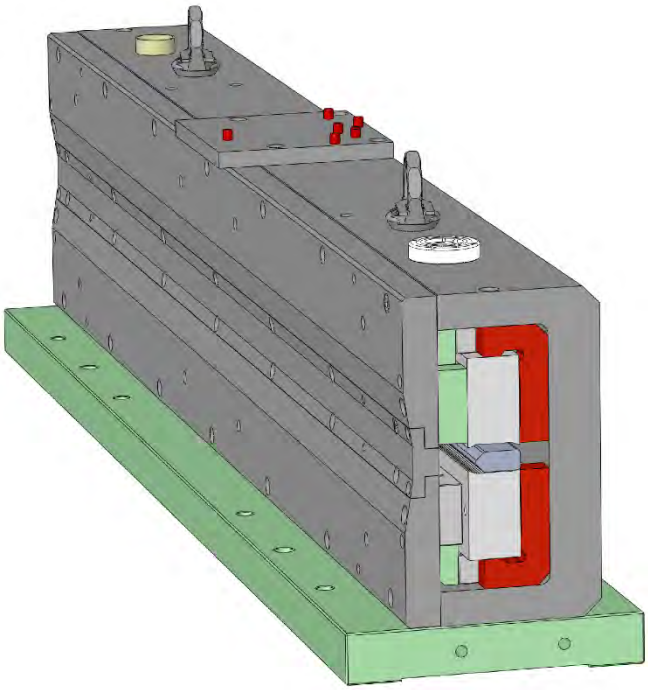

Figure 9.30: CAD view (SolidWorks) of the PM septum magnet.

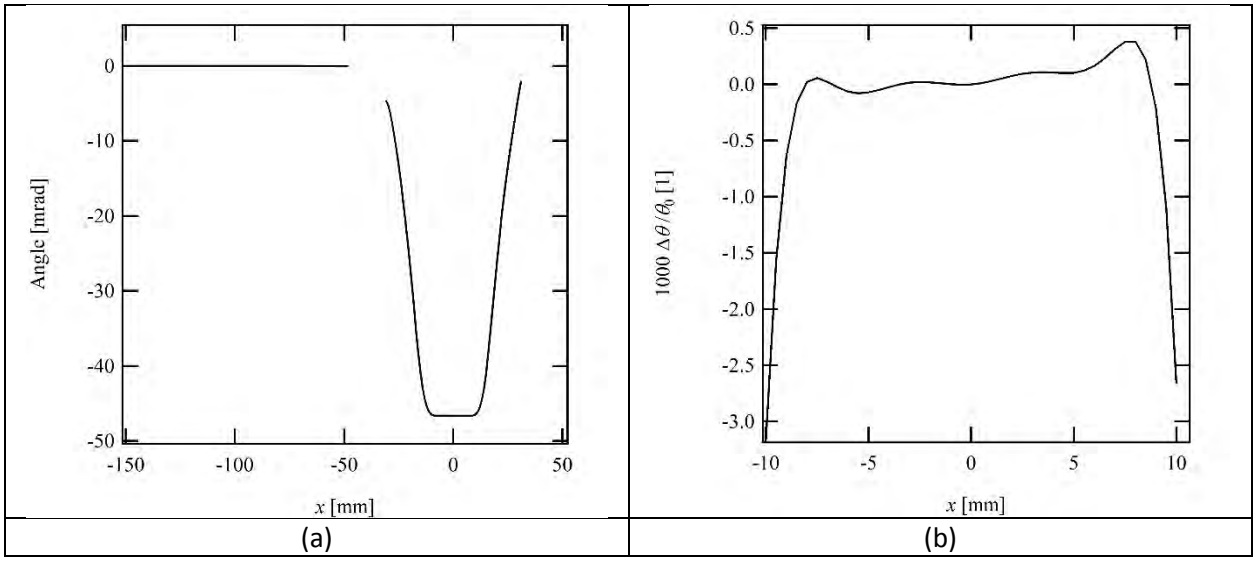


Figure 9.31: PM septum angle vs transverse position for 6 GeV electrons (3D Radia computations). (a) Angle induced on the injected beam (x = 0 mm) and on the injected beam (x = -123 mm). The angle before shimming is expected to be 46.5 mrad. It will be shimmed to 45 mrad before installation. (b) Transverse homogeneity of the septum angle.

## 9.19 Pulsed Power Supply S3

### Introduction

The ESRF complex accelerates the electrons with a 200 MeV linear accelerator and a 6 GeV synchrotron booster. Electrons are then injected into the storage ring at a repetition rate of 4Hz. An eddy current sheet type septum magnet S3 powered by a Pulsed Power Supply provides the final deflection of the injected beam from the Booster at the junction with the Storage Ring (Figure 9.32). A new Power Supply is designed to fulfil the requirements for the update project.

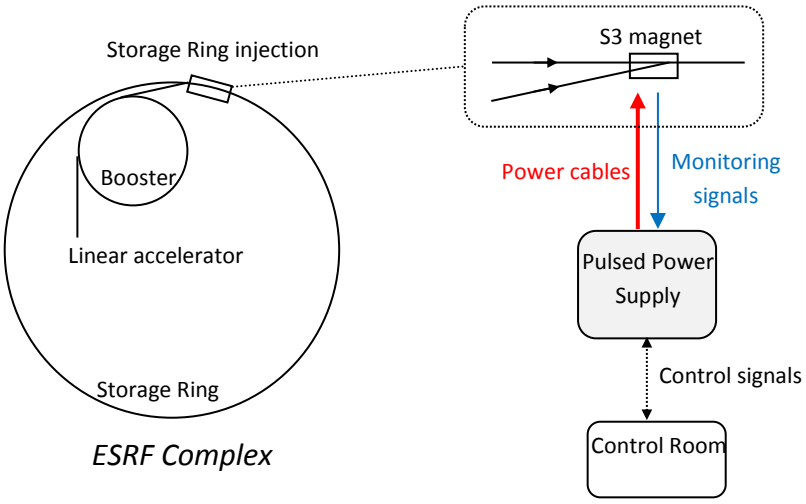


**Figure 9.32: An eddy current sheet type septum magnet S3 powered by a Pulsed Power Supply provides the final deflection of the injected beam from the Booster at the junction with the Storage Ring.**

### Power Supply main specification

The characteristics of the Pulsed Power Supply for the ½ sine waveform are indicated in Table 9.8.

**Table 9.8: Pulsed Power Supply output characteristics for ½ sinus waveform.**

| | |
|---|---|
| **Maximum pulse repetition of the ESRF trigger signal** | **4Hz (every 250ms)** |
| **Jitter (between START signal and crest of the waveform)** | < 100 ns |
| **Pulse shape** | ½ sinus |
| **Pulse duration** | 60µs ( ½ sinus) |
| **Current flat-top (crest of positive sine half wave)** | 2µs |
| **Long term current flat-top stability on positive half wave** | ±0.3% (during 2µs) |
| **Nominal Peak current on positive half wave** | 10kA |
| **Maximum Peak current on positive half wave** | 12kA |
| **Typical load L/R (magnet + cable)** | 3µH / 10mΩ |
| **Ambient temperature** | 25°C |
| **Cable length between power supply and magnet** | ~15 m |

The pulsed current at the output of the Pulsed Power Supply applied to the magnet is a Single shot ½ sine current waveform repeated every 250ms (Figure 9.33).

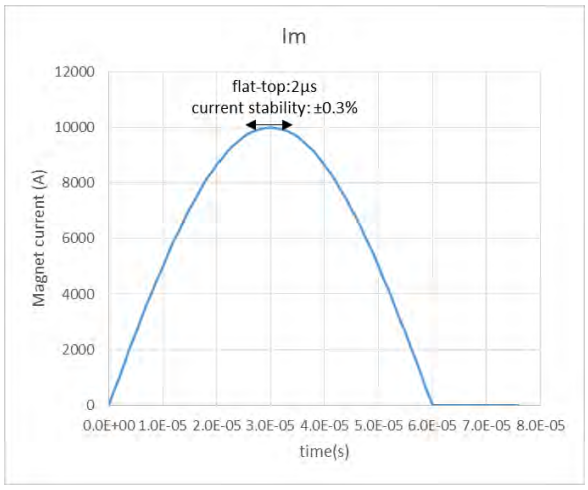


**Figure 9.33: The single shot ½ sine current waveform applied to the magnet by the pulsed power supply.**

The pulse timing generation is illustrated in Figure 9.34. The Pulsed Power Supply is synchronized with the two external signals FW and START:

- The FW signal triggers the Pulsed Power Supply to be ready to deliver the pulsed current in the magnet.
- The START signal enables the current in the magnet.
- Im is the current in the coil of the magnet

The current is pulsed in the magnet every 250ms and this sequence is repeated indefinitely.

The precision, repeatability and stability of the current in the magnet are extremely important:

- The value of the peak current in the magnet must reach the current reference at the first shot pulse within the ±0.3% precision.
- The peak current has to be the same over a long time period (±0.3% even after 24 hours of operation at 4 Hz): the Pulsed Power Supply must adapt itself to variations of the load parameters (L and R values).
- The time disparity of the peak current pulses over a long time period must be constant as much as possible (jitter < 100ns) taking START signal as time reference.

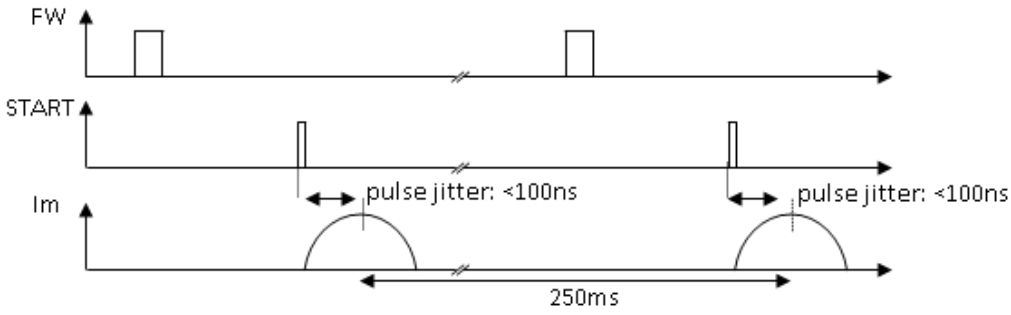


**Figure 9.34: The pulse timing generation of the pulsed power supply.**

## Power Supply design

The design and the assembly of the power supply is made internally by the ESRF RF team. The following sections describe the main parts of the design.

### Power electronics topology

The power electronics topology for making ½ sinus current waveform using classical discharge capacitor bank in a tuned LC circuit is shown in Figure 9.35. The main elements of the power supply are:

- The DC charger to charge the capacitor bank within a specified time (<250ms)
- Capacitor bank (100uF)
- Controlled firing switch (Th1-D1)
- Decoupling/Energy recovery path ($D_{recovery}$-$L_{recovery}$). Alternative solution is to use resistor instead of recovery inductance if the DC charger is strong enough to recharge the capacitor bank from 0V to its nominal value.

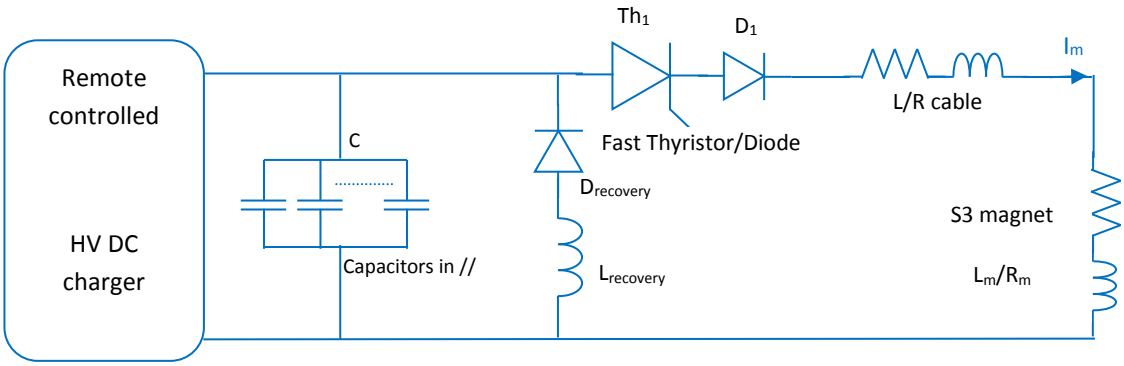


Figure 9.9: The power electronics topology for making ½ sinus current waveform using classical discharge capacitor bank in a tuned LC circuit.

| AC input | **400V – 3ph** |
|---|---|
| HV DC voltage range | 0-2500V |
| Regulation type | Voltage and current |
| Charging time | < 80ms for 100µF |
| Load profile | See Figures 5 |
| Remote controlled | yes |
| Period (Hz) | 4Hz |
| AC input | 400V – 3ph |
| Retained reference | TECHNIX CCR2.5KV-4KJ/s |

### HV DC Charger

A HV DC charger is used to make the charge of the capacitor. The characteristics of the capacitor charger required for the application are shown in Table 9.9.

Table 9.9: HV DC charger specifications.

The charge profile is defined by the following steps:

1. The 100µF capacitor bank is charged to nominal voltage value.
2. The charger is set OFF and disconnected (by use of an external semiconductor switch) within few ms just before the discharge order.
3. An external circuit (pulse thyristor) discharges the capacitor into the magnet.
4. Recovery energy circuit recharges the capacitor up to 80% nominal voltage.
5. The charger is set ON and charges the capacitor to its nominal voltage.
6. Repetition of the cycles 1) to 5) every 250ms

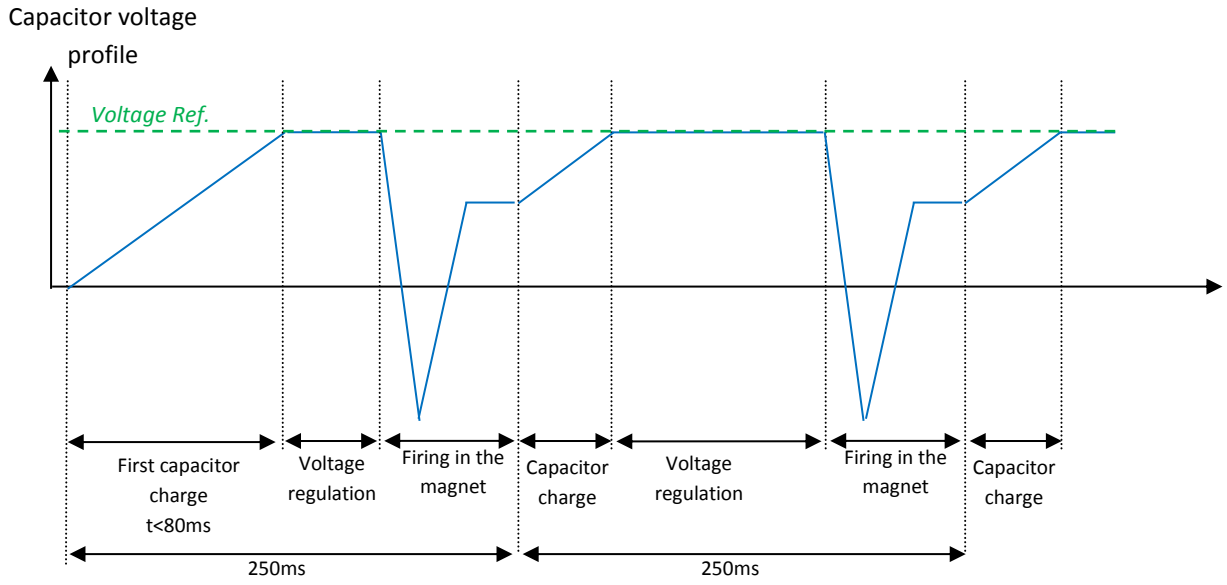


**Figure 9.36: Capacitor voltage profile.**

## Power electronics stack

The power stack is composed of a fast pulse thyristor (Th1) (presspack package) dedicated to pulsed application with high di/dt and pulsed peak current above tens of kA. The diode (D1) in series avoids reverse voltage across the thyristor.

The recovery circuit (Lrecovery, Drecovery) acts as a decoupling circuit during the pulse and re-charges the capacitor to around 80% of its nominal voltage within a few ms.

The characteristics of the power components required for application are shown in **Table 9.10**.

**Table 9.10: Characteristics of the power components required for application.**

| Thyristor $T_{h1}$ | Value |
|---|---|
| VDRM | 4.5kV |
| R.M.S current | > 120 Arms |
| di/dt | > 500A / µs |
| Peak current | 10 kA / 60µs / ½ sinus / each 250ms |
| Retained reference | DYNEX PT60QHx45 (4.5kV Asymmetrical – 100mm) |
| Diode $D_1/D_{recovery}$ | **Value** |
| VDRM | 4.5kV |
| R.M.S current | > 30 Arms |
| Peak current | 550A / ½ sinus / 1ms duration / each 250ms |
| Retained reference | DYNEX DSF20545SF (76mm) |

For size reduction, the above components are connected in series and clamped together by two external heat sinks. Busbar and heatsinks are used as electrical terminals to be connected to the capacitor bank, recovery path and output to the magnet (Figure 6).

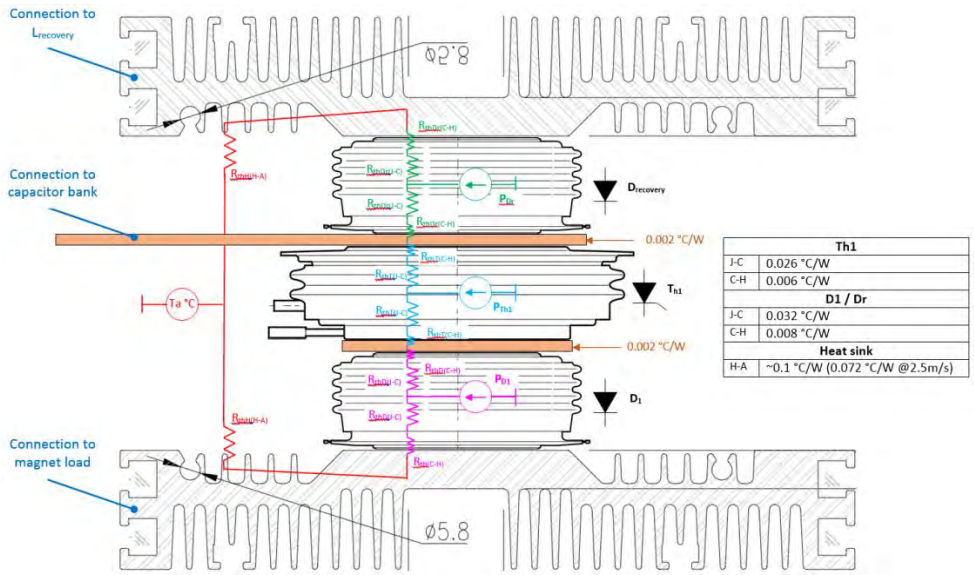


**Figure 9.37: Electrical scheme of power electronics stack.**

The junction temperatures of power semiconductors are computed based on thermal transient impedance given in the datasheet and dynamic simulations. These temperatures are indicated in Table 9.11 for a 12kA-60µs pulsed current.

Table 9.11: Power semiconductor junction temperatures.

| Ipeak=12kA | $T_{h1}$ | $D_1$ | $D_{recovery}$ |
|---|---|---|---|
| Dynamic T°C rise | 9°C | 1°C | 0.1°C |
| Peak Temperature vs ambient | 23 + 9 = +32°C | 22 + 1 = +23°C | 21 + 0.1 = |

## Power supply installation

All the parts of the power supply are integrated in a single 2000 x 800 x 800mm cubicle. The cubicle will be installed as close as possible of the magnet S3 in the technical zone. The connection between the power supply and the magnet is made through coax cables (~15 meters) to minimize the inductance/resistance values. Interfaces with the control room allow synchronization, configuration and feedback measurements with the power supply through Modbus Ethernet and TTL signals.

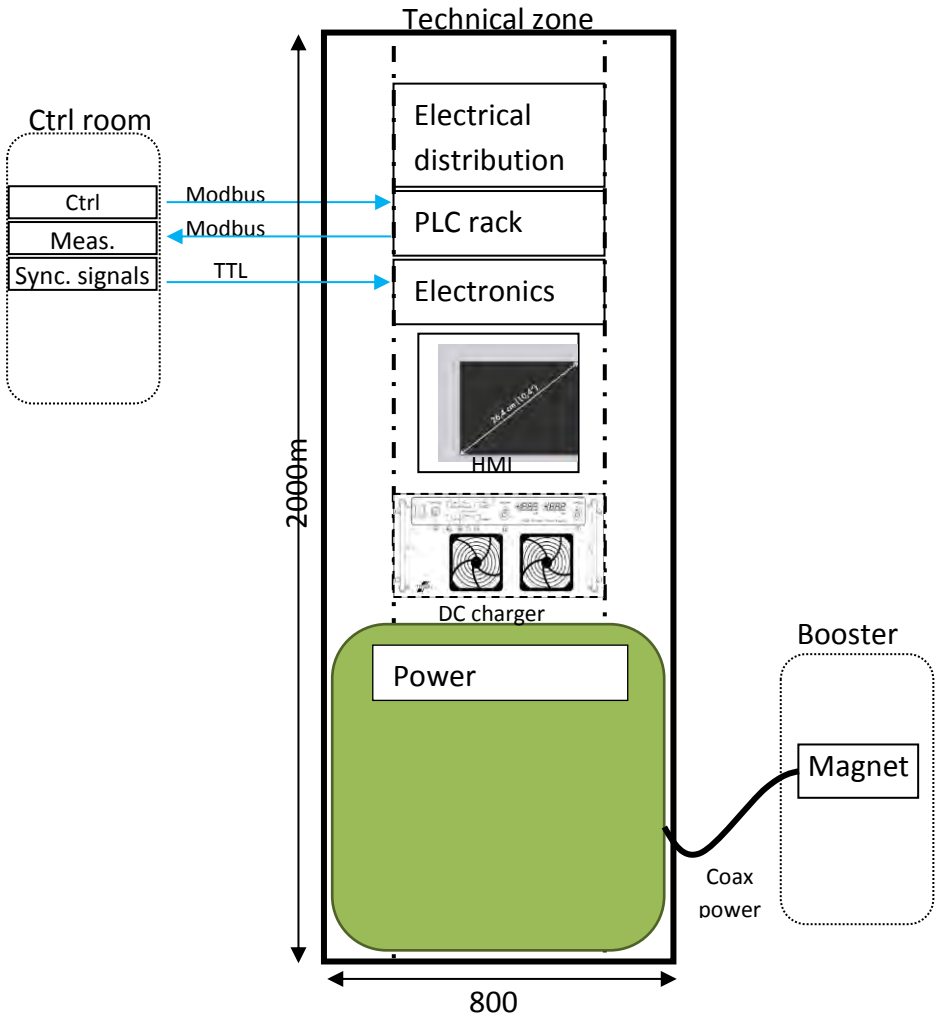


Figure 9.38: Installation and connection scheme of the power supply.

## Overall performances

To achieve ±0.3% error for the first shot in the magnet, the Pulsed Power Supply regulation mode is similar as an open loop control during the starting sequence. This implies that all errors, offsets and static parameters must be known in advance. Then, slow regulation is activated to maintain the current within the required limits during normal operation. The following error measurements have been taken into account to estimate the overall precision of the power supply:

### HV DC charger accuracy

DC capacitor charger typical voltage regulation is ±0.05%. This value is dependent of the charging sequence strategy (constant voltage regulation until firing or pre-charge of the capacitor and let the capacitor discharges itself in RC time constant before firing).

### Current transformer sensor

A passive current transformer (Pearson) will be used. Considering that the precision deviation is negligible and the measurement error/offset is constant, the current transformer introduces no error between two consecutive measurements. Internal adjustments / measurements will be carried out to optimize the reading of the current transformer information.

### Current feedback measurements

Based on the pessimist assumption of a standard 12-bit ADC, the measurement step is around 0.025%. By considering 2 LSB error introduced by the ADC during acquisition, the measurement error becomes +/-0.05%.

The cumulative error for the main parts is calculated as follows: ±0.05% (DC charger) + ±0.05% (ADC) = ±0.1%.

Additional error (electronics jitter, temperature deviation) will be evaluated and minimized during the pre-test of the power supply.

Taking into account the above errors, the remaining error margin to fulfill the specified ±0.3% of the spec. is ±0.2%.

## 9.20 Power converters for S1, S2, Se2/1 and Se2/2

### Introduction

The booster extraction and the storage ring injection have to be upgraded and, in particular, the S1, S2 and Se2 septum magnets have to be operated with increased operational currents in order to provide increased deflection angles. The septum magnet Se2 is divided in two parts named Se2/1 and Se2/2.

Two magnet configurations are envisaged for normal and redundant operations:

- Case 1 (baseline configuration): S2 and Se2/1 are new Electromagnetic Magnets (EM) powered by two new pulsed power supplies. S1 and Se2/2 are new Permanent Magnets (PM) developed in house.
- Case 2 (fall back configuration in case of problems with PM magnets): S1, S2 and Se2/1 are new Electromagnetic Magnets (EM). Se2/2 is also a new Electromagnetic Magnet (EM) powered by an existing ESRF power supply.

Three new power converters are needed, including one spare, and their connection to the septum magnet circuit can be configured in order to allow operational redundancy.

A collaboration with CERN is in progress to implement the MegaDiscap converters for the project. The following sections presents the requirements and technical data of this collaboration.

### Electrical requirements for S1, S2, Se2/1, Se2/2

The electrical parameters are identical for S1, S2, Se2/1 and Se2/2 magnets. These parameters and the operational requirements for beam injection are provided in Table 9.12.

**Table 9.12: Electrical parameters of the septa and operational requirements for beam injection.**

| Parameter | Unit | Value |
|---|---|---|
| **Magnet Inductance** | [µH] | 3 ±0.5 |
| **Magnet Resistance @ 20°C coil temperature** | [mOhms] | 0.35 < Rm < 0.85 |
| **Maximum operating current (Iop.max)** | [kA] | 12 |
| **Minimum operating current (Iop.min)** | [kA] | 8 |
| **Maximum voltage rating** | [V] | 300 |
| **Required precision level at Iop.max** | [A pk-pk] | 24 |
| **Maximum repetition rate** | [Hz] | 4 |

### Operating mode requirement

The septum magnet coils have to be supplied by pulsed currents whose waveform presents a stable flat-top during the total beam duration in order to deflect the beam. The power converters will deliver high current pulses with fast rise and fall times in order to minimize the thermal losses in the magnets and the power consumption from the mains.

For the actual ESRF configuration, the magnet pairs S1 and S2 as well as Se2/1 and Se2/2 are serially powered by single power converters. With the new powering scheme, the magnets will be powered according to two cases, shown below in Figures 9.39 and 9.40:

**Figure 9.39: Case 1 (normal operation): Electromagnetic Magnets S2 and Se2/1 are powered with power converters and S1 and Se2/2 are Permanent Magnets.**

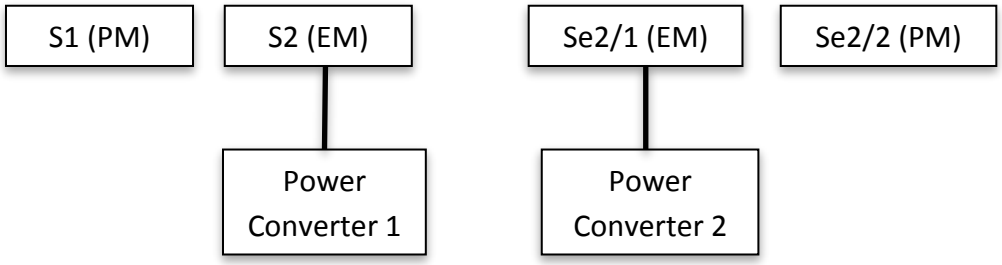


**Figure 9.40: Case 2 (redundant operation in case of degradation of the PM septum): Electromagnetic Magnets S1, S2, Se2/1 are powered with power MegaDiscap converters and Se2/2 is powered using an existing ESRF power converter.**

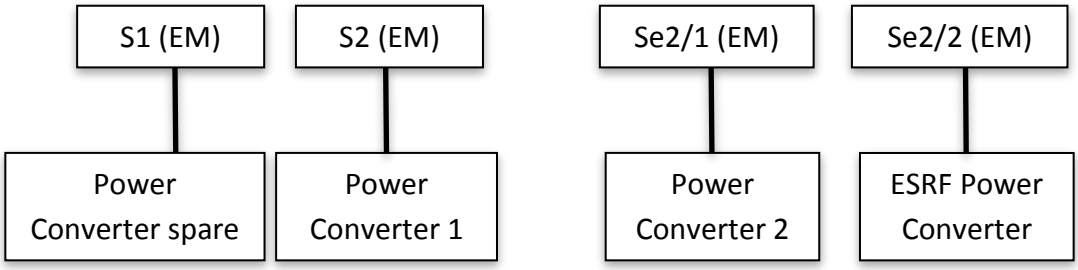

### Power converter specification

The septum magnet coils S1, S2, Se2/1 have to be supplied by pulsed currents whose waveform presents a stable flat-top of 500µs (Figure 9.41).

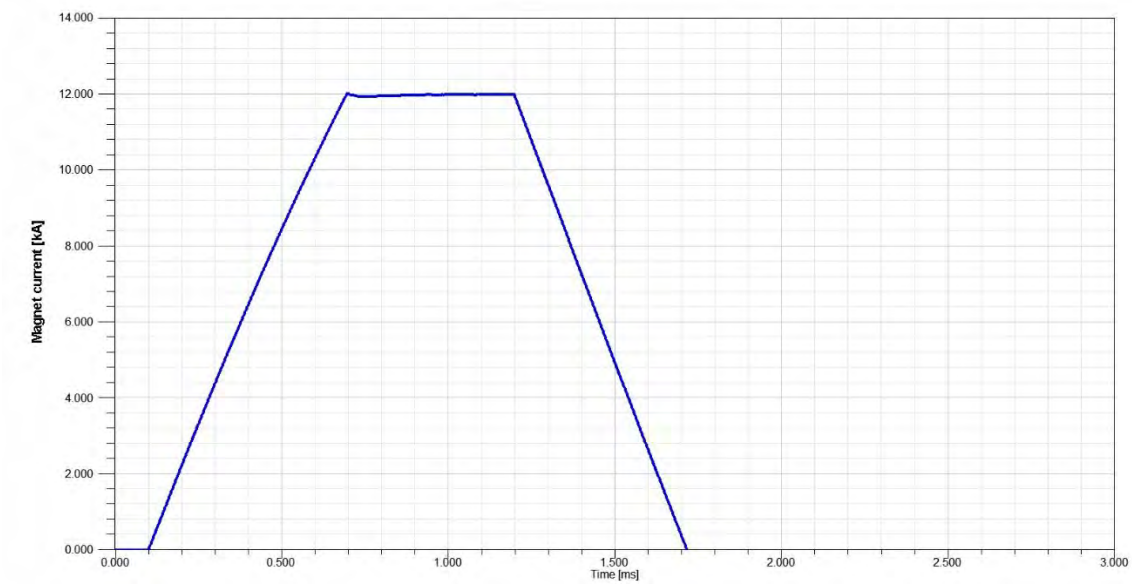


**Figure 9.41: Flat-top waveform of the pulsed current in the septa magnet coils.**

In order to deliver high current pulses, a step-up transformer (ratio 8/1) is installed for each septum magnet (S1, S2, Se2/1) and connected to the magnet using high current striplines (busbars). The location of the transformers and busbar has to be as close as possible to the magnets to minimize the line impedance. The converter parameters are given in Table 9.13.

**Table 9.13: Parameters.**

| Parameters | Unit | Value |
|---|---|---|
| Maximum operating current at secondary side of | [kA] | 12 |
| Minimum operating current at secondary side of | [kA] | 8 |
| Maximum flat-top duration (including current stabilization) | [µs] | 500 |
| Current precision (100µs minimum duration, peak to peak, pulse to pulse, single shot or uninterrupted operation | [A pk-pk] | 24 |
| Maximum voltage at the primary side of the matching | [kV] | 2.2 |
| Matching transformer ratio | [-] | 8 |
| Maximum repetition rate | [Hz] | 4 |
| Resistance seen at converter output (estimated) | [Ohms] | 0.124 |
| Inductance seen at converter output (estimated) | [µH] | 236 |
| Input voltage (3 phases with neutral) | [VRMS] | 400 |
| Maximum input current (per phase) | [ARMS] | 40 |
| Converter dimensions (height – width – depth) | [mm] | 2225 – 1150 - 1000 |

### Power supply installation

Two MegaDiscap power supplies (the "1" and the spare) will be installed in the technical zone near the location of the magnets S1 and S2 in the injection zone of TL2 (Figure 9.42). The MegaDiscap "2" will be installed close to the foot bridge just above the Se2/1 magnet. The transformers and the DCCTs are installed as close as possible to the magnets to minimize the loop inductance. The communication between the power supply and the control room is made through FGC Ethernet protocol for the settings and feedback measurements. TTL signals are used for firing trigger and measurement synchronization.

One existing ESRF power supply installed in the injection/extraction platform will be kept for the magnet Se2/2 (Figure 9.43) in case of problems with the PM septum. Interfaces with the control room allow synchronization, configuration and feedback measurements with the power supply through Modbus Ethernet and TTL signals.

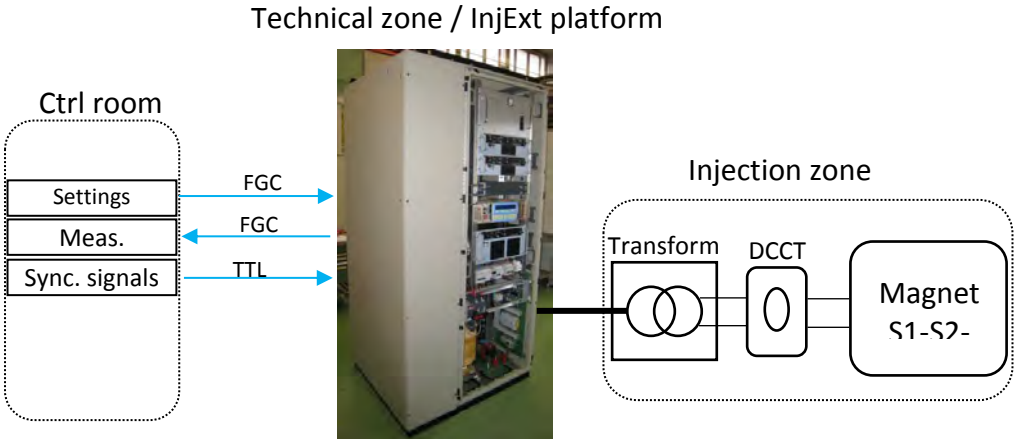


**Figure 9.42: MegaDiscap power supply installed near TL2 injection zone.**

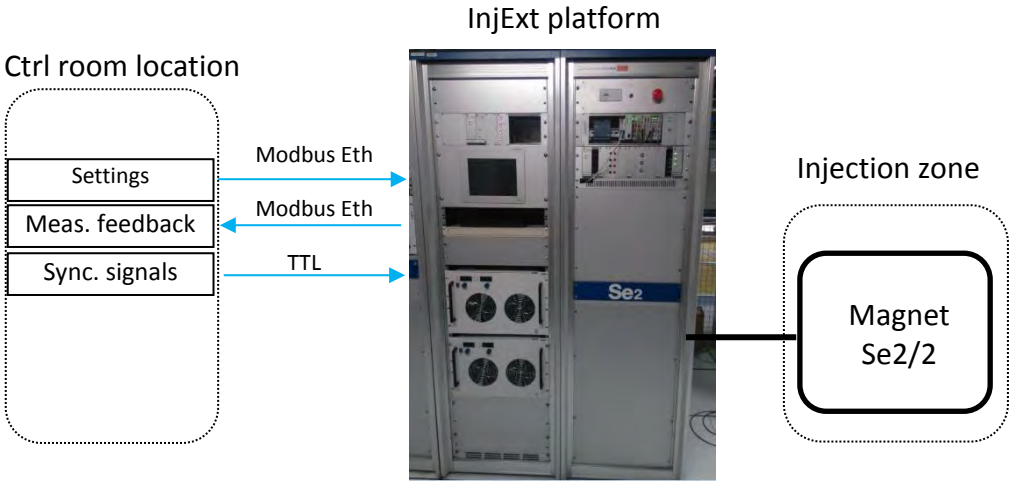


**Figure 9.43: Existing ESRF power supply in the injection/extraction platform (to be kept for the magnet Se2/2 in case of problems with the PM septum).**

## 9.21 Injection kickers power supply

It is foreseen to re-use the existing kickers power supplies. The four storage ring injection kickers are operated by four individual power supplies pulsing at 10 Hz with a pulse length of approximately 3μs, as shown in **Figures 9.44**, **9.45** and **9.46**. The pulse tracking of the four magnets, comprising pre-pulse rise, flat top, fall and post pulse ripple is specified to be better +/- 1% within a working range from 40 % to 100 % kick.

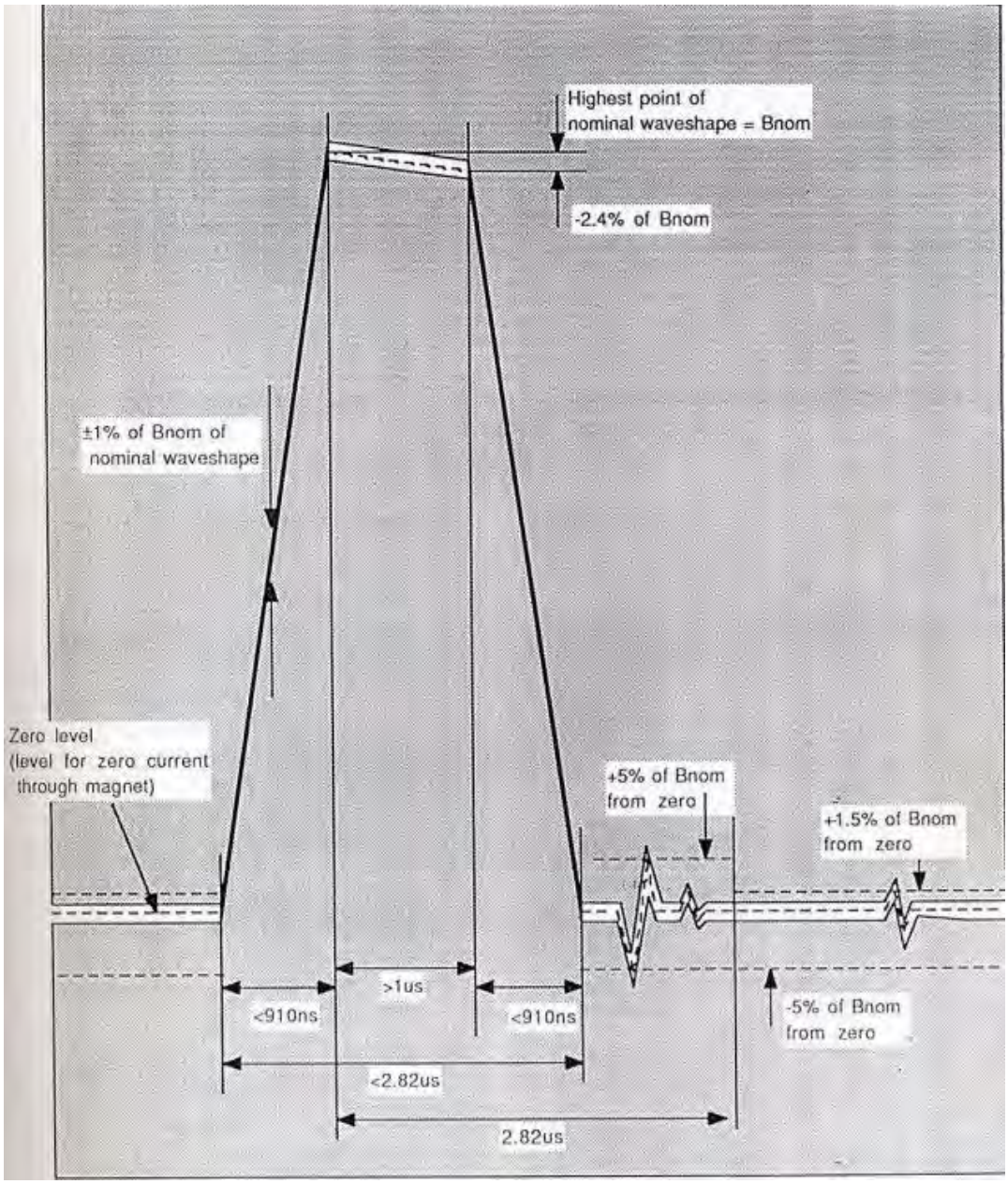


**Figure 9.44: Injection kicker pulse shape.**

**Figure 9.45: Top: Characteristics of the present pulsed power supplies, kickers are shown in blue. Bottom: Storage ring injection kickers schematic.**

| Magnet Type | Number | Current Wave form | Energy storage | I magnet | Adaptation Transformer | Switching Type |
|---|---|---|---|---|---|---|
| Booster Injection Septum Si | 1 | 1,2ms | C:2300uF Vc: 150 V | 6200 A | no | Thyristor |
| Booster Extraction Septum SE1 | 1 | 1,2ms | C:4700uF Vc: 150 V | 3200 A | no | Thyristor |
| Booster Extraction Septum SE2 | 1 | 1,4ms | C:13000uF Vc: 150 V | 9000 A | no | Thyristor |
| Booster Extraction Bumpers B1, B2, B3 | 3 | 3 ms | C:300uF Vc: 750 V | 750 A | yes | Thyristor |
| Storage ring injection Septum S1-2 | 1 | 2,2 ms | C: 640 uF Vc: 2 KV | 10 000 A | yes | Thyristor |
| Storage ring injection Septum S3 | 1 | 60 us | C: 200 uF Vc: 2 KV | 8 000 A | no | GTO |
| Booster Injection/Extraction Kickers Ki-Ke | 2 | 1 us | PFN:3 cables RG 220 in // Ve: 40 KV | Ki:400 A Ke:2000 A | no | Thyratron |
| Storage Ring Injection Kickers K1, K2, K3, K4 | 4 | 2,8 us | PFN:3 cables RG 220 in // Ve: 40 KV | 2200 A | no | Thyratron |

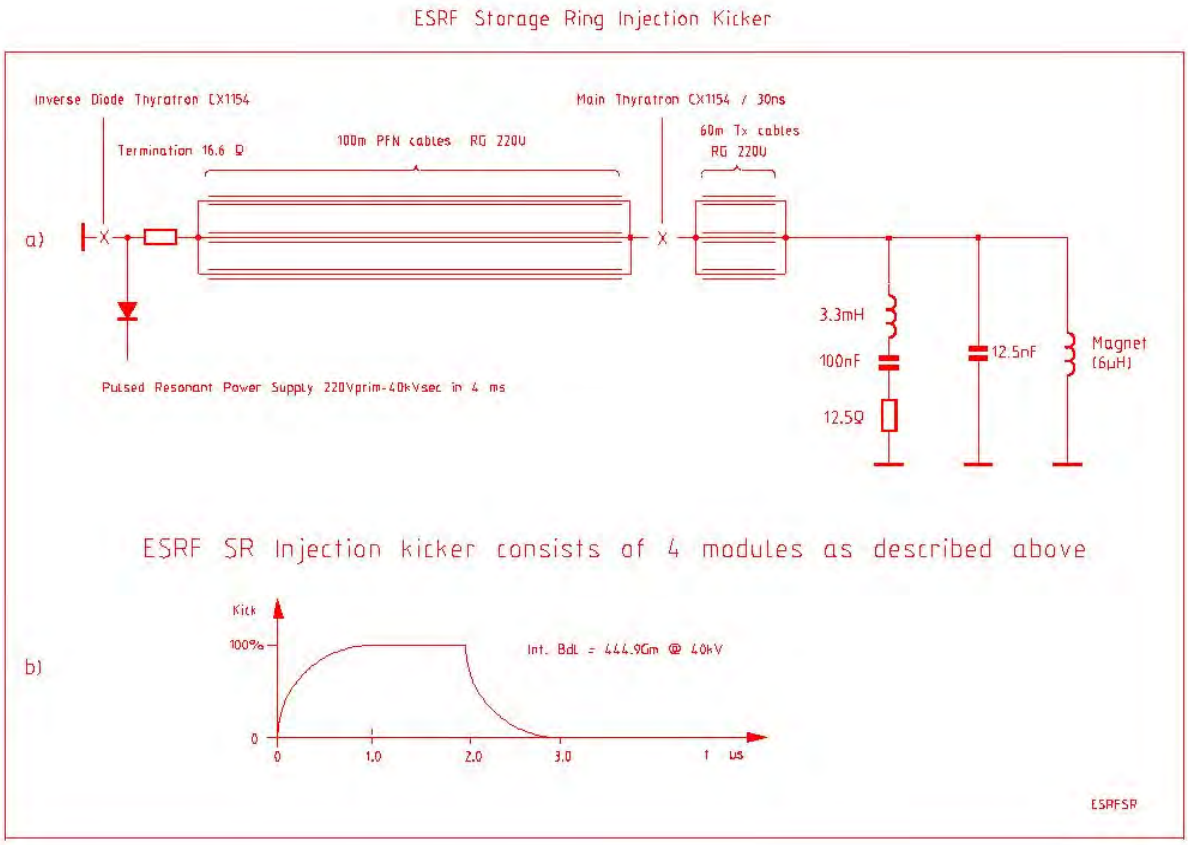

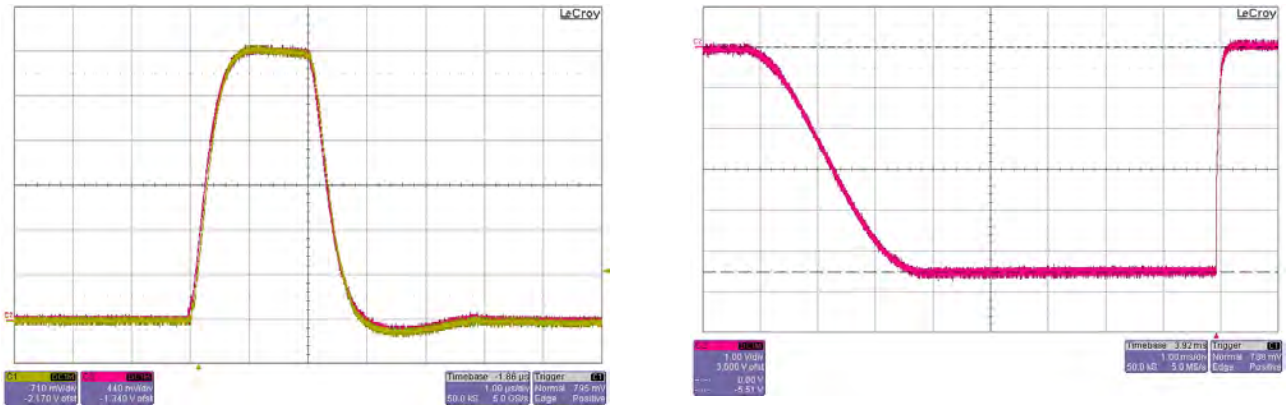


**Figure 9.46: Magnet current (left) and PFN voltage right.**

Recent measurements were performed to assess the present performance in term of stability and reproducibility of the injection kickers power supplies. Measurements were done on the kickers K1 only, but similar results can be expected for the remaining three kickers.

- PFN voltage stability (done at Vpfn = 26.7kV):
  - Losses on the cables and connectors: 0.69%
  - Pulse-by-pulse reproducibility: 0.28%

- Current seen by the magnet:
  - Flatness of the plateau: 2.6%
  - Tail of the main pulse: 4.8%
  - Amplitude jitter: +/-0.29% (~3A)

The flatness of the plateau and negative rebounds will not impact the perturbations on the stored beam as long as they are identical for the four kickers, flatness could affect the injection efficiency since all bunches will not see the same bump amplitude.

On the other hand, pulse-to-pulse reproducibility and amplitude jitter will have a negative impact on both the injection efficiency and perturbations onto the stored beam. The measured values, although better at nominal current than the initially specified 1%, are currently a factor 10 larger than what is needed to keep the perturbation below $0.1\sigma$. Power supply upgrade and the implementation of an active compensation maybe required to achieve transparent injection.

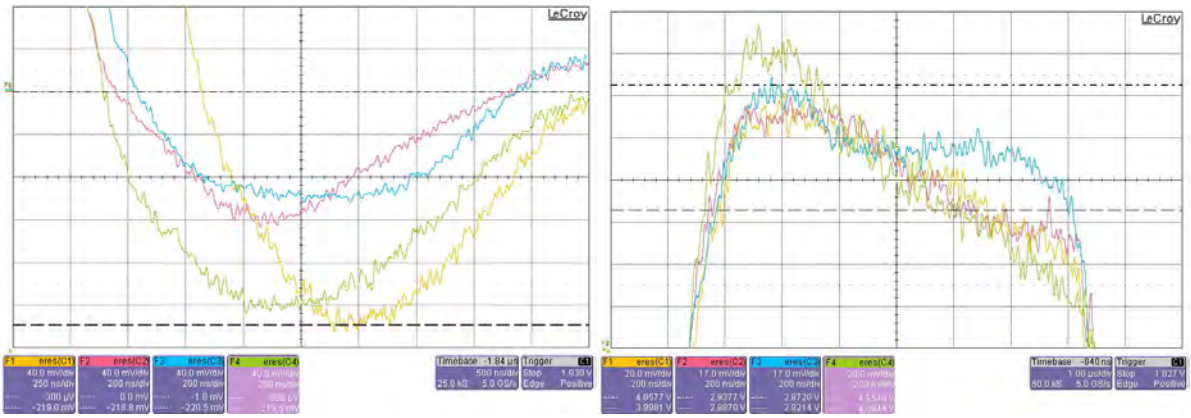

Figure 9.47: Flat-top and tail comparison of the four kickers.

Figure 9.47 shows a comparison of the flat-top and tails of the four kickers. In order for the bump to remains closed at all times the four kickers pulse shape should be identical. The measured rise-time, flatness of the plateau and tail are as follows:

- Flatness:
  - K1: 2.6%, K2: 2.7%, K3: 1.77%, K4: 2.9%
- Rise time:
  - K1: 455ns, K2: 485ns, K3:484ns, K4: 457ns.
- Tail amplitude:
  - K1: 4.8%, K2: 4.4%, K3: 3.7%, K4: 5.1%.

It is seen that there is significant, and most likely need, room for improvement on all three aspects in order to achieve transparent injection.

## 9.22 Mechanical engineering

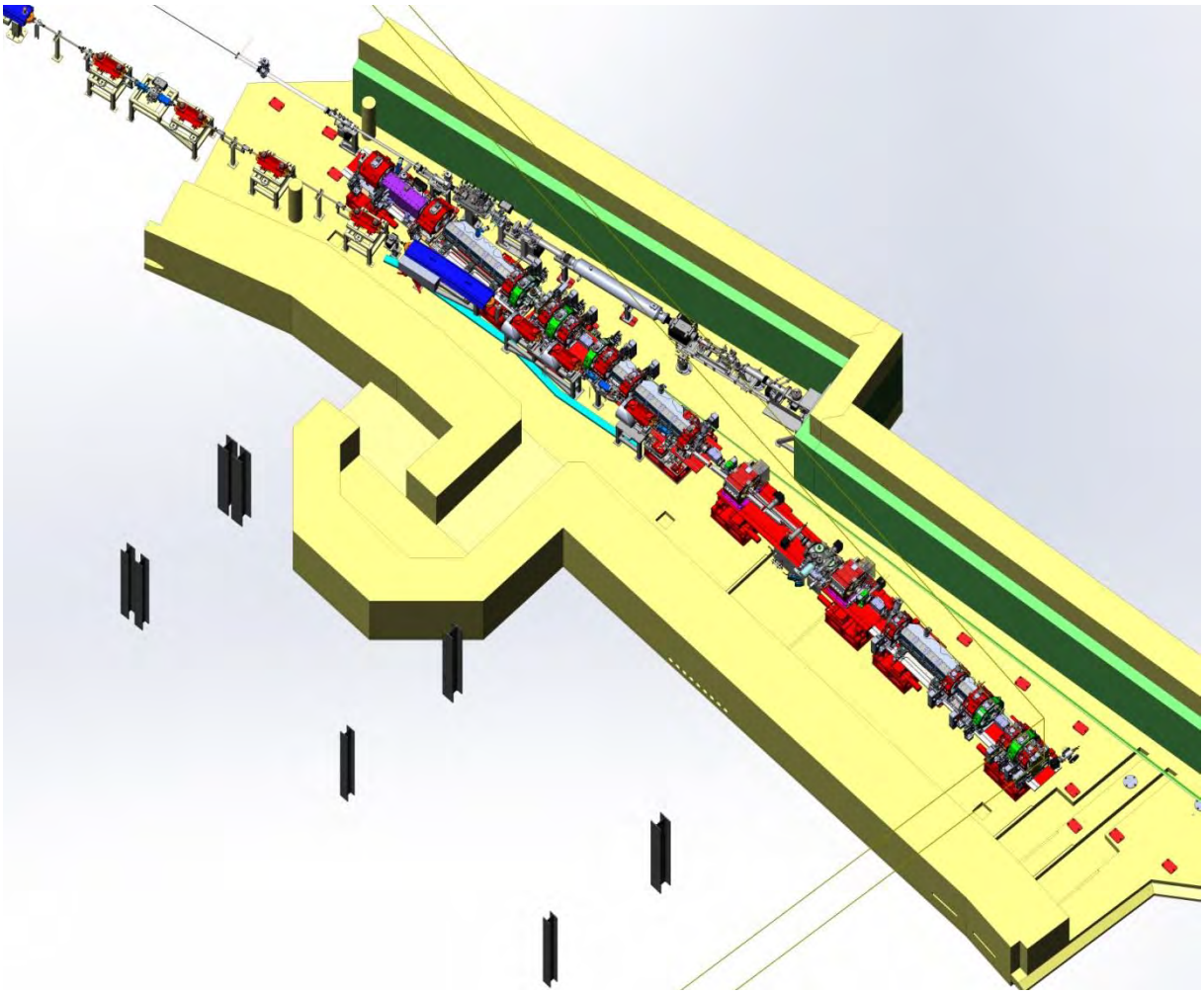

Figure 9.48: General top view of the injection cells and end of TL2.

Figure 9.48 shows the general layout of the injection zone (cell 3 and 4) including the tunnel walls and the end part of TL2. To be noted that ID03 front end exists and is shown whereas BM03 and ID04 will never exist. BM03 beamport is blocked within the dipole chamber as is the ID04 beam. The central girder of the injection zone is in the straight section ID04. An existing wide trench allows cables to be distributed to the special magnets. This section gives a description of the girders that need to be modified with respect to the standard cell girders.

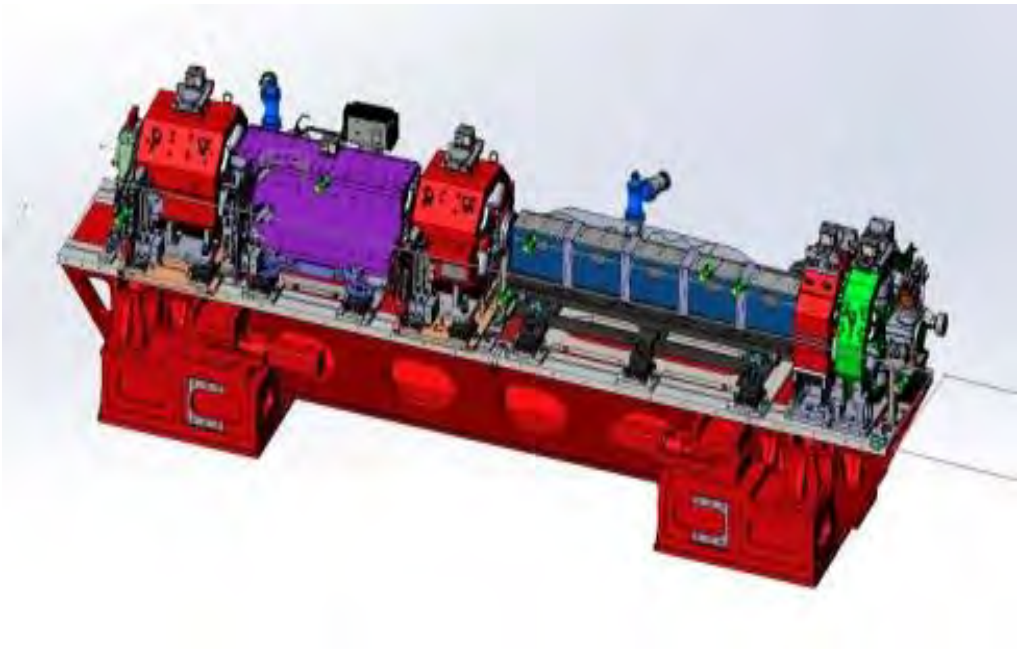

Figure 9.49: Girder 3, cell 3.

Figure 9.49 shows the girder 3 of cell 3 which is identical to the standard girder 3 except for the last quadrupole and sextupole electrical connection box located on the outer-side of the ring. BM03 dipole radiation stopped with dipole chamber and requires a special absorber.

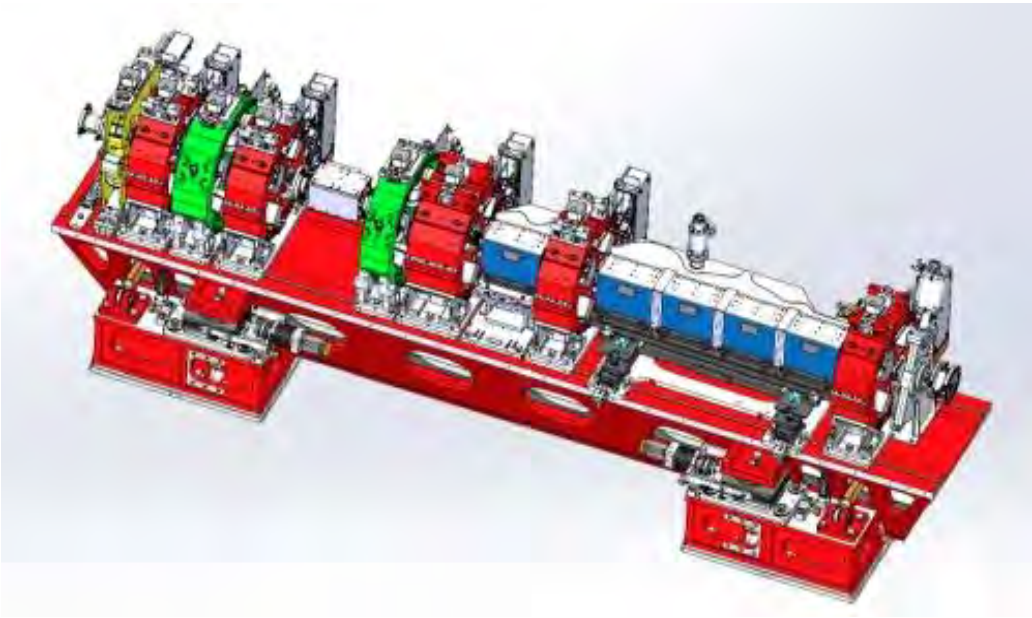

Figure 9.50: Girder 4, cell 3.

Figure 9.50 shows the girder 4 of cell 3. Similarities with girder 4 standard cell. The magnets are simple variants of the standard cell girders and the motorization is identical as well as the chamber CH11 and the sector valves. All magnets have their electrical box on the outside of the ring. The injection kicker with its ceramic chamber is installed in place of the chamber CH12. Special supports are required for the dipole modules and a non-standard aluminium dipole chamber is needed. The BPM bellow chamber CH14 and the absorber CH13 are also non-standard.

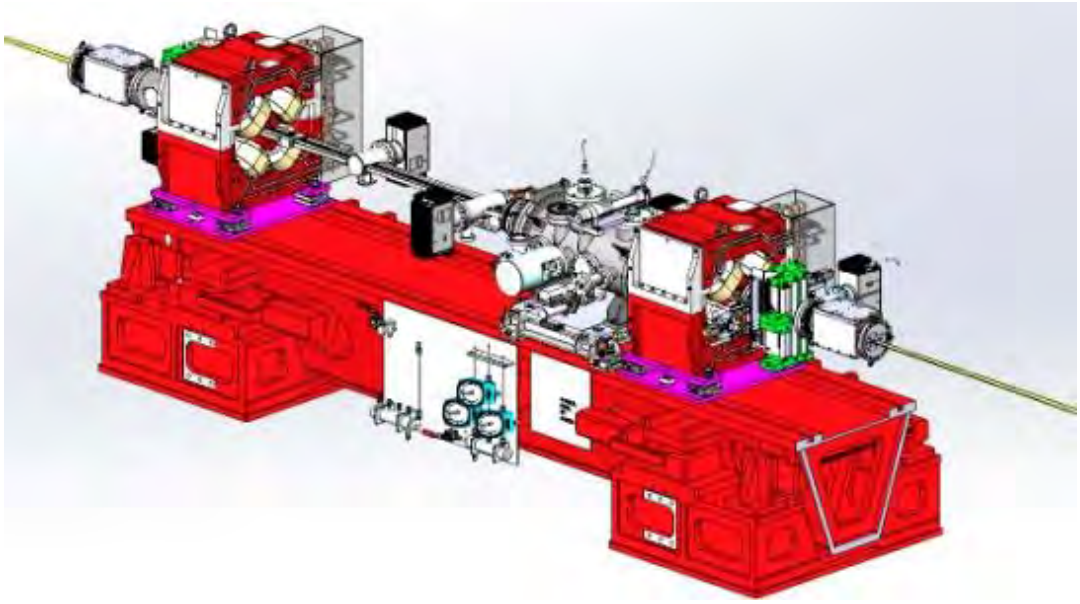

Figure 9.51: Dedicated central girder.

Figure 9.51 shows the dedicated central girder with is not present in the standard cell and is located in place of the straight section ID chambers. Although similar to the standard girder some modification such as shortening may be required. This girder is hosting the kickers K2 & K3, the in-vacuum septum S3 and correctors. The 2 central quadrupoles are recuperated from the existing machine. A horizontal scraper is inserted right after the second quadrupole for beam dynamics studies and special diagnostics are installed upstream the septum S3.

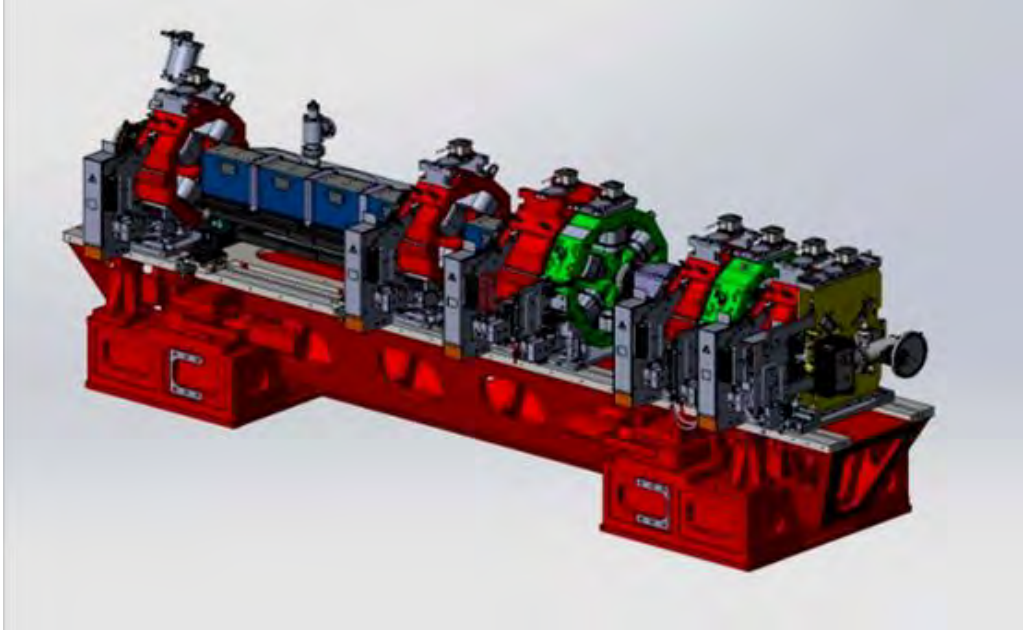

Figure 9.52: Girder 1 of cell 4.

Figure 9.52 shows the girder 1 of cell 4 which the last girder that differs from the standard cell. Again all magnet are variant from the standard and the girder motorization is identical as well as the sector valve. The electrical connection box are all located on the outside of the ring and the kicker K4 in installed in place of the crotch CH3. Special supports are required for the dipole modules and a non-standard aluminium dipole chamber CH2 is needed. The BPM bellow CH1, the absorbers CH2 and CH4 and the vacuum vessel CH3 and Ch4 are non-standard as well.

# 10 Vacuum System

## 10.1 Introduction

The vacuum system of the standard cell consists of 14 chambers. The arrangement of the chambers and the absorbers on the 4 girders of the standard cell is presented in Figures 10.1 to 10.4. The components of the vacuum system of the different girders are given in Figures 10.5 to 10.8. Chamber 2, 5, 9 and 13 are made of aluminum and the others made of stainless steel (316 LN). The details of the chambers and the absorbers are presented in Chapter 3: Accelerator Engineering

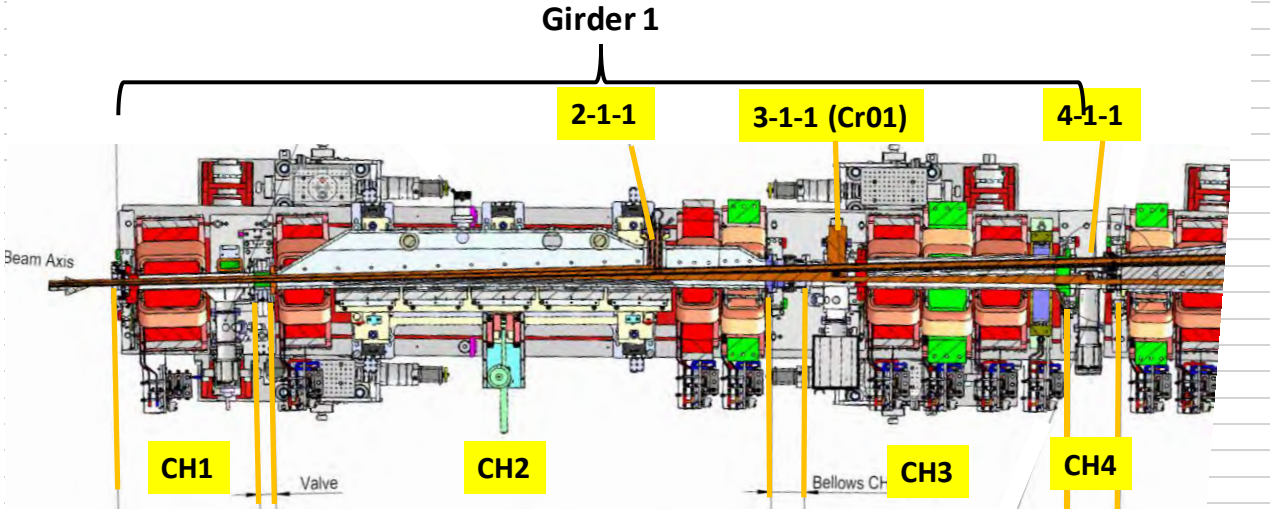


Figure 10.1: Location of the different vacuum chambers in girder 1.

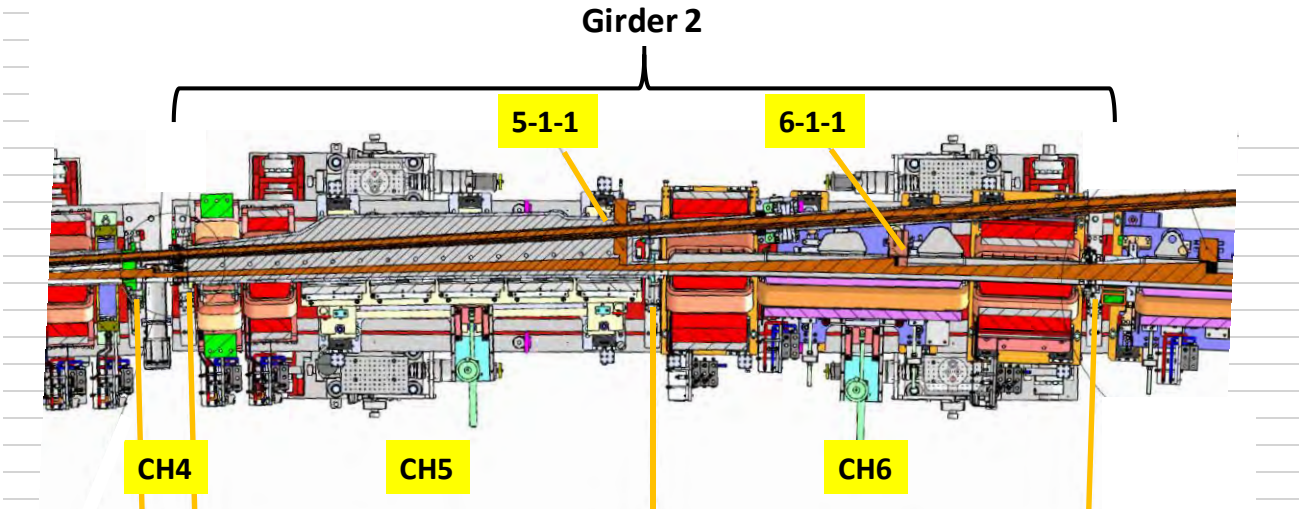


Figure 10.2: Location of the different vacuum chambers in girder 2.

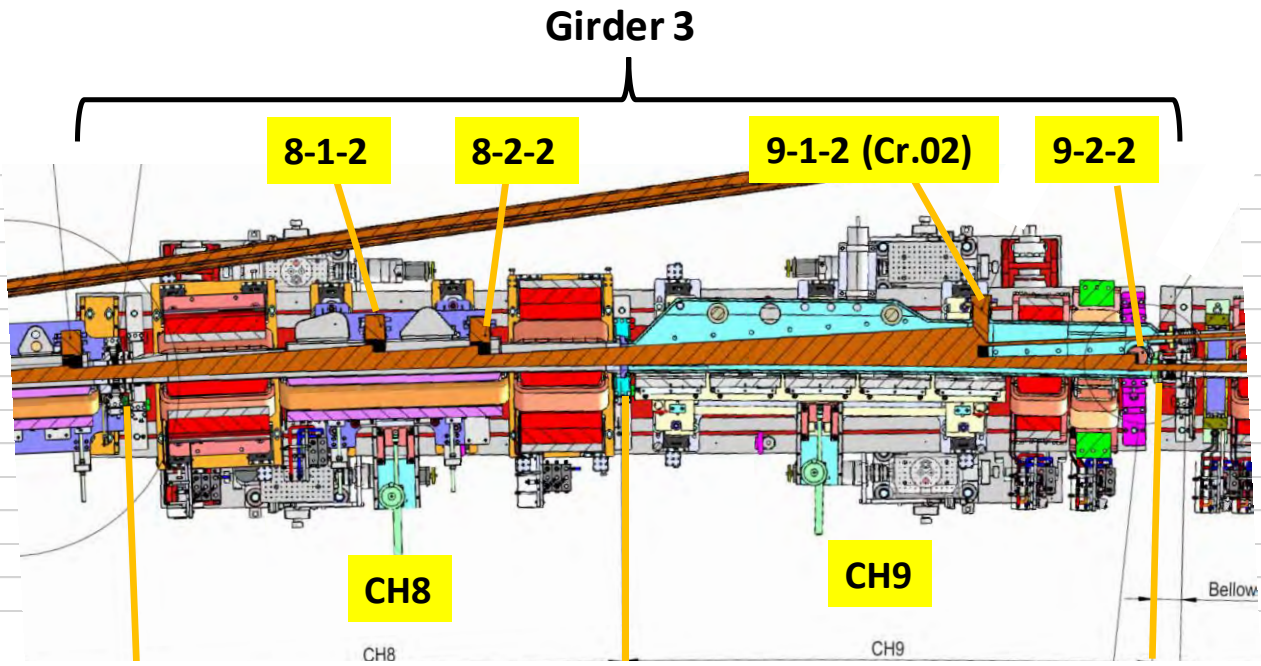


Figure 10.3: Location of the different vacuum chambers in girder 3.

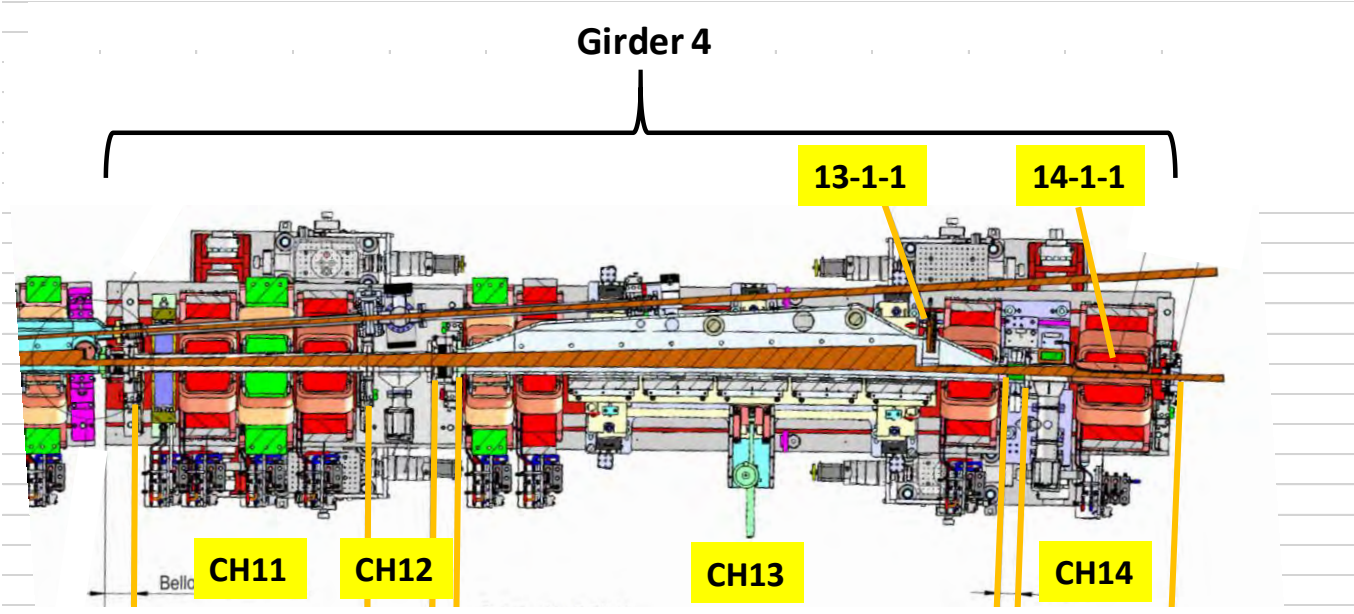


Figure 10.4: Location of the different vacuum chambers in girder 4.

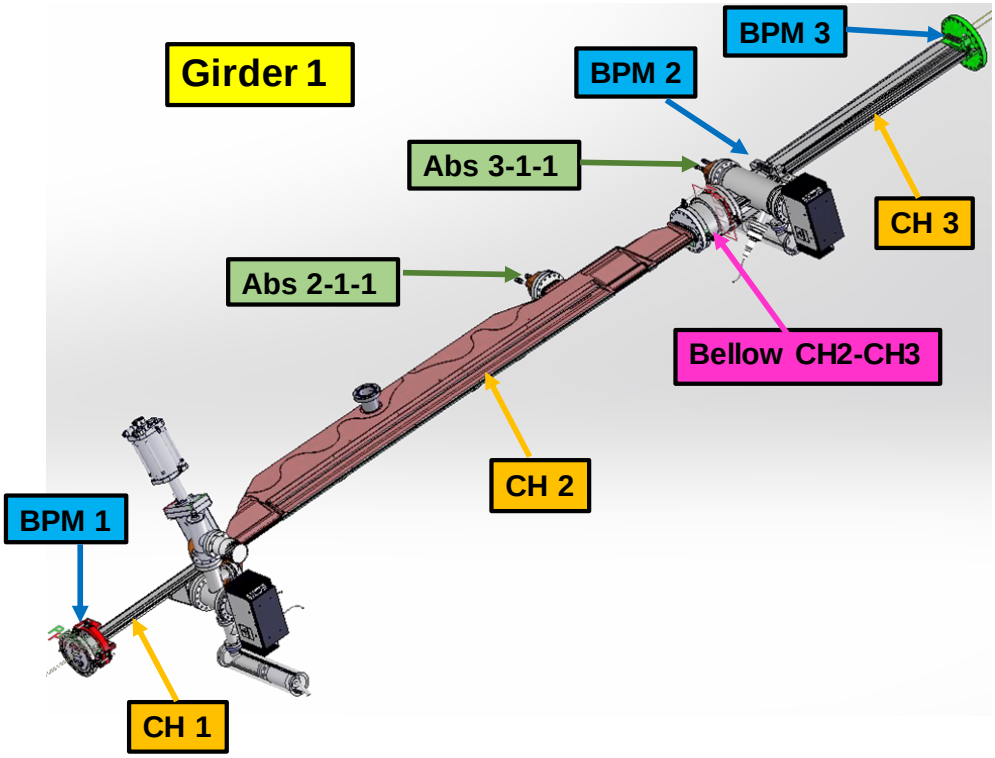


Figure 10.5: Components of the vacuum system installed on girder 1.

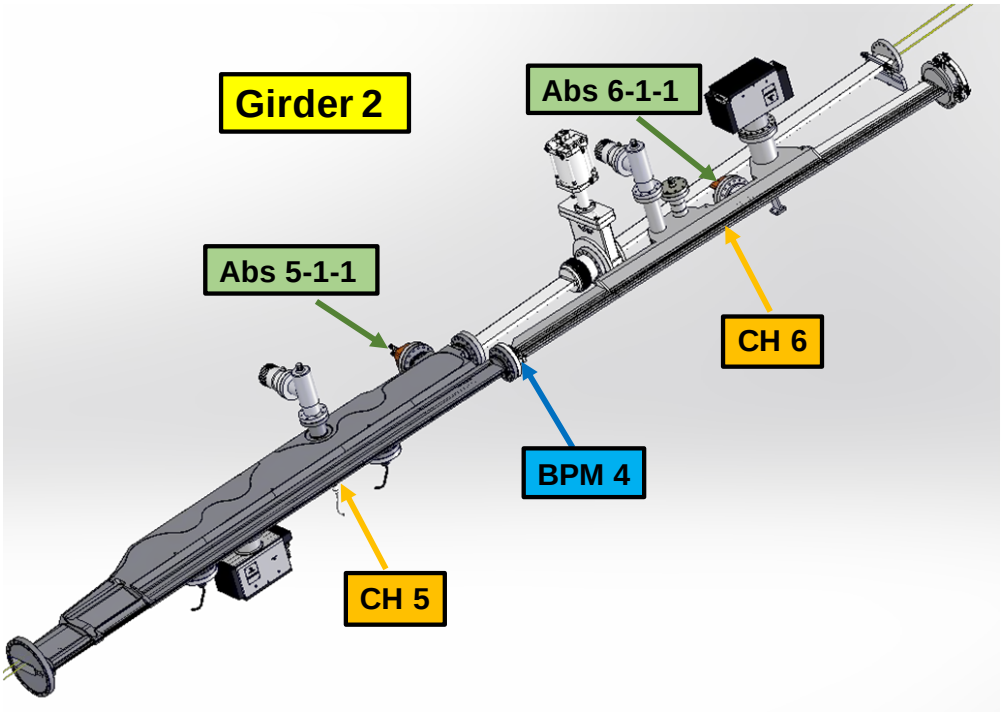


Figure 10.6: Components of the vacuum system installed on girder 2.

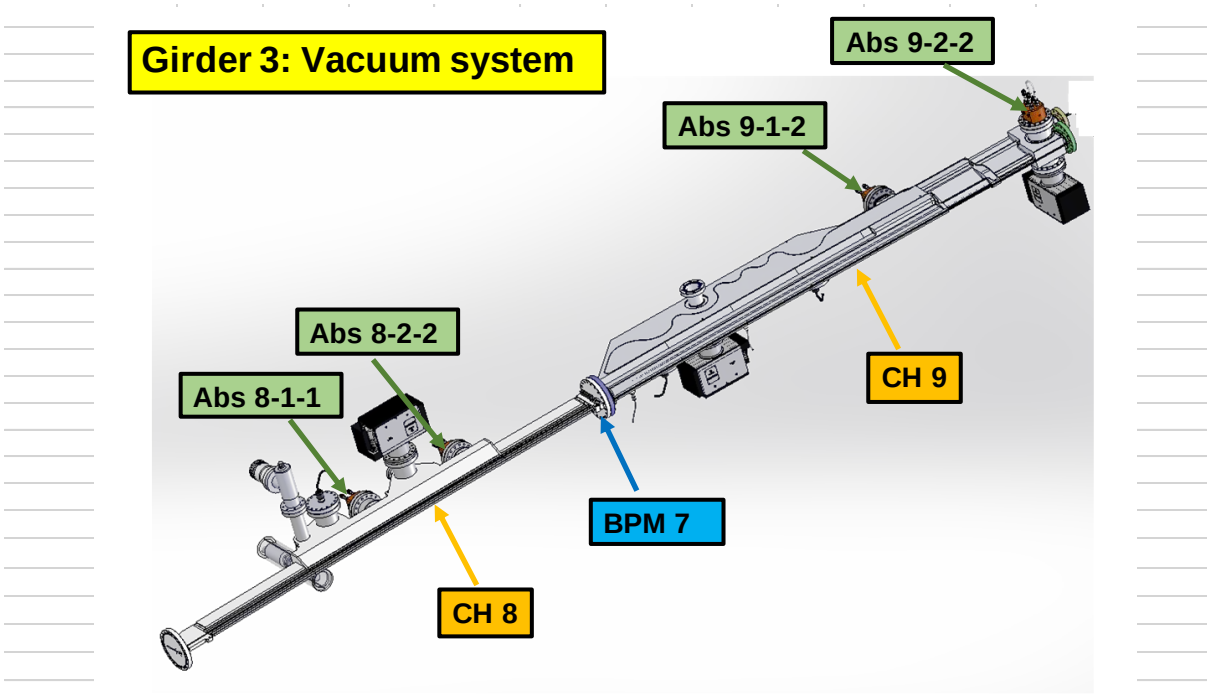


Figure 10.7: Components of the vacuum system installed on girder 3.

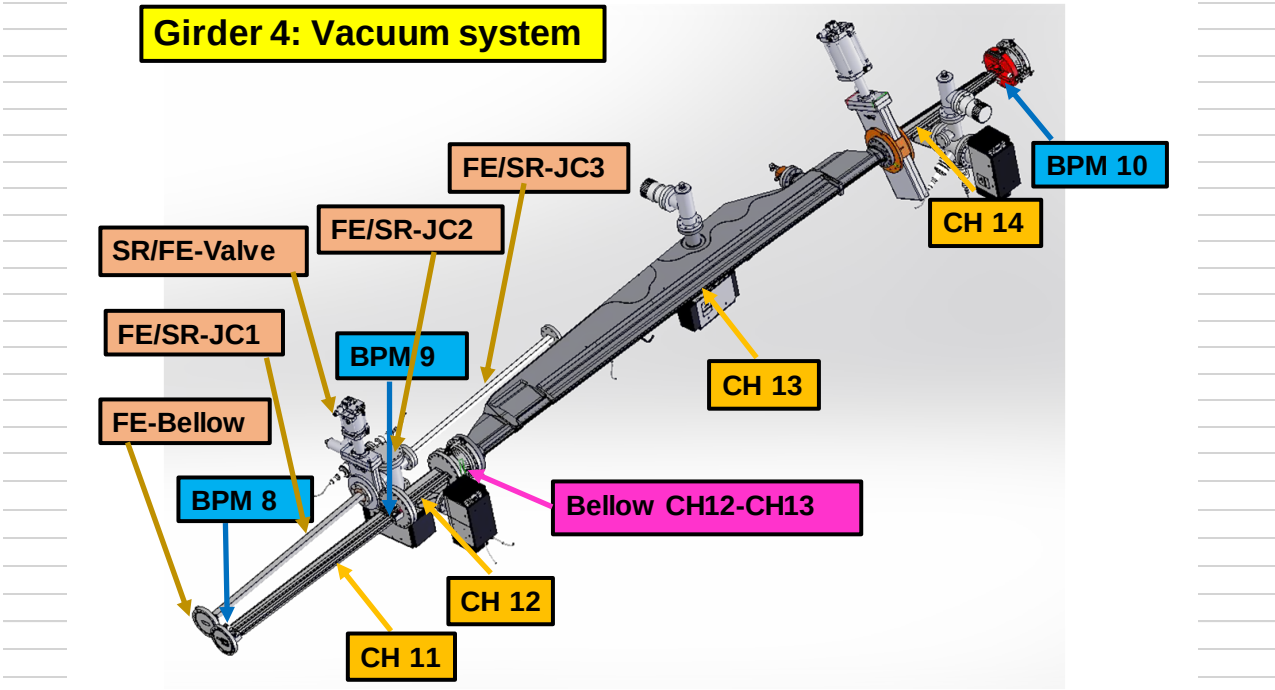


Figure 10.8: Components of the vacuum system installed on girder 4.

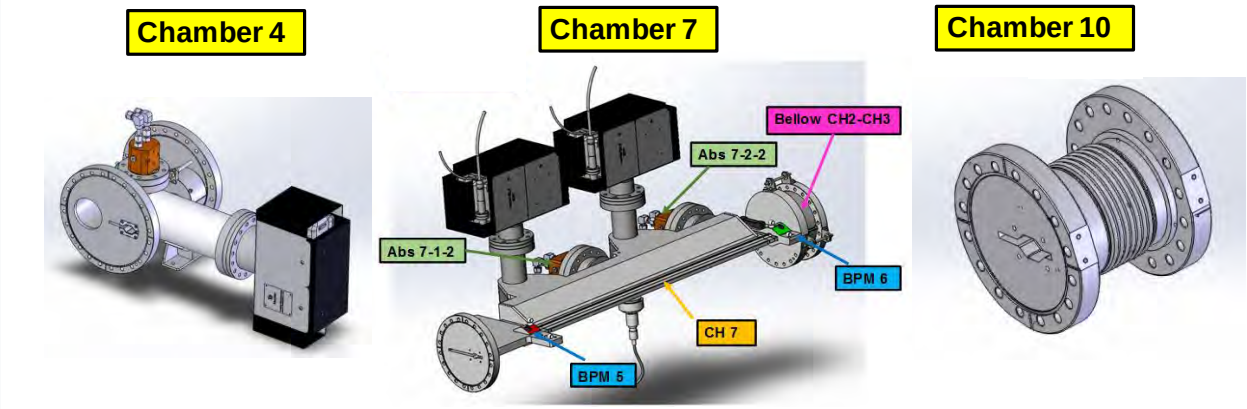


**Figure 10.9: Components of the vacuum chambers 4, 7 and 10, which are the connection between the girders 1-2, 2-3 and 3-4.**

The main duties defined for the work package concern the vacuum generation (pumping) and measurement/analysis, procurement of the vacuum system components, accompanying of the chamber design with vacuum simulation and preparation of the assembly of and installation of all ultra-high vacuum (UHV) items.

Two chambers of each cell the machine in the vicinity of insertion will be coated with a non-evaporable getter (NEG) film to reduce the photo-desorption and provide sorption pumping for getterable gases.

## 10.2 UHV pump and vacuum control layout

Lumped sputtering ion pumps and NEG-cartridge based pumps are the principal UHV pumps of the storage ring. For the ion pumps, ESRF selected a triode arrangement mainly to assure compatibility with existing ion pump power supplies (see Figure 10.10).

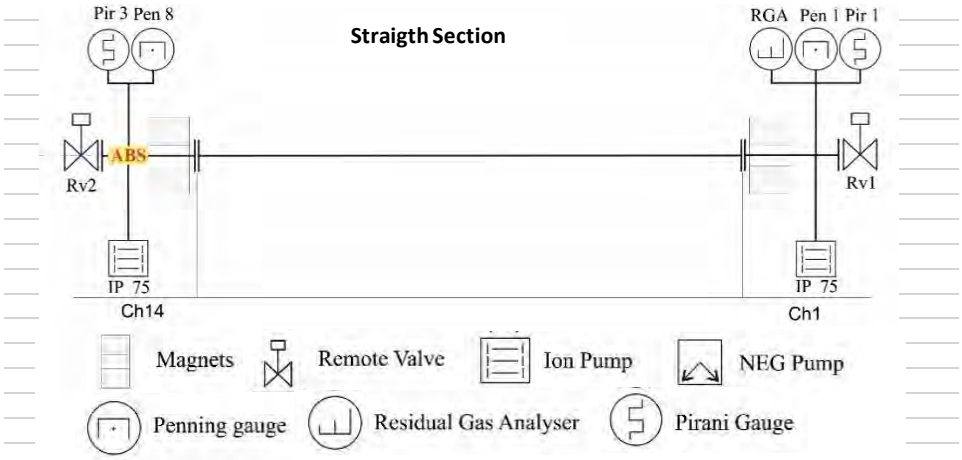


**Figure 10.10 : Vacuum layout of the straight section of an EBS standard cell.**

Cold cathode gauges of the inverted magnetron type will be used to measure the vacuum in the UHV regime, thermal conductivity gauges of the Pirani type for the fore-vacuum.

Quadrupole residual gas analyzers (RGA) will provide information about the gas composition in each vacuum sector and can be used for in-situ Helium leak detection.

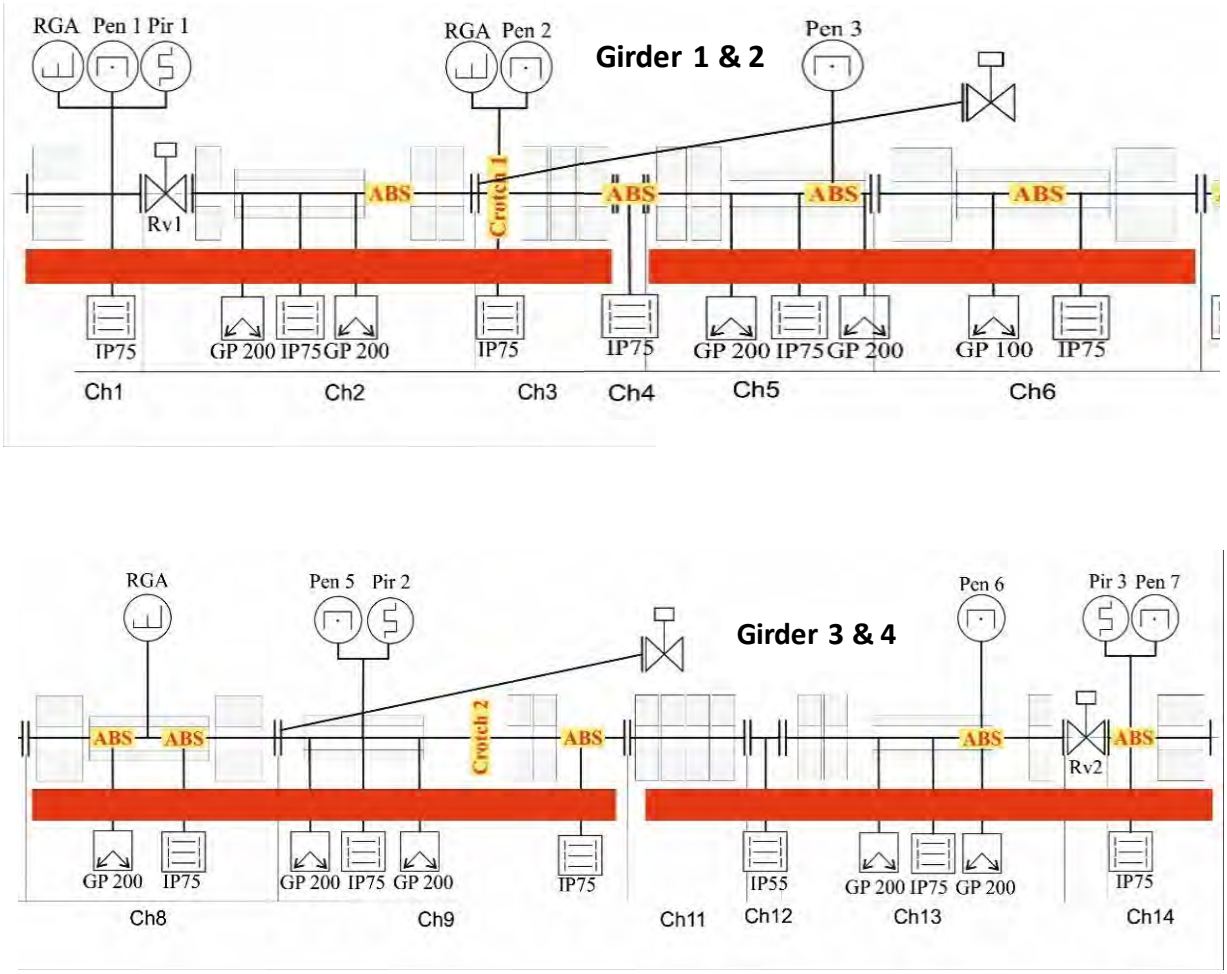


Figure 10.11: Vacuum layout of an EBS standard cell.

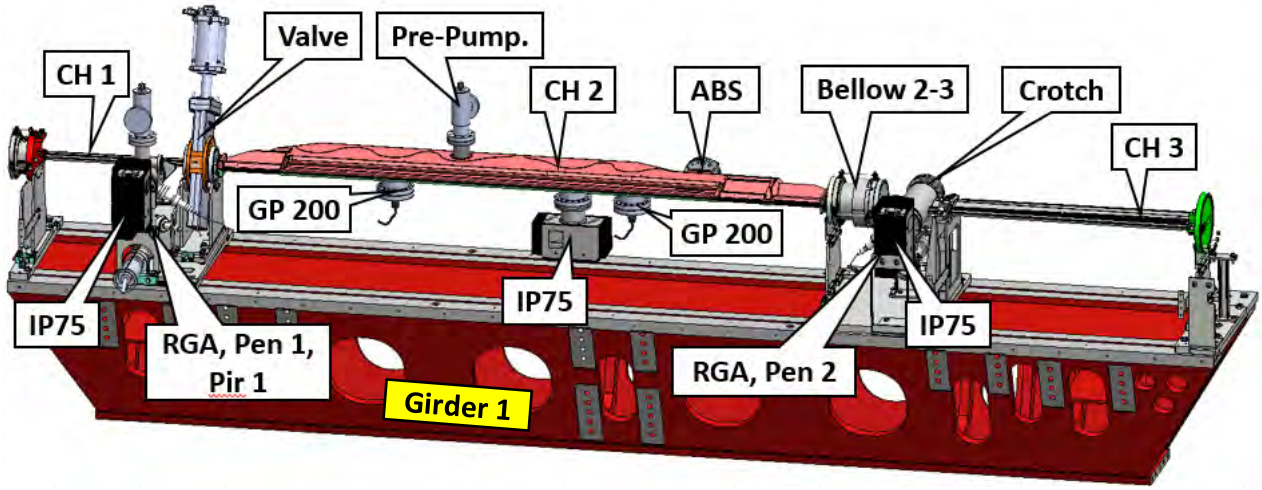


Figure 10.12: Vacuum chambers and components on girder 1.

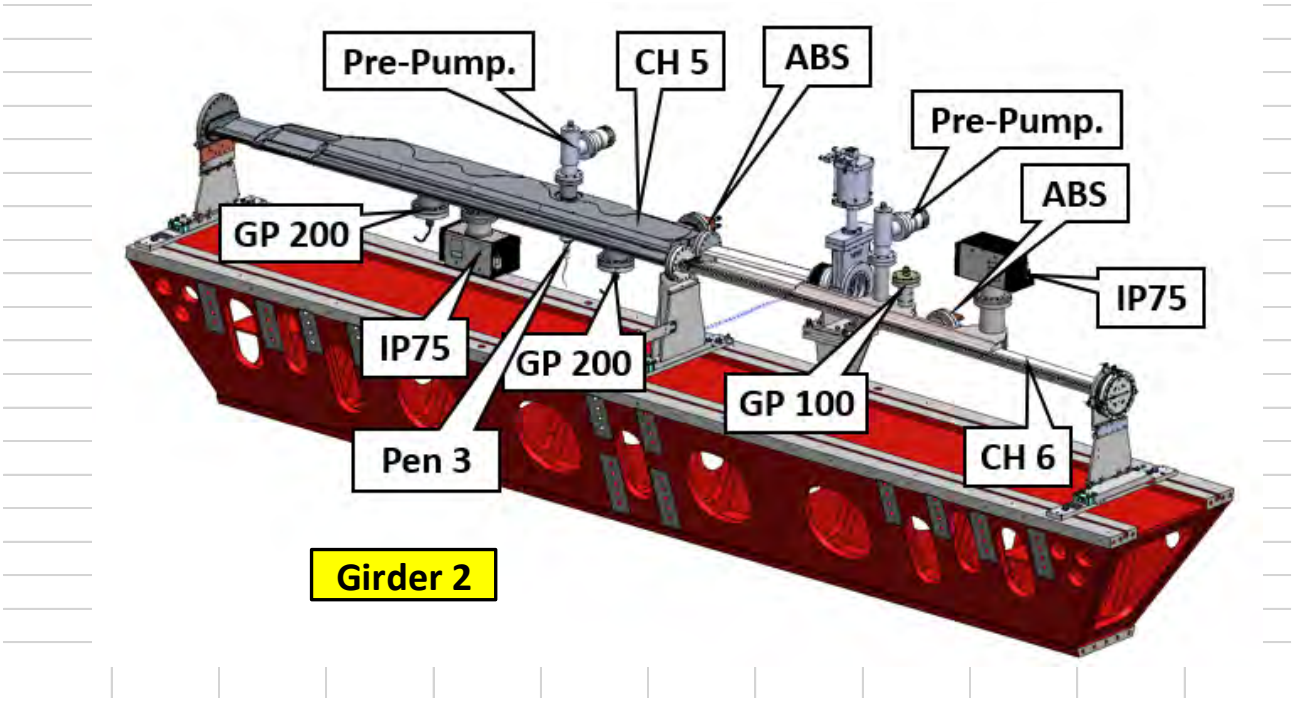


Figure 10.13: Vacuum chambers and components on girder 2.

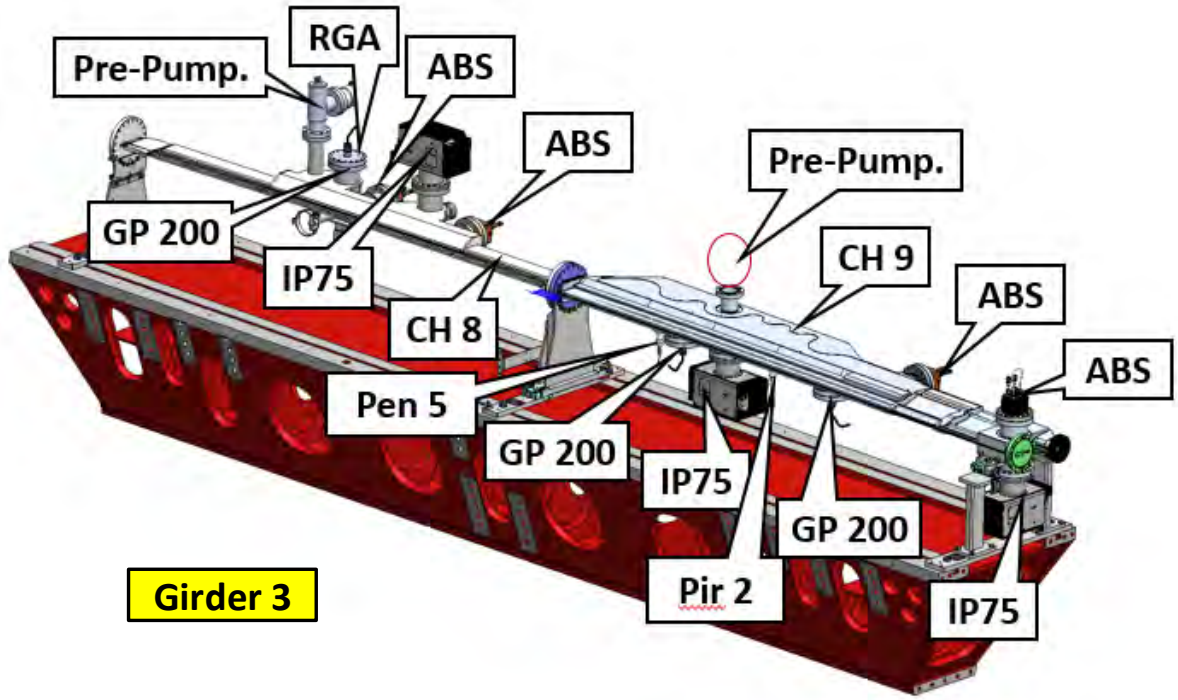


Figure 10.14: Vacuum chambers and components on girder 3.

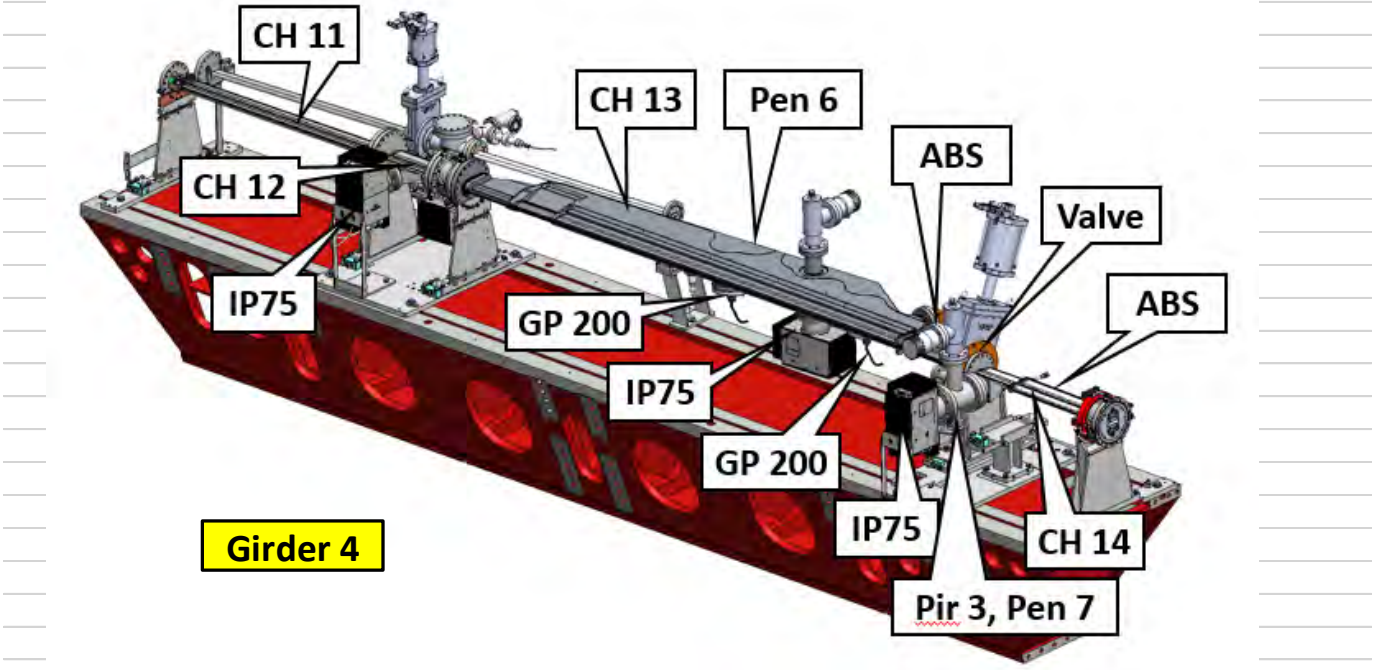


Figure 10.15: Vacuum chambers and components on girder 4.

The Vacuum Control will be handled by modern Programmable Logic Controllers (PLC) which allow failure analysis and troubleshooting via network. A fast PLC system will be installed in

addition, which does not interfere with the safety relevant principal PLC and allows for analysis of very fast pressure events.

## 10.3 Full metal sector valves and front end valves

Full metal sector valves (see Figure 10.11) with pneumatic actuator have been chosen for the 32 vacuum cells and the separation of the insertion device sector as well as for the separation between storage ring and front end module 1 (front end valves). The tight tolerances of the beam stay clear zone translates into tight tolerances between the movable part of the sector valves and the valve body to allow the precise alignment of the valve.

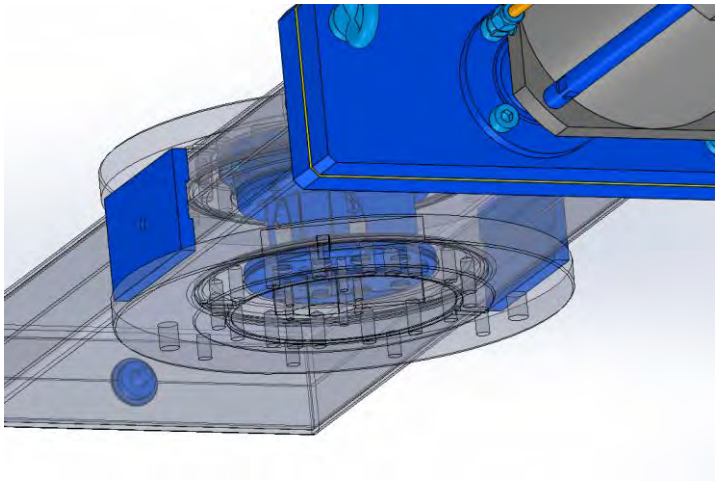

**Figure 10.16: EBS full metal sector valve with RF liner.**

The RF liner of the sector valves will be produced of copper beryllium sheets to improve thermal and electric conductivity. A production prototype of the sector valve is supposed to be installed in summer 2016 on the existing machine in order to verify the pressure and temperature prediction with beam.

## 10.4 Pressure simulation

The installed nominal pumping speed is approximately one third less as compared to what is installed on the existing machine. The presence of many more magnets and a smaller cross section of the vacuum chamber do not allow the installation of huge pumps with big connection flanges providing high conductance / high efficient pumping speed. The chamber design has been accompanied with pressure simulation in order to optimize the usage of the installed pumps. Figure 10.12 shows the expected pressure distribution in a standard cell

at beam current of 200 mA in multibunch mode after different values of Ampere Hours of beam conditioning. The cell is shown in length units and is starting with the middle of the insertion device straight section (s=0).

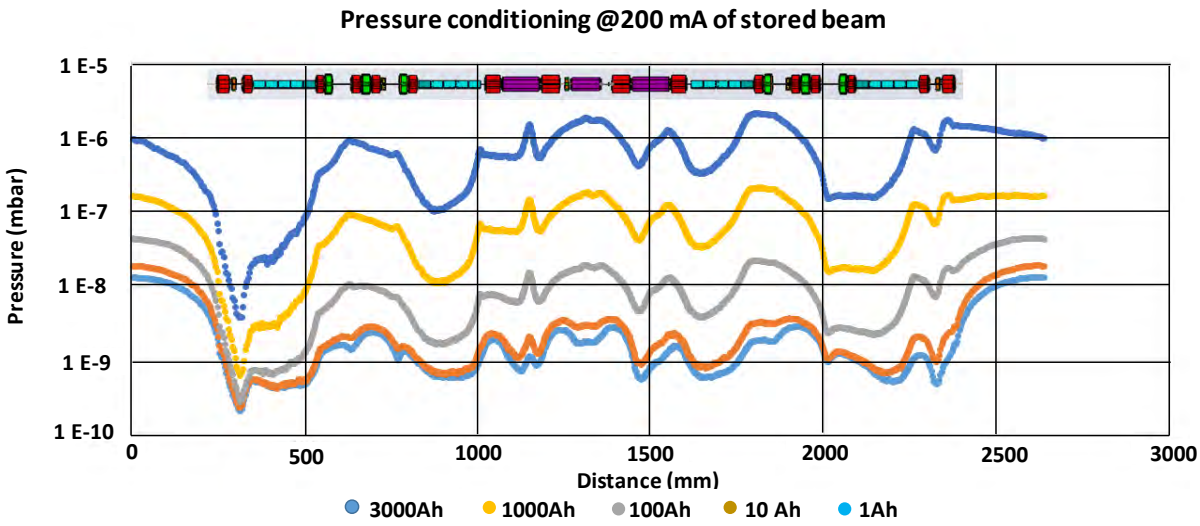


**Figure 10.17: Vacuum simulation of the EBS standard cell after 1, 10, 100, 1000 and 3000 Ah conditioning**

## 10.5 NEG coating

The chambers connecting the insertion device vacuum chambers in the straight section to the rest of the cell need to be NEG coated in order to reduce the pressure bump over this section. This concerns the so called CH01 and CH14. The chambers are going to be coated with a TiZrV alloy in the NEG coating facility at ESRF. The activation of the film will be done by means of the installed in-situ baking system which is described later.

## 10.6 In-situ baking system

The chambers and heaters are designed for a nominal baking temperature of 150°C (see Figure 10.13). The principal heaters used for the in-situ baking system are coaxial sheathed heaters composed of a CrNi conductor in a stainless steel sheath, besides some ribbons/jackets and heating collars. Alumized Kapton© foil will be used for thermal isolation of the chamber under bake.

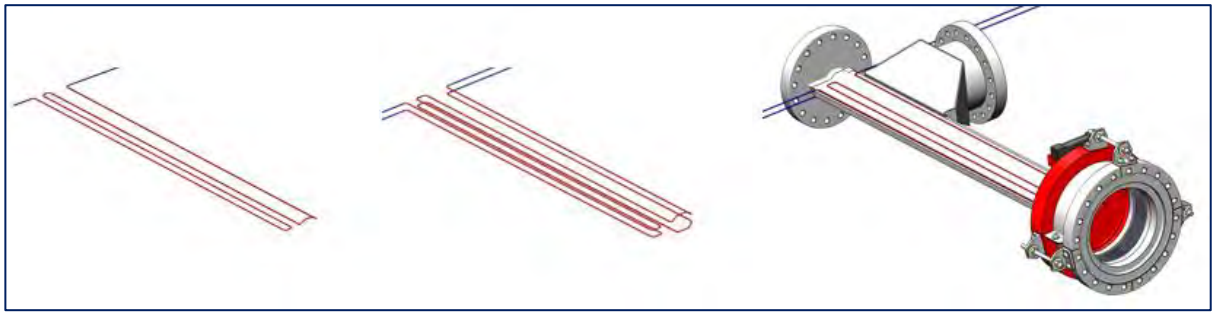

Figure 10.18: Preformed sheath heaters and their mounting on CH01.

The heaters are supposed to be fixed on the stainless steel chambers via point-welded bridges made of stainless steel sheets. On the aluminum chambers they will be put inside dedicated machined grooves as shown in the picture below.

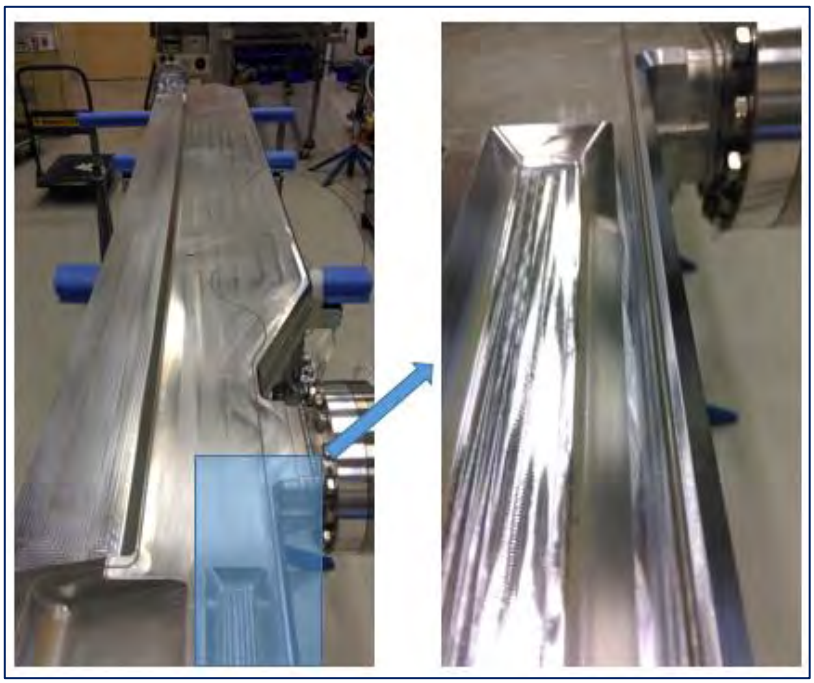

Figure 10.19: Sheath heaters installed into groove on aluminum chamber CH02 (prototype).

Bake controllers containing a simple PLC for the PID control of the baking loops as well as the power electronics are under development. The layout is done in a way that they cover the components of one girder each and they are supposed to be compatible with the pre-assembly and in-situ bake-out in the tunnel.

# Chapter 11 Alignment

## 11.1 Introduction

Alignment is an essential step in the assembly and installation of the new EBS machine. Aside from the very stringent alignment tolerances in the order of 50 µm, the EBS machine must be installed in the same place as the existing machine. We would like for the alignment of the new machine to be as transparent as possible for the existing beamlines and their operation. If the new machine is in the same place as the old one, then all things being equal, the new photon beam should also be in the same place as the old one.

Aligning magnets, BPMs and other sensitive elements on the individual girders and then aligning the girders in the tunnel to within 50 µm of one another while maintaining their position with respect to the existing beamlines comprises the EBS alignment challenge.

## 11.2 Magnet and BPM position alignment tolerances

The EBS tolerances are defined in the WP01 Design Report. The tolerances from the WP01 part of the Design Report are reproduced here for reference and convenience only. (Table 12.1)

**Table 11.7: WP01 Design Report Alignment tolerances.**

| Machine | Δx [µm] | Δz [µm] | Δs [µm] | Δψ [µrad] | ΔL/L |
|---|---|---|---|---|---|
| Long. Varying field dipoles | >100 | >100 | 1000 | 500 | $10^{-3}$ |
| High gradient quadrupoles, Combined function dipoles | 60 | 60 | 500 | 200 | $5\ 10^{-4}$ |
| Medium gradient quads | 100 | 85 | 500 | 500 | $5\ 10^{-4}$ |
| Sextupoles | 70 | 50 | 500 | 1000 | $3.5\ 10^{-3}$ |
| Octupoles | 100 | 100 | 500 | 1000 | $5\ 10^{-3}$ |

Apart from the dipoles, tolerances in the directions orthogonal to the beam travel Δx and Δz vary between 50 µm and 100 µm. Tolerances along the travel of the beam are still tight, but far more relaxed at 500 µm to 1000 µm.

The radial tilt (roll) tolerances required for the machine to function are between 200 µrad and 1000 µrad. However, because the survey references used to align the magnets are located on the top of the magnets, errors in the radial tilt (roll) will significantly influence the radial alignment Δx uncertainty. If we consider the survey references are located 0.5 m above the

beam position, then an error of 200 µrad will cause radial alignment error of 100 µm. This is close to twice the Δx tolerance. For this reason, despite the large radial tilt (roll) machine tolerances, very special attention must be given to the radial tilt (roll) uncertainty for alignment purposes. For the tilt to be a negligible part of the radial alignment error budget – say 20 µm to 50 µm – tilt uncertainties must be in the order of 40 µrad to 100 µrad.

## 11.3 The Survey and Alignment Coordinate System

The coordinate system used by the Survey and Alignment group (ALGE) is different than the one used to define the machine. The positive X direction is along the travel of the beam. The Y axis is positive to the left of the X axis in the horizontal plane. The Z axis is in the direction of the gravity vector. Rotations are in the clockwise direction looking from the origin along the axes ( Figure 11.2). Equivalencies between the *Machine* and *Survey* systems are given in Table 11.8

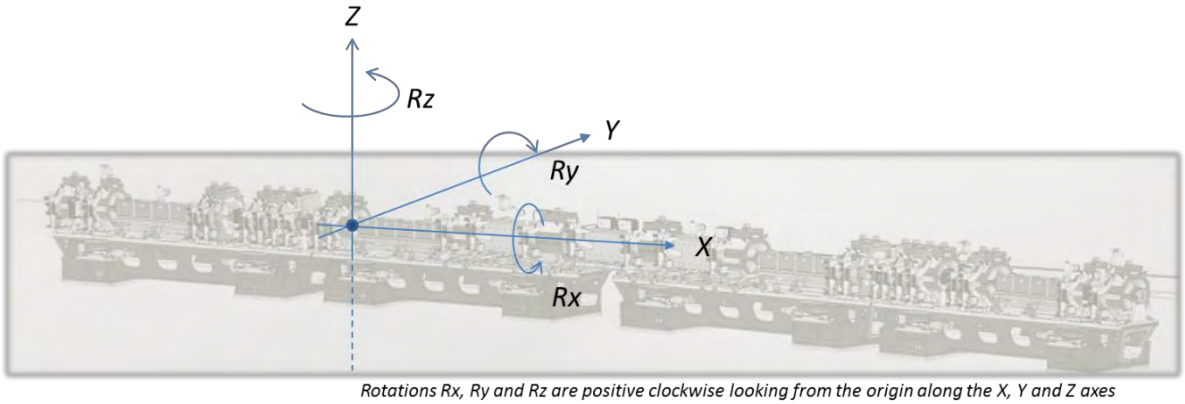


**Figure 11.2: Alignment coordinate system.**

**Table 11.8: Coordinate System equivalencies**

| | Survey | Machine |
|---|---|---|
| Along the beam | X | S |
| Orthogonal to X in the horizontal plane | Y | X |
| Orthogonal to X in the vertical plane | Z | Y |
| Rotation about the X axis | Rx[1)] | Psi[2)] |
| Rotation about the Y axis | Ry[1)] | Phi[2)] |
| Rotation about the Z axis | Rz[1)] | Theta[2)] |

*Notes on coordinate systems:*

1) *Rotation is clockwise looking from the origin along the axis*
2) *Rotation is counter clockwise looking from the origin along the axis*

## 11.4 Assembly of the magnets on the girders (*To be completed*)

The initial assembly and alignment of the magnets, BPMs and vacuum chambers on the girder in the B1 building will be done in three steps: installation and pre-alignment of the magnets to within 0.5 mm; fine alignment of the magnets to within 0.05 mm with respect to one another; and, installation and fine alignment of the BPMs and vacuum chambers to within 0.05 mm with respect to the magnets.

The first step is the assembly of the magnets on the girders. The magnets will be placed on

After the magnets have been fine aligned they will be disassembled (i.e. the top half removed) so that the vacuum string can be introduced. The BPM blocks (and vacuum

the girders using a special jig designed for this. It provides a means to preposition the magnets to within 0.5 mm of their nominal positions of the girders. This jig has been successfully tested on the prototype girder and shown to perform as expected.

After the magnets have been prepositioned on the girder they will be aligned to within 50 µm with respect to one another. Once again this alignment step has been successfully tested on the prototype girder.

The fine alignment will be done using one (or more) At 402 laser tracker(s). The manufacturer's stated 3D point[1] uncertainty for this instrument is +/- 15 µm + 6 µm/m. Tests made in August 2015[2] show that magnets can be aligned to an uncertainty of between 30 µm and 40 µm. These tests also showed that it takes approximately 6 hours for a team of two surveyors to fine align and measure all of the magnets on a girder.

chambers) will be aligned. Then the magnets will be reassembled and the overall alignment verified.

Alignment tests[3] made on the prototype girder using polystyrene model magnets and metal BPM supports have demonstrated that it is possible to achieve the desired alignment tolerances of 50 µm.

There are other foreseeable and/or potential tasks during the pre-assembly or even

[1] The measurement uncertainty of a coordinate $U_{xyz}$ is defined as the deviation between a measured coordinate and the nominal coordinate of that point. This measurement uncertainty is specified as a function of the distance between the laser tracker and the measured point.

[2] Refer to ESRF-TS-ALGE/1866CL dated August 28, 2015 for a detailed analysis of these tests

[3] Refer to ESRF-TS-ALGE/1894CL dated 9 March, 2016 for a detailed analysis of these tests.

procurement and assembly phases. A non-exhaustive list of these tasks include:

- alignment of the tables on which the vacuum strings will be assembled;
- control of the vacuum string alignment jigs;
- dimensional control of the vacuum chamber exterior and possibly interior geometry;
- dimensional control of the girders;
- dimensional control of the vacuum string assembly;
- control of the magnets fiducialisation;
- dimensional control of the magnet poles;
- dimensional control of the BPM blocks and possibly the BPM buttons themselves;

This is a bare bones approach to the assembly. Considerable detail is missing. The assembly process and techniques must be fleshed out and elaborated. This should advance with the mock-up scheduled in 2017.

## 11.5 Girder Transport

Once the magnets and BPMs have been aligned on the girders they will be transported, stored, and transported again to their final position in the tunnel. This involves a significant amount of handling (cranes, forklifts, trolleys etc…). There was concern that shocks (large accelerations) due to this handling would have a detrimental effect on the magnet alignment on the girders. To determine if there were damaging effects a number of transportation tests were performed[4].

Three tests were made. First the girder was simply lifted and put back into its support cradle. Second, it was lifted onto a set of rollers and moved around the Chartreuse hall. Finally it was taken outside, loaded onto a truck, unloaded back onto the rollers and repositioned on its cradle. These tests are highly representative of movements that will be made during the assembly and installation phase of EBS. Overall only very small movements were detected.

Although these tests do not validate future transportation systems, we can safely say that assembling the girders in the B1 building and transporting them with the same care (<3G accelerations) observed in these tests, there will be no significant deterioration in the overall alignment.

## 11.6 Alignment networks

[4] Refer to ESRF-TS-ALGE/1879DM dated 15 December 2015 for a detailed analysis of these tests.

The survey alignment network comprises the skeleton upon which all alignment work hangs (Figure 11.3). We determine the 3D positions of the points in the survey network. These points are then used to install new reference points or to align elements of the accelerator and beamlines in their nominal positions. Because everything moves and the networks deform over time, we re-measure them regularly so that we have the most accurate up to date coordinates available. Typically all of the survey networks are re-measured twice per year. Because of their importance, the machine networks are measured at each shutdown. The existing SR machine network is shown in Figure 11.4.

**Figure 11.3: The full interlinked ESRF system including TL1, Booster, TL2, SR, EXPH, EX2, D16 and Exterior site networks.**

To install the Phase I UPBLs we created a very extensive and highly redundant set of interlinked survey networks. (Figure 11.5) These networks are measured with high precision AT402 laser trackers.

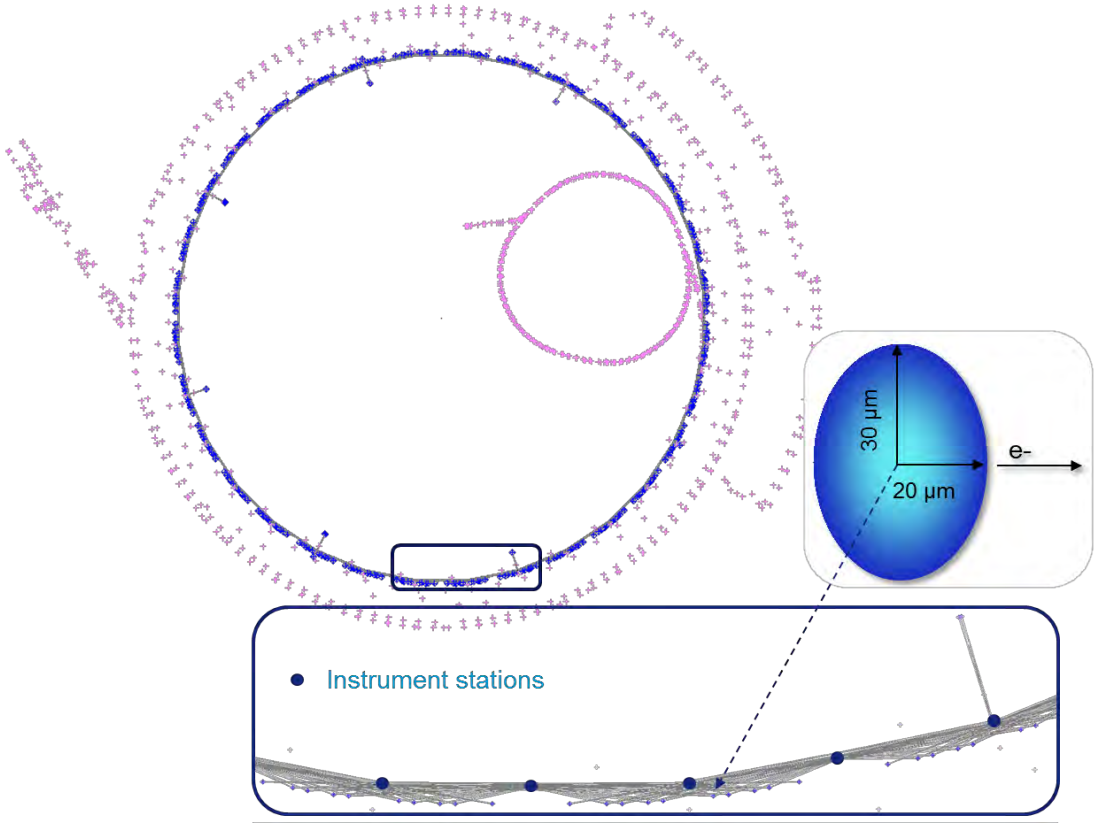


**Figure 11.4: The existing SR network.**

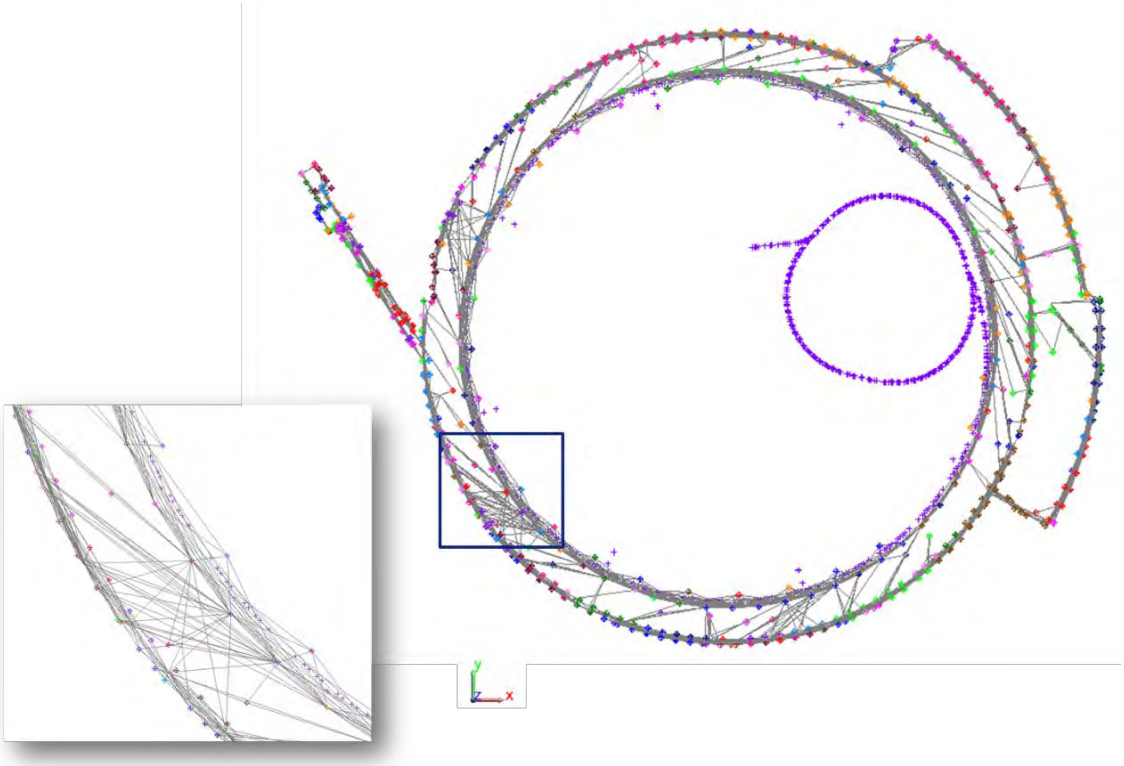

**Figure 11.5: The main EXPH-EX2 network (and detail of highly redundant observations – right) used to align the beamlines.**

Planimetric uncertainties issued from the least squares calculations on the SR are in the order of 30 µm in the *Y* direction (horizontal direction perpendicular to the beam), 25 µm in the *Z* direction and 20 µm in the *X* direction along the beam (at 1σ significance). These are absolute uncertainties in the overall network calculation. Relative uncertainties between adjacent girders are in the order of 10 µm[5]. Planimetric uncertainties are in the order of 30 µm at 1 sigma significance throughout the EXPH and EX2 halls ( Figure 11.6). Because of the network configuration and distance from the machine, uncertainties are larger in the ID16 satellite building.

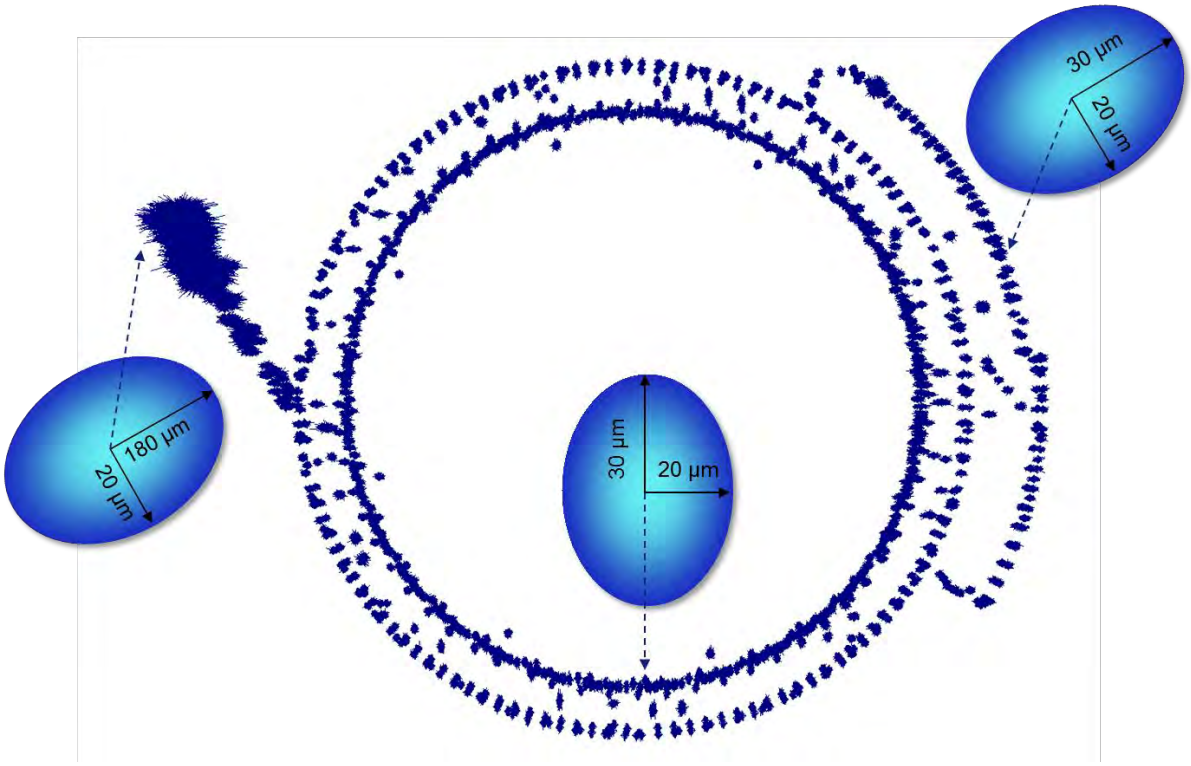


**Figure 11.6: EX2 survey network uncertainties.**

The existing survey network consisting of survey pillars and wall brackets will be removed when the new machine is installed. We have already installed a new network that will replace the existing network. This network comprises 7-8 points per cell – four points on the exterior walls, one or two points on the interior walls and two points in the floor. A prototype of this new network is shown in Figure 11.7. Measurements and simulations have shown the point uncertainty for this network will be compatible with the tolerance

[5] It is important to understand these are the uncertainties in the determination of a point position. They do not necessarily represent the precision to which we can align something.

requirements for the installation of the new machine. It will be measured regularly between now and the long 2019 shutdown.

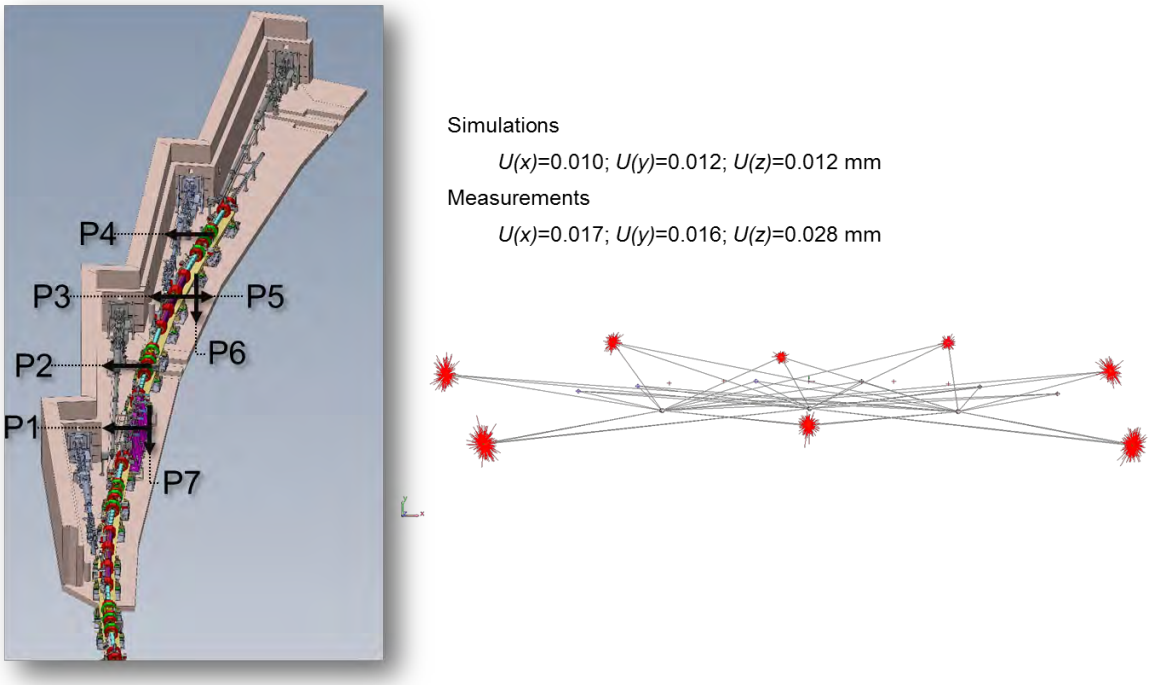


**Figure 11.7: The new network installed in 2016 for the installation and long term monitoring of the EBS.**

## 11.7 Alignment of the girders in the tunnel (*To be completed*)

The Survey and Alignment group is implicated in all stages of the installation. It will be among the first to start, and the last to finish work on the EBS. This section provides a very general overview of the activities in the SR during the installation phase.

On the first day of the shutdown – before anything is dismantled – the Survey and Alignment group will measure the TL1, Booster, TL2, SR, EXPH and EX2 networks. This will be the reference zero for all subsequent alignment work. This first measurement is critical for the success of the EBS in terms of alignment. It will take two to four days to complete.

Following the initial network measurements, the machine infrastructure will be dismantled and civil engineering works made. After these works are completed, the Survey and Alignment group will trace girder support plate positions on the floor. There will also setting out required for positions of the cable trays, piping networks and other infrastructure items.

After their positions are set out, the plates will be fixed and grouted to the floor - ready to receive the girders. The girders will be transported to their nominal positions in the SR and positioned to within 0.2 to 0.5 mm of their nominal positions (see also the discussion in

The Form of the existing SR Machine and the new EBS) below using the new SR survey network

discussed in the section on

Alignment networks above. In parallel the front end module 1s will be aligned.

At some point in the middle of the installation period a full survey of the SR network will be made. This is done to have up to date coordinates and will take approximately one week to complete.

When all of the girders have been installed. A full survey of the TL1, Booster, TL2, SR, EXPH and EX2 networks will be made again. From this survey we will smooth the machine. This is the final machine positioning and alignment operation. Smoothing entails adjusting the girders onto a *best fit* smooth curve to Beamlines below.

Although the smoothing is mainly applied in the horizontal direction, there is no reason that it cannot be equally applied in the vertical direction as well. However, by convention, all things being equal, it is better to align and maintain the machine on a horizontal plane.

At some point near the end of the long shutdown we will also verify the alignment, minimize the horizontal offset between adjacent girders. The radial position of the machine in December 2015 is shown in Figure 11.8. The offsets from the smooth (red) curve in Figure 11.8 are shown in Figure 11.9 We see from Figure 11.9 we have an offset standard deviation of 0.11 mm for the Quadrupole girders. The equivalent tolerance for the new machine is 0.05 mm. The situation is actually significantly more complex than this. We also have the additional constraint of positioning the new machine on the existing machine in such a way as to ensure the photon beam is correctly aligned for the beamlines. This is discussed in detail in section 11.13

and possibly realign the BPMs, the absorbers, the CV5000s or equivalent straight section vacuum chambers and the Front-end Module 2s (FEM2s). This is certainly a non-exhaustive list of elements that must be checked before the machine is started.

As with the assembly, this is a bare bones outline of what must be done. Considerable detail is missing and must be elaborated before the installation of EBS.

## 11.8 The Form of the existing SR Machine and the new EBS

The existing SR machine is not aligned in its nominal position (Figure 11.8 – for the radial position, and Figure 11.10 for the vertical position). These graphs show the difference between the actual and nominal (zero) positions in the radial and vertical directions perpendicular to the beam travel. The reason the machine is not in its nominal position is because of errors in the original alignment due to the precision of the instruments at our disposal in 1992; and, to long term site movements (Refer to the section on

Site Movements below).

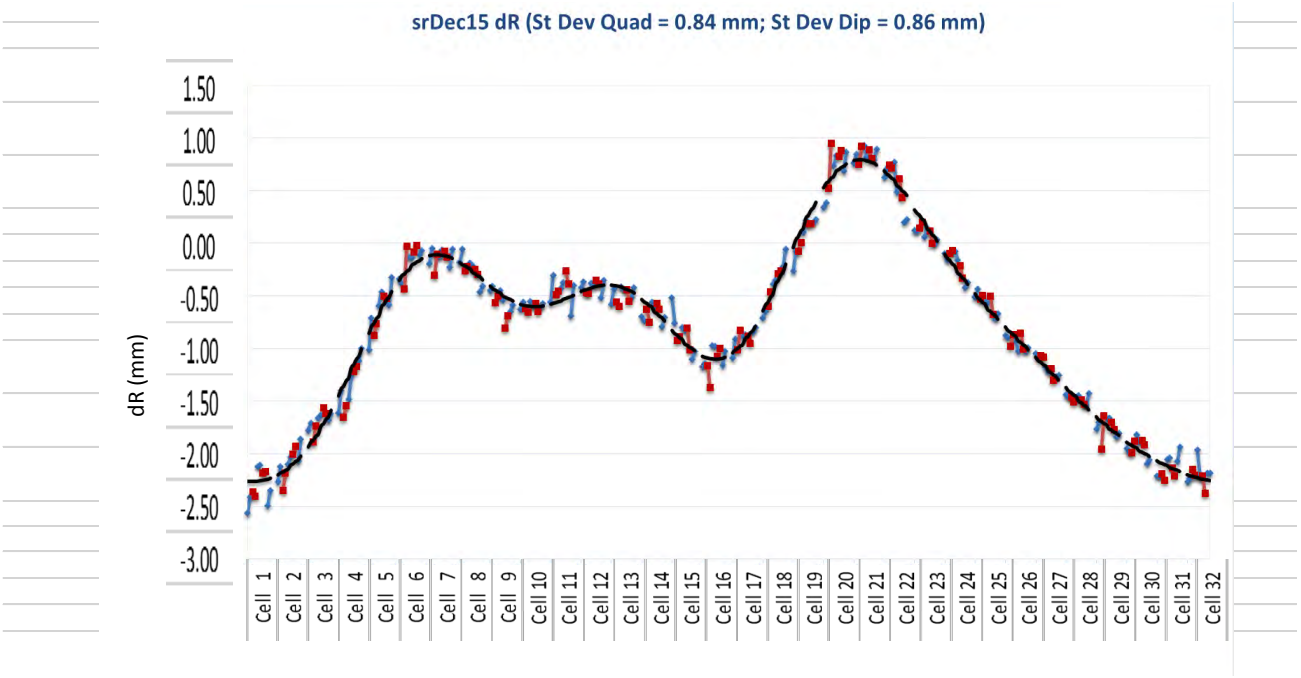


**Figure 11.8: Entry and exit radial positions of the machine quadrupole and dipole girders (points) and the best fit smooth curve through the points in December 2015. Note the machine nominal position is zero.**

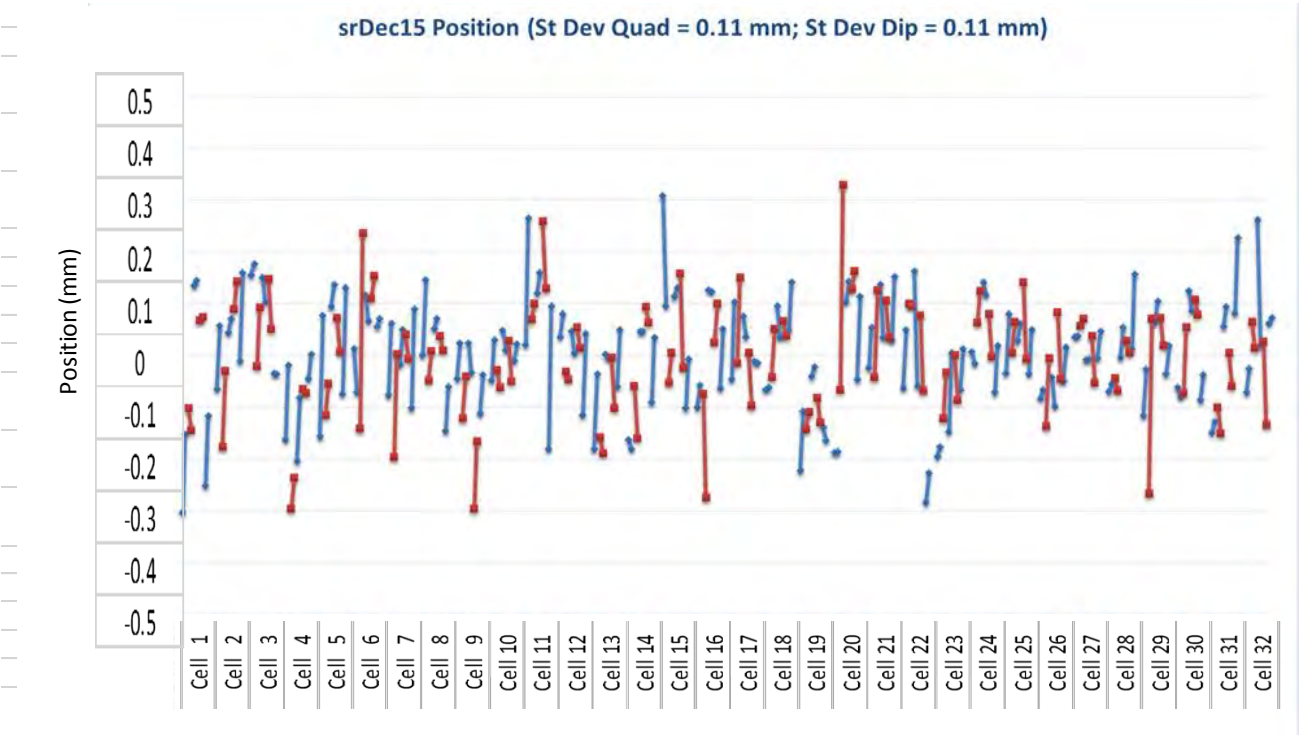


**Figure 11.9: Offsets with respect to the smooth curve in Figure 11.8. Red points are the quadrupole girder entry and exit point offsets and blue points the entry and exit points of the dipole girders with respect to the smooth curve**

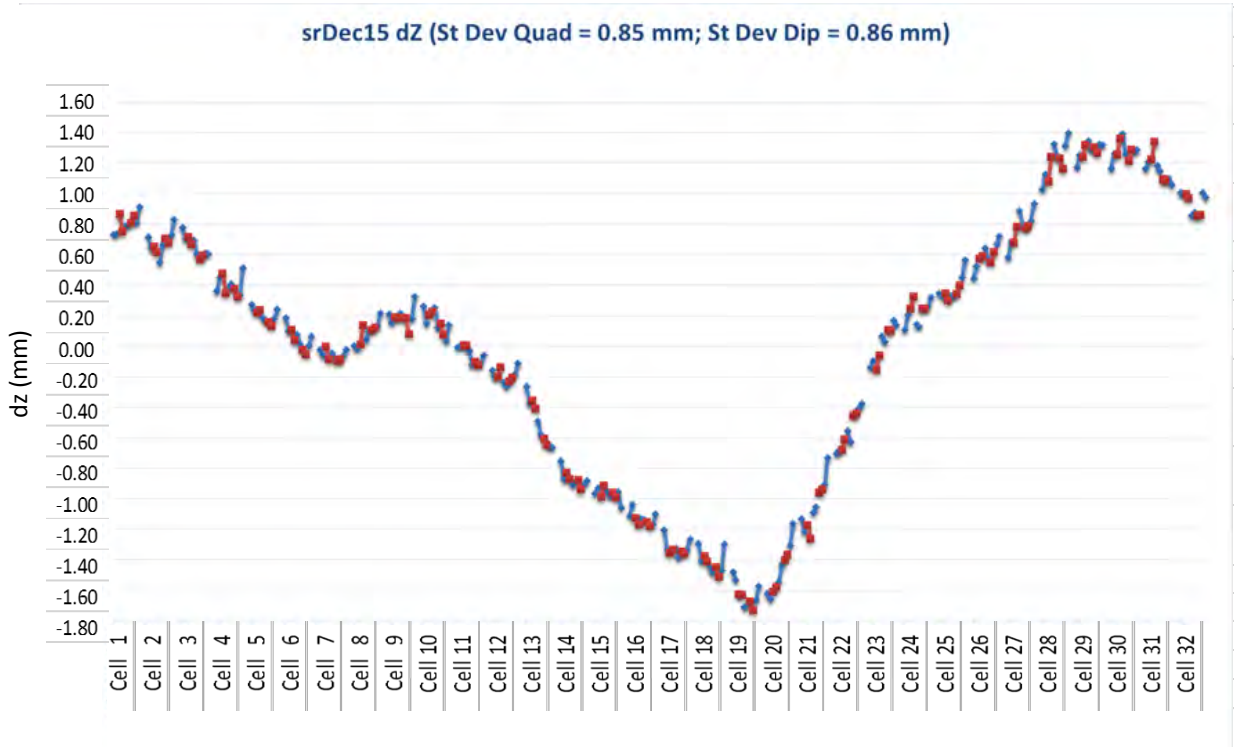


**Figure 11.10: Entry and exit vertical positions of the machine quadrupole and dipole girders (points) and the best fit smooth curve through the points in December 2015. Note the machine nominal position is zero.**

It has been decided to align the EBS on the existing SR position – or the position it will be in in 2018 – to minimize realignment on the Beamlines below.

beamlines. Beamline alignment is discussed in the section 11.13

## 11.9 Site Movements

The ESRF Survey and Alignment group has followed the evolution of the site since 1990. There are several highly characteristic site

movement signatures that have been identified.

The first characteristic site movement is the long-term geological and geomorphological movements of the Grenoble basin [6] (Figure

11.11 and Figure 11.12). The Vercors and Chartreuse mountain ranges are slowly moving apart from one another due to

[6] Menard, G., *Mesure de l'affaissement actuel de la cuvette grenobloise par comparaisons de nivellements*, Laboratoire EDYTEM, l'Université de Savoie, Mars 2008

tectonic movements. This is causing the Grenoble basin to sink and deform – flow – slowly down the Isere valley towards Voiron. It is a large scale movement. There are two effects on the ESRF site. The first is a long term tipping or tilting of the site along the axis ID06 to ID16; ID16 being consistently lower than lower than ID06. There is also an elongation along the same axis in the horizontal plane. Because these movements are smooth, they have no real consequence on the functioning of the SR machine or beamlines. They simply provide a regional backdrop to the other more significant movement signatures discussed below.


**Figure 11.11: Long-term geomorphological and geological movements in Grenoble basin 1989 to 2001.**

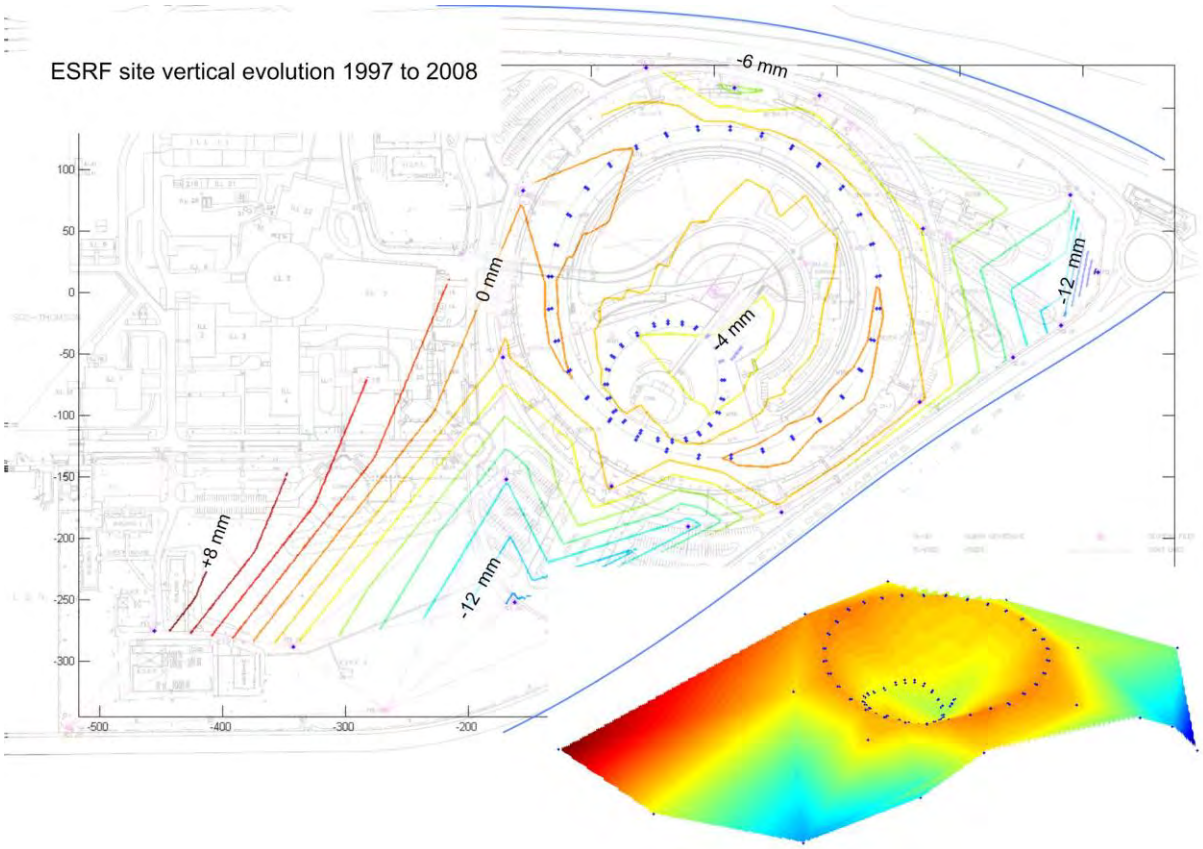


**Figure 11.12: Site movements over the period 1997 to 2008 showing the tipping of the site due to geological movements and the sinking of the Booster and the Central Building due to long-term settlement.**

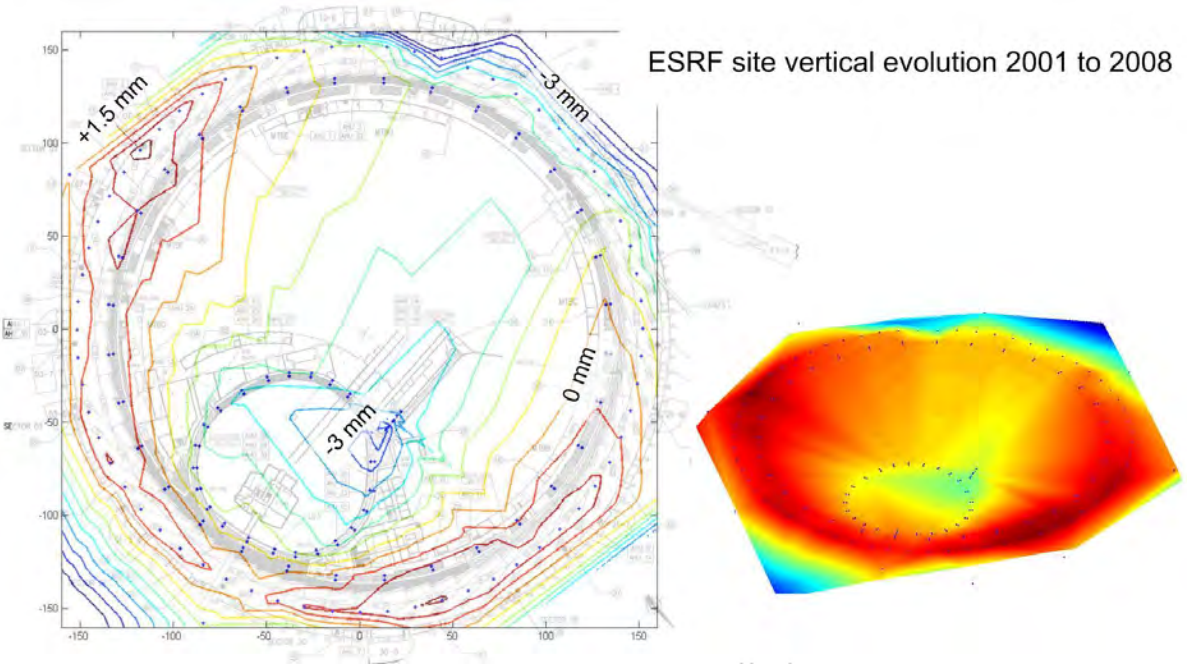


**Figure 11.13: Zoom of movements of the ESRF accelerators over the period 2001 to 2008.**

Far more significant movements were caused by the excavation works in 1992 after the completion of the ESRF (black line in Figure 11.14) and in 2012 during the construction of the EX2 hall extension. However after the initial site excavation works, other long-time term movements became evident. These movements are complex. With reference to Figure 11.11 through Figure 11.14 we can hypothesize:

- The sinking of the site centre – possibly due to the long term settlement of the mass of earth put on the Booster in 1992.
- The relative sinking of the area around the ID16 and ID17 experimental stations – possibly due to the confluence of the Drac and Isere rivers, or perhaps the leaching of sediment into the Presque-Isle drainage system – or the confluence of this drainage system – or proximity to the pumping station.
- The relative sinking along sides and in proximity to the Drac and Isere rivers – again possibly due to sediment leaching into the site drainage system – or possibly long term sediment (mass) build up in the river beds.
- The relative rising of the SR in the zones Cells 1 to 8 and 24 to 1 except near the central building – due to the tipping motion of the site and the long term sinking of the central building.

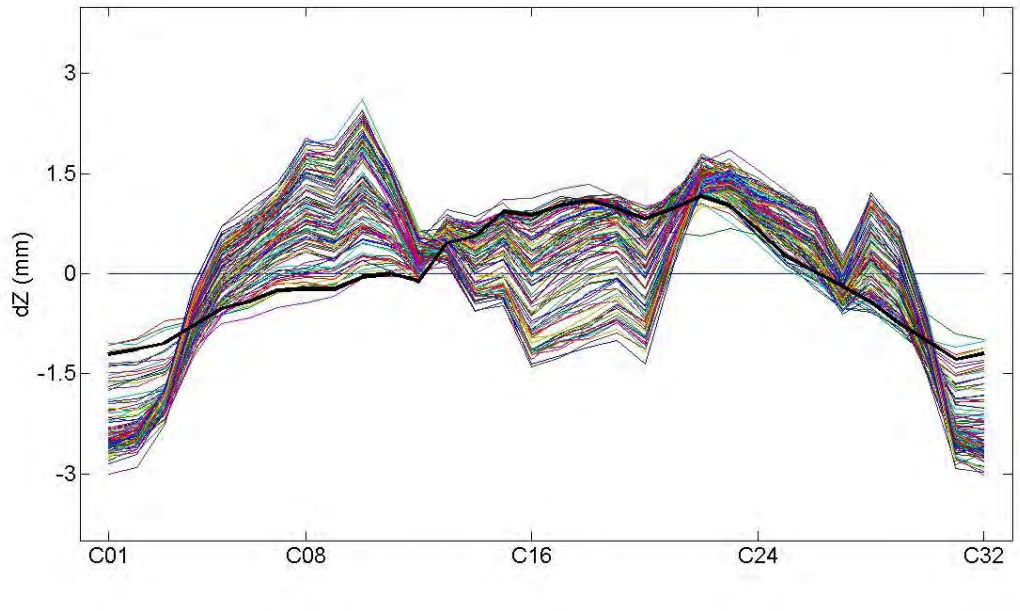


**Figure 11.14: Long term movements of the SR from 1992 to 2012 – just before the excavation of the EX2 hall.**

These background movements produce a smooth deformation of the site. They provoke a long wave deformation of the SR and are therefore virtually undetectable. Similarly, they have a virtually imperceptible effect on the beamlines. However, it is advisable to correct them periodically nonetheless.

Other similar long wave deformations have been observed. One example is the *chasse* or flushing of the Saint-Égrève dam. From time to time when conditions permit, EDF proceeds with what is referred to as a *chasse*. The aim of a *chasse* is to remove the sediment that builds up in the rever beds over time. It causes large site deformations and ground water variations when the dam is emptied and the river finds its natural state. Typically there is some permanent deformation after the event.

## 11.10 Movements in the SR Tunnel and on the Girders

Although the deformations described previously are generally innocuous, there are other movements that are far more detrimental to the machine operation. Specifically movements at the SR concrete floor slab joints are large and are clearly visible in the orbit plot (Figure 11.15). Movements at the slab joints are caused by slab curling.

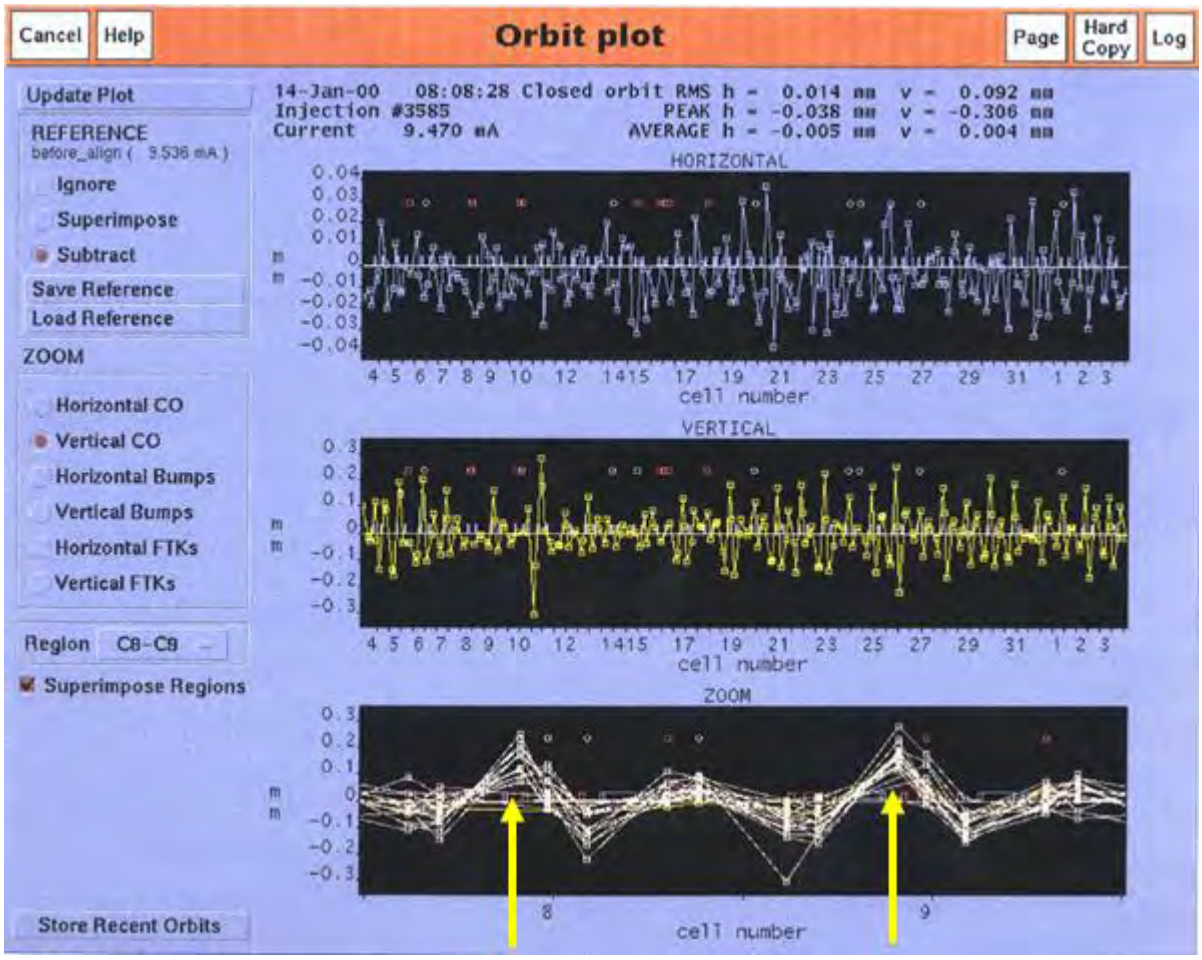


**Figure 11.15: SR orbit plot on 14 January 2000 showing peaks due to girder movements driven by movements at the slab joints.**

Slab curling is caused by gradients in temperature and moisture between the top and the bottom of the slab. The slab edges curl upward when the surface is drier and shrinks more, or is cooler and contracts more than the bottom. Curling is most noticeable at the construction joints but can also occur at saw-cut joints and random cracks. The curling moment is greater at the ends of the slab decreasing to almost zero at the slab centre. Due to gravity the internal stresses caused by curling are smallest near the slab ends and highest over a large centre area.

In the case of the SR, the main long term mechanism behind the slab curling is temperature gradient variation through the slabs. Ground temperature under the slab changes slowly in a sinusoidal cycle over the course of the year. The temperature of the top of the slab (i.e. the SR floor) varies more rapidly on diurnal and monthly cycles driven by outside temperature variations. These cycles cause gradient variations and drive the slab curling. Because bending is a function of the magnitude of the gradient, somewhat counter intuitively, thicker slabs bend more than a thin slabs for the same gradient. In relative terms, the 1 m thick SR slab bends quite a bit. Humidity gradient variations have never been studied in depth. However

they may also play a very important analogous role in slab bending. Typically the air is much drier in winter than in summer.

## 11.11 Automatic Monitoring and Girder Alignment (*To be written*)

The girders are equipped with four jacks and four Hydrostatic Levelling System (HLS) sensors so that they can be realigned and corrected for the ground and slab movements.

***A study is presently under way to estimate the magnitude of expected EBS girder movements and their realignment frequency.***

## 11.12 Booster

The radius of the Booster will be decreased by approximately 17 mm. This will be done in January and February 2019. At the same time both the TL1 and TL2 lines will be entirely realigned as well.

## 11.13 Beamlines

One of the key aims of the Survey and Alignment group will be to try to maintain the existing beamline alignment – or at least to minimize the beamline alignment interventions at the EBS start-up and commissioning. To do this we will take a number of important steps.

First and foremost we will try to ensure the source points and orientations of the straight sections of the new machine are coincident with those of the existing machine. This means the new machine will follow a peculiar trajectory based on the existing machine (see section 11.8

The Form of the existing SR Machine and the new EBS).

Secondly, we have scheduled a measurement campaign to estimate the beamline trajectories. This campaign will take place in 2017 and 2018. Preliminary tests made in 2014 showed that the actual beam trajectories determined by a fit through the measured source point, front end and primary silt positions on eight beamlines differed significantly from their nominal trajectories determined by the orientation of the straight section ( Figure 11.16). In fact the standard deviation in the difference between the measured and expected primary slit positions was 0.63 mm. This corresponds to a beamline angle uncertainty of 27 µrad at 1σ and implies alignment uncertainty of:

- ±3.2 mm at 2σ at 60 m in the EXPH,
- ±6.4 mm at 2σ at 120 m in the EX2, and
- ±9.7 mm at 2σ at 180 m on ID16.

This means even if we align the new machine where the existing machine is, the photon beam will not necessarily be where it is today.

For this reason, all of the beamline trajectories will be calibrated using white beam monitors before the long shutdown in 2019. This extensive campaign comprises two steps.

First, in the laboratory, the white beam monitors will be fiducialised – this is to say the white beam monitor image fiducials are measured with respect to our externally visible reference marks. When the beam monitors are installed and measured on the beamline; in principle, the beam image can be directly linked to the ESRF survey network reference system (see also section 11.2 Alignment networks).

We then aim to determine the differences between the nominal and actual beamline trajectories. This step comprises measuring the beam position with the front end slit(s), primary slit, white beam monitor, and any other element deemed useful for this purpose. The source point position is determined from the alignment of the magnets on either side of the ID straight section. Finally, this information will be used to align the EBS machine in its optimal position.

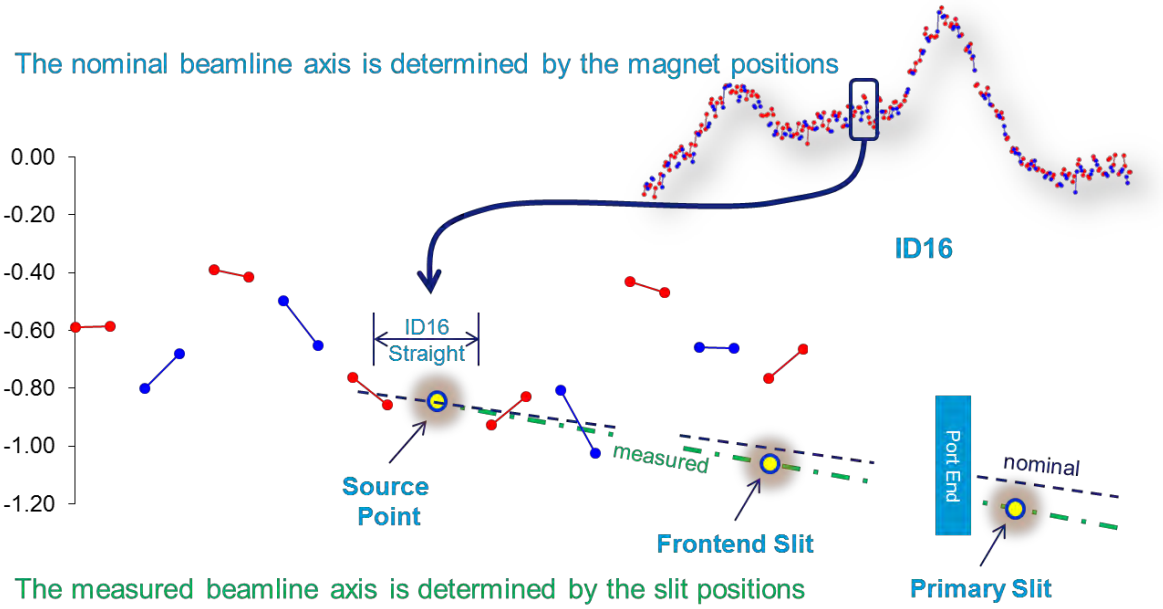


**Figure 11.16: Nominal and measured beamline trajectories.**

## 11.14 Resources

This section discusses the number of Survey and Alignment technicians needed, and the expertise they must have, to complete the EBS project. This estimate also includes anticipated work on the beamlines immediately after the EBS installation phase to ensure that they work.

With regards to expertise, we require trained survey technicians. These are typically people with a minimum education at the French BTS level, or equivalent, in surveying. However, it is advisable to employ people with at least two to five years of relevant field experience in

addition to the minimum education. Even for trained and experienced survey technicians to be fully independent, we must count an additional 6 to 14 months of in-house training so that they are conversant with our techniques, software and instrumentation.

The intrinsic job skill set and the required in-house training precludes using ESRF (beamline) technicians.

With regards to EBS manpower requirements. At present the Survey and Alignment group can field two survey teams of two people each. In addition there is logistical and administrative support provided by one half time post for planning, programming and calculations; and one full time post for electronics, and hardware and software support for instrumentation. In theory we can field two survey teams. In reality, with shift work and shift work recuperation (~50 days per year outside of shutdown), RTT, different types of leave, and constraints imposed during the shutdowns we can only consistently field one team. During the shutdowns we rely heavily upon exterior company support.

The best estimate for the workload over the coming five years[7] is given in Table 11.3. ***Note that all manpower requirements in this table are expressed in survey team units***. A survey team is composed of two people. Consequently to have the actual number of people required, multiply the number of teams by two. On the horizontal axis of this table are months and years. On the vertical axis are the following headings:

- ***Beamlines, Office, Instruments***
  typically a survey team can spend a maximum of 75% of its time in the field. In this category the work is essentially on the beamlines. For the remaining 25% of its time, the team has many other essential tasks to perform including: calculations, results and report preparation, instrument verification calibration and testing, general site work, installation and reparation of survey networks, preparation of field work, etc…. In addition, as discussed previously, there is leave and shift work to consider.
- ***Shutdown (weight length factor ½)***
  The manpower requirements for the shutdowns are weighted by the length of the shutdown. The Summer and Winter shutdowns are roughly 20 days long while the shorter shutdowns in March, May and October are 7 to 8 days long. Additionally we call upon exterior personnel periodically to work on the beamlines and/or exterior site outside of the shutdown periods. Taking all of this into account, we can consider that on the teams are used half-time in the months they are required.
- ***Phase II Girder (Pre) Assembly***
  this covers the pre-assembly and assembly phases of the magnets on the girders in the B1 building.

[7] Master Schedule – R. Dimper, MAC 24-25 September 2015.

- ***Booster resizing***
  this covers the re-alignment and measurement of the Booster, TL1 and TL2; and the measurement of Booster survey network.
- ***SR Installation***
  this will cover the tracing, setting out, and installation of the SR infrastructure (cable trays, piping networks; the pre-alignment and fine alignment of the girders, front ends and other machine elements. It also covers the measurement of the survey networks.
- ***Beamline commissioning***
  at present this represents an unknown quantity of work. However we do know that the beamlines will require assistance to become operational. There is also a tremendous amount of work on the CRG beamlines. In addition, once the existing beamlines are operational there will be periodic support required to fine tune them. Finally there are several (four) Upgrade Phase II beamlines to install.
- ***Required Field Teams***
  this is the total number of field teams that will be required for all current tasks (i.e. that column of the table). Note that sometimes the number do not add up. For example take March 2016. The number of *Required Field Teams* is 3. However we see there are 2 *Beamlines, Office, Instruments* teams and 2 *Shutdown* (…) teams - which we should multiply by a weight length factor ½. This gives the sum 2+2x½=3 found in this column. Note that because we cannot have ½ of a team, numbers are always rounded up to the nearest integer team.
- ***Difference (Required-Actual)***
  this is the difference between the number of field teams required to perform all of the tasks and the actual number of field teams available. We presently have 2 field teams available.
- ***Yearly Average Difference***
  this is the *Difference (Required-Actual)* averaged over the calendar year. For example, the Yearly Average Difference for 2016 is 1. This means we are missing - on average - one survey team of two people in 2016. Note this difference (i.e. the missing mean permanent manpower requirements) increases from one team (two people) in 2017, to two teams in 2017 (four people) to three teams (six people) in 2018, 2019 and 2020. Note that once again teams are rounded up to the nearest integer team.
- ***Equivalent Exterior Company Cost (k€)***
  this is how much it would cost per year if we were to use Exterior company personnel. This is determined by: *Yearly Average Difference x €688/day x 21 days/month x 12 months/year.* Under the present contract, an exterior company team costs €688 /day.

These are <u>minimum</u> personnel requirements based on the present planning. It does not take into account any events, or work that may be required on EBS outside of these generalised tasks. For example it does not provide for sick leave, or factory visits to control magnets or vacuum chambers. Furthermore, if for any reason different project stages overlap; for example, if the assembly stage overlaps with the realignment of the Booster and/or the SR installation phases, the required personnel will increase[8].

[8] ESRF-TS-ALGE/1895DM, Required EBS Survey and Alignment group personnel resources, 12/03/2016

In theory exterior company personnel could be used. Indeed, a common misconception is that and ESRF Survey and Alignment team can be integrated with and/or replaced by an exterior team. French labour law stipulates exterior personnel cannot be paired with ESRF personnel [9]. Exterior personnel must have clearly defined objectives and tasks that they are qualified to perform with a minimum of ESRF supervision. These tasks are defined in the Exterior Personnel CFT. There are only very specific types of work that an external team can perform with **minimum initiative and minimum supervision**. A typical example of this type of work is the regular Surveys we make to follow our networks.

This does not mean exterior personnel will not be used on the EBS project. Indeed they will be used extensively. For example, the external personnel will probably set out the girder feet and the fluids and electrical networks supports positions. However, **exterior personnel cannot be used** to: align the magnets on the girders with a tolerance of 50 um; align the girders in the tunnel with similar tolerances; align of the Front Ends, straight sections, diagnostic equipment, etc…; align the beamlines; …. They do not have the skills required to perform these complex tasks. And because they change regularly, there is little point in investing the considerable time and effort needed to train them properly to do these tasks[10].

Finally other instrument and material resources must be considered[11].

**Table 11.3: Estimated manpower requirements January 2016 through December 2020. Numbers represent the number of field survey teams required for a specific generalized task. The actual number of people is the number of teams multiplied by two.**

[9] There may be confusion over this because formerly, a Survey and Alignment team was composed of three people - a *Chef de brigade* (a senior survey technician), an *Operateur* (a survey technician) and an *Aide Géomètre* (an assistant). At the time the ESRF provided the senior survey technician and the other team members were from the external personnel contract. Mixing ESRF with external personnel is not/no longer permitted under French Law.

[10] ESRF-TS-ALGE/1930DM, Survey and Alignment Personnel, 11/08/2016

[11] ESRF-TS-ALGE/1942DM, Revised estimated alignment related costs for the EBS assembly and installation, 17/11/2016

| | 2017 | | | | | | | | | | | | 2018 | | | | | | | | | | | |
|---|---|---|---|---|---|---|---|---|---|---|---|---|---|---|---|---|---|---|---|---|---|---|---|---|
| | J | F | M | A | M | J | J | A | S | O | N | D | J | F | M | A | M | J | J | A | S | O | N | D |
| Beamlines, Office, Instruments | 2 | 2 | 2 | 2 | 2 | 2 | 2 | 2 | 2 | 2 | 2 | 2 | 2 | 2 | 2 | 2 | 2 | 2 | 2 | 2 | 2 | 2 | 2 | 2 |
| Shutdown (weight length factor 1/2 | 3 | | 2 | | 2 | | | 3 | | 2 | | 3 | 3 | | 2 | | 2 | | | 3 | | 2 | | 2 |
| Phase II Girder (Pre) Assembly | 1 | 1 | 1 | | | | | | | 2 | 2 | 2 | 2 | 2 | 2 | 2 | 2 | 2 | 2 | 2 | 2 | 2 | 2 | 2 |
| Booster | | | | | | | | | | | | | | | | | | | | | | | | |
| SR installation | | | | | | | | | | | | | | | | | | | | | | | | |
| Beamline Commissioning | | | | | | | | | | | | | | | | | | | | | | | | |
| | | | | | | | | | | | | | | | | | | | | | | | | |
| Required Field Teams | 5 | 3 | 4 | 2 | 3 | 2 | 2 | 4 | 2 | 5 | 4 | 6 | 6 | 4 | 5 | 4 | 5 | 4 | 4 | 6 | 4 | 5 | 4 | 6 |
| Difference (Required-Actual) | 3 | 1 | 2 | 0 | 1 | 0 | 0 | 2 | 0 | 3 | 2 | 4 | 4 | 2 | 3 | 2 | 3 | 2 | 2 | 4 | 2 | 3 | 2 | 4 |
| Yearly Average Difference | 2 | | | | | | | | | | | | 3 | | | | | | | | | | | |
| Equivalent Exterior Company (Cost) (k€) | 347 | | | | | | | | | | | | 521 | | | | | | | | | | | |

| | 2019 | | | | | | | | | | | | 2020 | | | | | | | | | | | |
|---|---|---|---|---|---|---|---|---|---|---|---|---|---|---|---|---|---|---|---|---|---|---|---|---|
| | J | F | M | A | M | J | J | A | S | O | N | D | J | F | M | A | M | J | J | A | S | O | N | D |
| Beamlines, Office, Instruments | 1 | 1 | 1 | 1 | 1 | 1 | 1 | 1 | 1 | 1 | 1 | 2 | 2 | 2 | 2 | 2 | 2 | 2 | 2 | 2 | 2 | 2 | 2 | 2 |
| Shutdown (weight length factor 1/2 | 3 | | | | | | | | | | | | 3 | | 2 | | 2 | | | 3 | | 2 | | 3 |
| Phase II Girder (Pre) Assembly | | | | | | | | | | | | | | | | | | | | | | | | |
| Booster | 1 | 1 | 1 | | | | | | | | | | | | | | | | | | | | | |
| SR installation | | | | 4 | 4 | 4 | 4 | 4 | 4 | 4 | 4 | | | | | | | | | | | | | |
| Beamline Commissioning | | | | | | | | | | | | 2 | 2 | 2 | 2 | 2 | 2 | 2 | 2 | 2 | 2 | 2 | 2 | 2 |
| | | | | | | | | | | | | | | | | | | | | | | | | |
| Required Field Teams | 4 | 2 | 2 | 5 | 5 | 5 | 5 | 5 | 5 | 5 | 5 | 4 | 6 | 4 | 5 | 4 | 5 | 4 | 4 | 6 | 4 | 5 | 4 | 6 |
| Difference (Required-Actual) | 2 | 0 | 0 | 3 | 3 | 3 | 3 | 3 | 3 | 3 | 3 | 2 | 4 | 2 | 3 | 2 | 3 | 2 | 2 | 4 | 2 | 3 | 2 | 4 |
| Yearly Average Difference | 3 | | | | | | | | | | | | 3 | | | | | | | | | | | |
| Equivalent Exterior Company (Cost) (k€) | 521 | | | | | | | | | | | | 521 | | | | | | | | | | | |

1) Offices refers to calculations of results, general site work, etc... Instruments refers to instrument verification, testing and calibration, etc...

2.) Shutdown personnel requirements are weighted for the length of the shutdown (long shutdown 18 - days-short shutdown 7 days). For example in March 2016 we will require roughly 2 teams (i.e. 4 exterior personnel) for 8 days. Today these people are provided by the external personal contract.

3) The numbers in this table do not take into account the logistics, administration and electronics support which comprises 2 1/2 additional ALGE personnel.